

Durham E-Theses

Synthesis, Characterisation and Reactivity of Cobalt(II) and Cobalt(I) Cyclopentadienyl, Diphosphine and α -Diimine Complexes

BRODIE, CLAIRE,NICOLE

How to cite:

BRODIE, CLAIRE,NICOLE (2020) *Synthesis, Characterisation and Reactivity of Cobalt(II) and Cobalt(I) Cyclopentadienyl, Diphosphine and α -Diimine Complexes*, Durham theses, Durham University. Available at Durham E-Theses Online: <http://etheses.dur.ac.uk/13558/>

Use policy

The full-text may be used and/or reproduced, and given to third parties in any format or medium, without prior permission or charge, for personal research or study, educational, or not-for-profit purposes provided that:

- a full bibliographic reference is made to the original source
- a [link](#) is made to the metadata record in Durham E-Theses
- the full-text is not changed in any way

The full-text must not be sold in any format or medium without the formal permission of the copyright holders.

Please consult the [full Durham E-Theses policy](#) for further details.



Synthesis, Characterisation and Reactivity of
Cobalt(II) and Cobalt(I) Cyclopentadienyl,
Diphosphine and α -Diimine Complexes

Department of Chemistry, Durham University

2016 - 2019

Thesis submitted for the degree of Doctor of Philosophy

By

Claire Nicole Brodie

Statement of Originality

This thesis is based on work conducted by the author, in the Department of Chemistry at Durham University, during the period October 2016 to December 2019. All the work described in this thesis is original, unless otherwise acknowledged in the text or in the references. None of this work has been submitted for any another degree in this or any other University.

The copyright of this thesis rests with the author. No quotation from it should be published without the author's prior written consent and information derived from it should be acknowledged.

Signed: _____

Date: _____

Abstract

This thesis presents the synthesis and characterisation of cobalt(II) and (I) complexes bearing cyclopentadienyl, α -diimine and diphosphine ligands, to provide an understanding of their physico-chemical properties to enable their future use as pro-catalysts in, *e.g.* selective linear α -olefin (LAO) to LAO oligomerisation. There has been considerable recent interest of (P^P)cobalt(I) complexes in a range of catalytic transformations, however the mechanism of formation of the cobalt(I) species has been little studied.

Chapter 2 describes the attempted synthesis of a series of analogues to the reported linear α -olefin (LAO) to LAO dimerisation pro-catalyst $[(\eta^5\text{-Cp}^*)\text{Co}(\eta^2\text{-C}_2\text{H}_4)(\text{P}(\text{OMe})_3)]$ (**1**), which only exhibits very low activity (TOF 3.7 h^{-1}). Analogues of complex **1** with general formula $(\text{L}_2\text{X})\text{Co}(\text{CO})_2$, where L_2X is Cp or Cp^* were synthesised (**2.17a**, **2.17b**). Attempts to prepare derivatives where L_2X was indenyl or fluorenyl, led to the formation of η^1 or η^2 complexes $(\text{Ind})_2\text{Co}_2(\text{CO})_6$ (**2.21**), $(\text{Ind})_2\text{Co}_2(\text{CO})_4(\text{THF})_2$ (**2.25**) and $\text{FluCo}(\text{CO})_4$ (**2.26**). To enhance the stability of pre-catalysts such as **1**, Cp-based ligands with a pendant L-type donor (PR_2 , NR_2), a series of $(\text{L}_2\text{X})\text{-CH}_2\text{CH}_2\text{-L}$ ligands ($\text{L}_2\text{X} = \text{Cp}, \text{Cp}^*, \text{Ind}, \text{Flu}, \text{L} = \text{PR}_2, \text{NR}_2$) were synthesised. Cp and Cp^* derivatives of these “tethered” ligands were derived from *spiro*[cyclopropane]precursors (**2.16a,b**); Ind and Flu derivatives were prepared from $\text{ClCH}_2\text{CH}_2\text{PR}_2$ (**2.7a-c**). Subsequent complexation of Cp^*PPh_2 (**2.15**) to produce a cobalt half-sandwich complex (**2.29**) revealed the flexibility of **2.15** to coordinate in, *e.g.*, mono-, bi-dentate or bridging modes.

In chapter 3 a series of variously-substituted α -diimine (**3.2a-d**) and diphosphine (**3.3-3.10**) cobalt(II) complexes are described and their electronic and steric properties probed by structural (XRD, $\%V_{\text{bur}}$) and spectroscopic (UV-Vis, Raman, IR) methods. The donor capacity of the ligands was found to have a significant impact on the structural and electronic properties of the resulting complexes.

Chapter 4 explores the reduction of $(\text{P}^{\wedge}\text{P})\text{CoX}_2$ complexes (**3.3-3.10**) with Zn and the characterisation of the resulting cobalt(I) derivatives (**4.1-4.8**) of general formula $[(\text{P}^{\wedge}\text{P})\text{Co}(\mu_2\text{-X})_2]$. This study showed that the outcome of the Zn-mediated reduction is governed by steric and electronic effects imposed by the $\text{P}^{\wedge}\text{P}$ ligand. The reaction of $(\text{P}^{\wedge}\text{P})\text{CoX}_2$ (where phosphine substituent is *not* Ph) with Zn resulted in formation of $(\text{P}^{\wedge}\text{P})\text{ZnX}_2$ complexes (**Zn-5.1-Zn-5.9**). The mechanism by which Co-Zn diphosphine ligand exchange occurs was found to proceed *via* disproportionation of “ $(\text{P}^{\wedge}\text{P})\text{CoX}$.” The lability of the $\text{P}^{\wedge}\text{P}$ ligand was found to play a key role in the formation of $(\text{P}^{\wedge}\text{P})\text{ZnX}_2$ complexes.

Chapter 5 describes development of an *inert atmosphere* approach for mass spectrometric analysis of air-/moisture-sensitive solid materials using the Atmospheric Solid Analysis Probe (ASAP), which is applied throughout this work. Chapters 6 and 7 contain all experimental and supporting information.

Acknowledgments

First and foremost, I'd like to thank my supervisor, Dr Phil Dyer for his enthusiasm and support throughout my time in Durham – especially when things weren't going to plan... Phil, I was once told you were known as “generous Phil” around the inorganic community. This is very true, and not just in your willingness to get a round in at the pub! Your generosity in the time you have spent helping me with (what seemed like an endless stream of) questions, curiosities, presentations, abstracts and, then finally, chapter drafts and in patience when I encountered new concepts and techniques. I couldn't have asked for a better supervisor.

I'd also like to extend thanks to Martin Hanton (previously of Sasol) for the brief time he was co-supervising this work. I wish you all the best for future and your new career outwith Sasol!

Drs Andrei Batsanov and Dimitry Yusif, thank you for your excellent crystallographic work. In particular, Andrei's fantastic work has been key to many of the points discussed within this thesis. To the Durham Mass Spec service (Dr Jackie Mosely, Dr David Parker and Mr Peter Stokes), thank you for all your hard work and collaboration with running air sensitive samples and the development of *i*ASAP MS. To Dr Juan Aguilar Malavia, Dr Alan Kenwright and Mrs Catherine Heffernan, thank you for your guidance and patience in all things NMR. Prof. Andy Beeby, Dr Mark Fox and Dr Ross Davidson, thank you for your teachings in Raman and EChem measurements.

To Kerry and Amy – thanks for being great students and putting up with me wittering on about diimines, diphosphines and nacnacs! You've done great work in little time and made the lab a brighter place.

To the Dyer group past and present: *good afternoon* – you've all been great. My particular thanks go to Stephen Rouse and Dominikius Heift – thank you for everything you've done for me – from coming to all my practice talks to providing extra hands in the lab – you guys have been incredibly supportive and continually picked me up when I was down. Thank you!

My best friend Ellen, you are fantastic. I couldn't ask for a better friend – you've supported me throughout this PhD and been my cheer leader when I needed it. Thanks for everything dear!

Finally, I'd like to thank Mark. I genuinely couldn't have done this without you. Thank you for putting up with the late nights, hectic schedules and stress throughout. In particular, the last couple of months while I've been writing, you've been unbelievably patient and supportive. I owe a lot to you and can't describe how much your support means to me. Thank you for everything you do.

Table of Contents

Statement of Originality.....	i
Abstract.....	ii
Acknowledgments.....	iii
Table of Contents.....	v
List of Abbreviations.....	xi
List of Compounds and Complexes: Chapter 2.....	xiv
List of Compounds and Complexes: Chapter 3.....	xv
List of Compounds and Complexes: Chapter 4.....	xvi

Chapter One: Introduction

1.1 Introduction	1
1.1 Commercial Importance of Linear α -olefins	2
1.2 Commercial Technologies for LAO Production	3
1.2.1 The Shell Higher Olefin Process	3
1.2.2 The AlphaButol Process	5
1.2.3 The Fischer-Tropsch Process	6
1.2.3.1 Mechanism for LAO production via Fisher-Tropsch Synthesis	8
1.3 LAO Chain Length Distribution for SHOP and FT Synthesis	9
1.4 Mechanism of Transition Metal-catalysed LAO Dimerisation and Oligomerisation	10
1.4.1 Cossee-Arman Mechanism (Step-Wise Addition)	11
1.4.2 Metallacycle Mechanism	14
1.4.3 Distinguishing Between Metallacycle and Step-wise Insertion Mechanisms	15
1.4.4 Regioselectivity in LAO to LAO Dimerisation Reactions	17
1.5 Processes Competing with LAO Dimerisation	19
1.5.1 Isomerisation of LAOs to LIOs Using Dimerisation Systems	19
1.5.2 Apparent "Trimerisation": The Co-dimerisation of Substrates and Products in Dimerisation Systems	20
1.6 Background Summary and Thesis Aims	21
1.7 References	23

Chapter Two: Synthetic Routes Towards Cobalt(I) Half-Sandwich Complexes: $(L_2X)CoL_n$

2.1 Introduction	26
2.1.1 LAO Trimerisation and Tetramerisation Systems	26
2.1.2 LAO Dimerisation Systems	28
2.1.2.1 Ni-based LAO dimerisation systems	28
2.1.3 Co- and Fe-based LAO Dimerisation Systems	29
2.1.3.1 Brookhart and Broene: Selective 1-Hexene Dimerisation	32
2.1.4 The Bonding of Cyclopentadienyl Ligands to Metals	35
2.1.5 Coordination Modes of Cp-type Ligands to a Metal	36
2.1.6 Cp-containing Hemi-labile Ligands	38
2.2 $[(L_2X)-L]$ -type Constrained Geometry Catalysts	39
2.2.1 Synthetic Routes towards $(L_2X-CH_2CH_2-ER_n)$ -type Ligands	40
2.2.1.1 Flu- and Ind-derivatives with a 'C ₂ -tether'	41
2.2.1.2 Synthesis of Cp- and Cp*-derivatives with a 'C ₂ -tether.'	56
2.2.1.2.2 Synthesis of $(Cp/Cp^*)-CH_2CH_2-PR_2$ type ligands	59
2.3 Synthesis of Cobalt(I) Half-Sandwich Complexes	62
2.3.1 Synthesis of Brookhart and Broene's Pro-catalyst: $[Cp^*Co(\eta^2-C_2H_4)(P(OMe)_3)]$	62
2.3.1.1 Single-crystal X-ray Structures of $Cp^*Co(CO)_2$, $Cp^*CoI_2(CO)$ and $[Cp^*Co(\mu_2 I)_3CoCp^*][I_3]$	64
2.3.2 Synthesis of Analogues to Complex $[Cp^*Co(CO)_2]$ (2.17a)	66
2.3.2.1 Identification and solid-state structure of $[Co(C_6H_8)(CO)(\mu_2-CO)]_2$ (2.22)	70
2.3.2.2 Mechanistic Study for the Formation of Complex 2.17a via Synthesis of 2.22	72
2.3.2.3 Attempted Synthesis of complexes 2.17c and 2.17d from a Cobalt(I) Source	76
2.3.2.4 The Hypothetical Bonding of Indenyl- and Fluorenyl-moities to Cobalt	81
2.3.3 Synthesis of $[\{(L_2X)-CH_2CH_2-(L)\}Co(CO)]$ Complexes	82
2.4 Summary and Conclusions	85
2.5 Future work and Outlook	87
2.5.1 Cobalt Half-Sandwich Complex Synthesis	87
2.5.2 Proposed Constrained Geometry Pre-Catalyst Synthesis	88
2.6 References	90

Chapter Three: Structural and Spectroscopic Investigations into α -Diimine and Diphosphine Cobalt(II) Halide Complexes

3.1 Introduction	95
3.1.1 α -Diimine Metal Complexes and their Application within Olefin Oligomerisation Reactions	95
3.1.2 Phosphine-Cobalt Complexes and their Reactivity towards Olefins	100
3.1.2.1 The Reactivity of $(\text{PPh}_3)_3\text{CoCl}$ towards Olefins	100
3.1.2.2 Diphosphine Cobalt Complexes and their Reactivity towards Olefins	103
3.1.3 The Bonding and Structure of Bidentate ($(\text{N}^{\wedge}\text{N})$ and $(\text{P}^{\wedge}\text{P})$) Ligands	108
3.1.3.1 The Bonding of Imines and Phosphines to Transition Metals	108
3.1.3.2 Assessing the Steric Demands of Diimines and Diphosphines	111
3.2 Preparation and Characterisation of a Series of (α -Diimine)cobalt(II) Bromide Complexes (3.2a-d)	113
3.2.1 Synthesis of α -Diimine (L_2) Ligands	113
3.2.2 Characterisation of α -Diimine Cobalt(II) Bromide Complexes	115
3.2.2.1 Structural Characterisation of α -Diimine Cobalt Complexes	115
3.2.2.2 Steric Contributions from α -Diimine Ligands	120
3.2.2.3 Investigating Vibrational Energies in $(\text{N}^{\wedge}\text{N})\text{CoBr}_2$ Complexes Through IR, Raman and DFT Spectroscopic Techniques	121
3.2.2.4 UV-Vis Spectroscopic Analysis of $(\text{N}^{\wedge}\text{N})\text{CoBr}_2$ Complexes	124
3.3 Diphosphine Cobalt(II) Halide Complexes	127
3.3.1 Investigating the Donor Capacity of Diphosphine Ligands in $(\text{P}^{\wedge}\text{P})\text{CoX}_2$ Complexes	129
3.3.2 Structural Characterisation of Diphosphine Cobalt(II) Halides	131
3.3.2.1 Distortions from Tetrahedral Geometry of $(\text{P}^{\wedge}\text{P})\text{CoX}_2$ complexes	135
3.3.2.2 $\%V_{\text{bur}}$ Analysis of Diphosphine Ligands	137
3.3.2.3 Non-tetrahedral $(\text{P}^{\wedge}\text{P})\text{CoX}_2$ Complexes	139
3.3.2.3.2 Solid-state structure of $[(\text{dppe})_2\text{CoBr}]^{+2}[\text{Br}_3\text{Co}(\mu_2\text{-dppe})\text{CoBr}_3]^{2-}$	140
3.3.3. Mass Spectrometric Analysis of $(\text{P}^{\wedge}\text{P})\text{CoX}_2$ Complexes	144
3.3.4 Spectroscopic Characterisation of Diphosphine Cobalt(II) Dihalides	147
3.3.4.1 Raman Spectroscopic Analysis of $(\text{P}^{\wedge}\text{P})\text{CoX}_2$ Complexes	147
3.3.4.2 Electronic Spectra of $(\text{P}^{\wedge}\text{P})\text{CoBr}_2$ Complexes	150

3.3.4.3 UV-Visible Spectroscopic Studies of (P [^] P)CoX ₂ Complexes	153
3.3.4.4 Racah Parameters and the Nephelauxetic Series	157
3.3.5 Effective Magnetic Moment (μ_{eff}) of (P [^] P)CoX ₂ Complexes	165
3.3.6 Investigations into the Oxidation Products of (P [^] P)CoX ₂ Complexes	167
3.3.6.1 An Unexpected Oxidation Product: (COOH) ₂ Co(OH) ₂	170
3.4 Summary and Outlook	173
3.5 References	175

Chapter Four: The Role of Zinc in the Reduction Chemistry of Diphosphine Cobalt(II) Halide Complexes

4.1 Introduction	179
4.1.1 Previously Reported Reduction of (P [^] P)CoX ₂ Complexes with Zn where Resulting “(P [^] P)CoX” species have been Isolated	179
4.1.2 Reported Reduction of (P [^] P)CoX ₂ Complexes with Zn <i>in situ</i>	182
4.1.3 Reported Reduction of (P [^] P)CoX ₂ Complexes <i>in</i> or <i>ex situ</i> : Non-Zn reductants	187
4.1.4 Literature Review Summary	189
4.2 Investigating the Reduction Chemistry of (P [^] P)CoX ₂ Complexes	191
4.2.1 Successful Single-electron Reduction of (P [^] P)CoX ₂ Complexes with Zn Dust	191
4.2.1.1 The Reduction of (dppp)CoX ₂ (X = Cl 3.4c and X = Br 3.4d) with Zn Metal	193
4.2.1.2 The Reduction of (dppb)CoX ₂ (X = Cl 3.4e , X = Br 3.4f) with Zn Metal	200
4.2.1.3 The Reduction of [BrCo(μ_2 -dppm) ₂ (μ_2 -Br) ₂ CoBr] (3.4a) with Zn Metal	202
4.2.1.4 The Reduction of (dppx)CoBr ₂ (3.6f) with Zn Metal	203
4.2.1.5 The Reduction of (PNNP-Ph)CoBr ₂ (3.7b) with Zn Metal	204
4.2.1.6 The Reduction of (dtbpx)CoBr ₂ (3.6b) with Zn Metal	205
4.2.1.7 The Reaction of (dtbpx)CoCl ₂ (3.6a) with Zn Metal	211
4.2.2 Reaction of Zn with (P [^] P)CoX ₂ Complexes Without Formation of Cobalt(I)	212
4.2.3 Summary of the Observed Reactions of Zn with (P [^] P)CoX ₂ Complexes	215
4.2.4 Attempted (P [^] P)CoX ₂ Single Electron-reductions in the Presence of a Stabilising Ligand	216
4.3 Synthesis of (P [^] P)ZnX ₂ Complexes	220
4.3.1 Spectroscopic and Spectrometric Characterisation of (P [^] P)ZnX ₂ Complexes	221
4.3.2 Structural Characterisation of (P [^] P)ZnX ₂ Complexes	223

4.4 Diphosphine Ligand Exchange Between CoX_2 and ZnX_2 Complexes	226
4.4.1 The Exchange of dppbz Between Zn^{II} and Co^{II} in THF	228
4.4.2 The Exchange of dtbpx Between Zn^{II} and Co^{II} in THF	228
4.4.3 The Exchange of dppp Between Zn^{II} and Co^{II} in THF	232
4.4.4 The Exchange of Diphosphine Ligands (dppp or dtbpx) Between Zn^{II} and Co^{II} in DCM	235
4.4.5 Summary of the Exchange of Diphosphine Ligands Between Zn^{II} and Co^{II}	236
4.5 Electrochemical Investigation into $(\text{P}^{\wedge}\text{P})\text{CoBr}_2$ Complexes	238
4.6 Attempted Reductions of $(\text{P}^{\wedge}\text{P})\text{CoX}_2$ Complexes Without Zn Metal	244
4.6.1 Attempted Single-electron Reduction of $(\text{PPh}_3)_2\text{CoX}_2$ (3.3a,b) with Magnesium	245
4.6.2 Attempted Single-electron Reduction of $(\text{PNNP-Ph})\text{CoBr}_2$ (3.7b) with SmI_2	245
4.6.3 Attempted Single-electron Reduction of $(\text{dtbpx})\text{CoBr}_2$ (3.6b) with KC_8	247
4.6.4 Attempted Single-electron Reduction of $(\text{dtbpx})\text{CoBr}_2$ (3.6b) with Zirconocene	247
4.6.5 Attempted Single-electron Reduction of $(\text{dtbpx})\text{CoBr}_2$ (3.6b) with Cobaltocene	248
4.7 A Direct Approach to the Synthesis of $(\text{L}^{\wedge}\text{L})\text{cobalt(I)}$ Complexes	250
4.7.1 The Attempted Synthesis of $(\text{P}^{\wedge}\text{P})(\text{PPh}_3)\text{CoCl}$ Complexes	252
4.7.2 The Attempted Synthesis of $(\text{N}^{\wedge}\text{N})(\text{PPh}_3)\text{CoCl}$ Complexes	255
4.7.3 Summary of Direct Approach to the Synthesis of $(\text{L}^{\wedge}\text{L})\text{Cobalt(I)}$ Complexes	258
4.8 A Molecular “A-Frame”: The Solid-state structure of $[\{\text{BrCo}(\mu_2\text{-dppm})\}_2(\mu_2\text{-Br})]$ (4.5)	259
4.9 Summary and Conclusions	262
4.10 Future Work	264
4.11 References	266

Chapter 5: Development of an *inert* Mass Spectrometric Analysis Technique

5.1 Introduction	268
5.1.1 Atmospheric Solids Analysis Probe (ASAP) Mass Spectrometry	268
5.2 Development of <i>inert</i> ASAP MS	270
5.2.1 Glass Probe Design and Implementation	271
5.2.2 Optimisation of the <i>i</i> ASAP ⁺ MS Process	272
5.2.2.1 Maximising Signal Intensity in <i>i</i> ASAP MS	273
5.3 Comparison of ASAP ⁺ with <i>i</i> ASAP ⁺	275
5.4 Conclusions and Future Work	278

5.5 References	279
----------------------	-----

Chapter 6: Experimental

6.1 General Considerations	280
6.1.1 NMR Spectroscopy	280
6.1.2 X-Ray Crystallography	281
6.1.3 Effective Magnetic Moment	281
6.1.4 Raman, Infrared, UV/Vis and NIR-UV/Vis Spectroscopies	281
6.1.7 Computational Details	282
6.1.5 Mass spectrometry, Elemental Analysis and Gas Chromatography	282
6.1.5.1 <i>i</i> ASAP	283
6.1.6 Electrochemical Measurements	284
6.2 Chapter 2 Experimental Details	285
6.2.1 L ₂ X-CH ₂ CH ₂ -X type ligands	285
6.2.2 X-CH ₂ CH ₂ -ER _n type ligands	286
6.2.3 L ₂ X-CH ₂ CH ₂ -ER _n type ligands	294
6.2.4 (L ₂ X)Co(L) _n Complexes	314
6.3 Chapter 3 Experimental	327
6.3.1 Synthesis of Diimine Ligands	327
6.3.1.1 Synthesis of <i>bis</i> (4-methoxyphenyl)-acenaphthylquininediimine {(<i>p</i> -OMe)-BIAN}	327
6.3.2 Synthesis of (N [^] N)CoBr ₂ Complexes	328
6.3.3 Synthesis of (P [^] P)CoCl ₂ Complexes	331
6.3.4 Synthesis of (P [^] P)CoBr ₂ complexes	339
6.3.5 Synthesis of diphosphinediselenides	348
6.4 Chapter 4 Experimental	349
6.4.1 Attempted Reductions of (P [^] P)CoX ₂ with Zn metal	349
6.4.2 Attempted Reductions of (P [^] P)CoX ₂ Complexes with Zn in the presence of L	361
6.4.2.1 Attempted synthesis of (P [^] P)(1-C ₆)CoBr	361
6.4.2.2 Attempted synthesis of [(dtbpx)(PPh ₃)CoBr]	363
6.4.2.3 Attempted synthesis of [(dtbpx)(PPh ₃) ₂ Co]	363

6.4.3 Synthesis of Diphosphine Zinc(II) Halides	364
6.4.4 Ligand Exchange Reactions	368
6.4.5 Attempted Reductions of (P [^] P)CoX ₂ Without Zn	373
6.4.6 Direct Synthesis of Cobalt(I) Diphosphines and Cobalt(I) Diimines	376
6.5 Example μ_{eff} calculations	379
6.5.1 JME Determination of Effective Magnetic Moment	379
6.5.2 Evans' Spectroscopic NMR Method for Determination of Effective Magnetic Moment	381
6.6 References	382

Chapter Seven: Appendices and Supplementary Information

7.1 Appendices	384
7.1.1 Conferences: Contributions and Prizes	384
7.1.2 Seminars attended	385
7.2 Supplementary Information	389
7.2.1 UV-Vis and Raman Spectroscopic data for diphosphine Cobalt(I) Complexes	389
7.2.2 Crystallographic Data	396
7.2.3 <i>i</i> ASAP MS Variable Optimisation Experiments	407

List of Abbreviations

General Abbreviations

Å	Angström (10 ⁻¹⁰ m)
BAO	Branched α -olefin
C	Celsius
DCM	Dichloromethane
DFT	Density Functional Theory
DMF	Dimethylformamide
EA	Elemental Analysis
FT	Fischer-Tropsch
h/hrs	Hour/hours
HAO	Higher α -olefin
HDPE	High density polyethylene
<i>in vacuo</i>	From Latin: within a vacuum
IPA	Isopropyl alcohol
IR	Infrared
K	Kelvin
LAO	Linear α -olefin
LIO	Linear internal-olefin
MeCN	Acetonitrile
min/mins	Minute/minutes
MS	Mass Spectrometry
NMR	Nuclear Magnetic Resonance
THF	Tetrahydrofuran
TOF	Turn over frequency
TON	Turn over number
UV-Vis	Ultraviolet-visible
UV-Vis-NIR	UV-Vis Near-IR
<i>vide infra</i>	From Latin: see below
<i>vide supra</i>	From Latin: see above

Spectroscopic Abbreviations

ASAP	Atmospheric Solid Analysis Probe
br	broad
COSY	Correlation Spectroscopy
d	Doublet
Da	Dalton
dd	Doublet of doublets
dt	Doublet of triplets
ds	Doublet of septets
ES	Electrospray
GC	Gas Chromatograph
HMBC	Heteronuclear Multiple Bond Coherence
HSQC	Heteronuclear Single Quantum Coherence
Hz	Hertz
<i>i</i> ASAP	<i>inert</i> ASAP
<i>J</i>	Scalar Coupling constant
m	Multiplet (NMR) or medium (IR)
min	minute
PONA	Paraffins, Olefins, Naphthenes and Aromatics
ppm	Parts per million
q	Quartet
qC	Quaternary carbon
quin	quintet
s	Singlet (NMR) or strong (IR)
spt	Septet
t	Triplet
td	Triplet of doublets
v	Stretch
$\nu_{1/2}$	Full width at half maximum
vw	Very weak
w	Weak

L₂X-Type Ligands:

Cp	cyclopentadienyl
CpH	cyclopentadiene
Cp*	1,2,3,4,5-pentamethyl-cyclopentadienyl
Cp*H	1,2,3,4,5-pentamethyl-cyclopentadiene
Ind	indenyl
IndH	indene

Flu	fluorenyl
FluH	fluorene
CHD	1,3-cyclohexadiene
COD	1,4-cyclooctadiene

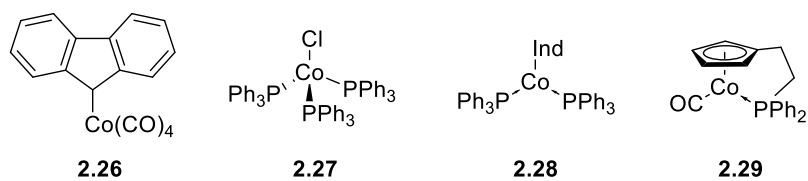
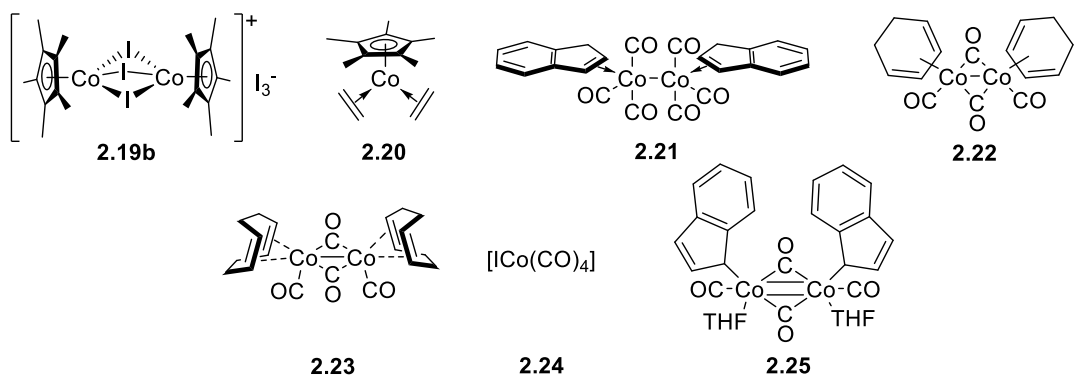
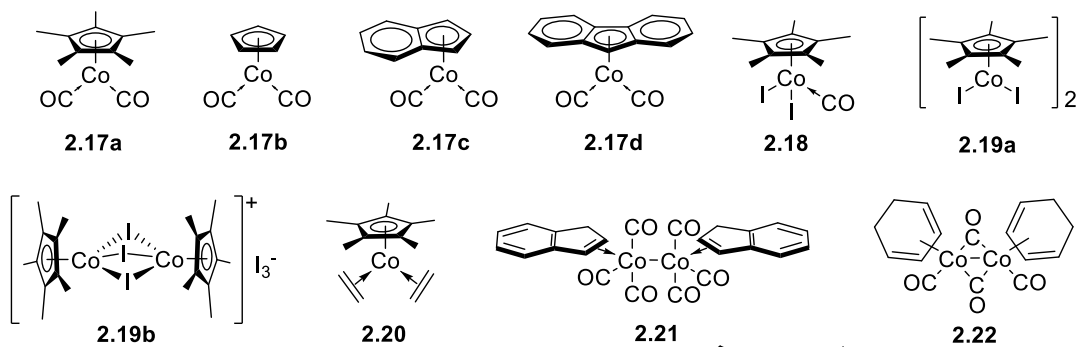
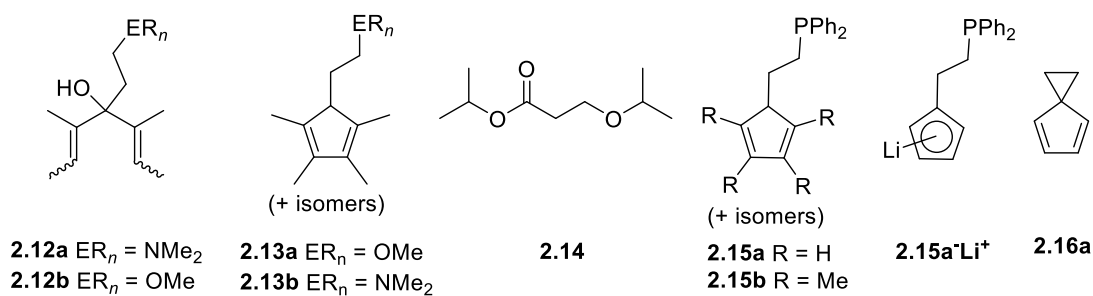
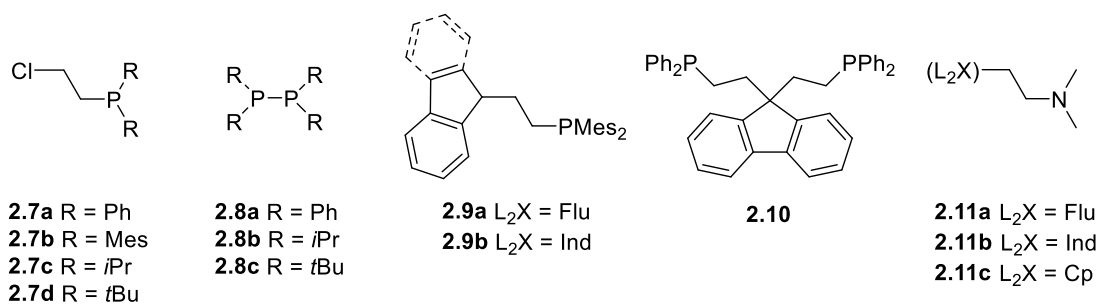
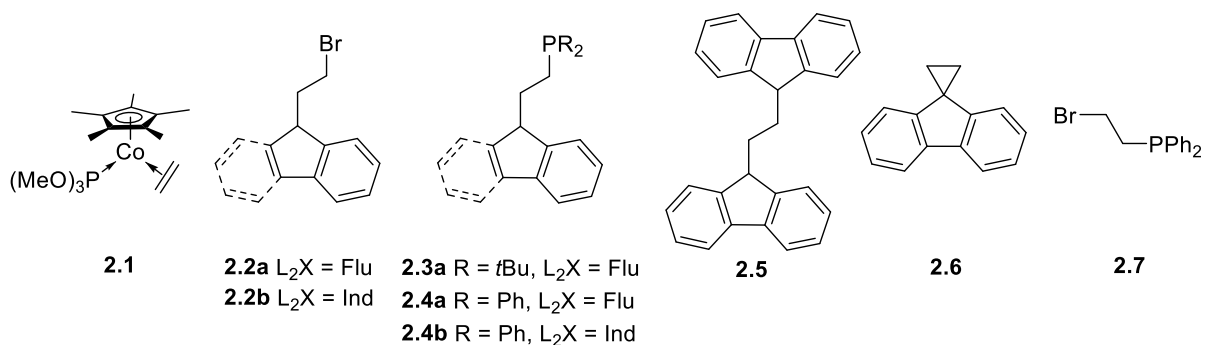
α -Diimine Ligands:

<i>p</i> -OMe-BIAN	<i>N,N'</i> -[<i>bis(p</i> -anisyl)imino]acenaphthene
<i>p</i> -Me-BIAN	<i>N,N'</i> -[<i>bis(p</i> -tolyl)imino]acenaphthene
<i>p</i> -OMe-BIE	<i>N,N'</i> -[<i>bis(p</i> -anisyl)imino]ethane
<i>p</i> -NMe ₂ -BIE	<i>N,N'</i> -[<i>bis(p</i> -dimethylanilyl)imino]ethane

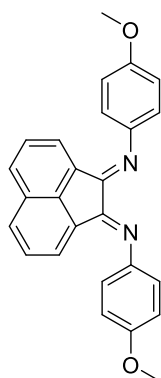
Diphosphine Ligands:

dppm	1,1- <i>bis</i> (diphenylphosphino)methane
dppe	1,2- <i>bis</i> (diphenylphosphino)ethane
dcype	1,2- <i>bis</i> (dicyclohexylphosphino)ethane
dppp	1,3- <i>bis</i> (diphenylphosphino)propane
dtbpp	1,3- <i>bis</i> (<i>tert</i> -butylphosphino)propane
dppb	1,4- <i>bis</i> (diphenylphosphino)butane
diprpb	1,4- <i>bis</i> (<i>di-isopropyl</i> phosphino)butane
dcypb	1,4- <i>bis</i> (dicyclohexylphosphino)butane
dppx	1,2- <i>bis</i> (diphenylphosphinomethyl)benzene
dtbpx	1,2- <i>bis</i> (<i>tert</i> -butylphosphinomethyl)benzene
dcypx	1,2- <i>bis</i> (dicyclohexylphosphinomethyl)benzene
diprpx	1,2- <i>bis</i> (<i>di-isopropyl</i> phosphinomethyl)benzene
dadpx	1,2- <i>bis</i> (<i>diadamantyl</i> phosphinomethyl)benzene
dppbz	1,2- <i>bis</i> (diphenylphosphino)benzene
BINAP	2,2'- <i>bis</i> (diphenylphosphino)-1,1'-binaphthyl
Xantphos	4,5- <i>bis</i> (diphenylphosphino)-9,9'-dimethylxanthene
PNNP-Ph	<i>N,N'</i> - <i>bis</i> (diphenylphosphino)- <i>N,N'</i> - <i>bis</i> (dimethyl)-1,2-diaminoethane
PNNP- <i>t</i> Bu	<i>N,N'</i> - <i>bis</i> (<i>tert</i> -butylphosphino)- <i>N,N'</i> - <i>bis</i> (dimethyl)-1,2-diaminoethane
PNNP- <i>t</i> Bu/Py	<i>N,N'</i> - <i>bis</i> ((2-pyridyl)phenylphosphino)- <i>N,N'</i> - <i>bis</i> (dimethyl)-1,2-diaminoethane
diphosphineSe	<i>e.g.</i> dppeSe = 1-(diphenylphosphine selenide)-2-(diphenylphosphino)ethane
diphosphineSe ₂	<i>e.g.</i> dppeSe ₂ = 1,2- <i>bis</i> (diphenylphosphine selenide)ethane
diphosphineO	<i>e.g.</i> dppeO = 1-(diphenylphosphine oxide)-2-(diphenylphosphino)ethane
diphosphineO ₂	<i>e.g.</i> dppeO ₂ = 1,2- <i>bis</i> (diphenylphosphine oxide)ethane

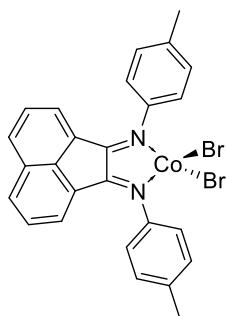
List of Compounds and Complexes: Chapter 2



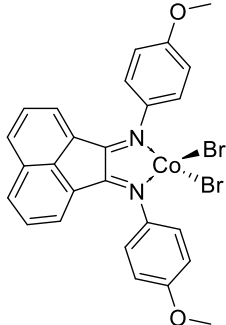
List of Compounds and Complexes: Chapter 3



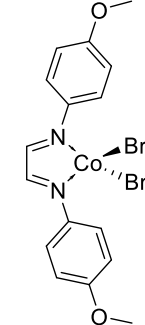
3.1



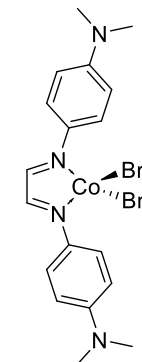
3.2a



3.2b



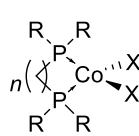
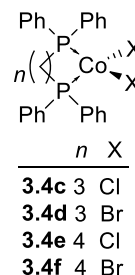
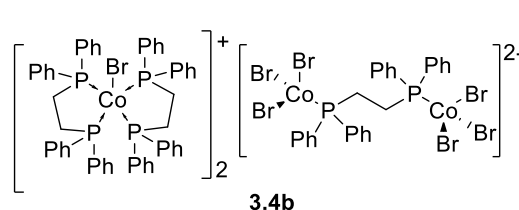
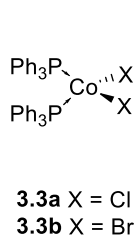
3.2c



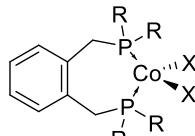
3.2d



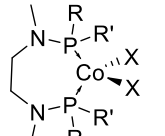
3.2e



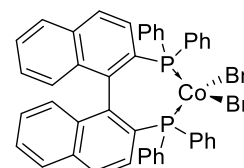
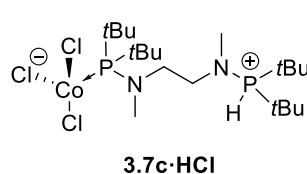
n	R	X
3.5a	<i>t</i> Bu	Br
3.5b	<i>i</i> Pr	Cl
3.5c	Cy	Br



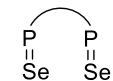
R	X
3.6a	<i>t</i> Bu
3.6b	<i>t</i> Bu
3.6c	Cy
3.6d	Ad
3.6e	Ad
3.6f	Ph
3.6g	<i>i</i> Pr



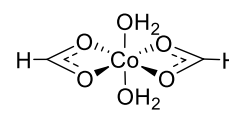
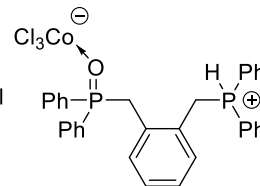
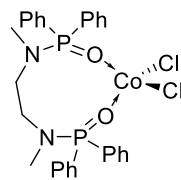
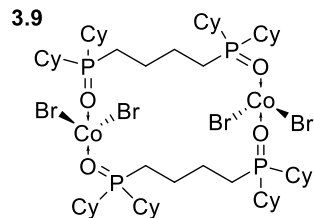
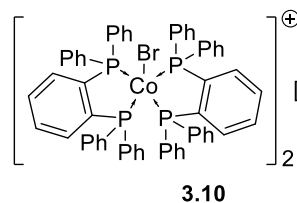
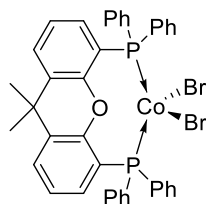
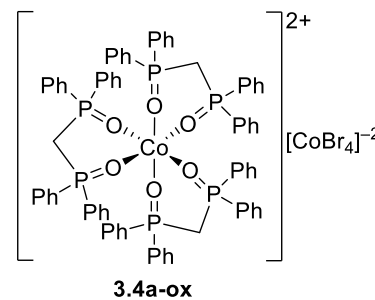
R	R'	X
3.7a	Ph	Cl
3.7b	Ph	Br
3.7c	<i>t</i> Bu	<i>t</i> Bu
3.7d	<i>t</i> Bu	2-Py



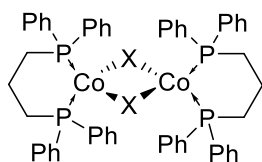
3.8



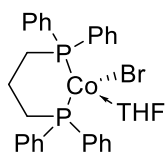
(P ^A P)
3.11a
3.11b
3.11c
3.11d
3.11e
3.11f
3.11g
3.11h
3.11i
3.11j
3.11k



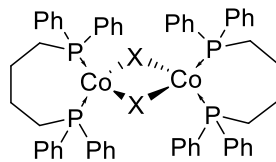
List of Compounds and Complexes: Chapter 4



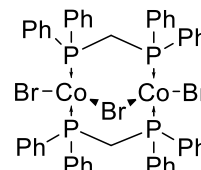
4.1 X = Cl
4.2 X = Br



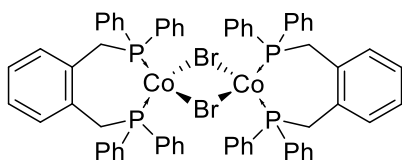
4.2·THF



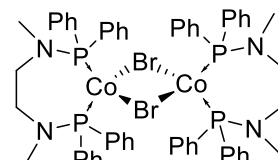
4.3 X = Cl
4.4 X = Br



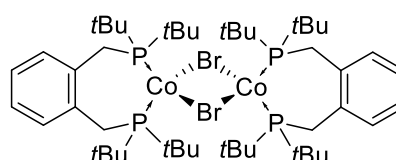
4.5



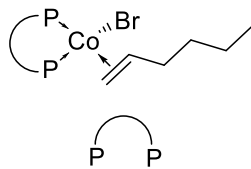
4.6



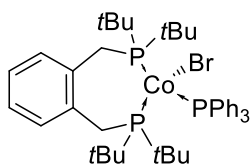
4.7



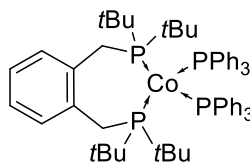
4.8



4.9 dtbpx
4.10 diprpx
4.11 dpppbz



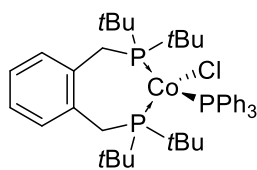
4.12



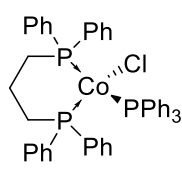
4.13

[(dtbpx)CoBr₂][Cp₂Co]
4.14

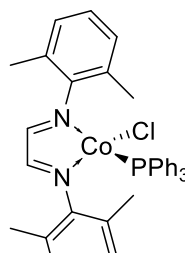
[Cp₂Co]₂[CoBr₄]
4.15



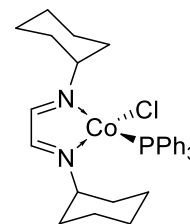
4.16



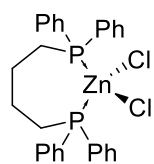
4.17



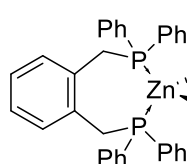
4.18



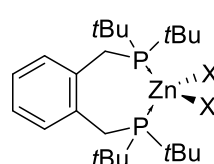
4.19



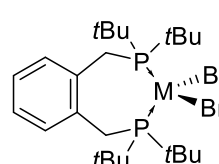
Zn-5.1



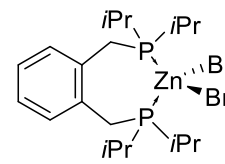
Zn-5.2



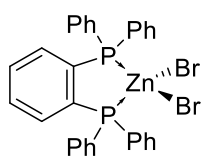
Zn-5.3 X = Br
Zn-5.4 X = Cl



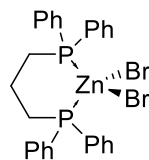
ZnCo-5.3
M = Zn:Co (3:1)



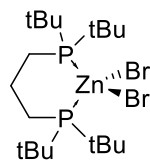
Zn-5.5



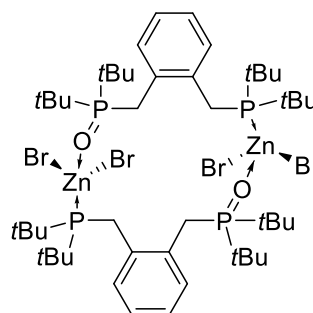
Zn-5.6



Zn-5.7



Zn-5.8



Zn-5.9

CHAPTER 1

– Introduction

The work presented in this thesis, which has been carried out in collaboration with Sasol Technology UK, is interested in the synthesis and subsequent reactivity of cobalt-based organometallic complexes. The overarching aim of this work is to provide underpinning background understanding to enable the future development of cobalt-based, homogeneous catalysts for the formation of linear α -olefins (LAOs) from linear α -olefins. In this context, this first chapter describes the general background to the research focussing, in particular, on the commercial importance of LAOs, the mechanistic pathways by which they may be produced and competing reactions that may occur during LAO production.

1.1 Introduction

The development of earth-abundant transition metal catalysis has become a research topic of great interest as the significance of the scarcity of 'traditional' precious metals going forward has been realised. Development of the chemistry and reactivity of earth-abundant first-row transition metals for use in homogeneous catalysis is therefore an area worthy of research. In this context, cobalt-based systems are attractive since cobalt is produced as a by-product in the extraction and refining of nickel and copper, so is cheap and has plentiful availability.

The Group 9 elements employed in homogeneous catalysis reactions are traditionally iridium and rhodium, however, their lighter 3d metal cobalt counterpart is an interesting alternative to these platinum-group elements. While use of the lighter 3d elements is attractive from a financial/sustainability stance, the chemistry of the first row elements is much more complex and less "predictable" when compared to that of their heavier congeners. This is principally a result of the ease with which these light elements can access a range of different spin states and also their ability to readily undergo single electron transfer reactions. The work presented in this thesis works towards developing underpinning knowledge of the synthesis, characterisation and reactivity of cobalt-based organometallic complexes, primarily with the aim that this will aid in the development of cobalt-catalysed regio- and stereo-selective olefin oligomerisation reactions in the future.

The selective oligomerisation of linear α -olefins (LAOs) to longer chain linear α -olefins has been of industrial interest for some time. This current work was, in part, funded by Sasol Technology UK, who run the largest Fisher-Tropsch process in the world. Sasol currently produce large quantities of underexploited short chain (C_2 – C_5) α -olefins. Development of a homogeneous, transition metal catalytic system that could selectively oligomerise these underexploited carbon fractions into high value, longer chain α -olefins is therefore of great economic value to Sasol. At present, many of both the commercial and LAO dimerisation systems reported in the academic literature inherently yield

internal olefin products and so research into the selective formation of LAOs from LAOs *via* a dimerisation system is of interest.

1.1 Commercial Importance of Linear α -olefins

Linear α -olefins (LAOs) are straight-chain hydrocarbons with the general formula C_nH_{2n} with a terminal carbon-carbon double bond. These LAOs are commodity chemicals that have a range of end use applications (**Figure 1.1**) including as plasticisers and as co-monomers for the production of linear low density polyethylene (LLDPE) and high density polyethylene (HDPE).

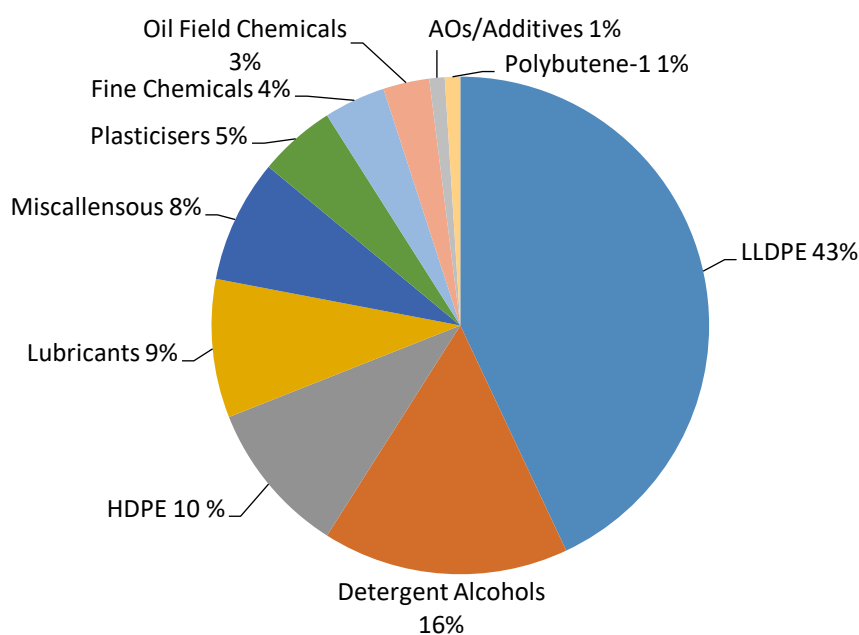


Figure 1.1 Global LAO demand by application.¹

The largest market share for LAO usage comes from the demand for the production of LLDPE (commonly used in the production of plastic bags along with plastic films, wraps, *etc.*), which accounts for 43% of their end use application.^{1,2} The high demand for LLDPE has resulted in a lucrative global market, with LLDPE sales totalling \$40 billion over the course of 2013.³ As a part of the manufacturing process of LLDPE and HDPE, 1-hexene and 1-octene are added in low weight percentages (~ 2%) as co-monomers with ethylene. Their addition provides stress-crack resistance to the end product materials (**Table 1.1**).^{2,4} As a result of their extensive use as co-monomers for plastics, a route to the selective formation of 1-hexene and 1-octene is of great industrial interest.

Table 1.1 Example end use applications of LAOs by carbon chain length.

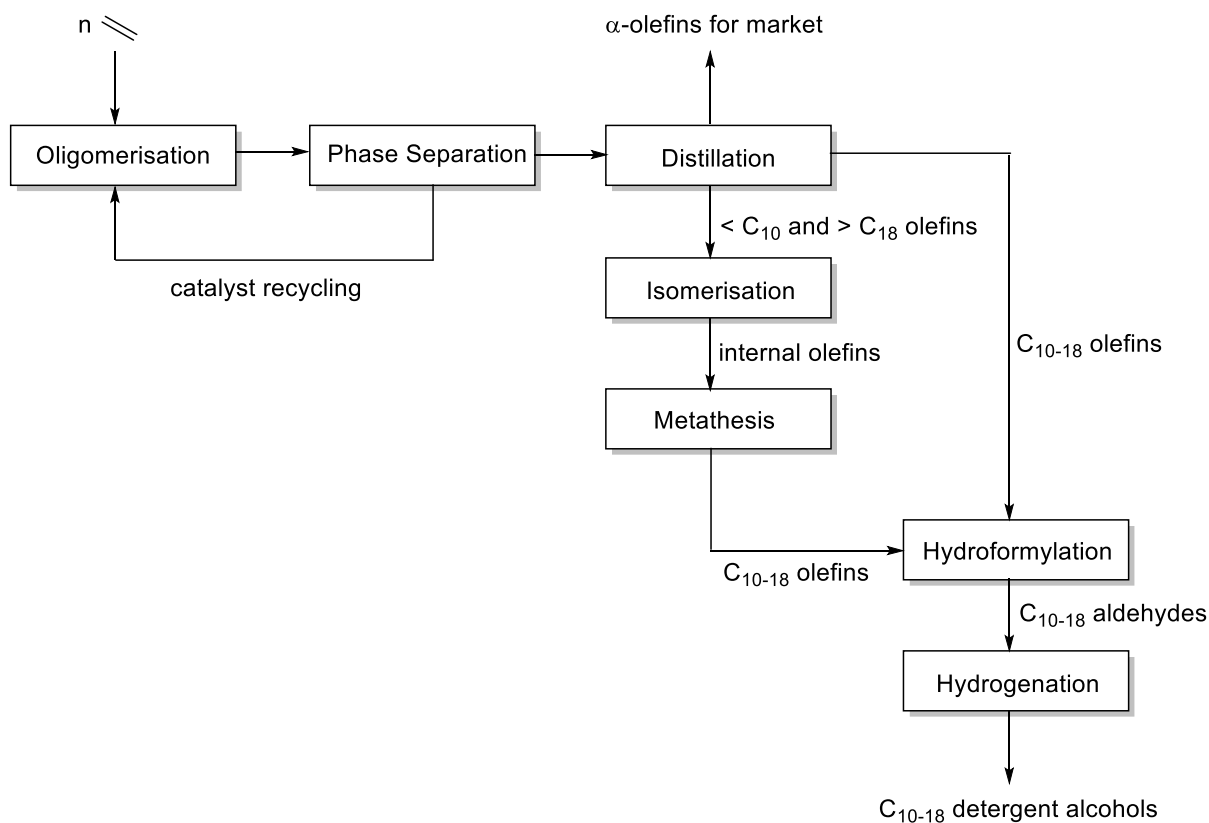
Carbon Number	Applications
C ₄	Polybutylene
C ₄ -C ₈	Plasticisers, alcohols
C ₆ -C ₈	Co-monomers for LLDPE
C ₈ -C ₁₀	Synthetic base oils
C ₁₀ -C ₁₆	Household surfactants
C ₁₆ -C ₂₀₊	Industrial surfactants
C ₁₈ -C ₂₀₊	Drilling fluids

Furthermore, the global market demand for 1-hexene and 1-octene now currently exceeds production capacity achievable through traditional production methods.⁵ Commercial technologies that currently provide the majority of LAOs for market consumption rely upon the oligomerisation of C₂ (ethylene) or C₁ (CO and H₂) feedstocks and, as such, produce a range of varying chain length olefins, which have to then be separated for their differing end uses. Examples of current technologies for LAO production include the Shell Higher Olefins Process (SHOP: ethylene oligomerisation), Axens Solutions' AlphaButol process (ethylene dimerisation to 1-butene) and the Fischer Tropsch synthesis (syngas to hydrocarbon liquids); these processes are covered in detail in the following sections.^{6,7}

1.2 Commercial Technologies for LAO Production

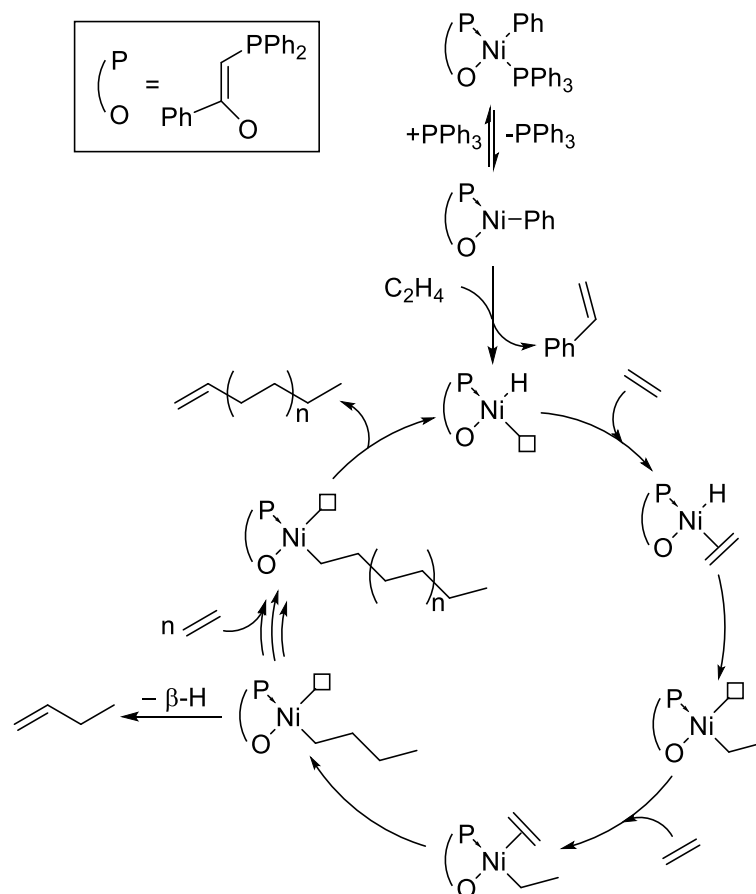
1.2.1 The Shell Higher Olefin Process

The Shell Higher Olefin Process (SHOP) is used to oligomerise ethylene to produce a range of even-numbered LAOs with a Schulz-Flory distribution. The process itself is not trivial, as it involves a series of reactions: ethylene oligomerisation, linear hydroformylation, isomerisation and metathesis (**Scheme 1.1**). This combination of oligomerisation, metathesis and hydroformylation allows SHOP to produce and separate (through distillation) olefin-based products that are in commercial demand, resulting in a process that can react to the global market.^{6,8-11}



Scheme 1.1 Flow sheet representation of the Shell Higher Olefin Process (SHOP) and downstream processes.^{11,12}

SHOP achieves oligomerisation of ethylene through the use of a nickel-based homogeneous catalyst, which can be recycled using a two-phase solvent system. Oligomerisation occurs after initial catalyst activation *via* phosphine ligand dissociation followed by the first insertion of ethylene and β -hydride elimination. Post activation, the SHOP catalyst mediates ethylene oligomerisation to LAO products through stepwise ethylene coordination and insertion followed by subsequent β -hydride eliminations. The generally accepted mechanism for SHOP oligomerisation is shown in **Scheme 1.2**.

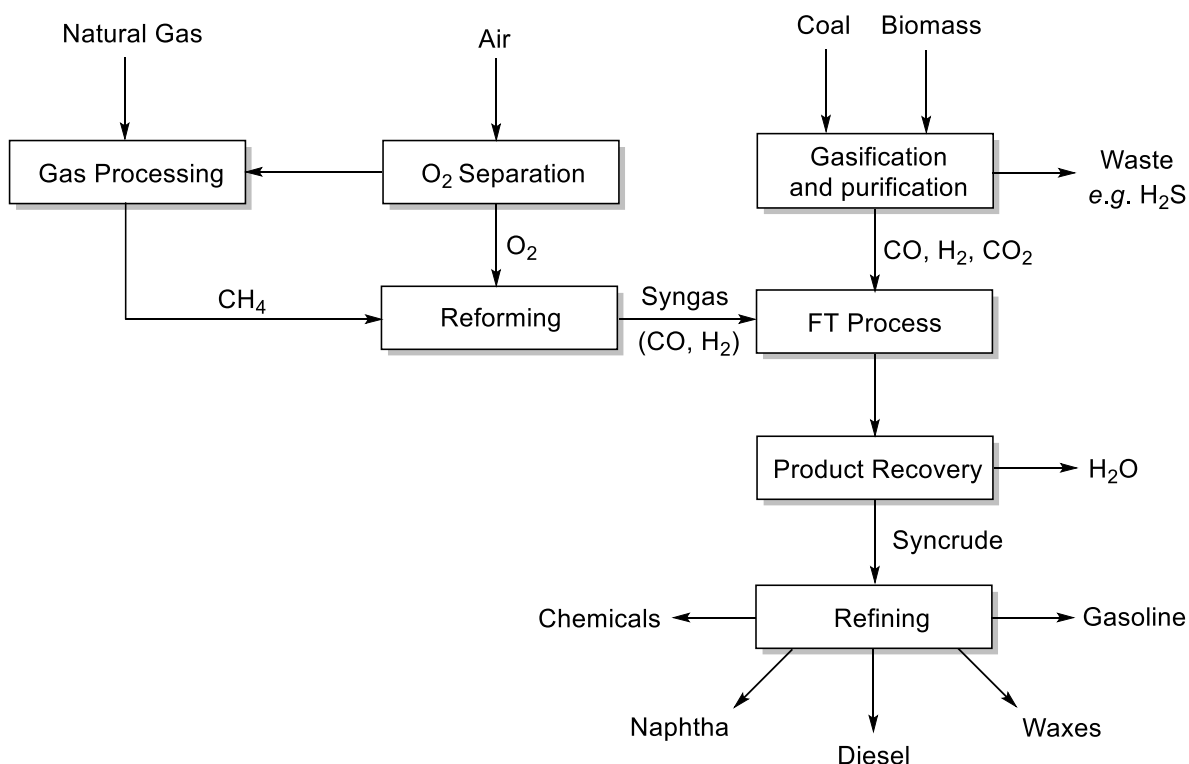


Scheme 1.2 Mechanism for SHOP oligomerisation of ethylene to α -olefins.^{11,13,14}

After the oligomerisation stage of SHOP, the liquid LAOs produced, which are not directly sold as LAOs (*i.e.* $<C_{10}$ and $>C_{18}$), are passed over a heterogeneous catalyst to isomerise them to their corresponding linear internal olefin (LIO). This isomerisation process is usually carried out using a solid potassium metal catalyst.¹⁵ At this point it is important for the proportion of LAOs present to be as low as possible to prevent high molecular weight and low molecular weight products from being produced in the next process step, namely olefin metathesis.¹⁶ The cross-metathesis catalyst in use is an alumina-supported molybdate system (derived from MoO_3/Al_2O_3) and is used to convert the LIOs into a mixture of both odd- and even-numbered LIOs.^{15,17} This allows for formation of desired C_{10} - C_{18} internal alkenes, which can be separated by distillation and converted into commodity chemicals such as detergent alcohols.^{11,16}

1.2.2 The AlphaButol Process

The AlphaButol Process for selective dimerisation of ethylene to 1-butene was developed by Axens Solutions together with SABIC.¹⁸ The AlphaButol Process uses a soluble titanium-based catalyst, which



Scheme 1.5 Generalised process scheme for the manufacture of petrochemical products from, *e.g.* coal, biomass or natural gas, where a Fisher-Tropsch (FT) step is included.^{19,24,25}

As shown in **Scheme 1.5**, FT synthesis can begin with a carbon-based feedstock (*e.g.* coal, biomass), which goes through a gasification process at temperatures between 600 – 1200 °C. Purification during gas processing allows removal of sulfur-containing impurities such as H₂S, as well as any tars, oils or phenols that can be produced at the high temperatures required for gasification. The purified mixture of CO, H₂ and CO₂ produced from biomass or coal during gasification are then fed to the FT reactor bed. Alternatively, a natural gas source can be used, which undergoes gas processing to remove impurities before being combined with an O₂ stream, which enables a steam reforming reaction to produce syngas, which is then introduced into the FT process step. The resulting syncrude from the FT reactor can be refined and distilled to allow separation of products by carbon number for their varying end uses.²⁵

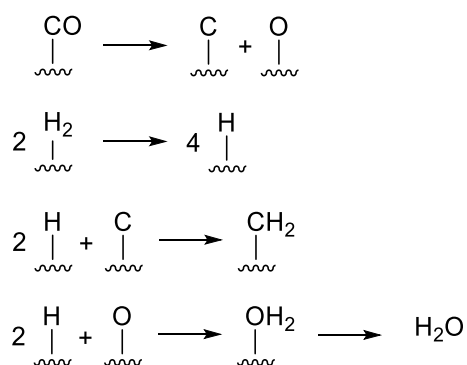
Oxygenates, olefins and alkanes are all observed to form during FT synthesis and can be separated easily by distillation. Mechanistically, Fisher-Tropsch is complex, with two incompatible catalytic cycles occurring on the surface of the heterogeneous catalyst employed (typically either iron- or cobalt-based) in tandem, where successive CO or methylene insertions occur.²⁶ Selectivity towards a desired product range can be controlled through choice of reaction conditions including: catalyst, temperature, reactor residence time, pressure and syngas composition.²⁴

Chapter 1

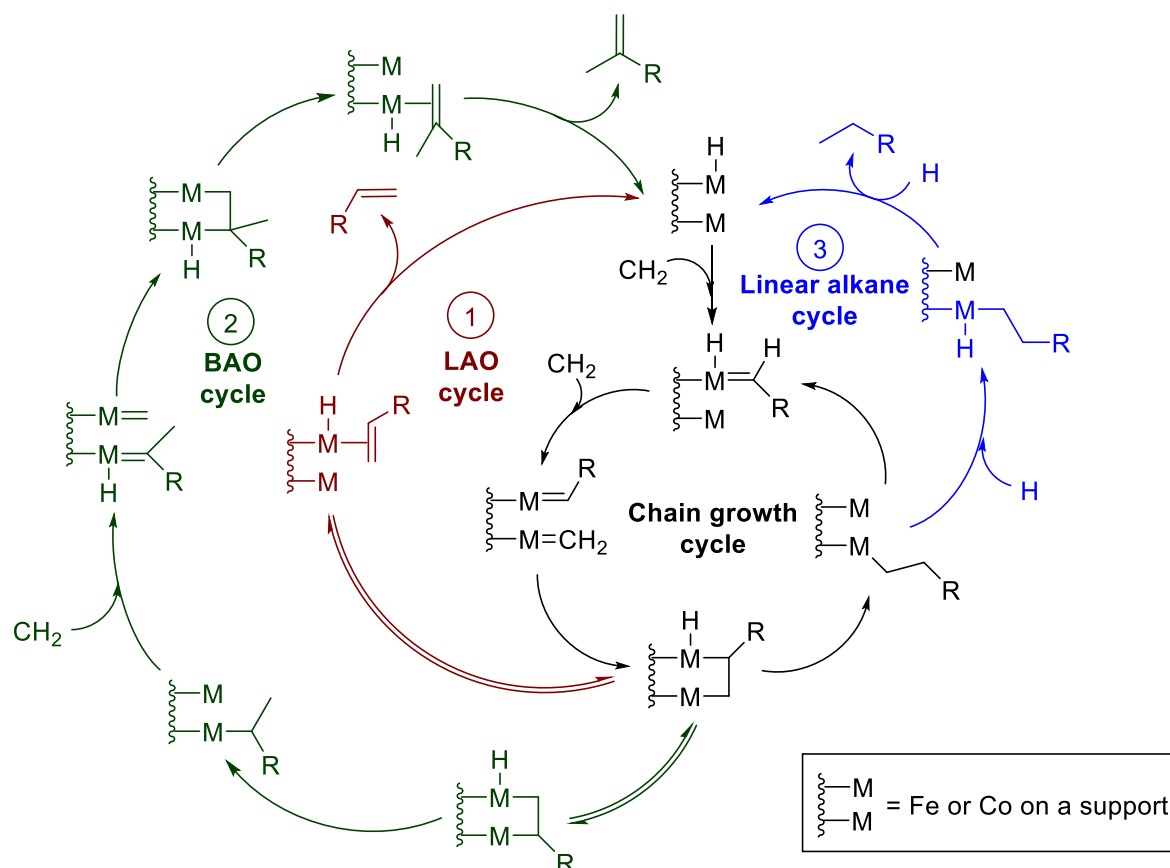
1.2.3.1 Mechanism for LAO production *via* Fisher-Tropsch Synthesis

Fisher-Tropsch (FT) synthesis commonly uses iron- or cobalt-based heterogeneous catalysts to perform the transformation of syngas into syncrude.²⁵ The temperature at which FT is carried out has a substantial effect on the products obtained. For example, high temperature FT (HTFT, 300 – 350 °C) uses mainly Fe catalysts and results in the majority of products being olefins within the C₃-C₁₁ range. Conversely, low temperature FT (LTFT, <300 °C) uses Co and Fe catalysts and produces waxes with n > C₂₀, where n is chain length.^{27,28}

The mechanism of LAO formation by HTFT iron catalysts is widely accepted to go *via* formation of an active surface Fe-CH₂ species.²⁸ This moiety arises upon adsorption and redistribution of two dihydrogen molecules and one carbon monoxide molecule, forming water as a by-product, as illustrated in **Scheme 1.6**.



Scheme 1.6 Schematic representation for the formation adsorbed CH₂ species on a FT heterogeneous catalyst surface.²⁸



Scheme 1.7 Proposed schematic representation mechanism for FT formation of LAOs, where LAO = Linear α-olefins, and BAO = branched α-olefins.^{26,29,30}

Once the active adsorbed CH₂ species has formed, it can then mediate chain growth through successive CH₂ insertions on the active site. Isomerisation and termination reactions, *via* α- or β-eliminations, then allow formation of the ① LAOs, ② branched α-olefins (BAOs) and ③ alkanes that together make up the syncrude mixture, the proposed mechanisms of which are given in **Scheme 1.7**.^{24,29}

1.3 LAO Chain Length Distribution for SHOP and FT Synthesis

The stepwise mechanism (through consecutive insertions of C_n units, n = 1 for FT, n = 2 for SHOP) for LAO production during FT and SHOP results in an Anderson-Schultz-Flory distribution of products being obtained.^{6,31} After each successive insertion of a C_n unit to the growing chain with length n, there is the probability, α, of propagation to a longer chain, or of a termination event (with probability α-1) occurring *via* β-hydride elimination; this relationship is given in equation 1.^{31,32}

$$f(n \text{ wt}\%) = \alpha^n (1 - \alpha)^{n-1} \quad (1)$$

$$\alpha = \frac{k_T}{k_T + k_G} \quad (2)$$

As the chain length increases, the likelihood of termination therefore increases, resulting in an exponential decay function, which is termed Schultz-Flory; this is independent of residence time and as such is modelled by the rate of termination (k_T).^{33,34} The rate of termination from β -hydride elimination vs the rate of growth (k_G) from insertion events therefore determines the value given to α , as shown in equation 2. A typical Anderson-Schulz-Flory distribution of Sasol process-derived FT LAOs is shown in **Figure 1.2**.

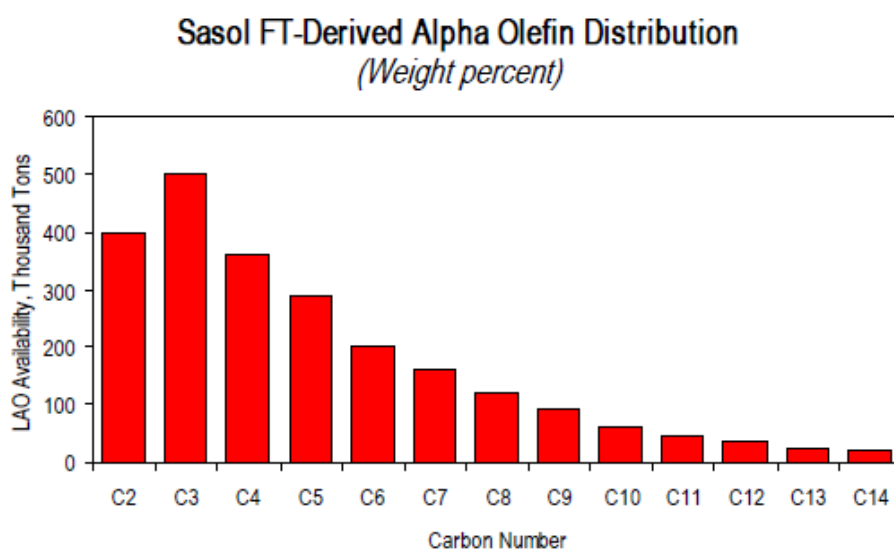


Figure 1.2 Sasol Fisher-Tropsch (FT) α -olefin product range, displaying Anderson-Schulz-Flory distribution: decreasing availability as carbon number increases.¹⁶

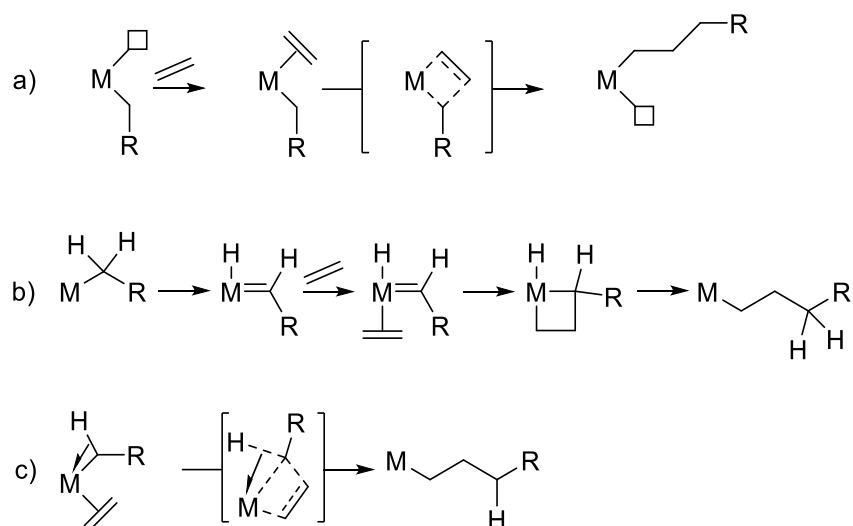
As mentioned in Section 1.1, currently LAOs with carbon numbers C₆-C₈ are in the highest demand due to their use as co-monomers for LLDPE production. The Anderson-Schulz-Flory distribution of Sasol FT feed-derived LAOs means that such FT process streams have comparatively low concentrations of the highly desired C₆-C₈ fraction. Consequently, there is considerable demand for the development of a system to convert low molecular weight and high abundance FT-derived LAOs (C₃-C₄) into these more in demand fractions. A system to convert C₃-C₄ into C₆-C₈ would therefore be of great interest.

1.4 Mechanism of Transition Metal-catalysed LAO Dimerisation and Oligomerisation

The dimerisation of linear α -olefins to longer-chained linear α -olefins is inherently difficult due to the more stable, and therefore thermodynamically favoured, internal olefin arising preferentially.³⁵ To design a system whereby the thermodynamic barriers are overcome to allow selective LAO production, the mechanisms by which oligomerisation occurs must first be understood. There are two widely accepted mechanisms for LAO oligomerisation: the *metallacycle mechanism* (oxidative coupling) and the *Cossee-Arlman mechanism* (step-wise addition).

1.4.1 Cossee-Arlman Mechanism (Step-Wise Addition)

The dimerisation, oligomerisation and polymerisation of LAOs by a step-wise addition mechanism was first introduced by Cossee and Arlman in 1964.^{32,36} Cossee and Arlman proposed that LAOs could be inserted into a growing chain at an octahedrally-coordinated active transition metal centre (*e.g.* Ti) with a vacant site (**Scheme 1.8a**). This vacant site would allow coordination of the LAO through a “ π -bond.” At the moment this π -bond was formed, it was postulated that the existing metal-alkyl bond to the growing chain would easily break due to the formation of a new molecular orbital (MO). This new lower energy MO, lowers the thermal excitation barrier required to allow breaking of the metal-alkyl bond to radicals, allowing LAO insertion into the metal-alkyl bond and formation of a new vacant site for propagation.^{32,36}



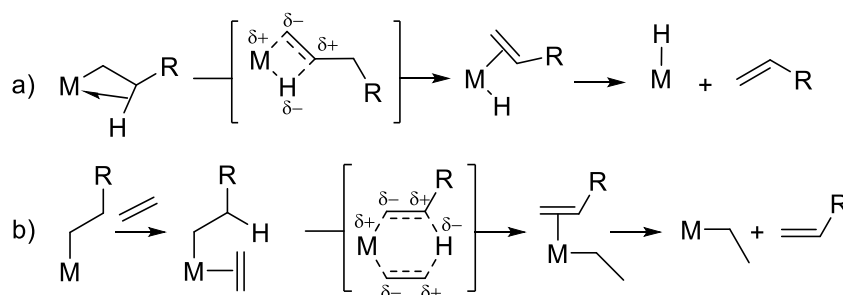
Scheme 1.8 Step-wise addition pathways for LAO dimerisation: a) Cossee-Arlman, b) Green-Rooney (carbene-hydride) and c) Modified Green-Rooney (α -agostic-assisted).^{32,37,38}

In 1978 Green and Rooney contested the Cossee-Arlman mechanism, suggesting instead that the mechanism of LAO insertion to a growing chain is similar to that of cross-metathesis.³⁷ From evidence of olefin dimerisation and oligomerisation by metathesis catalysts, Green and Rooney proposed that the key steps of C-C bond formation in LAO oligomerisation must be the interconversion of metal-olefin-carbenes and metallacyclobutanes. Green and Rooney suggest a 1,2-hydrogen shift from the growing chain to form a metal-olefin-carbene species, which, upon coordination of a LAO, can interconvert to a metallacyclobutane species (**Scheme 1.8b**). This metallacyclobutane once more forms a linear metal alkyl chain through reductive elimination, giving rise to the name carbene-hydride mechanism for LAO oligomerisation (**Scheme 1.8b**).³⁷

A modification to their mechanism was made in 1982 by Green, Rooney and Brookhart (**Scheme 1.8c**).³⁸ This α -agostic pathway can be viewed as a hybrid of the Cossee-Arman and Green-Rooney mechanisms, with stepwise insertions of LAOs going through a four-membered intermediate, which is stabilised by an α -agostic interaction between the metal centre and α -proton of the growing chain. It is thought that this α -agostic interaction could facilitate the rotation of C sp^3 orbital, allowing for LAO insertion into the growing chain. More recent evidence suggests the α -agostic interactions of the modified Green-Rooney mechanism only arise when olefin insertion is the rate-limiting step.^{38,39}

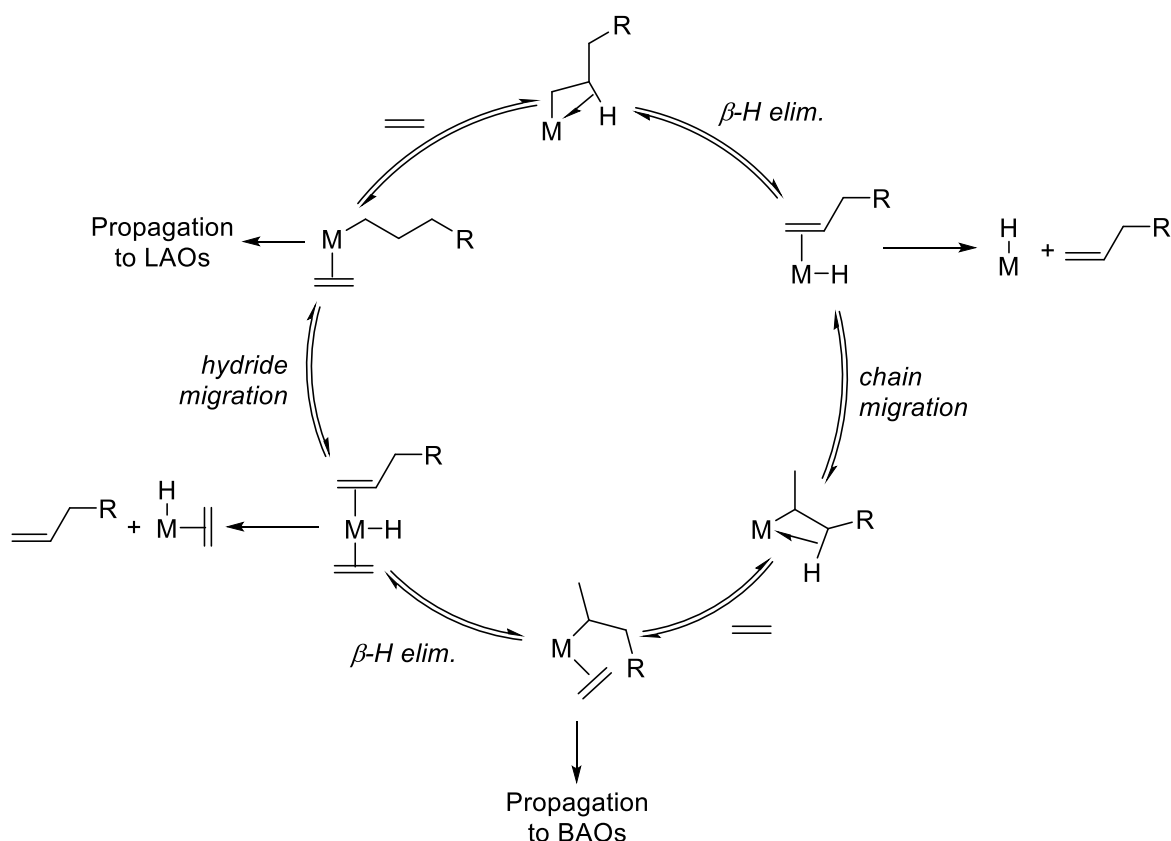
Both metal alkyl and metal hydride species have been shown to be catalytically active in step-wise insertion mechanisms. The distribution of products obtained is largely dependent upon the rate of chain growth (k_G) vs the rate of termination (k_T). Dimerisation occurs when $k_T \gg k_G$, oligomerisation occurs when k_T is approximately equal to k_G , and polymerisation occurs when $k_T \ll k_G$. The rates of termination and chain growth are determined through metal choice, ligand steric and electronic effects, solvent choice, *etc.*, factors that together permit a degree of tuning to enable selective dimerisation to be achieved.^{40,41} The termination step of such pathways can occur by one of two methods: β -hydride elimination or β -hydride transfer (**Scheme 1.9**), resulting in a metal hydride and metal alkyl species, respectively.⁴⁰⁻⁴²

During β -hydride elimination, which proceeds *via* formation of a four-membered, polar transition state, to form a metal hydride with an LAO coordinated. Dissociation of the LAO then regenerates the catalytically active metal hydride that can then re-enter the cycle.⁴⁰⁻⁴² This process is shown in **Scheme 1.9a**. β -Hydride transfer occurs when an additional LAO coordinated to the metal alkyl species. A six-membered, polar transition state can then arise, allowing direct β -hydrogen transfer to the incoming LAO. This direct transfer allows dissociation of the newly formed LAO from the metal centre, regenerating the active metal alkyl species in the process.⁴⁰⁻⁴² A representation of β -hydride transfer is shown in **Scheme 1.9b**, with ethylene chosen to demonstrate the incoming LAO.



Scheme 1.9 Termination mechanisms for Cossee-Arman-type LAO dimerisation: a) β -hydride elimination, b) β -hydride transfer.⁴⁰⁻⁴²

Step-wise insertions of LAOs in a *Cossee-Arlman-type mechanism* do give high yields of LAOs. However, a chain walking mechanism is also potentially operative, which gives rise to branched α -olefins (BAOs). BAOs occur when chain migration occurs after a metal alkyl species has undergone β -hydride elimination to form a metal hydride species.^{40,41} Chain migration is the reformation of a metal alkyl species, also with a stabilising β -agostic interaction, through migratory insertion of hydride on the metal-centre, however the M-C bond has now moved to the 2-position on the growing chain, resulting in propagation of branched products.^{40,41} This mechanism is shown in **Scheme 1.10**.

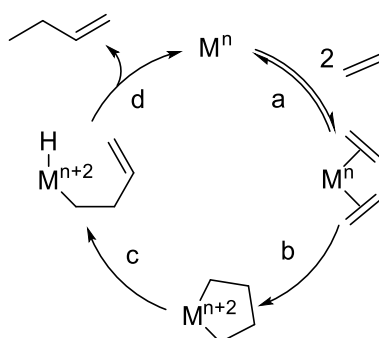


Scheme 1.10 Mechanism for chain walking during step-wise olefin dimerisation. β -H elim. = β -hydride elimination. ^{40,41}

As chain walking is the result of fast rates of β -hydride elimination, reducing the rate of β -hydride elimination will therefore reduce the quantity of BAOs produced. For example, in ethylene oligomerisation processes such as SHOP, the pressure of ethylene can simply be increased to reduce the rate of β -hydride elimination through coordinative saturation of the metal centre, and therefore reduce the rate of chain walking.⁴¹

1.4.2 Metallacycle Mechanism

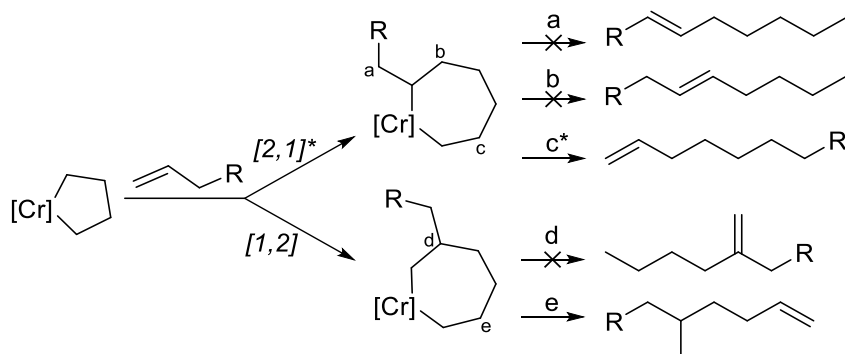
Selectivity towards LAO dimerisation can be obtained through operation of a so-called *metallacycle mechanism* (**Scheme 1.11**). Initial coordination of two alkene (*e.g.* ethylene) units to the metal centre results in a metal-olefin species that can then undergo oxidative coupling to form a metallacyclopentane. β -Hydride elimination from the metallacycle followed by reductive elimination liberates the LAO product and regenerates the catalyst for further cycles. At each stage, additional LAO insertion or termination can occur.^{6,43}



Scheme 1.11 Metallacycle mechanism: ethylene dimerisation to 1-butene: a) ethylene association; b) oxidative coupling; c) β -hydride elimination; d) reductive elimination.⁶

The metallacycle mechanism has been shown to be very selective towards 1-butene, 1-hexene and 1-octene formation from ethylene oligomerisation.⁴⁵ The stability of the metallacyclic intermediate determines the selectivity for given molecular weight LAO products. As additional ethylene insertions take place, the metallacycle formed becomes less stable, with the stability of metallocyclopentane > metallacycloheptane > metallacyclononane, which gives rise to the observed chain length control.⁴⁴

Ethylene trimerisation *via* metallacycle-mediated transition metal catalysts is well documented, with industrial applications achieving > 95% selectivity to 1-hexene.⁴⁵ However, there is still scope for enabling the isomerisation of LAOs to BAOs, as found by Bercaw and Labinger in their 2007 study.⁴⁶ Bercaw and Labinger used co-trimerisation of ethylene and propylene to demonstrate formation of both LAOs (1-heptene) and BAOs *via* a metallacycle-mediated chromium-based catalytic system. During trimerisation, Bercaw and Labinger postulated that several pathways for product isomerisation were possible, resulting from the initial mode of LAO insertion (2,1 vs 1,2) and the resulting β -hydride elimination pathway possibilities.⁴⁶ Routes to potential isomeric products are given in **Scheme 1.12**.



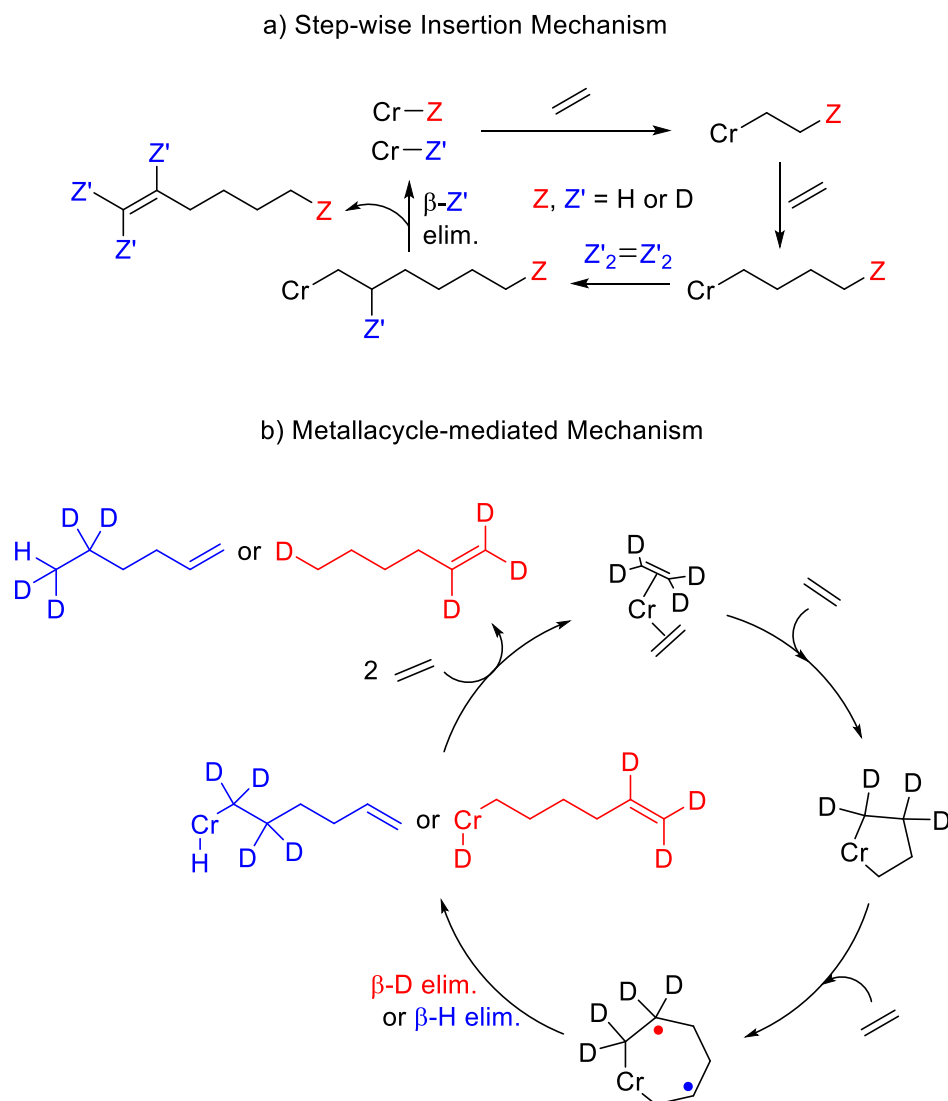
Scheme 1.12 Example modes of insertion of LAO into a pre-formed metallacyclopentane and subsequent products of possible β -hydride eliminations; a-e are sites of β -hydride elimination; *denotes favoured pathway.⁴⁶

The favoured insertion mode of an LAO into a metallocyclopentane was found to be a 2,1-insertion, which allows for β -hydride elimination to result in the LAO product, 1-heptene. Isomerisation to the LIO was postulated through β -hydride elimination at positions denoted as *a* and *b* in **Scheme 1.12**, however no evidence of LIO formation was observed.⁴⁶ Evidence of BAO formation was observed (namely formation of 3-methyl-1-hexene, 4-methyl-1-hexene and 5-methyl-1-hexene) after β -hydride elimination from the metallacycle formed post LAO 1,2-insertion.⁴⁶

While ethylene trimerisation catalysts can be extraordinarily selective to 1-hexene, the observation of BAO formation by Bercaw and Labinger must be taken into account when considering dimerisation processes. It could be postulated that the same BAO production pathway could exist in a metallacycle-mediated transition metal catalytic system for LAO dimerisation, the results of which are discussed in Section 1.4.4.

1.4.3 Distinguishing Between Metallacycle and Step-wise Insertion Mechanisms

As isomerisation mechanisms to BAOs and LIOs are available in both the metallacycle-mediated pathway and within step-wise insertion oligomerisation, it is necessary to find an alternative method of determining the mechanistic route by which oligomerisation occurs with a given catalyst. One strategy for aiding in the determination of the pathway by which LAO oligomerisation occurs is through the use of isotopic labelling studies. Using a 1:1 mixture of ethylene and deuterated ethylene (C_2D_4) in conjugation with an ethylene trimerisation catalyst, Labinger demonstrated a method for determining the reaction pathway in operation.⁴⁶ Here, the isotopologic product distribution observed will clearly indicate the pathway by which the trimerisation occurs. This technique can be applied to find the route by which any oligomerisation catalyst proceeds.⁴⁶



Scheme 1.13 Example products of deuterium-labelled ethylene trimerisation from a) a step-wise mechanism and b) a metallacycle-mediated mechanism.^{46,47}

During step-wise insertion of ethylene in a Cossee-Arlman type mechanism, H/D scrambling can be expected within the products; liberation of the LAO product goes *via* β -hydride elimination, reforming the active metal-hydride or metal-deuteride species. Therefore, using a mixture of ethylene and deuterium labelled ethylene will allow possible formation of isotopologues, as termination could occur *via* β -H or β -D elimination (**Scheme 1.13a**). The eliminated H or D is then incorporated into the subsequently bound LAO, resulting into an isomeric mixture of products with H/D-scrambling.⁴⁶ A step-wise insertion mode for formation of 1-hexene, for example, results in the expected isotopologic mixture containing both odd and even numbers of D as shown in **Table 1.2**.

However, no H/D scrambling would be expected if the mode of trimerisation of ethylene goes *via* a metallacycle-mediated mechanism. β -H or β -D elimination from the metallacycle to form the metal-

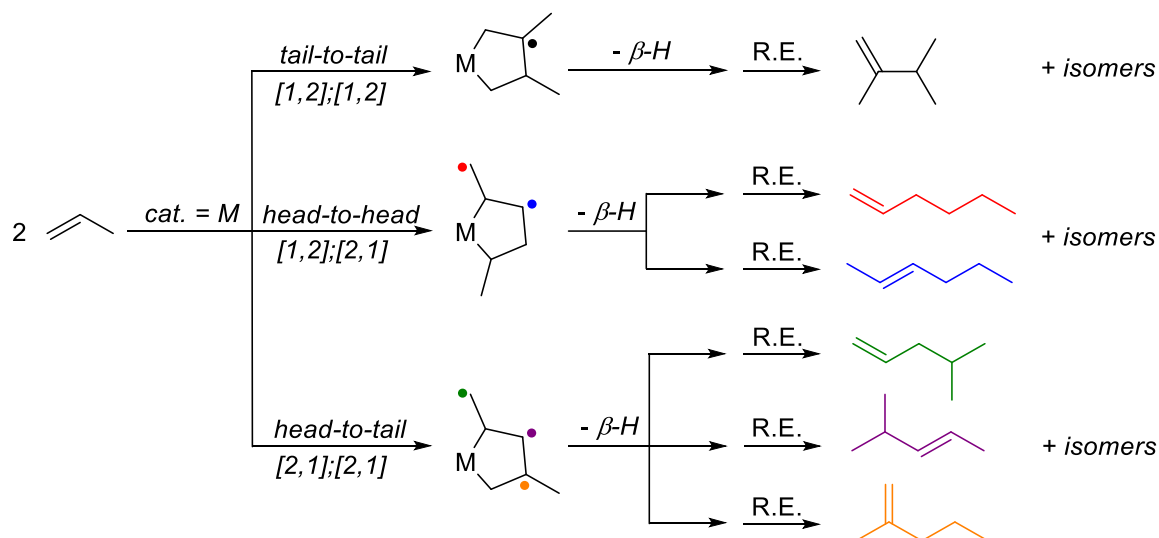
hydride/deuteride-alkyl species does not change the overall isotopic ratio observed in the product. Termination of the metallacycle goes *via* reductive elimination, resulting in a distribution of even numbered H/D-containing products due to the incorporation of the previously eliminated H/D into the product (**Scheme 1.13b**). Possible isotopomeric products formed from a mixture of $C_2D_4:C_2H_4$ are shown in **Table 1.2**. The use of isotopic labelling experiments with LAO dimerisation/oligomerisation catalysts is therefore of great use, enabling the mechanism of chain growth to be determined unambiguously.⁴⁶

Table 1.2 Expected product isotopomers for 1-hexene formation from trimerisation of a 1:1 mixture of C_2H_4 and C_2D_4 by both metallacycle and step-wise insertion mechanisms.

Step-wise Insertion		Metallacycle-mediated	
Formula	Relative Ratio	Formula	Relative Ratio
C_6H_{12}	1	C_6H_{12}	1
C_6DH_{11}	1	$C_6D_8H_4$	3
$C_6D_3H_9$	1	$C_6D_4H_8$	3
$C_6D_4H_8$	3	C_6D_{12}	1
$C_6D_5H_7$	2		
$C_6D_7H_5$	2		
$C_6D_8H_4$	3		
$C_6D_9H_3$	1		
$C_6D_{11}H$	1		
C_6D_{12}	1		

1.4.4 Regioselectivity in LAO to LAO Dimerisation Reactions

The regioselectivity of dimer formation achieved during transition metal-mediated LAO dimerisation is determined by the mode of insertion of the olefins: 1,2-insertion vs 2,1-insertion and combinations thereof.⁴⁸ **Scheme 1.14** presents the isomeric product mixture obtained for dimerisation with a propylene substrate and the associated substituted metallacyclopentane intermediates.

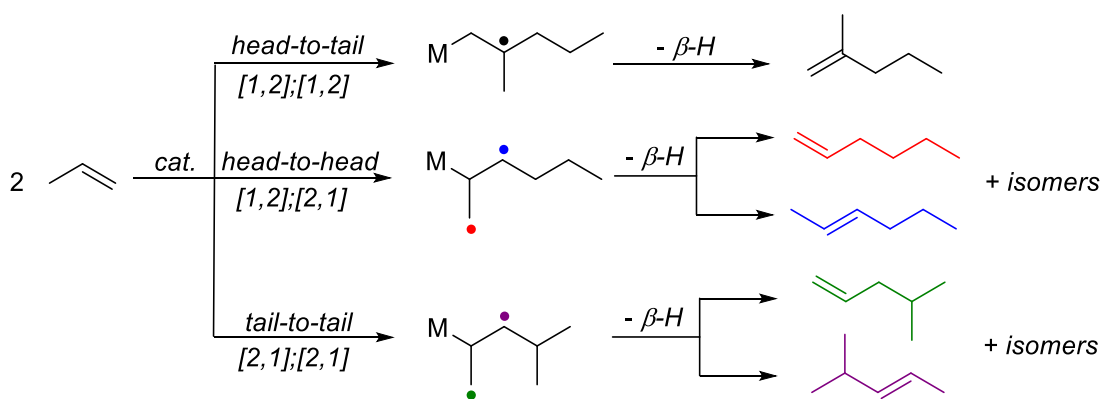


Scheme 1.14 Isomeric products formed during dimerisation of propylene *via* a metallacycle mechanism, where R.E. is reductive elimination. • denotes position of β -hydride elimination.

As shown in **Scheme 1.14**, tail-to-tail insertion (both olefins undergo 1,2-insertion) of two propylene molecules with subsequent β -hydride elimination and reductive elimination will liberate undesired and highly branched 2,3-dimethyl-1-butene. Similarly, head-to-tail insertion (both olefins undergo 2,1-insertion) will liberate branched internal and terminal olefins.⁴⁸

Head-to-head insertion (1,2 then 2,1) metallacyclic intermediates are desirable since subsequent β -hydride elimination will result in linear olefin products. However, this head-to-head insertion can also give rise to internal olefinic materials. A transition metal system that promotes head-to-head insertion modes, and is also an isomerisation catalyst towards terminal olefins, can therefore be imagined as a viable combination to achieve selective LAO dimerisation to LAOs.

It should also be noted that in step-wise dimerisation systems, the same isomeric mixture will be obtained, as 1,2- and 2,1-insertions are both possible.⁴⁹ The dimerisation of propylene is used as an example in **Scheme 1.15** to demonstrate the metal alkyl intermediates and products obtained by head-to-head, head-to-tail and tail-to-tail modes of insertion.



Scheme 1.15 Isomeric products formed during dimerisation of propylene *via* a step-wise mechanism mediated by a metal hydride species. •denotes position of β -hydride elimination.

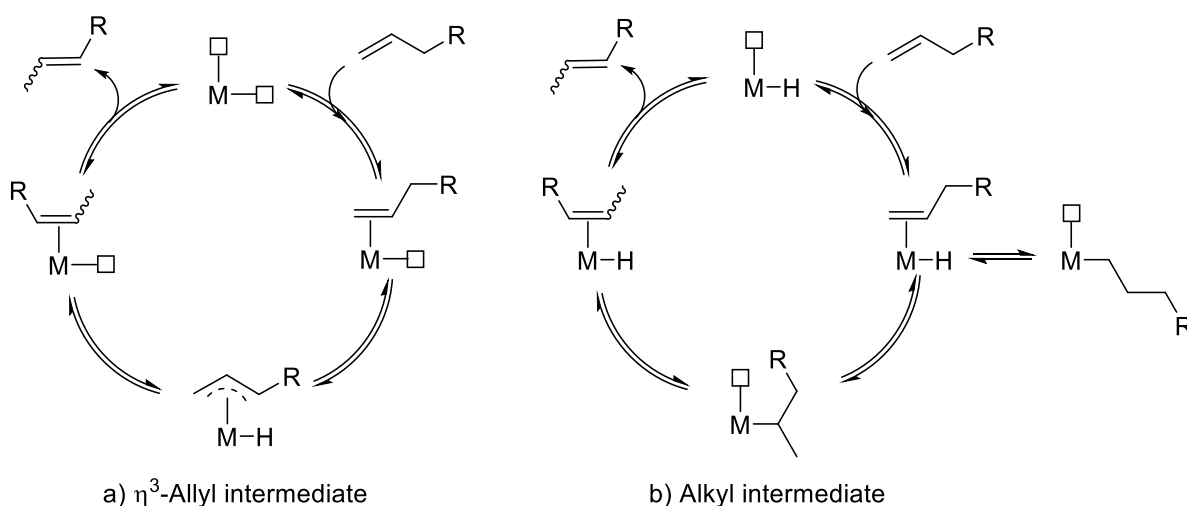
1.5 Processes Competing with LAO Dimerisation

There are many reports in the literature of system that display excellent selectivity towards dimerisation.^{6,50–56} However, dimerisation systems for LAOs that are both selective towards dimerisation and towards the LAO product are not yet well established. Within LAO dimerisation systems, isomerisation of LAOs to LIOs will compete with the production of LAOs. Additionally, co-dimerisation within LAO dimerisation systems can result in longer than dimeric LAO formation. In the following sections, processes that compete with LAO dimerisation will be discussed.

1.5.1 Isomerisation of LAOs to LIOs Using Dimerisation Systems

Isomerisation within olefin dimerisation catalytic processes often refers to the migration of the double bond from the α -olefinic position to afford the thermodynamically favoured linear internal olefin.⁵⁷ The isomerisation of the double bond from the terminal position to an internal one is possible through two mechanisms.

Isomerisation can occur through formation of an η^3 -allyl intermediate (**Scheme 1.16a**). Allyl-mediated isomerisation is prevalent in metallacycle-based dimerisation systems.⁶ Formation of an allyl-intermediate can arise if the active metal centre contains two vacant sites *cis* to one another. After coordination of the olefin to the metal centre, the activated C-H bond at the allylic centre can then undergo oxidative addition to form the allyl-intermediate, which can subsequently undergo reductive elimination to release the isomerised alkene.⁵⁷

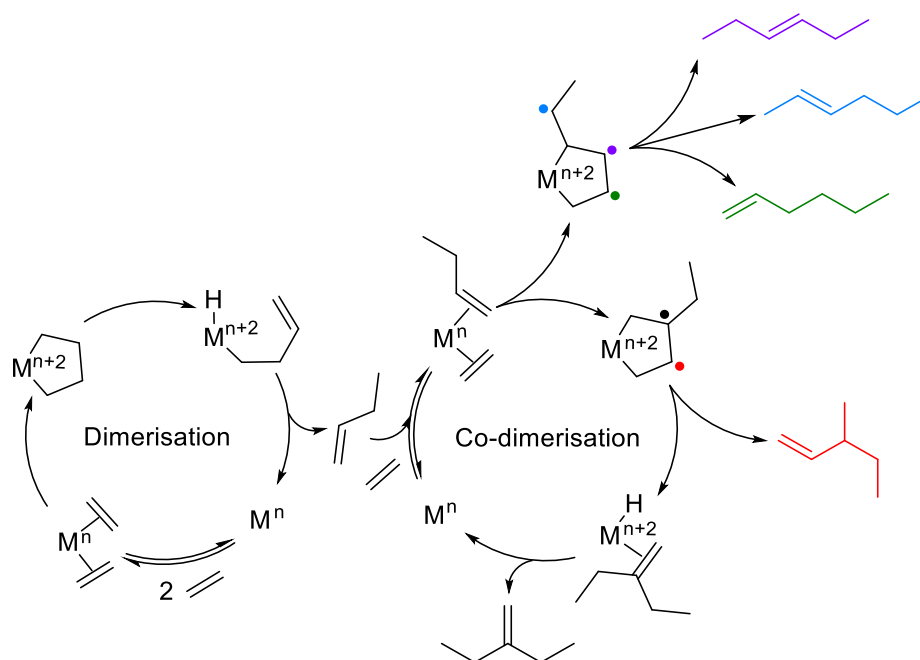


Scheme 1.16 Possible isomerisation mechanisms associated with olefin dimerisation catalytic cycles: a) *via* an η^3 -allyl intermediate and b) *via* an alkyl intermediate

When the active site is a metal hydride species with a vacant site, an alternative isomerisation mechanism may be envisaged *via* an alkyl intermediate (**Scheme 1.16b**). The latter type of isomerisation is prevalent for dimerisation systems where the mechanism is step-wise insertion; the active site required for isomerisation is identical to that required for step-wise chain growth (Section 1.4.1). After alkene coordination to the metal centre, migratory insertion of the hydride can result in a secondary metal-alkyl intermediate. β -Hydride elimination from this secondary metal-alkyl intermediate and reductive elimination can then result in the formation of a new internal alkene. However, when the primary (linear) metal-alkyl species is formed after initial migratory insertion, this species can only regenerate the linear 1-alkene through β -hydride elimination.

1.5.2 Apparent “Trimerisation”: The Co-dimerisation of Substrates and Products in Dimerisation Systems

During operation of an olefin dimerisation process, it is also possible for co-dimerisation to occur. Co-dimerisation is the process by which, after an initial dimerisation of the alkene substrate, the dimer product re-enters the cycle and undergoes further chain growth with an additional substrate molecule. Co-dimerisation therefore can result in the apparent formation of a ‘trimer’ product.^{58,59} The co-dimerisation of ethylene with 1-butene is explored in **Scheme 1.17** as an example.



Scheme 1.17 Possible co-dimerisation products of 1-butene and ethylene in a metallacycle-mediated dimerisation pathway. •location of β -hydride elimination.⁵⁹

As shown in **Scheme 1.17**, the co-dimerisation of ethylene with 1-butene results in a mixture of isomeric olefins. Following initial 1-butene formation through dimerisation of ethylene, it can re-enter as a dimerisation substrate to result in co-dimerisation with an additional ethylene unit. Metallacycle formation followed by β -hydride elimination then determines the possible isomers produced with, in this example, 1-hexene, 2-hexene, 3-hexene, 3-methyl-1-pentene and 2-ethyl-1-butene all being formed.^{58,59}

1.6 Background Summary and Thesis Aims

From the preceding sections, it can be seen that the regio- and stereo-selective production of linear α -olefins from ethylene or linear α -olefin feedstock offers a great synthetic challenge. However, with judicious design, the use of a homogeneous catalytic system for the production of linear α -olefins can be envisioned to allow control over the regio- and stereo-selectivity. Indeed, the large degree of control over the reactivity of the homogeneous catalytic system possible through modifications to the ligand system present on the metal centre is ubiquitous in this arena. With this in mind, the main objective of this thesis is to develop fundamental understanding of the nature of the metal-ligand bonding interactions present and their subsequent effect upon the reactivity of the resulting system. This aim is actualised through the synthesis of various cobalt-based systems (and ligands for use therein), with an emphasis upon the characterisation of these systems and exploration into the rudimentary behaviour of these cobalt complexes.

Chapter 1

Chapter 2 builds upon the work of Brookhart and Broene who employed a cationic $[\text{Cp}^*\text{CoH}\{\text{P}(\text{OMe})_3\}]$ -based system for the unusual cobalt-catalysed dimerisation of α -olefins to give linear α -olefin products, and aims to develop synthetic routes towards cobalt(I) half-sandwich complexes with general formula $(\text{L}_2\text{X})\text{Co}(\text{L})$. These systems are ultimately designed for use as pro-initiator systems in the catalytic transformation of propene to 1-hexene or 1-butene to 1-octene. A brief literature review on existing systems for LAO to LAO dimerisation and reported systems for selective production of 1-hexene and 1-octene is included. This chapter focuses on ligand design and synthesis. Subsequent complexation of these ligands to cobalt, to produce cobalt(I) half-sandwich complexes is explored.

Chapter 3 describes the synthesis and characterisation of two series of $(\text{L}^{\wedge}\text{L})\text{CoX}_2$ systems, where $(\text{L}^{\wedge}\text{L})$ = diimine or diphosphine and $\text{X} = \text{Cl}, \text{Br}$. Based upon literature review, these systems offer promise for use within selective ethylene oligomerisation reactions to produce short chain linear α -olefinic products such as 1-octene. The fundamental reaction and reduction chemistry of the synthesised diphosphine complexes, $(\text{P}^{\wedge}\text{P})\text{CoX}_2$, to produce cobalt(I) analogues is explored in Chapter 4. The influence of the diphosphine ligand present within these complexes upon observed reduction chemistry is reported. Alternative (non-reduction) routes to the synthesis of cobalt(I) complexes with general formula “ $(\text{P}^{\wedge}\text{P})\text{CoX}$ ” has also been investigated and the results reported herein.

Finally, Chapter 5 briefly describes the development of an *inert* delivery method for performing ASAP mass spectrometric analysis of air- and moisture sensitive samples. Termed ‘*i*ASAP MS’, this technique was used throughout the work herein.

1.7 References

- 1 L. M. Farrell, *Developments in LAO Comonomer Technologies for Polyethylene*, PERP 2011S11, 2012, p1-53.
- 2 Plastics Europe, *Linear Low Density Polyethylene (LLDPE)*, Brussels, Belgium, 2008, p1-4.
- 3 Ceresana, *Market Study: Polyethylene LLDPE (2nd edition)*, Constance, Germany, 2014, p1-480.
- 4 G. R. Lappin and J. D. Sauer, *Alpha Olefins Applications Handbook*, Marcel Dekker Inc., New York, U.S.A, 1st edn., 1989, p1-13.
- 5 B. Tooze, *Sasol Technology (UK) Ltd: Cobalt catalysed generation of α -olefins via olefin dimerisation - A computational approach towards the design of new catalysts*, 2009.
- 6 D. S. Mcguinness, *Chem. Rev.*, 2011, **111**, 2321–2341.
- 7 C. T. O'Connor and M. Kojima, *Catalysis Today*, 1990, **6**, 329–349.
- 8 D. Bézier, O. Daugulis and M. Brookhart, *Organometallics*, 2017, **36**, 443–447.
- 9 H. Wittcoff and B. Reuben, *J. Chem. Educ.*, 1988, **65**, 605–607.
- 10 E. F. Lutz, *J. Chem. Educ.*, 1986, **63**, 202.
- 11 W. Keim, *Angew. Chemie Int. Ed.*, 2013, **52**, 12492–12496.
- 12 W. Keim, F. H. Kowaldt, R. Goddard and C. Kruger, *Angew. Chem. Int. Ed. Engl.*, 1978, **6**, 466–467.
- 13 C. Wang, S. Friedrich, T. R. Younkin, R. T. Li, R. H. Grubbs, D. A. Bansleben and M. W. Day, *Organometallics*, 1998, **17**, 3149–3151.
- 14 E. R. Freitas and C. R. Gum, *Chem. Eng. Prog.*, 1979, 73–76.
- 15 J. C. Mol, *J. Mol. Catal. A Chem.*, 2004, **213**, 39–45.
- 16 Nexant Chem Systems, *PERP Report: Alpha Olefins 06/07-5*, 2008, p1-32.
- 17 T. M. Trnka and R. H. Grubbs, *Acc. Chem. Res.*, 2001, **34**, 18–29.
- 18 A. Forestière, H. Olivier-Bourbigou and L. Saussine, *Oil Gas Sci. Technol.*, 2009, **64**, 649–667.
- 19 D. Leckel, *Energy & Fuels*, 2009, **23**, 2342–2358.
- 20 A. J. V. Underwood, *Ind. Eng. Chem.*, 1936, **32**, 449–454.
- 21 O. Glebova, *Gas to Liquids: Historical Development and Future Prospects*, Oxford, 2013, p1-53.
- 22 F. Fisher and H. Tropsch, DE. Pat., DE484337, 1925.
- 23 D. J. Wilhelm, D. R. Simbeck, A. D. Karp and R. L. Dickenson, *Fuel Process. Technol.*, 2001, **71**, 139–148.
- 24 A. de Klerk, *Green Chem.*, 2008, **10**, 1249–1279.
- 25 M. E. Dry, *Catalysis Today*, 2002, **71**, 227–241.
- 26 J. Gaube and H. F. Klein, *J. Mol. Catal. A Chem.*, 2008, **283**, 60–68.
- 27 D. Lamprecht, L. P. Dancuart and K. Harrilall, *Energy and Fuels*, 2007, **21**, 2846–2852.

Chapter 1

- 28 P. Biloen and W. M. H. Sachtler, *Adv. Catal.*, 1981, **30**, 165–216.
- 29 O. R. Inderwildi and S. J. Jenkins, *Chem. Soc. Rev.*, 2008, **37**, 2163–2171.
- 30 I. M. Ciobîcă, G. J. Kramer, Q. Ge, M. Neurock and R. A. van Santen, *J. Catal.*, 2002, **212**, 136–144.
- 31 G. J. P. Britovsek, R. Malinowski, D. S. McGuinness, J. D. Nobbs, A. K. Tomov, A. W. Wadsley and C. T. Young, *ACS Catal.*, 2015, **5**, 6922–6925.
- 32 P. Cossee, *J. Catal.*, 1964, **3**, 80–88.
- 33 P. J. Flory, *J. Am. Chem. Soc.*, 1936, **58**, 1877–1885.
- 34 G. V. Z. Schulz, *Phys. Chem. (B)*, 1935, **30**, 379.
- 35 R. D. Broene, M. Brookhart, W. M. Lamanna and A. F. Volpe, *J. Am. Chem. Soc.*, 2005, **5**, 17194–17195.
- 36 E. J. Arlman and P. Cossee, *J. Catal.*, 1964, **3**, 99–104.
- 37 K. J. Ivin, J. J. Rooney, C. D. Stewart, M. L. H. Green and R. Mahtab, *J. Chem. Soc. Chem. Commun.*, 1978, 604–606.
- 38 M. Brookhart and M. L. H. Green, *J. Organomet. Chem.*, 1983, **250**, 395–408.
- 39 R. H. Grubbs and G. W. Coates, *Acc. Chem. Res.*, 1996, **29**, 85–93.
- 40 S. D. Ittel, L. K. Johnson and M. Brookhart, *Chem. Rev.*, 2000, **100**, 1169–1203.
- 41 S. Pillai, M. Ravindranathan and S. Sivaram, *Chem. Rev.*, 1986, **86**, 353–399.
- 42 J. Skupinska, *Chem. Rev.*, 1991, **91**, 613–648.
- 43 D. S. McGuinness, *Organometallics*, 2009, **28**, 244–248.
- 44 J. T. Dixon, M. J. Green, F. M. Hess and D. H. Morgan, *J. Organomet. Chem.*, 2004, **689**, 3641–3668.
- 45 *Mitsubishi Chemical Co.*, US Pat., US5865612, 1999.
- 46 T. Agapie, J. A. Labinger and J. E. Bercaw, *J. Am. Chem. Soc.*, 2007, **129**, 14281–14295.
- 47 R. H. Grubbs and G. W. Coates, *Acc. Chem. Res.*, 1996, **29**, 85–93.
- 48 J. J. Zuckerman and A. D. Norman, Eds., *Inorganic Reactions and Methods, Reactions Catalyzed by Inorganic Compounds*, John Wiley and Sons, Volume 16., 1993.
- 49 B. L. Small and A. J. Marcucci, *Organometallics*, 2001, **20**, 5738–5744.
- 50 A. Carter, S. A. Cohen, N. A. Cooley, A. Murphy, J. Scutt and D. F. Wass, *Chem. Commun.*, 2002, **3**, 858–859.
- 51 M. Uemura, H. Yorimitsu and K. Oshima, *Chem. Comm.*, 2006, 4726–4728.
- 52 A. Jabri, C. B. Mason, Y. Sim, S. Gambarotta, T. J. Burchell and R. Duchateau, *Angew. Chemie - Int. Ed.*, 2008, **47**, 9717–9721.
- 53 J. R. Briggs, *J. Chem. Soc. Chem. Commun.*, 1989, 674.
- 54 *Philips Petroleum Company*, US Pat., US5523507, 1996.

- 55 *Philips Petroleum Company*, EP Pat., EP0608447A1, 1994.
- 56 *Philips Petroleum Company*, US Pat., US5856257, 1999.
- 57 R. H. Crabtree, *The Organometallic Chemistry of the Transition Metals*, John Wiley & Sons, Inc, New Jersey, Fifth., 2001, p239-244.
- 58 E. W. Abel and F. G. A. Stone, Eds., *Organometallic Chemistry*, Royal Society of Chemistry, Volume 18., 1989, p370-373.
- 59 R. Ugo, Ed., *Aspects of Homogeneous Catalysis: A Series of Advances*, D. Reidel Publishing Company, Boston, USA, Volume 2., 1974, p81-84.

CHAPTER 2

- Synthetic Routes Towards Cobalt(I)
Half-Sandwich Complexes: $(L_2X)CoL_n$

“It is well known that a vital ingredient of success is not knowing that what you’re attempting can’t be done.”

– Terry Pratchett

2.1 Introduction

As described in Chapter 1, the oligomerisation of LAOs and ethylene has attracted substantial attention in both academic and industrial settings.¹⁻⁸ This interest is the result of the high value HAO products possibly obtained, which have a range of uses such as co-monomers for LLDPE production.^{9,10}

In the following sections, a brief literature review including examples of significant systems within the field of dimerisation and oligomerisation of LAOs will be presented along with rationale for the development of complexes containing *hemi*-labile ligands. For instance, ligands based upon Cp, Cp* and derivatives with “tethered” donor moieties are produced. Consequently, this chapter is primarily interested in establishing synthetic routes towards half-sandwich complexes of cobalt(I) and the synthesis of dual-functionality ligands. The complexation of these ligands to cobalt is explored with the aim of better understanding the synthetic challenges involved for the production of pro-catalyst complexes containing ligands with *hemi*-labile functionality. Ultimately it is hoped that this work will aid in the development of a new series of pro-catalyst complexes for use within olefin oligomerisation reactions.

2.1.1 LAO Trimerisation and Tetramerisation Systems

The first commercial catalytic ethylene trimerisation system was introduced by Reagen in 1994 for the Phillips Petroleum Company.¹¹ This so-called Phillips trimerisation system uses a catalyst derived from reaction of CrCl₃ with sodium pyrrolide and triethylaluminium using THF as a solvent (**Figure 2.1a**). However, alterations to this system were quickly established to improve selectivity and activity further.⁸ The second generation Phillips catalyst package uses a different chromium source (chromium(III)2-ethylhexanoate) and a slightly different ligand, 2,5-dimethylpyrrolide, along with the addition of a chloride source (diethylaluminiumchloride) (**Figure 2.1b**). This modified Phillips ethylene trimerisation system allowed activities of up to 156,666 g (g Cr)⁻¹ h⁻¹ with 93.2 % selectivity to 1-hexene to be obtained by 1999.⁸

More recently, the Mitsubishi Chemical Company have improved upon the Phillips system, achieving a substantial increase in catalyst activity and higher selectivity to 1-hexene (**Figure 2.1c**). Through introduction of a new chloride source, hexachloroethane, and an *in situ* activation process, Mitsubishi’s ethylene trimerisation system can offer 95.4% selectivity towards 1-hexene with activities up to 3,780,000 g (g Cr)⁻¹ h⁻¹.^{12,13}

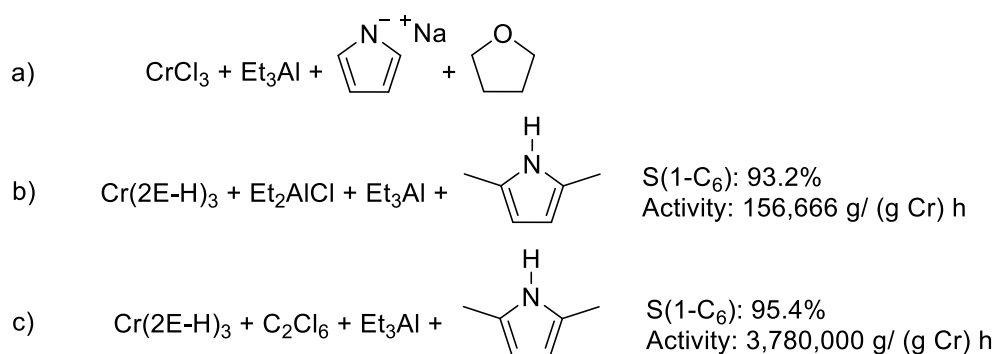
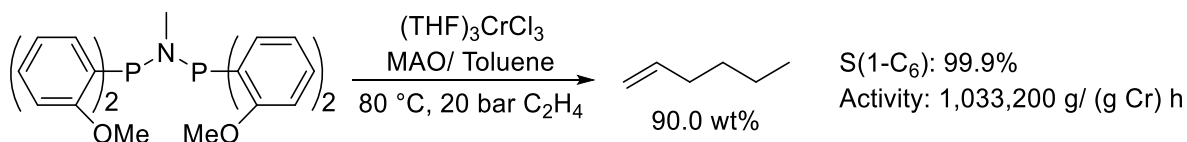


Figure 2.1 Commercial ethylene trimerisation systems: a) Phillips Petroleum generation I, b) Phillips Petroleum generation II, c) Mitsubishi Chemical Corporation

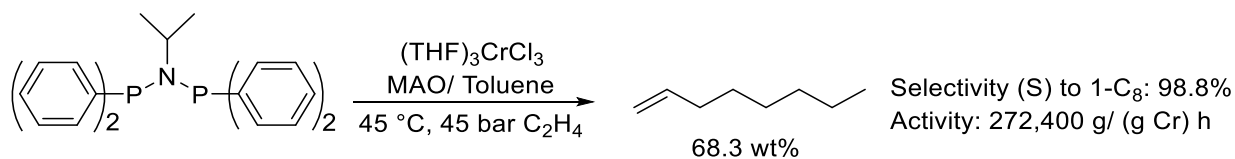
In 2002, BP published an alternative chromium-based ethylene trimerisation system using methylaluminoxide (MAO) as an activator with a P-N-P tridentate catalyst (**Scheme 2.1**) and reported obtaining selectivity towards 1-hexene within the C₆ fraction of up to 99.9% with activities reaching 1,033,200 g (g Cr)⁻¹ h⁻¹.¹ Wass *et al.* hypothesised that the *ortho*-methoxy groups present at the periphery of P-N-P ligand of this BP system could act as pendant donors, increasing the coordinative saturation of the Cr centre, which was thought to aid selectivity and activity.¹



Scheme 2.1 BP chromium-based system for ethylene trimerisation using a P-N-P tridentate ligand and MAO activator.¹

Using the BP catalyst as a starting point, Bollmann *et al.* investigated structural variations of the P-N-P ligand and their subsequent effects upon selectivity for ethylene oligomerisation at Sasol.¹⁴ Sasol's investigation demonstrated that through removal of the *ortho*-methoxy groups present on the BP trimerisation catalyst, the selectivity of the system could be moved towards tetramerisation of ethylene (**Scheme 2.2**). Bollmann and co-workers found that the substituent present on the nitrogen-backbone had little effect on selectivity, but did have a large influence on the activity of the system. Through use of an *iso*-propyl group on the N-backbone and simple diphenylphosphine moieties, Sasol was able to obtain selectivity towards 1-octene of up to 70 wt%. Interestingly, Sasol's study also revealed that addition of alkyl groups to the *ortho*-position of aryl groups present on the phosphine moiety moves the selectivity of their system back towards trimerisation. This finding could suggest

that the *ortho*-methoxy group favoured by BP could be simply acting as a sterically demanding group, which limits chain growth and hence reduces tetramerisation.^{2,14}

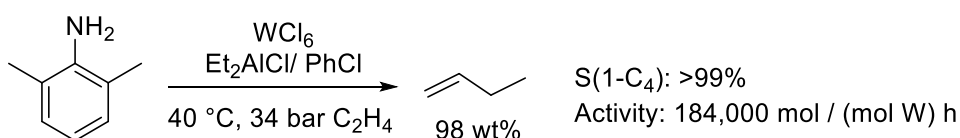


Scheme 2.2 Sasol system for selective ethylene tetramerisation.¹⁴

2.1.2 LAO Dimerisation Systems

While this PhD program is interested in the selective dimerisation of LAOs of chain length greater than ethylene, it would be remiss not to include an example of ethylene dimerisation to 1-butene due to this transformation's industrial importance and wide coverage in the literature.^{15,16}

In 1974, *The Goodyear Tire and Rubber Company* reported the preparation of 1-butene from ethylene.¹⁷ At 40 °C and through dissolving tungsten hexachloride with 2,6-dimethylaniline in chlorobenzene, subsequent treatment with diethylaluminium chloride allowed selective dimerisation of ethylene to 1-butene in yields up to 98% (**Scheme 2.3**).¹⁷ The tungsten catalyst activity reached up to 184000 mol (mol W)⁻¹ h⁻¹ with 34 bar pressure ethylene. However when this pressure was reduced to 27 bar, the catalytic activity also reduced to 176000 mol (mol W)⁻¹ h⁻¹.¹⁷



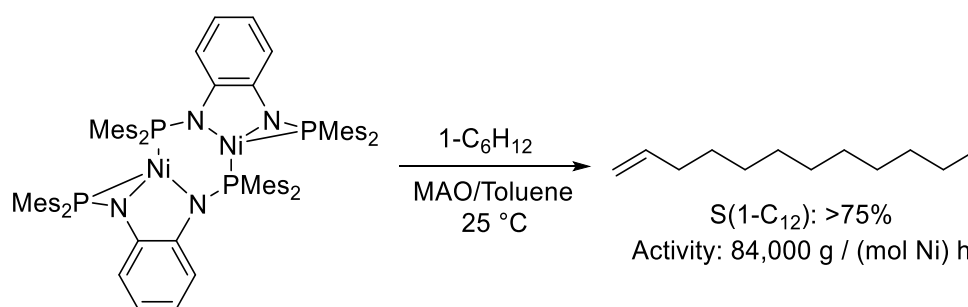
Scheme 2.3 Goodyear Tire and Rubber Company system for selective ethylene dimerisation.¹⁷

2.1.2.1 Ni-based LAO dimerisation systems

An early example of a selective higher α -olefin (HAO) dimerisation process was presented by Jones and Symes in 1971, who probed the selective dimerisation of 1-butene and 1-hexene.^{18,19} Using a Ni(acac)₂-Et₂AlOEt catalyst at 40 °C, they were able to obtain selectivity towards linear dimer formation of between 75–85% for the HAOs tested. Unfortunately, they also encountered co-dimerisation product formation alongside isomerisation to the internal alkene product. Jones and Symes found the rates of 1-hexene isomerisation to 2-hexene and 3-hexene at 40 °C to be twice as great as the dimerisation process, resulting in exponential decay of the activity observed for dimerisation as the substrate is

isomerised. Furthermore, the activities measured for these systems were very low, with the highest turnover frequency (TOF) recorded as $9.6 \text{ g (g Ni)}^{-1} \text{ h}^{-1}$ for 1-butene dimerisation. The high selectivity towards linear dimer formation by head-to-head insertion observed by Jones and Symes was rationalised through a step-wise insertion pathway with the active species being a Ni-H.¹⁹ This finding was confirmed in 1997 in a similar study by da Rosa *et al.* using the same catalyst in a study of 1-butene oligomerisation reactions.²⁰ da Rosa found very similar results, observing 73% selectivity for 1-butene dimerisation to internal octenes, with >98% of these internal octenes within the linear fraction.²⁰

More recently, the dimerisation of 1-hexene by a dimeric *bis(amido)* nickel complex was reported by Hey-Hawkins and Eisen.²¹ Using $[\text{Ni}\{\text{1-N}(\text{PMe}_2)\text{-2-N}(\mu\text{-PMe}_2)\text{C}_6\text{H}_4\text{-}\kappa^3\text{N,N',P,-}\kappa^1\text{P}'\}]_2$ with MAO as an activator in toluene at 25 °C, Hey-Hawkins and Eisen observed 100% conversion of 1-hexene to dodecenes, with 75% selectivity towards 1-dodecene and activities of up to $84,000 \text{ g (mol Ni)}^{-1} \text{ h}^{-1}$ (**Scheme 2.4**). However, it was also observed that the resulting organic product mixtures isomerised to a mixture of linear internal dodecene olefins over time.



Scheme 2.4 Selective dimerisation of 1-C₆ to 1-dodecene as reported by Hey-Hawkins and Eisen.²¹

2.1.3 Co- and Fe-based LAO Dimerisation Systems

There are several examples of cobalt- and iron-based HAO dimerisation transition metal catalysts in the literature. Small *et al.* reported a series of pyridine *bis(imine)* iron catalysts (**Figure 2.2**) for selective dimerisation of LAOs to LIOs *via* a step-wise insertion mechanism. Through systematic variation of the substituents present on the ligand, Small demonstrated a system that resulted in 23–80% selectivity towards *n*-dodecenes from 1-hexene.^{22,23}

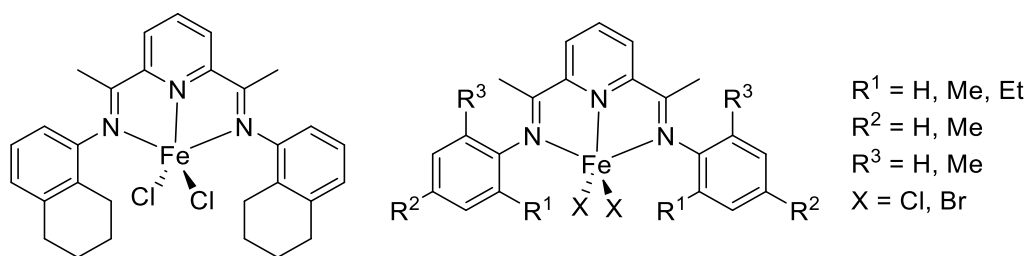
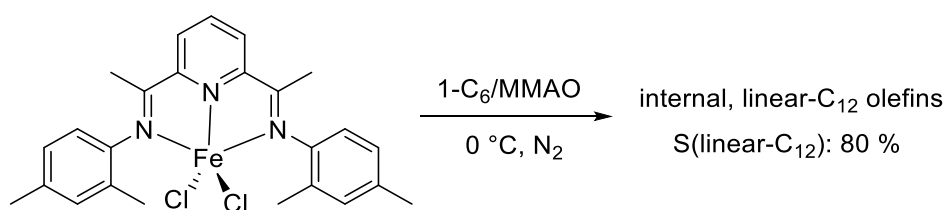


Figure 2.2 Representative catalysts tested by Small *et al.* for selective dimerisation of 1-hexene.²²

The highest selectivity observed for linear dodecene formation from 1-hexene was found with an Fe-catalyst with N-N-N ligand with *ortho*- and *para*-methyl groups (shown in **Scheme 2.5**). Using modified methylaluminoxane (mMAO) as an activator with an Al:Fe ratio of 390 at 0 °C under a purge of nitrogen, Small *et al.* were able to demonstrate 1-hexene dimerisation with 80% selectivity towards linear, internal-dodecene formation.²²



Scheme 2.5 Selective 1-hexene dimerisation to linear dodecenes as reported by Small *et al.*²²

In 2003, Small expanded upon his previous study with an additional investigation around pyridine *bis*(imine) cobalt complexes (**Figure 2.3**).²⁴ Here, Small investigated the selective dimerisation of propylene to linear hexenes, obtaining the highest known selectivity at the time to linear dimerisation of 99.8% with reasonable activities ranging from 7,400–17,100 g (g Co)⁻¹ h⁻¹.²⁴

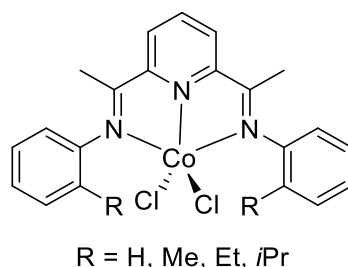
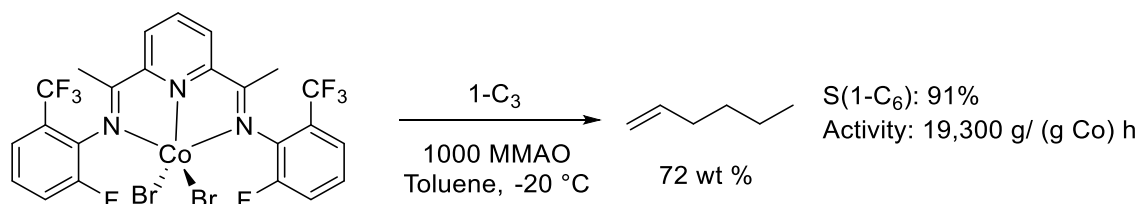


Figure 2.3 Pyridine *bis*(imine) cobalt complexes for selective propylene dimerisation.²⁴

Small found that by substituting the *ortho*-position on the phenyl ring bound to the imine (Figure 2.3, R) with an isopropyl group, the catalyst precursor formed resulted in 70% selectivity to hexene, with 99.8% selectivity for linear hexenes, of which 59% were found to be 1-hexene.²⁴ This percentage of 1-hexene within the C₆ fraction is much greater than would be predicted based on thermodynamic arguments (<5%), as the internal olefin is inherently thermodynamically more stable. The process of isomerisation from an LAO to an LIO is driven by the relative rates of olefin insertion into M-H vs M-C bonds. The relative rate for olefin insertion into an M-H bond is usually ~10⁵ greater than insertion to an M-C bond, resulting in internal isomer formation.²² Consequently, this results in isomerisation being facile and hence the formation of LIOs.

The organic product distributions obtained by Small suggested a simple step-wise mechanism for the dimerisation of propylene with cobalt and iron *bis*(imino)pyridine catalysts due to the high degree of selectivity towards linear products observed.²⁴ While the pyridine *bis*(imine) cobalt complexes were successful for exceptional linearity within hexene formation, the activities found were lower than those of their previously investigated iron analogues.^{22–24}

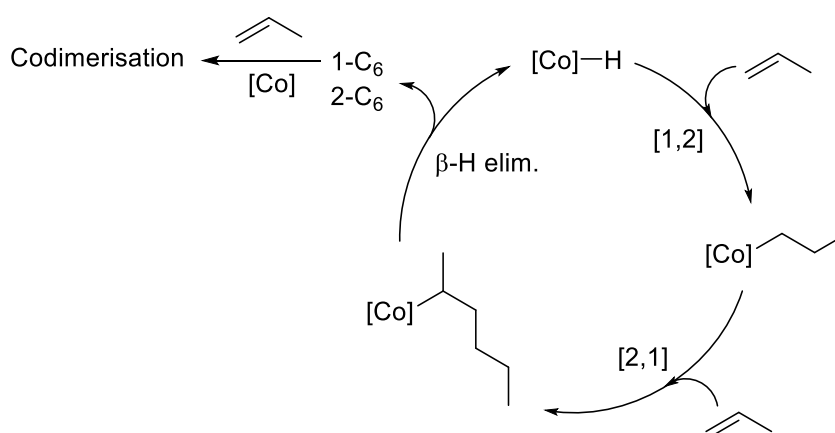
In 2005 Gibson and Tellmann investigated the effect of trifluoromethyl substituents at the *ortho*-position on the phenyl bound to imine upon the selectivity of propylene dimerisation by cobalt *bis*(imino)pyridine catalysts.²⁵ Using catalysts of the type displayed in **Scheme 2.6**, Gibson and Tellman were able to dimerise propylene with selectivity ranging between 72 and 92%.²⁵



Scheme 2.6 Selective dimerisation of propylene as described by Gibson *et al.*²⁵

In a similar fashion to Small, Gibson and co-workers also observed a high selectivity for propylene dimerisation to linear hexene. However, the addition of *ortho*-trifluoromethyl and *ortho*-fluoride groups within the systems tested by Gibson and co-workers resulted in increasing the observed activities, which ranged from 261–27,200 g (g Co)⁻¹ h⁻¹.^{24,25} Using the cobalt *bis*(imino)pyridine catalyst and conditions displayed in **Scheme 2.6**, propylene was dimerised to linear hexene, making up 72 wt% of the products obtained; additional products observed were mostly C₉ and C₁₂ fractions. While the dimerisation selectivity does not match what has been observed in previous systems, within the C₆ fraction, it was noted that the selectivity towards 1-hexene formation was up to 91%. Again, the high selectivity towards linearity was attributed to step-wise (1,2- then 2,1-insertion) addition of

propylene.²⁵ However, after analysis of the higher ($n > 2$) oligomerisation products obtained (C_9/C_{12}), the mechanism by which the observed selectivity occurs was re-evaluated. The high linearity observed in $n > 2$ fractions suggest stepwise insertion of $n > 2$ propylene cannot be the mechanism by which the highly linear C_9 and C_{12} fractions were forming.²⁵ Gibson therefore suggests a mechanism by which initial propylene units insert in (1,2) then (2,1) modes to obtain the linear dimer.²⁵ At this point, the linear C_6 olefin is released *via* β -hydride elimination, resulting in the active “Co-H” species and a range of hexenes. To obtain high linearity in the C_9/C_{12} fractions, Gibson suggests co-dimerisation of 1-hexene produced with propylene occurs to afford the apparent ‘trimer’ product, carrying the assumption that for cobalt *bis*(imino)pyridine systems, chain termination rates are greater than propagation through a 1-hexene insertion pathway.²⁵ A representation of this mechanism is shown in **Scheme 2.7**.



Scheme 2.7 Proposed mechanism for selective 1-hexene and linear C_9 fractions formation.²⁵

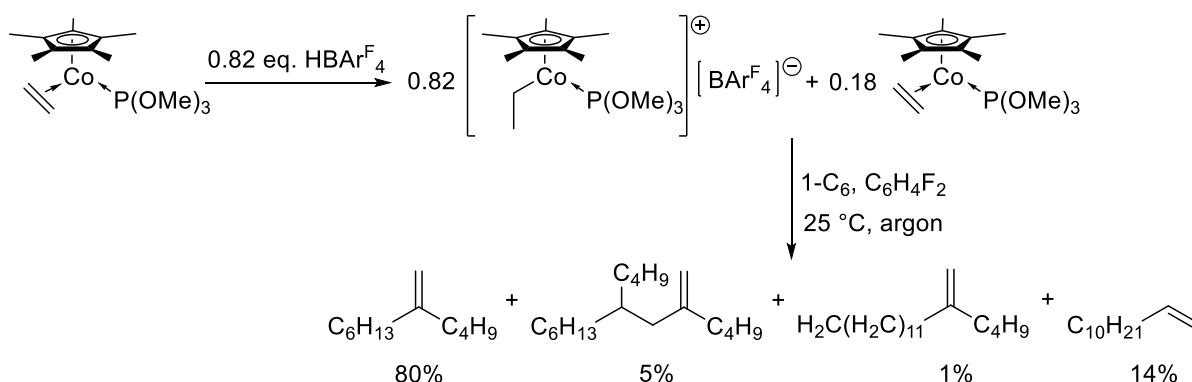
While these results for propylene dimerisation to 1-hexene are encouraging, unfortunately when Gibson *et al.* tested these systems on 1-butene and 1-hexene substrates, the linear, internal olefins were formed almost exclusively.²⁵

2.1.3.1 Brookhart and Broene: Selective 1-Hexene Dimerisation

The most significant example of selective LAO dimerisation was published in 2005 by Brookhart and Broene. This study reports unprecedented selectivity towards dimerisation of 1-hexene to 1-dodecene, affording the linear α -olefin as 14% of the product mixture.²⁶ While 14% selectivity may seem low, when the aforementioned mechanisms of isomerisation to branched products and the inherent thermodynamic preference for formation of the internal olefins are taken into consideration, obtaining 14% selectivity to 1-dodecene is an extraordinarily significant result.

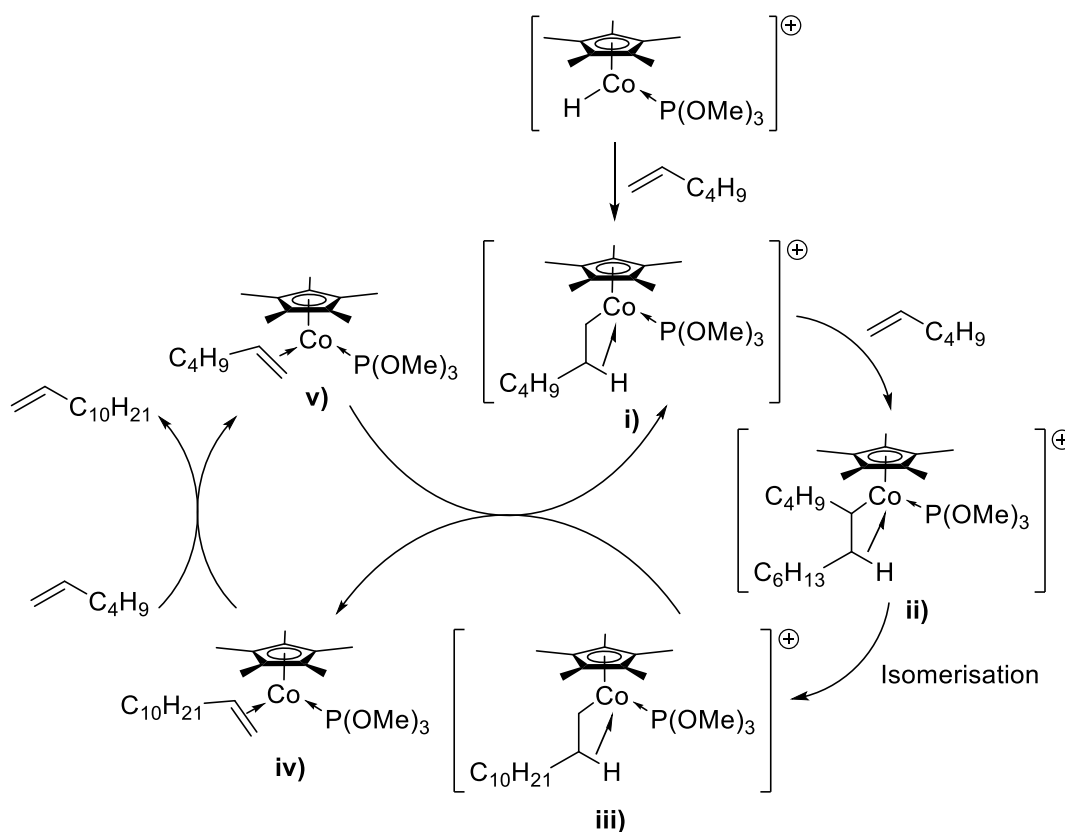
Brookhart and Broene reported oligomerisation of 1-hexene by the catalytic precursor $Cp^*Co(P(OMe)_3)(\eta^2-C_2H_4)$ in the presence of a sub-stoichiometric quantity of $HBAr^F_4$ ($\{[3,5-$

$(\text{CF}_3)_2\text{C}_6\text{H}_3)_4\text{B}][(\text{Et}_2\text{O})_2\text{H}]$) in 1,2-difluorobenzene solution (40 vol. % 1-C₆) at 25 °C under argon to result in the products displayed in **Scheme 2.8**.²⁶ Using the conditions described in **Scheme 2.8**, 1-dodecene was formed as 14% of the product mixture by GC analysis, alongside vinylidene dimers and trimers after 3.5 hours. This system also displayed similar reactivity for the dimerisation of 1-octene and 1-butene, demonstrating the potential for versatility within dimerisation reactions. Under the same conditions, with the run time extended to 12 hours, the product mixture was found to be the same, but with isomerisation of 1-dodecene to internal olefins.²⁶



Scheme 2.8 Catalyst formation and organic product mixture obtained reported by Brookhart and Broene for selective 1-hexene di- and tri-merisation.²⁶

Brookhart and Broene proposed that the approximate 4:1 ratio of ethyl salt, $[\text{Cp}^*\text{Co}(\text{P}(\text{OMe})_3)_2\text{C}_2\text{H}_5][\text{BARF}_4]$, to the neutral, unactivated ethylene complex obtained through use of a deficit of HBARF_4 was key to obtaining selectivity towards 1-dodecene. After the initiation cycle (one turnover and loss of the ethyl group) the active species can be described with a hydride as a chain carrier.²⁶ The step-wise insertion mechanism proposed to explain the observed reactivity with sub-stoichiometric HBARF_4 is given in **Scheme 2.9**.



Scheme 2.9 Proposed mechanism for selective 1-hexene dimerisation by Brookhart's pentamethylcyclopentadienylcobalt catalyst.²⁶

It could be envisaged that the steric bulk of the Cp* moiety at the Co centre dictates initial 1,2-insertion of 1-hexene, followed by 2,1-insertion of an additional 1-hexene (**Scheme 2.9(ii)**). Rapid isomerisation to the favoured, linear metal-alkyl cationic species can then occur, resulting in a primary, β -agostic-stabilised intermediate (iii).²⁶ This intermediate is required to give rise to the production of linear α -olefin dimers. The linear metal-alkyl complex (iii) will result due to the steric bulk imposed by the Cp* moiety, disfavoring branched (ii) metal alkyl species. The agostic dodecyl complex (iii) could then undergo hydride exchange with the neutral (unactivated) 1-hexene complex (v), allowing regeneration of the cationic, agostic hexyl species (i) and in a new, neutral 1-dodecene complex (iv). Ligand exchange between another molecule of 1-hexene with the coordinated 1-dodecene on (iv) will liberate free 1-dodecene and regenerate the neutral, unactivated, 1-hexene complex (v).²⁶

The turnover frequency of the catalytic system reported by Brookhart and Broene is low (3.7 h^{-1}).²⁶ The poor activity of this catalytic system can be attributed to catalyst instability. It is therefore of interest to develop this system such that catalyst stability, and therefore activity, is improved. For instance, introduction of a pendant neutral donor ligand to the Cp-functionality to act as a *hemi*-labile donor ligand could aid the overall stability of the system.

2.1.4 The Bonding of Cyclopentadienyl Ligands to Metals

One aspect of the work described in this thesis chapter aims to use the system employed by Brookhart $[\text{Cp}^*\text{Co}(\text{H})\{\text{P}(\text{OMe})_3\}]$, as a starting point and expand the ligand series through systematic variation of the L_2X (Cp derivative) moiety and neutral L-type $\{\text{P}(\text{OMe})_3\}$ donor. However, in order to better understand the role of the ligands and to gain insight into how a catalyst can be tuned, it is important to understand the nature of the bonding of cyclopentadienyl moieties to a metal centre. For simplicity, the focus of this discussion will be between metal d orbitals and cyclopentadienyl moiety; the interactions between metal p orbitals and cyclopentadienyl will not be discussed.

To understand the bonding between a metal and a Cp moiety, first the atomic orbitals within the Cp unit must be understood. The linear combination of atomic orbitals (LCAOs) for a Cp moiety are shown in **Figure 2.4** and consist of a_1 , e_1 and e_2 levels, which have 0, 1 and 2 nodal planes, respectively.

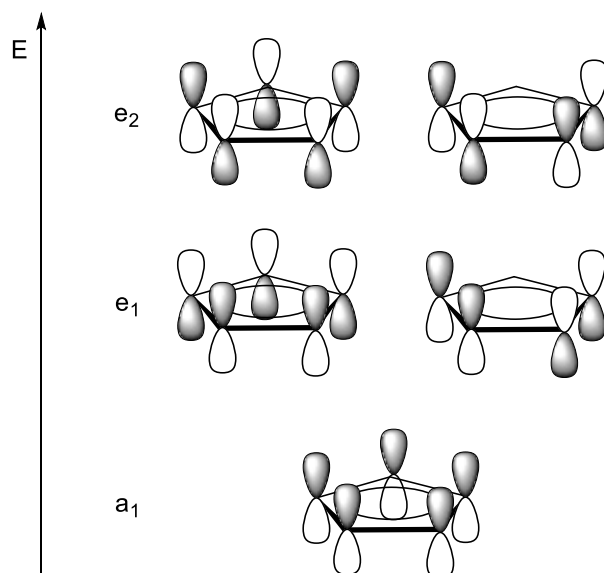
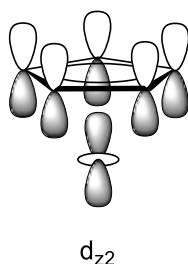


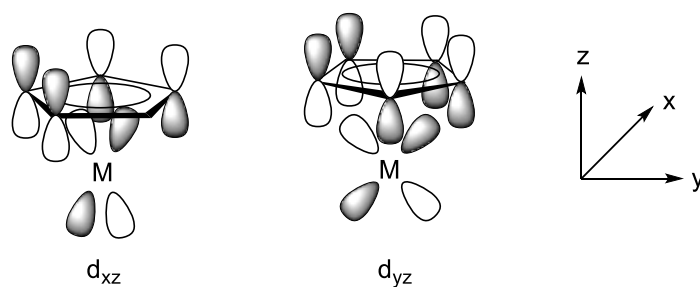
Figure 2.4 Linear combination of the atomic orbitals of a cyclopentadienyl moiety.

The bonding between Cp and a metal can be thought of as having three components: the bonding between a_1 , e_1 and e_2 LCAOs with d orbitals on the metal, which are shown in **Figure 2.5**. First consider the face-on σ -interaction between d_{z^2} and $\text{Cp-}a_1$, which essentially amounts to a non-bonding interaction. Typically, σ -interactions would be expected to exhibit the strongest bonding, however in the case of ring systems there is negligible orbital overlap and so this is the weakest interaction observed. The d_{xz} and d_{yz} orbitals on the metal do have good overlap with $\text{Cp-}e_1$ and strong π -interaction results: $M(d_{xz}, d_{yz}) \leftarrow \text{Cp}(e_{1g})$. Finally, a δ -type ‘face-on’ interaction exists between metal $d_{x^2-y^2}$ and d_{xy} orbitals and $\text{Cp-}e_2$, this $[\text{Cp}(e_{2g}) \leftarrow M(d_{x^2-y^2}, d_{xy})]$ π -interaction is weak due to poor overlap.

- a) Non-bonding σ -interaction between d_{z^2} orbital on M and cyclopentadienyl a_1 LCAO



- b) π -donation by cyclopentadienyl e_1 LCAOs to d_{xz} and d_{yz} orbitals on M



- c) δ interaction: π -acceptance by cyclopentadienyl e_2 LCAOs from d_{xy} and $d_{x^2-y^2}$ orbitals on M

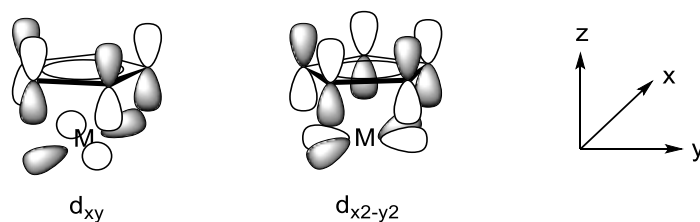


Figure 2.5 Partial frontier MO diagrams depicting the interactions between a cyclopentadienyl-moiety and d orbitals on a metal.

The interactions discussed above assume a η^5 -coordination of the cyclopentadienyl moiety, however cyclopentadienyl moieties and derivatives (*e.g.* Cp*, indenyl, fluorenyl) are capable of multiple coordination modes depending on the environment of the metal centre. It is therefore important to consider alternative binding modes of Cp derivatives.

2.1.5 Coordination Modes of Cp-type Ligands to a Metal

The different coordination modes Cp moieties and derivatives are capable of have been widely studied.²⁷ The metal environment has been shown to direct the coordination mode of these moieties through steric and electronic influence, as such, any additional ligands coordinated to the metal and the oxidation state of the metal can alter the binding mode. For instance, cyclopentadienyl, indenyl

and fluorenyl ligands have been shown to be susceptible to ring-slippage (e.g. $\eta^5 \rightarrow \eta^3$, $\eta^3 \rightarrow \eta^1$), a depiction of which is shown in **Figure 2.6**.

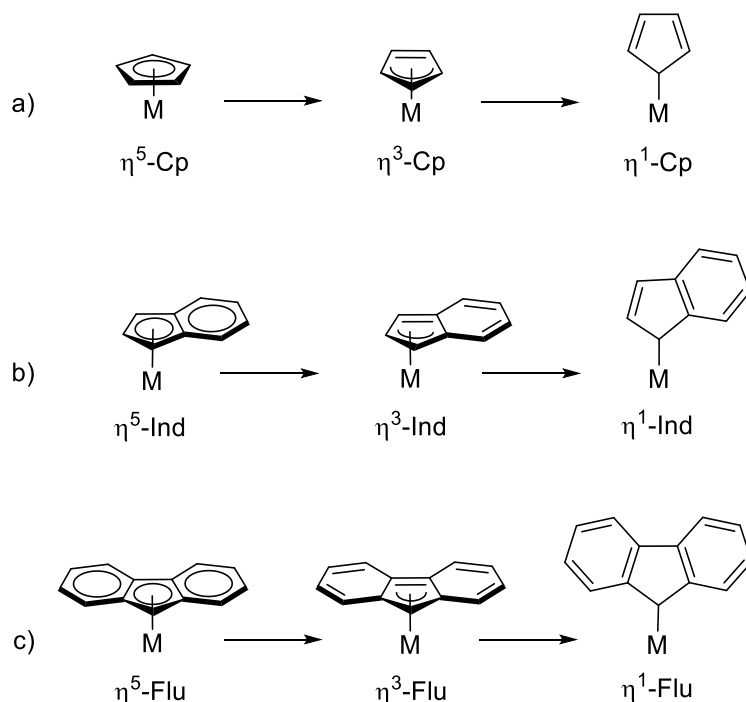
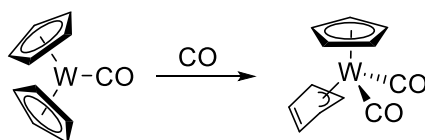


Figure 2.6 Ring slippage of a) cyclopentadienyl, b) indenyl and c) fluorenyl ligands.^{27,28}

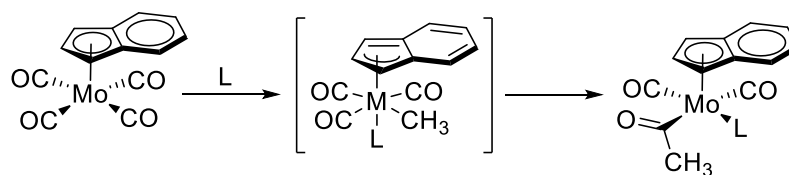
The first, non-disputed, example of ring-slippage occurring for a cyclopentadienyl system was not reported until 1978 when Huttner and co-workers obtained a single crystal molecular structure of ring-slipped Cp ligand within a tungsten complex. The non-planarity of the ‘slipped’ Cp ring is clear evidence of the reduction in the ligand’s hapticity from η^5 to η^3 as a result of coordination of a second CO molecule, thus allowing the complex to avoid a high energy $20 e^-$ configuration (**Scheme 2.10**).²⁹



Scheme 2.10 Ring-slipped Cp moiety induced by CO binding to avoid a $20e^-$ configuration.^{29,30}

While examples of ring-slipped Cp moieties are still rare, indenyl- and fluorenyl-systems have much stronger propensity for isomerisation from $\eta^5 \rightarrow \eta^3$ as a result of the fused benzene ring systems present, which can stabilise the η^3 -coordination through delocalisation of electron density within the aromatic fused ring systems.²⁷ This ring-slipping has been termed ‘the indenyl effect’ and has been shown to play a crucial role in many catalytic transformations.³¹ For instance, the flexibility of the

hapticity of the indenyl moiety allows catalytic carbonylation when induced by the binding of an additional neutral donor ligand. Ring-slippage of indenyl from $\eta^5 \rightarrow \eta^3$ creates a vacant site for coordinating a ligand (L) that, for instance, can enable migratory insertion (**Scheme 2.11**).^{32–35} The ‘indenyl effect’ described above has been shown to be even more pronounced for fluorenyl-moieties.³¹



Scheme 2.11 Variation in the hapticity of the indenyl ligand allows carbonylation when promoted by coordination of additional ligand, L (PPh₃).^{33,34}

The multiple binding modes available to these ligands make these very interesting choices for use in transition metal catalysed transformations. The flexibility within coordination mode that these ligands have can allow transformations to take place through creation of vacant sites to allow substrate binding.

2.1.6 Cp-containing *Hemi*-labile Ligands

The unique coordination modes possible within *hemi*-labile ligand systems makes these ligands of great interest within homogeneous catalytic applications. The presence of a *hemi*-labile donor moiety can allow reversible creation of a vacant site on the metal centre for reaction to occur at, or can fill a vacant site (stabilising the metal complex) when required.

The introduction of pendant neutral donor functionalities to, *e.g.* cyclopentadienyl fragments, is an established means by which the chemistry of resulting metal complexes can be altered.^{36–38} The coordination of a pendant donor group is entropically favoured when compared to coordination of a ‘free’ donor group, making ‘tethered’ ligands an attractive prospect. These dual-functionalised ligands have two possible bonding modes: *inter*- or *intra*-molecular (**Figure 2.7**), where intramolecular bonding is typically favoured.³⁶

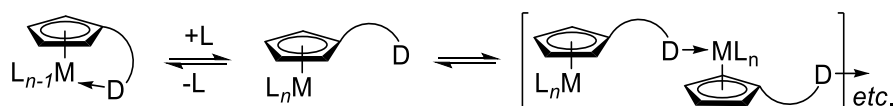
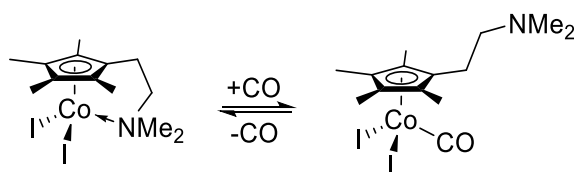


Figure 2.7 *Hemi*-labile coordination of a pendant donor group: *intra*-molecular (LHS) and *inter*-molecular (RHS) bonding modes possible for Cp-fragments with pendant donor, D.

The strength of the interaction between the ligand moieties (*e.g.* Cp or D) and metal can be approximated using Pearson's Hard Soft Acid Base (HSAB) theorem: hard ligands (*e.g.* poorly polarisable C-, O-, N-donors, *etc.*) combine preferentially with hard metals (*e.g.* early transition metals) and soft ligands (*e.g.* polarisable P-, S-donors, *etc.*) combine preferentially with soft metals (*e.g.* late transition metals).³⁹ For instance, in hard metal-based systems, it has been suggested that the hard donor moiety will be strongly bound to the metal, but a soft pendant donor will be less strongly bound to the metal and, as a result, is potentially labile.^{36–38} Stabilisation as a result of the chelate effect allows stabilisation of unflavoured hard-soft interactions. Therefore, the pendant soft donor moiety could be labile in its coordination to the metal centre (**Figure 2.7**); these ligands are termed '*hemi-labile*'.⁴⁰

Some of the most commonly employed *hemi-labile* donor pairs within Cp-chemistry are Cp[∧]P^{3,38,41–50} Cp[∧]N,^{36,47,51–61} Cp[∧]O^{36,37,52,62–65} and Cp[∧]S^{36,38,66–68}. For instance, the *hemi-lability* of Cp-N complexes on cobalt(III) has been demonstrated by Jutzi and co-workers, through the dissociation/association of a CO ligand with amino-functionality acting as a *hemi-labile* donor moiety (**Scheme 2.12**).⁶⁹



Scheme 2.12 *Hemi-labile* behaviour of Cp^{*}-CH₂CH₂-NMe₂ with CO association/dissociation on cobalt(III).⁶⁹

2.2 [(L₂X)-L]-type Constrained Geometry Catalysts

The low activity of the [Cp^{*}Co(P(OMe)₃)C₂H₄][BAR^F₄] catalyst presented by Brookhart and Broene for LAO dimerisation can be attributed to poor catalyst stability.²⁶ It is postulated that this low activity can be improved through stabilising the catalyst precursor (**1**) through the addition of a *hemi-labile* pendant-donor to Cp^{*} or derivative (Cp, Ind, Flu, *etc.*). These catalysts would therefore have a so-called constrained geometry, dictated by the chain length of the “tether” in use.⁶⁹ Electronic and steric controls can be imposed on the catalyst through choice of both the pendant donor and of the Cp^{*} derivative. Examples of targeted constrained geometry catalysts (CGCs) are shown in **Figure 2.8**.

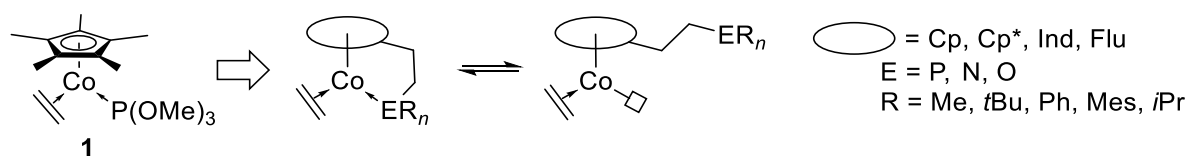
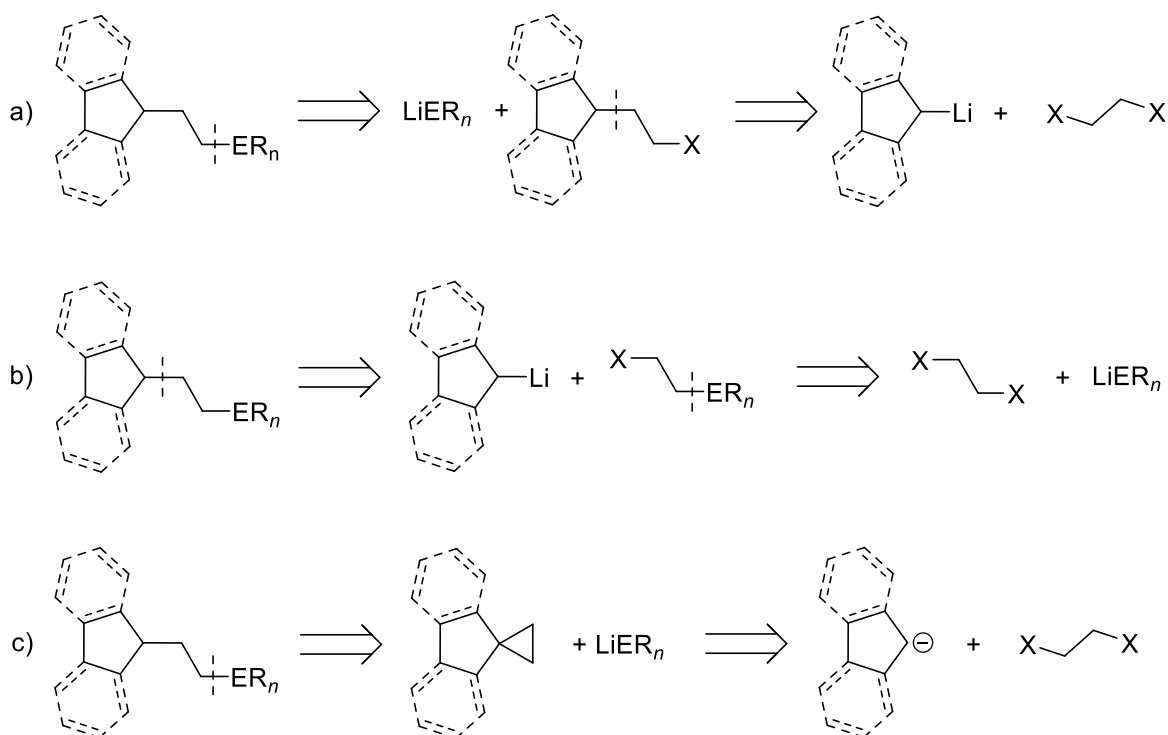


Figure 2.8 Proposed stabilisation of the pro-catalyst, **1**, through introduction of a *hemi*-labile donor moiety capable of introduction and filling of a vacant site, □, with example targeted constrained geometry type-catalyst precursors.

2.2.1 Synthetic Routes towards (L₂X-CH₂CH₂-ER_n)-type Ligands

Three retrosynthetic routes towards the synthesis of the target L₂X-CH₂CH₂-ER_n type ligands can be envisioned (**Scheme 2.13**). The synthetic route shown in **Scheme 2.13a** yields a ubiquitous intermediate (L₂X-CH₂CH₂-X type) for quick successive reactions to produce “tethered” ligands with varying ER_n groups. The synthetic route shown in **Scheme 2.13b** would allow quick successive reactions to produce “tethered” ligands with various different L₂X groups *via* an X-CH₂CH₂-ER_n intermediate. In contrast, the approach depicted in **Scheme 2.13c** requires ring-opening of a *spiro* cyclopropane-moiety through reaction with, *e.g.* Li-ER_n, a reaction driven by the release of ring-strain within the cyclopropane-moiety.



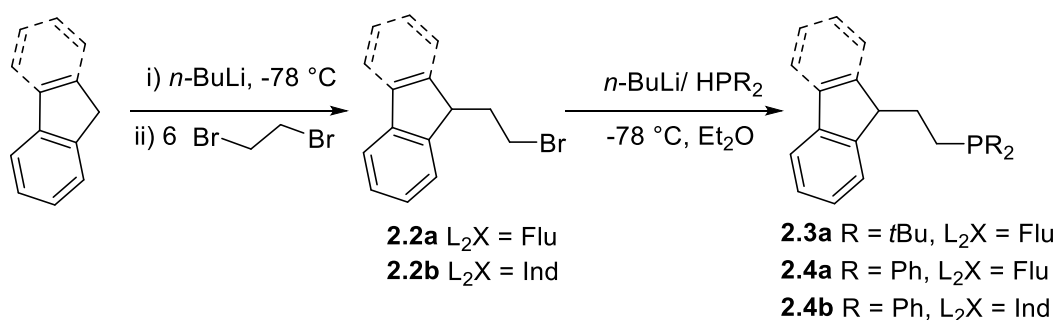
Scheme 2.13 Example retrosynthetic pathways for the synthesis of (L₂X)-CH₂CH₂-ER_n type ligands.

The work presented within this thesis chapter targets several ligand structures, as shown in **Figure 2.8**. It was found that the synthetic routes required to produce compounds with various different ER_n and L_2X -moieties depends on the moiety in question. For ease, synthetic route outlined below are therefore split into two main sections: those concerned with Cp- and Cp* derivatives and those concerned with Flu- and Ind-derivatives.

2.2.1.1 Flu- and Ind-derivatives with a 'C₂-tether'

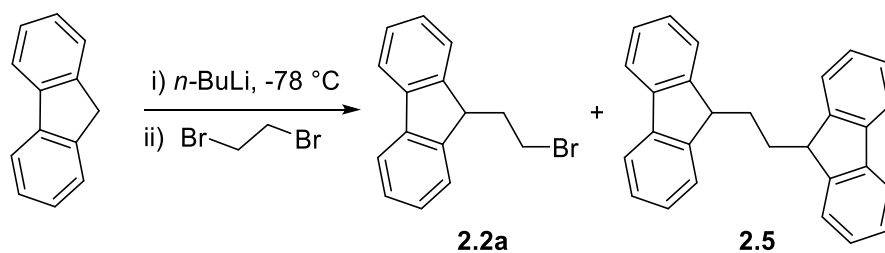
2.2.1.1.1 Synthesis of $(L_2X)-CH_2CH_2-PR_2$ where L_2X = Indenyl or fluorenyl

Initially, the retrosynthetic route shown in **Scheme 2.27a** was used in attempts to produce ligands functionalised with Flu- and Ind-moieties. The synthetic route shown in Scheme 2.14 was proposed in an attempt to synthesise compounds such as **2.3** and **2.4** (derivatives of Flu- $CH_2CH_2-PR_2$ and Ind- $CH_2CH_2-PR_2$) *via* the synthesis of **2.2** (L_2X)- CH_2CH_2-Br). The desired ligands **2.3** and **2.4** have not previously been reported, however routes to the synthesis of **2.2** are well known.⁷⁰



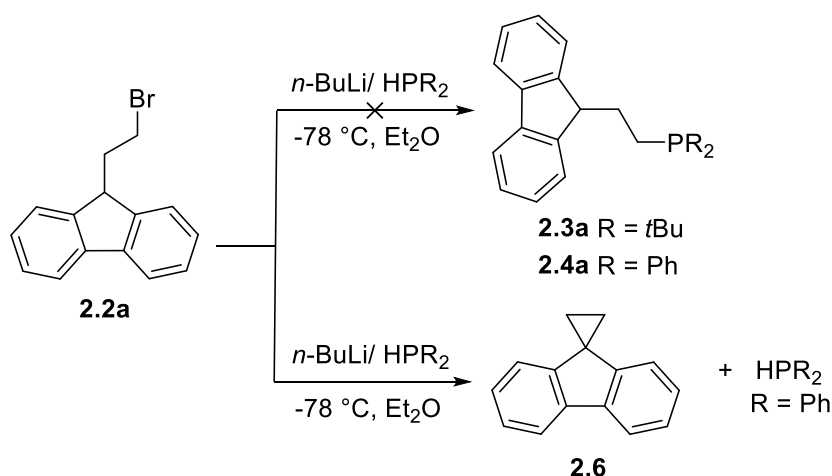
Scheme 2.14 Proposed synthesis of $L_2X-CH_2CH_2-PR_2$ -type ligands, from **2.2**.⁷⁰

1-Bromo-(9'-fluorenyl)ethane (**2.2a**) can be readily prepared by the route presented in the literature, which uses *n*-butyllithium to deprotonate fluorene before subsequent reaction with an excess of 1,2-dibromoethane.⁷⁰ The first attempt at synthesis of **2.2a** was disrupted through a hotplate failure, resulting in loss of stirring of the reaction post 1,2-dibromoethane addition. The results of this loss of stirring clearly display the requirement for an excess of 1,2-dibromoethane, as the major product obtained was 1,2-*bis*-(9'-fluorenyl)ethane (**2.5**), shown in **Scheme 2.15**, which was separated from **2.2a** through exploitation of their different rates of crystallisation from diethyl ether. The synthesis of **2.2a** was repeated with no interruption to stirring, which produced **2.2a** in 68% yield. The identities of both **2.2a** and **2.5** were confirmed through comparison of ^1H and $^{13}\text{C}\{^1\text{H}\}$ NMR spectra to known values.^{70,71}



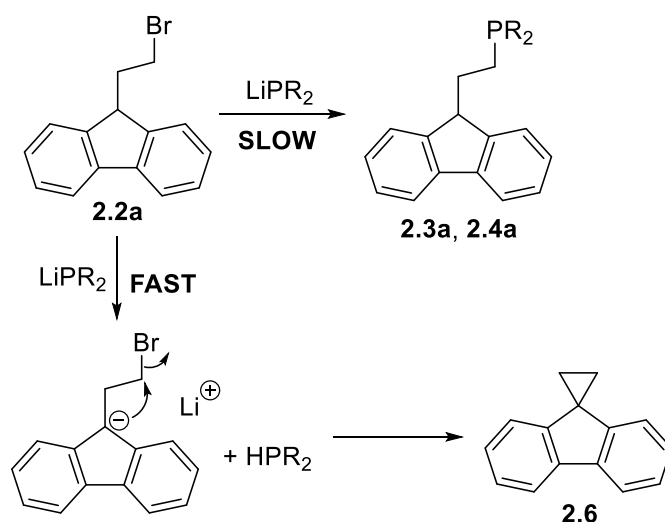
Scheme 2.15 Production of 1,2-bis(9'-fluorenyl)ethane (**2.5**), formed when 1,2-dibromoethane is not available in excess.⁷¹

Using 1-bromo-(9'-fluorenyl)ethane (**2.2a**), it was proposed that the synthesis of Flu- $\text{CH}_2\text{CH}_2\text{-PR}_2$ -type ligands (**2.3a**, **2.4a**) could be achieved through use of a lithium-halogen exchange. However, when these reactions were performed with HPPH_2 (prepared in accordance to literature procedure, 80% yield)⁷² and HP^tBu_2 (obtained from group supplies), in both cases the major product obtained was *spiro*[cyclopropane-1,9'-fluorene] (**2.6**) (**Scheme 2.16**).



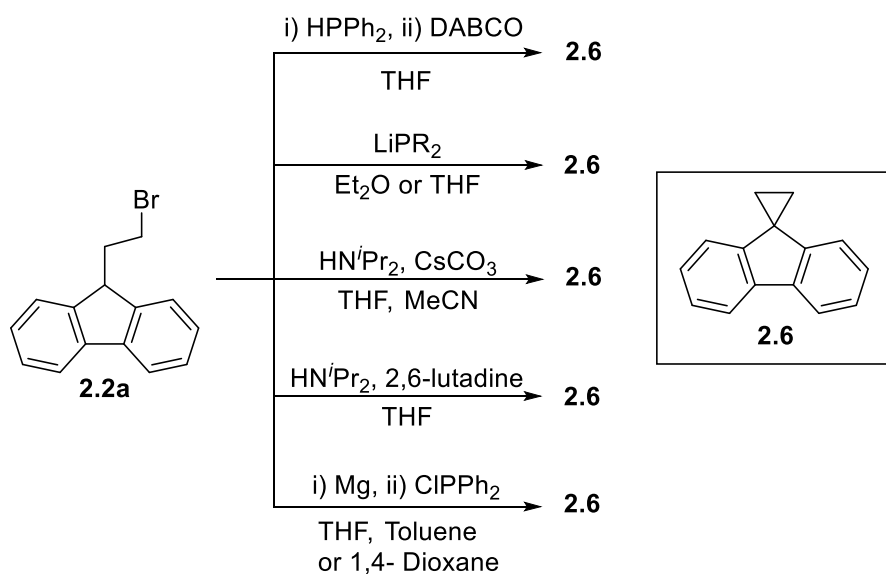
Scheme 2.16 Formation of *spiro*[cyclopropane-1,9'-fluorene], **2.6**, from **2.2a** upon treatment with LiPR_2 .

It is postulated that the rate of deprotonation competes with the desired nucleophilic substitution reaction. In the above reactions, LiPR_2 was formed independently and added slowly to a solution of **2.2a**, resulting in the concentration of **2.2a** to be much greater than LiPR_2 , allowing complete consumption of the lithium salt *via* deprotonation of **2.2a**. Subsequent *intramolecular* nucleophilic substitution allows formation of the *spiro*-cycle (**Scheme 2.17**).



Scheme 2.17 Proposed mechanism for the formation of *spiro*[cyclopropane-1,9'-fluorene] (**2.6**).

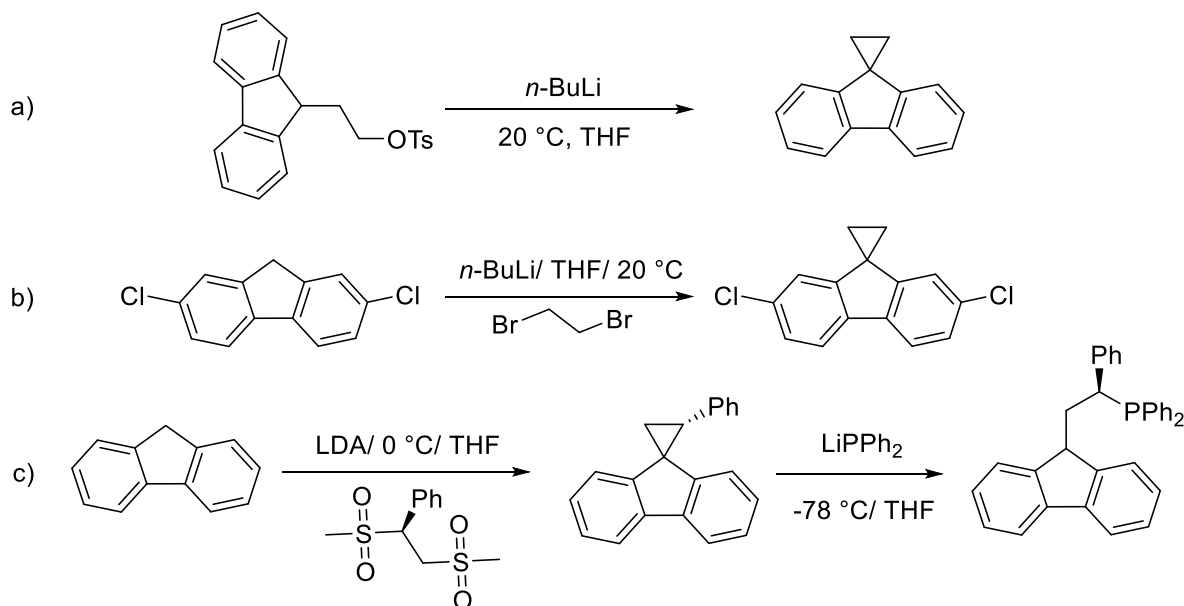
The formation of *spiro*[cyclopropane-1,9'-fluorene], **2.6**, was also observed within many additional reactions whenever attempts to synthesise Flu-CH₂CH₂-ER_n from the intermediate Flu-CH₂CH₂-Br (**2.2a**) were undertaken. A summary of the reaction conditions used which led to the formation of **2.6** as the major product is shown in **Scheme 2.18**.



Scheme 2.18 Observed formation of *spiro*[cyclopropane-1,9'-fluorene] (**2.6**), from **2.2**.

The formation of **2.6** and derivatives of **2.6** are well documented within literature, when attempts have been made to produce asymmetric 1,2-substituted ethanes where 9'-fluorenyl is one of the substituents for use in, *e.g.* metal-catalysed ethylene oligomerisation reactions.⁷³ Some examples of such reactions are shown in **Scheme 2.19a,b**.^{74,75} Notably, the synthesis of (*S*)-[2-(9'-fluorenyl)-1-

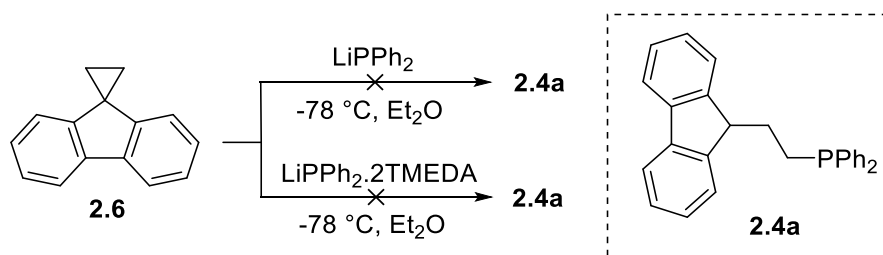
phenyl-ethyl]-diphenylphosphane has been reported through ring opening of (*S*)-*spiro*-1-(9'-fluorenyl)-2-phenyl-cyclopropane through use of LiPPh₂ (Scheme 2.19c).⁷³



Scheme 2.19 Reported formation of *spiro*[cyclopropane-1,9'-fluorenyl]-derivatives.^{73–75}

Frustratingly, deliberate attempts to produce the *spiro*-cyclopropane compound, **2.6** were met with little success (Scheme 2.20). When 1,2-dichloroethane is reacted with fluorene in the presence of NaOH, no reaction was observed to have taken place by ¹H NMR spectroscopic analysis of the products. This may be the result of the poorer leaving ability of chloride when compared to bromide and that NaOH is a weaker base than *e.g.* *n*-butyllithium (*c.f.* pK_a 14.7 vs 50, respectively). When **2.2a** is treated with NaOH, again, no reaction was observed to have taken place, further suggesting this base is not strong enough (note: NaOH is the base of choice for formation of *spiro*[cyclopropane-1,1'-cyclopentadiene]).⁷⁶

within this work were met with little success, seemingly a result of the lack of substitution of the cyclopropane ring (**Scheme 2.22**).



Scheme 2.22 Attempted synthesis of **2.4a** from **2.6** using *n*BuLi/HPPH₂ or *n*BuLi/HPPH₂/TMEDA.⁷³

The attempted synthesis of **2.4a** from HPPH₂ and **2.6** was followed by ³¹P{¹H} NMR spectroscopy. The first attempt was performed in accordance with the literature procedure, however, over the course of 2 days, regeneration of HPPH₂ was observed through growth of the characteristic peak at δ_p −40.3 ppm.^{72,73} The regeneration of HPPH₂ is not the result of incomplete deprotonation by *n*BuLi, as a signal corresponding to 100% conversion to LiPPh₂ at δ_p −35.3 ppm was observed within the ³¹P{¹H} NMR spectrum obtained prior to reaction with **2.6**. It was hypothesised at this point that the diphenylphosphide species generated was not nucleophilic enough, and so the use of TMEDA (*N,N*-tetramethylethylenediamine) was employed in an attempt to increase the nucleophilicity of the anion. A gauge of the nucleophilicity of the anion can be gathered by the relative shift to higher frequency measured by ³¹P{¹H} NMR spectroscopy, as shown in **Figure 2.9**.

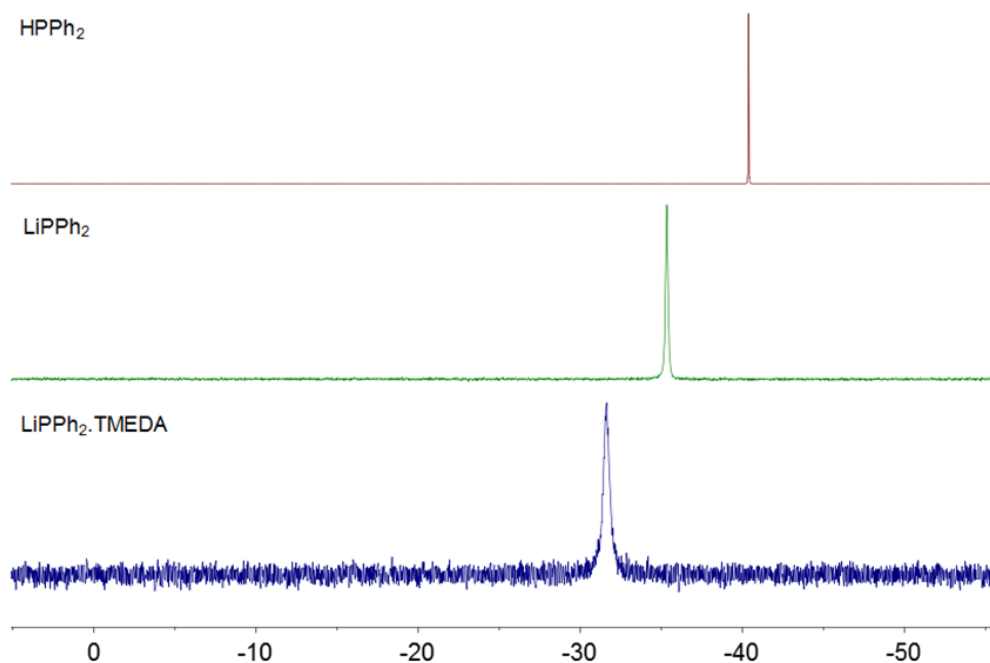
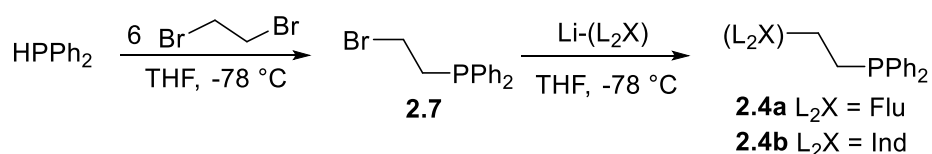


Figure 2.9 $^{31}\text{P}\{^1\text{H}\}$ NMR (Et_2O , 162.0 MHz) spectra displaying shift to higher frequency moving from HPPh_2 to LiPPh_2 and $\text{LiPPh}_2\cdot\text{TMEDA}$.

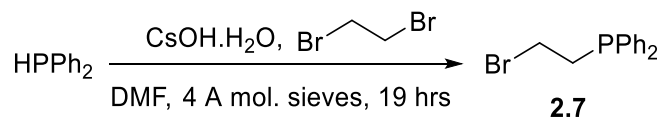
Despite successfully increasing the nucleophilicity of the diphenylphosphide moiety, the successful ring opening of **2.6** could not be confirmed. After formation of the $\text{LiPPh}_2\cdot 2\text{TMEDA}$ species, **2.6** was added and the mixture was heated at reflux for 60 hours, over which time the regeneration of HPPh_2 was observed by $^{31}\text{P}\{^1\text{H}\}$ NMR spectroscopy. After work-up of the reaction mixture, a precipitate was collected at -78°C , however, due to the small quantity of precipitate formed, analysis was unfeasible.

At this point, the method for production of $\text{Flu-CH}_2\text{CH}_2\text{-PR}_2$ type ligands was re-evaluated due to the inherent formation of **2.6** when reactions were attempted using **2** as an intermediate. A new synthetic route for the production of **2.4a** and **2.4b** [1-(diphenylphosphino)-2-(2'-indenyl)ethane] was therefore proposed *via* the synthesis of 1-bromo-2-(diphenylphosphino)ethane (**2.7**), a general scheme for this transformation is shown in **Scheme 2.23**.



Scheme 2.23 Proposed route for the synthesis of **2.4** *via* **2.7**.

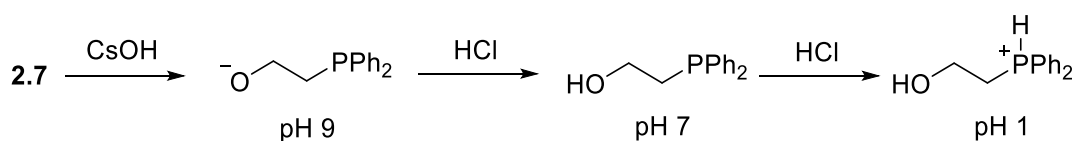
The synthesis of **2.7** has been reported in the literature starting from diphenylphosphine and 1,2-dibromoethane, as shown in **Scheme 2.24**. Honaker *et al.* reported the synthesis of **2.7** in 89% yield under mild conditions (room temperature, 19 hours) using CsOH.H₂O to mediate the reaction in DMF (dimethylformamide).⁷⁷ However, no spectroscopic data for **2.7** are disclosed in the literature.



Scheme 2.24 Literature procedure for the synthesis of **2.7**.⁷⁷

The attempted synthesis of **2.7** was carried out in accordance with the literature procedure and the reaction followed by ³¹P{¹H} NMR spectroscopy.⁷⁷ After work-up under basic conditions, a single peak was observed within the aqueous DMF solution at δ_P 21.2 ppm by ³¹P{¹H} NMR spectroscopy. At this point, the literature procedure calls for extraction of the product using DCM, however, when this was attempted, no phosphorus-containing species were observed within the ³¹P{¹H} NMR spectrum obtained. Attempts at extraction of the phosphorus-containing species into an organic medium were then carried out using hexane, diethyl ether and xylenes; in each case, a single peak was observed at δ_P 21.2 ppm within the aqueous/DMF layer, with no signal from a phosphorus-containing product being observed in the organic layer. The aqueous DMF solution was then saturated within an excess of NaCl in the presence of DCM in an additional attempt to drive extraction of the phosphorus-containing species into a DCM layer. However, ³¹P{¹H} NMR spectra obtained of the aqueous and DCM layers displayed a single peak (δ_P 21.2 ppm) within the aqueous layer only.

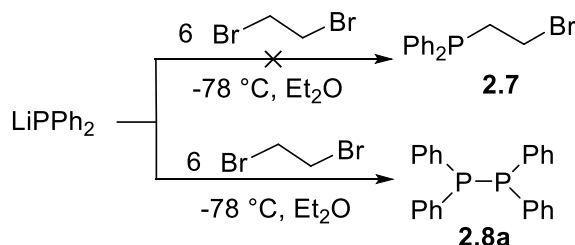
The procedure for the synthesis of **2.7** includes a basic work-up, and so it was hypothesised at this point that the transformation shown in Scheme 2.25 could have occurred due to the use of CsOH in excess. At pH 9 therefore, it was hypothesised that a 2-diphenylphosphinoethoxide species could be present, at pH 7 therefore, protonation to form 2-diphenylphosphinoethanol could aid extraction of this hypothesised product from the aqueous/DMF layer.



Scheme 2.25 Suspected transformation of **2.7** to 2-diphenylphosphinoethanol in the presence of excess CsOH.H₂O.

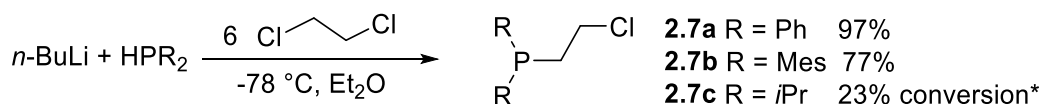
Extractions of the aqueous/DMF solution produced during the attempted synthesis of **2.7** were performed using DCM and the pH of the solution was lowered sequentially through portion-wise addition of an aqueous HCl solution to pH 7, pH 4 and pH 1, respectively. No change to previous observations were observed when the pH value was 7 or 4. However, when the pH of the solution was lowered to pH 1, a precipitate was observed. The $^{31}\text{P}\{^1\text{H}\}$ NMR spectrum of this precipitate displayed a single peak with a shift at higher frequency (when compared to the signal observed previously) at δ_p 30.8 ppm, however, due to the small quantity of precipitate isolated, additional analysis was not performed. It could be speculated that this shift at higher frequency could result from the presence of the phosphonium salt of 2-diphenylphosphinoethanol (**Scheme 2.25**).

Due to the difficulties highlighted above that were encountered using the previously-reported literature synthesis of **2.7**, an alternative synthetic route was proposed.⁷⁷ Under the same conditions used within the synthesis of **2.2**, the synthesis of **2.7** was attempted using an excess of 1,2-dibromoethane and LiPPh_2 (**Scheme 2.26**).⁷⁰ However, from comparison of the ^1H , $^{13}\text{C}\{^1\text{H}\}$ and $^{31}\text{P}\{^1\text{H}\}$ MMR spectra obtained of the white powder product produced within this reaction, to literature values the product was determined to be tetraphenyldiphosphine (**2.8a**).⁷⁸ The formation of tetraphenyldiphosphine *via* reductive coupling of ClPPh_2 is a common occurrence, the formation of **2.8a** is well documented within literature.⁷⁹



Scheme 2.26 Attempted synthesis of **2.7**, where the observed product is tetraphenyldiphosphine (**2.9**).

It is proposed that the use of 1,2-dibromoethane results in the formation of **2.8a** *via in situ* formation of BrPPh_2 , due to the moderately good leaving ability of a bromide group, followed by reductive coupling of the generated bromophosphine species. While the use of 1,2-dibromoethane did not yield the desired results, when 1,2-dichloroethane is used instead, the desired compound **2.7a** can be synthesised successfully along with derivatives (**Scheme 2.27**).



Scheme 2.27 Synthesis of Cl-CH₂CH₂-PR₂ compounds, **2.7a-c**, from 1,2-dichloroethane. *Determined by ³¹P{¹H} NMR spectroscopy

The successful syntheses of **2.7a-c** were confirmed by NMR (¹H, ¹³C{¹H}, ³¹P, ³¹P{¹H}) spectroscopic methods. Compounds **2.7a** and **2.7b** were produced in good to excellent yield (97% and 77%, respectively) and show similar characteristic singlet signals in their ³¹P NMR spectra with shifts at δ_P – 20.1 and –28.3 ppm, respectively. The synthesis of compound **2.7c** is less straightforward, and as such a sample of **2.7c** was not able to be isolated from the mixture of other phosphorus-containing products that were also present, as shown in the ³¹P NMR spectrum obtained (**Figure 2.10**).

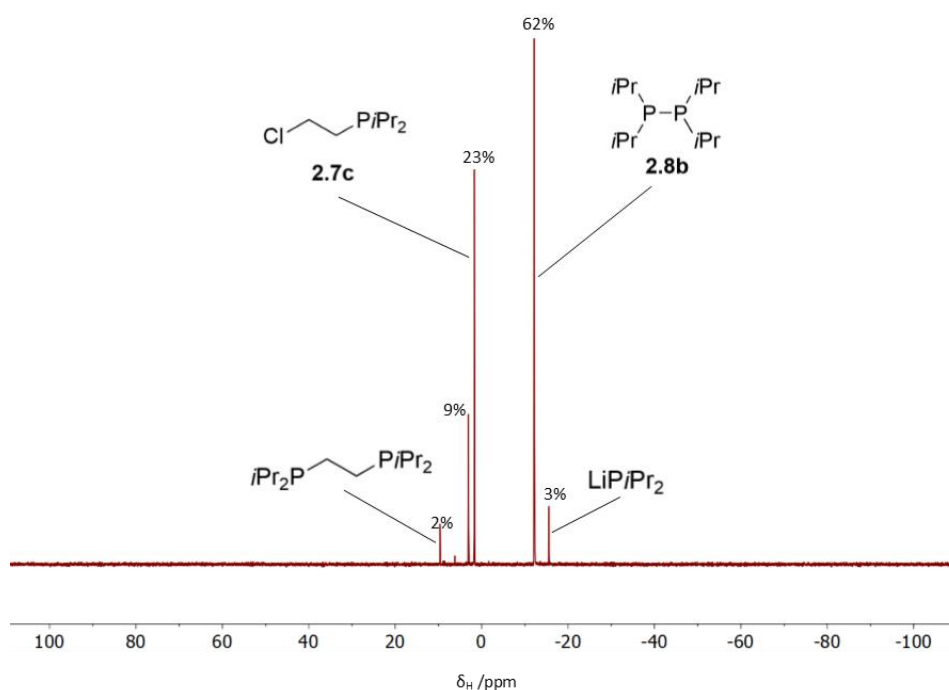
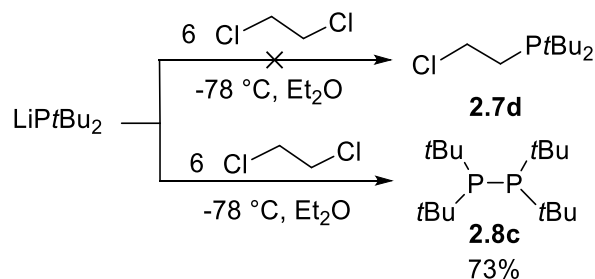


Figure 2.10 ³¹P{¹H} NMR (Et₂O, 162 MHz) spectrum of the reaction mixture obtained during attempted synthesis of **2.7c**.

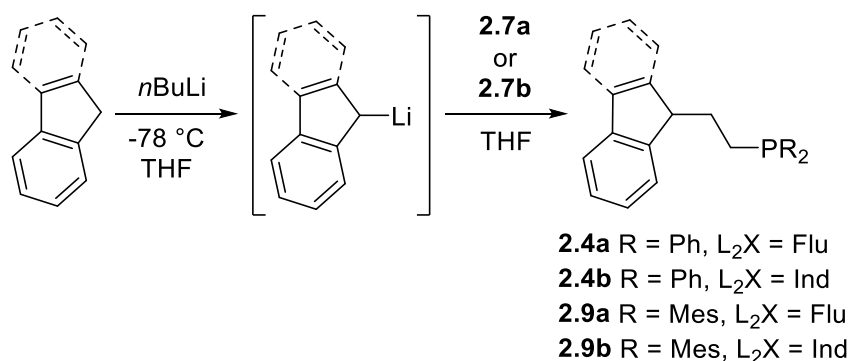
The major phosphorus-containing species formed during reaction of LiP*i*Pr₂ and 1,2-dichloroethane is tetraisopropyldiphosphine, **2.8b**, as 62% of the phosphorus-containing products. It is hypothesised that increasing the donating power of the substituents on phosphorus of the phosphine used drives the reaction towards the formation of diphosphine products. This hypothesis is reinforced when di*tert*butylphosphine is used in an attempt to synthesise **2.7d** (1-chloro-2-

(*di**tert*butylphosphino)ethane), as 73% of the reaction mixture is converted to *di**tert*butyldiphosphine, **2.8c**, Scheme 2.28.



Scheme 2.28 Attempted synthesis of 1-chloro-2-(*di**tert*butylphosphino)ethane (**2.7d**)

Following from the successful synthesis of intermediates **2.7a-c**, the synthesis of phosphine-tethered L_2X substituents could be considered *via* a simple lithium-halogen exchange using the synthesis outlined in **Scheme 2.29**. A solution of lithium salt is added dropwise to a solution of **2.7a** or **2.7b** in THF or Et_2O and the resulting reaction progress followed by ^{31}P NMR spectroscopy.



Scheme 2.29 Proposed synthesis of indenyl- (Ind) and fluorenyl (Flu) derivatives of $(\text{L}_2\text{X})\text{-CH}_2\text{CH}_2\text{-PR}_2$.

When compound **2.7b** (R = Mes) was employed in the lithium halogen exchange with either Ind-Li or Flu-Li, no reaction was observed to occur within 24 hours at room temperature. Exchange of the solvent from THF to Et_2O to help promote the exchange still yielded no conversion. The reactions were also heated at reflux for 48 hours in THF, after which time only the only phosphorus-containing species present was **2.7b** ($\delta_{\text{P}} = -28.0$ ppm) and the reactions were abandoned.

When **2.7a** (R = Ph) was employed in the lithium halogen exchange shown in **Scheme 2.29**, **2.4b** (L_2X = Ind) was produced in 33% yield. This yield could potentially be improved upon as the product was precipitated from a solution in hexanes and no attempts were made to obtain additional precipitation from the mother liquor. NMR spectroscopic analysis determined the substitution reaction to have taken place on the 2-position of indene to give rise to the structure shown in **Figure 2.11**.

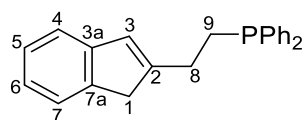


Figure 2.11 Structure of 1-(diphenylphosphino)-2-(2'-indenyl)ethane, **2.4b**.

The ^{31}P NMR spectrum obtained of compound **2.4b** showed a singlet at $\delta_{\text{P}} -15.7$ ppm (*c.f.* **2.7a** $\delta_{\text{P}} -20.1$ ppm), thus showing complete conversion of **2.7a** into **2.4b**. The ^1H NMR spectrum obtained of **2.4b** showed that characteristic loss of the H-2 proton in indene had occurred, along with a shift to low frequency for the indene protons (Figure 2.12). Additionally, in the spectrum of **2.4b**, H-1 integrated as equivalent to 2-protons, which showed substitution and tether introduction had taken place at the C-2 position.

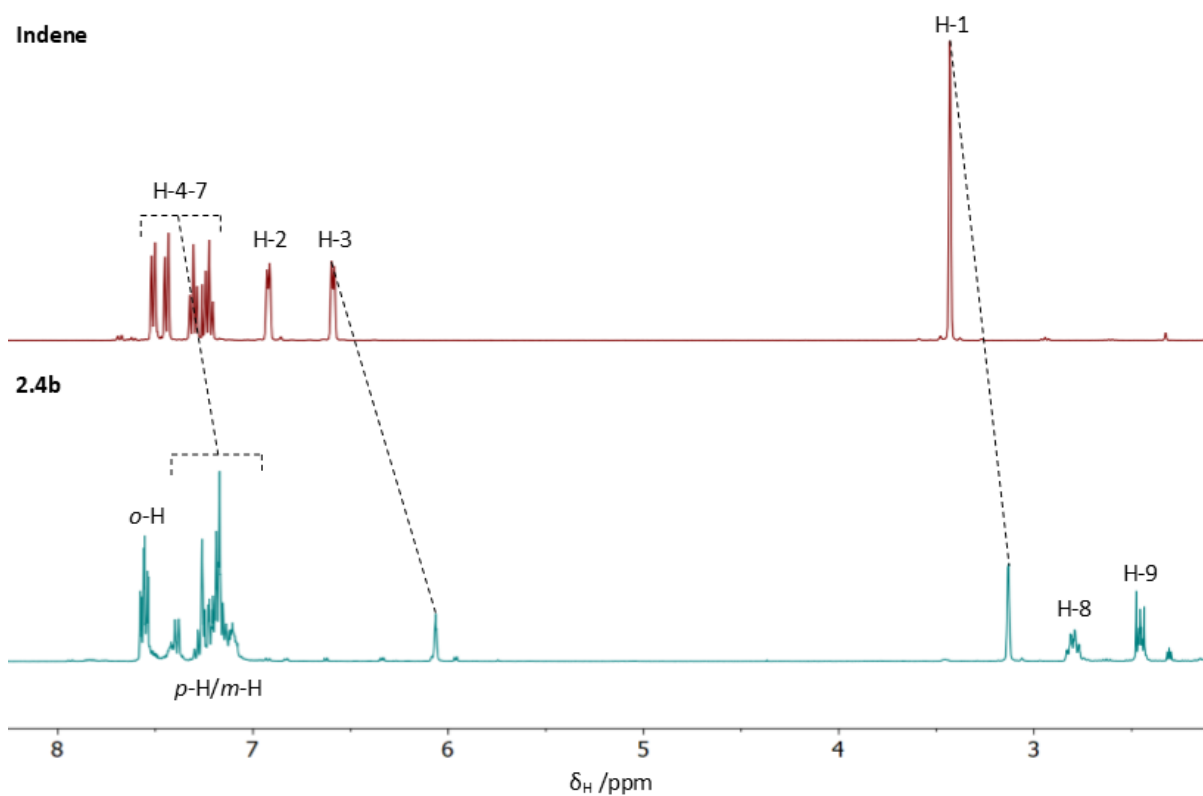
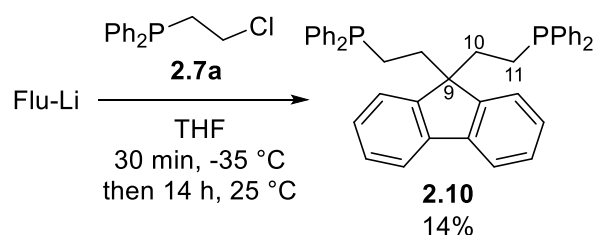


Figure 2.12 Comparison of ^1H NMR spectra (400 MHz) of indene (top, CDCl_3) and **2.4b** (bottom, C_6D_6).

When the same reaction was carried out between fluorenyl lithium and $\text{PPh}_2\text{-CH}_2\text{CH}_2\text{-Cl}$ (**2.7a**), an unexpected reaction was observed. Double substitution occurs at the fluorenyl group, resulting in formation of 9,9'-bis[2-(1-(diphenylphosphinoethyl))]fluorene (**2.10**) which was isolated in 14% yield (**Scheme 2.30**).



Scheme 2.30 Synthesis of 9,9'-bis[2-(1-(diphenylphosphinoethyl))]fluorene, **2.10**.

The identity of compound **2.10** was confirmed by NMR spectroscopic analysis. The ^{31}P NMR spectrum showed a singlet at δ_{P} -15.3 ppm. The ^1H NMR spectrum showed no resonance corresponding to a fluorenyl-9H proton, additionally the signal integration of any aromatic fluorenyl proton to *e.g.* C-10 or C11 is 1:4; both observations are consistent with double substitution. The 2D NMR spectra obtained clearly showed substitution has taken place at the 9-position of the fluorenyl-moiety, with correlation observed between H-10 and C-9 (δ_{C} 56.4 ppm) in the 2D correlation HMBC NMR spectrum (**Figure 2.13**). C-9 appeared as a triplet in the $^{13}\text{C}\{^1\text{H}\}$ NMR spectrum due to $^3J_{\text{CP}}$ coupling to two equivalent phosphine moieties.

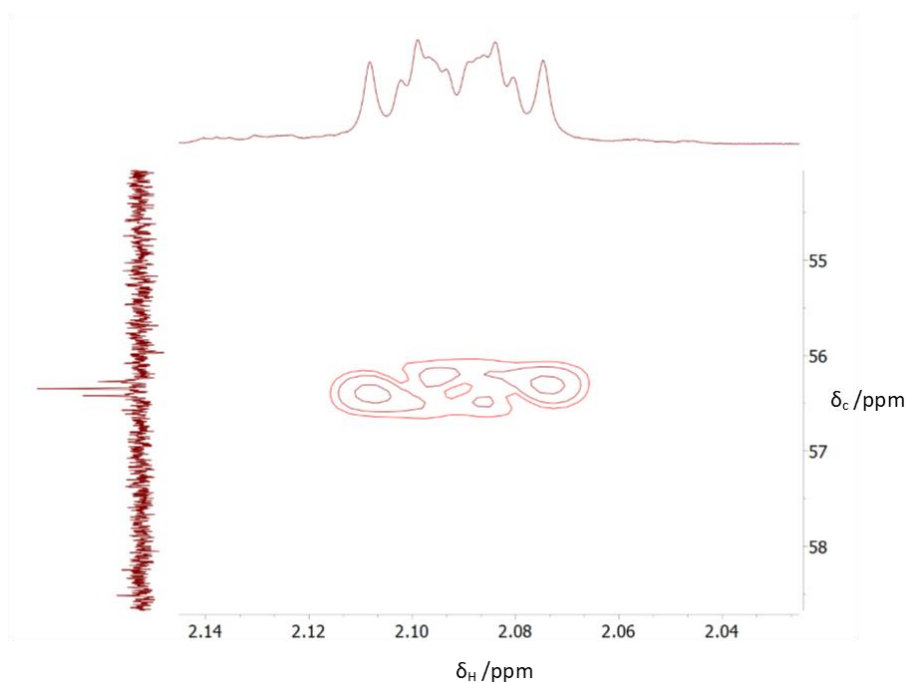


Figure 2.13 Section of the 2D-HMBC ($^1\text{H}-^{13}\text{C}\{^1\text{H}\}$) NMR spectrum (C_6D_6 , 700 MHz, 176 MHz) showing correlation between C-9 and H-10 in compound **2.10**.

The low yield obtained during the synthesis of 9,9'-bis[2-(1-(diphenylphosphinoethyl))]fluorene (**2.10**) was likely due to slow deprotonation of mono-substituted (*i.e.* **2.4a**) fluorenyl-species by additional

Flu-Li, reminiscent of the observations made for the formation of **2.6** *via* Flu-Li. The formation of the doubly-substituted compound **2.10** displays the acidity of fluorenyl-9-H proton even after mono-substitution has occurred.

Deliberate synthesis of compound 9,9'-bis[2-(1-(diphenylphosphinoethyl)]fluorene (**2.10**) was attempted using the same reaction conditions as those described in **Scheme 2.30**, with 2 equivalents of $\text{PPh}_2\text{-CH}_2\text{CH}_2\text{-Cl}$ (**2.7a**) and 2 equivalents of *n*-butyllithium. However, the ^{31}P NMR spectrum of the products obtained displayed a change to selectivity in this reaction, with the major product giving a signal at δ_{p} -16.4 ppm. It is thought that this signal arises from the mono-substituted product, Flu- $\text{CH}_2\text{CH}_2\text{-PPh}_2$ (**2.4a**), although a pure sample has not been isolated for confirmation. However, by integration of the ^{31}P NMR spectrum only 17% of the reaction mixture was the desired compound **2.10**, with 25% being P_2Ph_4 (**2.8a**). Additionally a small amount of dppe was produced in the reaction along with two unidentified phosphorus-containing species. The $^{31}\text{P}\{^1\text{H}\}$ NMR spectrum of the reaction products is shown in **Figure 2.14**.

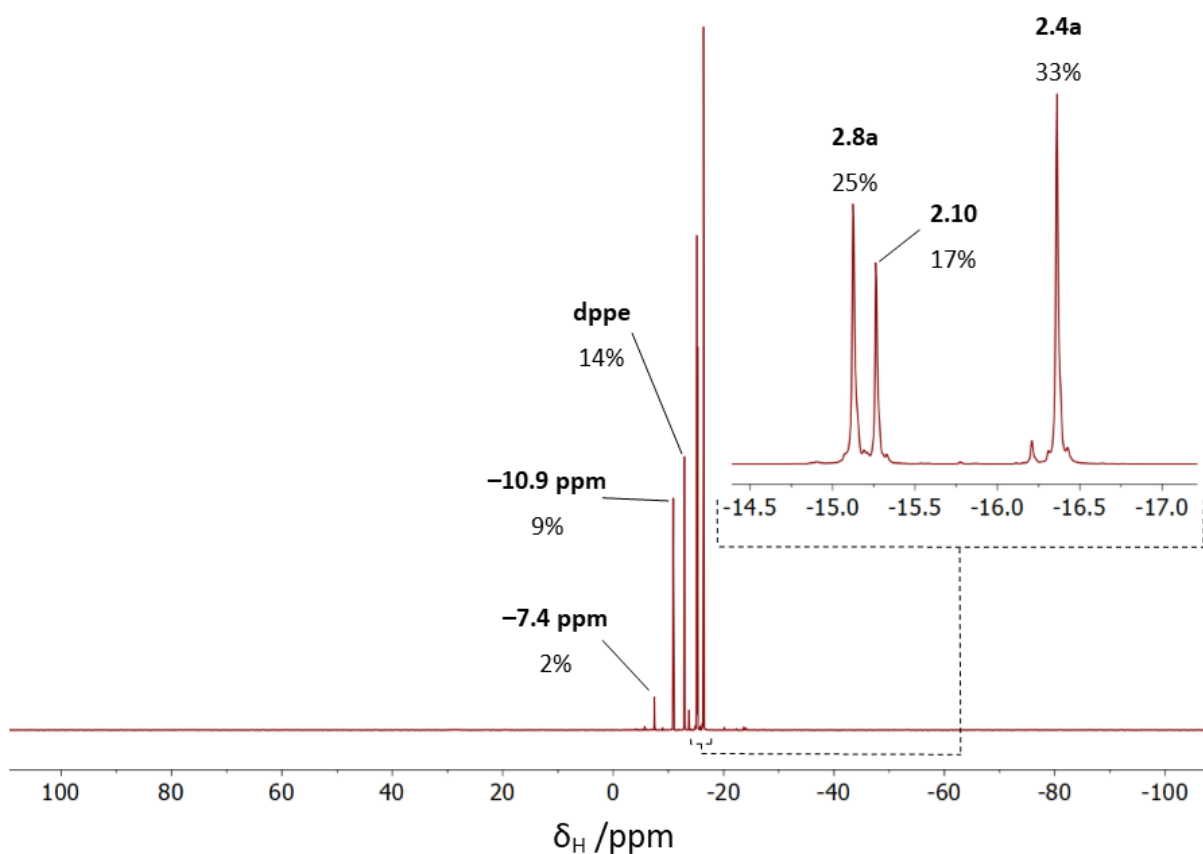
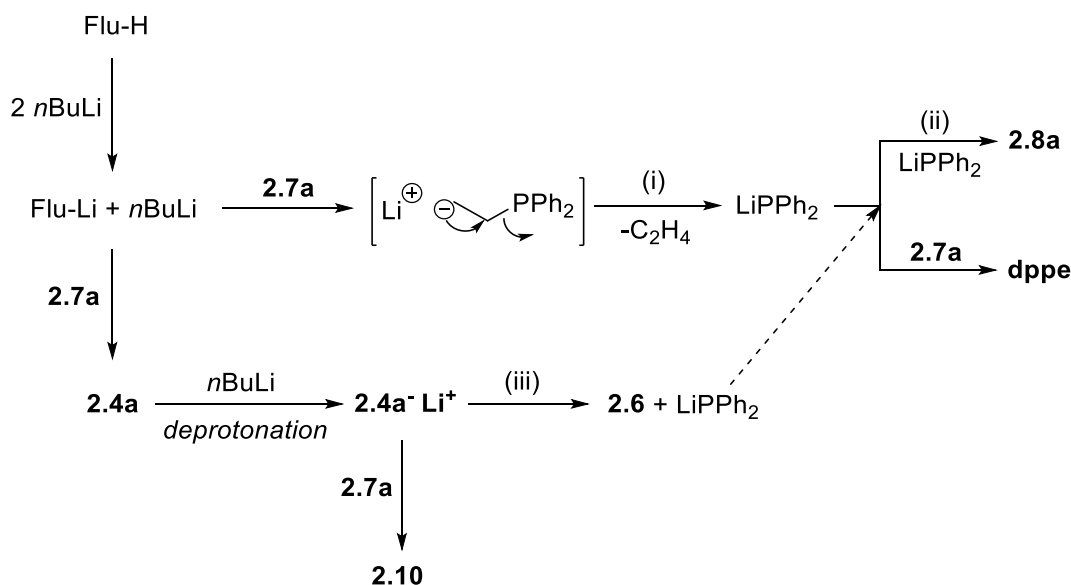


Figure 2.14 $^{31}\text{P}\{^1\text{H}\}$ NMR spectrum (162 MHz, C_6D_6) of the products obtained during attempted synthesis of **2.10**.

It is postulated that the poor selectivity of this reaction to 9,9'-bis[2-(1-(diphenylphosphinoethyl))]fluorene (**2.10**) is the result of the presence of a second equivalent of *n*-butyllithium. A summary of the proposed competing reactions is shown in **Scheme 2.31**. The first equivalent of *n*-butyllithium allows formation of fluorenyllithium, which can undergo nucleophilic substitution to produce Flu-CH₂-CH₂-PPh₂ (**2.4a**). The second equivalent of *n*-butyllithium is immediately available for lithium-halogen exchange with PPh₂-CH₂CH₂-Cl (**2.7a**), which appears to be able to undergo *intramolecular* nucleophilic substitution (i) to release LiPPh₂ and ethene. The LiPPh₂ can then undergo a reductive coupling reaction to produce tetraphenyldiphosphine (**2.8a**) (ii) as a major portion of the reaction mixture, or react with an additional molecule of PPh₂-CH₂CH₂-Cl (**2.7a**) to produce dppe. To allow formation of 9,9'-bis[2-(1-(diphenylphosphinoethyl))]fluorene (**2.10**), first, **2.4a** must be deprotonated by *n*-butyllithium to form **2.4a⁻Li⁺** which can then undergo reaction with **2.7a** to produce **2.10**. It is also possible **2.4a⁻Li⁺** could undergo *intramolecular* nucleophilic substitution (iii), as was seen repeatedly with Flu-CH₂CH₂-Br (**2.2a**), to produce *spiro*-compound (**2.6**) and LiPPh₂. No characteristic signal corresponding to cyclopropane CH₂ could be observed within the ¹H NMR spectrum. Although the ¹H NMR spectrum obtained contained a complex mixture of overlapping multiplets within the region where cyclopropane CH₂ would be expected.

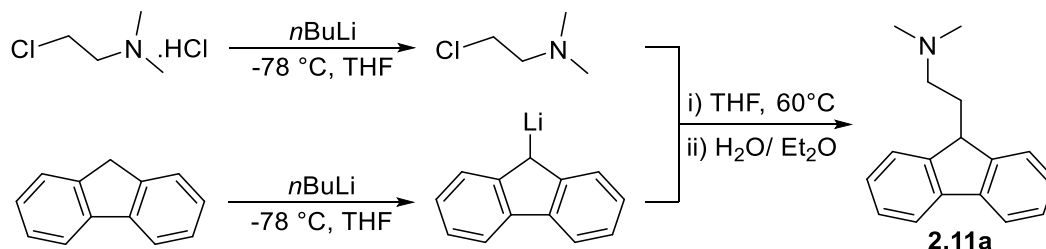


Scheme 2.31 Proposed competing reactions possible during the attempted synthesis of **2.10**.

2.2.1.1.2 Synthesis of (L₂X)-CH₂CH₂-NR₂ where L₂X = Indenyl or fluorenyl

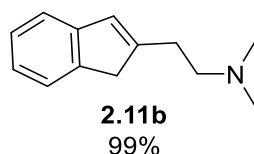
The synthesis of 2-(9'-H-fluorenyl)-*N,N*-dimethylethylamine, **2.11a**, from fluorene and 2-chloro-*N,N*-dimethylethylamine hydrochloride has previously been reported (**Scheme 2.32**). Compound **2.11a** was

successfully synthesised in 55% yield using the synthesis shown in **Scheme 2.32**, and comparison of ^1H and $^{13}\text{C}\{^1\text{H}\}$ NMR spectra obtained to literature data determined the product to be **2.11a**.⁸⁰



Scheme 2.32 Synthesis of **2.11a**, Flu-CH₂CH₂-NMe₂, from fluorene and 2-chloro-*N,N*-dimethylethylamine hydrochloride.⁸⁰

Using modifications to the literature procedure outlined in **Scheme 2.32**, the synthesis of 2-(2'-indenyl)-*N,N*-dimethylethylamine (**2.11b**) was achieved in quantitative yield. Characteristic loss of a signal corresponding to indene H-2 along with the observation of 2-protons present on the 3-position with correlation within the 2D HMBC spectrum between 'tether'-protons and C-2 all suggested that, as seen within the phosphine-derivatives, the synthesis of **2.11b** is regioselective to the 2-position on indene. The EI (GC-MS) spectrum obtained of **2.11b** shows the molecular ion at m/z 181.10 Da.



Scheme 2.33 Structure of **2.11b**, synthesised using a modified literature procedure.⁸⁰

2.2.1.2 Synthesis of Cp- and Cp*-derivatives with a 'C₂-tether.'

2.2.1.2.1 Synthesis of Cp/Cp*-CH₂CH₂-ER_n type ligands where E = O, N.

The cyclopentadienyl derivative of **2.11a,b** can be synthesised through a similar synthesis as that outlined in **Scheme 2.32** for the preparation of 2-(cyclopentadienyl)-*N,N*-dimethylethylamine (**2.11c**), which exists in three isomeric forms (**Figure 2.15**). The sodium salt of cyclopentadiene was used in place of the lithium salt during synthesis, and possibly as a result, the yield obtained (33%) within this reaction is lower than those for **2.11a** or **2.11b**. Spectroscopic data for **2.11c** has been reported previously and the values found in this work are in good agreement.⁸¹

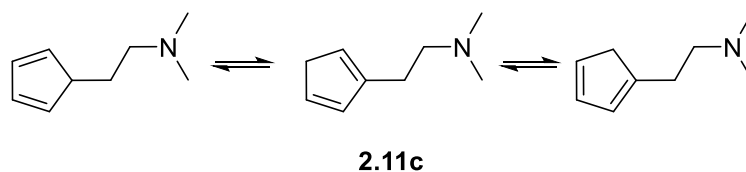
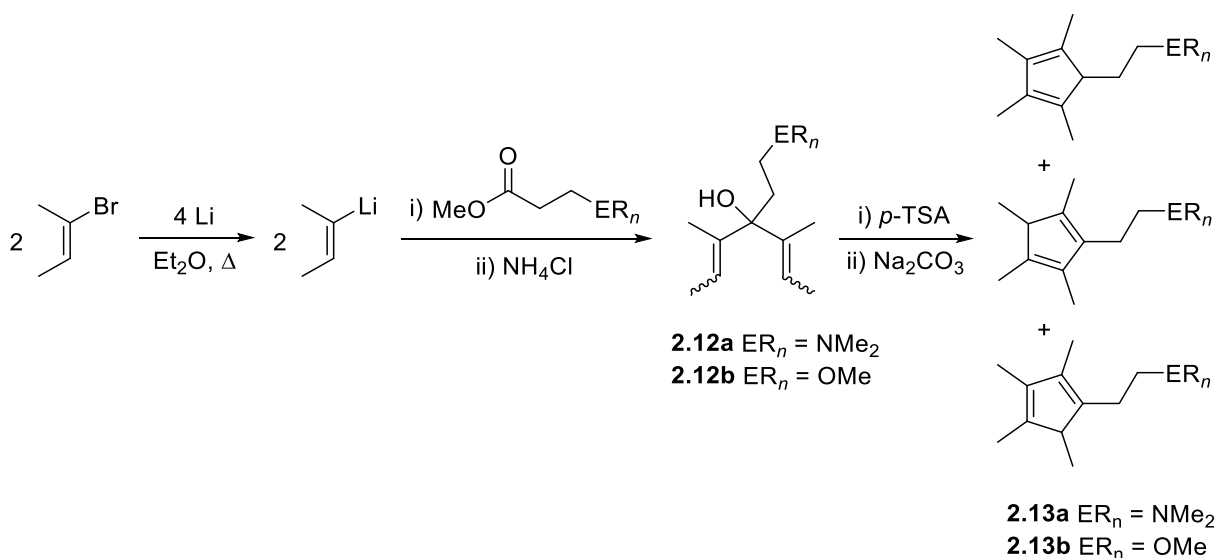


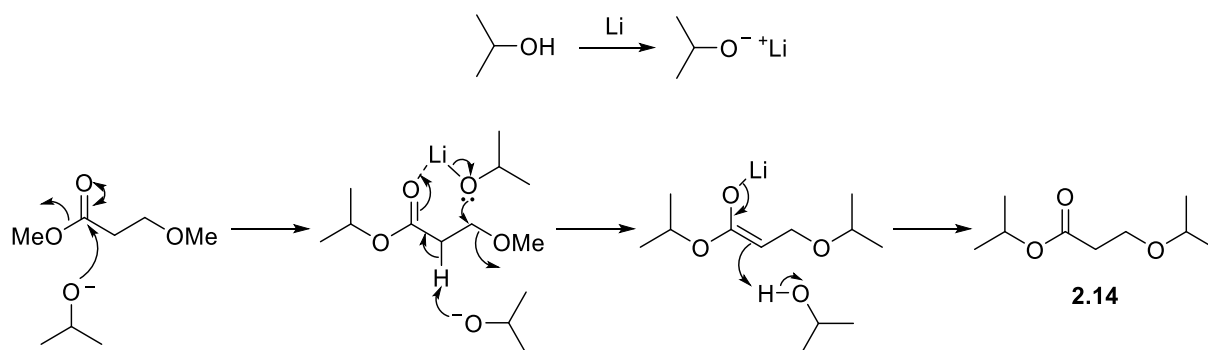
Figure 2.15 Isomeric structures of 2-(cyclopentadienyl)-*N,N*-dimethylethylamine, **2.11c**.

The synthesis of compounds Cp^{*}-CH₂CH₂-NMe₂ (**2.13a**) and Cp^{*}-CH₂CH₂-OMe (**2.13b**) were reported in 1993 by Jutzi and Dahlhaus (**Scheme 2.34**).⁶⁷ From 2-bromo-2-butene and 3-functionalised-methylpropionate, the corresponding dienol (**2.12a** and **2.12b**) can be produced, subsequent acid-catalysed ring closure of the dienol will result in ligands of the type Cp^{*}-CH₂CH₂-ER_{*n*} (**2.13a** and **2.13b**).



Scheme 2.34 Synthetic route towards Cp^{*}-CH₂CH₂-ER_{*n*} type ligands, ER_{*n*} = NMe₂ (**2.13a**) or OMe (**2.13b**).⁶⁷

Using the route developed by Jutzi and Dahlhaus (**Scheme 2.34**) dienols **2.12a,b** were produced as orange oils in moderate yield (56% and 51%, respectively). Notably, during a first attempt of the synthesis of **2.12b**, excess lithium was quenched *in situ* through dropwise addition of propan-2-ol (IPA). This *in situ* quench resulted in unfavourable conditions whereby methyl-3-methoxypropionate is consumed to form isopropyl-(2-isopropoxy)ethanoate (**2.14**) as 55% of the product mixture obtained. A mechanism for this transformation is proposed in **Scheme 2.35**. The identity of **2.14** was confirmed through isolation *via* vacuum transfer and comparison of ¹H and ¹³C{¹H} NMR spectra obtained to literature values.⁸² Subsequent synthesis of **2.12b** was therefore performed without an *in situ* quench of excess lithium; rather, the reaction mixture was filtered away from the metal prior to its quench.



Scheme 2.35 Proposed mechanism for the formation of **2.14** from propan-2-ol, excess lithium and methyl-3-methoxypropionate.

The successful synthesis of **2.12a,b** was confirmed through comparison of the ^1H NMR spectra obtained to values reported in literature, which were found to be in good agreement.⁶⁷ The ^1H and $^{13}\text{C}\{^1\text{H}\}$ NMR spectra obtained are complex as a result of the isomers of **2.12a,b** formed, *i.e.* EE, ZZ and EZ isomers (**Figure 2.16**).

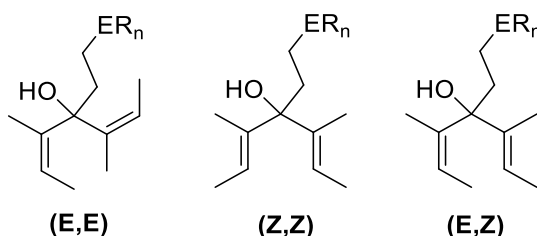
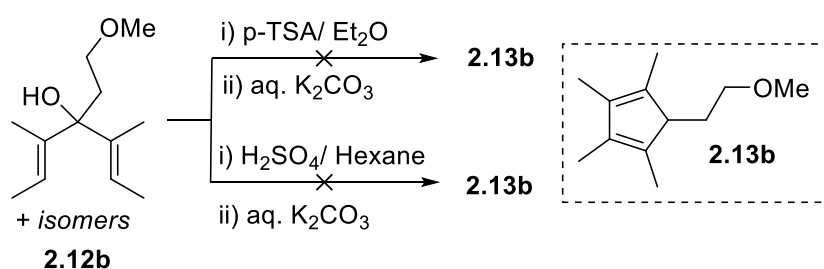


Figure 2.16 Possible alkene isomers of dienols **2.12a,b**.

From the dienols the ligands **2.13a,b** have been reported to be readily prepared through the literature procedure by Jutzi and Dahlhaus.⁶⁷ However, the attempted ring closure of these dienols using this methodology met with little success. In the attempted ring closure of **2.12a** a crude product was obtained as a yellow oil. The ^1H NMR spectrum of this oil displayed a complex mixture of overlapping multiplets, however, signals corresponding to the ring-closed **2.13a** were the predominant component. In an attempt to purify this oil, distillation under reduced pressure using a Kugelrohr was attempted. However, due to the small volume of crude **2.13a** produced, the temperature required for distillation had to be increased, eventually resulting in the decomposition of the product.

Ring closure attempts for the synthesis of **2.13b** were unsuccessful. The first attempt gave rise to a product mixture with a non-attributable ^1H NMR spectrum. Although small peaks associated with residual dienol **2.12b** could be observed, no clear signals could however, be identified within the alkyl region of the spectrum. Consequently, TLC (thin layer chromatography) separation was attempted following solvent system optimisation. Using a solvent mixture of hexane and ethyl acetate (10:1), separation of the crude product to three spots was observed. However, when applied to column chromatography, co-elution of the compounds present was observed.

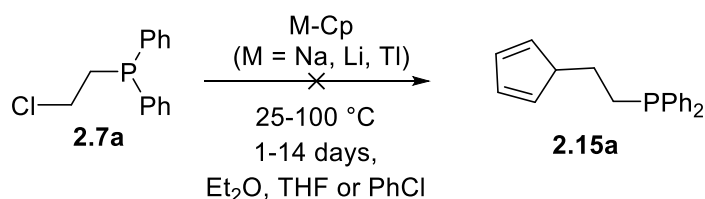
The synthesis of compound **2.13b** was re-attempted according to the literature procedure, however, a similar, complex ^1H NMR spectrum were obtained.⁶⁷ It was hypothesised at this point that the solubility of *p*-TSA (*p*-toluenesulfonic acid) in diethyl ether was too poor to achieve complete ring closure. In an attempt to complete the ring closure, after one treatment with *p*-TSA, the crude oil was dissolved in hexane and treated with an excess of conc. sulfuric acid and stirred for 2 hours. After an aqueous work-up, a red oil was obtained, however, the ^1H NMR spectrum collected was not-attributable. As the same unattributable ^1H NMR spectrum was obtained through use of both *p*-TSA and sulfuric acid, it can therefore be concluded that the solubility of the acid is not accountable for the mixture of products obtained (**Scheme 2.36**). It is now proposed that the reaction is not going to completion as a result of the second step, which is treatment with potassium carbonate.



Scheme 2.36 Attempted synthesis of **2.13b**.⁶⁷

2.2.1.2.2 Synthesis of (Cp/Cp*)-CH₂CH₂-PR₂ type ligands.

Several attempts to produce 1-(diphenylphosphinoethyl)cyclopentadiene (**2.15a**) *via* reaction of Cl-CH₂CH₂-PPh₂ (**2.7a**) with a metal-cyclopentadienyl salt were undertaken (**Scheme 2.37**).



Scheme 2.37 Attempted synthesis of **2.15a**.

For clarity, the conditions trialled for the synthesis of Cp*-CH₂CH₂-PPh₂ (**2.15a**) have been summarised in **Table 2.1**. When Cp-Li or Cp-Tl are employed within this reaction, no conversion to **2.15a** was seen by ^{31}P NMR spectroscopic analysis. When Cp-Na is used within this reaction, no reaction is observed to take place using THF as a solvent, despite heating the reaction to reflux. However, when the solvent is changed to Et₂O, good conversion to **2.15a** can be achieved (**Table 2.1**: Entry 9).

Table 2.1 Conditions trialled and the resulting phosphorus species observed during the attempted synthesis of **2.15a** as determined by ^{31}P NMR spectroscopy.

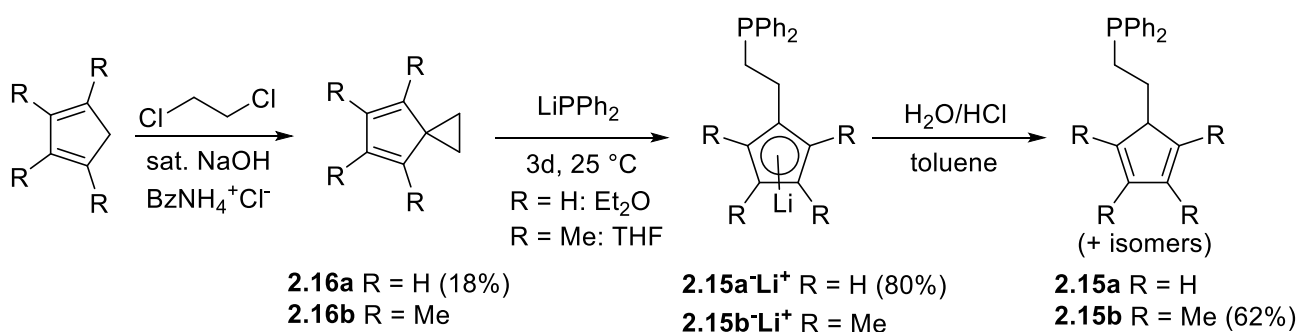
Entry	M	Solvent	Temp / $^{\circ}\text{C}$	Time /days	Observed P-containing species
1	Li	Et ₂ O	25	2	2.7a
2	Li	Et ₂ O	50	5	2.7a
3	Li	THF	25	8	2.7a
4	Tl	THF	25	10	2.7a
5	Tl	THF	60	8	2.7a
6	Tl	PhCl	100	12	2.7a, 2.8a , $\delta_{\text{P}} -11.1$ ppm
7	Na	THF	25	14	2.7a
8	Na	THF	60	19 h	2.7a
9	Na	Et ₂ O	25	6	2.7a, dppe, 2.8a, 2.15a (77%)

In the reactions outlined in **Table 2.1**, exchange to allow formation of **2.15a** was only observed when Et₂O was used a solvent with Na-Cp (Entry 9). As no exchange was observed using THF as a solvent, this change is likely indicative of the degree of aggregation of Na-Cp within solution.⁸³ Et₂O is less polar than THF, which is perhaps what is needed for the dissolution and disaggregation of Cp-Na within solution, allowing successful sodium/halogen exchange to occur (**Scheme 2.38**). The exchange between metal (M) and halogen (X) is also likely very dependent upon the nature and water content of the solvent in use as these reactions are proposed to proceed *via* a single electron transfer (SET) process.⁸⁴

**Scheme 2.38** Equilibrium of alkali metal (M)/halogen (X) exchange.

When the conditions shown in **Table 2.1**, Entry 9 were employed, the desired product, **2.15a**, is observed in the ^{31}P NMR spectrum obtained of the reaction mixture. However, there were also a mixture of side-reactions occurring that produced dppe and **2.8a**. As such, the literature methods for preparation of **2.15a** and **2.15b** (Cp*-CH₂CH₂-PPh₂) were employed.⁴⁵ To this end, *spiro*[2.4]hepta-4,6-diene, (**2.16a**) and 1,2,3,4-tetramethyl-*spiro*[2.4]hepta-4,6-diene (**2.16b**) were obtained using

literature procedures.^{45,76} The ring-opening of **2.16** with LiPPh₂ gave a clean reaction with quantitative conversion to **2.15a⁻Li⁺**, which was isolated in 80% yield and stored. Comparison of the ¹H, ³¹P and ¹³C NMR spectroscopic data for **2.15a⁻Li⁺** to the prior literature data confirmed its identity. In addition, the *i*ASAP⁺ MS spectrum showed [M-Li+H]⁺ in 100% abundance (*m/z* 279.103 Da).



Scheme 2.39 Reported procedures for the synthesis of **2.15a** and **2.15b** from **2.16a** and **2.16b**, isolated yields are shown in parenthesis.^{45,76}

The ³¹P NMR spectrum obtained of **2.15b⁻Li⁺** displayed a small LiPPh₂ impurity, so the lithium salts were quenched through aqueous work up and washing with dilute HCl to produce **2.15b** as a pyrophoric oil, although residual HPPPh₂ remains. The *i*ASAP⁺ MS spectrum of **2.15b** shows the protonated-molecular ion [M+H]⁺ in 100% abundance (*m/z* 335.172 Da). The ³¹P{¹H} NMR spectrum obtained shows three singlets at δ_p -14.3, -15.6 and -16.1 ppm, for the three expected isomers. ¹H and ¹³C{¹H} NMR spectroscopic data are also in good agreement with the reported values for **2.15b**.^{45,85}

2.3 Synthesis of Cobalt(I) Half-Sandwich Complexes

As discussed in the introduction, the literature system that has reported the most significant potential for achieving LAO to LAO dimerisation is that described by Brookhart and Broene.²⁶ In this system, Brookhart and Broene employ $[\text{Cp}^*\text{Co}\{\text{P}(\text{OMe})_3\}\{\eta^2\text{-C}_2\text{H}_4\}]$ (**2.1**) in combination with a sub-stoichiometric quantity of HBAr^{F_4} . This system could therefore be used to obtain a “baseline” of catalytic activity to which future complexes synthesised within this PhD program can be compared. Thus, the first part of this work outlines the synthesis of this system according to known preparative routes, before describing attempts to synthesise analogues to the Brookhart system. In order to develop understanding of the steric effect(s) that the 1,2,3,4,5-pentamethylcyclopentadienyl ligand has upon selectivity within LAO dimerisation reactions using the Brookhart system, the synthesis of a series of analogues to **2.17a** $[\text{Cp}^*\text{Co}(\text{CO})_2]$ was planned.²⁶ Through replacing the Cp^* group on the pre-catalyst **2.17a** with ligands of varying size, but with similar coordination modes, the steric effects this ligand has upon selectivity of LAO dimerisation could be determined. The analogues planned were $\text{CpCo}(\text{CO})_2$ (**2.17b**), $\text{IndCo}(\text{CO})_2$ (**2.17c**) and $\text{FluCo}(\text{CO})_2$ (**2.17d**), **Figure 2.17**.

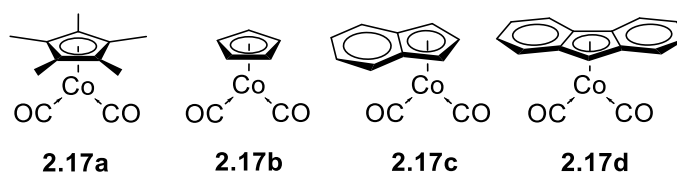
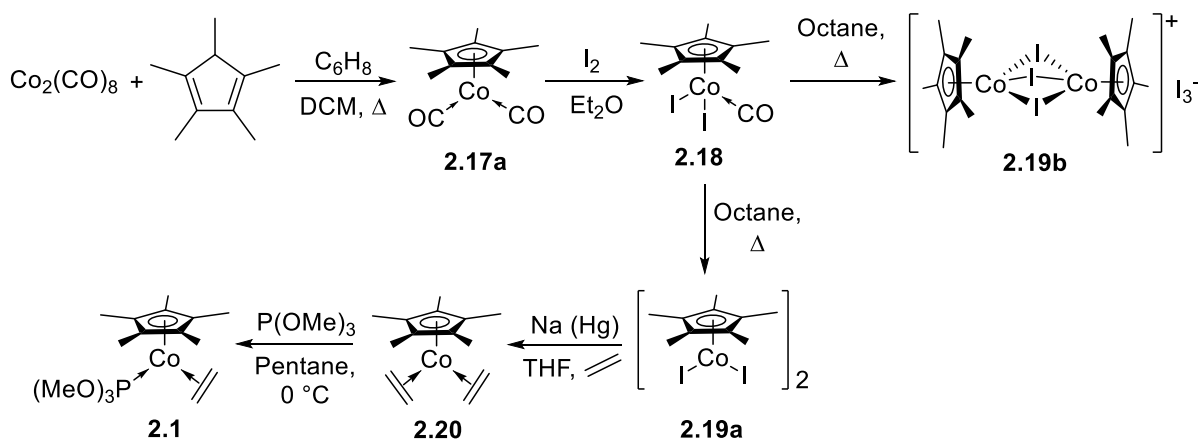


Figure 2.17 Analogues to complex **2.17a**: $\text{CpCo}(\text{CO})_2$ (**2.17b**), $\text{IndCo}(\text{CO})_2$ (**2.17c**), $\text{FluCo}(\text{CO})_2$ (**2.17d**).

2.3.1 Synthesis of Brookhart and Broene’s Pro-catalyst: $[\text{Cp}^*\text{Co}(\eta^2\text{-C}_2\text{H}_4)(\text{P}(\text{OMe})_3)]$

The pro-catalyst $\text{Cp}^*\text{Co}(\eta^2\text{-C}_2\text{H}_4)(\text{P}(\text{OMe})_3)$ (**2.1**) can be synthesised through modifications of literature procedures as shown in **Scheme 2.40**.^{86–90} This five-step pathway for the synthesis of **2.1** should also be applicable to the synthesis of analogues of **2.1** through synthesis of **2.17a-d**. Complexes **2.17a** and **2.18** were synthesised successfully, however, attempts to synthesise $[\text{Cp}^*\text{Co}(\text{I})_2]$ (**2.19a**) resulted in production of the complex $[\text{Cp}^*\text{Co}(\mu_2\text{-I})_3\text{CoCp}^*][\text{I}_3]$, **2.19b**.



Scheme 2.40 Proposed five-step synthesis of $[\text{Cp}^*\text{Co}(\eta^2\text{-C}_2\text{H}_4)(\text{P}(\text{OMe})_3)]$ (**2.1**) adapted from literature procedures.^{86–90}

A modification to the literature procedure was used for the synthesis of $\text{Cp}^*\text{Co}(\text{CO})_2$ (**2.17a**).⁸⁶ As shown in **Scheme 2.40**, dicobaltoctacarbonyl and 1,2,3,4,5-pentamethylcyclopentadiene were heated at reflux in DCM in the presence of 1,3-cyclohexadiene to yield **2.17a** as red/brown crystals (95% yield) suitable for single crystal X-ray diffraction. The successful synthesis of **2.17a** was confirmed through NMR (^1H and $^{13}\text{C}\{^1\text{H}\}$) and IR spectroscopic studies, along with single-crystal X-ray diffraction. The ^1H NMR spectrum of complex **2.17a** displayed a single peak at δ_{H} 1.62 ppm corresponding to the Cp^* CH_3 protons, in good agreement with the literature value.⁸⁶ The $^{13}\text{C}\{^1\text{H}\}$ NMR spectrum had not previously been reported in the literature. Consequently, the $^{13}\text{C}\{^1\text{H}\}$ NMR data was obtained for complex **2.17a** and showed a broad signal at δ_{C} 208.7 ppm, corresponding to the carbonyl group. Additionally, peaks were recorded at δ_{C} 96.3 and 10.4 ppm, corresponding to the Cp^* ring carbons and methyl carbons, respectively. The IR spectrum of complex **2.17a** displayed two strong signals at 2006 and 1946 cm^{-1} , corresponding to the asymmetric and symmetric stretching modes of the carbonyl groups present on cobalt, respectively.

The complex $\text{Cp}^*\text{CoI}_2(\text{CO})$ (**2.18**) was prepared from reaction of **2.17a** with iodine using a modification of the literature procedure, which gave complex **2.18** as a black powder in quantitative yield.⁸⁷ Notably, the crude product mixture produced during the synthesis of **2.18** required a total of >96 hours under dynamic vacuum and three recrystallisations from DCM to ensure removal of excess iodine. The ^1H NMR spectrum of **2.18** displayed a single peak at δ_{H} 1.58 ppm, which was very similar to that obtained for **2.17a** (δ_{H} 1.62 ppm). Small shifts in the $^{13}\text{C}\{^1\text{H}\}$ NMR spectrum of **2.18** when compared to that of **2.17a** were also observed, with peaks corresponding to ring and methyl carbons at δ_{C} 100.5 and 11.0 ppm, respectively, being observed. Due to the poor solubility of complex **2.18**, the carbonyl carbon signals could not be detected within the $^{13}\text{C}\{^1\text{H}\}$ NMR spectrum. However, the successful synthesis of **2.18** was evidenced by the IR spectrum obtained, which confirmed the loss of a carbonyl stretching

band when compared to the spectrum of **2.17a**, with only one carbonyl stretching signal observed at 2055 cm^{-1} . A single CO stretching band within the IR spectrum of **2.18** at higher wavenumber than those observed in **2.17a** was indicative of the loss of a carbonyl group. This shift to higher wavenumber is expected due to the loss of electron density on the cobalt centre as a result of the introduction of electron-withdrawing iodide ligands and the loss of a σ -donating carbonyl. Decreased electron density on cobalt due to iodide introduction at the metal will result in decreased π -back donation from cobalt d -orbitals to the carbonyl, lowering the π^* -character of the CO bond. This results in a shorter C-O bond distance, and thus increases the stretching frequency and therefore absorption occurs at higher wavenumber. A schematic representation of metal-CO bonding is shown in **Figure 2.18**.

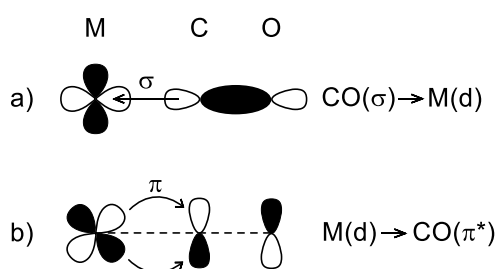


Figure 2.18 Schematic representation of M-CO bonding, a) σ -donation and b) π -back donation.

The attempted synthesis of $[\text{Cp}^*\text{CoI}_2]_2$ (**2.19a**) was carried out using adaptations to the literature procedure.⁸⁷ Nitrogen was continuously passed over a solution of complex $\text{Cp}^*\text{Co}(\text{I})_2(\text{CO})$ (**2.18**), which was heated at reflux in octane for 56 hours to ensure all CO was driven from the reaction mixture. Subsequently, after removal of volatile components, the crude product was extracted in a Soxhlet apparatus over a 96 hour period in DCM to yield a black powder, which was determined to be $[\text{Cp}^*\text{Co}(\mu_2\text{-I})_3\text{CoCp}^*][\text{I}_3]$ (**2.19b**) by single crystal X-ray diffraction (81% yield). The production of **2.19b** from this reaction suggests that excess iodine remained within the mixture of **2.18**, despite 96 hours under dynamic vacuum. The ^1H NMR spectrum obtained of complex **2.19b** was very similar to those obtained for complexes **2.17a** and **2.18**, with a single resonance corresponding to methyl protons at δ_{H} 1.60 ppm. The $^{13}\text{C}\{^1\text{H}\}$ NMR spectrum of **2.19b** was, again, similar to that obtained for **2.18**, with ring and methyl carbon environments observed at δ_{C} 100.4 and 10.9 ppm, respectively. Additionally, the IR spectrum of does not contain any bands that can be attributed to CO stretching.

2.3.1.1 Single-crystal X-ray Structures of $\text{Cp}^*\text{Co}(\text{CO})_2$, $\text{Cp}^*\text{CoI}_2(\text{CO})$ and $[\text{Cp}^*\text{Co}(\mu_2\text{-I})_3\text{CoCp}^*][\text{I}_3]$

Single crystal X-ray diffraction was used to obtain additional support for the successful synthesis of complexes **2.17a** and **2.18**. The single-crystal X-ray structure of complex **2.17a** has been previously reported, however that of **2.18** had not.⁹¹ The X-ray structures of complexes **2.17a** and **2.18** are shown

in **Figure 2.19** for comparison. Crystals of **2.18** suitable for single crystal X-ray diffraction were grown through slow evaporation of DCM. The unit cell of compound $[\text{Cp}^*\text{Co}(\text{CO})(\text{I})_2]$ (**2.18**) is comprised both of a molecule of iodine (I_2) and the expected piano-stool cobalt complex. This suggested that complete removal of iodine had not been achieved at the time of crystallisation. Further steps were undertaken to remove excess iodine from the sample before its use in the preparation of **2.19a**, as discussed in Section 2.2.1, however, complete removal of excess iodine was not achieved. Consequently, $[\text{Cp}^*\text{Co}(\mu_2\text{-I})_3\text{CoCp}^*][\text{I}_3^-]$ (**2.19b**) was formed. The unit cell of **2.19b** was comprised both of a triiodide anion (I_3^-) and the dinuclear complex **2.19b**, the single-crystal X-ray molecular structure of **2.19b** is shown in **Figure 2.19**.

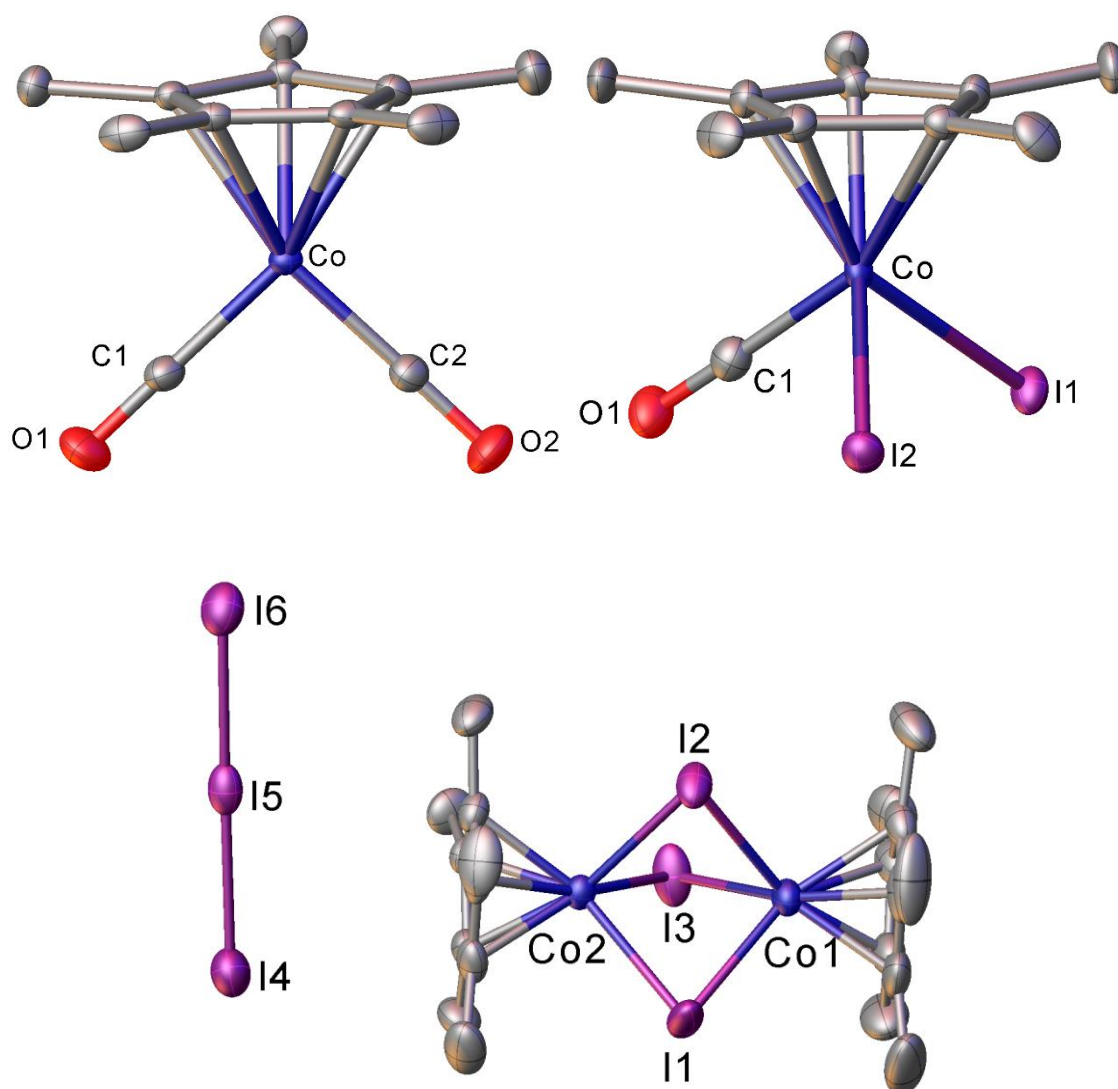


Figure 2.19 Molecular structure obtained by single crystal X-ray diffraction of $\text{Cp}^*\text{Co}(\text{CO})_2$ (**2.17a**), $\text{Cp}^*\text{CoI}_2(\text{CO})$ (**2.18**) and $[\text{Cp}^*\text{Co}(\mu_2\text{-I})_3\text{CoCp}^*][\text{I}_3^-]$ (**2.19b**). The structure of **2.19b** is disordered at iodide ligands and I_3^- anion (0.85:015). ORTEPs are set at 50% probability and hydrogen atoms, an iodine molecule in **2.18** and disorder in **2.19b** are omitted for clarity.

No significant change to the C-O bond length measured in **2.18** (1.128(10) Å) is observed when compared to those measured for complex **2.17a** (1.1473(14) and 1.1491(17) Å) (Table 2.2). However, the Co-C1 bond distance measured in **2.18** is longer than that observed within **2.17a** (Co-C1/2 in **2.17a** = 1.732(1) - 1.739(1) Å and Co-C1 in **2.18** (1.783(8) Å), which suggests decreased π -back donation from Co to CO in complex **2.18**. Values for Cp*-Co bond lengths measured within complexes **2.17a**, **2.18** and **2.19b** do not differ significantly (Table 2.2). The Co-I bond lengths measured in complex **2.18** are comparable to those for the reported complex CpCoI₂(CO) (*c.f.* ~2.58 Å in **2.18** and 2.56(5) Å).⁹² The Co-I bond lengths measured in **2.19b** are longer (2.590(1)-2.635(1) Å) than those measured in **2.18** due to their bridging two cobalt centres, the Co-I bond distances are within the reported range for Co-I-Co structures (2.61-2.70 Å).⁹³

Table 2.2 Selected bond lengths (Å) from single-crystal structures **2.17a**, **2.18**, CpCoI₂(CO) and **2.19b**.⁹²

Bond	2.17a	2.18	CpCoI ₂ (CO)	2.19b
Co-C1	1.7387(14)	1.783(8)	1.764(12)	
Co-C2	1.7324(14)			
C1-O1	1.1473(14)	1.128(10)	1.136(17)	
C2-O2	1.1491(17)			
Co-C _{ring} ^a	2.093(2)	2.101(15)	2.042(25)	2.065(14)
Co-I1		2.576(6)	2.565(3)	2.590(1) ^a
Co-I2		2.5779(8)	2.565(3)	2.635(1) ^a
Co-I3				2.627(1) ^a

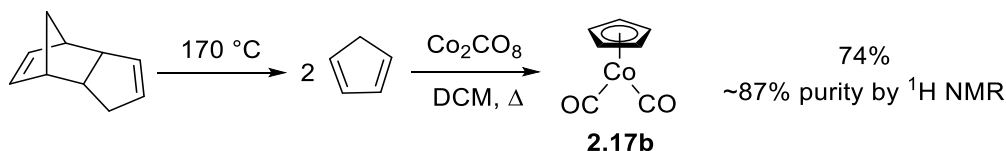
^aMean value

2.3.2 Synthesis of Analogues to Complex [Cp*Co(CO)₂] (**2.17a**)

The synthesis of a series of analogues to complex **2.17a** was planned where the steric and electronic properties of the possible L₂X ligand were modified.²⁶ The analogues proposed were CpCo(CO)₂ (**2.17b**), IndCo(CO)₂ (**2.17c**) and FluCo(CO)₂ (**2.17d**), as shown previously in Figure 2.17.

The synthesis of (η^5 -C₅H₅)Co(CO)₂ (**2.17b**) was performed in accordance to the literature procedure from freshly prepared cyclopentadiene and dicobaltoctacarbonyl in DCM (Scheme 2.41).⁹⁴ Notably, **2.17b** is a liquid under ambient conditions, the volatility of which results in difficulties in separation

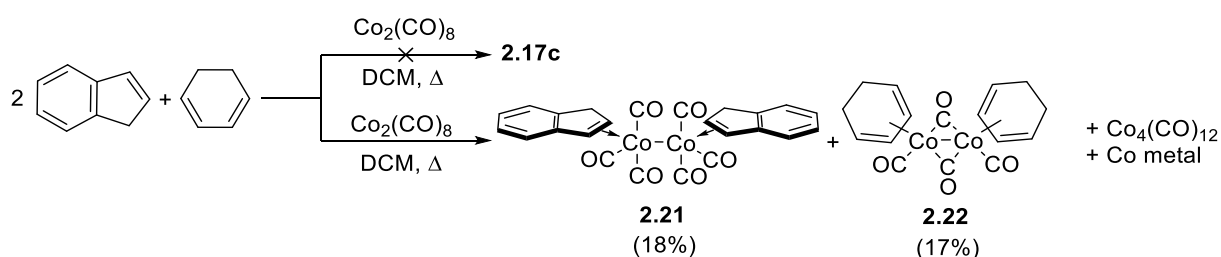
from DCM. In an attempt to separate the two, DCM was first removed *via* distillation at atmospheric pressure and 40 °C, before **2.17b** was collected through distillation at reduced pressure and ambient temperature. However, small impurities of DCM remain within the sample, as observed by ^1H NMR spectroscopic analysis (DCM δ_{H} 5.30 ppm in CDCl_3).



Scheme 2.41 Preparation of **2.17b** from dicyclopentadiene and $\text{Co}_2(\text{CO})_8$.⁹⁴

The successful synthesis of complex **2.17b** was however confirmed through NMR (^1H , $^{13}\text{C}\{^1\text{H}\}$) and IR spectroscopies. The ^1H NMR spectrum obtained displays a single peak at δ_{H} 4.42 ppm, confirming the successful complexation of cyclopentadiene to cobalt through loss of signals corresponding to the alkyl protons (δ_{H} 2.90 ppm), and through observation of only one vinyl proton environment.⁹⁵ Additionally, the $^{13}\text{C}\{^1\text{H}\}$ NMR spectrum obtained displays a single peak corresponding to the single carbon environment present within bound (η^5) cyclopentadienylcobalt complexes at δ_{C} 84.6 ppm, along with a broad peak at δ_{C} 205.5 ppm corresponding to the carbonyl groups of $\text{CpCo}(\text{CO})_2$. The NMR spectra obtained were in agreement with those reported in the literature.⁹⁴ The IR spectrum of complex **2.17b** was obtained as Nujol mulls on KBr plates and, in accordance with literature data, displayed two ν_{CO} bands at 2029 and 1968 cm^{-1} corresponding to the asymmetric and symmetric CO stretches, respectively.⁹⁶

A modification to the literature procedure for the synthesis of **2.17a** was used in the attempted synthesis of $(\eta^5\text{-C}_9\text{H}_7)\text{Co}(\text{CO})_2$ (**2.17c**).⁸⁶ Over the course of a four day reflux, $\text{Co}_2(\text{CO})_8$ in DCM was treated with an excess of indene in the presence of 1,3-cyclohexadiene, after which time an orange precipitate (**2.22**) was observed to form, **Scheme 2.42**. The filtrate was collected and volatile components were removed *in vacuo*, with the complex $[\{(\eta^2\text{-Indene})(\text{CO})_3\text{Co}\}_2]$ (**2.21**) subsequently being isolated as a yellow oil, leaving behind a mixture of cobalt metal and complex **2.22**. The orange precipitate observed during the attempted synthesis of complex **2.17c** was determined to be di-carbonyl-*bis*[carbonyl-(π -cyclohexa-1,3-diene)cobalt] (**2.22**) through a combination of NMR (^1H and $^{13}\text{C}\{^1\text{H}\}$) and IR spectroscopic analyses and a single crystal X-ray structure determination. The structure of **2.22** is shown in **Scheme 2.42**. Discussion of this undesired side product is covered in detail in Section 2.3.2.1.



Scheme 2.42 Attempted synthesis of $\text{IndCo}(\text{CO})_2$ (**2.17c**) that instead produced **2.21** and **2.22**. Isolated yields are shown in parenthesis.

The ^1H NMR spectrum of complex **2.21** displayed five broad signals at δ_{H} 7.47, 7.27, 6.94, 6.61 and 3.45 ppm, which have relative integrals of 2:2:1:1:2, respectively, which suggested no deprotonation to the indene has occurred. The line broadening of the ^1H NMR spectrum obtained is proposed to be the result of the fluxional behaviour of the η^2 -indene. (**Figure 2.20**). The IR spectrum obtained of the yellow oil (**2.21**) isolated contained three ν_{CO} bands at 2052m, 1980s and 1940w cm^{-1} , suggesting three terminal carbonyl ligands are present upon each cobalt. Additionally, within the ASAP (Atmospheric Solids Analysis Probe) mass spectrum obtained of **2.21**, the highest molecular weight ion was observed at m/z 519.15 Da (0.90% $[\text{M}]^+$) along with 231.12 Da (100% $[\{(\eta^2\text{-Indene})(\text{CO})_3\text{Co}\}_2]^+$). A black precipitate consisting of cobalt metal and $\text{Co}_4(\text{CO})_{12}$ was also isolated from this reaction. The presence of $\text{Co}_4(\text{CO})_{12}$ was determined through IR spectroscopy, with three ν_{CO} bands observed within the spectrum at 2062, 2053 and 1865 cm^{-1} corresponding to the terminal and bridging carbonyls present within the cobalt cluster.⁹⁷

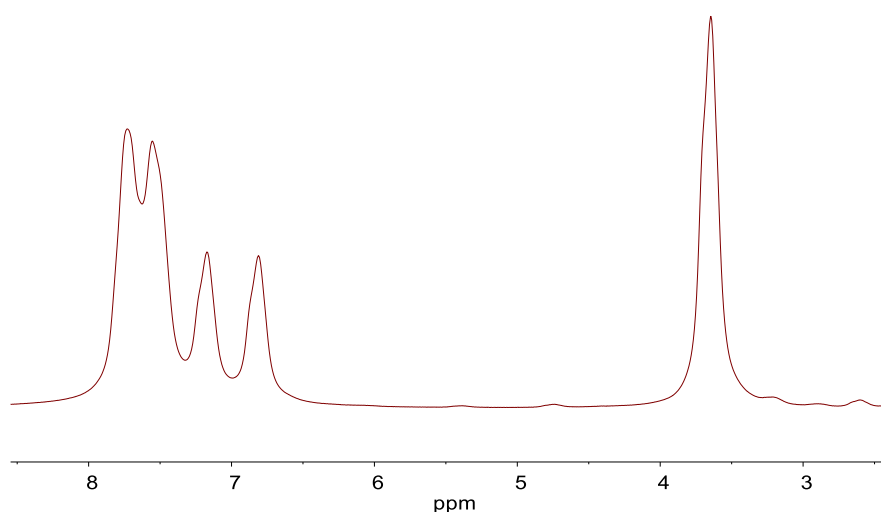
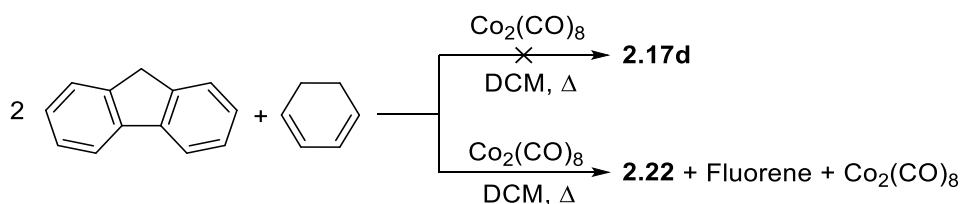


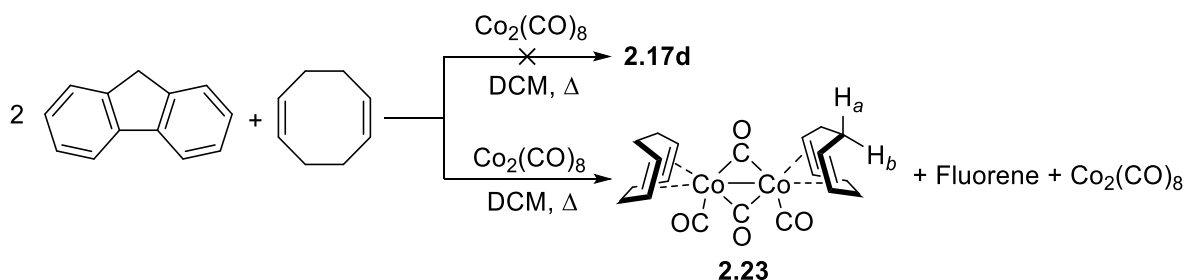
Figure 2.20 ^1H NMR (400 MHz, C_6D_6) spectrum obtained of complex $[\{(\eta^2\text{-Indene})(\text{CO})_3\text{Co}\}_2]$, **2.21**.

The synthesis of ($\eta^5\text{-C}_{13}\text{H}_9$)Co(CO)₂ (**2.17d**) was attempted using a modification to the procedure used to prepare **2.17a**.⁸⁶ Thus, Co₂(CO)₈ and fluorene, in the presence of 1,3-cyclohexadiene, were heated at reflux in dichloromethane for four hours. Unfortunately, after volatile components were subsequently removed *in vacuo*, a mixture of unreacted fluorene, Co₂(CO)₈ and complex **2.22** was confirmed through ¹H, ¹³C{¹H} NMR and IR spectroscopic analysis. Unbound fluorene is easily detected through ¹H NMR spectroscopy due to the presence of two alkyl protons at δ_{H} 3.92 ppm, confirming deprotonation had been unsuccessful.



Scheme 2.43 Attempted synthesis of FluCo(CO)₂ (**2.17d**) using a modification to the literature used for the preparation of complex **2.17a**.⁸⁶

The synthesis of **2.17d** was attempted again, this time using 1,4-cyclooctadiene (COD) in place of cyclohexadiene, since any cyclooctadiene complex formed during the course of the reaction is likely to be less stable than the cyclohexadiene complex, and thus may favour formation of **2.17d**. However, analysis of the products resulting from this reaction suggested formation of a COD-cobalt dimer, **2.23**, similar in structure to **2.22** (**Scheme 2.44**). The ¹H NMR spectrum of **2.23** contained three broad resonances at δ_{H} 6.82, 3.11 and -0.09 ppm (each with $\nu_{1/2}$ 170-180 Hz), corresponding to a coordinated cyclooctadiene in which the CH₂ protons are inequivalent. In addition, the IR spectrum obtained of **2.23** shows three carbonyl stretches at 2062s and 2054s (ν_{CO} terminal CO) and 1865m (ν_{CO} bridging CO). Unfortunately, attempts to isolate single crystals of **2.23** in order to confirm the analysis by X-ray diffraction were unsuccessful.



Scheme 2.44 Attempted synthesis of **2.17d** using COD to mediate the reaction, resulting in formation of **2.23**.

2.3.2.1 Identification and solid-state structure of $[\text{Co}(\text{C}_6\text{H}_8)(\text{CO})(\mu_2\text{-CO})]_2$ (**2.22**).

As mentioned previously, di- μ_2 -carbonyl-*bis*[carbonyl-(π -cyclohexa-1,3-diene)cobalt] (**2.22**) was isolated during the attempted synthesis of complex **2.17c** and **2.17d**. The identity of complex **2.22** was confirmed through a single-crystal X-ray diffraction study and NMR (^1H , $^{13}\text{C}\{^1\text{H}\}$) and IR spectroscopic techniques. The synthesis of complex **2.22** has been reported through reaction of $\text{Co}_2(\text{CO})_8$ with 1,3-cyclohexadiene at elevated temperatures (the literature reports temperatures >130 °C will result in greater yields).⁹⁸ The IR spectrum obtained of complex **2.22** was in good agreement with that has reported in the literature previously, with strong bands recorded at 1982 and 1768 cm^{-1} corresponding to terminal and bridging CO stretches, respectively.⁹⁹ The IR spectra obtained of samples of complex **2.22** were taken in the solid state (ATR-FTIR or Nujol mull on KBr) and support the claims made in the literature that complex **2.22** exists almost exclusively as the *cis*-isomer within the solid state, as additional bands (expected at lower wavenumbers) corresponding to the *trans*-isomer were not observed.⁹⁹

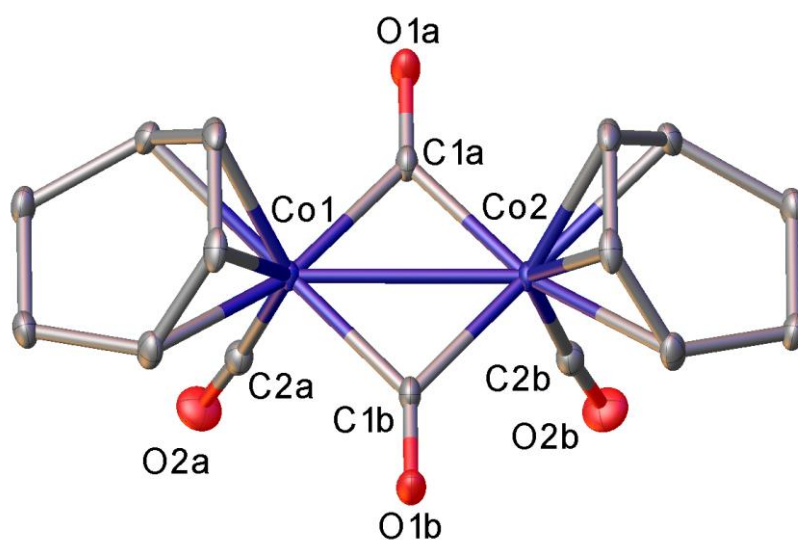


Figure 2.21 Single crystal X-ray molecular structure of $[\text{Co}(\mu_2\text{-CO})(\text{CO})(\eta^4\text{-C}_6\text{H}_8)]_2$ (**2.22**). Hydrogen atoms have been omitted for clarity and ORTEPs are set at 50% probability.

Crystals of complex **2.22** suitable for X-ray diffraction were grown from slow cooling of a solution of complex **2.22** in xylenes with the resulting molecular structure shown in **Figure 2.21**; no structure has previously been reported for **2.22**.¹⁰⁰ Selected bond lengths and angles are displayed in Table 2.3. The Co-Co bond distance of 2.550(1) Å, lies slightly out with the standard range for Co-Co bonds reported with similar structures (2.4–2.5 Å).⁹⁷ The Co-C1 distance (1.9212(15) Å) is longer than that measured for Co-C2 (1.776(2) Å) as would be expected as a result of σ -donation to two metal centres.¹⁰¹ The Co-C1-Co (\angle 83.15(1)°) and C1a-Co-C1b (\angle 96.76(1)°) bond angles are very similar to those within the

previously reported *cis*-[Fe(Cp)(μ -CO)(CO)]₂ complex (*c.f.* \angle 82.8(3) $^\circ$ and \angle 96.0(3) $^\circ$).¹⁰² Additionally, as in the *cis*-[Fe(Cp)(μ ₂-CO)(CO)]₂ complex, the 1,3-cyclohexadiene groups of **2.22** are eclipsed, as reflected by the measured torsion angle of 0 $^\circ$ for C2a-Co1a-Co1b-Co2b.¹⁰² Finally, the carbonyl bridge present within complex **2.22** is planar, further suggesting that Co-(π -diene) dimer structures are more similar to iron analogues than to Co₂(CO)₈, which contains a puckered CO bridge.^{99,102}

Table 2.3 Selected bond distances (Å), bond angles ($^\circ$) and torsion angles ($^\circ$) measured for complex **2.22**.

Bond Distances (Å)	
Co1-Co2	2.550(1)
Co-C1 ^a	1.9212(15)
Co-C2 ^a	1.776(2)
C1-O1 ^a	1.173(1)
C2-O2 ^a	1.138(1)
Bond angles ($^\circ$)	
Co1-C1-Co2	83.15(1)
C1a-Co1-C1b	96.76(1)
C1-Co-C2 ^a	99.20(7)
Torsion angles ($^\circ$)	
C1a-Co1-Co2-C1b	3.2(1)
C2a-Co1-Co2-C2b	0.000

The NMR spectra of complex **2.22** have not previously been reported. Both the NMR spectra (¹H and ¹³C{¹H}) obtained here displayed signals within the expected regions when compared to similar [Co(η ⁴- π -diene)(CO)(μ ₂-CO)]₂ complexes.¹⁰³ The choice of deuterated solvent for the analysis of complex **2.22** by NMR spectroscopy was found to be important. When complex **2.22** was dissolved in CDCl₃ broad, uninterpretable spectra were obtained, possibly the result of the presence of trace HCl in the solvent. However, dissolution of **2.22** in either *d*₆-acetone or *d*₆-benzene resulted in sharp ¹H NMR spectra, with *cis*- and *trans*-**2.22** isomers observed in the solution state when either of these solvents were used (**Figure 2.22**). The ¹³C{¹H} NMR spectrum obtained also revealed the presence of *cis*- and *trans*-isomers

of complex **2.22**, with chemical shift differences between *cis*- and *trans*-**2.22** in the region of 1–3 ppm. While the alkyl carbon signal of the 1,3-cyclohexadiene moiety measured by $^{13}\text{C}\{^1\text{H}\}$ NMR spectroscopy did not display a significant coordination chemical shift ($\Delta\delta$) when compared to “free” 1,3-cyclohexadiene, the signals associated with the vinyl carbons in complex **2.22** were found at lower frequency with $\Delta\delta$ up to 46 ppm. This dramatic shift to a lower frequency is expected upon 1,3-cyclohexadiene coordination to Co as a result of increased shielding of this environment by the electron-rich metal centre. Carbonyl carbon environments were not observed in the $^{13}\text{C}\{^1\text{H}\}$ NMR spectra of complex **2.22** obtained as a result of the poor solubility of this sample and the low intensity of these quaternary carbons.

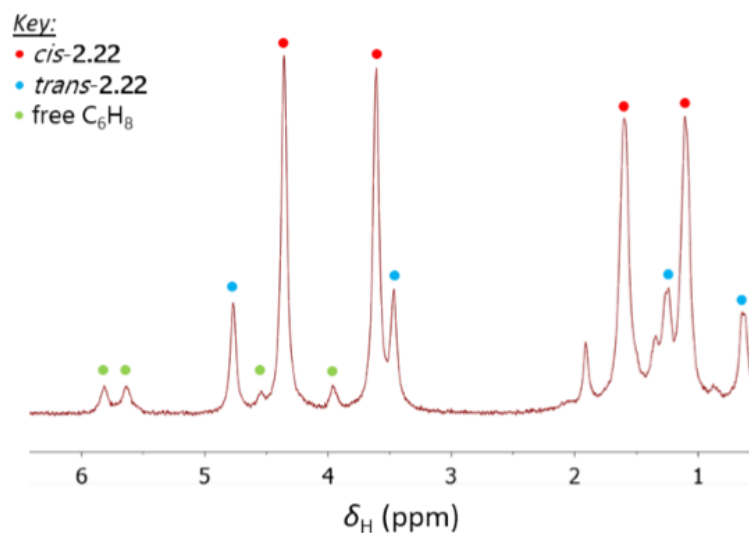


Figure 2.22 ^1H NMR (400 MHz, C_6D_6) spectrum of *cis*- and *trans*-**2.22**.

2.3.2.2 Mechanistic Study for the Formation of Complex **2.17a** via Synthesis of **2.22**.

The production of complex di- μ_2 -carbonyl-*bis*[carbonyl-(π -cyclohexa-1,3-diene)cobalt (**2.22**) during the attempted synthesis of complex $\text{IndCo}(\text{CO})_2$ (**2.17c**) is proposed to be the result of weak binding of indene to cobalt, resulting in preferential coordination of 1,3-cyclohexadiene. In order to gain a better understanding of how to push selectivity towards coordination of indene preferentially, a study was undertaken to determine the mechanism for the formation of complex **2.22** from $\text{Co}_2(\text{CO})_8$. The formation of complex **2.22** was investigated through a series of experiments between $\text{Co}_2(\text{CO})_8$ and 1,3-cyclohexadiene where conditions (temperature, time, treatment with ultrasound) were varied. The conditions used and the resulting products that were isolated are summarised in **Table 2.4**.

Table 2.4 Conditions and products isolated during attempted synthesis of $[\text{Co}(\text{C}_6\text{H}_8)(\text{CO})(\mu_2\text{-CO})]_2$ (**2.22**).

Entry	Solvent	Temperature / °C	Time/ h	$[\text{Co}(\text{C}_6\text{H}_8)(\text{CO})(\mu_2\text{-CO})]_2$ Observed	Additional Observed Products ^a
1	DCM	25	48	-	No observed reaction
2	DCM	40	48	Yes	Co metal, $\text{Co}_2(\text{CO})_8$
3	DCM	40	96	Yes	Co metal, $\text{Co}_2(\text{CO})_8$, C_6H_8 ^b
4 ^c	DCM	~30	48	Yes	$\text{Co}_2(\text{CO})_8$, C_6H_8 ^b
5	PhCl	60	48	Yes	Co metal, $\text{Co}_2(\text{CO})_8$, C_6H_8 ^b
6	Pet-ether ^d	90	4	-	Metallic Co mirror
7	Xylenes	130	48	-	Metallic Co mirror

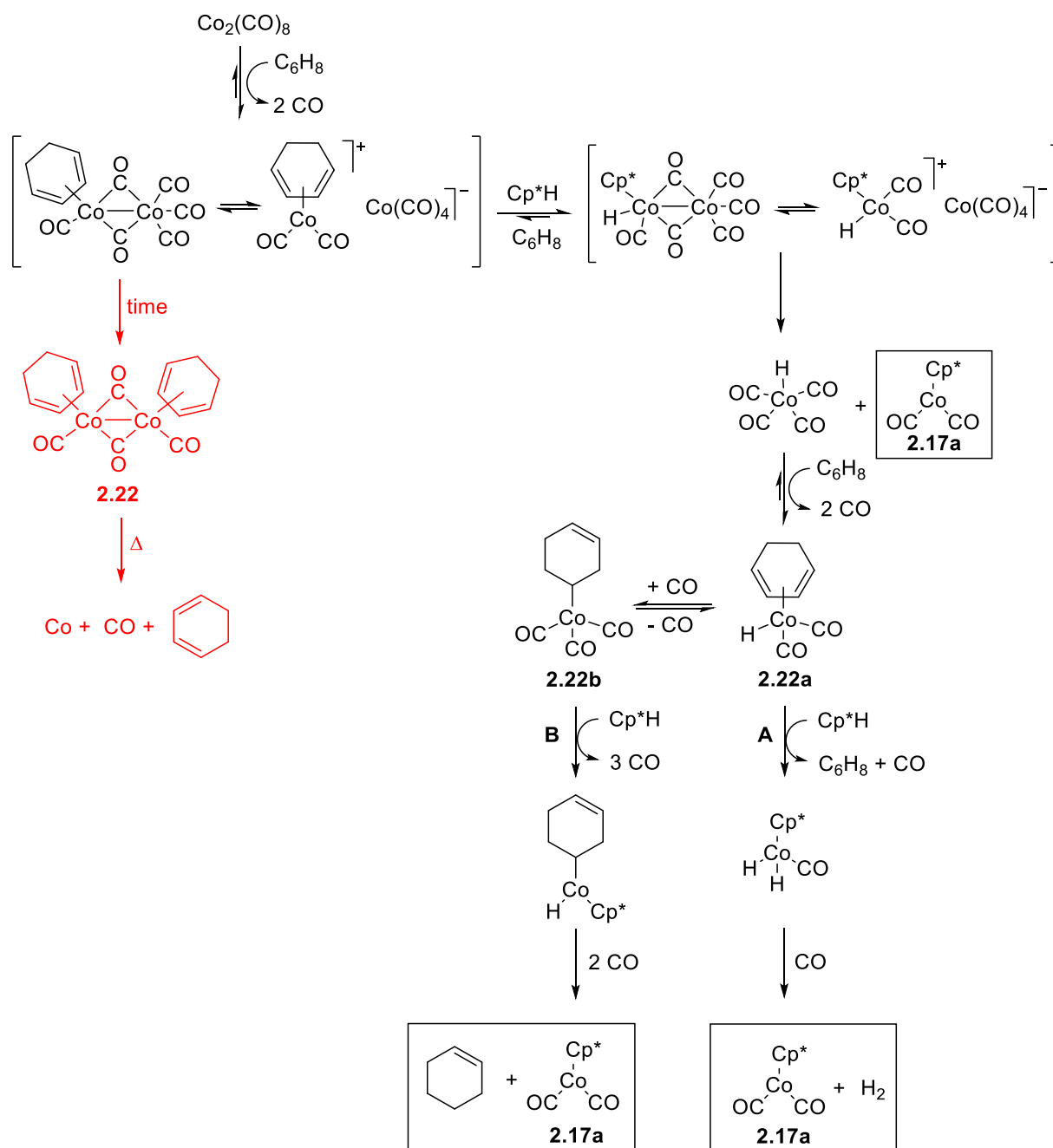
^aDue to the volatility of 1,3-cyclohexadiene, attempts were not made to specifically isolate this starting material. ^bObserved in the ¹H NMR spectrum only. ^cSample placed in an ultrasound bath. ^dHigh b.p. petroleum ether (100–120 °C)

From the results shown in **Table 2.4**, it can be concluded that higher temperatures (>60 °C) are detrimental to the formation of complex **2.22**, through the decomposition of $\text{Co}_2(\text{CO})_8$ to pyrophoric cobalt metal and carbon monoxide. It can therefore be inferred that temperatures greater than 60 °C will be disadvantageous for the synthesis of analogues of **2.17a** ($\text{Cp}^*\text{Co}(\text{CO})_2$) using $\text{Co}_2(\text{CO})_8$ as a starting material. These observations are in agreement with the known decomposition of $\text{Co}_2(\text{CO})_8$ above 52 °C, however they are in direct contrast to literature reports for the synthesis of complex **2.22** that describe temperatures up to 130 °C.^{98,99,104} Interestingly, when sonication was used to agitate the reaction (**Table 2.4: Entry 4**), no decomposition to cobalt metal was observed, whereas small quantities of decomposition products were observed in all other experiments performed within this study - even under the mild conditions which are used within the synthesis of complex **2.17a** (**Table 2.4: Entry 2**).

It is proposed that during the synthesis of complex $\text{Cp}^*\text{Co}(\text{CO})_2$ (**2.17a**), 1,3-cyclohexadiene would displace CO in $\text{Co}_2(\text{CO})_8$ before dissociation of this neutral $\eta^4\text{-C}_6\text{H}_8$ moiety and oxidative addition of $\eta^5\text{-Cp}^*$. However, during the attempted synthesis of complex $\text{IndCo}(\text{CO})_2$ (**2.17c**), the complex $[(\text{C}_6\text{H}_8)(\text{CO})\text{Co}(\mu_2\text{-CO})]_2$ (**2.22**) was produced preferentially at this point. Evidence for the production of complex **2.22** was also observed during the attempted synthesis of complex $\text{FluCo}(\text{CO})_2$ (**2.17d**).

An experiment was performed whereby complex **2.22** was reacted with 1,2,3,4,5-pentamethylcyclopentadiene under the same conditions used for the synthesis of complex **2.17a** however, no reaction was observed within this experiment, suggesting that complex **2.22** is not an

intermediate within the synthesis of complex **2.17a**. A proposed mechanism for the formation of complex **2.22** is shown in **Scheme 2.45**.



Scheme 2.45 Proposed mechanism for formation of complex **2.17a** (black) and **2.22** (red) from $\text{Co}_2(\text{CO})_8$ and 1,3-cyclohexadiene with two possible routes **A** and **B** for the formation of complex **2.17a**.

As shown in **Scheme 2.45**, after successful oxidative addition of Cp^*H , it could be postulated that hydride transfer could occur to result in the formation of $\text{HCo}(\text{CO})_4$ and the complex **2.17a**. Subsequent displacement of two CO ligands on $\text{HCo}(\text{CO})_4$ by 1,3-cyclohexadiene could then result in formation of

a new 18 electron species $[\text{HCo}(\text{C}_6\text{H}_8)(\text{CO})_2]$ (**2.22a**). Pathway **A** in **Scheme 2.45** describes possible reaction of an additional molecule of Cp^*H with **2.22a** to form the 18 electron intermediate $\text{Cp}^*\text{Co}(\text{H})_2$, which could liberate H_2 upon additional CO complexation to regenerate 1,3-cyclohexadiene and produce **2.17a**. An alternative reaction pathway is shown from the postulated intermediate **2.22b**, whereby migratory insertion of the hydride present on **2.22a** is driven by CO coordination. Reaction of **2.22b** with an additional molecule of Cp^*H and loss of a CO ligand could result in the 17 electron intermediate shown, which could then undergo additional hydride insertion and CO complexation to liberate cyclohexene and **2.17a**.

In an effort to understand the mechanism by which complex **2.17a** is formed, the synthesis of complex **2.17a** was repeated and an aliquot of the reaction mixture (separated from Co-containing products by distillation) was taken and analysed by gas chromatography (**Figure 2.23**). The gas chromatogram (GC) of the reaction mixture (**a**) obtained displayed two non-solvent signals at retention times of ~ 3.4 and ~ 3.6 minutes (slight time variations result as an artefact of manual injection). In order to assign these signals, standards of possible resulting products were run under the same conditions, including: 1,3-cyclohexadiene, cyclohexene, cyclohexane and 1,4-cyclohexadiene (**Figure 2.23b-e**, respectively) and compared to the GC trace obtained of the reaction mixture (**Figure 2.23a**). While analysis indicated no formation of 1,4-cyclohexadiene as a product, and indicated formation of cyclohexene, simple comparison of the retention times does not allow differentiation between 1,3-cyclohexadiene and cyclohexane (**Figure 2.23b** and **Figure 2.23d**, respectively).

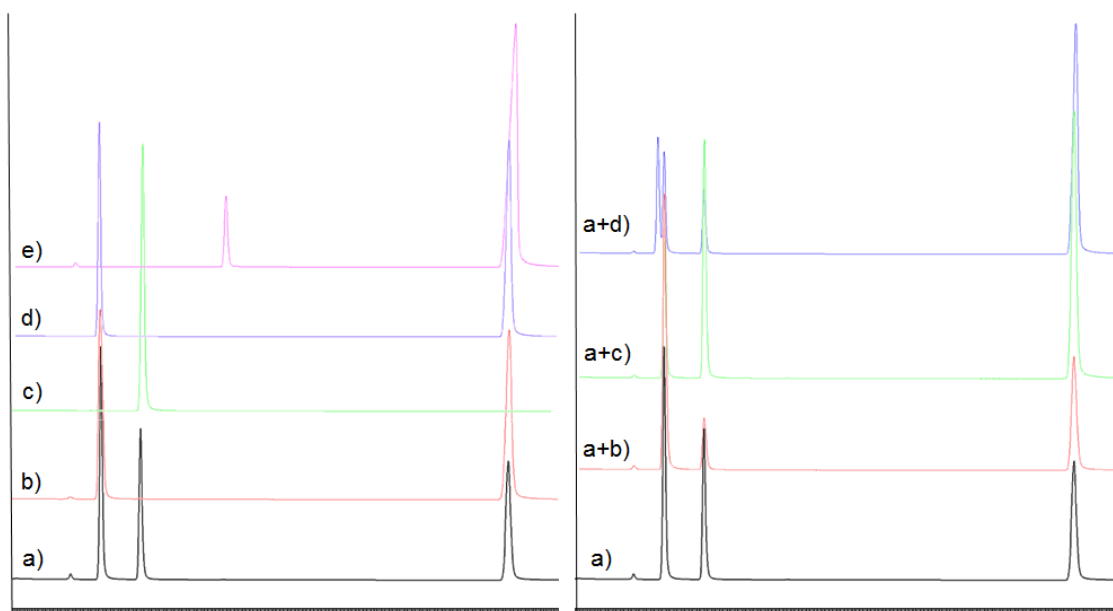


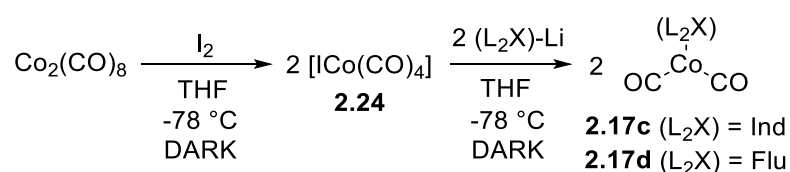
Figure 2.23 Gas chromatographs (PONA column) obtained of volatiles components of the reaction mixture during the synthesis of complex **2.17a** (**a**), compared with standards **b-e** where **b**) 1,3-cyclohexadiene, **c**) cyclohexene, **d**) cyclohexane and **e**) 1,4-cyclohexadiene) and reaction mix (**a**) spiked with standards (**b-d**).

To confirm the presence of cyclohexene and to distinguish between 1,3-cyclohexadiene and cyclohexane, GC traces were obtained where the reaction mixture was spiked with these standards (**Figure 2.23**, RHS). The data presented in **Figure 2.23(a+b)** and **Figure 2.23(a+c)** confirm the presence of 1,3-cyclohexadiene and cyclohexene within the reaction mixture, respectively. This suggests that either pathway **A** or pathway **B** (**Scheme 2.45**) could be operative for the formation of complex **2.17a**. Complete hydrogenation of 1,3-cyclohexadiene to cyclohexane is not observed, something reflected in the appearance of a discreet cyclohexane signal within the GC curve obtained for reaction mixture spiked with cyclohexane (**Figure 2.23(a+d)**).

The GC traces obtained (**Figure 2.23(a+b)** and **Figure 2.23(a+c)**) give clear evidence for the formation of **2.17a** through pathway **B** (**Scheme 2.45**), however do not provide evidence for or against pathway **A**. 1,3-Cyclohexadiene is used within the synthesis of complex **2.17a** in slight excess and so it is ambiguous as to whether the observed 1,3-cyclohexadiene is the result of pathway **A** or residual starting material.

2.3.2.3 Attempted Synthesis of complexes **2.17c** and **2.17d** from a Cobalt(I) Source

As the syntheses of $\text{IndCo}(\text{CO})_2$ (**2.17c**) and $\text{FluCo}(\text{CO})_2$ (**2.17d**) from $\text{Co}_2(\text{CO})_8$ were unsuccessful, it was proposed that a cobalt(I) starting material may be a better option. As such, a synthetic route starting from the reactive cobalt(I) species $[\text{Co}(\text{CO})_4]$ (**2.24**), which has to be kept in the dark at $-78\text{ }^\circ\text{C}$, was planned such that lithium halogen exchange between Ind-Li or Flu-Li with $[\text{Co}(\text{CO})_4]$ could be used to yield **2.17c** or **2.17d** (**Scheme 2.46**).



Scheme 2.46 Proposed synthetic route to prepare **2.17c** and **2.17d** from a cobalt(I) source, **2.24** $[\text{Co}(\text{CO})_4]$.

When the reaction shown in **Scheme 2.46** was performed with indenyl-lithium, an oil was obtained that contained a THF impurity (by ^1H NMR spectroscopic analysis). The sample was therefore placed under dynamic vacuum for a total of 14 days in an attempt to remove residual THF. After this time, the ^1H NMR spectrum of the oil displayed the presence of coordinated THF (broadened peaks) along with signals arising from an indene species consistent with an asymmetric η^1 -binding mode of indene to

cobalt (*i.e.* 7 discrete proton environments). The spectrum is shown in **Figure 2.24**, some residual free indene is also observable within the ^1H NMR spectrum obtained.

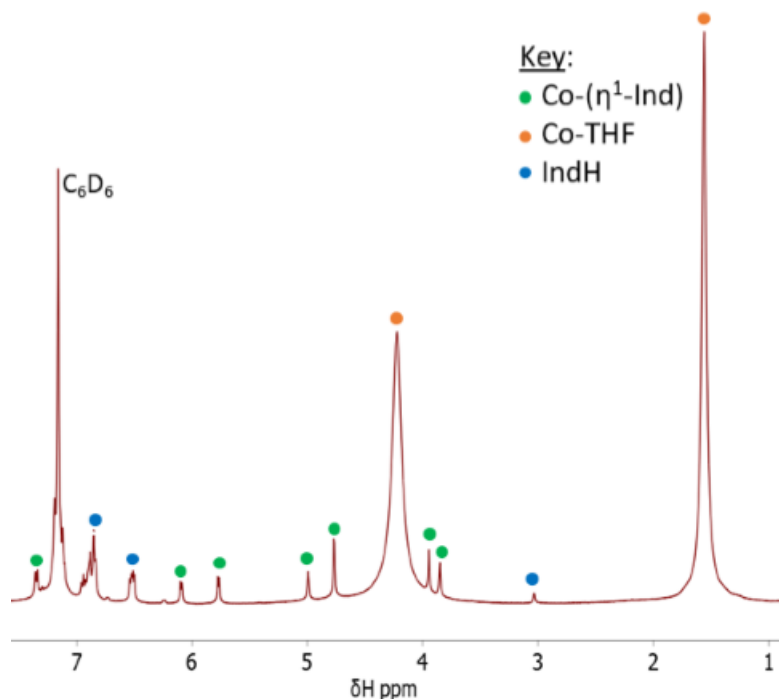
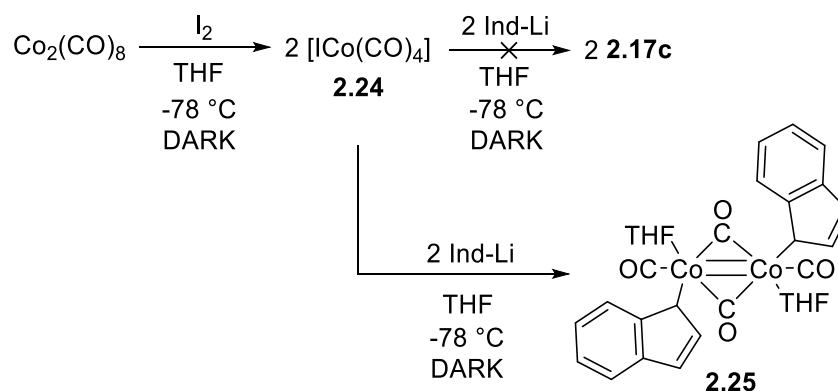


Figure 2.24 ^1H NMR (C_6D_6 , 400 MHz) obtained of the product from reaction of **2.24** with Ind-Li .

IR spectroscopic analysis of the resulting viscous oil revealed multiple bands corresponding to carbonyl stretches at 2013s, 1909s, 1887s and 1837s cm^{-1} ; the energies of these stretches suggest there are both bridging and terminal carbonyl species present. The mass spectrum of the oil displays fragments with m/z 130.084 Da (79.74% $[(\text{Ind})\text{Co}(\text{CO})_2]^+$) and 289.011 (100% $[(\text{Ind})_2\text{Co}]^+$) along with fragments at much higher molecular weight which are not attributable.

When the IR and NMR spectroscopic and mass spectrometric data are taken together, a tentative structure for the reaction product can be proposed. The reaction product, **2.25**, is suggested to be a dimeric cobalt species (with bridging and terminal carbonyls) containing bound THF and an indenyl-moiety bound in an η^1 -fashion, as shown in **Scheme 2.47**.



Scheme 2.47 Attempted synthesis of complex **2.17c** from **2.24** and proposed reaction product, **2.25**.

In accordance with **Scheme 2.46**, the reaction of fluorenyl sodium with **2.24** was also performed in an attempt to produce $\text{FluCo}(\text{CO})_2$ (**2.17d**). In this instance, a dark green waxy substance was obtained as the product of the reaction following work-up. IR spectroscopic analysis of the product showed seven very weak carbonyl bands with energies corresponding to terminal carbonyl groups only, which could be tentatively assigned as $[(\eta^1\text{-Flu})\text{Co}(\text{CO})_4]$ (**2.26**) (**Figure 2.25**). However, the very low intensity of these bands suggested any carbonyl-containing species were likely to be a very minor product of this reaction. *i*ASAP MS analysis showed the presence of fluorene (m/z 166.062 Da (100%)) along with a small fragment (1.68%) corresponding to $[\text{CoFlu-H}]^+$ (m/z 223.047 Da), however the vast majority of the spectrum is dominated by a repeating pattern corresponding to a polymer with repeat mass units of 72 Da and 16 Da: this is assigned as the polymeric product of ring-opened THF, as a result of the presence of anionic fluorene in the reaction.

be the result of the fluxional behaviour of PPh_3 in **2.27**. The ^1H NMR spectrum of complex **2.27** was collected in C_6D_6 solvent and showed three broad resonances corresponding to coordinated triphenylphosphine at δ_{H} 9.85 ($\nu_{1/2}$ 35 Hz), 3.33 ($\nu_{1/2}$ 407 Hz) and 1.65 ($\nu_{1/2}$ 22 Hz) ppm. These broad signals in the ^1H NMR spectrum are attributed to the paramagnetic nature of the *pseudo*-tetrahedral complex **2.27**. In addition, signals corresponding to free triphenylphosphine were observed in the ^1H NMR spectrum as a result of their fluxionality on cobalt. The Raman spectrum of complex **2.27** shows a band at 309 cm^{-1} that is assigned as Co-Cl.

With complex **2.27** in hand, the lithium halogen exchange between **2.27** and Ind-Li was attempted in accordance to **Scheme 2.48**. After two hours at $-78\text{ }^\circ\text{C}$, the reaction was observed to change colour from green to red, it was then left for an additional 14 hours at room temperature. After work-up of the reaction, a red solid was obtained. Spectroscopic analysis (NMR, UV-Vis, Raman, IR) of this red solid showed that the reaction was only partially successful, as residual **2.27** was observed ($\nu_{\text{Co-Cl}}$ 306 cm^{-1} , δ_{H} 9.85 ($\nu_{1/2}$ 42 Hz), 3.42 ($\nu_{1/2}$ 405 Hz), 1.65 ($\nu_{1/2}$ 34 Hz) ppm) (**Figure 2.26**). The UV-Vis spectrum obtained of the mixture containing **2.27** and **2.28** showed a shouldered band at λ 532 nm, which could indicate indenyl coordination to cobalt. However, the clear presence of the starting material **2.27** renders this reaction unsuccessful. In addition, no indication as to the possible coordination mode of the indenyl moiety to cobalt was observed. With further work, it is possible that this lithium halogen exchange reaction between **2.27** and Ind-Li could be pushed to completion (*e.g.* increased temperature, time, addition of TMEDA *etc.*) however, additional attempts were not completed due to the ambiguous outcome of the performed reaction.

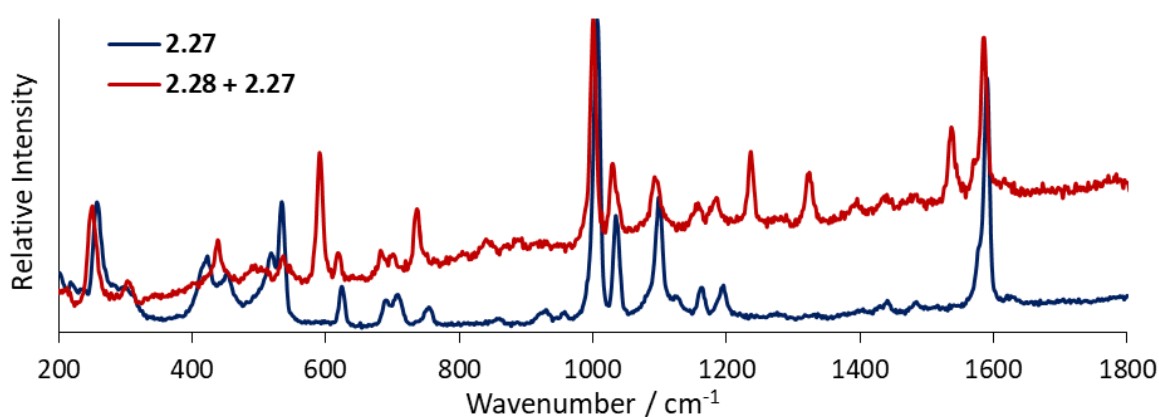


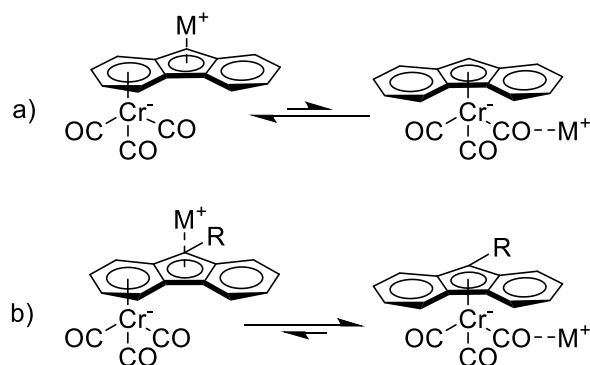
Figure 2.26 Comparison of the Raman spectra (LIR, 532 nm) obtained of $[(\text{PPh}_3)_3\text{CoCl}]$ (**2.27**) and the product of the reaction from **2.27** with Ind-Li (**2.28**).

2.3.2.4 The Hypothetical Bonding of Indenyl- and Fluorenyl-moieties to Cobalt

Complexes **2.17a**, **2.17b** (Cp*H and CpH parent L₂X ligands, respectively) were produced in good yields (95% and 74%) while all attempts for the synthesis of complexes **2.17c** and **2.17d** (indene and fluorene parent L₂X ligands) were unsuccessful. The pK_a values of the parent L₂X ligands investigated follow the trend: Cp*H > fluorene > indene > CpH (26.1 > 22.6 > 20.1 > 18.0)^{106–109}, and as such, the poor rate of oxidative addition to cobalt by indene and fluorene suggest the effect in play is not related to pK_a. It is hypothesised that cobalt complexes containing η⁵-indenyl and η⁵-fluorenyl are inherently less stable than Cp- or Cp* derivatives as a result of the fused aromatic systems present within indenyl- and fluorenyl-derivatives. Consider the bonding within a cyclopentadienyl-metal complex: as discussed within Section 2.1.4. σ-Interaction is non-bonding as a result of poor orbital overlap, and the predominant force arises from M(d_{xz}, d_{yz})←Cp(e_{1g}). As cobalt is a 3d transition metal, this π-interaction is weaker in cobalt complexes than, for instance, rhodium and iridium; η⁵-indenyl and η⁵-fluorenyl complexes of rhodium and iridium are well established within the literature, but the cobalt complexes are not. Extension of the π-system beyond a simple five-membered ring (as in indenyl and fluorenyl) results in delocalisation of the charge produced, weakening the π-interaction. Conversely, the addition of electron donating methyl groups on Cp* acts to strengthen the π-interaction.

This effect has been observed previously for rhodium and iridium complexes. A review on the subject by White, Thompson and Maitlis showed that the relative stability of arene ligands complexed to rhodium and iridium followed the trend: η⁶-naphthalene < η⁶-phenanthrene < η⁶-benzene < η⁶-alkylbenzenes < η⁶-indole < η⁵-indenyl > η⁶-indene, η⁶-indolyl. White *et al.* did also attempt to include fluorene and fluorenyl complexes of rhodium and iridium within their study, but found that the data obtained were not conclusive towards any one clear coordination mode.¹¹⁰

Ustynyuk and co-workers have reported the tendency of η⁵→η⁶-rearrangements of fluorenyl-chromium complexes, the rate of which was decreased upon addition of alkyl-donor groups on C9-position of the fluorenyl-moiety (Scheme 2.49).¹¹¹



Scheme 2.49 Preferential binding modes of fluorenyl-chromium complexes, where R = alkyl group and M = Cs, Ca, Rb salt.¹¹¹

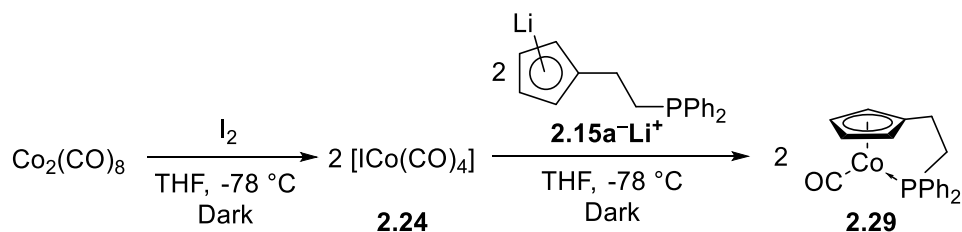
Additionally, a study by Carpentier and co-workers observed a strong bias towards η^6 -coordination of the fluorenyl-anion within iron complexes (47:1 η^6 : η^5), which could only be reversed during heating.¹¹² Ferreira de Silva and co-workers were able to produce iron complexes of *bis*-cyclopentadienyl and *bis*-indenyl, but not *bis*-fluorenyl and attribute this observation to the delocalisation of charge as the aromatic system is extended.¹¹³

In fact, η^5 -indenyl and η^5 -fluorenyl complexes of the 3d metals have been reported for Ti, V, Cr and Mn, with η^6 -coordination modes also observed for Mn and Fe. To date only two reports claim to have produced an η^5 -indenyl cobalt complex. Lucherini reports formation of $[(\text{Flu})\text{Co}\{\text{P}(\text{OMe})_3\}_2]$ and $[(\text{Ind})\text{Co}\{\text{P}(\text{OMe})_3\}_2]$ with η^5 -coordination mode of the supposed L_2X -ligand. However, in both cases, the ^1H NMR data reported for these complexes actually suggests η^1 or η^3 coordination mode.¹¹⁴

In each attempt within the work presented in this thesis, in which indenyl- or fluorenyl-moieties have been successfully coordinated to cobalt, the coordination modes observed have been neutral or (likely) η^1 -coordination. It is therefore proposed in this report that obtaining a η^5 -coordinated indenyl- or fluorenyl-moiety to cobalt is very unlikely. For this reason, additional attempts to synthesise η^5 -indenyl or fluorenyl complexes of cobalt were not undertaken. Instead, work was refocussed on the coordination of 'tethered' ligand systems to cobalt.

2.3.3 Synthesis of $\{[(\text{L}_2\text{X})\text{-CH}_2\text{CH}_2\text{-(L)}]\text{Co}(\text{CO})\}$ Complexes

The synthesis of $(\text{Cp-CH}_2\text{CH}_2\text{-PPh}_2)\text{Co}(\text{CO})$ (**2.29**) was attempted *via* a lithium-halogen exchange reaction between the reactive complex $[\text{Co}(\text{CO})_4]$ (**2.24**) and $(\text{Cp-Li})\text{-CH}_2\text{CH}_2\text{-PPh}_2$ (**2.15a**Li⁺), as shown in **Scheme 2.50**.



Scheme 2.50 Proposed synthetic route to form **2.29**.

The IR spectrum of the product obtained from this reaction showed multiple CO environments, all within the range expected for a terminal CO (ν_{CO} 2012, 1979, 1944 and 1901 cm^{-1}), a comparison between the IR spectra of the product obtained and starting material, $\text{Co}_2(\text{CO})_8$, is shown in **Figure 2.27**. The multiple bands within the IR spectra obtained of complex **2.29** corresponding to CO stretching suggests the structure of this complex (**2.29**) is not as simple as the one suggested in **Scheme 2.50**, as the structure proposed would only be expected to have one strong stretching frequency associated with it. As such, it is likely that a mixture of products had been obtained.

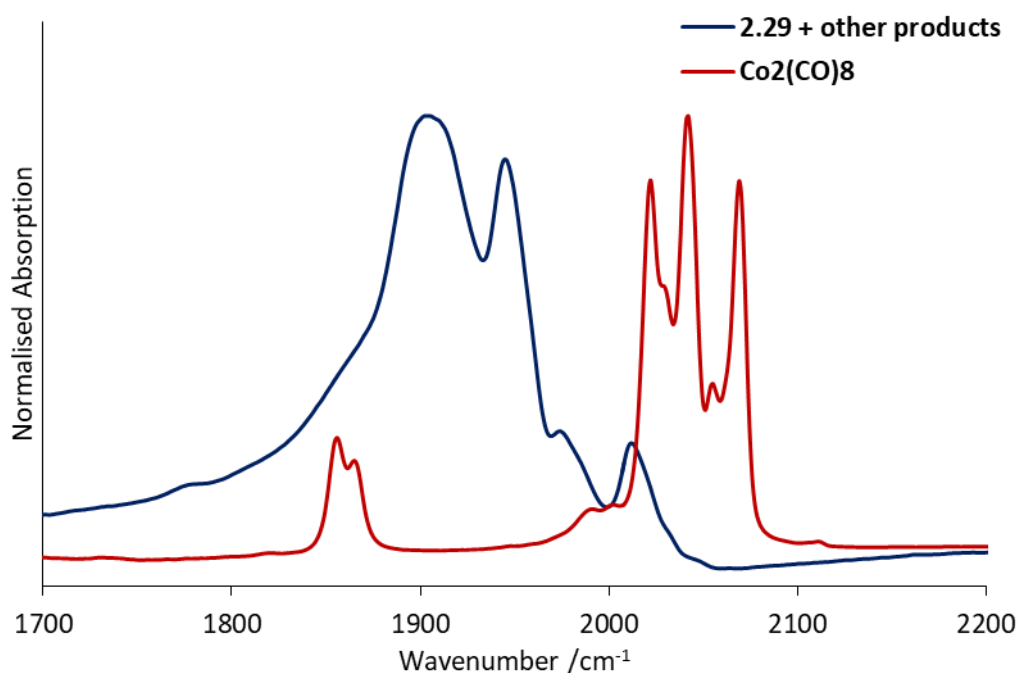


Figure 2.27 Comparison of parts of the IR spectra (in the range 1700-2200 cm^{-1}) obtained of **2.29** and $\text{Co}_2(\text{CO})_8$.

Within the ^1H NMR spectra of the product(s) of the reaction shown in **Scheme 2.50**, overlapping signals corresponding to aromatic phenyl-protons were observed within the aromatic region, suggesting that there are multiple phenyl environments present. This would be expected within the structure of **2.29** proposed in **Scheme 2.50**, as there can be no free rotation around the Co-P bond, locking the two

phenyl substituents into different environments. The ^1H NMR spectrum obtained at 400 MHz also showed four inequivalent protons corresponding to the aliphatic 'C₂-tether', which suggests the structure has a constrained geometry as a result of the phosphine moiety coordinating to cobalt. However, the resolution of these 'tether' protons was lost within the ^1H NMR spectrum obtained at 700 MHz (*i.e.* two signals each corresponding to two protons), suggesting the labile nature of the phosphine-moiety. The ^1H NMR collected at 700 MHz also displays two broad singlets, which are shown to couple to each other in the 2D COSY spectrum at δ_{H} 3.99 ($\nu_{1/2}$ 30 Hz) and 1.95 ($\nu_{1/2}$ 15 Hz) ppm. These broadened singlets had 1:1 integration and were assigned as tetrahydrofuran that is coordinated to Co through oxygen. In addition, the ^{31}P NMR spectrum obtained at 283 MHz contained multiple broadened signals (δ_{P} 85.4 ($\nu_{1/2}$ 149 Hz), 84.4 ($\nu_{1/2}$ 84 Hz), 83.7 ($\nu_{1/2}$ 84 Hz), 49.2 ($\nu_{1/2}$ 354 Hz) and one sharp signal (δ_{P} 48.7 ppm) suggesting there were multiple cobalt-bound phosphorus-species present and at least one where the phosphine donor moiety was not coordinated to cobalt (sharp). The mass spectrum obtained of the products of the reaction (**Scheme 2.50**) sample has m/z 364.008 (100%, $[\text{M}]^+$), along with 435.061 (0.76% $[\text{M}+\text{THF}-\text{H}]^+$), suggesting there was coordination of THF to cobalt. Additional, higher molecular weight, fragments were also observed, *i.e.* m/z 700.032 (7.91% $[\text{2M}-\text{CO}]^+$), and 798.941 (28.67% $[\text{2M}+\text{THF}]^+$). When these data are considered together, it is likely there is a mixture of products present, with the *hemi*-labile phosphine-moiety reversibly coordinating to cobalt to allow THF to coordinate to cobalt, and the dual-functionalised ligand sometimes acting to bridge between two cobalt centres (**Figure 2.28**).

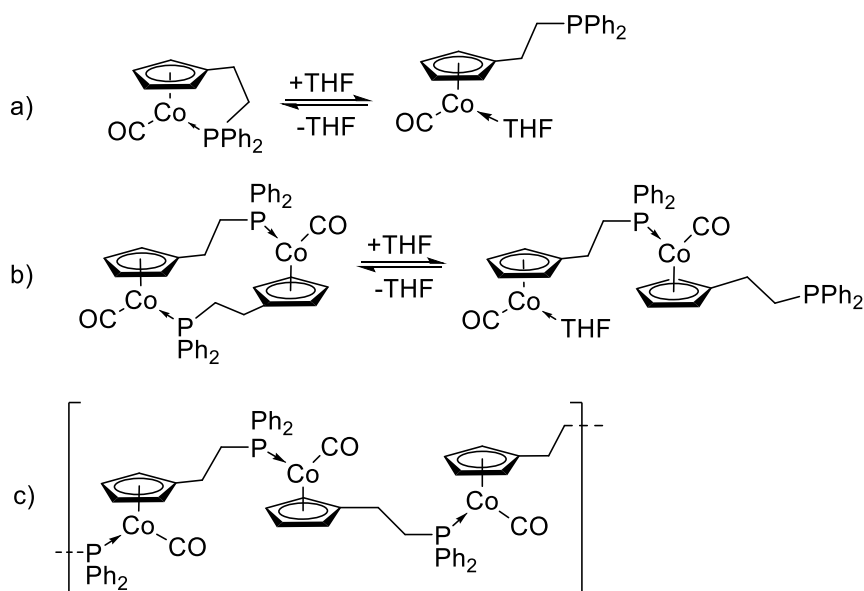


Figure 2.28 Proposed structures relating to 2.29 a) reversible coordination of phosphine-moiety and THF, b) dimeric with bridging ligands and c) polymeric with bridging ligands.

2.4 Summary and Conclusions

The main aims of the work presented here in Chapter 2 were to develop synthetic routes for the synthesis of a series of precursors to Brookhart and Broene's pre-catalyst $[(\eta^5\text{-C}_5\text{Me}_5)\text{Co}(\eta^2\text{-C}_2\text{H}_4)(\text{P}(\text{OMe})_3)]$ (**2.1**) through exploration of the synthesis of "tethered" $(\text{L}_2\text{X})\text{-CH}_2\text{CH}_2\text{-L}$ -type ligands and cobalt(I) half-sandwich complexes of Cp, Cp*, indenyl and fluorenyl. The modes by which these moieties can coordinate to cobalt have been explored. It has been proposed that the poor selectivity of the system presented by Brookhart and Broene could be attributed to poor catalyst stability. Consequently, a series of ligands with pendant donor groups to act as *hemi*-labile stabilisers to the catalyst were therefore targeted. Variations on the pendant L-type donor upon Cp, Cp*, indenyl and fluorenyl-tethered ligands were attempted with the ultimate goal of investigations upon the electronic influence of the pendant donor upon selectivity and activity within catalytic LAO to LAO dimerisation reactions.

Multiple synthetic routes were explored in attempts to synthesise $(\text{L}_2\text{X})\text{-CH}_2\text{CH}_2\text{-L}$ -type ligands (**2.3a**, **2.4a,b**, **2.9a,b**, **2.11a-c**, **2.13a,b** and **2.15a,b**). However, attempts to produce "tethered" fluorenyl ligands, $\text{Flu-CH}_2\text{CH}_2\text{-L}$ ($\text{L} = \text{PR}_2, \text{NR}_2$), from the compound $\text{Flu-CH}_2\text{CH}_2\text{-Br}$ (**2.2a**) almost always resulted in the formation of *spiro*[cyclopropane-1,9-fluorene] (**2.6**). Attempts to deliberately synthesise **2.6** and attempts to ring-open **2.6** with, *e.g.* lithium phosphide, to produce $\text{Flu-CH}_2\text{CH}_2\text{-PR}_2$ ($\text{R} = t\text{Bu}$ **2.3a**, Ph **2.4a**) were unsuccessful. However, tethered ligands $(\text{L}_2\text{X})\text{-CH}_2\text{CH}_2\text{-L}$ ($\text{L}_2\text{X} = \text{Ind, Flu, L} = \text{PPh}_2, \text{NMe}_2$, **2.4b** and **2.11a,b**) were successfully synthesised from lithium halogen exchange between $\text{L}_2\text{X-Li}$ and $\text{Cl-CH}_2\text{CH}_2\text{-L}$ ($\text{L} = \text{PR}_2$ where $\text{R} = \text{Ph}$ **2.7a** (97%), Mes **2.7b** (77%); NMe_2) in poor to excellent yield (33-99%). Attempted synthesis of $\text{Flu-CH}_2\text{CH}_2\text{-PPh}_2$ (**2.4a**) from reaction of **2.7a** with fluorenyl lithium resulted in the formation of the doubly-substituted product $\text{Flu}(\text{CH}_2\text{CH}_2\text{PPh}_2)_2$ (**2.10**) which was isolated in 14% yield. Attempts to deliberately synthesise **2.10** met with little success.

The corresponding lithium halogen exchange reaction between M-Cp ($\text{M} = \text{Li, Na, Tl}$) and $\text{Cl-CH}_2\text{CH}_2\text{-PPh}_2$ (**2.7a**) to produce $\text{Cp-CH}_2\text{CH}_2\text{-PPh}_2$ (**2.15a**) did not yield the desired products, therefore Cp and Cp* derivatives were produced from ring-opening of *spiro*[cyclopropane]derivatives **2.16a** and **2.16b** to produce $\text{Cp-CH}_2\text{CH}_2\text{PPh}_2$ (**2.15a**) (isolated in 80% yield as the lithium salt **2.15a-Li⁺**) or $\text{Cp}^*\text{-CH}_2\text{CH}_2\text{-PPh}_2$ (62%, **2.15b**). The compound $\text{Cp-CH}_2\text{CH}_2\text{-NMe}_2$ (**2.11c**) was successfully synthesised from $\text{Cl-CH}_2\text{CH}_2\text{-NMe}_2$ in 33% yield as an isomeric mixture. The dienol precursors (**2.12a** and **2.12b**) to $\text{Cp}^*\text{-CH}_2\text{CH}_2\text{-L}$ type ligands ($\text{L} = \text{OMe}$ **2.13a** and $\text{L} = \text{NMe}_2$ **2.13b**) were synthesised in moderate yields (56 and 51%, respectively). During the synthesis of **2.12b**, an *in situ* IPA quench of unreacted lithium was found to produce the undesired ester side product **2.14**. Ring closure of the dienol **2.12a** proved difficult, resulting in a complex mixture of products as shown by the ^1H NMR spectrum obtained.

Thus, a short series of tethered ligands with general structure $(L_2X)-CH_2CH_2-L$ has been produced where $L_2X = Cp, Cp^*, Ind, Flu$ and $L = PPh_2, NMe_2$ and the successful synthesis of these compounds was confirmed by spectroscopic and mass spectrometric techniques. It was found that the synthetic route required for formation of $L_2X-CH_2CH_2-L$ type ligands largely depends upon the L_2X -moiety, *i.e.* successful routes for indenyl and fluorenyl derivatives cannot generally be applied to Cp and Cp^* derivatives and *vice versa*. It is proposed that this is a direct result of the extended conjugated systems present in indenyl and fluorenyl when compared to Cp and Cp^* . For instance, *spiro*[cyclopropane] derivatives of Cp and Cp^* are difficult to form and easy to ring open by e.g. lithium phosphide, whereas, *spiro*[cyclopropane-1,9-fluorene] is formed under a variety of conditions and could not be ring-opened.

The complete synthesis of complex **2.1** was targeted, however this work remains incomplete. The synthesis of pre-cursors to complex **2.1** ($Cp^*Co(CO)_2$ (**2.17a**) and $Cp^*CoI_2(CO)$ (**2.18**) has been successful and these were obtained in excellent yields (89 – 99%). During the attempted synthesis of $Cp^*Co(\mu^2-I)_4CoCp^*$ (**2.19a**), incomplete removal of excess iodine from the reaction results in formation of $[Cp^*Co(\mu^2-I)_3CoCp^*][I_3]$ (**2.19b**). Complexes **2.17a**, **2.18** and **2.19b** were characterised by 1H , $^{13}C\{^1H\}$ NMR and IR spectroscopic techniques and investigations into the solid state structures of **2.17a** (previously reported) and **2.18** and **2.19b** (new structures) were carried out through single crystal X-ray diffraction.

A series of cobalt dicarbonyl complexes that are analogous to $Cp^*Co(CO)_2$ (**2.17a**) was planned to produce cobalt(I) half sandwich complexes $CpCo(CO)_2$ (**2.17b**), $IndCo(CO)_2$ (**2.17c**) and $FluCo(CO)_2$ (**2.17d**). The half sandwich complex **2.17b** was prepared in 74% yield through application of the literature procedure. However, during attempts to produce **2.17c** and **2.17d** from reaction of $Co_2(CO)_8$ with indene or fluorene in the presence of a mediator, 1,3-cyclohexadiene or 1,4-cyclooctadiene (COD), the major product of these reactions were found to be $(C_6H_8)(CO)Co(\mu^2-CO)_2Co(CO)(C_6H_8)$ (**2.22**) and $(COD)(CO)Co(\mu^2-CO)_2Co(CO)(COD)$ (**2.23**). A mechanistic study on the formation of **2.17a** from reaction of $Co_2(CO)_8$ with Cp^*H in the presence of 1,3-cyclohexadiene showed that **2.22** is not an intermediate formed during the reaction. Additional attempts to produce indenyl and fluorenyl derivatives with general structure $(L_2X)Co(L_2)$ ($L_2X = Ind, Flu, L = CO, PPh_3$) were not successful from a variety of cobalt starting materials *e.g.* $[Co(CO)_4]$ (**2.24**), $(PPh_3)_3CoCl$ (**2.27**). Where complexation of indenyl or fluorenyl to cobalt was observed to occur, the coordination modes observed were never the desired η^5 -fashion. Observed coordination modes include η^1-Ind (**2.25**, **2.28**), η^2-Ind (**2.21**) and η^1-Flu (**2.26**). Consideration of the reported 'indenyl effect' (which is amplified in fluorenyl systems) leads to the conclusion that obtaining the desired η^5 -coordination of indenyl or fluorenyl moieties to, the first row transition metal, cobalt is unlikely.

The complexation of the phosphine tethered ligand (CpLi)CH₂CH₂PPh₂ (**2.15**^{-Li⁺}) to cobalt was explored through a lithium halogen exchange with the reactive complex [ICo(CO)₄] (**2.24**) and was determined to form a mixture of half-sandwich cobalt(I) complexes (**2.29** mixture) that include both *intra*- and *inter*-molecular coordination of the *hemi*-labile phosphine moiety.

2.5 Future work and Outlook

There remains a lot of work to be done within this project in order to obtain understanding of both the mechanism and the electronic and steric parameters by which olefin dimerisation occurs through the use of Cp*Co(P(OMe)₃)(η²-C₂H₄) (**2.1**). The following sections will discuss what should be attempted in the future to develop understanding of the factors governing dimerisation of α-olefins within systems related to that of Brookhart and Broene.

2.5.1 Cobalt Half-Sandwich Complex Synthesis

The selectivity observed towards dimerisation of LAOs to LAOs through use of a homogeneous catalyst is likely the result of steric and electronic demands on the system. In the system reported by Brookhart and Broene, the steric bulk of the Cp* group is attributed to preventing oligomerisation to a certain extent. In lieu of the difficulties associated with obtaining η⁵-coordination of indenyl and fluorenyl to cobalt, a more convenient route to the exploration of the steric effects in play during dimerisation would be to investigate Cp and Cp* derivatives *e.g.* 1,2,3,4,5-Et, 1,2,3,4,5-Ph, 1,2,3,4,5-Pr, *etc.* Additionally, the electronic and (to a lesser extent) steric demands imposed by the phosphine also play a role in the selectivity observed. Investigation of the role of the phosphine ligand would be straightforward through systematic changes to the steric and electronic effects of the phosphine ligand. To investigate the electronic role of the neutral phosphine ligand alongside steric role of the L₂X-type ligands, the system presented by Brookhart and Broene can be roughly equated to catalysts of the type shown in **Figure 2.29**. Refocussing of efforts towards Cp-derivative L₂X moieties and phosphine substitution should enable a straightforward investigation into the structure-property relationship between derivatives of **2.1** and reactivity towards olefins. Not least since many phosphines and cyclopentadiene derivatives are commercially available or synthetic routes to their preparation have been reported previously.^{115,116}

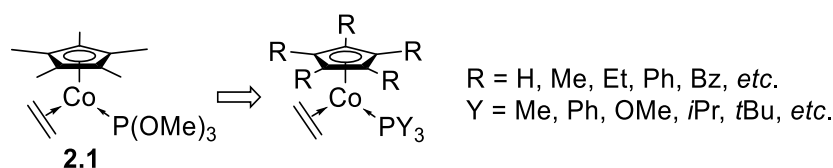


Figure 2.29 Representation of Cp*Co(P(OMe)₃)(η²-C₂H₄) displaying possible future ligand variation.²⁶

2.5.2 Proposed Constrained Geometry Pre-Catalyst Synthesis

The low activity of the catalyst presented by Brookhart and Broene for LAO dimerisation can be attributed to poor catalyst stability.²⁶ It is postulated that this low activity can be improved through stabilising the catalyst precursor through the addition of a fluxional pendant-donor to Cp* or derivative. These catalysts would therefore have a constrained geometry, dictated by the chain length of the “tether” in use. Electronic and steric controls can be imposed on the catalyst through choice of both the pendant donor and of the Cp* derivative. Examples of possible future targets for constrained geometry catalysts are shown in **Figure 2.30**.

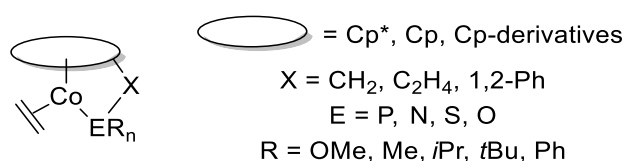
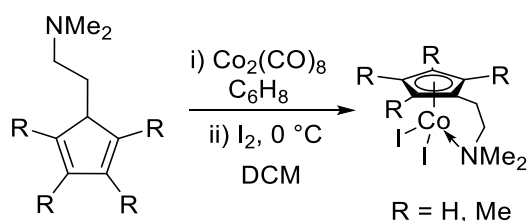


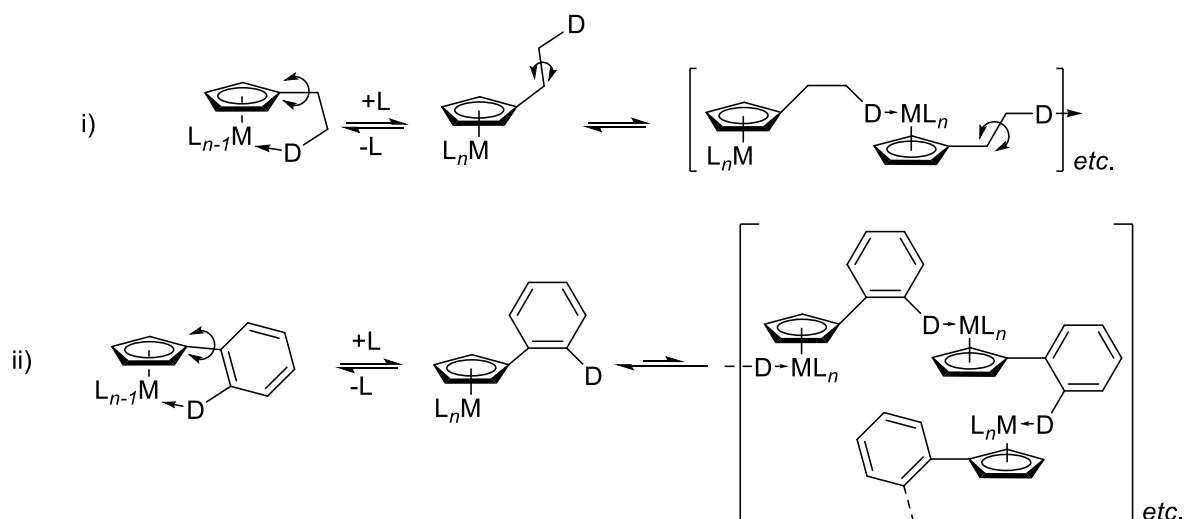
Figure 2.30 Representation of variables in constrained geometry type catalyst precursors.

Complexation of pendant-donor ligands to cobalt could be achieved through use of modifications to the literature procedures.^{48,69} This would allow for the formation of CGCs, and the subsequent effect on catalytic activity within LAO to LAO dimerisation reactions. For example, the complexation of 1-[2-(N,N-dimethylamino)ethyl]-2,3,4,5-tetramethyl-cyclopentadienyl to cobalt can be carried out from $\text{Co}_2(\text{CO})_8$ and 1,3-cyclohexadiene, as shown in **Scheme 2.51**.



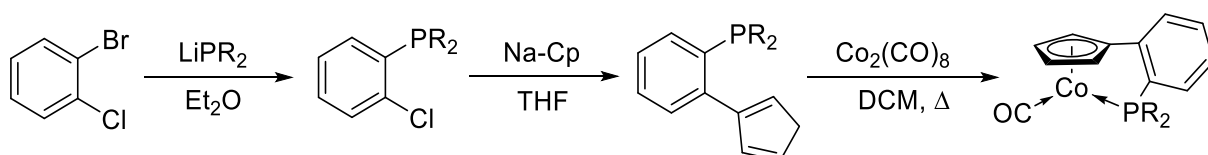
Scheme 2.51 Proposed synthetic route to pendant-dimethylamino-catalyst precursors.^{48,69}

In some instances the use of an ethyl C_2 -tether was problematic (*e.g.* repeated formation of *spiro*[cyclopropane-1,9-fluorene] and the formation of a mixture of products (**2.29**) after complexation of $\text{CpCH}_2\text{CH}_2\text{PPh}_2$ (**2.15a**) to cobalt. However, the use of a 1,2-substituted benzene to create a “ C_2 -tether” will prevent the formation of *spiro*[cyclopropane] derivatives. In addition, the flexibility of the ligand will be reduced when compared to an aliphatic derivative, and so use of a 1,2-substituted benzene may also help to reduce the formation of *inter*-molecular coordination of the ligand moieties (**Scheme 2.52**).



Scheme 2.52 Hemi-labile coordination of a pendant donor group: *intra*-molecular (LHS) and *inter*-molecular (RHS) bonding modes possible for Cp-fragments with pendant donor, D with postulated reduction in the formation of inter-molecular when 1,2-disubstituted benzene is used (ii) in place of ethyl (i) as the “tether.”

The preparation of a 1,2-disubstituted benzene ligand containing L_2X - and L-type functionality could conceivably be prepared through use of 1-bromo-2-chloro-benzene and sequential reaction with lithium phosphide and cyclopentadienyl sodium. If successful, complexation of the proposed ligand should be able to be achieved through modification of the literature procedure for the preparation of $CpCo(CO)_2$ (**Scheme 2.53**).⁹⁴



Scheme 2.53 Proposed synthetic route for the formation of constrained geometry catalyst with a phenyl tether.⁹⁴

Finally, it would also be of interest to determine the relative stabilities of indenyl and fluorenyl moieties, which are coordinated to cobalt. For this reason a computational study to calculate the relative energies of complexes of cobalt with η^1 , η^2 , η^5 and η^6 coordinated indenyl and fluorenyl-moieties should be undertaken. In particular, the available orbital mixing and degree of electron delocalisation within indenyl and fluorenyl when compared to Cp and Cp* would be interesting.

2.6 References

- 1 A. Carter, S. A. Cohen, N. A. Cooley, A. Murphy, J. Scutt and D. F. Wass, *Chem. Commun.*, 2002, **3**, 858–859.
- 2 D. S. McGuinness, *Chem. Rev.*, 2011, **111**, 2321–2341.
- 3 M. Uemura, H. Yorimitsu and K. Oshima, *Chem. Comm.*, 2006, 4726–4728.
- 4 A. Jabri, C. B. Mason, Y. Sim, S. Gambarotta, T. J. Burchell and R. Duchateau, *Angew. Chemie - Int. Ed.*, 2008, **47**, 9717–9721.
- 5 J. R. Briggs, *J. Chem. Soc. Chem. Commun.*, 1989, 674.
- 6 *Philips Petroleum Company*, US 5523507, 1996.
- 7 *Philips Petroleum Company*, EN 0608447A1, 1994.
- 8 *Philips Petroleum Company*, US 5856257, 1999.
- 9 L. M. Farrell, *Developments in LAO Comonomer Technologies for Polyethylene*, PERP 2011S11, 2012.
- 10 Plastics Europe, *Linear Low Density Polyethylene (LLDPE)*, Brussels, Belgium, 2008.
- 11 *Mitsubishi Chemical Corporation*, EN 0608447A1, 1994.
- 12 *Mitsubishi Chemical Corporation*, EP 0611743, 2000.
- 13 *Mitsubishi Chemical Corporation*, US 5856612, 1999.
- 14 A. Bollmann, K. Blann, J. T. Dixon, F. M. Hess, E. Killian, H. Maumela, D. S. McGuinness, D. H. Morgan, A. Neveling, S. Otto, M. Overett, A. M. Z. Slawin, P. Wasserscheid and S. Kuhlmann, *J. Am. Chem. Soc.*, 2004, **126**, 14712–14713.
- 15 S. Pillai, M. Ravindranathan and S. Sivaram, *Chem. Rev.*, 1986, **86**, 353–399.
- 16 A. M. Al-Jarallah, J. A. Anabtawi, M. A. B. Siddiqui and A. M. Aitani, *Catalysis Today*, 1992, **14**, 1–124.
- 17 *Goodyear Tire and Rubber Company*, US 3813453, 1971.
- 18 J. R. Jones, *J. Chem. Soc. C Org.*, 1968, 1117–1124.
- 19 J. R. Jones and T. J. Symes, *J. Chem. Soc. C Org.*, 1971, 1124–1130.
- 20 R. G. da Rosa, M. O. de Souza and R. F. de Souza, *J. Mol. Catal. A Chem.*, 1997, **120**, 55–62.
- 21 F. Majoumo-Mbe, P. Lonneck, V. Volkis, M. Sharma, M. S. Eisen and E. Hey-Hawkins, *J. Organomet. Chem.*, 2008, **693**, 2603–2609.
- 22 B. L. Small and A. J. Marcucci, *Organometallics*, 2001, **20**, 5738–5744.
- 23 *Chevron Philips Chemical Company*, US 7223893, 2007.
- 24 B. L. Small, *Organometallics*, 2003, **22**, 3178–3183.
- 25 K. P. Tellmann, V. C. Gibson, A. J. P. White and D. J. Williams, *Organometallics*, 2005, **24**, 280–286.
- 26 R. D. Broene, M. Brookhart, W. M. Lamanna and A. F. Volpe, *J. Am. Chem. Soc.*, 2005, **5**,

17194–17195.

- 27 J. M. O'Connor and C. P. Casey, *Chem. Rev.*, 1987, **87**, 307–318.
- 28 I. A. Lobanova and V. I. Zdanovich, *Russ. Chem. Rev.*, 1988, **57**, 967–980.
- 29 G. Huttner, H. H. Brintzinger and L. G. Bell, *J. Organomet. Chem.*, 1978, **145**, 329–333.
- 30 P. R. Schonberg, R. T. Paine, C. F. Campana and E. N. Duesler, *Organometallics*, 1982, **1**, 799–807.
- 31 M. E. Rerek, L. N. Ji and F. Basolo, *J. Chem. Soc. Chem. Commun.*, 1983, 1208–1209.
- 32 D. J. Jones and R. J. Mawby, *Inorganica Chim. Acta*, 1972, **6**, 157–160.
- 33 A. J. Hart-Davis, C. White and R. J. Mawby, *Inorganica Chim. Acta*, 1970, **4**, 441–446.
- 34 C. White and R. J. Mawby, *Inorganica Chim. Acta*, 1970, **4**, 261–266.
- 35 A. J. Hart-davis and R. J. Mawby, *J. Am. Chem. Soc. Inorg. Phys. Theor.*, 1969, 2403–2407.
- 36 C. Müller, D. Vos and P. Jutzi, *J. Organomet. Chem.*, 2000, **600**, 127.
- 37 U. Siemeling, *Chem. Rev.*, 2000, **100**, 1495–1526.
- 38 H. Butenschon, *Chem. Rev.*, 2000, **100**, 1527–1564.
- 39 P. Atkins, T. Overton, J. Rourke, M. Weller and F. Armstrong, *Shriver and Atkins: Inorganic Chemistry*, Oxford University Press, Oxford, 5th edn., 2009, p138.
- 40 J. C. Jeffrey and T. B. Rauchfuss, *Inorg. Chem.*, 1979, **18**, 2658–2666.
- 41 R. M. Bellabarba, M. Nieuwenhuyzen and G. C. Saunders, *Dalton Trans.*, 2001, 512–514.
- 42 D. P. Krut'ko, M. V. Borzov, E. N. Veksler, R. S. Kirsanov, A. V. Churakov and D. A. Lemenovskii, *Pure Appl. Chem.*, 2001, **73**, 367–371.
- 43 D. P. Krut'ko, M. V. Borzov, E. N. Veksler, R. S. Kirsanov and A. V. Churakov, *Eur. J. Inorg. Chem.*, 1999, 1973–1979.
- 44 S. Ciruelos, U. Englert, A. Salzer, C. Bolm and A. Maischak, *Organometallics*, 2000, **19**, 2240–2242.
- 45 A. C. McConnell, P. J. Pogorzelec, A. M. Z. Slawin, G. L. Williams, P. I. P. Elliott, A. Haynes, A. C. Marr and D. J. Cole-Hamilton, *Dalton Trans.*, 2006, 91–107.
- 46 D. P. Krut'ko, M. V. Borzov, E. N. Veksler, A. V. Churakov and K. Mach, *Polyhedron*, 2003, **22**, 2885–2894.
- 47 D. P. Krut'ko, M. V. Borzov, E. N. Veksler, A. V. Churakov and L. G. Kuz'mina, *J. Organomet. Chem.*, 2005, **690**, 4036–4048.
- 48 D. P. Krut'ko, M. V. Borzov, V. S. Petrosyan, L. G. Kuz'mina and A. V. Churakov, *Russ. Chem. Bull.*, 1996, **45**, 1740–1744.
- 49 J. Sztmونيak, J. Besancon, A. Dormond and C. Moise, *J. Org. Chem.*, 1990, **55**, 1429–1432.
- 50 P. Jutzi and U. Siemeling, *J. Organomet. Chem.*, 1995, **500**, 175–185.
- 51 P. Jutzi and J. Dahlhaus, *Coord. Chem. Rev.*, 1994, **137**, 179–199.
- 52 W. S. Rees and K. A. Dippel, *OPPI Briefs*, 1992, **24**, 527–532.

- 53 M. Enders, G. Ludwig and H. Pritzkow, *Organometallics*, 2001, **20**, 827–833.
- 54 V. Bertolasi, R. Boaretto, M. R. Chierotti, R. Gobetto and S. Sostero, *Dalton Trans.*, 2007, **8**, 5179–5189.
- 55 G. Liu, X. Lu, M. Gagliardo, D. J. Beetstra, A. Meetsma and B. Hessen, *Organometallics*, 2008, **27**, 2316–2320.
- 56 S. A. Belov, R. S. Kirsanov, D. P. Krut'ko, D. A. Lemenovskii, A. V. Churakov and J. A. K. Howard, *J. Organomet. Chem.*, 2008, **693**, 1912–1918.
- 57 J. Dahlhaus, M. Bangel and P. Jutzi, *J. Organomet. Chem.*, 1994, **474**, 55–58.
- 58 P. Jutzi, M. O. Kristen, J. Dahlhaus, B. Neumann and H. G. Stammler, *Organometallics*, 1993, **12**, 2980–2985.
- 59 P. Jutzi, C. Müller, A. Stammler and H. Stammler, *Organometallics*, 2000, **19**, 1442–1444.
- 60 P. Jutzi and T. Redeker, *Organometallics*, 1997, **16**, 1343–1344.
- 61 P. Jutzi and J. Kleimeier, *J. Organomet. Chem.*, 1995, **486**, 287–289.
- 62 Y.-X. Chen, P.-F. Fu, C. L. Stern and T. J. Marks, *Organometallics*, 1997, **16**, 5958–5963.
- 63 Y. Zhang and Y. Mu, *Organometallics*, 2006, **25**, 631–634.
- 64 E. E. C. G. Gielens, J. Y. Tiesnitsch, B. Hessen and J. H. Teuben, *Organometallics*, 1998, **17**, 1652–1654.
- 65 D. P. Krut'ko and A. V. Churakov, *Seriya K.*, 1996, **7**, 1828–1832.
- 66 O. Daugulis, M. Brookhart and P. S. White, *Organometallics*, 2003, **22**, 4699–4704.
- 67 P. Jutzi and J. Dahlhaus, *Synthesis (Stuttg.)*, 1993, 684–686.
- 68 D. P. Krut'ko and A. V. Churakov, *Seriya K.*, 1996, **4**, 984–992.
- 69 P. Jutzi, M. O. Kristen, J. Dahlhaus, B. Neumann and H. G. Stammler, *Organometallics*, 1993, **12**, 2980–2985.
- 70 J. Kukral, P. Lehmus, M. Klinga, M. Leskelä and B. Rieger, *Eur. J. Inorg. Chem.*, 2002, 1349–1356.
- 71 H. G. Alt, *J. Organomet. Chem.*, 1994, **472**, 113–118.
- 72 Z. Rohlík, P. Holzhauser, J. Kotek, J. Rudovský, I. Němec, P. Hermann and I. Lukeš, *J. Organomet. Chem.*, 2006, **691**, 2409–2423.
- 73 A. Doppiu, U. Englert and A. Salzer, *Chem. Commun.*, 2004, 2166–2167.
- 74 P. M. Nedorezorva, E. N. Veksler, E. S. Novikova, V. A. Optov, A. O. Baranov, A. M. Aladyshev, V. I. Tsvetkova, B. F. Shklyaruk, D. P. Krut'ko, A. V. Churakov, L. G. Kuz'mina and J. A. K. Howard, *Russ. Chem. Bull. Int. Ed.*, 2005, **54**, 400–413.
- 75 A. R. Siedle, R. A. Newmark, B. F. Duerr and P. C. Leung, *J. Mol. Catal. A Chem.*, 2004, **214**, 187–198.
- 76 E. V. Shulishov, O. A. Pantyukh, L. G. Menchikov and Y. V. Tomilov, *Tetrahedron Lett.*, 2019, **60**, 2043–2045.
- 77 M. T. Honaker, B. J. Sandefur, J. L. Hargett, A. L. McDaniel and R. N. Salvatore, *Tetrahedron*

- Lett.*, 2003, **44**, 8373–7377.
- 78 D. Crich, Ed., *Handbook of Reagents for Organic Synthesis, Reagents for Radical and Radical Ion Chemistry*, John Wiley and Sons, Online Edi., 2013, p1-728.
- 79 N. J. Lawrence and H. Beynek, *Synlett*, 1998, 497–498.
- 80 F. Taullaj, D. Armstrong, A. J. Lough and U. Fekl, *Polyhedron*, 2016, **108**, 30–35.
- 81 P. W. Causey, M. C. Baird and S. P. C. Cole, *Organometallics*, 2004, **23**, 4486–4494.
- 82 M. Helms and H. Fullbier, *J. Pract. Chem.*, 1986, **328**, 643–647.
- 83 W. F. Bailey, M. R. Luderer and K. P. Jordan, *J. Org. Chem.*, 2006, **71**, 2825–2828.
- 84 E. C. Ashby and T. N. Pham, *J. Org. Chem.*, 1987, **52**, 1291–1300.
- 85 D. P. Krut'ko, M. V. Borzov, E. N. Veksler, R. S. Kirsanov and A. V. Churakov, *Eur. J. Inorg. Chem.*, 1999, **5**, 1973–1979.
- 86 S. A. Frith and J. L. Spencer, *Inorganic Synthesis*, Wiley-Interscience, Vol. 23., 1985, p.278-279.
- 87 D. M. Roe and P. M. Maitlis, *J. Chem. Soc. A*, 1971, 3173–3175.
- 88 R. G. Beevor, S. A. Frith and J. L. Spencer, *J. Organomet. Chem.*, 1981, **446**, C25–C27.
- 89 C. P. Lenges, M. Brookhart and B. E. Grant, *J. Organomet. Chem.*, 1997, **528**, 199–203.
- 90 M. Brookhart, D. M. Lincoln, A. F. Volpe and G. F. Schmidt, *Organometallics*, 1989, **8**, 1212–1218.
- 91 L. R. Byers and L. F. Dahl, *Inorg. Chem.*, 1980, **19**, 277–284.
- 92 T. Avilés, A. Dinis, J. Orlando Gonçalves, V. Félix, M. J. Calhorda, Â. Prazeres, M. G. B. Drew, H. Alves, R. T. Henriques, V. da Gama, P. Zanello and M. Fontani, *J. Chem. Soc., Dalton Trans.*, 2002, **2**, 4595–4602.
- 93 I. Knopf, M. A. Courtemanche and C. C. Cummins, *Organometallics*, 2017, **36**, 4834–4843.
- 94 R. A. Genetti and M. D. Rausch, *J. Org. Chem.*, 1970, **35**, 3888–3897.
- 95 N. J. R. van Ekiema Hommes and T. Clark, *J. Mol. Model.*, 2005, **11**, 175–185.
- 96 O. Crichton, D. J. Taylor and J. Rest, Antony, *J. Chem. Soc. Dalton Trans.*, 1980, 167–173.
- 97 H. Wadepohl, S. Gebert, H. Pritzkow, F. Grepioni and D. Braga, *Chem. - A Eur. J.*, 1998, **4**, 279–288.
- 98 E. O. Fischer and H. Werner, *Metal π -complexes: Vol. 1 - Complexes with Di- and Oligo-olefinic Ligands*, Elsevier Publishing Company, Amsterdam, 1966, p63-73.
- 99 P. Mcardle and A. R. Manning, *J. Chem. Soc. A Inorganic, Phys. Theor.*, 1969, **3**, 2123–2128.
- 100 Cambridge Structural Database, <http://webo.csd.ccdc.cam.ac.uk/index.php>, Nov 2019.
- 101 J. C. Green, M. L. H. Green and G. Parkin, *Chem. Commun.*, 2012, **48**, 11481.
- 102 R. F. Bryan, P. T. Greene, J. Newlands, Michael and D. S. Field, *J. Chem. Soc. A Inorganic, Phys. Theor.*, 1970, 3068–3074.
- 103 R. Pankayatselvan and K. M. Nicholas, *J. Organomet. Chem.*, 1990, **384**, 361–380.

- 104 L. Bretherick, *Handbook of Reactive Chemical Hazards*, Butterworth-Heinemann Ltd., Boston, 4th edn., 1990, p730.
- 105 M. Aresta, M. Rossi and A. Sacco, *Inorganica Chim. Acta*, 1969, **3**, 227–231.
- 106 F. G. Bordwell and G. E. Drucker, *J. Org. Chem.*, 1980, **45**, 3325–3328.
- 107 F. G. Bordwell, G. E. Drucker and H. E. Fried, *J. Org. Chem.*, 1981, **46**, 632–635.
- 108 W. S. Matthews, J. E. Bares, J. E. Bartmess, F. J. Cornforth, G. E. Drucker, R. J. McCallum, G. J. McCollum, N. R. Vanier, F. G. Bordwell and Z. Margolin, *J. Am. Chem. Soc.*, 1975, **97**, 7006–7014.
- 109 A. W. Parkins and R. C. Poller, *An introduction to organometallic chemistry*, Macmillian Publishers LTD, London, 1986, p81-84.
- 110 C. White, S. J. Thompson and P. M. Maitlis, *J. Chem. Soc. Dalton Trans.*, 1977, 1654–1661.
- 111 N. A. Ustynyuk, Y. F. Oprunenko, S. G. Malyugina, O. I. Trifonova and Y. A. Ustynyuk, *J. Organomet. Chem.*, 1984, **270**, 185–199.
- 112 E. Kirillov, S. Kahlal, T. Roisnel, T. Georgelin, J. Y. Saillard and J. F. Carpentier, *Organometallics*, 2008, **27**, 387–393.
- 113 F. G. . N. Cloke, A. R. Dias, A. M. Galvao and J. L. Ferreira da Silva, *J. Organomet. Chem.*, 1997, **548**, 177–183.
- 114 P. Diversi, A. Giusti, G. Ingrosso and A. Lucherini, *J. Organomet. Chem.*, 1981, **205**, 239–246.
- 115 D. Stein and H. Sitzmann, *J. Organomet. Chem.*, 1991, **402**, 249–257.
- 116 C. Zhao, P. Li, X. Cao and Z. Xi, *Chem. - A Eur. J.*, 2002, **8**, 4292–4298.

CHAPTER 3

– Structural and Spectroscopic
Investigations into α -Diimine and
Diphosphine Cobalt(II) Halide
Complexes

“Short cuts make long delays.”

– J. R. R. Tolkien

3.1 Introduction

For homogeneous metal-catalysed reactions it is well established that the choice of ligand has a great impact upon a particular system's selectivity and activity, with small variations in the electronic or steric properties of the ligand having significant impact. The use of bidentate ligands rather than monodentate ligands in such processes can be beneficial, conferring additional catalyst stability as a result of the reduced lability of the bidentate metal scaffold through the chelate effect, imposition of geometric/structural constraints to the metal coordination sphere, and subsequent altered reactivity.¹

Among the wide variety of bidentate ligands that have been used in homogeneous catalysis applications diphosphine ligands, in particular, have found wide-spread use as a result of their readily tuned steric, geometric, and electronic characteristics.²⁻⁹ Similarly, α -diimines have been used broadly in a range of applications, combining straightforward syntheses with significant electronic variability through judicious choice of N-N backbone and substituents at the imine nitrogen.¹⁰⁻¹⁴ Of particular relevance to this thesis is the use of α -diimine and diphosphine ligands in homogeneous transition metal-catalysed selective olefin oligomerisation reactions, an arena in which such metal scaffolds have found widespread utility. Consequently, a brief literature review of the use of diimine and diphosphine complexes as catalysts/procatalysts in olefin oligomerisation and polymerisation is included at the start of this chapter. Subsequently, the remainder of this chapter will focus on the structural and spectroscopic properties obtained for series of (α -diimine)CoBr₂ and (diphosphine)CoX₂ (X = Cl, Br) complexes, which were prepared within this work, with a view to the use of such systems as selective oligomerisation catalysts in the future.

3.1.1 α -Diimine Metal Complexes and their Application within Olefin Oligomerisation Reactions

The use of α -diimines in late transition metal-catalysed ethylene oligomerisation has been studied extensively by Brookhart and co-workers.¹⁴ In particular, the use of nickel and palladium complexes bearing α -diimine ligands in the oligomerisation and polymerisation of ethylene has found particular success; some representative examples of such complexes are shown in **Figure 3.1**.¹⁴⁻¹⁶

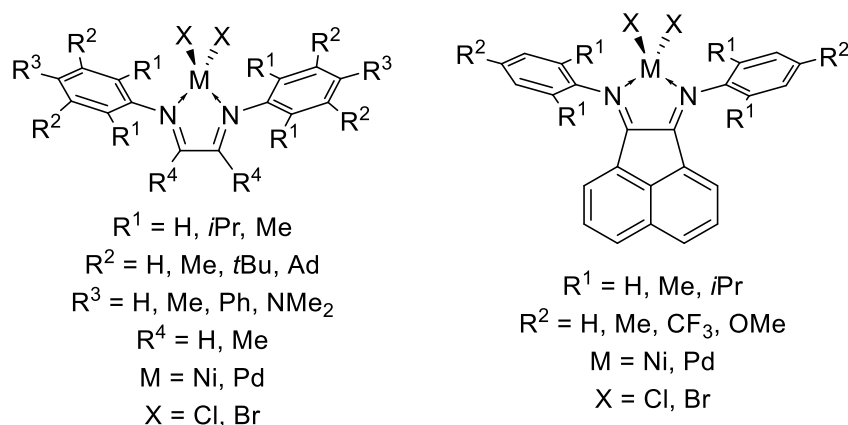
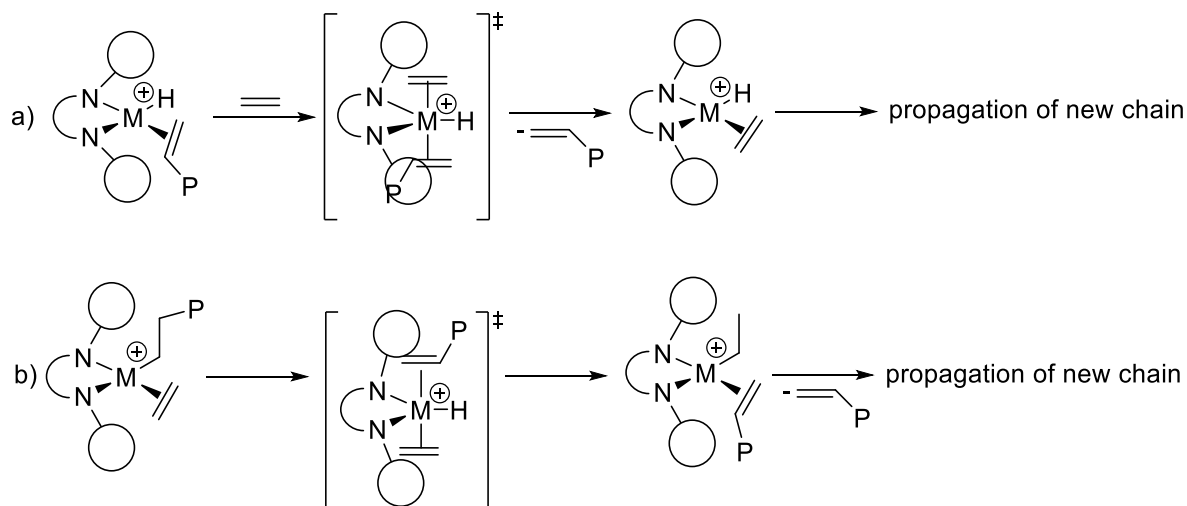


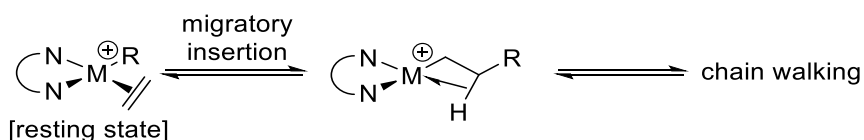
Figure 3.1 Representative examples of α -diimine complexes of Ni and Pd used for ethylene homo- and co-polymerisation.¹⁴

The structural and electronic versatility of design of α -diimine ligands, as illustrated in **Scheme 3.1**, has allowed the development of ethylene polymerisation systems that give excellent selectivity to high molecular weight polyethylene and with controllable degrees of chain branching. In this context, it has been demonstrated that the use of bulky N-aryl substituents on the α -diimine ligand, in particular, can be used to gain control over molecular weight distribution of the polyethylene produced. There are two proposed mechanisms by which the molecular weight of the polyethylene can be enhanced through addition of steric bulk (**Scheme 3.1**). In **Scheme 3.1a**, steric congestion about the metal coordination sphere by substitution of the N-aryl group (R^1 -position in **Figure 3.1**) helps to reduce the available space within the coordination sphere, blocking axial approach of monomer (ethylene) and thus reducing the rate of chain transfer, allowing high molecular weight polyethylene to be produced. In **Scheme 3.1b**, direct β -hydride transfer to the monomer from the alkyl-olefin resting state is suggested. The transition states for both pathways shown in **Scheme 3.1a** and **b** place the olefins in axial positions, and thus, the rate of chain transfer is reduced through introduction of steric bulk as the transition state is destabilised.^{15,17–20}



Scheme 3.1 Proposed mechanism of chain transfer in Ni α -diimine-mediated ethylene polymerisation, a) associative displacement from olefin hydride intermediate and b) direct β -hydride transfer to monomer from alkyl-olefin resting state.¹⁴

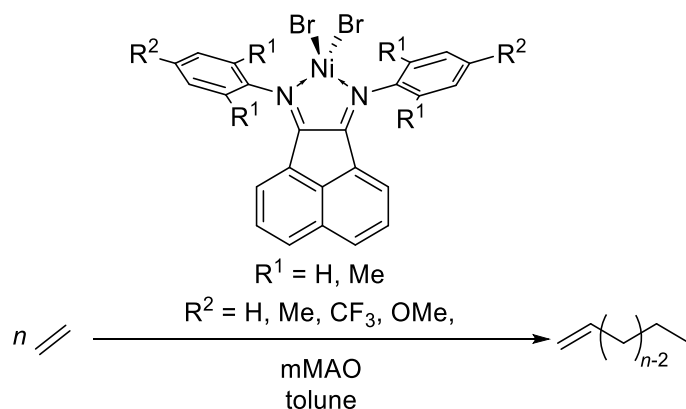
The addition of steric bulk to the aryl-N substituent within the α -diimine Ni or Pd complexes (**Figure 3.1**) investigated by Brookhart and co-workers also has the effect of increasing branching within the resulting polyethylene polymer chain.¹⁴ This increase in branching is attributed to an increase in the rate of chain-walking within these complexes (discussion of the mechanism of chain-walking can be found in Chapter 1, Section 1.5.1). The increase of steric bulk on N-aryl substituents acts to destabilise the metal-alkyl resting state (**Scheme 3.2**) as a result of geometric constraints, thus increasing the rate of migratory insertion to produce the β -agostic-stabilised transition state that can then undergo chain-walking to result in branched polymer formation (**Scheme 3.2**).



Scheme 3.2 Migratory insertion to produce β -agostic stabilised transition state, which undergoes chain-walking.

The conditions (*e.g.* temperature, pressure, *etc.*) under which the polymerisation reaction of ethylene is performed (using either Ni or Pd α -diimine pro-catalysts) are also observed to have a significant effect upon the selectivity of the reaction. For instance, Brookhart and co-workers tested a series of α -diimine complexes in which the diimine has an acenaphthyl-backbone (**Scheme 3.3**) for ethylene oligomerisation reactions, and found a high propensity for the production of linear α -olefinic (LAO) products.¹⁶ In this study carried out by Brookhart *et al.* the authors found that an increase in ethylene pressure resulted in an increase in the tendency to produce linear alpha-olefin (LAO) products. This

was attributed to an increasing rate of chain transfer relative to the rate of chain-walking (required for the formation of branched chains). Furthermore, increasing the electrophilicity of the metal centre (*e.g.* when $R^2 = \text{Me}$ vs $R^2 = \text{CF}_3$), saw an 2-fold increase in the TOF. Thus, an increase in the electrophilicity of the metal centre therefore allows increased rate of ethylene insertion. Increasing temperature saw a decrease in the Schulz Flory value, α , towards the formation of lower oligomeric products with a decrease in the selectivity for α -olefinic products. This suggests that as temperature increases, the rate of chain-transfer relative to propagation is increased.¹⁶ The systems described in **Scheme 3.3** have much less steric congestion around the metal (R^1 is H or Me vs $R^1 = i\text{Pr}$) centre than those discussed for the production of high molecular weight polyethylene (**Figure 3.1** where $R^1 = i\text{Pr}$), it is therefore postulated that a decrease in steric bulk on the N-aryl substituent of an α -diimine ligand acts to increase the rate of chain-transfer relative to the rate of chain-walking, resulting in shorter oligomers with a higher propensity for LAO formation.



Scheme 3.3 Oligomerisation of ethylene to LAOs through use of an α -diimine Ni(II) pro-catalyst, as reported by Brookhart and co-workers.¹⁶

In the vast majority of the α -diimine nickel or palladium systems investigated by Brookhart and co-workers, the polymerisation rates and productivities of the catalytic polymerisation of olefins observed are less when the substrate is any olefin of greater chain length than ethylene.¹⁴ This is also true of the α -diimine nickel systems shown in **Scheme 3.3**; these systems were tested for reactivity with propylene and 1-butene and the TOFs calculated for 1-butene reactions were <5% of those found in propylene reactions.¹⁶ Together these observations highlight the significant impact of the steric demands of the N-imine substituents upon the reactivity of the bound metal centre.

When the systems shown in **Scheme 3.3** were tested for reactivity with propylene, the value of α was seen to dramatically decrease compared to what was observed during reaction with ethylene. The reaction of these acenaphthyl-substituted α -diimine complexes with propylene was seen to produce hexenes as the primary product (>99% selectivity), with up to 42% selectivity for linear hexene

products. This remarkable observation suggests that the major dimerisation pathway involves a head-to-head insertion. The propensity of these acenaphthyl-diimine systems to produce linear olefins as a major component of the reaction products suggests that the rate of chain transfer is much higher relative to the rate of chain walking, thus reducing the rate of isomerisation to branched olefinic products. At longer reaction times (>3 h), a small degree (<10%) of isomerisation was observed suggesting that some chain-walking does still occur within these systems, but that its rate is much lower than that of chain transfer.¹⁶

As indicated above, the relative rates of β -hydride elimination vs olefin insertion is crucial in controlling the catalysis outcomes of polymerisation versus oligomerisation. By its very nature, β -hydride elimination will be favoured for metal centres with greater d^n configurations since electron retrodonation from the metal centre into C-H σ^* orbitals will be favoured. Furthermore, such retrodonation will be very dependent on the geometry around the metal centre. Consequently, there has been significant interest in exploring a range of metals for their performance in olefin oligomerisation/polymerisation. In this context, investigations into the reactivity of α -diimine cobalt-based systems with olefins are not as developed as those for nickel or palladium.¹⁴ Within ethylene polymerisation reactions, cobalt-based systems tend to have lower activity than their nickel analogues.¹⁴ A study into the ability of α -diimine cobalt complexes to polymerise ethylene in the presence of mMAO was undertaken by Ribeiro and co-workers. The complexes investigated are shown in **Figure 3.2**.²¹

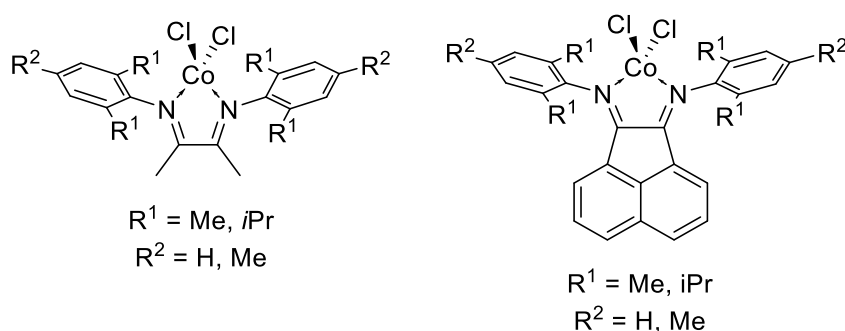


Figure 3.2 Reported examples of cobalt α -diimine complexes investigated for ethylene polymerisation.²¹

In this study by Ribeiro and co-workers, the activities of the pro-catalysts in ethylene polymerisation reactions were determined to be very low ($<1 \text{ g polyethylene (mmol cat)}^{-1} \text{ hour}^{-1} (\text{bar C}_2\text{H}_4)^{-1}$) and produced low molecular weight, branched, polyethylene materials.²¹ Attempts were made by the authors to look for the presence of short chain oligomers through GC-analysis of the volatile components of the reaction mixtures. However, no short chain oligomeric products were observed. However, the fact that no short chain oligomeric products were observed is surprising in this instance

as the polymer produced has a high degree of branching, suggesting chain transfer and chain walking events were taking place. Notably, however, the conditions under which GC analyses were undertaken by the authors means that the observation of low molecular weight olefinic products is unlikely if they had been formed. Most notably, the GC analysis runs were started at a temperature of 60 °C, which makes observation of low molecular weight oligomers such as butenes unlikely.²¹

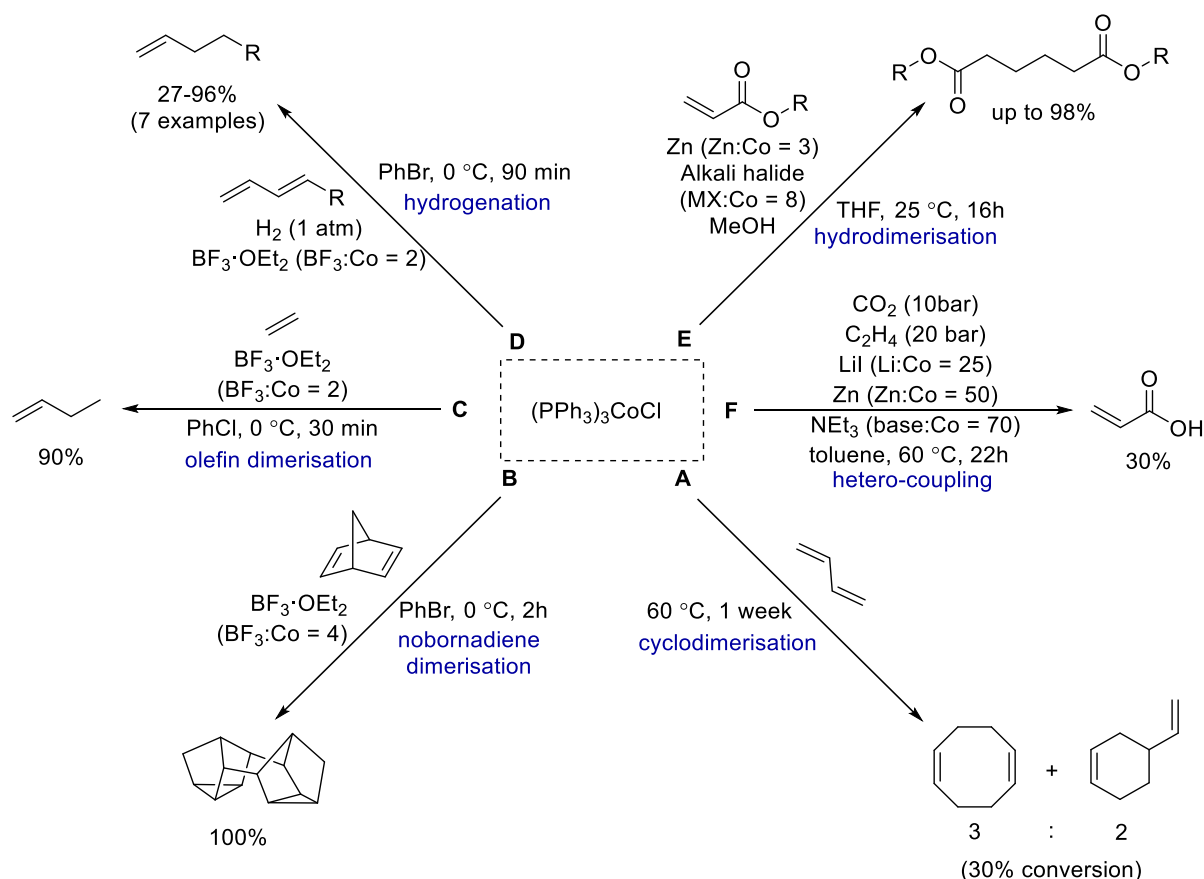
3.1.2 Phosphine-Cobalt Complexes and their Reactivity towards Olefins

Diphosphine cobalt-based systems have recently attracted significant attention for use in catalytic transformations of olefins. In particular, cobalt(I) complexes containing diphosphine or monophosphine ligands have been shown to be active olefin hydrosilylation, heterodimerisation, polymerisation and hydrogenation catalysts.^{22–28} Building on these reported studies, this thesis is primarily interested in the use of multi-dentate, chelating diphosphine ligands to stabilise cobalt(I) complexes. The available literature of well characterised diphosphine cobalt(I) complexes remains sparse, therefore this review will also include perhaps the best known cobalt(I) catalytic system, *tris*(triphenylphosphine)cobalt(I) chloride. This *pseudo*-tetrahedral system, $(\text{PPh}_3)_3\text{CoCl}$, is commercially available and contains the readily available and cheap monodentate triphenylphosphine ligand.

3.1.2.1 The Reactivity of $(\text{PPh}_3)_3\text{CoCl}$ towards Olefins

As *tris*(triphenylphosphine)cobalt(I) chloride is relatively stable under ambient conditions, cheap to prepare and already in the desired 1+ oxidation state, $(\text{PPh}_3)_3\text{CoCl}$ has been employed in a number of catalytic transformations, such as: hydrogenation, dimerisation and coupling reactions of various olefinic feedstocks.^{29–37} Some examples of transformations mediated by $(\text{PPh}_3)_3\text{CoCl}$ are shown in

Scheme 3.4.

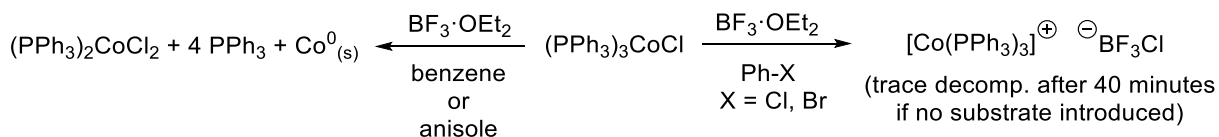


Scheme 3.4 Some examples of reported transformations using $(\text{PPh}_3)_3\text{CoCl}$.^{29–37}

Carins and Nixon reported the cyclodimerisation of 1,3-butadiene catalysed by $(\text{PPh}_3)_3\text{CoCl}$ in 0.2 mol% loading at 60 °C over the course of a week (**Scheme 3.4A**).³⁰ While conversion to the products was low (30%) the reaction did show exclusive selectivity to the cyclodimeric products, rather than the formation of linear olefinic dimers that may have been expected.^{30,38} In a similar vein, Nakayama and co-workers have reported the dimerisation of nornbornadiene with 100% conversion using $(\text{PPh}_3)_3\text{CoCl}$ (0.5 mol%) in the presence of a Lewis acid, *i.e.* $\text{BF}_3 \cdot \text{OEt}_2$ (4 eq. to Co), using bromobenzene as a solvent (**Scheme 3.4B**).³⁵ In this study on nornbornadiene dimerisation, the Lewis acid was varied and it was found that $\text{BF}_3 \cdot \text{OEt}_2$ was far superior to the commonly employed³⁷ ZnBr_2 in formation of the active cationic cobalt species, $[\text{Co}(\text{PPh}_3)_3]^+$.³⁵

In contrast to the cyclodimerisations described above, Ozaki and co-workers have reported the use of $(\text{PPh}_3)_3\text{CoCl}$ to catalyse the dimerisation of ethylene to produce 1-butene in up to 90% selectivity (**Scheme 3.4C**).^{33,34} Ozaki reports that a variety of catalyst loadings (0.6–28 mol%; based upon ethylene consumption) in the presence of a Lewis acid ($\text{BF}_3 \cdot \text{OEt}_2$) can be used to selectively dimerise ethylene to the linear α -olefinic product. The authors show that there is a one-to-one interaction between cobalt and Lewis acid, suggesting that $\text{BF}_3 \cdot \text{OEt}_2$ allows formation of the active cationic catalyst

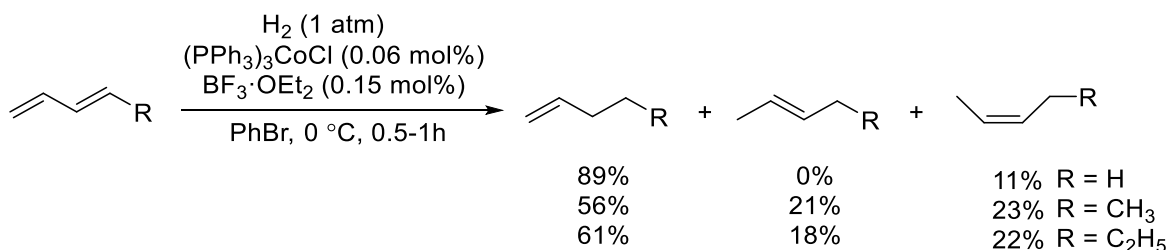
$[\text{Co}(\text{PPh}_3)_3]^+$. Ozaki and co-workers also noted that this cationic species is most stable in halo-benzene solutions. However, they did notice some trace decomposition after 40 minutes in solution if no ethylene was introduced, indicating this catalyst is stabilised by both halo-benzene and olefin substrate.³³ Complete disproportionation of $(\text{PPh}_3)_3\text{CoCl}$ in the presence of $\text{BF}_3\cdot\text{OEt}_2$ was noted when the solvent used was benzene or anisole (**Scheme 3.5**).³³



Scheme 3.5 Reported solvent-dependant stability of $(\text{PPh}_3)_3\text{CoCl}$ in the presence of $\text{BF}_3\cdot\text{OEt}_2$.³³

Based upon the observations made by Ozaki, the solvent system used for any catalytic transformations using cobalt(I) catalysts is therefore likely of great importance to prevent unwanted catalytic decomposition, such as disproportionation to cobalt(II) and cobalt(0) (**Scheme 3.5**). Additionally, it is envisaged that the use of a bidentate diphosphine ligand (rather than monodentate phosphines) should aid in stabilising any cobalt(I) complexes that are generated through the chelate effect. Aspects of the work presented in this thesis aim to help stabilisation of cobalt(I) species towards disproportionation/decomposition through introduction of bidentate diphosphines.

Ozaki and co-workers have extended their study on the reactivity of $(\text{PPh}_3)_3\text{CoCl}$ and found it is an active catalyst for the hydrogenation of 1,3-dienes (**Scheme 3.4D**).³⁷ The ability of $(\text{PPh}_3)_3\text{CoCl}$ (7 mol%) to hydrogenate a variety of dienes was explored in the presence of activator, $\text{BF}_3\cdot\text{OEt}_2$ (15 mol%), under a hydrogen atmosphere in bromobenzene; conversions to the terminal alkene product of up to 89% were reported.³⁷ Notably, this hydrogenation study emphasises that using $(\text{PPh}_3)_3\text{CoCl}$ results in little/no isomerisation of olefinic products into the thermodynamically more stable internal olefinic products. This may be inferred since some of the substrates are very rapidly hydrogenated, which would not be the case had they undergone initial isomerisation. For instance, 89% of the product mixture obtained during hydrogenation of 1,3-butadiene was isolated as 1-butene, whereas if this system was isomerising alkenes a greater proportion of 2-butenes (*cis* and *trans* isomers, thermodynamically more stable than the 1-alkene) might be expected (**Scheme 3.6**).



Scheme 3.6 Representative examples of reported hydrogenation of dienes catalysed by $(\text{PPh}_3)_3\text{CoCl}/\text{BF}_3\cdot\text{OEt}_2$.³⁷

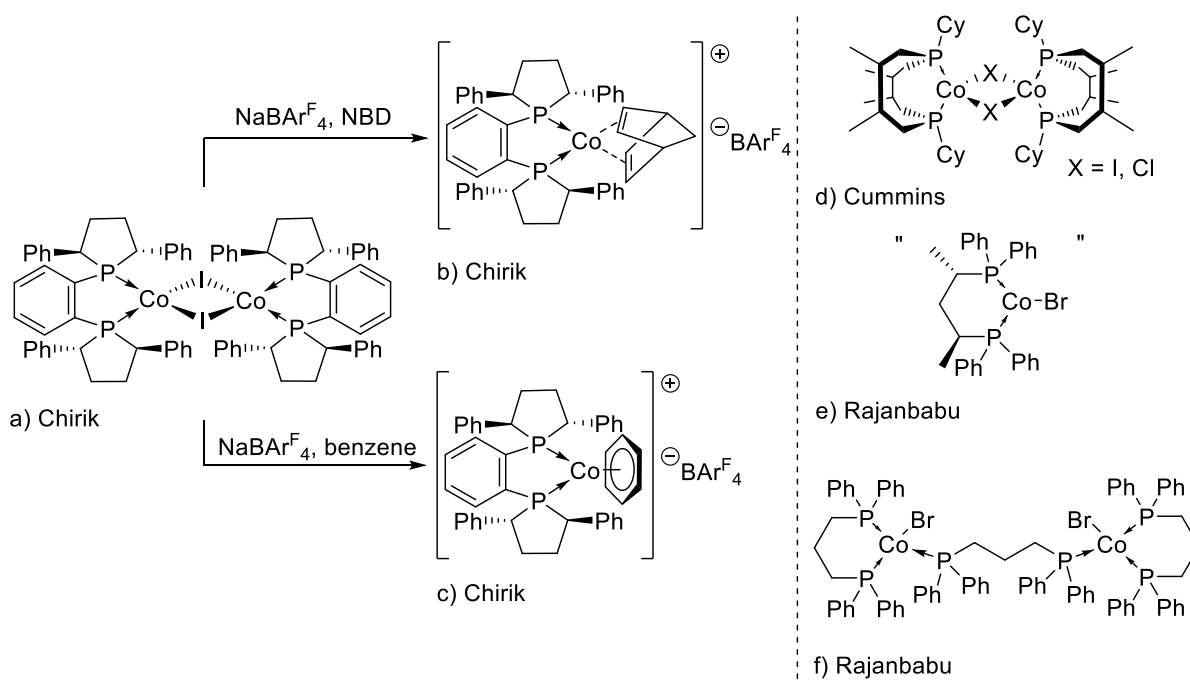
Kanai, Ishii and Okada have demonstrated the use of $(\text{PPh}_3)_3\text{CoCl}$ to mediate the hydrodimerisation of methyl acrylate to dimethyl apidate with up to 98% conversion at loadings of 6 mol% Co in the presence of Zn metal and an alkali halide (**Scheme 3.4E**).^{31,32} The authors proposed that a cobalt(I)/cobalt(II) cycle was operative where an excess of Zn dust and an alkali metal were used to aid regeneration of the active cobalt(I) species through reduction of an intermediary cobalt(II) complex.³¹ However, no detailed studies were made to investigate this mechanism and so further discussion is not warranted.

More recently, Cummins *et al.* have shown that $(\text{PPh}_3)_3\text{CoCl}$ can catalyse the coupling of ethylene and CO_2 at high pressure (20 bar C_2H_4 and 10 bar CO_2) to produce methyl acrylate in up to 30% conversion using chlorobenzene as a solvent (**Scheme 3.4F**).³⁹ Of note, Cummins and co-workers did not report any formation of dimethyl apidate, which (based upon the work of Okada) might have been expected to result from this reaction.^{31,32} Despite good selectivity, the conversions obtained by Cummins *et al.* during heterocoupling were low, despite significant efforts having been made by the authors to increase them. For example, longer reaction times did not yield any more methyl acrylate, so the authors report an unknown deactivation pathway of the cobalt(I) catalyst employed. However, the majority of the optimisation experiments performed as a part of the study by Cummins used anisole as a solvent, which from the work of Ozaki, could be the cause of catalytic decomposition through disproportionation of $(\text{PPh}_3)_3\text{CoCl}$ in the presence of a Lewis acid (LiI_2) and anisole (as shown in **Scheme 3.5**).³³

3.1.2.2 Diphosphine Cobalt Complexes and their Reactivity towards Olefins

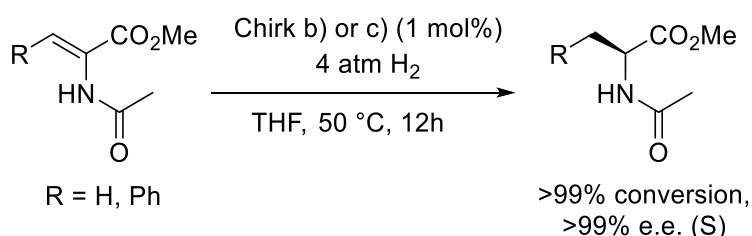
The work on diphosphine cobalt complexes for catalytic transformations by the group of Chirik has, in particular, advanced the field of diphosphine cobalt(I) mediated catalytic transformations in recent years.^{22,23,40-43} In Chirik's work, the vast majority of diphosphine cobalt pro-catalysts are cobalt(I) complexes. These cobalt(I) complexes are generally prepared *in situ* during catalysis from the cobalt(II) precursor through addition of a reducing agent (usually an excess of Zn metal). However, there are a

few examples within the literature of isolated and characterised cobalt(I) pro-catalysts, which are shown in **Scheme 3.7**.^{22,23,27,39} Of these previously-reported complexes, a), d), e) and f) were all prepared from a $(P^{\wedge}P)Co^{II}X_2$ precursor through single-electron reduction with zinc metal. In **Scheme 3.7**, the cationic cobalt(I) complexes reported by Chirik *et al.* are prepared from the cobalt(I) complex, a).



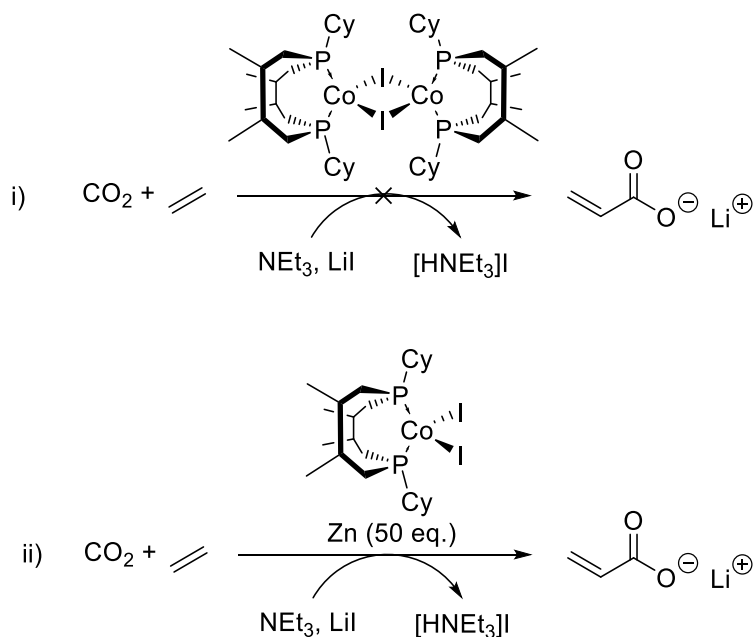
Scheme 3.7 Examples of diphosphine cobalt(I) complexes active towards olefins; all have been isolated with the exception of e).^{22,23,27,39}

The cationic pro-catalysts prepared by Chirik *et al.* shown in **Scheme 3.7** have been demonstrated to be highly active for asymmetric alkene hydrogenation reactions.²² These cationic species were tested for hydrogenation of MAA (methyl 2-acetamidoacrylate) and MAC ((*Z*)-2-acetamido-3-phenylacrylate), with full conversion to the *S*-enantiomeric products being observed after 12 hours for both substrates (**Scheme 3.8**).



Scheme 3.8 Asymmetric hydrogenation of MAA and MAC with Chirik b) or c).³⁶

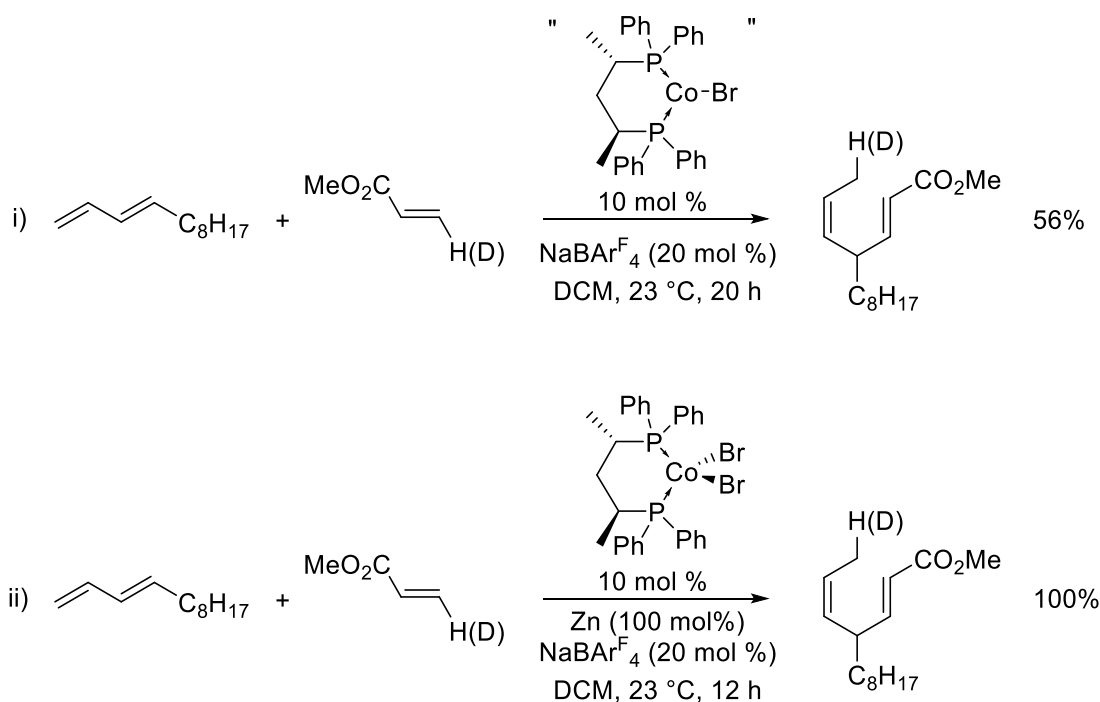
Cummins and co-workers reported the synthesis and isolation of a halide-bridged dimeric cobalt complex stabilised by a chelating macrocyclic diphosphine ligand, **Scheme 3.9**. This dimeric complex has been tested for reactivity towards coupling of ethylene and CO₂ to produce acrylates. However, the activity of the pre-formed cobalt(I) complex was found to be negligible (**Scheme 3.9i**). Acrylate production (6% conversion) from ethylene and CO₂ was observed when the reduction of the cobalt(II) pre-cursor to d) was performed *in situ* using a large excess of zinc metal (**Scheme 3.9ii**). Cummins *et al.* suggest that the lack of activity observed from the preformed dimeric cobalt(I) species could be the result of either poor solubility of the dimeric complex or through stability in solution. It was also suggested that *in situ* reduction of the cobalt(II) complex in the presence of ethylene prevents the formation of the dimeric cobalt(I) complex that, in turn, aids in increasing activity. However, the large excess of zinc metal used for the *in situ* reduction could also be playing a part in the catalytic transformation taking place. While the authors did run a control experiment with just zinc and no cobalt complex and saw no conversion to acrylate, unfortunately, the corresponding test where reaction was undertaken with zinc metal in the presence of diphosphine ligand was not performed. The role of zinc in the reduction of cobalt(II) diphosphine complexes is the primary focus of Chapter 4 herein and is a feature that will be discussed in depth.³⁶



Scheme 3.9 Attempted coupling of CO₂ and ethylene by Cummins *et al.* using pre-formed cobalt(I) complex, d).³⁶

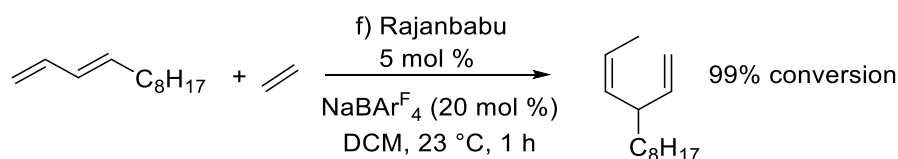
Rajanbabu and co-workers have demonstrated the use of cobalt(I) diphosphine complexes for the catalytic heterodimerisation of 1,3-dienes with acrylates. They report the use of bdpp [1,3-(dimethyl)-1,3-(diphenylphosphino)propane] cobalt(I) complexes within the heterodimerisation reactions they

describe. Similar to the results reported by Cummins, the activity of these complexes was higher during an *in situ* reduction of the cobalt(II) precursor than when compared to that achieved using a preformed cobalt(I) complex (*c.f.* **Scheme 3.10i** and **ii**). It should be noted here that the cobalt(I) complex shown in **Scheme 3.10i** was not characterised in any way by Rajanbabu *et al.* nor was any experimental detail given for the preparation of this presumed cobalt(I) complex reported. As such, it is difficult to draw any conclusions from these results.^{27,44}



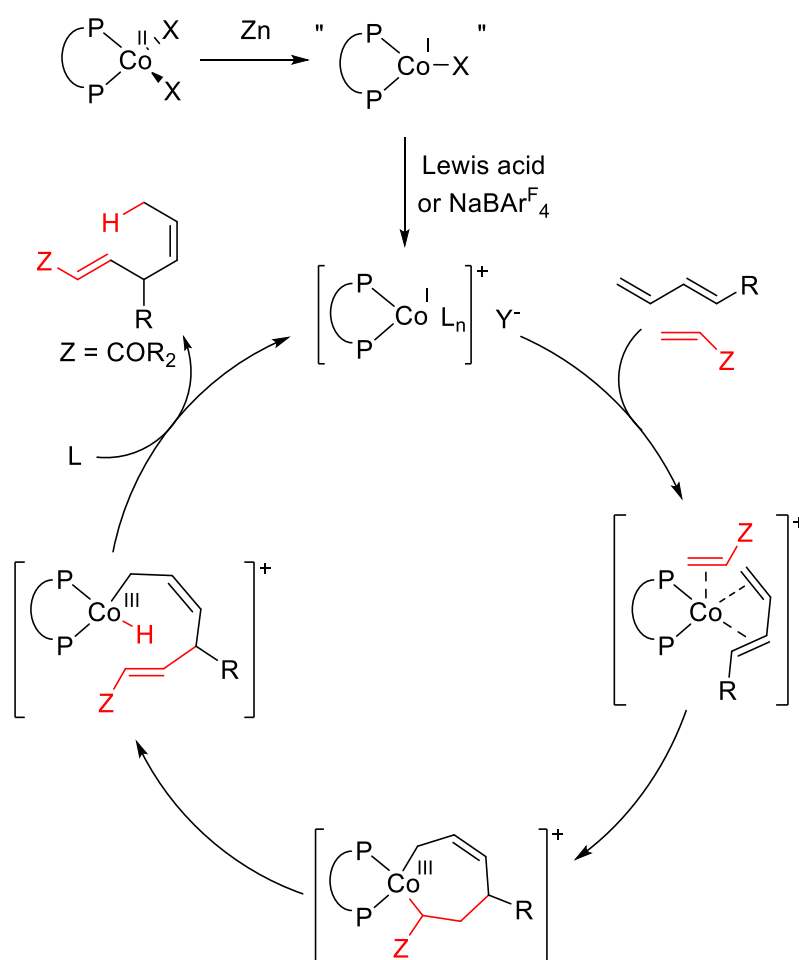
Scheme 3.10 1,3-Diene and acrylate coupling with pre-formed cobalt(I) complex or reduction *in situ* as reported by Rajanbabu *et al.*²⁷

As a part of the study by Ranjanbabu and co-workers, one cobalt(I) complex was prepared, isolated and characterised by single crystal X-ray diffraction. This complex, **Scheme 3.7f** $[(\mu_2\text{-dppp})\{(\text{dppp})\text{CoBr}_2\}_2]$, was tested for reactivity towards the coupling of 1,3-dodecadiene with ethylene and gave a 99% conversion to the coupled product after 1 hour (**Scheme 3.11**). Unfortunately, a comparison reaction with *in situ* reduction of the precursor, $(\text{dppp})\text{CoBr}_2$, was not reported by the authors and hence speculation about the catalytic pathway and species involved is impossible.²⁷



Scheme 3.11 1,3-Diene and ethylene coupling by $[(\mu_2\text{-dppp})\{(\text{dppp})\text{CoBr}_2\}_2]$ as reported by Ranjanbabu *et al.*²⁷

The chloride analogue of $[(\mu_2\text{-dppp})\{\text{dppp}\text{CoBr}\}_2]$ was also reported within the same study, although no characterisation data were included. Rajanbabu *et al.* presume a similar structure to that obtained for **f**) in **Scheme 3.7**, and found this derivative to have similar reactivity towards ethylene and 1,3-dodecadiene under the conditions shown in **Scheme 3.11** as with the bromide counterpart. Interestingly, full conversion to the coupled olefinic product was also observed when using this presumed “(dppp)CoCl” species in the presence of ZnX_2 ($\text{X} = \text{Cl}, \text{Br}, \text{I}$) in place of NaBARF_4 . A tentative mechanism for the reported heterodimerisation, as proposed by Rajanbabu, is shown in **Scheme 3.12**. This catalytic cycle accounts for the requirement of the Lewis acid (ZnI_2) or NaBARF_4 within their reactions, with either generating a counter ion to the active cationic cobalt species. The reactivity of ZnX_2 with cobalt diphosphine complexes is discussed at length in Chapter 4 herein.²⁷



Scheme 3.12 Proposed mechanism for the heterodimerisation of 1,3-dienes with acrylates modified from Stanley *et al.*²⁷

While the work from Rajanbabu is missing any meaningful characterisation of the complexes used and focuses on the formation of regio- and enantiopure 1,4-dienes, this work does suggest the likelihood that similar “(P²)Co⁺”-based systems could be utilised within the dimerisation reactions of

1-alkenes.²⁷ If a similar Co(I)/Co(II) redox system could be achieved, then selective 1-alkene dimerisation could be envisioned through a metallacyclic intermediate.^{45,46} However, the steric and electronic effects upon such a system would need to be carefully balanced to allow the desired “head-to-head” insertion of the 1-alkenes to take place.

With the above in mind, the work in this chapter is primarily focused upon development of the understanding of the bonding interactions within cobalt complexes containing diimine and diphosphine ligands. Therefore the next sections describe the general bonding of phosphines and imines to metals. In addition, the general routes to assessing steric demands within diphosphine and diimine metal complexes are discussed, as the steric properties of the system have been shown to be important in determining the outcome of olefin oligomerisation reactions, *e.g.* in (N[^]N)M catalysed olefin oligomerisation reactions.

3.1.3 The Bonding and Structure of Bidentate ([N[^]N] and {P[^]P}) Ligands

Both α -diimine and diphosphine ligands offer great opportunity for structural variation as indicated previously (**Figure 3.3**). The substituents on the N- and P-donor components of these metal scaffolds can be altered systematically to change the steric and electronic impact of the ligand upon the metal centre. Additionally, it is well-established that altering the backbone between the two donor centres of α -diimine and diphosphine ligands can have dramatic effects on the resulting properties of the metal complex, not least through variation in the bite angle at the metal centre, which, in turn, significantly influences the metal's reactivity.

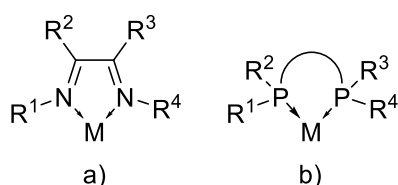


Figure 3.3 Opportunities for structural variation within α -diimine (a) and diphosphine ligands (b).

3.1.3.1 The Bonding of Imines and Phosphines to Transition Metals

In order to understand the effects of structural variations of α -diimine and diphosphines ligands upon the resulting reactivity of their metal complexes, it is first important to understand the fundamental bonding properties of the individual imine and phosphine moieties to a metal centre.

3.1.3.1.1 The Bonding of Phosphines to Transition Metals

By way of introduction, the MO diagram for phosphine, PH_3 , under C_{3v} symmetry is shown in **Figure 3.4**.

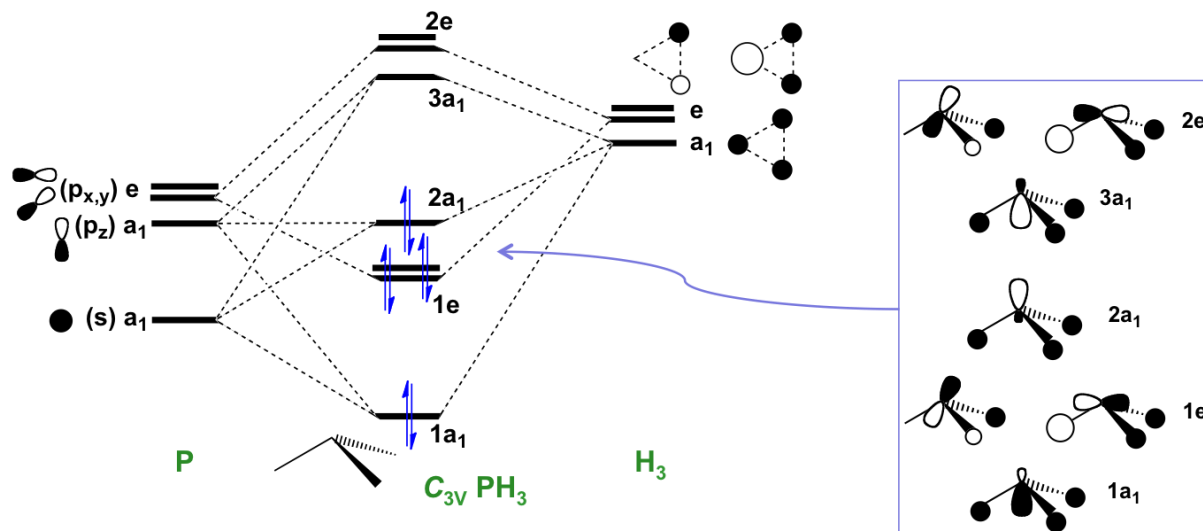


Figure 3.4 MO diagram for a PH_3 moiety under C_{3v} symmetry showing the HOMO and LUMO MOs available for bonding between the phosphine and a metal.

From the MO diagram of the phosphine (**Figure 3.4**) it is easy to understand how simple variation of the substituent at phosphorus can dramatically alter both the σ -donor and also π -acceptor character of a phosphine (**Figure 3.5**). For example, for a phosphine PR_3 , when R is electron-withdrawing in character (*e.g.* Ph, OR, F) the HOMO is lowered in energy, resulting in the phosphine being a weaker σ -donor and stronger π -acceptor.

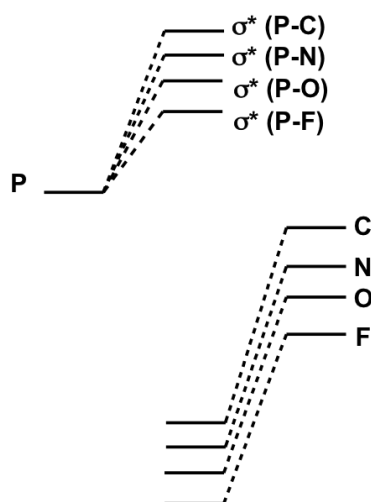
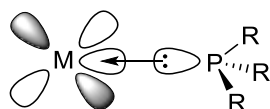


Figure 3.5 Impact upon the HOMO-LUMO gap of a phosphine upon variation in the character of the substituents at phosphorus.

The bonding of a phosphine to a metal centre can be considered to have two components. This coordination is dominated by σ -donation from a filled sp^3 hybrid-type orbital on phosphorus to an empty or partially filled σ -symmetry orbital on the metal, *i.e.* lone pair donation (**Figure 3.6a**). More rigorously, this interaction is better viewed as the donation of a pair of electrons from the $2a_1$ HOMO of a simplified phosphine (PH_3) motif (**Figure 3.4**). Phosphines also have the ability to act as π -acceptors and as such participate in ' π -back bonding' from a filled d orbital on the metal to the phosphine (**Figure 3.6b**). The unoccupied LUMO hybrid orbitals on phosphorus capable of π -acceptance can be thought of as a P_π , and is the combination of σ^* anti-bonding orbitals (P-R) and $3d$ orbitals on phosphorus (**Figure 3.6c**),⁴⁷⁻⁴⁹ it is generally recognised that the contribution from phosphorus d -orbitals is extremely minor.

- a) σ -donation from filled P-centered $2a_1$ MO to an empty σ symmetry orbital on M



- b) π -acceptance by P_π LUMO (P-R σ^* MO) on P from filled d orbital on M



- c) Combination of P-R σ^* anti-bonding MO and P $3d$ orbital to give doubly degenerate PR_3 LUMO

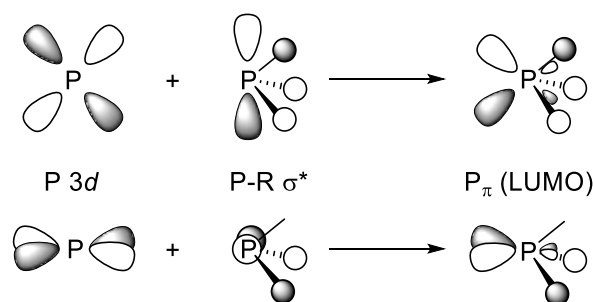


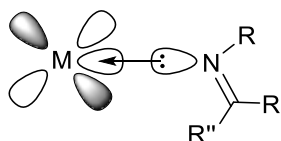
Figure 3.6 The two principal frontier orbital components involved in the bonding between a phosphine and a metal.

3.1.3.1.2 The Bonding of Imines to Transition Metals

The bonding between an imine to a metal can also be considered to have two components: σ -donation from the lone pair of the imine nitrogen to the metal and π -acceptance by the imine from the metal. The σ -donor component is lone pair donation from a formally sp^2 hybrid orbital on nitrogen to an empty or partially filled metal d -orbital with σ -symmetry (**Figure 3.7a**). The π -acceptor ability of the

imine is of differing significance depending on whether the imine C=N bond is conjugated or not. For an unconjugated imine, the antibonding $\pi^*_{\text{C=N}}$ can act to accept electron density from a metal d orbital (**Figure 3.7b**), however this effect is not believed to be significant.⁵⁰ For imines which are part of an extended π -system, acceptance by the π^* antibonding orbital of the conjugated π -systems is significant. However, when α -diimine ligands are compared with β -diimine ligands, there is typically no appreciable difference in the bond order of M-N (as determined by M-N bond lengths) observed, suggesting that no significant conjugation exists between imine moieties in α -diimine complexes (metallacycle).⁵¹⁻⁵³

- a) σ -donation from filled N sp^2 -type hybrid orbital to empty σ symmetry orbital on M



- b) π -acceptance by π^* anti-bonding N=C MO from filled d orbital on M

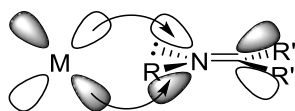


Figure 3.7 MO diagrams representing the bonding between an imine and a metal.

3.1.3.2 Assessing the Steric Demands of Diimines and Diphosphines

Assessing the steric demands imposed upon a metal centre by a ligand is of great interest and importance as it determines to what extent the coordination sphere of the metal is occupied or blocked by the ligand. This is of particular consequence when considering catalytic processes, as the available space within a metal's coordination sphere can determine not only the ease and mode of binding of a substrate, but subsequently also the regio- or stereoselectivity within a given catalytic process. See section 3.1.1 (*vide supra*) for examples.

The steric bulk of the bidentate ligands on a metal can be investigated through use of the 'percentage buried volume' ($\%V_{\text{bur}}$ values) approach.⁵⁴ Analysis of the $\%V_{\text{bur}}$ values is a more useful tool for analysis of chelating ligands than the Tolman cone angle, which is more applicable to, for instance, monophosphines.⁵⁴⁻⁵⁶ For a symmetric monophosphine ligand, the Tolman cone angle is defined as twice the angle between the outer edge of the van der Waals radii of the substituents at phosphorus and the M-P axis. The Tolman cone angle can be used to gain a good indication of relative steric bulk within symmetric monophosphines, but when asymmetric phosphines or bidentate ligands are investigated, the cone angle becomes much more complex (**Figure 3.8**). The use of percentage buried

volume (%V_{bur}) approach is much more applicable to bidentate ligand systems (e.g. diphosphines, diimines) as it allows measurement of the steric congestion within the metal coordination sphere directly from crystallographic data. Representations of both the Tolman cone angle and %V_{bur} are shown in **Figure 3.8**. The free, on-line software SambVca 2.1 was used to calculate the %V_{bur} and works by placing the ligand of interest at a set distance (2.0 Å) from the metal centre, and surrounding the metal centre with a sphere with arbitrary radius (3.5 Å).⁵⁴ The percentage of the sphere that is then occupied by the ligand is therefore the value of %V_{bur}. Thus, for example, for a set of ligands with increasing values of %V_{bur} means that there is increasing steric congestion imposed by the ligand close to the metal centre. The software SambVca 2.1 can also be used to generate ‘steric maps’ of a ligand when coordinated to a metal centre in the solid state. These maps can be particularly useful for visualising how sterically congested the space around the metal centre is when considering how a substrate molecule could approach the metal centre (**Figure 3.8**).

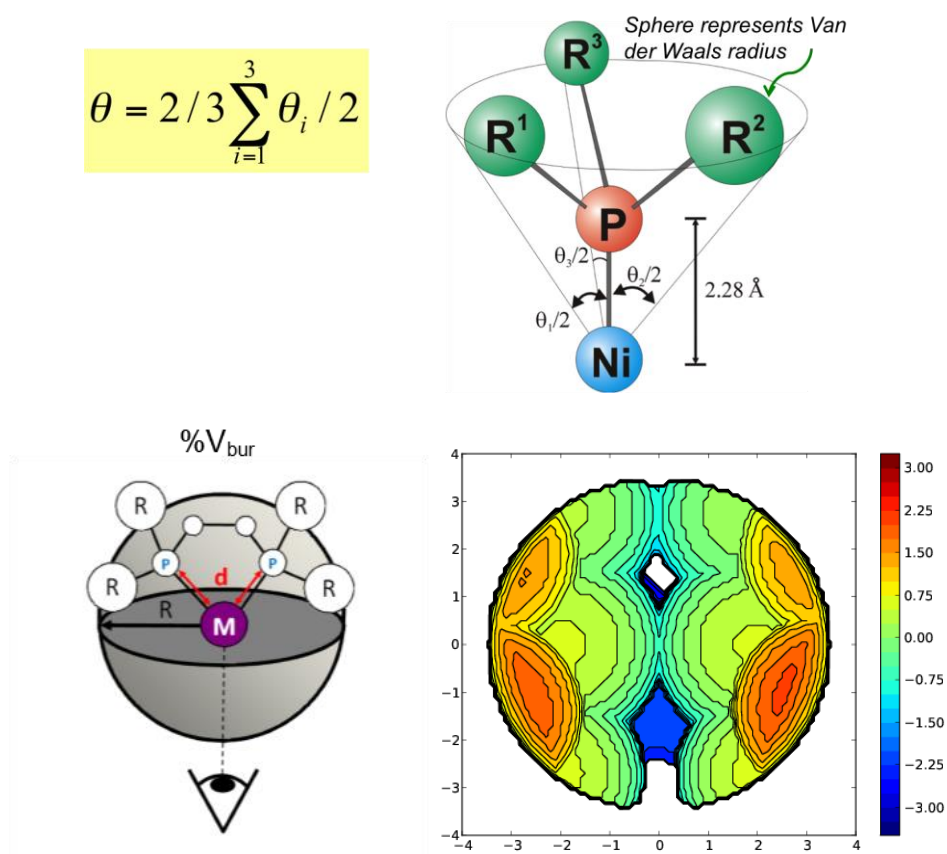


Figure 3.8 Top: Representations of Tolman's cone angle (asymmetric monophosphine ligand). Bottom LHS: %V_{bur} (diphosphine ligand) with direction of view for steric maps generated highlighted. Bottom RHS: Representative steric map of a chelating diphosphine generated by SambVca 2.1.⁵⁴

This chapter is focussed on the synthesis and characterisation of series of (P[^]P)CoX₂ and (N[^]N)CoBr₂ complexes. Where possible, structural investigations are launched, including the use of %V_{bur}, through

analysis of the molecular structures of the prepared cobalt(II) complexes that were obtained by single crystal X-ray diffraction.

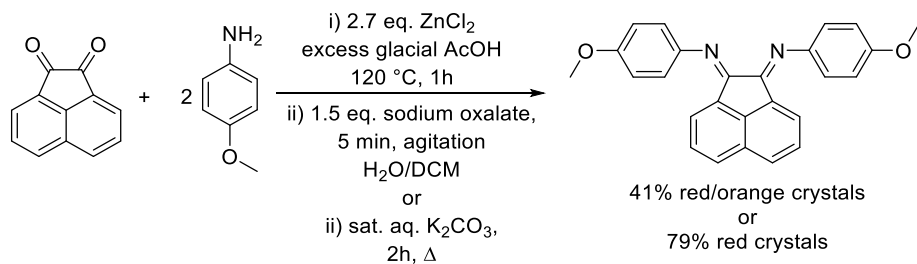
3.2 Preparation and Characterisation of a Series of (α -Diimine)cobalt(II) Bromide Complexes (**3.2a-d**)

The use of α -diimine cobalt complexes within olefin oligomerisation reactions has not yet been explored in great detail. Applying the same logic used within the nickel and palladium systems reported by Brookhart *et al.*, it seems likely that similar systems to those reported by Ribeiro could be used to catalyse olefin oligomerisation reactions (with low values of α).^{14,21} Therefore, the work presented in this thesis will include the preparation of α -diimine cobalt systems with low steric bulk on the N-aryl substituent. Future reaction of these prepared complexes with ethylene under conditions favouring oligomerisation, *e.g.* high ethylene pressures and moderate temperatures, could be a viable route to achieving regio- and stereoselective ethylene oligomerisation to LAOs. For this reason, a small series of (α -diimine)cobalt(II) bromide complexes (**3.2a-d**) were prepared and the electronic and structural characteristics of the resulting species investigated.

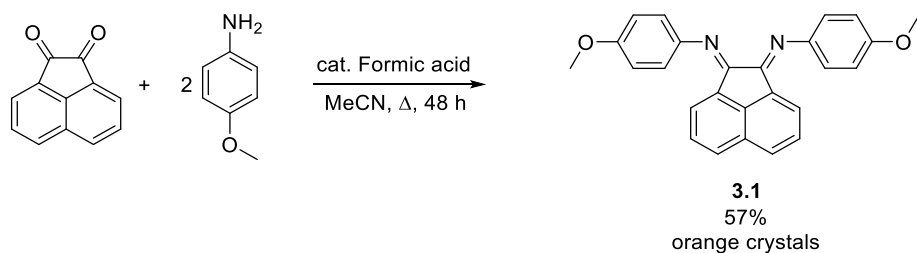
3.2.1 Synthesis of α -Diimine (L_2) Ligands

The synthesis of α -diimine ligands is well established. As such, modifications to existing literature procedures can be employed for the synthesis of a range of α -diimine compounds with substitutional variation in good yields. All α -diimine ligands used within this work were synthesised previously within the PWD group, through adaptation of literature procedures, with the exception of *bis*-(4-methoxyphenyl)-acenaphthylquininediimine (*p*-(OMe)-BIAN}. Existing literature syntheses of {*p*-(OMe)-BIAN} employ multiple steps and use a large excess of concentrated acid followed by basic work up (**Scheme 3.13A**). Here, in this thesis it has been shown that the synthesis of {*p*-(OMe)-BIAN} using an acid-catalysed condensation reaction, followed by recrystallization from ethanol, could be used to produce the target α -diimine in good yield (57%). The spectroscopic data obtained for {*p*-(OMe)-BIAN} match those reported previously.⁵⁷

A) literature procedure:



B) this work:



Scheme 3.13 Synthesis of $\{(p\text{-OMe})\text{-BIAN}\}$ from the reaction of acenaphthenequinone with p -anisidine.⁵⁷

With a range of variously-substituted α -diimine ligands in hand, the preparation of $(\text{N}^{\wedge}\text{N})\text{CoBr}_2$ complexes was achieved through simple ligand coordination with cobalt(II) bromide in THF using standard Schlenk techniques. The complexes synthesised within this work are shown in **Figure 3.9**.

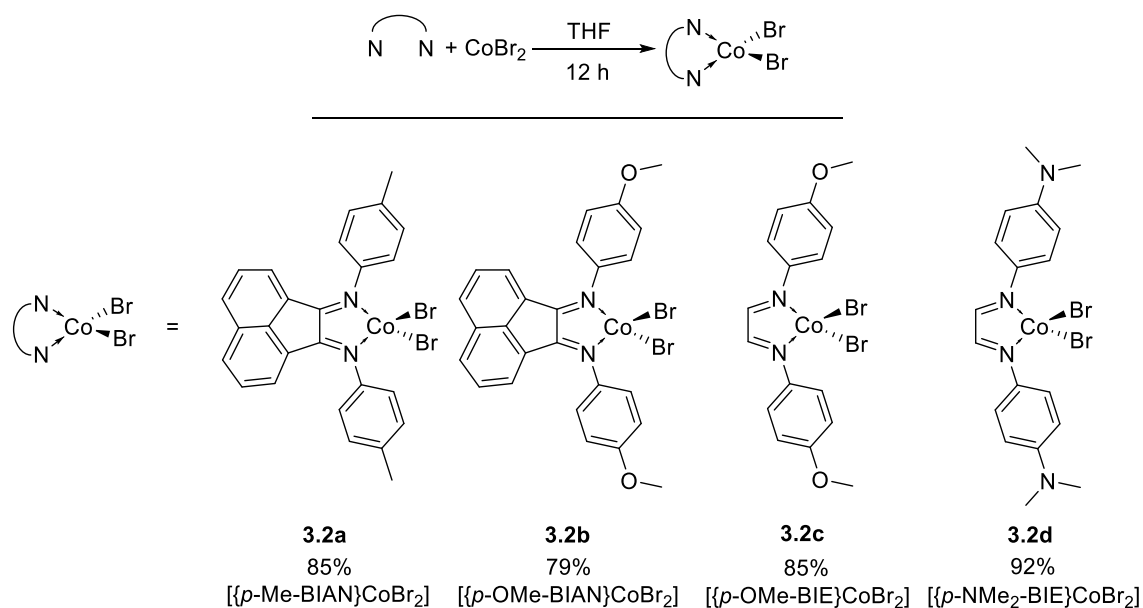


Figure 3.9 General synthesis of $(\alpha\text{-diimine})\text{Co(II)}$ bromide complexes (Top) and complexes synthesised with yield (%) shown underneath (Bottom).

The complexes shown in **Figure 3.9** were prepared in good yield (85-92%) and were obtained as intensely coloured powders. The $(\text{N}^{\wedge}\text{N})\text{CoBr}_2$ complexes (**3.2a-d**) synthesised were prepared and

stored under inert atmosphere conditions to prevent, *e.g.* water coordination to the metal centre (discussed in Section 3.2.2.1).

3.2.2 Characterisation of α -Diimine Cobalt(II) Bromide Complexes

The (N[^]N)CoBr₂ complexes synthesised in this work have been fully characterised by single crystal X-ray diffraction, mass spectrometry and IR, Raman and UV-Vis spectroscopies. The mass spectra (ASAP⁺) obtained of these complexes all show characteristic molecular ions [M]⁺, along with fragmentation resulting from Co-Br and N-Co bond cleavage (**Table 3.1**).

Table 3.1 MS (ASAP⁺) fragmentation data from the synthesised (N[^]N)CoBr₂ series. Masses are in Da, with % intensities in parentheses.

(N [^] N)CoBr ₂	[M] ⁺	[M-Br] ⁺	[M-CoBr ₂] ⁺
3.2a { <i>p</i> -Me-BIAN}	576.896 (59.70)	497.981 (50.68)	360.139 (16.09)
3.2b { <i>p</i> -NMe ₂ -BIE}	510.922 (5.51)	432.010 (2.63)	294.161 (100)
3.2c { <i>p</i> -OMe-BIAN}	608.892 (25.25)	529.977 (34.80)	392.132 (100)
3.2d { <i>p</i> -OMe-BIE}	484.863 (7.12)	405.949 (12.84)	268.096 (100)

In addition to the fragments shown in **Table 3.1**, the mass spectra of (N[^]N)CoBr₂ complexes (**3.2a-d**) also show the presence of fragments with mass and isotope pattern corresponding to [(N[^]N)₂Co₂Br₃]⁺ and [(N[^]N)₂CoBr]⁺. However, these higher molecular weight fragments have been attributed to recombination products formed within the mass spectrometer after ionisation of the initial complex, and are not a true representation of the structure of the complexes. Molecular structures determined by single-crystal X-ray diffraction show the complexes to be monomeric in the solid-state. Previous work within the Dyer group (performed by Amy Buckley) has shown that α -diimine cobalt halide complexes are monomeric in the solution-state (*i.e.* (N[^]N)CoBr₂) through the use of the Signer cryoscopic method for molecular weight determination in solution.⁵⁸

3.2.2.1 Structural Characterisation of α -Diimine Cobalt Complexes

Structural analysis through single crystal X-ray diffraction of the (N[^]N)CoBr₂ complexes prepared herein was undertaken to afford insight into the steric and electronic differences incurred as a result of changing the α -diimine ligand. Single crystals of complexes with (N[^]N) = {*p*-Me-BIAN}, {*p*-NMe₂-BIE} and {*p*-OMe-BIAN} were grown under inert atmosphere (crystals grown in air discussed below)

conditions and, as a result, have a 4-coordinate *pseudo*-tetrahedral cobalt centre. However, single crystals suitable for XRD studies of $\{p\text{-OMe-BIE}\}\text{CoBr}_2$ proved harder to obtain. Very small crystals of **3.2d** were grown under inert conditions and were submitted for neutron diffraction; unfortunately, these crystals decomposed during irradiation. Crystals of $\{p\text{-OMe-BIE}\}\text{CoBr}_2$ were then successfully grown from a solution in MeCN under an air atmosphere *via* slow evaporation. However, as a result, the resulting structure contains *pseudo*-octahedral cobalt with complexed MeCN and H₂O where two bromide ligands lie above and below the plane defined by N, N, O, N, to give rise to $[\{p\text{-OMe-BIE}\}\text{Co}(\text{NCMe})(\text{OH}_2)]$, **3.2e** (Figure 3.10).

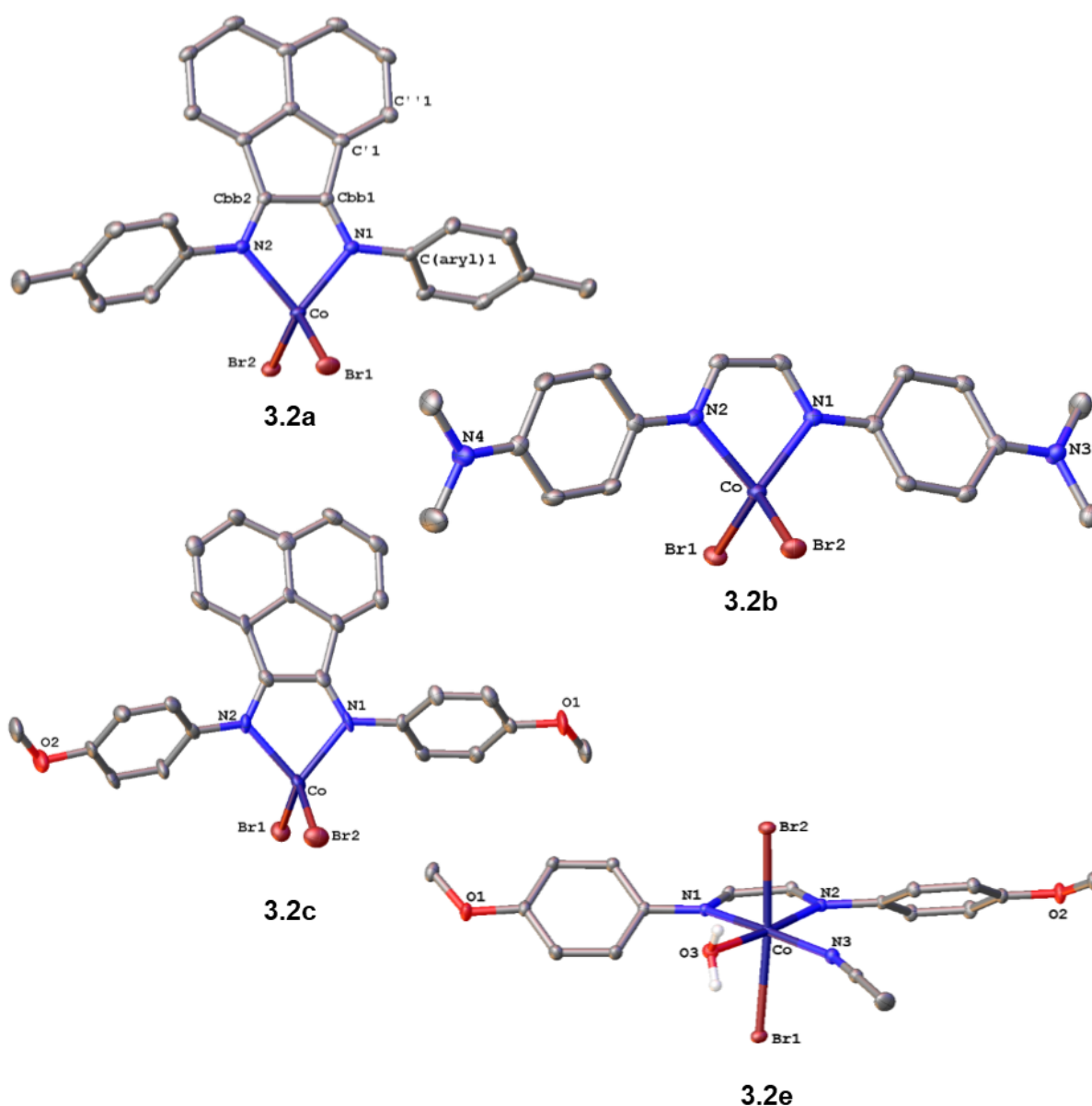


Figure 3.10 Molecular structures of diimine-cobalt complexes determined as part of this work. ORTEPs are set at 50% possibility. $\{p\text{-Me-BIAN}\}\text{CoBr}_2$ (**3.2a**), $\{p\text{-NMe}_2\text{-BIE}\}\text{CoBr}_2$ (**3.2b**), $\{p\text{-OMe-BIAN}\}\text{CoBr}_2$ (**3.2c**), $[\{p\text{-OMe-BIE}\}\text{CoBr}_2\cdot\text{H}_2\text{O}\cdot\text{MeCN}]$ (**3.2e**). ORTEPs are set at 50% probability and H-atoms are omitted for clarity in all case except within H₂O, a molecule of DCM solvate has been removed from structures **3.2a-c**.

From the data obtained from X-ray diffraction of the various (N[^]N)CoBr₂ complexes (summarised in **Table 3.2**), it can be seen that varying the *para*-substituent on N-aryl group does not have an effect on the C=N bond distance (1.285(3) Å and 1.29(2) Å in **3.2a** and **3.2c**, respectively). In addition, changing the backbone from acenaphthene to a simple C-C motif also appears not to have a significant effect upon the C=N bond distance measured (1.299(6)) Å in **3.2b**).

Table 3.2 Selected bond distances and bond angles for (N[^]N)CoBr₂ complexes **3.2a-c,e**

(N [^] N)CoBr ₂ =	3.2a	3.2b	3.2c	3.2e^a
	<i>Selected bond distances /°</i>			
Co-Br ^b	2.3575(6)	2.3644(7)	2.350(1)	2.5571(4)
Co-N(imine) ^b	2.051(1)	2.044(3)	2.050(8)	2.160(2)
C=N(imine) ^b	1.285(3)	1.299(6)	1.29(2)	1.284(1)
Co-O3				2.1581(9)
Co-N(MeCN)				2.117(1)
N-C(aryl)	1.427(3)	1.399(6)	1.43(2)	1.425(2)
Cbb-Cbb	1.5171(19)	1.422(4)	1.493(11)	1.4247(16)
	<i>Selected bond angles /°</i>			
β	88.20(2)	82.62(8)	82.1(2)	77.30(4)
Br-Co-Br	114.23(2)	117.06(2)	111.15(5)	173.59(1)
N1-Co-Br1	112.33(4)	110.52(6)	113.1(2)	88.73(3)
N1-Co-Br2	114.34(4)	118.13(6)	117.4(2)	91.37(3)
N2-Co-Br1	111.42(4)	110.57(6)	112.4(2)	95.97(3)
N2-Co-Br2	118.14(4)	112.90(6)	117.4(2)	90.29(3)
C(aryl)-N=C	123.5(1)	124.2(3)	122.8(8)	117.6(2)
N=Cbb-Cbb	117.3(1)	118.9(4)	117.8(10)	119.0(1)
Cbb-C'-C''	135.0(1)		135.6(10)	
θ	55.56	12.73	55.40	35.63
τ ₄ ^c	0.90	0.89	0.89	

^a[*p*-OMe-BIE]Co(MeCN)(OH₂)Br₂ ^bmean value, ^c4-coordinate geometry index⁵⁹

Small changes to the geometry around the cobalt centre also appear not to have a significant effect upon the C=N bond distance: 1.284(1) Å in the *pseudo*-octahedral complex **3.2e** and 1.285(3) Å in four-coordinate **3.2a**). The lack of a change in the C=N bond distance despite changing geometry and aryl-

groups suggest that there is no significant conjugation of the aryl substituent π -system and that of the imine C=N bond. Based on literature precedent, (Section 3.1.1) no significant back bonding from cobalt to the imine $\pi^*_{\text{C=N}}$ would be expected in these non-conjugated systems. Not least as within a *pseudo*-tetrahedral complex, π -symmetry orbitals of the metal are largely orientated in the wrong directions for a rigid bidentate ligand in a five-membered metallacycle.

The measured Co-N(imine) bond distance for these (N[^]N)CoBr₂ complexes (**3.2a-c**) do not change dramatically as the imine is varied across structurally comparable samples. However, for complex **3.2e** the Co-N distance is measured as 2.160(2) Å, a significantly longer bond when compared to the Co-N bond distances determined for tetrahedral systems **3.2a**, **3.2b** and **3.2c**: Co-N, ~2.050(8) Å. A greater Co-N distance is expected for **3.2e** as this octahedral complex is formally 19e⁻ and hence dictates weaker imine_N to cobalt donation due to the greater charge density on cobalt. A significantly greater Co-Br bond length of 2.5571(4) Å is observed for **3.2e** compared with ~2.357(2) Å in the tetrahedral systems **3.2a-c**.

The N-Co-N bite angle, β , measured for the *pseudo*-tetrahedral complexes **3.2a-c**, ranges from 82.1(2)^o in **3.2c** to 88.20(2)^o in **3.2a**. However, the Car-C=N, N=Cbb-Cbb and Cbb-C'-C'' (representative labels shown for **3.2a** in **Figure 3.10**) bond angles measured for each of these tetrahedral complexes remains the same, suggesting that the value of β for the α -diimine must be fairly flexible. The variation in the N-Co-N bite angle (β) determined for these complexes **3.2a-c** in the solid-state is therefore thought, in part, to be a result of crystal packing forces and can be envisaged to be a 'snapshot' of C-C=N wagging vibrations. Indeed, tetrahedral metal complexes with an α -diimine ligand have previously reported values of β ranging between 67-92^o (mode average 83^o) according to a search of the Cambridge Structural Database.⁶⁰

The complexes **3.2a** and **3.2c** containing acenaphthyl-functionalised diimine backbones both have smaller N-C(aryl) bond distances than those with simple C-C skeletons. The structures of complexes **3.2a** and **3.2c** also exhibit large dihedral angles θ (>55^o), measured between the plane of the aryl-substituent on N and the plane of the metallacycle (**Figure 3.11**). As previously reported in the literature, the value of θ can be used as an indication of the degree of π -system conjugation.⁶¹ Small θ values suggest significant conjugation as orbitals involved in the π -system are all orientated for transfer of electron charge, while large values of θ show that the conjugation of the π -system has been interrupted. In complexes **3.2a** and **3.2c** the acenaphthyl functionality of the diimine backbone causes steric repulsion between the aryl-groups and backbone, resulting in an increase in θ and thus a decrease in the N-C(aryl) bond order as the π -conjugation is interrupted. In contrast, θ is much smaller

(12.73°) in complex **3.2b** where the simple C–C backbone is small enough to allow N-aryl groups to rotate into plane to produce an extended π -system.

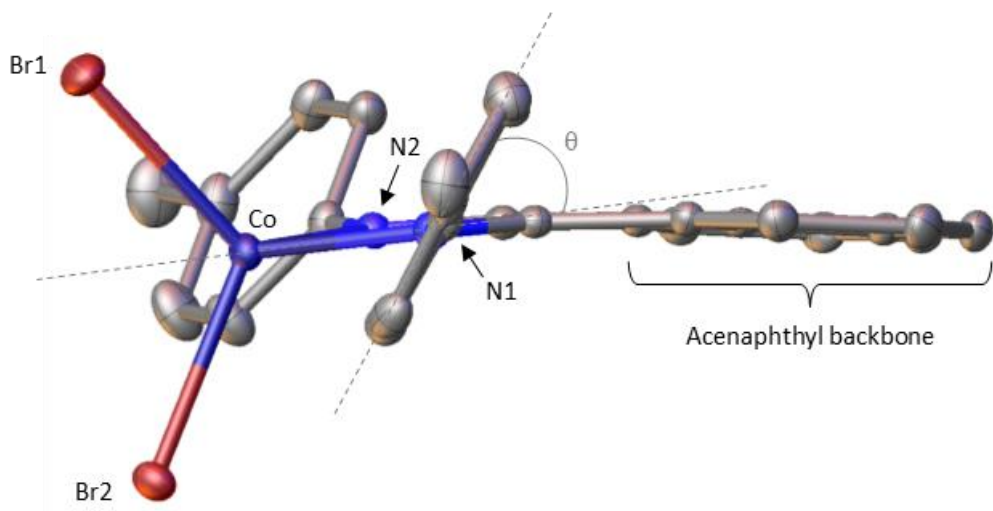


Figure 3.11 Representation of dihedral angle, θ , measured between the metallacycle and N-aryl, $\{p\text{-NMe}_2\text{-BIE}\}\text{CoBr}_2$ (**3.2a**) shown with ORTEPs set at 50% probability, H-atoms and a DCM solvate molecule have been omitted for clarity.

The *pseudo*-tetrahedral geometry of the synthesised complexes **3.2a-c** can be described in terms of the four-coordinate geometry index, τ_4 .⁵⁹ This four-coordinate geometry index, τ_4 , gives an indication of the distortion from ‘perfect’ tetrahedral geometry. The four-coordinate geometry index is determined using **Equation 3.1** where α and β are the greatest angles (*e.g.* N-Co-N, Br-Co-Br, *etc.*) measured around the four-coordinate metal centre.

Equation 3.1: Calculation of the 4-coordinate geometry index, τ_4 ⁵⁹

$$\tau_4 = \frac{360^\circ - (\alpha + \beta)}{141}$$

In this instance, τ_4 can be used to quantify the distortion from perfect tetrahedral geometry. For which $\tau_4 = 1.00$, towards trigonal pyramidal geometry, where $\tau_4 = 0.85$, **Figure 3.12**.

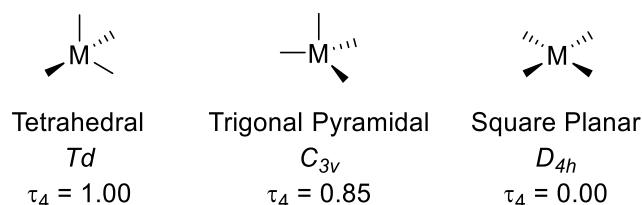


Figure 3.12 Examples of four-coordinate geometries with corresponding point group and τ_4 value.⁵⁹

The value of τ_4 is not found to change significantly (**Table 3.2**) across the small series of four-coordinate cobalt complexes (**3.2a-c**) and as such it can be concluded that changing the *para*-substituent on N-

aryl and the changes to the backbone of α -diimine ligand do not significantly influence the bonding around Co.

3.2.2.2 Steric Contributions from α -Diimine Ligands

The $\%V_{\text{bur}}$ values and corresponding steric maps for each of the diimine ligands coordinated to cobalt under investigation **3.2a-c** were generated (**Figure 3.13**). The values of $\%V_{\text{bur}}$ for diimine ligands within complexes **3.2a-c** were all found to be 39-41%. As the $\%V_{\text{bur}}$ values for **3.2a-c** are all very close, this shows that substituent changes in the *para*-position of N-aryl group and changes to the α -diimine backbone do not have a significant impact upon the steric congestion around the metal centre, as expected. The value of $\%V_{\text{bur}}$ determined for the diimine ligand of the octahedral complex **3.2d** (35.6%) is slightly lower than those for the tetrahedral cobalt diimine complexes **3.2a-c** as a result of tilting of the N-aryl groups to avoid steric repulsion between introduced, bound water and MeCN ligands. The highest $\%V_{\text{bur}}$ value was determined for the $\{p\text{-NMe}_2\text{-BIE}\}$ ligand (in complex **3.2b**), something that has been attributed to the planarity of the ligand (due to its extended π -system) resulting in a greater impact from the N-aryl groups. The planarity of the N-aryl groups in **3.2b** and their resulting greater contribution to the steric congestion around the metal centre is clearly visualised within the steric map obtained (**Figure 3.13**).

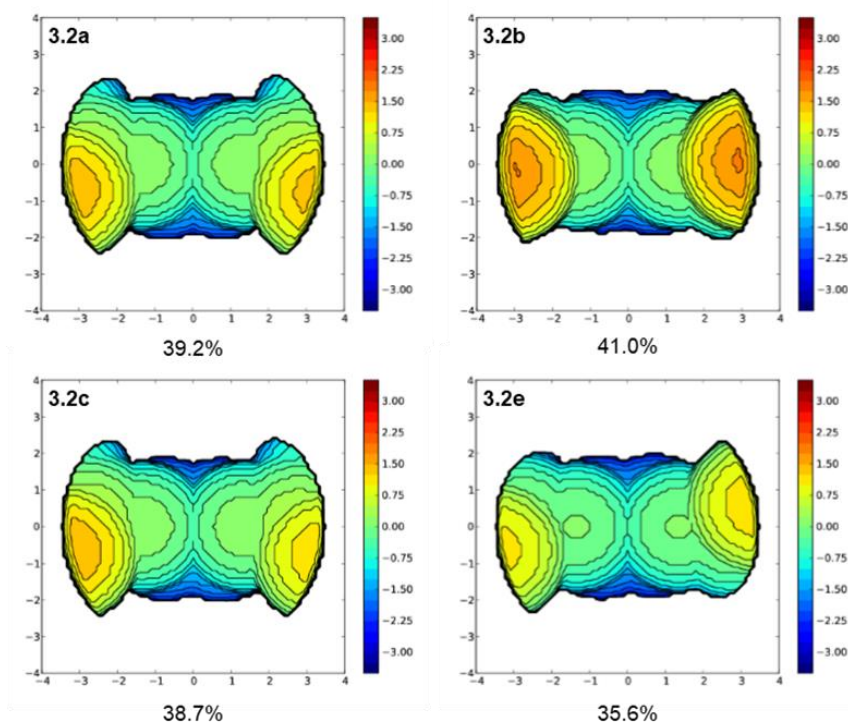


Figure 3.13 Steric maps generated from the solid-state structures obtained for $(\alpha\text{-diimine})\text{CoBr}_2$ complexes with $\%V_{\text{bur}}$ shown beneath. $\{p\text{-Me-BIAN}\}\text{CoBr}_2$ (**3.2a**), $\{p\text{-NMe}_2\text{-BIE}\}\text{CoBr}_2$ (**3.2b**), $\{p\text{-OMe-BIAN}\}\text{CoBr}_2$ (**3.2c**), $\{[p\text{-OMe-BIE}]\text{-CoBr}_2(\text{H}_2\text{O})(\text{MeCN})\}$ (**3.2e**).

3.2.2.3 Investigating Vibrational Energies in (N[^]N)CoBr₂ Complexes Through IR, Raman and DFT Spectroscopic Techniques

Structural analysis of (N[^]N)CoBr₂ complexes suggests that there is no significant π -backbonding within these complexes between $\pi^*_{C=N} \leftarrow d_{Co}$. In order to verify this hypothesis, Infrared (IR) spectroscopic analysis of $\nu_{C=N}$ can be used: if the diimine ligands present are acting as π -acceptors, a shift in the value of $\nu_{C=N}$ to lower wavenumber upon complexation to cobalt would be expected as a result of decreasing C=N bond order. To this end, the IR spectra of the free diimines and the corresponding complexes **3.2a-d** were collected and an investigation into variations in $\nu_{C=N}$ launched.

Assignment of $\nu_{C=N}$ stretching (symmetric and asymmetric) bands observed by IR spectroscopy is not always straightforward. These bands are expected to have strong absorptions and have frequencies falling within the range 1300 – 1600 cm⁻¹, which is a similar region to that expected for $\nu_{C=C}$ stretches. Indeed, the complexes **3.2a-d** and free diimines investigated all have contributions in their IR spectra obtained arising from $\nu_{C=C}$. Consequently, care must be taken when assigning these $\nu_{C=N}$ bands. This is particularly important for BIAN-substituted ligand derivatives due to the multiple $\nu_{C=C}$ bands expected from their acenaphthyl-backbone. For this reason, Raman spectra were also recorded of the complexes **3.2a-d**. Raman spectroscopy relies on a change in polarizability of the complex, rather than a change to the dipole moment as in IR spectroscopy, and so the number of complex overlapping bands corresponding to $\nu_{C=C_{asym}}$ are reduced within the Raman spectra obtained. Thus, comparison of a diimine's IR and Raman spectra aids in the correct assignment of the $\nu_{C=N}$ band. In addition, further corroboration of the spectral assignments has been made by determining the gas-phase vibrational frequencies computationally, which have been calculated at the B3LYP/3-21G* level with calculations starting from the solid-state structural data obtained where available. A summary of the experimental and calculated $\nu_{C=N}$ frequencies for the diimines used as part of this study is provided in **Table 3.3**.

Table 3.3 $\nu\text{C}=\text{N}$ frequencies (cm^{-1}) before and after complexation of diimine to cobalt(II) as measured experimentally by IR and Raman spectroscopies (accuracy to within $\pm 4 \text{ cm}^{-1}$); values determined computationally by DFT. at the B3LYP/3-21G* level are given in parenthesis with an applied scalar correction of 0.9625.⁶²

Entry	Complex	Infrared		Raman
		$\nu\text{C}=\text{N}_{\text{symm}}$	$\nu\text{C}=\text{N}_{\text{asymm}}$	$\nu\text{C}=\text{N}_{\text{symm}}$
1	3.2a	1488m (1478s)	1588m (1589m)	1502vw (1478vs)
2	3.2b	1299m (1302w)	1482sh (1481m)	1308w (1302vs)
3	3.2c	1480sh (1488w)	1589m (1592s)	1480w (1476w)
4	3.2d	1372m	1463s	1371m
	Free Ligand	$\nu\text{C}=\text{N}_{\text{symm}}$	$\nu\text{C}=\text{N}_{\text{asymm}}$	
5	<i>p</i> -Me-BIAN	1489m	1589m	
6	<i>p</i> -NMe ₂ -BIE	1307w	1488sh	
7	<i>p</i> -OMe-BIAN	1485m	1584m	
8	<i>p</i> -OMe-BIE	1377m	1457s	

vw: very weak, w: weak, m: medium, s: strong, vs: very strong, sh: shoulder.

For all cases the experimentally determined Raman and IR spectroscopic data are in good agreement where common bands are observed (e.g. $\nu\text{C}=\text{N}_{\text{symm}}$ stretch). Additionally, the experimental data are in good agreement with the DFT-calculated data for each compound. Examples of the IR, Raman and calculated spectra obtained for $\{p\text{-OMe-BIAN}\}$ and $\{p\text{-OMe-BIAN}\}\text{CoBr}_2$ (**3.2c**) are shown in **Figure 3.14**.

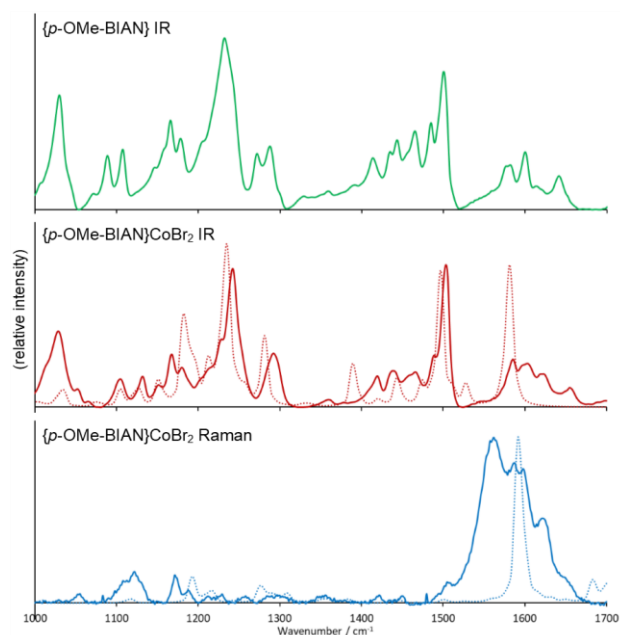


Figure 3.14 Comparison of experimental (solid line) and calculated (dotted line) vibrational (IR and Raman) spectra for $\{p\text{-OMe-BIAN}\}$ and $\{p\text{-OMe-BIAN}\}\text{CoBr}_2$ (**3.2c**). Experimentally-determined spectra have been subject to manual baseline correction.

Within the series of α -diimine ligands and in the series of cobalt complexes (**3a-d**), the same trend in value of $\nu_{\text{C=N}}$ is observed, such that $\{p\text{-NMe}_2\text{-BIE}\} < \{p\text{-OMe-BIE}\} < \{p\text{-OMe-BIAN}\} \approx \{p\text{-Me-BIAN}\}$. This follows the Hammett parameters (σ) for the *para*-substituents present ($p\text{-}\sigma$) on N-aryl groups where $p\text{-}\sigma$: $p\text{-NMe}_2$ (-0.83) $<$ $p\text{-OMe}$ (-0.27) $<$ $p\text{-Me}$ (-0.17).⁶³ The trend is as expected, namely, introduction of a strongly electron donating group (such as $p\text{-NMe}_2$: **3.2b** $\nu_{\text{C=N}_{\text{symm}}}$ 1299 cm^{-1}) vs a poorer electron donating group ($p\text{-OMe}$: **3.2d** $\nu_{\text{C=N}_{\text{symm}}}$ 1372 cm^{-1}) results in an increase in electron density within the π -system, resulting in an increased electron density populating $\pi^*_{\text{C=N}}$, subsequent decrease in bond order and observation of $\nu_{\text{C=N}}$ at lower energy.

For all the α -diimine ligands ($\text{N}^{\wedge}\text{N}$) and their corresponding ($\text{N}^{\wedge}\text{N}$) CoBr_2 complexes (**3.2a-3.2d**) there is no significant shift in the frequency of the $\nu_{\text{C=N}}$ band upon ligand complexation to cobalt (**Table 3.3**). The similarity of all the experimentally-determined values of $\nu_{\text{C=N}}$ in the free ligands and in the complexes **3.2a-3.2d** support the claims in literature that there is little back-bonding from d orbitals on the metal to $\pi^*_{\text{C=N}}$ within *pseudo*-tetrahedral complexes.⁵¹⁻⁵³ This conclusion is further supported by the fact that Co-N ($\sim 2.05\text{ \AA}$) and C=N ($\sim 1.29\text{ \AA}$) bond distances measured for complexes **3.2a-3.2c** do not change across the series. Similarly, no change to the value of $\nu_{\text{C=N}}$ upon coordination of $\{p\text{-OMe-BIE}\}$ to form $\{p\text{-OMe-BIE}\}\text{CoBr}_2$ (**3.2d**) was observed (**Table 3.3**, Entries 4 and 8). Again, this suggests there is no significant back-bonding to $\pi^*_{\text{C=N}}$ within **3.2d**.

There is also no significant change to the values of the $\nu_{\text{C=N}}$ band measured when comparing BIAN-based ligand systems with different *para*-substituents, for instance, in complexes **3.2a** and **3.2c** the value of $\nu_{\text{C=N}_{\text{symm}}}$ is 1485 cm^{-1} and 1488 cm^{-1} , respectively. This is attributed to the orientation of the N-aryl groups away from coplanarity with the imine fragment as a result of the presence of a sterically demanding acenaphthyl-backbone. This 'twisting' of these N-aryl groups breaks the conjugation of the π -system, resulting in no propagation of the electronic effects introduced by variation of the N-aryl *para*-substituent to the imine fragment. The value of $\nu_{\text{C=N}}$ measured for the BIAN-based systems is therefore likely dictated solely by the inductively-withdrawing nature of the acenaphthyl-backbone.

The structural analysis of $\{p\text{-NMe}_2\text{-BIE}\}\text{CoBr}_2$ (**3.2b**) showed the N-aryl substituents to be close to planarity with the metallacycle. This co-planar orientation of the N-aryl substituent suggests that conjugation to the π -system by C=N could be possible. Addition of electron donating *para*-substituent ($p\text{-NMe}_2$) in complex **3.2b** in an extended π -system to the imine C=N bond in combination with the electron donating BIE-backbone results in a decrease in the value of $\nu_{\text{C=N}_{\text{symm}}}$ in **3.2b** (1299 cm^{-1}) when compared to **3.2a** and **3.2c** (1485 and 1488 cm^{-1} , respectively) (**Table 3.3**).

3.2.2.4 UV-Vis Spectroscopic Analysis of (N[^]N)CoBr₂ Complexes

To compliment the structural and spectroscopic data obtained, the UV-Vis spectra of free α -diimine ligands (N[^]N) and the corresponding (N[^]N)CoBr₂ complexes were obtained in DCM solution (selected for its non-coordinating nature and polarity). The free diimines and their corresponding complexes are very intensely coloured as a result of the extent of conjugation within these compounds. The UV-Vis spectra obtained for the free (N[^]N) ligands and corresponding [(N[^]N)CoBr₂] complexes are shown in **Figure 3.15**.

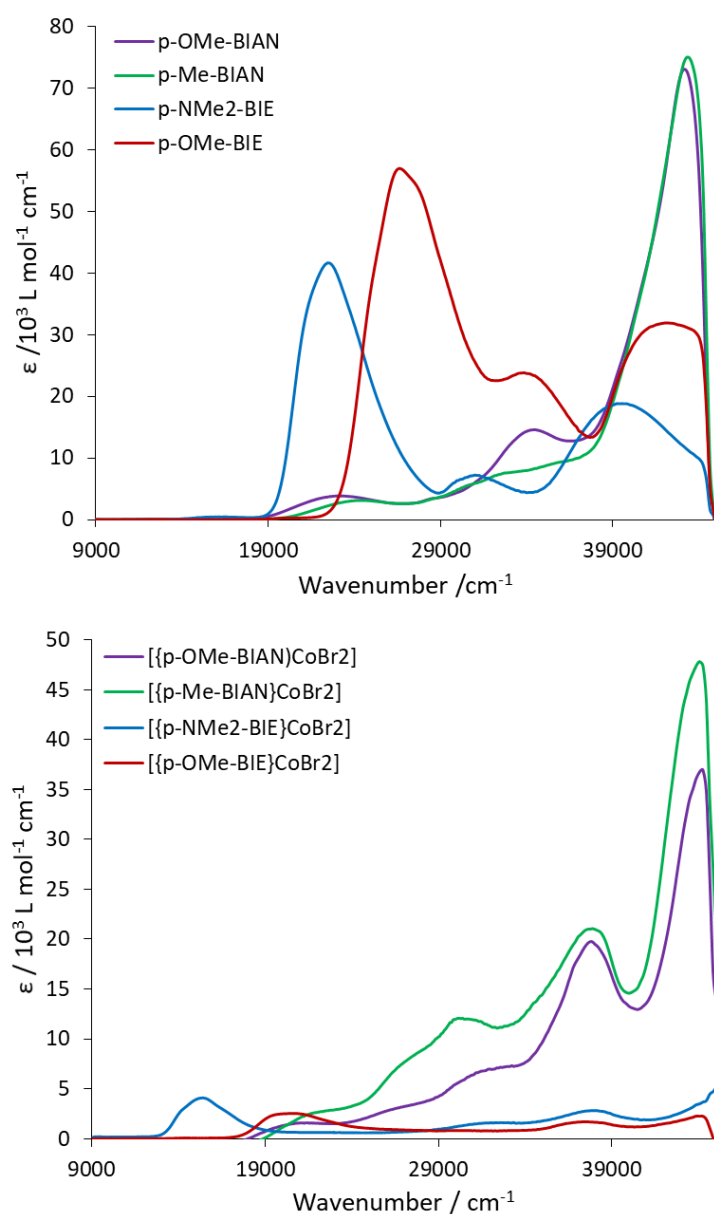


Figure 3.15 UV-Vis spectra (DCM solution) recorded for free diimine ligands (top) and (N[^]N)CoBr₂ Complexes **3.2a-d** (bottom).

The highest intensity bands (around 44000 cm⁻¹) are assigned as ligand centred (¹LC) $\pi^* \leftarrow \pi$ transitions, with contributions from N-aryl and (within BIAN containing compounds) acenaphthyl and are not observed to shift significantly upon complexation of the diimine ligand to CoBr₂ (**Table 3.4**)⁵⁷. In the spectra of the free diimine ligands there are several hypochromic bands observed between 19000 and 35000 cm⁻¹, which have been previously reported as intra-ligand charge transfer (¹ILCT) bands primarily on the N-aryl, but with some contribution from the acenaphthyl group where present.⁶¹

As has been shown previously for complexes of α -diimine ligands, the ¹ILCT bands within the UV-Vis spectrum of complexes of these ligands are bathochromically shifted upon complexation as they mix with ¹MLCT (metal-ligand charge transfer) bands.^{61,64-67} The extent of the bathochromic shift observed within the series of spectra obtained for complexes **3.2a-d** can be rationalised through considerations of the available conjugation within the π -system (i.e. θ°). Complimentary to the structural data obtained, the largest bathochromic shift is observed upon complexation of {*p*-NMe₂-BIE} to CoBr₂ to produce **3.2b** (**Table 3.4**). This large decrease in energy upon complexation is attributed to the planarity of the π -system within **3.2b** ($\theta = 12.73^\circ$) as a result of extended conjugation of the π -system. Bathochromically shifted bands are also observed within **3.2d**, to a lesser extent than **3.2b**, suggesting this complex can also obtain an extended π -system through planarity between imino-groups and the N-aryl substituent. In contrast, both complexes containing BIAN-functionalised ligands (**3.2a** and **3.2c**) only showed a small shift in energies upon complexation to cobalt; this can be attributed to the orientation of N-aryl groups relative to the metallacycle, which approaches orthogonality (θ is 55.56° and 55.40°, respectively).

Table 3.4 Selected bands within the UV-Vis spectra of (N[^]N) and [(N[^]N)CoBr₂]. λ_{\max} values shown in nm (ϵ /L mol⁻¹ cm⁻¹). Where ¹LC is Ligand centred and ¹ILCT is *intraligand* charge transfer and ¹MLCT is metal-ligand charge transfer (only highest and lowest λ_{\max} values observed shown).

Free ligand =	{ <i>p</i> -Me-BIAN}	{ <i>p</i> -NMe ₂ -BIE}	{ <i>p</i> -OMe-BIAN}	{ <i>p</i> -OMe-BIE}
$\pi^* \leftarrow \pi$ ¹ LC	231 (74959)	235 (11815)	232 (73016)	237 (31911)
¹ ILCT	296sh (7921) -	322 (7211) -	290 (14515) -	296 (23801) -
	408 (3116)	445 (41625)	431 (3850)	376 (56926)
(N [^] N)CoBr ₂ =	3.2a	3.2b	3.2c	3.2d
$\pi^* \leftarrow \pi$ ¹ LC	227 (47822)	<230 ^a	226 (36956)	228 (2263)
¹ ILCT/ ¹ MLCT	264 (21055) -	264 (2817) -	265 (19746) -	268 (1702) -
	471 (2255)	649 (4088)	479 (1566)	484 (2530)

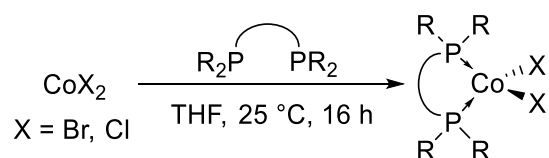
^aobscured due to a baseline subtraction error.

Chapter 3

With spectroscopic and structural characterisation of these (α -diimine)cobalt(II) complexes in hand, it is of interest to determine the reactivity of these complexes within catalytic transformations. For instance, the reactivity of these complexes towards ethylene oligomerisation. Unfortunately, an investigation into the catalytic activity of complexes **3.2a-d** is yet to be performed. However, these experiments will be performed within the PWD group in the near future. The following sections discuss the synthesis and characterisation of a library of (P[^]P)CoX₂ complexes.

3.3 Diphosphine Cobalt(II) Halide Complexes

As discussed in Section 3.1.2, pro-catalysts containing diphosphine ligands are of interest for use in selective olefin oligomerisation reactions. To this end, a library of diphosphine[†] cobalt(II) halide complexes (P[^]P)CoX₂ was prepared through modifications to the literature procedures (**Scheme 3.14**).²⁷



Scheme 3.14 General scheme for the synthesis of (P[^]P)CoX₂ complexes.²⁷

The cobalt(II) dihalide diphosphine complexes that have been synthesised within this project are shown in **Figure 3.16**; the corresponding reaction yields are given in parentheses. The synthesis of diphosphine cobalt(II) halide complexes is straightforward and reaction yields range from poor (29%, **3.6d**) to excellent (99%, **3.10**) depending on the diphosphine. The lower yield associated with the preparation of **3.6d** has been attributed to the difficulty in isolating all the product obtained due to this reaction being performed on a small (10 mg) scale due to the cost/availability of the diphosphine. It should be noted here that for ease of diphosphine ligand comparison, the structures of the various complexes described in **Figure 3.16** are all represented as being four-coordinate at cobalt with *pseudo*-tetrahedral geometry. However, there are a few exceptions to this: “dppeCoBr₂” (**3.4b**) exists as the salt [(dppe)₂CoBr₂]₂[Br₃Co(μ₂-dppe)CoBr₃], “(dppm)CoBr₂” (**3.4a**) is the dimeric complex BrCo(μ₂-Br)₂(μ₂-dppm)₂CoBr and “(dppbz)CoBr₂” (**3.10**) is the salt [(dppbz)₂CoBr]₂⁺[Br₂Co(μ₂-Br)₂CoBr₂]₂⁻. The structures of these non-tetrahedral complexes (**3.4a**, **3.4b** and **3.10**) are discussed in Section 3.3.2.3.

[†] Throughout Chapters 4, 5, 6 and 7, diphosphine ligands investigated will be referred to by their common abbreviated terms. *e.g.* dppe = 1,2-bis(diphenylphosphino)ethane. A table of these abbreviations is provided in on page xiii.

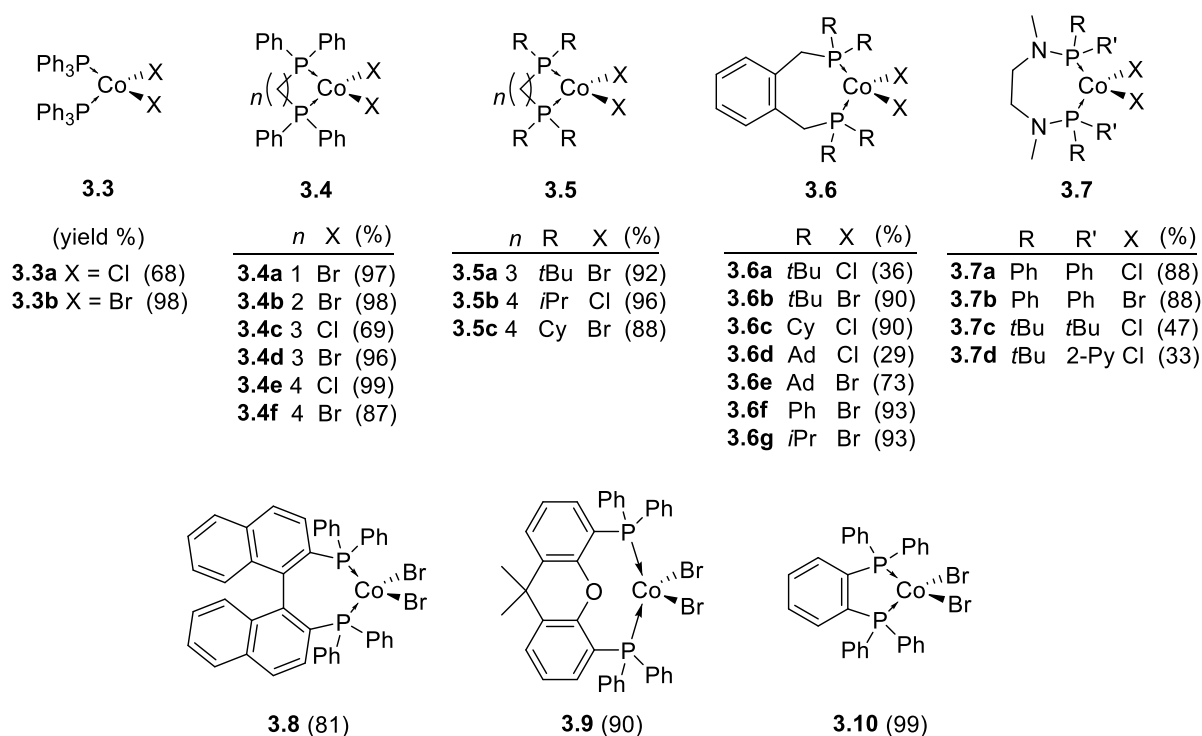


Figure 3.16 (P^AP)CoX₂ complexes synthesised herein (% yield).

The library of diphosphine cobalt(II) dihalide derivatives prepared (**Figure 3.16**) was assembled to establish systematic changes to the P-substituent and the backbone of diphosphine ligands. This series of diphosphine cobalt complex derivatives (**3.3-3.10**) allow the effects of varying the diphosphine on the subsequent reactivity of the cobalt centre to be understood. The donor capacities of the diphosphine ligands used within this study are discussed below in Section 3.3.1 and the steric properties of diphosphine ligands are discussed within the structural characterisation in Section 3.3.2.

Diphosphine cobalt(II) halide complexes are inherently difficult to characterise. These complexes are, for the most part, highly sensitive to oxygen and water and so care needs to be taken to ensure, where possible, all characterisation is carried out under inert atmosphere conditions. For instance, the phosphorus atoms present within the ligand scaffold are susceptible to oxidation, often with the resulting phosphine oxide becoming sequestered by the cobalt. In addition, cobalt(II) has a d⁷ electron configuration, resulting in these complexes being paramagnetic in nature, which results in broadened and shifted NMR spectra as a result of shortened T₂ relaxation times.^{68,69} These (P^AP)CoX₂ complexes (**3.3-3.10**) have been characterised by structural, spectrometric and spectroscopic techniques, the results of which are discussed in complimentary sections below.

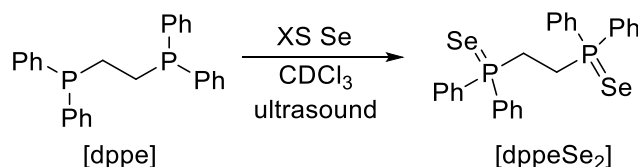
3.3.1 Investigating the Donor Capacity of Diphosphine Ligands in (P^ΛP)CoX₂ Complexes

The electronic influence of the diphosphine ligand used can be indicated through comparison of phosphorus-selenide coupling constants, which can be measured by ³¹P NMR spectroscopy. Here it has been established that this measured coupling constant has an inverse relationship with the σ-donor capacity of the phosphine ligand, such that decreasing |¹J_{SeP}| is equivalent to an increase in σ-donor capacity, **Equation 3.2**.⁷⁰

Equation 3.2: Relationship between P-Se coupling constant and donor capacity:

$$|{}^1J_{SeP}| \propto \frac{1}{\text{donor capacity}}$$

To this end, a series of diphosphine-diselenide compounds was synthesised in accordance to established literature procedures:⁷⁰ to a solution of diphosphine in CDCl₃ in a J Young's NMR tube, an excess of elemental selenium was added and the resulting suspension subject to ultrasonication. The transformations were followed by ³¹P NMR spectroscopy until complete conversion to the corresponding diphosphine-diselenide was achieved. An example is shown in **Scheme 3.15**.



Scheme 3.15 Representative synthesis of *bis*(phosphine-selenide) compounds, where *bis*(phosphine) is dppe.⁷⁰

The selenide compounds were not isolated as only the |³¹P-⁷⁷Se| coupling constant was of interest and so no yield data or any characterisation outwith ³¹P NMR spectroscopy was obtained. A summary of ³¹P NMR shifts and |³¹P-⁷⁷Se| coupling constants measured for prepared diphosphineSe₂ compounds can be found in **Table 3.9**. All NMR spectra obtained were measured in CDCl₃ at 262 MHz to enable reliable comparisons to be made between compounds.

Table 3.5 ^{31}P NMR shifts (ppm) and $|^{31}\text{P}-^{77}\text{Se}|$ coupling constants (Hz) of synthesised diphosphine-diselenide compounds measured in CDCl_3 at 262 MHz.

No.	Compound	δ_{P} /ppm	$ ^1J_{\text{SeP}} $ /Hz
3.11a	dppmSe ₂	25.1	744
3.11b	dppeSe ₂	36.0	735
3.11c	dpppSe ₂	33.0	722
3.11d	dppbSe ₂	33.7	720
3.11e	dppbzSe ₂	38.3	747
3.11e	dcypeSe ₂	57.6	697
3.11f	dcypbSe ₂	53.3	680
3.11g	dtbppSe ₂	76.8	689
3.11h	dtbpxSe ₂	76.7	696
3.11i	dadpxSe ₂	69.7	635
-*	dppxSe ₂	32.9	724
3.11j	BINAPSe ₂	33.6	738
3.11k	XantphosSe ₂	31.5	757

*value obtained from the literature⁷¹

From the values of $|^1J_{\text{SeP}}|$, as determined by ^{31}P NMR spectroscopy, the trend in donor capacity as the diphosphine ligand composition was varied have been identified. The largest $|^{31}\text{P}-^{77}\text{Se}|$ coupling constants measured were 757 Hz for XantphosSe₂, 747 Hz for dppbzSe₂ and 738 Hz for BINAPSe₂. These large coupling constants are indicative of the lessened donor capability of xantphos, dppbz and BINAP due to all phosphine substituents having sp^2 -hybridised C ($\text{PR}(\text{sp}^2)_3$) in electron withdrawing aromatic environments. *bis*(Phosphines) with phenyl substituents and an aliphatic P-C(backbone) ($\text{PR}_2(\text{sp}^2)_2\text{R}(\text{sp}^3)$) have $|^1J_{\text{SeP}}|$ values ranging between 744 Hz – 720 Hz, which decrease with increasing aliphatic backbone chain length, *i.e.* $|^1J_{\text{SeP}}|$ dppbSe₂ < dpppSe₂ < dppeSe₂ < dppmSe₂. Changing the P-substituent, as expected, has a significant effect on the measured $|^1J_{\text{SeP}}|$ values: all the diphosphines with aliphatic substituents have smaller $|^1J_{\text{SeP}}|$ values compared with their aryl-substituted counterparts. The coupling constants for $[\text{PR}(\text{sp}^3)_3]$ compounds range between 697 Hz – 635 Hz and follow the trend: dadpxSe₂ < dcypbSe₂ < dtbppSe₂ < dtbpxSe₂ < dcypeSe₂. The lowest $|^1J_{\text{SeP}}|$ measured was obtained for dadpxSe₂ (635 Hz) and reflects the strongly inductively donating character of the adamantyl-substituents present on phosphorus.

3.3.2 Structural Characterisation of Diphosphine Cobalt(II) Halides

Where possible, solid state molecular structures of the diphosphine cobalt(II) halide complexes prepared have been obtained. Investigation into these solid state structures allows insight into the steric and electronic effects the diphosphine ligand has upon the resulting $(P^*P)CoX_2$ species to be probed. The solid-state molecular structures of tetrahedral $(P^*P)CoX_2$ complexes, which have not been previously reported, are shown in **Figure 3.17**.

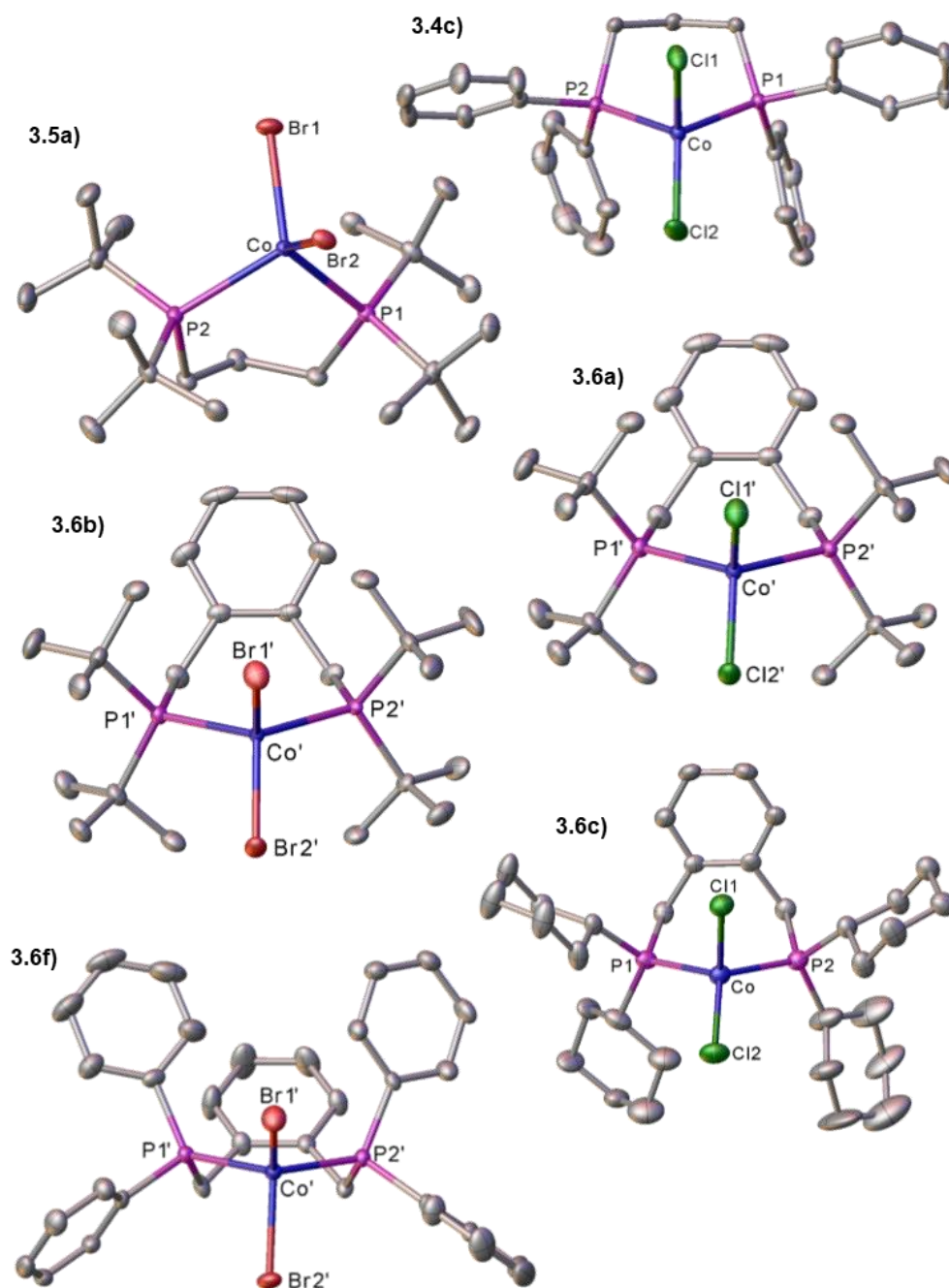


Figure 3.17 Solid-state molecular structures of various $(P^*P)CoX_2$ complexes determined by X-ray diffraction dtbppCoBr₂ (**3.5a**), dtbpxCoBr₂ (**3.6d**), dppxCoBr₂ (**3.6f**), dpppCoCl₂ (**3.4c**), dtbpxCoCl₂ (**3.6a**), dcyppCoCl₂ (**3.6c**). ORTEPs are set at 50% probability and hydrogen atoms; a DCM solvate in the crystal lattice of **3.5b** and independent crystallographic structures in **3.6a,b,f** are removed for clarity.

A summary of selected bond distances and bond angles measured in the solid-state structures of (P[^]P)CoX₂ complexes are reported in **Table 3.6** and **Table 3.7** for (P[^]P)CoBr₂ and (P[^]P)CoCl₂ complexes, respectively. To allow a more complete comparison, selected (P[^]P)CoX₂ structures that have been reported previously in the literature, but that correspond to complexes synthesised within this work, have also been included.⁶⁰ X-ray diffraction data obtained for (P[^]P)CoX₂ complexes from the Cambridge Structural Database are indicated in **Table 3.6** and **Table 3.7** with the appropriate reference included in the table.⁶⁰

Table 3.6 Selected bond distances (Å) and bond angles (°) of *pseudo*-tetrahedral (P[^]P)CoBr₂ complexes in the solid state at 120 K. [†]Z' = 2: values shown are the average of two independent crystallographic sites.

Complex:	3.3b	3.4d	3.5a	3.6b [†]	3.6f [†]	3.9 [†]
	<i>Selected bond distances / Å</i>					
Co-Br ^a	2.3497(5)	2.3594(6)	2.3874(6)	2.396(2)	2.3472(18)	2.357(1)
Co-P ^a	2.3846(5)	2.3458(8)	2.4334(9)	2.452(2)	2.3474(15)	2.367(4)
P-R ^a	1.8207(7)	1.828(5)	1.864(5)	1.879(6)	1.833(12)	1.817(24)
	<i>Selected bond angles / °</i>					
β	117.45(1)	98.07(2)	102.03(2)	105.97(3)	107.96(4)	114.68(10)
Br-Co-Br	115.23(1)	119.25(2)	104.05(2)	101.25(1)	119.056(4)	116.48(6)
θ	-	40.5	12.0	6.7	35.2	68.7
Ref:	72	27				73

^amean value, [†]Z' = 2: values shown are the average of two crystallographic sites.

Table 3.7 Selected bond distances (Å) and bond angles (°) of *pseudo*-tetrahedral (P[^]P)CoCl₂ complexes in the solid state at 120 K.

Complex:	3.3a	3.4c*	3.6a [†]	3.6c [†]	(dppx)CoCl ₂ [†]	(xantphos)CoCl ₂ [†]
	<i>Selected bond distances / Å</i>					
Co-Cl ^a	2.2121(7)	2.2153(7)	2.245(2)	2.247(4)	2.211(3)	2.225(2)
Co-P ^a	2.3841(6)	2.3417(6)	2.4373(9)	2.364(4)	2.392(3)	2.383(2)
P-R ^a	1.8250(9)	1.827(2)	1.875(6)	1.842(19)	1.829(14)	1.820(5)
	<i>Selected bond angles / °</i>					
β	115.87(1)	96.64(1)	104.86(3)	104.31(8)	106.19(5)	114.16(4)
Cl-Co-Cl	117.25(1)	117.90(2)	102.67(3)	110.25(8)	109.49(6)	116.36(4)
θ	-	41.4	8.7	25.0	11.4	68.1
Ref:	72				74	75

^amean value, [†]Z' = 2: values shown are the average of two crystallographic sites. *solid-state structure has been reported at 200 K,⁷⁶ however, all other samples were recorded at 120 K and so data was collected for a sample of **3.4c** at 120 K for consistency.

As the halide is varied between chloride and bromide, the Co-P bond distances (where the diphosphine is kept the same) are not observed to change significantly. For instance, within the series of bromide derivatives, the Co-P bond lengths range from 2.3458(8) Å in **3.4d** to 2.452(2) Å in **3.6b**; upon moving to the chloride derivatives, corresponding complexes have Co-P bond distances of 2.3417(6) Å and 2.4373(9) Å (**3.4c** and **3.6a**, respectively). The Co-X bond lengths are longer when X = Br (2.3472(18)-2.396(2) Å) than X = Cl (2.211(3)-2.2247(4) Å) as anticipated and consistent with the standard ranges.⁴⁷ In both series of CoBr₂ and CoCl₂ dihalide complexes, the Co-X bonds are shortest when the diphosphine present is dppx and longest when the diphosphine is dtbpx. This can be attributed to there being greater electron density on cobalt in dtbpx complexes when compared to dppx complexes (as indicated by the $|^1J_{\text{SeP}}|$ values – see **Table 3.5**), resulting in a decrease in any halide to cobalt π -donation and longer Co-X bond lengths when the diphosphine is dtbpx.

For all of the (R₂P[^]PR₂)CoX₂ complexes described herein, the experimentally-determined P-C bond distances associated with the “PR₂” moiety (where R = Ph, tBu, Cy) were comparable to those reported for the corresponding free phosphine moieties or analogues thereof. Data for the free phosphines were obtained from the CSD according to the parameters defined in **Figure 3.18** and data in **Table 3.8**.

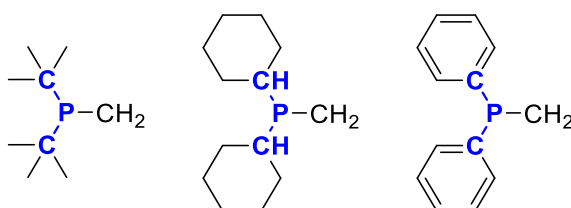


Figure 3.18 Search parameters used to extract P–C bond distances (highlighted in blue) for R₂PCH₂ (R=Ph, Cy, tBu) moieties from the Cambridge Structural database. In each case, the P atom was constrained to have only three bonded atoms.

For instance, for the (R₂P[^]PR₂)CoX₂ complexes where R = tBu (**3.5a**, **3.6b**, **3.6a**) the P-C bond distances measured experimentally ranged between 1.875(6) Å (**3.6a**) and 1.864(5) Å (**3.5a**). From the analysis of the CSD data reported for the free “PtBu₂CH₂” phosphine moieties the P-C distances spanned the range 1.83 – 1.977 Å (mean 1.89(15) Å).⁶⁵ (R₂P[^]PR₂)CoX₂ complexes where R = Ph (**3.3a,b**, **3.4c,d**, **3.6f**, **3.9**) the P-C bond distances measured lie within the range of 1.817(24) Å (**3.9**) to 1.833(12) Å (**3.6f**), which is within the range found for free “Ph₂PCH₂” moieties (1.700 – 1.987 Å, mean 1.84(15) Å).⁶⁵ The same is true for (Cy₂P[^]PCy₂)CoCl₂ (**3.6c**) where the P-C bond distance was 1.849(19) Å (*c.f.* free “PCy₂CH₂” phosphine moiety: P-C 1.831-1.926 Å (mean 1.87(15) Å)⁶⁵. Analysis of these data indicate that as the P-C bond distances measured within these (R₂P[^]PR₂)CoX₂ complexes are comparable to those of the free phosphines, it is unlikely that there is any (significant) π -back donation from the cobalt

centre to the phosphine P_{π} LUMO (P-R σ^* MO; see Section 3.1.3.1.1); back-donation would be expected to result in a lengthening of the P-C bond distances as result of population of a P-C σ^* MO.^{47,77,78}

Table 3.8 Range of P-C bond distances for free phosphine motifs as determined by a search of the Cambridge Structural Database.⁶⁰

Phosphine motif	No. Structures	Min. P-C distance / Å	Max. P-C distance / Å	Mean	Std. dev.	Outliers
Cy ₂ PCH ₂	902	1.831	1.926	1.865	0.015	1
Ph ₂ PCH ₂	902	1.700	1.9870	1.837	0.015	3
tBu ₂ PCH ₂	119	1.8300	1.9770	1.889	0.015	0

Within the series of (P[^]P)CoBr₂ complexes, the \angle P-Co-P (β) angle spans a wide range of angles between 98.07(2)° and 117.45(1)° (for **3.4d** and **3.3b**, respectively) (Table 3.6). The (P[^]P)CoBr₂ complexes can therefore be ordered in terms of β such that: **3.4d** < **3.5a** < **3.6b** < **3.6f** < **3.9** < **3.3b**. The smallest value of β measured is for **3.4d**, something attributed to a combination of decreasing steric bulk on the P-substituent (*i.e.* Ph < tBu) and the flexibility of the 1,3-*bis*(phosphino)propane backbone compared to 1,2-*bis*(phosphinomethyl)benzene, which results in decreased P-Co-P bond angle. This trend is mirrored within the series of (P[^]P)CoCl₂ complexes, which when ordered according to the magnitude of β follow: **3.4c** < **3.6c** < **3.6a** < (dppx)CoCl₂ < (xantphos)CoCl₂ < **3.3a** and range between 96.64(1)° and 115.87(1)°. Both series (X = Br or Cl) show that when the backbone is 1,2-*bis*(phosphinomethyl)benzene (7-membered metallacycle), β is smaller with tBu-P, and when the backbone is 1,3-*bis*(phosphino)propane (6-membered metallacycle), β is smaller with Ph-P. This observation has been attributed to a combination of the generally larger β associated with 7-membered metallacycles and steric hindrance between the tBu-substituents and the bromide ligands. When the solid-state structures of the various complexes are viewed along the plane of the backbone, a displacement of the bromide ligands as a result of steric repulsion from the tBu-substituents is clear. The dihedral angle, θ , between the planes P1-Co-P2 and P1-C...C-P2 of the backbone (Figure 3.19) can be used as a measure of this displacement. The values of θ follow the same trend as the values of \angle P-Co-P, such that **3.6b** < **3.5a** < **3.6f** < **3.4d** (θ = 6.71°, 12.00°, 35.97° and 40.47°, respectively).

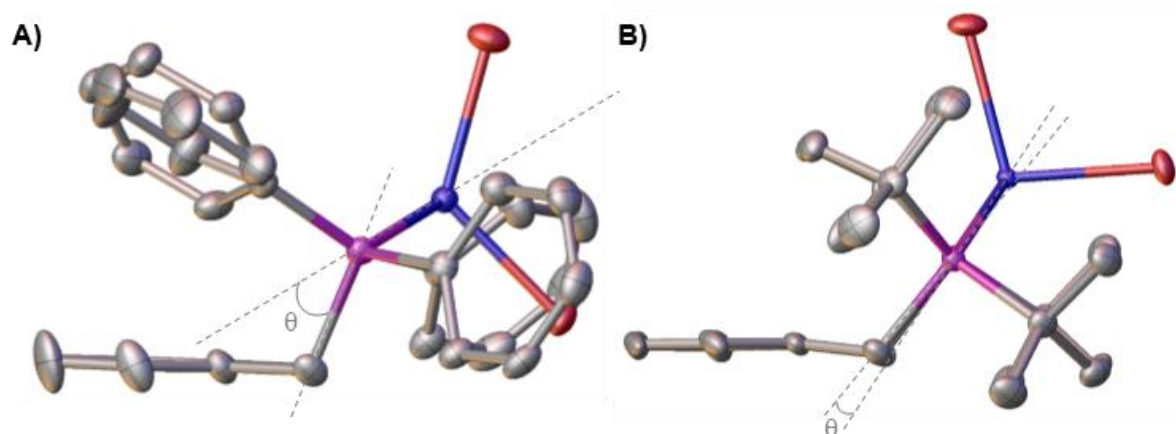


Figure 3.19 Solid-state structures as determined by X-ray diffraction of A) **3.6f** and B) **3.6b**, showing bromide ligand displacement due to steric repulsion and a representation of dihedral angle, θ .

When the X-Co-X bond angles are compared within the series of (P[^]P)CoX₂ complexes, the trend found is the same for both the series of chloride and of bromide derivatives. In both series, (dtbpx)CoX₂ adopts a structure with the smallest value of \angle X-Co-X, while (dppp)CoX₂ has the largest, with angles ranging between 101.68(2) – 119.25(2)° (X = Br) and 102.67(4) – 119.25(2)° (X = Cl). The value of \angle X-Co-X for (dppx)CoX₂ changes dramatically when X is changed (*c.f.* 119.056(4)° (**3.6f**; (dppx)CoBr₂) and 109.46(6)° ((dppx)CoCl₂). This large change in the \angle X-Co-X is mirrored by the θ value, which decreases from 35.2° (**3.6f**) to 11.4° ((dppx)CoCl₂) when bromide ligands are replaced by the less sterically demanding chloride ligands.

3.3.2.1 Distortions from Tetrahedral Geometry of (P[^]P)CoX₂ complexes

From the solid-state structures obtained by single crystal X-ray diffraction, the diphosphine cobalt(II) halide complexes under investigation can be ordered according to the extent to which their structures show distortions from a regular tetrahedral geometry. A summary of the τ_4 parameters (see Section 3.2.2.1) calculated for (P[^]P)CoX₂ complexes is given in **Table 3.9**.

Table 3.9 Calculated τ_4 parameters for (P[^]P)CoX₂ complexes.⁵⁹

Entry	(P [^] P)	τ_4 (P [^] P)CoBr ₂	τ_4 (P [^] P)CoCl ₂
1	2 PPh ₃	3.3b	3.3a
		0.903	0.900
2	dppp	3.4d	3.4c
		0.888	0.874
3	dtbpp	3.5a	-
		0.937	-
4	dppx	3.6f	
		0.894	0.949
5	dtbpx	3.6b	3.6a
		0.929	0.939
6	dcypx	-	3.6c
		-	0.920
7	xantphos	3.9	
		0.914	0.918

Comparisons of the τ_4 values of (P[^]P)CoBr₂ complexes versus those of the corresponding (P[^]P)CoCl₂ complexes show, for the most part, that the values are similar for the same diphosphine ligand. Comparing complexes with X = Cl or Br, with the same diphosphine ligand show all entries (excluding entry 4) varying between 0.3-1.6%. However, an increase ($\Delta\tau_4$ 5.8%) in the distortion value of (dppx)CoBr₂ (**3.6f**) when compared to (dppx)CoCl₂ is observed (0.894 and 0.949, respectively), suggesting that the bromide complex is closer to trigonal pyramidal geometry and the chloride complex is closer to tetrahedral in geometry. This is proposed to be the result of the steric influence of bulkier bromide ligand (when compared to chloride) combined with the flexibility of the dppx ligand that allows the complex to minimise steric repulsions between ligand moieties; resulting in a greater distortion to the structure of (dppx)CoBr₂ (**3.6f**). When just the cobalt(II) bromide complexes are considered, there is a clear trend associated with their τ_4 parameters. When the P-substituent is *t*Bu, the value of the τ_4 parameter is consistently higher than when the P-substituent is Ph, with the τ_4 parameter for (P[^]P)CoBr₂ complexes varying (P[^]P) = dppp < dppx < 2(PPh₃) < xantphos < dtbpx < dtbpp. This trend is mirrored in the series of (P[^]P)CoCl₂ complexes with the exception of (dppx)CoCl₂, which has the highest τ_4 value (0.949). Intuitively, it might be expected that *t*Bu-substituted phosphines would exhibit greater distortion from tetrahedral geometry, as these systems typically exhibit impose greater steric constraints than Ph-substituted phosphines. Thus, distortions from tetrahedral geometry could therefore be expected for *t*Bu-substituted diphosphine ligands to minimise *intra*-ligand steric repulsions. However, as the Ph-substituted diphosphines have been shown to have greatest deviation from tetrahedral geometry in the solid state by X-ray diffraction, it is clear this is not the case.

The backbone of the diphosphine ligand does not appear to have a great impact on the value of τ_4 . For example, the complexes (dppp)CoBr₂ (**3.4d**) and (dtbpp)CoBr₂ (**3.5a**) both have propyl backbones, but appear at the extremes of the scale observed for τ_4 (**Table 3.9**). However, the values of τ_4 found for (P[^]P)CoBr₂ complexes appears to trend with X-Co-X bond angle (**Figure 3.20**).

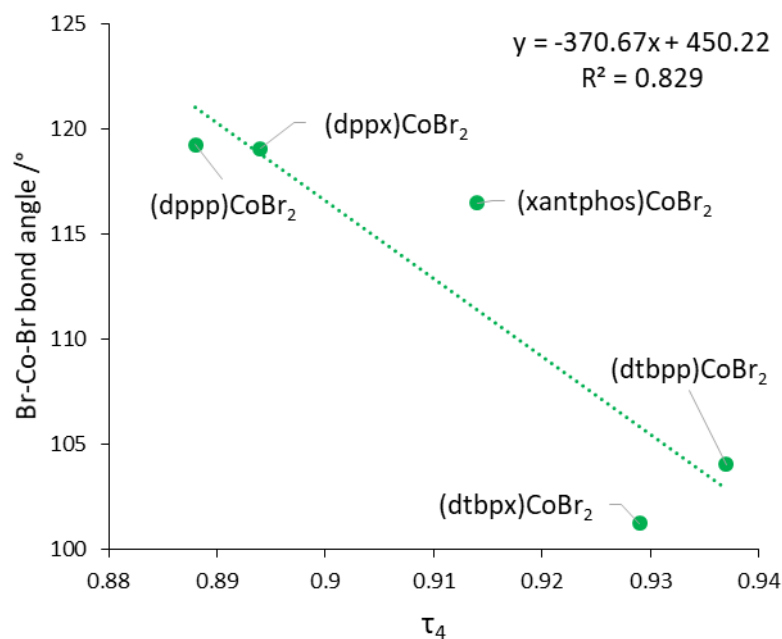


Figure 3.20 Relationship between the value of τ_4 and Br-Co-Br bond angle in (P^P)CoBr₂ complexes.

The observed trend between Br-Co-Br bond angle and the degree of distortion within (P^P)CoBr₂ complexes (**Figure 3.20**) suggests that these complexes distort from tetrahedral geometry as a result of the influence of steric constraints imposed by the different P-substituents and halide ligands. However, as this trend is not perfect ($R^2 = 0.829$), it is clear that other factors, not just sterics, contribute to structural distortion about the Co-centre. A spectroscopic study of these (P^P)CoX₂ complexes within the solution state to probe electronic effects was therefore necessary to further probe the origins of the observed effects (Section 3.3.4).

3.3.2.2 %V_{bur} Analysis of Diphosphine Ligands

To gain insight into the steric effect of changing diphosphine ligand, the magnitude of %V_{bur} and corresponding steric maps were generated for all the (P^P)CoX₂ complexes that had been structurally characterised by X-ray diffraction. The results of this investigation are shown in **Figure 3.21**.

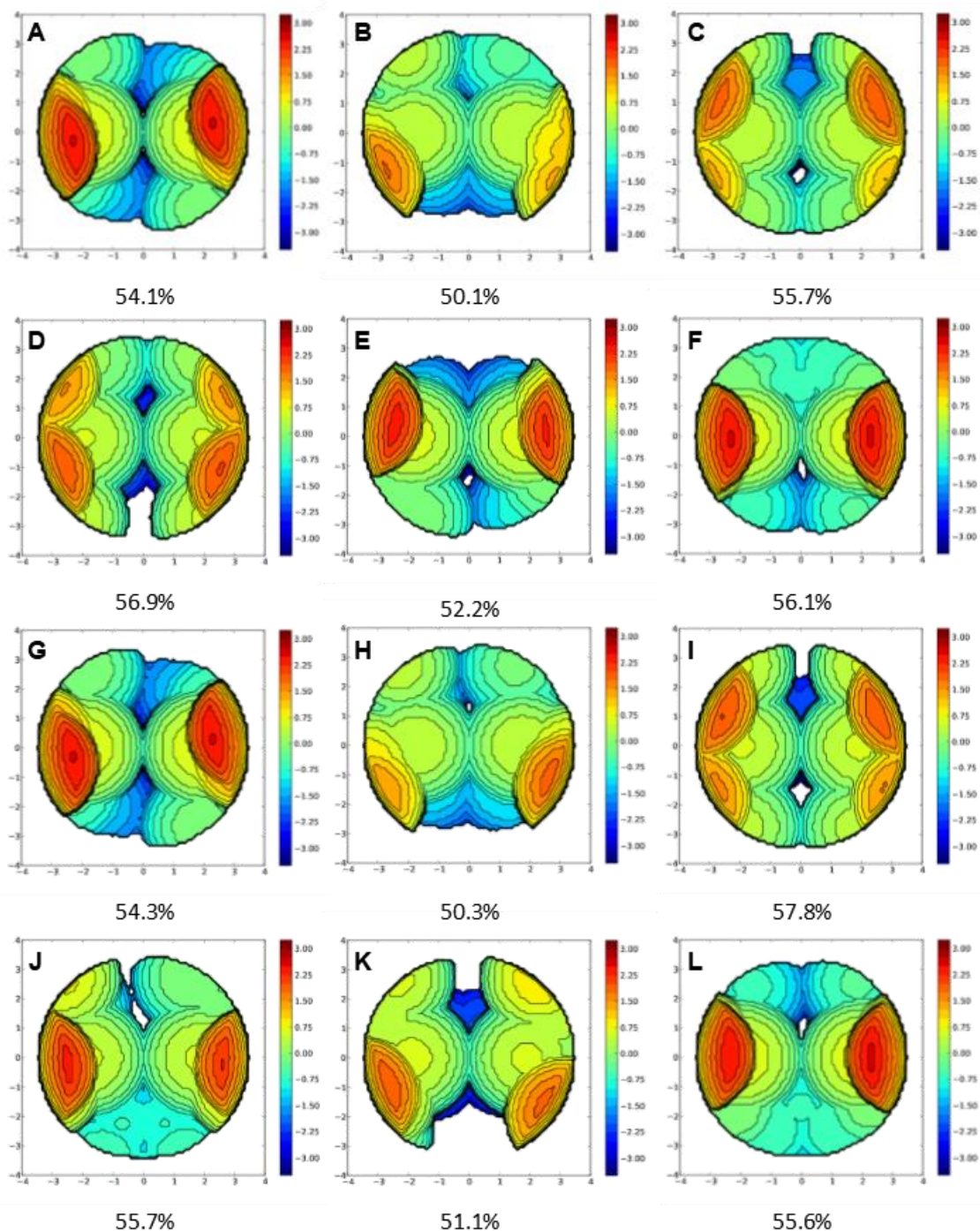


Figure 3.21 Steric maps obtained for diphosphine ligands when coordinated to CoX_2 (where $X = \text{Br}$, A-F and $X = \text{Cl}$, G-L) with $\%V_{\text{bur}}$ shown. Where $(P^{\wedge}P) =$ **A**: $2(\text{PPh}_3)$, **B**: dppp, **C**: dtbpp, **D**: dtbpx, **E**: dppx, **F**: xantphos, **G**: $2(\text{PPh}_3)$, **H**: dppp, **I**: dtbpx, **J**: dcypx, **K**: dppx and **L**: xantphos.

The values of $\%V_{\text{bur}}$ determined for the various $(P^{\wedge}P)\text{CoX}_2$ complexes investigated range between 50.1–57.8%, and follow the expected trends. For instance, when moving from Ph-substituted diphosphine to *t*Bu-substituted diphosphine, the steric congestion around the metal centre is increased as the bulk of the substituent increases (e.g. **Figure 3.21B** vs **C**; $\%V_{\text{bur}}$ dppp 50.1% vs dtbpp 55.7%). This trend is

also mirrored when the more rigid 1,2-*bis*(disubstitutedphosphinomethyl)benzene backbone is present, for instance, when maps **I**, **J** and **K** are compared the % V_{bur} is found to decrease: 57.8% > 55.7% > 51.1% (*t*Bu-P, Cy-P and Ph-P, respectively) upon moving to less sterically demanding phosphine substituents.

The backbone of the diphosphine ligand is also seen to have a significant effect upon the % V_{bur} value determined: when the backbone is changed from an aliphatic 1,3-*bis*(disubstitutedphosphino)propane unit to 1,2-*bis*(disubstitutedphosphinomethyl)benzene the value of % V_{bur} increases to 102–104% of that determined for the propyl-backbone value (comparing **B** and **E**, **C** and **D** and **H** and **K**). When the phosphine ligand(s) are 2 PPh₃, dppp and dtbpx, a small increase in the values of % V_{bur} is observed on replacing bromide by chloride ligands. This increase in % V_{bur} values is expected as the smaller chloride ligand will result in less steric repulsions, allowing the phosphine ligand to relax its geometry. However, when the diphosphine ligand is dppx or xantphos, a decrease in the magnitude of % V_{bur} is observed when the halide is changed from bromide to chloride. This has tentatively been attributed to a combination of the presence of the backbone and the ability of the phenyl groups present on phosphorus to rotate out of the way of the bulkier bromide ligands.

3.3.2.3 Non-tetrahedral “(P[^]P)CoX₂” Complexes

While the vast majority of (P[^]P)CoX₂ complexes synthesised in this work have *pseudo*-tetrahedral geometry at cobalt, this is not always the case. In a few instances, the geometry of prepared complexes is significantly different [where (P[^]P) = dppm, dppe, dppbz]. The structure of these complexes is discussed below.

3.3.2.3.1 The Structure of [BrCo(μ₂-dppm)(μ₂-Br)₂CoBr]

The reaction between diphenylphosphinomethane (dppm) with cobalt(II) bromide was performed in an attempt to produce the four-coordinate product (dppm)CoBr₂ (**Scheme 3.16**). However, a search of the Cambridge Structural Database for cobalt complexes containing a dppm ligand reveals dppm to almost exclusively coordinate as a bridging ligand.⁶⁰ For example, Puddephatt and co-workers reported a series of dinuclear-cobalt complexes containing bridging dppm ligands, an example of which is shown in **Figure 3.22**.⁷⁹

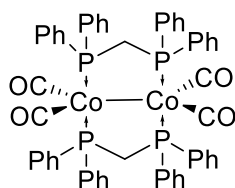
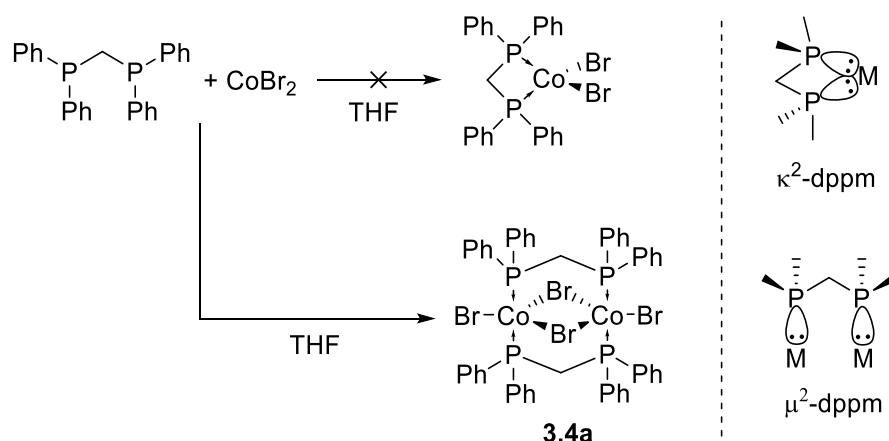


Figure 3.22 Reported molecular structure of a bimetallic Co⁰ complex containing bridging dppm ligands.⁷⁹

Based upon the preference of dppm to bridge two metal centres, the product obtained from the reaction of dppm with CoBr_2 has tentatively been assigned as a dicobalt dimer with bridging dppm and bromide ligands with general formula $[\text{Co}(\text{dppm})\text{Br}_2]_2$. It is thought that the small dppm bite angle could lead to considerable electronic conflict between the lone pairs on each P atom; a schematic representation of this proposed orbital overlap is shown in **Scheme 3.16**. Hence, it is proposed that the dppm ligand adopts a binding mode in which it bridges between two cobalt centres to prevent unfavourable lone pair-lone pair interactions in complex **3.4a**. Unfortunately, the solid-state molecular structure of this complex **3.4a** could not be obtained, so the proposed structure cannot be confirmed. However, Raman spectroscopic analysis of complex **3.4a** showed multiple overlapping bands in the expected region for $\nu_{\text{Co-Br}}$, which suggests complex **3.4a** is not *pseudo*-tetrahedral (which would only be expected to give rise to a single $\nu_{\text{Co-Br}_{\text{symm}}}$ band: discussed in Section 3.3.4.1). In addition, the solid-state structure of the product obtained upon reduction of **3.4a** with Zn metal (discussed in Chapter 4) contains two bridging dppm ligands, terminal bromides and a single bridging bromide ligand. These data support the proposed structure of **3.4a** shown in **Scheme 3.16**.



Scheme 3.16 Proposed structure of **3.4a** where dppm ligands bridge two metal centres to avoid repulsions between phosphine moiety lone pairs.

3.3.2.3.2 Solid-state structure of $[(\text{dppe})_2\text{CoBr}]^+_2[\text{Br}_3\text{Co}(\mu_2\text{-dppe})\text{CoBr}_3]^{2-}$

When 1,2-*bis*(diphenylphosphino)ethane (dppe) is reacted with cobalt(II) bromide in THF and recrystallised from DCM and hexanes, a salt is formed with general formula $[(\text{dppe})_2\text{CoBr}]^+_2[\text{Br}_3\text{Co}(\mu_2\text{-dppe})\text{CoBr}_3]^{2-}$ (**3.4b**). The two cationic species have square pyramidal geometry around cobalt with dppe ligands in the *xy* plane; the anion has two tetrahedral cobalt centres with a bridging dppe ligand (**Figure 3.23**). The solid-state structures of “ dppeCoX_2 ” ($\text{X} = \text{Cl}, \text{Br}, \text{I}$) complexes have been studied in

depth previously.⁸⁰ The solid-state structure as determined by X-ray diffraction as a part of this current work is shown in **Figure 3.23** the structure is very similar to that reported previously.⁸⁰ However, the previously reported structure of $[(dppe)_2CoBr]^+_2[Br_3Co(\mu_2-dppe)CoBr_3]^{2-}$ has a smaller unit cell compared to that for **3.4b** determined here as part of this work, since the latter contains two DCM solvate molecules, which were not in the previously reported structure. Severin *et al.* noted that the formation of salts with formula $[(dppe)_2CoX]^+_2[X_3Co(\mu_2-dppe)CoX_3]^{2-}$ ($X = Cl, Br$) was not affected by solvent choice or even through the stoichiometry of the reaction used to form the dppe complexes of cobalt (1:1, 1:2 and 1:3 dppe:Co tested), with all the resulting complexes having general formula $[(dppe)_2CoX]^+_2[X_3Co(\mu_2-dppe)CoX_3]^{2-}$ regardless of reaction stoichiometry.⁸⁰

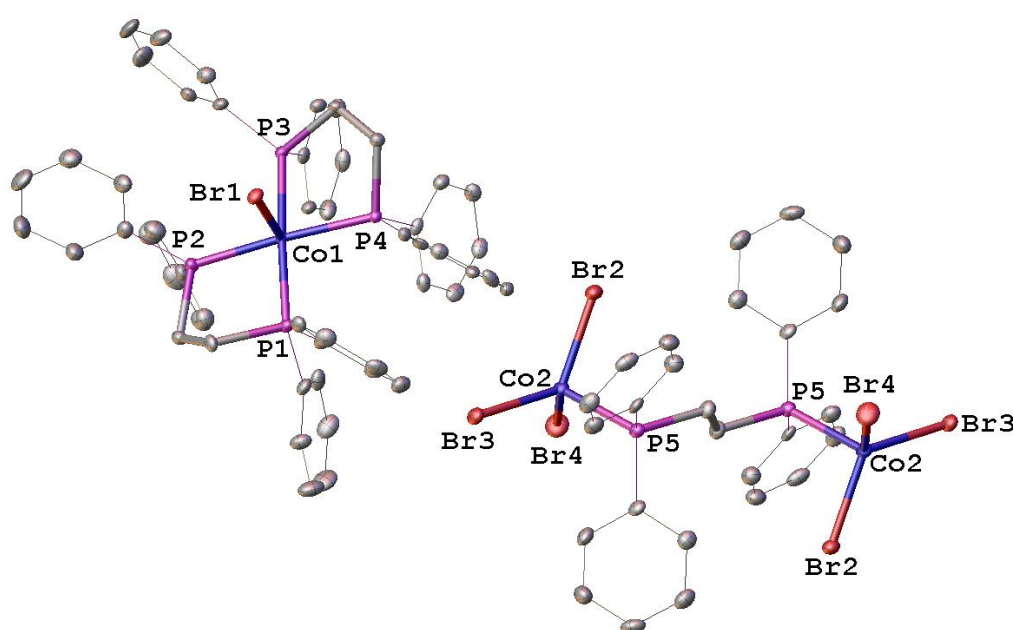


Figure 3.23 Solid-state structure of $[(dppe)_2CoBr]^+_2[Br_3Co(\mu_2-dppe)CoBr_3]^{2-}$ (**3.4b**). ORTEPs set at 50% probability. Hydrogen atoms and two DCM solvate molecules are omitted for clarity and phenyl groups are reduced to wireframe for clarity. *NB* There are two $[(dppe)_2CoBr_2]^+$ cations per $[Br_3Co(\mu_2-dppe)CoBr_3]^{2-}$ anion.

When the previously reported structure of $[(dppe)_2CoBr]^+_2[Br_3Co(\mu_2-dppe)CoBr_2]^{2-}$ is compared to that obtained in this current study, *i.e.* **3.4b** that has two molecules of DCM included (**Table 3.10**), the structures are very similar, with only small differences being observed. For instance the average Co-P bond distance within the cation of the structure of **3.4b** is 2.2101(35) Å and in the previously reported structure Co-P is 2.278(2) Å, the Co-Br bond distance is also observed to change slightly, *c.f.* 2.5377(8) Å and 2.5600(9) Å for **3.4b** and the previously reported structure of $[(dppe)_2CoBr]^+_2[Br_3Co(\mu_2-dppe)CoBr_2]^{2-}$ respectively. When the solid-state structures of the anion in **3.4b** and the previously reported structures are compared no difference to the bond distances measured is observed.

Table 3.10 Selected bond angles and bond distances comparing the previously reported structure⁸⁰ of $[(dppe)_2CoBr]^+_2[Br_3Co(\mu_2-dppe)CoBr_2]^{2-}$ to that obtained within this work. Values shown in parenthesis are standard deviation.

Complex		Co-Br ^a /Å	Co-P ^a /Å	∠Br-Co-P/°	∠β /°
3.4b	<i>cation</i>	2.5377(8)	2.2101(35)	89.34(4), 92.32(4), 93.77(4), 98.09(4)	81.58(5), 85.31(5)
	<i>anion</i>	2.3900(17)	2.372(2)	97.30(4), 105.94(5), 111.14(5)	
Ref	<i>cation</i>	2.5600(9)	2.278(2)	88.15(3), 91.37(2), 92.42(3), 98.12(3)	81.03(4), 84.53(4)
	<i>anion</i>	2.4002(14)	2.377(1)	97.06(3), 107.03(3), 110.70(3)	

^amean value

The structure of $[(dppe)_2CoBr]^+_2[Br_3Co(\mu_2-dppe)CoBr_2]^{2-}$ obtained by Severin *et al.* shows π -stacking of the phenyl groups between two dppe ligands. The solid-state structure of **3.4b** shows rotation of a phenyl group on P3 (**Figure 3.23**). The small changes to the solid-state structure of the cation of **3.4b**, when compared to the reported structure, are therefore attributed to the loss of some π -stacking character

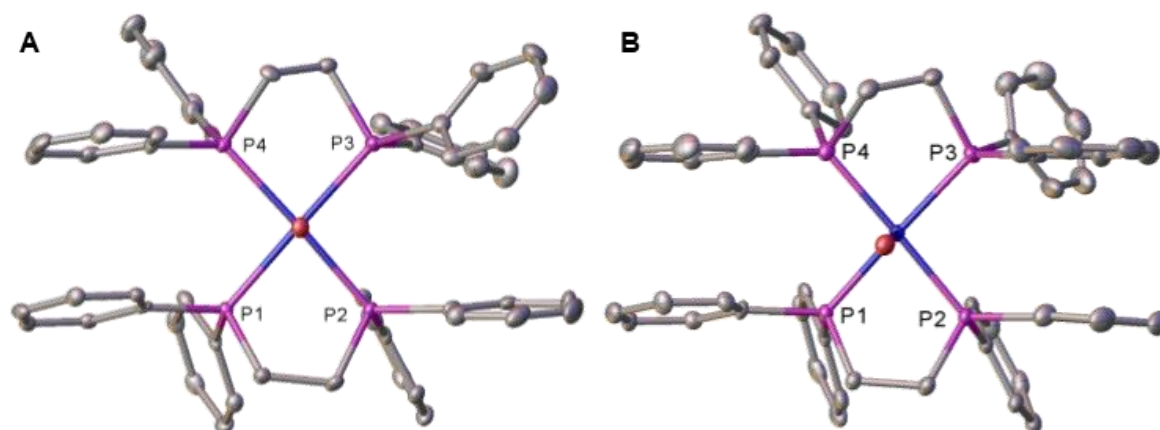


Figure 3.24 Comparison of solid-state structures of $[(dppe)_2CoBr]^+_2[Br_3Co(\mu_2-dppe)CoBr_2]^{2-}$ obtained in this work (**A**, **3.4b**) and previously reported (**B**), viewed down the z-axis. ORTEPs set at 50% probability, DCM solvate molecules and anions have been removed for clarity.

3.3.2.3.3 Solid-state structure of $[(dppbz)_2CoBr]^+_2[Br_2Co(\mu_2-Br)_2CoBr_2]^{2-}$

As has been reported previously for the reaction of $CoBr_2$ with dppe, when 1,2-*bis*(diphenylphosphino)benzene (dppbz) was reacted with cobalt(II) bromide, the resulting product is a disproportionated salt (**3.10**, **Figure 3.25**). However, due to the rigidity of the dppbz ligand, the salt formed has a simple $[Co_2Br_6]^{2-}$ dianion in place of the diphosphine bridged dianion seen for the analogous reaction with dppe (*i.e.* for complex **3.4b**), resulting in a structure with formula $[(dppbz)_2CoBr]^+_2[Br_2Co(\mu_2-Br)_2CoBr_2]^{2-}$ (**3.10**). The solid-state structure of complex **3.10** determined by single crystal X-ray diffraction shows square pyramidal geometry around the cationic cobalt centre and

tetrahedral geometry of the anionic cobalt centre, as was observed for the solid-state structure of **3.4b**.

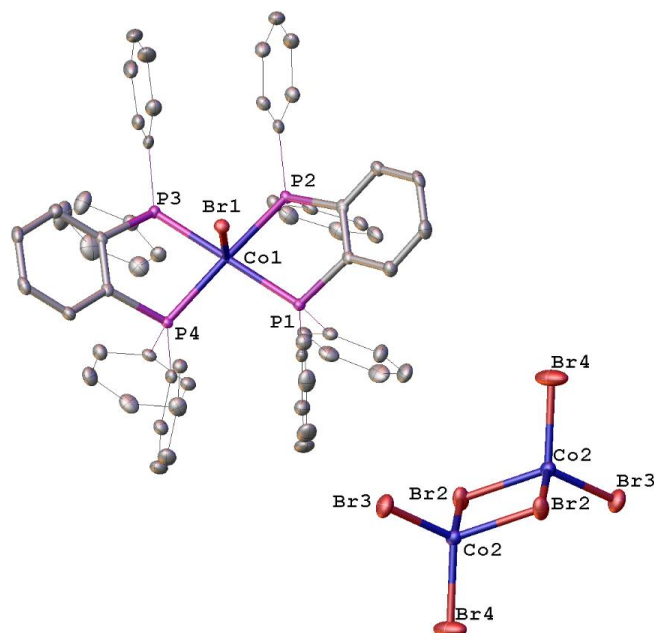


Figure 3.25 Solid-state structure of $[(\text{dppbz})_2\text{CoBr}]^+_2[\text{Co}_2\text{Br}_6]^{2-}$ (**3.10**). ORTEPs set at 50% probability. Hydrogen atoms and nine DCM solvate molecules are omitted for clarity and phenyl groups are reduced to wireframe for clarity. *NB* There are two $[(\text{dppbz})_2\text{CoBr}]^+$ cations per $[\text{Co}_2\text{Br}_6]^{2-}$ anion.

The bond distances and angles measured by X-ray diffraction for complex **3.10** are all within standard ranges (**Table 3.11**). The anion of complex **3.10** shows Co-Br bond distances of 2.3497(11) Å and 2.4582(9) Å, with the longer distance being found for the bridging bromide between the two cobalt centres.

Table 3.11 Selected bond angles and bond distances of $[(\text{dppbz})_2\text{CoBr}]^+_2[\text{Br}_2\text{Co}(\mu_2\text{-Br})_2\text{CoBr}_2]^{2-}$ (**3.10**).

	cation	anion
Co-Br ^a /Å	2.5141(8)	2.3497(11), 2.4582(9) ^b
Co-P ^a /Å	2.262(2)	
Br-Co-P/ ^o	91.41(3), 91.96(3), 93.05(3), 94.49(3)	
Br-Co-Br/ ^o		110.66(2), 111.19(2) ^c , 114.50(2) ^c
Co-Br-Co		86.07(2)
β / ^o	81.84(3), 82.35(3)	

^amean value, ^bCo-(μ_2 -Br), ^cBr-Co-(μ_2 -Br)

3.3.3. Mass Spectrometric Analysis of (P[^]P)CoX₂ Complexes

The *i*ASAP MS spectra of (P[^]P)CoX₂ complexes **3.3-3.10** were obtained under standard *i*ASAP conditions. For detailed discussion of development of *inert*ASAP MS technique and the experimental conditions used, see Chapter 5. A summary of characteristic fragments observed in the *i*ASAP MS spectra of (P[^]P)CoX₂ complexes **3.3-3.10** is shown in **Table 3.12**.

Table 3.12 MS (*i*ASAP⁺) fragmentation data from the synthesised (P[^]P)CoX₂ series. Masses are in Da, with % intensities in parentheses.

Entry	No.	Complex	[M] ⁺	[M-X] ⁺	[M-CoX ₂] ⁺
1	3.3a	(PPh ₃) ₂ CoCl ₂			263.08 ^a (100)
2	3.3b	(PPh ₃) ₂ CoBr ₂			263.07 ^a (100)
3 ^b	3.4a	(dppm)CoBr ₂	723.14 (0.9) ^c		385.10 ^a (100)
4 ^d	3.4b	(dppe)CoBr ₂		535.19 (3.1)	399.15 ^a (100)
5	3.4c	(dppp)CoCl ₂	541.01 (7.8)	506.05 (1.8)	413.15 ^a (42.1)
6	3.4d	(dppp)CoBr ₂		550.01 (7.9)	413.16 ^a (100)
7	3.4e	(dppb)CoCl ₂		519.12 (1.0)	427.15 (100)
8	3.4f	(dppb)CoBr ₂	602.89 (3.1)	564.0 (1.8)	426.10 (100)
9	3.5a	(dtbpb)CoBr ₂	549.02 (1.68)	470.11 (20.6)	333.27 (74.2)
10	3.5b	(diprpb)CoCl ₂	419.20 (10.6)	384.19 (100)	291.28 (33.5)
11	3.5c	(dcypb)CoBr ₂	667.07 (7.9)	588.14 (11.7)	451.32 (66.4)
12	3.6a	(dtbpx)CoCl ₂	555.15 (0.9) ^e	488.19 (3.0)	395.36 ^a (100)
13	3.6b	(dtbpx)CoBr ₂		532.15 (1.4)	395.00 ^a (100)
14	3.6c	(dcypx)CoCl ₂	627.19 (43.4)	592.23 (100)	499.34 (87.7)
15	3.6d	(dadpx)CoCl ₂		800.36 (2.3)	707.47 (100)
16	3.6e	(dadpx)CoBr ₂		844.27 (5.7)	746.43 (67.7)
17	3.6f	(dppx)CoBr ₂	960.95 (6.4)	612.03 (10.7)	474.18 (4.5)
18	3.6g	(diprpx)CoBr ₂	555.01 (42.8)	476.09 (42.8)	339.24 ^a (66.7)
19	3.6h	(dppx)CoCl ₂			
20	3.7a	(PNNP-Ph)CoCl ₂			457.18 ^a (59.2)
21	3.7b	(PNNP-Ph)CoBr ₂	672.92 (1.0)	594.01 (0.8)	457.17 ^a (100)
22	3.7c	(PNNP-tBu)CoCl ₂	No expected isotope patterns		
23	3.7d	(PNNP-tBtBu/Py)CoCl ₂		512.2 (100)	
24	3.8	(BINAP)CoBr ₂		760.06 (2.7)	623.21 ^a (100)
25 ^f	3.9	(xantphos)CoBr ₂		716.03 (2.0)	579.19 ^a (100)
26	3.10	(dppbz)CoBr ₂	1030.55 (2.2) ^f	583.95 (39.7) ^g	447.11 ^h (78.3)

^aObserved [M-CoX₂+H]. ^b[BrCo(μ₂-dppm)₂(μ₂-Br)CoBr], ^cASAP MS: [(dppmO)Co+H₂O]⁺, ^d[(dppe)₂CoBr]⁺₂[Br₃Co(μ₂-dppe)CoBr₃]²⁻, ^eASAP MS: [M+2O], ^f[(dppbz)₂CoBr]⁺₂[Br₂Co(μ₂-Br)₂CoBr₂]²⁻, ^g[(dppbz)CoBr]⁺, ^h[dppbz+H]⁺

The molecular ion can be observed for most, but not all, of the complexes analysed. As a result of *i*ASAP MS running without the presence of an aqueous lock-mass solution, the molecular ion is observed as $[M]^+$ rather than the more commonly observed $[M+H]^+$ ion by ASAP MS. Where $[M]^+$ was not observed, the most commonly observed highest molecular mass ion was $[M-X]^+$, for the complexes investigated. However, there were complexes for which this ion was not observed; these are discussed below.

Unfortunately, for complexes containing triphenylphosphine (TPP) ligands (**Table 3.12**: Entries 1, **3.3a**, and 2, **3.3b**), the *i*ASAP MS spectra obtained gave inconclusive results. This was a consequence of the strong ionisation of TPP that masked any signals that may have arisen from these samples, which was observed repeatedly throughout the work of this thesis. The observed ionisation patterns for samples **3.3a** and **3.3b** were confirmed to match that of TPP by running an authentic sample of TPP under standard *i*ASAP MS conditions. A comparison of the *i*ASAP MS spectra obtained for under identical conditions for $(PPh_3)_3CoBr_2$ and TPP is shown in **Figure 3.26**.

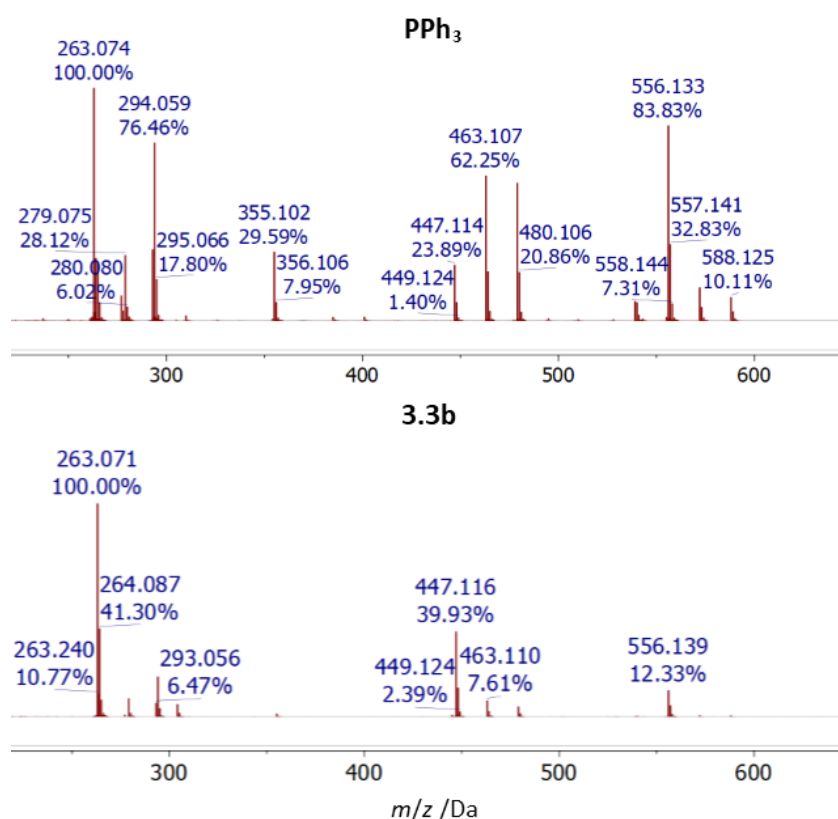


Figure 3.26 Comparison of *i*ASAP MS Spectra obtained of TPP (Top) and $(PPh_3)_3CoBr_2$ (**3.3b**) (Bottom); masses are in Da.

Analysis of the dimeric complex $BrCo(\mu_2-dppm)_2(\mu_2-Br)_2CoBr$ (**3.4a**), **Table 3.12**, **Entry 3**, afforded no $[M]^+$ or $[M-X]^+$ ions. This sample was run using standard ASAP methods. Under standard ASAP MS

conditions, the molecular ion of **3.4a** was not observed; the highest molecular weight ion observed was found to correspond to $[(\text{dppmO})\text{Co}+\text{H}_2\text{O}]$ with an intensity of 0.94% at m/z 723.14 Da.

Analysis of the complex $(\text{PNNP-Ph})\text{CoCl}_2$ (**3.7a**) (Table 3.12 Entry 19), gave a complicated mass spectrum with ion fragments that were hard to unambiguously assign. One ion that has been assigned tentatively had m/z 791.056 (0.98%), which was assigned to $[(\text{PPh}_2)_4\text{CoCl}+2\text{O}+2\text{H}]$, which is proposed to result from partial oxidation and hydrolysis of the complex **3.7a**. From the expected ions for complex **3.7a**, only $[(\text{PNNP-Ph})+\text{H}]^+$ was observed. The complex **3.7a** was run using *i*ASAP MS conditions, and so the observed presence of oxygen in the mass spectrum suggests the bulk material has, unfortunately, been exposed to air/moisture outwith the mass spectrometric measurement. Discussions of oxidation and hydrolysis products of $(\text{P}^{\wedge}\text{P})\text{CoX}_2$ complexes has been included in Section 3.6.6.

The *i*ASAP MS spectrum obtained of complex $\{1,2\text{-bis}(\text{di}t\text{er}t\text{butylphosphinoethylamino})\text{ethane}\}\text{CoCl}_2$ (**3.7c**; “ $(\text{PNNP-}t\text{Bu})\text{CoCl}_2$ ”) (Table 3.12: Entry 21) afforded some difficult to interpret signals with isotope patterns not associated with the predicted CoCl_2 species **3.7c**. Analysis of the spectrum obtained from **3.7c** shows the presence of CoCl_3 species. The *i*ASAP MS spectrum obtained of the sample could be interpreted as that containing a hydrolysis product, **3.7c·HCl** (Figure 3.27) with the following fragments observed: 447.429 (46.2%, $[\text{M}-\text{C}_4\text{H}_{11}\text{Cl}]$), 377.381 (100%, $[\text{M}-\text{CoCl}_3\text{H}]$), 319.300 (6.7% $[\text{M}-\text{CoCl}_3\text{C}_4\text{H}_{11}]$) Da. This was indeed confirmed from a single crystal X-ray diffraction study, which revealed the structure to be that shown in Figure 3.27, **3.7c·HCl**. Thus, the mass spectrometric data suggest that the molecular structure obtained by single crystal X-ray diffraction is indeed representative of the bulk material, **3.7c·HCl**.

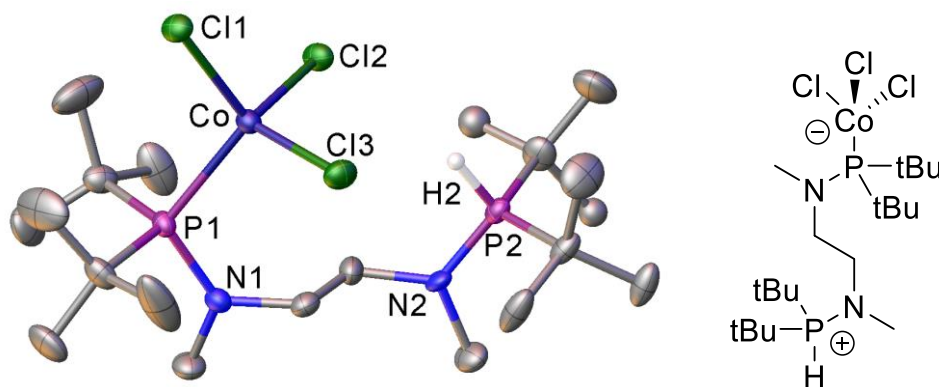


Figure 3.27 Solid-state structure of **3.7c·HCl** as determined by X-ray diffraction. ORTEPS set at 50%. Hydrogen atoms and two molecules of DCM have been omitted for clarity.

3.3.4 Spectroscopic Characterisation of Diphosphine Cobalt(II) Dihalides

The synthesised cobalt(II) dihalide complexes (**3.3-3.10**) were analysed by NMR, UV-Vis, NIR-UV-Vis and Raman spectroscopies in an effort to understand the effect of diphosphine variation upon the resulting structure and bonding within these (P[^]P)CoX₂ systems. As discussed in Section 3.3.2.1, the structure and bonding within *pseudo*-tetrahedral (P[^]P)CoX₂ complexes is controlled through the steric and electronic properties of the diphosphine ligand present. The results of these spectroscopic investigations are discussed below.

3.3.4.1 Raman Spectroscopic Analysis of (P[^]P)CoX₂ Complexes

Raman spectroscopic analysis of the vibrational energies of bonds has the advantage over IR spectroscopy of being able to probe low frequency vibrations, allowing cobalt-halide vibrations to be observed routinely. Determining Co-X bond vibration allows the effect of the diphosphine ligand upon the relative energies of Co-X bonds to be investigated. Consequently, Laser Induced Raman (LIR) spectroscopic measurements were performed on the various (P[^]P)CoX₂ complexes synthesised (**3.3-3.10**). For brevity only an analysis of Co-X bonds will be discussed in full (**Table 3.13**). However, for completeness, fully assigned Raman vibrational spectra are included in the experimental section. To compliment the experimental data and to aid band assignment, Raman spectra were determined computationally for those complexes for which structural data were available; the calculated data are included in parenthesis in **Table 3.13**.

Table 3.13 Summary of ν Co-X stretching frequencies within (P^P)CoX₂ complexes in the solid-state by LIR (λ 532 nm). Where possible, calculated spectra (B3LYP/3-21G*) energies are included in parenthesis.

Entry	(P^P)		ν Co-Cl /cm ⁻¹		ν Co-Br /cm ⁻¹
1	-		256s, 1001w ^a		261m, 488m, 950s
2	2 PPh ₃	3.3a	318m (320w)	3.3a	273m
3	dppm			3.4a	254-278m*
4	dppe			3.4b	254s ^b 300w
5	dppp	3.4c	318m (321w)	3.4d	284sh (304m)
6	dtbpp			3.5a	279sh (282sh)
7	dppb	3.4e	310m	3.4f	286m
8	dcypb			3.5c	270w
9	diprpb	3.5b	309m		
10	dppx			3.6f	283m (279m)
11	dtbpx	3.6a	318m	3.6b	282m (279m)
12	dcypx	3.6c	312m		
13	diprpx			3.6g	296sh
14	dadpx	3.6d	315sh	3.6e	297w
15	dbbpz			3.10	250s ^b , 298w ^c , 345m ^d , 373m ^{e/f} (239s ^b 304w ^c , 348m ^d , 365s ^e , 382m ^f)
16	BINAP			3.8	279w
17	xantphos			3.9	275m (264w)
18	PNNP-Ph	3.7a	321m	3.7b	293sh
19	PNNP- <i>t</i> Bu	3.7c	No bands ^g		
20	PNNP- <i>t</i> Bu/Py	3.7d	334m		

^alattice vibrations, w: weak, m: medium, s: strong, sh: shoulder, ^banion: ν Co-(μ -Br)_{symm}, ^ccation: ν Co-Br, ^danion: ν Co-(μ -Br)_{asymm}, ^eanion: ν Co-Br_{asymm} ^fanion: ν Co-(μ -Br)_{symm asymm} ^gCl₃Co(PNNP-*t*Bu·H⁺). *multiple overlapping bands.

From the Raman spectra obtained, it can be seen that upon moving from (P^P)CoCl₂ to (P^P)CoBr₂, the frequency of ν Co-X_{symm} stretch moves to lower wavenumber (**Table 3.13**: Entries 5, 7, 11, 14 and 18). This follows the expected trend when one considers Hooke's law (**Equation 3.3**), which uses the reduced mass, μ , (**Equation 3.4**) to determine the expected vibrational frequency of a bond between two atoms with masses m_1 and m_2 . Upon moving to a heavier atom, *e.g.* Cl to Br, the value of μ will increase, decreasing the observed vibrational frequency.

Equation 3.3 Hooke's Law: where c is $3 \times 10^{10} \text{ cm s}^{-1}$, k is the force constant ($5 \times 10^5 \text{ g s}^{-2}$), and μ is the reduced mass.

$$\bar{\nu} = \frac{1}{2\pi c} \sqrt{\frac{k}{\mu}}$$

Equation 3.4 Formula for reduced mass, μ , for a bond between two atoms with masses m_1 and m_2 .

$$\mu = \frac{m_1 m_2}{m_1 + m_2}$$

The Raman spectra obtained of complexes (P[^]P)CoBr₂ **3.4a**, **3.4b** and **3.10** (where (P[^]P) = dppe, dppbz, respectively), show multiple bromide environments in overlapping bands as a result of the multiple bromide environments present within these non-tetrahedral structures. These observed Co-Br stretches are within the range expected for $\nu_{\text{Co-Br}}$ in the Raman spectra obtained.⁸¹ Similar wavenumber ranges for the multiple bands were observed for complexes described in Entries 3, 4 and 15, suggesting similar structures for each. On reaction with CoBr₂ both dppbz and dppe have been shown to form disproportionated ion pairs (**3.4b** and **3.10**), resulting in multiple halide environments: one in the cation, and two (dppe) or four (dppbz) in the anion.

For the *pseudo*-tetrahedral complexes investigated within this work, no significant change to the Co-X bond vibration is observed when comparing diphosphine ligands with different substituents on phosphorus and the same backbones, for example, $\nu_{\text{Co-Br}_{\text{symm}}}$ is 284 cm^{-1} in (dppp)CoBr₂ (**3.4d**) and 279 cm^{-1} in (dtbpp)CoBr₂ (**3.5a**), and $\nu_{\text{Co-Br}_{\text{symm}}}$ is 283 cm^{-1} in (dppx)CoBr₂ (**3.6f**) and 282 cm^{-1} in (dtbpx)CoBr₂ (**3.6b**). The lack of a change to $\nu_{\text{Co-X}}$ upon changing phosphine substituent is surprising, as the σ -donor character of the ligands dramatically changes, as shown by the respective values of $|^1J_{\text{SeP}}|$ within diselenide compounds; $|^1J_{\text{SeP}}|$ measured for dpppSe₂ (**3.11c**) is 722 Hz, dtbppSe₂ (**4.11g**) is 689 Hz, dppxSe₂ is 724 Hz⁷¹ and dtbpxSe₂ (**3.11h**) is 696 Hz. In addition, no significant change to $\nu_{\text{Co-Br}}$ was observed upon changing the backbone of the diphosphine ligand. Insignificant variations in the value obtained of $\nu_{\text{Co-Br}_{\text{symm}}}$ were observed when comparing the Co-X stretching frequencies for complexes (dppp)CoCl₂ [318 cm^{-1} ; **3.4c**] with (dppp)CoBr₂ [310 cm^{-1} ; **3.4e**] and (dppb)CoCl₂ [284 cm^{-1} ; **3.4d**] with (dppb)CoBr₂ [286 cm^{-1} ; **3.4f**]. Both dppp and dppb ligands have very similar donor characteristics (*c.f.* $|^1J_{\text{SeP}}|$ 722 Hz in dpppSe₂ (**3.11c**) and 720 Hz in dppbSe₂ (**3.11d**)) and so no significant difference in $\nu_{\text{Co-X}}$ would be expected.

These observations of no significant change to the values of $\nu_{\text{Co-X}}$ upon diphosphine ligand variation where the donor properties of the diphosphine are changed suggests that there is no significant π -donation from the halide ligand to the metal. This lack of change to $\nu_{\text{Co-X}}$ values suggests that considering the P-Co and Co-X bonds in terms of simple σ -donor and resulting π -donor character is not a good representation of the bonding present.

3.3.4.2 Electronic Spectra of (P[^]P)CoBr₂ Complexes

The overarching aims of this thesis include the development of an understanding of the structure and bonding within cobalt(II) complexes supported by a bidentate ligand (P[^]P) or (N[^]N), with the ultimate goal of using this information to control the activity of these pre-catalyst complexes towards olefin oligomerisation. In this context, analysis of electronic absorption spectroscopic data is particularly useful when it comes to investigating the structure and bonding within transition metal complexes. UV-Vis spectroscopy is particularly useful in the characterisation of transition metal complexes due to their characteristic d←d transitions. Cobalt(II) complexes will absorb electromagnetic radiation within the near-infrared (NIR), visible and ultraviolet (UV) regions of the spectrum. Obtaining electronic absorption spectra of the (P[^]P)CoX₂ complexes (**3.3-3.10**) using UV-Vis spectroscopy allows the electronic structure and bonding within these complexes to be probed through investigation of the observed band energies and widths. Near-IR-UV-Vis spectroscopic studies have also been undertaken here on a small series of (P[^]P)CoBr₂ complexes: (dppp)CoBr₂ (**3.4d**), (dtbpp)CoBr₂ (**3.5a**), (dtbpx)CoBr₂ (**3.6b**) and (dppx)CoBr₂ (**3.6f**) to further the investigation into structure and bonding within (P[^]P)CoBr₂ complexes through determination of an experimentally-determined nephelauxetic series through implementation of a Tanabe Sugano diagram. A brief introduction into Term symbols, Tanabe-Sugano analysis and the nephelauxetic series and the derivation thereof is included.

3.3.4.2.1 Term Symbols

The ways in which angular momenta is associated with orbital spin in a many electron atom can be described by one of three main types: spin-spin coupling, orbit-orbit coupling or spin-orbit coupling. In Russell Saunders (also known as *LS* coupling) coupling, it is assumed that spin-spin coupling (*S*) > orbit-orbit coupling (*L*) > spin-orbit coupling. *LS* coupling has been found to be a good approximation for the first row transition metal elements, where spin-orbit coupling (*J*) can largely be ignored.⁸²

In Russell-Saunders coupling, *S* is the total spin angular momentum, *L* is the total orbital angular momentum and *J* is the total angular momentum, where:

$$\{2S, L, 2J\} \geq 0 \in \mathbb{Z}$$

The total orbital angular momentum is described by a symbol following the order: S, P, D, F, G, H... (alphabetical thereafter; excluding J) for values of *L* = 0, 1, 2, 3, 4, 5, 6..., respectively. *L* can take values within the range $|l_1 + l_2|, \dots, |l_1 - l_2|$ where *l*₁ and *l*₂ are orbital (azimuthal) quantum numbers. Within the naming of electronic states, the labels A, E and T are used to describe non-degenerate, doubly degenerate and triply degenerate states, respectively.^{83,84}

The total spin angular momentum can have values within the range $|s_1 + s_2|, \dots, |s_1 - s_2|$ where s_1 and s_2 are spin quantum numbers. The multiplicity of the term is described by $2S + 1$. Some example multiplicities are shown in **Table 3.14**.⁸³

Table 3.14 Multiplicity of a state as described within the term symbol.

S	2S + 1	Multiplicity
0	1	Singlet
$\frac{1}{2}$	2	Doublet
1	3	Triplet
$\frac{3}{2}$	4	Quartet
3	5	Quintet
$\frac{5}{2}$	6	Sextet
		<i>etc.</i>

The total angular momentum, J , is obtained by coupling the spin angular momentum and the orbital angular momentum and can have values $|L + S| \geq J \geq |L - S|$. A representation of the total angular momentum due to LS coupling where $J = L + S$ is shown in **Figure 3.28**.

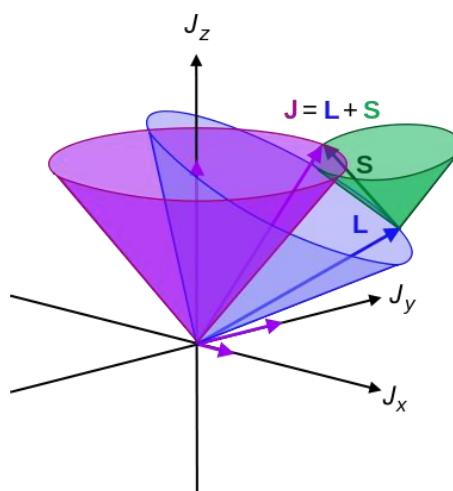


Figure 3.28 LS coupling where $J = L + S$.⁸⁵

It is helpful to have notation to describe distinct electronic states. In Russell-Saunders coupling, degenerate microstates are grouped into terms and given a unique term symbol descriptor, which follows the formula shown below. The resulting notation is called a 'term symbol.'⁸³

$$^{2S+1}L_J$$

For instance, Co^{2+} has a total orbital angular momentum $L = 3$ and a total spin angular momentum $S = 3/2$ ($2S+1=4$, quartet). These then give rise to a ${}^4\text{F}$ ground state.⁸² This ground state term is included within the Tanabe-Sugano analysis of $(\text{P}^{\wedge}\text{P})\text{CoX}_2$ complexes. These Tanabe-Sugano diagrams can then be used to determine which electronic transitions to excited states (in Term symbol notation) are observed within experimentally obtained electronic spectra.

3.3.4.2.2 Tanabe-Sugano Diagrams for Tetrahedral Complexes

Tanabe-Sugano (TS) diagrams are used in a ligand field model to correlate experimentally observed bands in electronic spectra with the corresponding electronic transitions from which they arise. From Tanabe-Sugano analysis, it is possible to order the ligands under investigation in terms of the degree of covalency they exhibit within the cobalt(II) system based upon the d-electron delocalisation to the ligands in question. This is termed a nephelauxetic series.^{82-84,86}

TS diagrams show the energies of electronic states of a complex, with specified d-electron count, as a function of the ligand field strength exhibited. The ligand field strength (Δ) is expressed as Δ/B' and plotted against the term energies (E) as E/B' , where B' is the so-called Racah parameter. The ground state is always taken to be that of the zero energy term and each line within the diagram represents the energy of an electronic state of the complex in an octahedral field.⁸²

As indicated, TS diagrams are usually expressed in terms of the electronic states of a complex within an octahedral field. For complexes where the geometry of the ligands around a metal centre is tetrahedral with d^n configuration, the corresponding octahedral-TS diagram with d^{10-n} can be used. However, it must be noted that $\Delta_{\text{tet}} \approx 4/9\Delta_{\text{oct}}$ when calculating the ligand field strength. Additionally, upon moving from octahedral (centrosymmetric) to tetrahedral (non-centrosymmetric) geometries, the gerade expressions can be removed from the term symbols describing the electronic states as the Laporte selection rule (transitions between states with no change in parity are forbidden) no longer applies.

The diphosphine cobalt(II) dihalide (d^7) complexes under investigation in this thesis have (distorted) tetrahedral geometry; the appropriate TS diagram is therefore octahedral field d^{10-7} , *i.e.* d^3 . The TS diagram for d^3 is shown in **Figure 3.29** where $C = 4.5B$. From the d^3 Tanabe sugano diagram, it is clear three allowed transitions are expected to be observed within measured electronic absorption spectra of cobalt(II) complexes, that should correspond to: $\nu_1: {}^4\text{T}_2({}^4\text{F}) \leftarrow {}^4\text{A}_2$, $\nu_2: {}^4\text{T}_1({}^4\text{F}) \leftarrow {}^4\text{A}_2$ and $\nu_3: {}^4\text{T}_1({}^4\text{P}) \leftarrow {}^4\text{A}_2$.

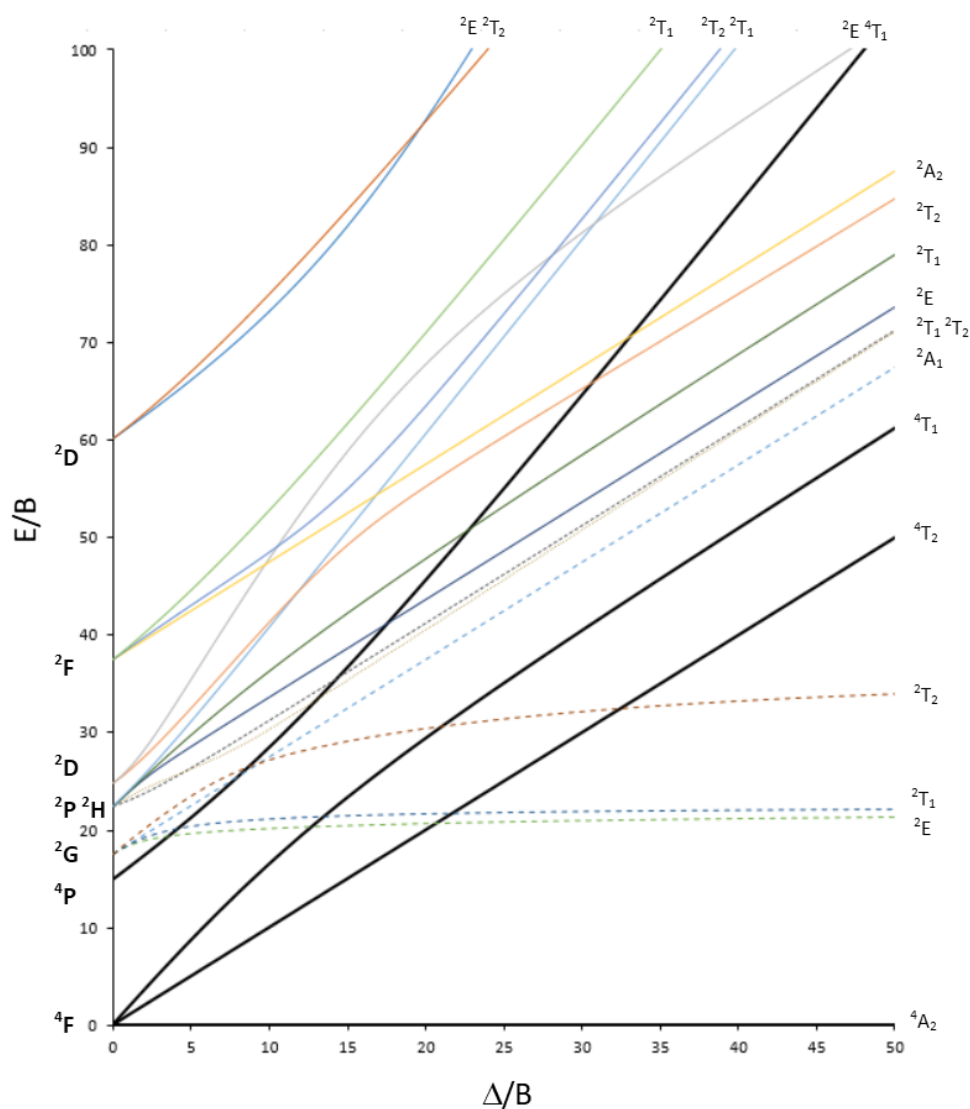


Figure 3.29 Tanabe-Sugano diagram of a d^3 complex in an octahedral field, or a d^7 complex in a tetrahedral field.⁸⁷

3.3.4.3 UV-Visible Spectroscopic Studies of (P^ΛP)CoX₂ Complexes

UV-Vis spectroscopy is a useful tool especially for the characterisation of transition metal complexes due to their characteristic $d \leftarrow d$ transitions, which occur in this spectral window. Consequently, UV-Vis spectra were recorded for (P^ΛP)CoX₂ complexes (3.3-3.10) as solutions in THF. For each of the (P^ΛP)CoX₂ complexes a broad band consisting of three distinct transitions was observed within the visible region (Figure 3.30). From the Tanabe-Sugano diagram appropriate for a tetrahedral cobalt(II) complex, three allowed transitions would be expected: ν_1 : ${}^4T_2({}^4F) \leftarrow {}^4A_2$, ν_2 : ${}^4T_1({}^4F) \leftarrow {}^4A_2$ and ν_3 : ${}^4T_1({}^4P) \leftarrow {}^4A_2$. The broad band observed within the visible region is assigned as ${}^4T_1({}^4P) \leftarrow {}^4A_2({}^4F)$ (ν_2).

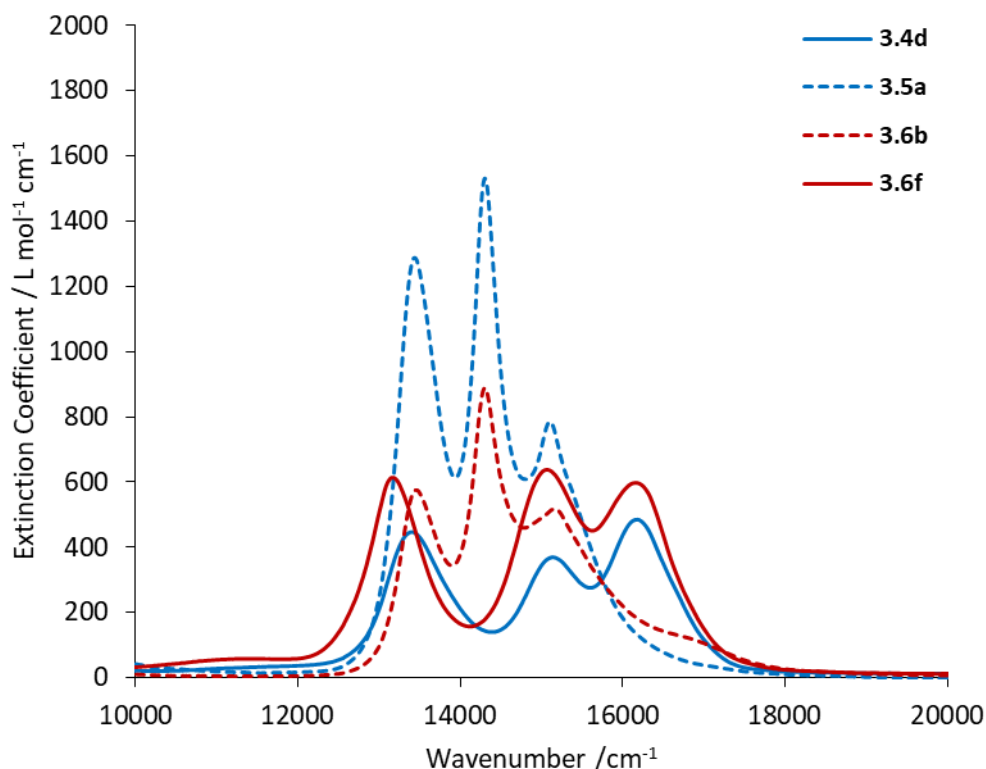


Figure 3.30 Visible region of the electronic absorption spectra of selected representative (P[^]P)CoBr₂ complexes (**3.4d**, **3.5a**, **3.6b** and **3.6f**) as their THF solutions.

The structure of the band (three peaks) observed within the visible region of the spectra of (P[^]P)CoX₂ complexes is as expected. As mentioned in the introduction to this chapter, Co²⁺ has a ⁴F ground state ($2S+1 = 4$, the result of three unpaired electrons). To understand the structure of the band observed arising from ⁴T₁(⁴P) ← ⁴A₂ transition in (P[^]P)CoX₂ complexes, the orbital degeneracy within a d⁷ complex with perfect tetrahedral geometry has to be considered. Within a complex with pure tetrahedral symmetry, the *d*_{xy}, *d*_{yz} and *d*_{zx} orbitals are degenerate and so a transition from any of these orbitals to the LUMO would be expected to have the same energy, giving rise to one transition (and hence band) within the electronic spectrum. However, in *pseudo*-tetrahedral complexes, a lifting of degeneracy for these three orbitals is likely, resulting in the three observed transition bands for the same base transition. A summary of the observed electronic transitions within the visible region for (P[^]P)CoX₂ complexes is shown in **Table 3.15**.

Table 3.15 Summary of observed electronic transitions in the visible region (THF solutions) for (P[^]P)CoX₂ complexes.

Entry	(P [^] P) =	⁴ T ₁ (⁴ P) ← ⁴ A ₂ / cm ⁻¹	
		(P [^] P)CoBr ₂	(P [^] P)CoCl ₂
1	-	16779sh, 15361sh, 14599	-
2	2 PPh ₃	3.3b 16779sh, 15314sh, 14556*	3.3a 17241, 15773, 14430*
3	dppm	3.4a 16807, 15361, 14577*	-
4	dppe	3.4b 16207sh, 15337sh, 14430 ¹	-
5	dppp	3.4d 16129, 15083, 13369	3.4c 17153, 15748, 13624
6	dtbpp	3.5a 15106, 14306, 13441	-
7	dppb	3.4f 16077, 14749 ¹	3.4e 16892, 15601, 14493, 13532 ^{1,2}
8	dcypb	3.5c 15576sh, 14706, 13423	-
9	diprpb	-	3.5b 16181, 15314sh, 13624
10	dtbpx	3.6b 15198, 14306, 13441	3.6a 15974, 14881, 13699
11	dppx	3.6f 16155, 15060, 13175	-
12	dadpx	3.6e 15129, 14205, 13550	3.6d 147606, 14771, 13774
13	diprpx	3.6f 15848sh, 15060, 13405	-
14	dcypx	-	3.6c 16694, 15699, 13643
15	BINAP	3.8 16750sh, 15361sh, 14620sh ^{1,3}	-
16	Xantphos	3.9 15949sh, 15198, 13228	-
17	dppbz	3.10 16287sh, 15848, 14104	-
18	PNNP-Ph	3.7b 16155, 14859, 13423	3.7a 17241, 15601, 14472*
19	PNNP- <i>t</i> Bu	-	3.7c 16949, 15528, 14556
20	PNNP- <i>t</i> Bu/Py	-	3.7d 17182, 15480sh, 14556*

sh: shoulder, *ligand dissociation, ¹poor solubility in THF, ²oxidised complex: dppbO₂ bridging two Co centres, ³green precipitate observed.

Across the series of (P[^]P)CoX₂ complexes **3.3-3.10** changes to the diphosphine ligand results in only small variations in the lowest energy component of the ν₂ band, but significant shifts in the energies of the two higher energy components of this ν₂ band. The highest energy component is observed to have a hypsochromic shift of up to ~2500 cm⁻¹ in (P[^]P)CoCl₂ complexes (*c.f.* 14706 cm⁻¹ in **3.6d**, Entry 12, and 17153 cm⁻¹ in **3.4c**, Entry 5 in **Table 3.15**) and up to ~1000 cm⁻¹ in (P[^]P)CoBr₂ complexes (*c.f.* 15106 cm⁻¹ in **3.5a**, Entry 6, and 16129 cm⁻¹ in **3.4d**, Entry 5 in **Table 3.15**). The highest energy

component of the ${}^4T_1({}^4P) \leftarrow {}^4A_2$ band for $(P^{\wedge}P)CoX_2$ complexes is observed to have the greatest shift upon ligand variation. From this shift, a general trend is apparent in the series of $(P^{\wedge}P)CoX_2$ complexes examined. As the substituents on the phosphine moiety become increasingly donating in character the highest energy component of the ${}^4T_1({}^4P) \leftarrow {}^4A_2$ moves to lower energy (**Figure 3.31**). The trend is towards a smaller band gap transition as the diphosphine ligand σ -donor character is increased, which suggests stabilisation of the T_2 d orbitals from increasing electron density on cobalt through σ -donation.

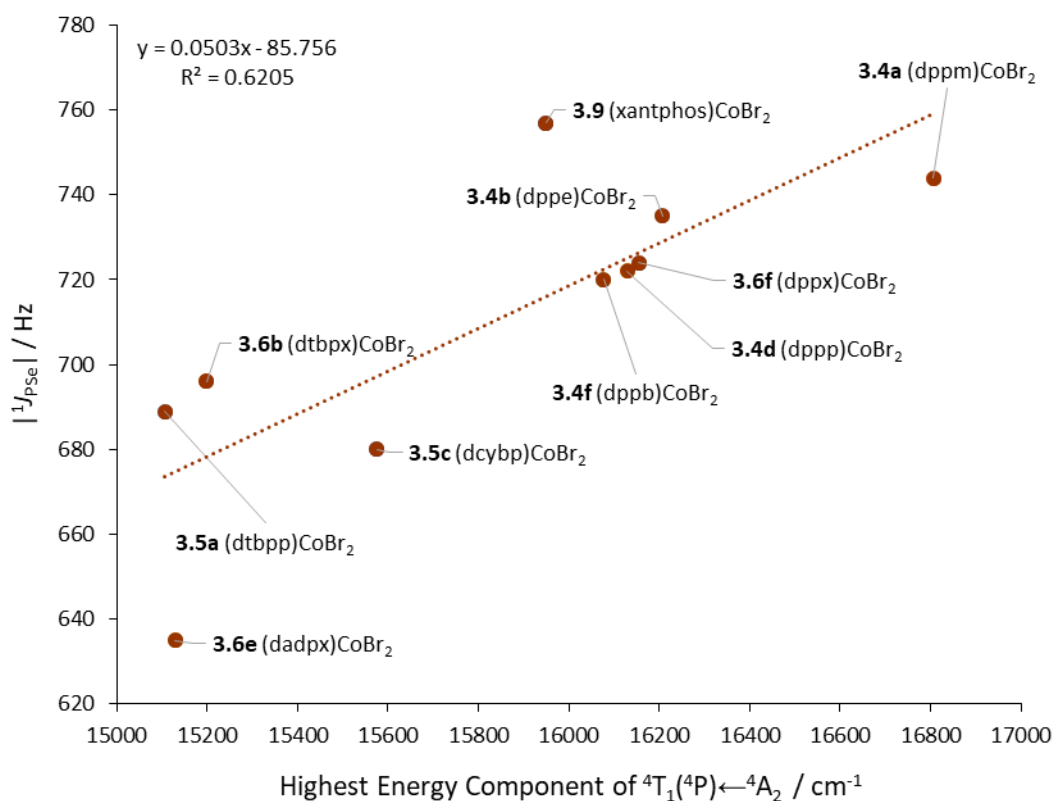


Figure 3.31 Attempted correlation between the donor capacity of the free ligand ($|{}^1J_{Pse}|$) and resulting energy of the highest energy component of the ${}^4T_1({}^4P) \leftarrow {}^4A_2$ transition.

The bandwidth of the transition corresponding to the transition ${}^4T_1({}^4P) \leftarrow {}^4A_2$ in $(P^{\wedge}P)CoX_2$ complexes **3.3-3.10** is very wide, ranging between 2500 cm^{-1} in $(dtbpx)CoBr_2$ (**3.6b**) to 3000 cm^{-1} in $(dppx)CoBr_2$ (**3.6f**) (quoted to the nearest 50 cm^{-1}). This is wider than the band width recorded for $[CoCl_4]^{2-}$ and $[CoBr_4]^{2-}$ by $1500\text{-}2500\text{ cm}^{-1}$.^{88,89} The observation of large bandwidths for the ${}^4T_1({}^4P) \leftarrow {}^4A_2$ component of the electronic spectra of *pseudo*-tetrahedral cobalt complexes have been noted previously by Lever and Nelson, who attributed the increasing width of the spectral envelope to result from a lowering of symmetry within their investigated series of *bis*(amine) cobalt halides from regular tetrahedral geometry towards C_{2v} .⁸⁶ In turn, Lever and Nelson attributed a lowering in symmetry to steric

hindrance induced by the introduction of sterically demanding amine ligands, which resulted in distortion about the metal centre. In the series of (P[^]P)CoX₂ complexes investigated herein, the largest bandwidths were measured for samples containing phenyl-substituted diphosphine ligands, *e.g.* (dppx)CoBr₂ (**3.6f**) and (dppp)CoBr₂ (**3.4d**) and the narrowest in complexes containing *tert*butyl-substituted diphosphine ligands, *e.g.* (dtbpx)CoBr₂ (**3.6b**) and (dtbpp)CoBr₂ (**3.5a**). Based upon the conclusions drawn by Lever and Nelson, the bandwidths measured for **3.5a** and **3.6b** would be expected to be greater than those with less sterically demanding phenyl-substituents on phosphorus (**3.6f** and **3.4b**). However, as the largest bandwidths are observed within phenyl-substituted diphosphines within this study, it can be concluded that bandwidth does not correlate simply to the steric demands of the ligand, as was indicated through investigation into the τ_4 values of (P[^]P)CoX₂ complexes (*vide supra*, Section 3.3.2.1). More likely, it is going to be a result of a combination of both the steric and electronic demands of the ligands and the ability of the resulting cobalt complex to accommodate the ligand through perturbations to the underlying symmetry. This effect is demonstrated by comparison of the values of τ_4 (four-coordinate geometry index) and the bandwidths measured for comparable (P[^]P)CoX₂ complexes. For instance, the values of τ_4 follow the trend: 0.888 (**3.4d**) \approx 0.894 (**3.6f**) < 0.929 (3.6b) \approx 0.937 (3.5a) and the corresponding bandwidths measured follow the same trend such that: **3.6f** (2950 cm⁻¹) \approx **3.4d** (2800 cm⁻¹) \gg **3.6b** (1750 cm⁻¹) \approx **3.5a** (1700 cm⁻¹). To gain additional insight into the observed greater extent of lowering of symmetry for P-phenyl-substituted diphosphine cobalt complexes compared to *tert*butyl-substituted diphosphine cobalt complexes, an investigation into the ligand field splitting and the nephelauxetic parameters for **3.4d**, **3.5a**, **3.6b** and **3.6f** was launched.

3.3.4.4 Racah Parameters and the Nephelauxetic Series

When using a TS diagram to determine ligand field strength based upon experimentally-determined energies of electronic states, it is useful to determine the value of the Racah parameter B'. There are three Racah parameters A, B' and C, which all describe how the energies that arise from a given term are affected by electron-electron repulsion. The value of A is the same for all terms (it is an average of the total inter-electron repulsion) and so it can be discounted when comparing relative energies. The electron repulsion felt for individual d-electrons is described by the parameters B and C. However, when comparing the value of relative triplet energies, the value of C is not required.⁸² The parameter B' gives an indication of the delocalisation of the d-electrons present within a complex as a result of the covalency of the ligand-metal bonding. As such, comparison of B'_{LCo} for a complex LCo²⁺ with B'_{Co} for the free Co²⁺ metal ion allows the effect of the ligand on d-electron delocalisation to be determined, something known as the nephelauxetic [*translation: cloud-expanding*] parameter, β :

$$\beta = \frac{B'_{LCo}(complex)}{B'_{Co}(free\ ion)}$$

Thus, through comparison of β values, ligands can be ordered according to the reduction in B' felt in comparison to B' of the free ion. This method of ordering ligands is known as the nephelauxetic series and is useful in cases where the spectrochemical series falls short, *e.g.* when ligands present have no significant π -acceptor/-donor character, something upon which the spectrochemical series relies. As discussed in Section 3.3.2, the diphosphine ligands investigated herein in *pseudo*-tetrahedral complexes have little π -acceptor character. As such, investigation into the nephelauxetic series to attempt to gain insight into the fundamental bonding within these (P[^]P)CoX₂ complexes is warranted.

Removing consideration of contributions arising from A and C during analysis of electronic spectra to obtain β is a widely employed technique.^{82,83,90} However, a recent report has noted that the interaction parameter C may have more of an effect upon values obtained for β .⁹¹ As such, any nephelauxetic series obtained cannot be regarded as being quantitative, but can still be used as a qualitative tool for comparing the relative degree of covalency within a series of comparable metal/ligand systems as a result of the ligands present.

3.3.4.5 Determination of a Small Nephelauxetic Series of (P[^]P)CoBr₂ Complexes

Tanabe-Sugano diagrams can be used to determine the nephelauxetic parameter for a given complex. Through use of NIR-UV-Vis spectroscopy, it is possible to observe both the ν_2 (⁴T₁(⁴F)←⁴A₂) and ν_3 (⁴T₁(⁴P)←⁴A₂) transition bands for (P[^]P)CoX₂ complexes. Thus, a nephelauxetic series (based upon the nephelauxetic parameter, β) can be constructed. To this end, the NIR-UV-Vis spectra of selected (P[^]P)CoBr₂ complexes (**3.4d**, **3.5a**, **3.6b** and **3.6f**) were measured.

Tanabe-Sugano diagrams make use of the measured energy of transition bands through the ratio of the positions of these bands. To effectively compare energies of the measured bands, one must ensure the weighted centre of the band is taken. Therefore, it is necessary for measured spectra to be fitted with Gaussian functions (equation for a Gaussian curve, g_1 , shown below).

$$f(g_1) = I_1 e^{-\frac{(x-c_1)^2}{2w_1^2}}$$

where I_1 = peak intensity, c_1 = centre of the band and w_1 is the band width.

To ensure a good fit could be obtained when fitting calculated Gaussian curves to measured spectra, the quality of the experimentally-measured spectra is important. Consequently, the spectroscopic data discussed below were all collected using single-beam UV-Vis-NIR spectroscopic techniques. Single beam spectroscopy prevents small deviations within the data associated with dual beam techniques,

which can result from, for example, use of unpaired cuvettes or impurities only present within one of the two cuvette solutions, *etc.* A detailed description of the single-beam spectroscopic methods used herein can be found in the Experimental Chapter 6.

For completeness, an example of the process used for peak fitting and subsequent band centre analysis is discussed for (dtbpx)CoBr₂ below; all other samples were treated similarly. The electronic absorption spectra and subsequent Gaussian curve fittings for (dtbpx)CoBr₂ are shown in **Figure 3.32**.

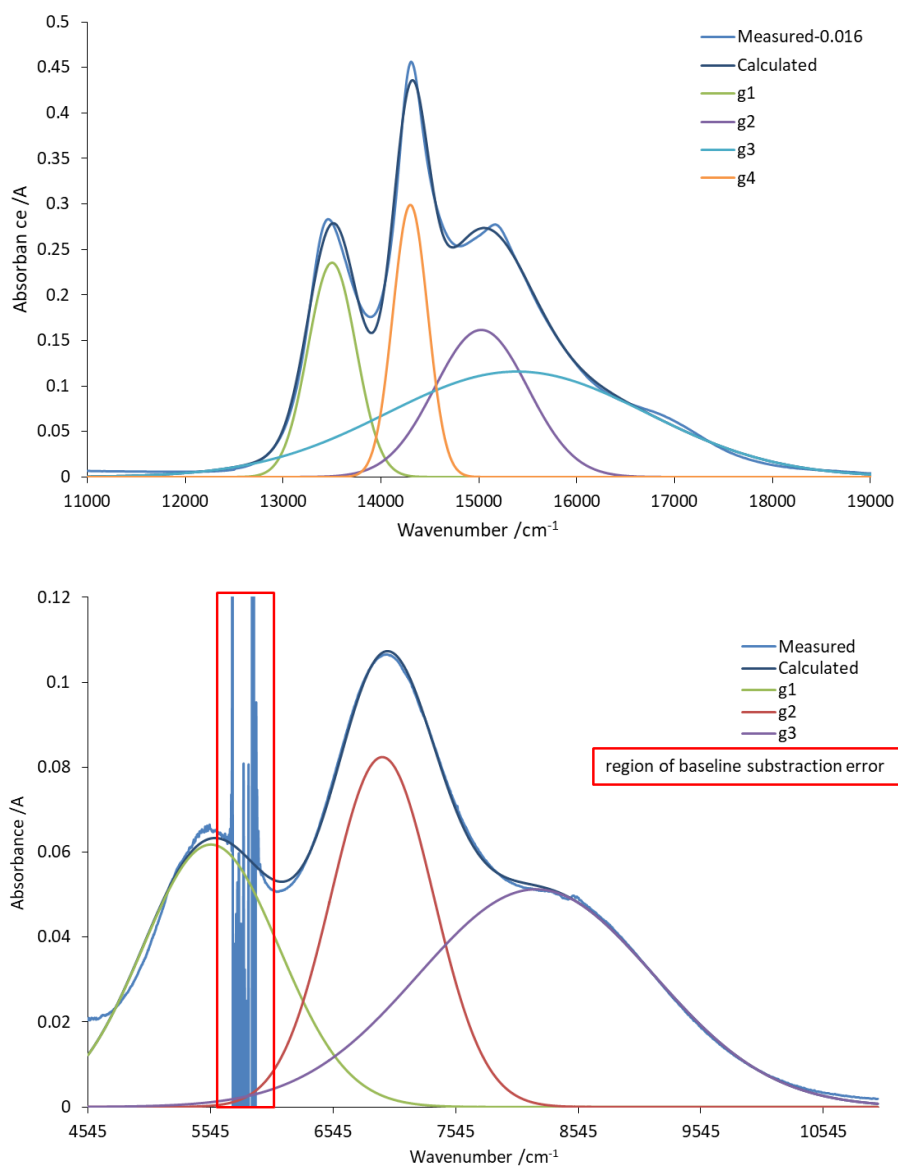


Figure 3.32 Measured and calculated electronic absorption spectra of (dtbpx)CoBr₂ (**3.6b**) within visible (Top, SS = 0.0148, showing ${}^4T_1({}^4P) \leftarrow {}^4A_2$) and near-IR (Bottom, SS = 0.0048, showing ${}^4T_1({}^4F) \leftarrow {}^4A_2$) regions with peak-fitted Gaussian curves (g) displayed.

Within the visible region of the spectra for all of the samples measured (**3.4d**, **3.5a**, **3.6b** and **3.6f**), it was necessary to use four Gaussian curves to allow for minimum variance when compared to the measured spectral data. This is attributed, in part, to a sloped baseline and contributions from forbidden quartet-doublet transitions on the high energy edge of the band of interest.⁸² Within the near-IR region for all complexes investigated, a region with a baseline subtraction error was identified, which arose as a result of strong absorbance of the solvent used;[‡] this region can be seen in the bottom spectra of **Figure 3.32**. To allow fitting around this error, the contribution from SS (sum of the difference squared: measured–calculated) within this region was discounted.

From the Gaussian curves obtained through fitting the experimental data, the weighted centre, \bar{x} , of each band can be obtained *via* centroid analysis. Here the area under the curve is found and used to determine the weighted centre of that band in either x or y plane. In this instance, the functions need only be solved for the x plane to obtain \bar{x} .

For a Gaussian curve, g_1 , the area, A_1 , can be determined *via*:

$$A_1 = \int_b^a f(g_1). dx$$

where a and b are set points on the x-axis where $y = 0$.

The total area, A_{tot} , under the band comprised of $\sum(g_1 + g_2 + g_3)$ is therefore:

$$A_{tot} = A_1 + A_2 + A_3$$

This allows the weighted centre of the band, \bar{x} , to be determined *via*:

$$\bar{x} = 1/A_{tot} \int_d^c x.f(g_1). dx + x.f(g_2). dx + x.f(g_3). dx$$

where c and d are set points on the x-axis where $y = 0$ for $\sum(g_1 + g_2 + g_3)$.

Using the Tanabe-Sugano diagram for a tetrahedral d^7 complex and the ratio between transition band centres, $(\nu_3 \bar{x})/(\nu_2 \bar{x})$, calculated from the experimental data obtained within the NIR-UV-Vis spectra of $(P^{\wedge}P)CoBr_2$ complexes collected, the value of Δ/B' can be calculated through finding a value of Δ/B' where $((\nu_3 \bar{x})/(\nu_2 \bar{x})) = ((\nu_3/B')/(\nu_2/B'))$; a representation is shown in **Figure 3.33**.

[‡]THF was selected as a solvent to aid solubility of the $(P^{\wedge}P)CoX_2$ complexes.

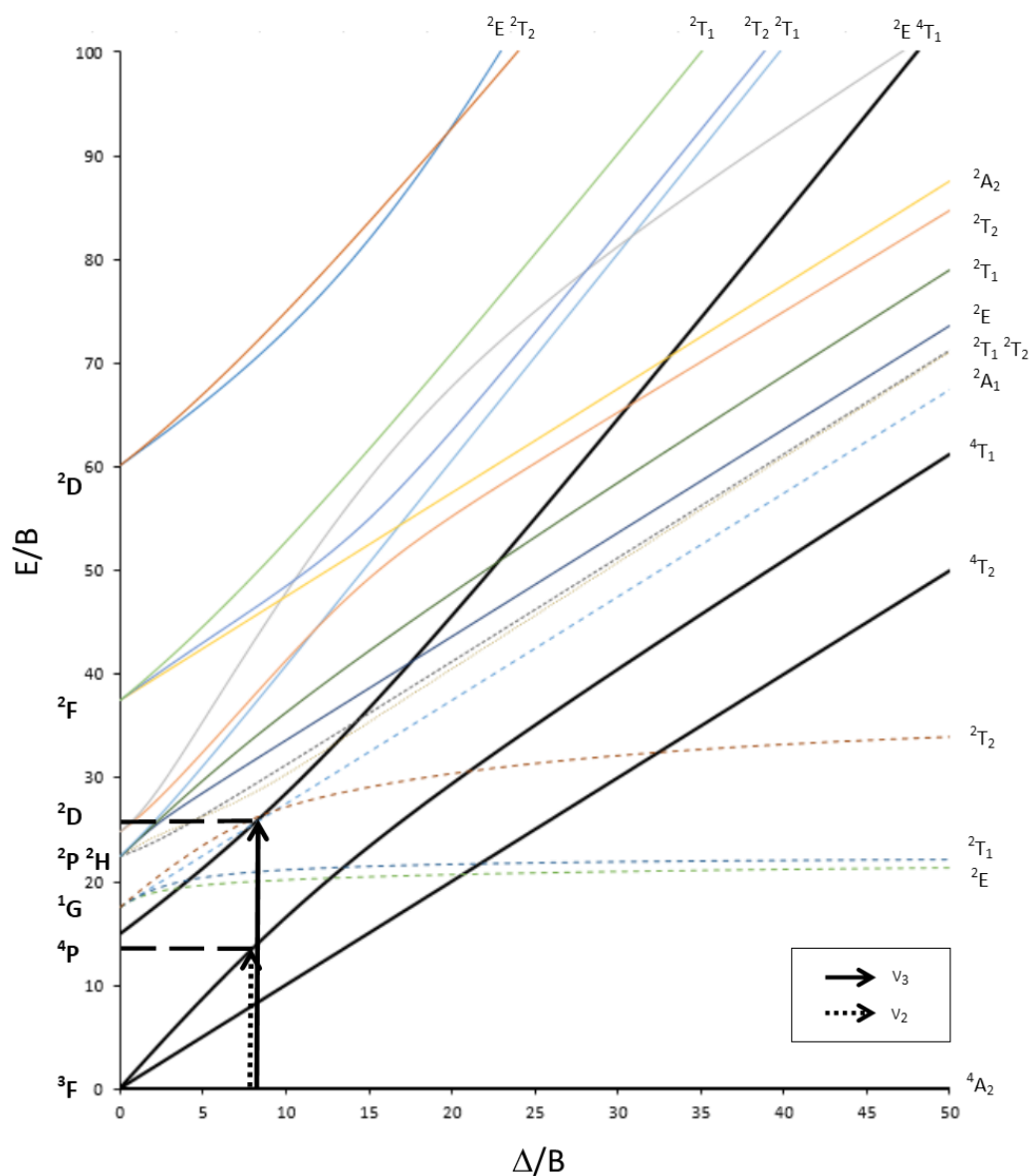


Figure 3.33 d^7 (tetrahedral) Tanabe-Sugano diagram where, e.g. $\Delta/B \approx 7$ when $((v_3 \bar{x})/(v_2 \bar{x})) = ((v_3/B')/(v_2/B')) = \sim 2$.

With Δ/B' in hand, the Racah parameter, B' , can be extracted through application of the observed transition band centres for each complex. From B' , the ligand field strength within a tetrahedral field can be directly obtained (Δ_{tet}), as can the nephelauxetic parameter, β . The resulting experimentally-determined data for the diphosphine cobalt(II) bromide complexes investigated are summarised in **Table 3.16**.

Table 3.16 Observed transitions, ν_2 and ν_3 , and corresponding Tanabe-Sugano analysis with calculated Racah parameters (B'), crystal field splitting, Δ , nephelauxetic parameter, β , and four-coordinate geometry index, τ_4 .

	3.6b (dtbpx)CoBr ₂	3.5a (dtbpp)CoBr ₂	3.4d (dppp)CoBr ₂	3.6f (dppx)CoBr ₂
$\nu_3 \bar{\chi} (^4T_1(^4P) \leftarrow ^4A_2) / \text{cm}^{-1}$	14641	15456	15480	14556
$\nu_2 \bar{\chi} (^4T_1(^3F) \leftarrow ^4A_2) / \text{cm}^{-1}$	7740	8217	7634	7246
$(\nu_3 \bar{\chi}) / (\nu_2 \bar{\chi})$	1.89160	1.88098	2.02777	2.00883
Δ / B'	8.016	8.118	6.953	7.081
ν_3 / B'	25.544	25.693	24.017	24.198
ν_2 / B'	13.504	13.660	11.844	12.046
ν_1 / B'	8.016	8.118	6.953	7.081
$(\nu_3 / B') / (\nu_2 / B')$	1.89159	1.88089	2.02777	2.00880
$B' \nu_3 / \text{cm}^{-1}$	573.17	601.57	644.54	601.54
$B' \nu_2 / \text{cm}^{-1}$	573.16	601.54	644.55	601.52
$B' \text{ avg} / \text{cm}^{-1}$	573	602	645	602
Δ / cm^{-1}	4593	4887	4485	4263
$\Delta_{\text{tet}} / \text{cm}^{-1}$	2041	2172	1993	1895
β	0.51	0.54	0.58	0.54
P-Co / Å	2.452(2)	2.4334(9)	2.3458(8)	2.3472(18)
Co-Br / Å	2.396(2)	2.3874(6)	2.3594(6)	2.3474(15)
τ_4	0.929	0.937	0.888	0.894

As these (P[^]P)CoBr₂ complexes (**3.6b**, **3.5a**, **3.4d** and **3.6f**) all exhibit distortions from regular tetrahedral geometry, the absolute values of β and of Δ_{tet} are not too significant. For this reason, only the overarching trends observed will be discussed.⁸⁶

From the values of Δ_{tet} obtained experimentally, a small spectrochemical series can be prepared for the diphosphine ligands present in complexes **3.6b**, **3.5a**, **3.4d** and **3.6f**, such that:

Series 1: $\text{dppx} < \text{dppp} < \text{dtbpx} < \text{dtbpp}$

This spectrochemical series (**Series 1**) arising from the experimental data from the various (P[^]P)CoBr₂ complexes suggests that aliphatic diphosphine ligands are stronger field ligands than their aryl phosphine counterparts. This trend is mirrored within the values of $|^1J_{\text{SeP}}|$ measured for the diphosphine ligands (**Figure 3.34**) such that, as donor capacity increases (lower $|^1J_{\text{SeP}}|$ value), the ligand field strength increases and a larger ligand field splitting parameter (Δ_{tet}) results.

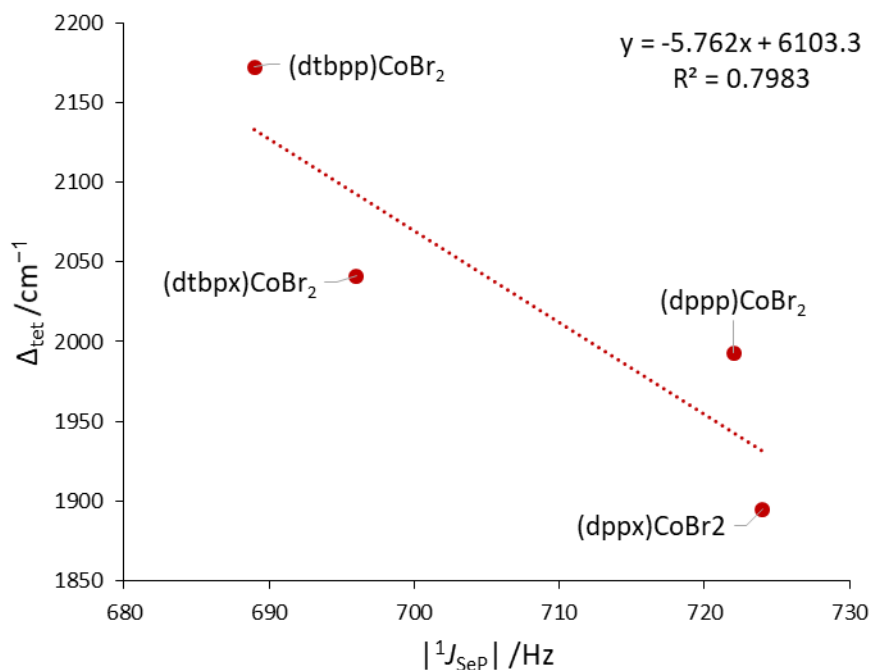


Figure 3.34 Relationship between ligand field splitting (Δ_{tet}) and donor capacity of the diphosphine ligand.

From the β values obtained, a short nephelauxetic series can be constructed to demonstrate the covalent character of the cobalt(II) complexes formed from the ligands investigated such that:

Series 2: (dtbpx)CoBr₂ (**3.6b**) < (dtbpp)CoBr₂ (**3.5a**) \approx (dppx)CoBr₂ (**3.6f**) < (dppp)CoBr₂ (**3.4d**)

An increase in the β value signifies a decrease in d -electron delocalisation onto the ligand, as such the complex can be considered to be less covalent in character. Examples of the derivation of nephelauxetic parameters from experimental data are not abundant in the literature. As such, the magnitude of the differences in values of nephelauxetic parameters calculated herein cannot be commented upon.^{86,88} The nephelauxetic series determined therefore implies an increase in covalent bond character for *t*Bu-substituted P-ligands. These data therefore suggest that the dtbpx ligand results in a greater reduction in electron repulsion within the metal ion than dppp through expansion of the d -orbitals. The order of this nephelauxetic series of (P[^]P)CoBr₂ complexes does not follow the same trends observed for: donor capacity of the diphosphine ligands ($|^1J_{SeP}|$ values), any bond angles within the complexes (P-Co-P, X-Co-X, *etc.* from XRD data) or bandwidth of the $^4T_1(^4P) \leftarrow ^4A_2$ transition (UV-Vis analysis).

The order of diphosphine complexes obtained within the above nephelauxetic series (**Series 2**) is counter-intuitive, as one would expect *t*Bu-substituted phosphine ligands to have less covalent character compared with their Ph-substituted phosphine ligand counterparts. This would be expected due to the relative increased electron density present on phosphorus from electron-rich *t*Bu groups

when compared to Ph-substituted phosphines (coupled with the potential for limited P-aryl pi-system interactions), thus P-Co bond character for *t*Bu-substituted phosphines would be expected to be more dative. In fact, the Co-P bond lengths measured for complexes with *t*Bu-substituted diphosphines (**3.5a** and **3.6b**) are longer than those measured in complexes with Ph-substituted diphosphines (**3.4d** and **3.6f**) (Table 3.16), which suggests that the bonding between cobalt and *t*Bu-substituted phosphines is more dative than the bonding between cobalt and Ph-substituted phosphines. In an effort to understand this notable and apparent increase in covalency upon moving from “*t*Bu-P” to “Ph-P” substituents, the observed distortions within the geometries of the complexes investigated (τ_4) should be considered. In addition, the orientation of the ligands (phosphine moiety vs halide on the apex) around cobalt must also be considered.

When considering the orbital interactions within (P[^]P)CoX₂ complexes that may give rise to the observed nephelauxetic series, it is important to consider the relative positions of the diphosphine and halide ligands about the cobalt centre. To determine whether a phosphine moiety or a halide ligand is present in the apex position within complexes **3.4d**, **3.5a**, **3.6b** and **3.6f**, the solid-state structural data obtained by single crystal X-ray diffraction can be used. Herein, the moiety in the apical position is defined as that where the minimum sum of the angles surrounding the moiety under scrutiny is found (Figure 3.35).

$$apex = \min \sum (\alpha^\circ + \beta^\circ + \gamma^\circ)$$

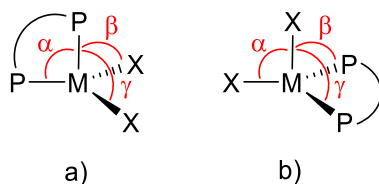


Figure 3.35 Schematic representation of a distorted tetrahedral complex displaying angles α , β and γ , used to calculate which ligand is on the apex. Where a) phosphine on the apex and b) halide (X) on the apex.

Using the equation shown in Figure 3.35 and the crystallographic data of complexes **3.4d**, **3.5a**, **3.6b** and **3.6f**, the ligand in the apical position for each structure was determined. In both complexes (dppp)CoBr₂ (**3.4d**) and (dtbpp)CoBr₂ (**3.5a**), a phosphine moiety is located in the apical position, while for both (dtbpx)CoBr₂ (**3.6b**) and (dppx)CoBr₂ (**3.6f**), a halide ligand resides in the apical position. Notably, both complexes investigated with a 1,3-disubstituted backbone (**3.4d** and **3.5a**) have a phosphine moiety on the apex, and both complexes with a 1,2-(disubstituted)methylbenzene backbone (**3.6b** and **3.6f**) have a halide on the apex. Consequently, the flexibility of the backbone of

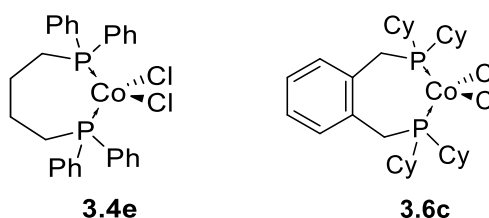
the diphosphine ligand, along with the steric and electronic contributions of the phosphine substituents are therefore implicated within the nephelauxetic series determined.

When the structural data obtained from X-ray diffraction studies was considered alongside the values of the nephelauxetic parameters for complexes **3.4d**, **3.5a**, **3.6b** and **3.6f**, there was no obvious correlation between the apparent increase in covalency per the observed trend of **3.6b** < **3.5a** \approx **3.6f** < **3.4d** (Series 2). Complexes **3.4d** and **3.6f** have a greater degree of distortion from regular tetrahedral geometry than **3.6b** and **3.5a**. However, as these complexes also have different ligand moieties on the apex of the distorted tetrahedra, no clear conclusions can therefore be drawn about the origin of the apparent nephelauxetic series obtained for these (P[^]P)CoBr₂ complexes. Therefore, for this small series of (P[^]P)CoBr₂ complexes, an accurate description of the bonding and structure cannot be obtained through use of nephelauxetic parameters obtained. A computational investigation to investigate the structure and bonding characteristics of these complexes, in particular the factors that dictate significant distortions from C_{2v} symmetry is currently underway by Dr Mark Fox (Durham University).

3.3.5 Effective Magnetic Moment (μ_{eff}) of "(P[^]P)CoX₂" Complexes

The effective magnetic moment (μ_{eff}) of selected complexes (**3.4e** and **3.6**) were recorded using a JME (Johnson-Matthew Evans) balance. A comparison between the μ_{eff} and the spin-only magnetic moment calculated ($\mu_{\text{s.o}}$) is shown in **Table 3.17**. An example calculation for the determination of the value of μ_{eff} is given in Chapter 6, Section 6.5.

Table 3.17 Effective magnetic moments (μ_{eff}) and spin only magnetic moments ($\mu_{\text{s.o}}$) of complexes (dppb)CoCl₂ (**3.4e**) and (dycpx)CoCl₂ (**3.6c**). Units are in Bohr Magnetons, μ_{B} , and all Co centres are regarded as being *pseudo*-tetrahedral.



Entry	1	2
Electronic configuration	d ⁷ (e ⁴ t ₂ ³)	d ⁷ (e ⁴ t ₂ ³)
$\mu_{\text{s.o}} = \sqrt{n(n+2)}$	3.88	3.88
μ_{eff}	4.98	4.20

Both of the complexes (dppb)CoCl₂ (**3.4e**) and (dcypx)CoCl₂ (**3.6c**) have values of μ_{eff} within the expected observed range for high spin tetrahedral cobalt(II) complexes (4.0-5.0 B.M).⁹² This range is typically higher than that expected from spin only contributions ($\mu_{\text{s.o}}$) alone (**Table 3.17**). The calculated spin-only effective magnetic moment, $\mu_{\text{s.o}}$, of Co(II) (d⁷) where n is the number of unpaired electrons is 3.88 μ_{B} as a result of the three unpaired electrons within the T₂ level. Differences in the spin-only magnetic moment and effective magnetic moment arise due to the spin-orbit coupling constant (λ) for d⁷ such that $\lambda < 0$ (full e_g and half full T₂, therefore no first-order orbital momentum; A, E ground terms) resulting in greater contribution to the observed magnetic moment coming from the angular momentum (L) as the spin-orbit contribution has not been quenched.

A d⁷ (e.g. Co(II)) configuration displays a positive and large deviation from the spin-only expectation (c.f. $\mu_{\text{s.o}} = 3.88 \mu_{\text{B}}$ and $\mu_{\text{eff}} = 4.98 \mu_{\text{B}}$ for **3.4e**). This is because (T₂)ⁿ configurations behave magnetically like (p)ⁿ configurations, when the sub-shells are more than half-filled, i.e. S and L are parallel, so any orbital contribution increases μ_{eff} beyond the spin-only value (**Figure 3.36**).

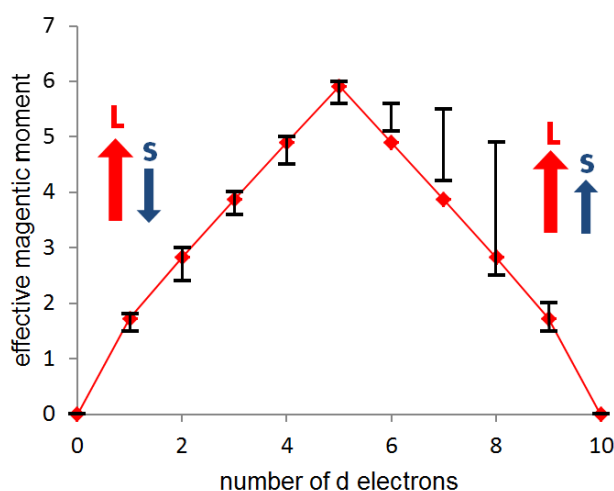


Figure 3.36 Spin-only magnetic moment as d-electron count increases, with measured values highlighted as a result of angular orbital moments and spin becoming parallel at $>d^5$.⁹³

Using the orbital angular momentum (L) and spin (S) to calculate the magnetic moment of a d⁷ complex can be beneficial due to the magnetic moment associated with L:

$$d^7: L = 3, S = 3/2$$

$$\mu = [4S(S + 1) + L(L + 1)]^{1/2}$$

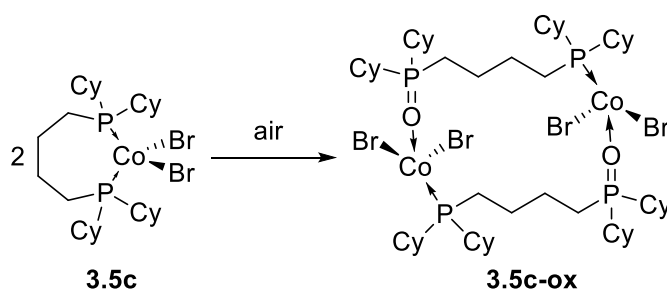
$$\mu = 5.20 \mu_{\text{B}}$$

In an attempt to confirm the values of μ_{eff} measured in the solid state, an attempt was made to determine the μ_{eff} of **3.4e** using the Evans' NMR spectroscopic method, whereby the μ_{eff} of the complex

can be calculated in the solution state. Details of this method and the associated calculation can be found in Chapter 6. However, the poor solubility of $(\text{dppb})\text{CoCl}_2$ (**3.4e**) and the other cobalt(II) diphosphine complexes prevented the determination of μ_{eff} *via* the Evans' NMR method, as the concentrations required to preserve the sample in solution were so low that the relative paramagnetic shift in CDCl_3 signal becomes less than the width of the standard signal.

3.3.6 Investigations into the Oxidation Products of $(\text{P}^{\wedge}\text{P})\text{CoX}_2$ Complexes

Cobalt(II) halides have been shown previously to catalyse the oxidation of phosphines, especially in solvents such as DCM or chloroform.⁹⁴ The resulting phosphorus oxide complexes formed are often observed in the solid state as dimeric structures with non-chelating phosphine oxide ligand bridges (example in **Scheme 3.17**).⁹⁴



Scheme 3.17 Representative example of the oxidation products from $(\text{P}^{\wedge}\text{P})\text{CoX}_2$ complexes. Shown in scheme: partial oxidation of $(\text{dcpb})\text{CoBr}_2$ (**3.5c**).

Throughout this work, there have been problems with solvent purity (water contamination) as obtained from the departmental Solvent Purification System (SPS), as a result, oxidation products have been occasionally observed, some of which have been discussed in previous sections.⁵ In this section, examples of additional oxidation products observed are noted. However, as these complexes were often only obtained as a small portion of the bulk samples produced herein and were not used in any further reactions, the structures of these oxidation products will not be discussed at any length.

The first attempt to synthesise $(\text{dcpb})\text{CoCl}_2$ (**3.5c**) resulted in the formation of a partial oxidation product $[\text{Br}_2\text{Co}(\mu_2\text{-dcpbO})_2\text{CoBr}_2]$ (**3.5c-ox**). Crystals suitable for single crystal X-ray diffraction were grown through layering of a solution of **3.5c-ox** in THF with hexanes. The molecular structure was determined to consist of partially oxidised dcpb ligands, *i.e.* dcpbO, which bridge two *pseudo*-tetrahedral cobalt(II) centres (formed as a result of oxygen contamination to a sample of $(\text{dcpb})\text{CoBr}_2$

⁵ Once this problem was identified, affected solvents (DCM, THF, Toluene) were freshly dried, distilled and degassed before use within the PWD Lab.

dissolved in THF) (**Figure 3.37**) presumably to avoid formation of a disfavoured eight-membered metallacycle (as would be the case if the ligand was chelating).

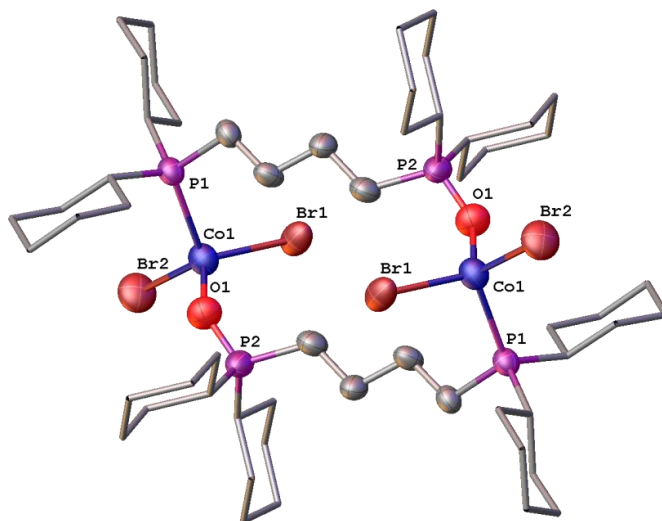


Figure 3.37 Solid state molecular structure of $[\text{Br}_2\text{Co}(\mu_2\text{-dcypbO})_2\text{CoBr}_2]$ (**3.5c-ox**), determined by single crystal X-ray diffraction. Hydrogen atoms and a solvate molecule of THF have been removed and cyclohexyl groups simplified for clarity. OTREPs set at 50%.

When a solution of $\text{BrCo}(\mu_2\text{-dppm})_2(\mu_2\text{-Br})_2\text{CoBr}$ (**3.4a**) was left to stand in air, crystals with the molecular structure $[(\text{dppmO}_2)_3\text{Co}][\text{CoBr}_4]$ (**3.4a-ox**) (shown in **Figure 3.38**) were observed to form. The structure of **3.4a-ox** consists of three oxidised dppm ligands (dppmO_2) that are bound in a bidentate fashion about a single cationic cobalt centre, giving rise to an overall octahedral coordination geometry; the complex is charge-balance by a tetrahedral $[\text{CoBr}_4]$ dianion. Here, it is proposed that a disproportionation reaction of the starting cobalt(II) complex **3.4a** takes place in DCM solution, possibly induced by oxidation of the phosphine moieties. This results in the formation of **3.4a-ox**. As a result of the oxidation of the dppm ligand, the oxidised dppm moiety can now chelate to a single metal centre since this oxidation removes the electronic/geometric constraints precluding mono-metal chelation, namely repulsion of the two phosphine lone-pairs (as is suggested to account for the bimetallic complex **3.4a**).

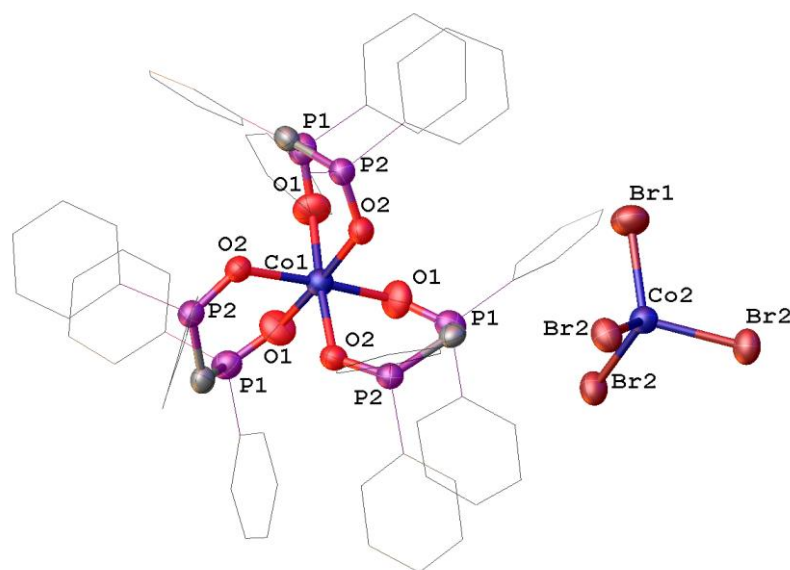


Figure 3.38 Molecular structure of the product resulting from initial oxidation of $[\text{BrCo}(\mu_2\text{-Br})_2(\mu_2\text{-dppm})_2\text{CoBr}]$ (**3.4a-ox**) followed by a subsequent disproportionation reaction. ORTEPs are set at 50% probability and two DCM solvate molecules and hydrogen atoms are omitted for clarity. Phenyl groups are reduced to wire-frame for clarity.

When a sample of $(\text{dtbpx})\text{CoCl}_2$ (**3.6a**) was prepared as a solution in THF (unexpectedly containing a water impurity) and layered with hexanes, crystals corresponding to the hydrolysis product of **3.6a** were formed *i.e.* $(\text{dtbpxO})\text{CoCl}\cdot\text{HCl}$ (**3.6aO·HCl**). The molecular structure of **3.6aO·HCl** obtained (**Figure 3.39**) is similar to that obtained of **3.7c·HCl** (Section 3.3.3).

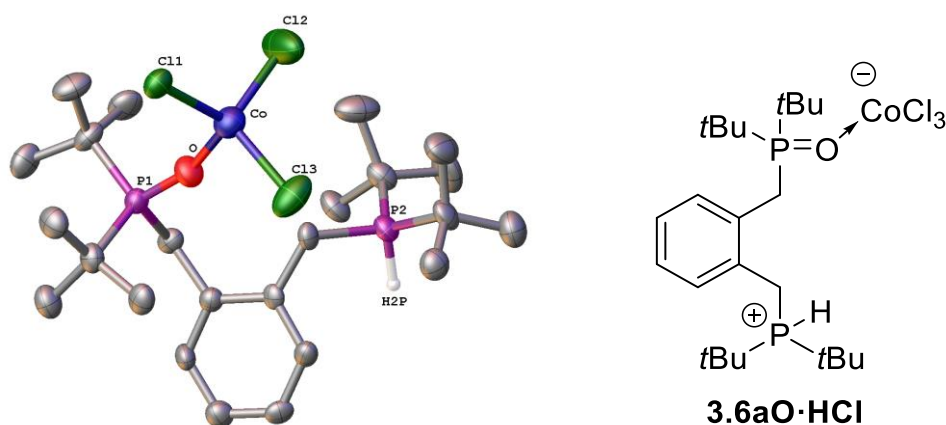
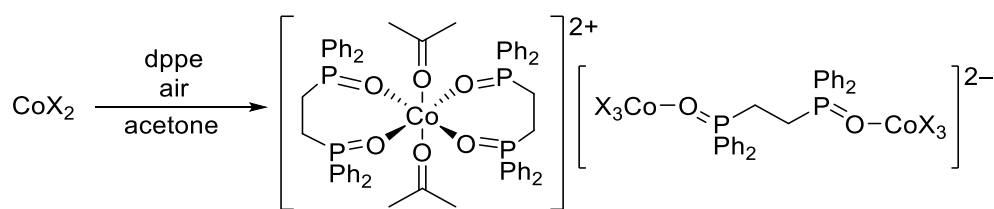


Figure 3.39 Molecular structure of **3.6aO·HCl**. ORTEPs are set at 50% probability and hydrogen atoms are omitted for clarity.

These partially or fully oxidised complexes obtained (namely **3.4a-ox**, **3.4c-ox**, **3.6aO·HCl** and **3.7c·HCl**) are similar to those previously reported example by Severin *et al.* who noted the oxidation of dppe on cobalt upon exposure of the sample of CoX_2/dppe to air (**Scheme 3.18**).⁸⁰ The complex observed by Severin contains fully oxidised dppe ligands (dppeO_2), which are present in both chelating (cation) and bridging (anion) coordination modes.⁸⁰



Scheme 3.18 Reported oxidation of dppe ligands in the presence of air and cobalt(II) dihalide halide where X = Cl, Br.⁸⁰

3.3.6.1 An Unexpected Oxidation Product: $(\text{COOH})_2\text{Co}(\text{OH}_2)_2$

To allow investigation into the complete oxidation/hydrolysis products of $(\text{P}^\wedge\text{P})\text{CoX}_2$ complexes, a selection of $(\text{P}^\wedge\text{P})\text{CoX}_2$ complexes ($(\text{PPh}_3)_2\text{CoCl}_2$ (**3.3a**), $(\text{dtbpx})\text{CoCl}_2$ (**3.6a**), and $(\text{PNNP-Ph})\text{CoCl}_2$ (**3.7a**)) were prepared as solutions in THF for recrystallisation in air. For the three complexes tested (**3.3a**, **3.6a** and **3.7a**), slow evaporation of THF led to the growth of red/brown crystals, which were identified by single crystal X-ray diffraction as the unexpected product, $[(\text{COOH})_2\text{Co}(\text{OH}_2)_2]$, **3.12** (**Figure 3.40**) in all cases.⁹⁵

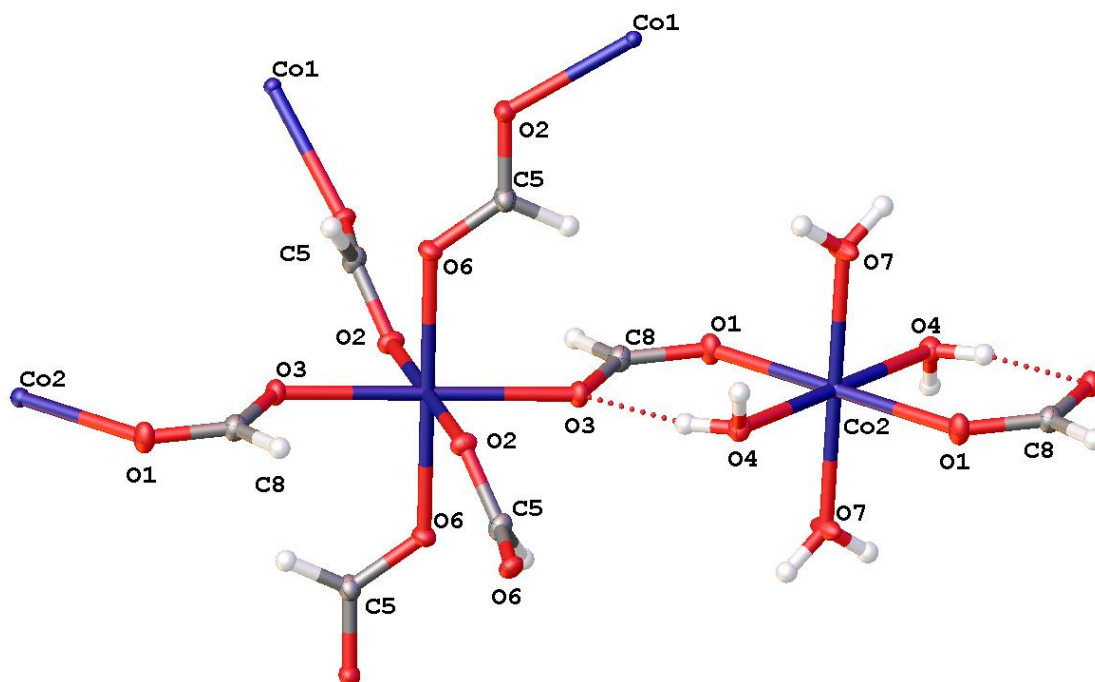


Figure 3.40 single crystal X-ray structure obtained of $[(\text{COOH})_2\text{Co}(\text{OH}_2)_2]$, **3.12**; ORTEPs set at 50% probability level.

Attempts were made to establish an unambiguous and intentional synthesis of **3.12**. To this end, CO_2 was bubbled through a sample of **3.6a** in dry, oxygen-free THF. No colour change was observed, which was deemed crudely to indicate that no reaction had taken place. This is consistent with the proposed operation of a redox process (thus requiring air/ O_2) and the necessity for the presence of water.

Consequently, this reaction was repeated using “hydrous” THF (*i.e.* not dried or degassed) to dissolve complex **3.7a**. After one week of standing in air, small crystals were observed to form. However, this material was identified as (PNNP-PhO₂CoCl₂ (**3.7a-ox**) as shown in **Figure 3.41**. It was therefore hypothesised that the cobalt complexes containing partially or fully oxidised diphosphine ligands could be an intermediate during the formation of **3.12**.

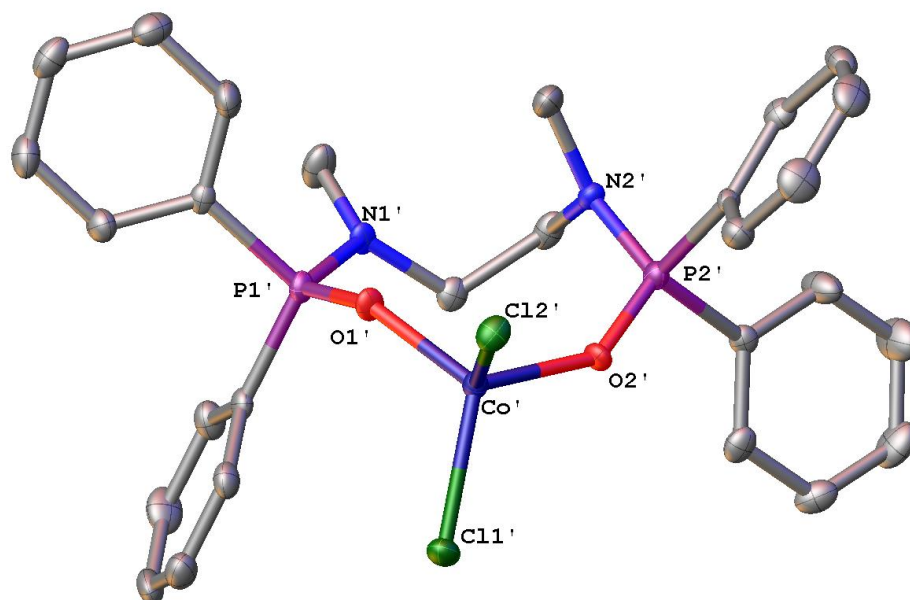
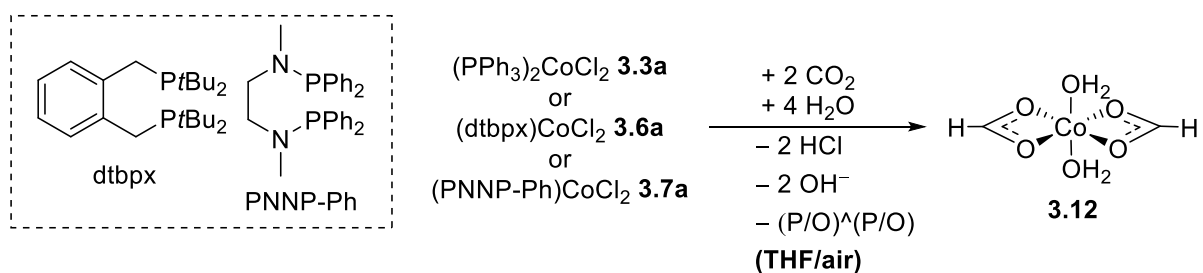


Figure 3.41 Molecular structure of [(PNNP-Ph)O₂]CoCl₂ (**3.7a-ox**), the oxidation product of [(PNNP-Ph)CoCl₂] (**3.7a**). ORTEPs set at 50% probability and hydrogen atoms and a second molecule in the unit cell (Z=2) are omitted for clarity.

It is postulated that the formation of (COOH)₂Co(OH)₂ (**3.12**) is the result of a cobalt-mediated redox process, which facilitates a proton-assisted multi-electron reduction of CO₂ (**Scheme 3.19**). To account for the formation of complex **3.12** it is tentatively proposed that the diphosphines act as redox non-innocent ligands becoming oxidised or partly oxidised on exposure to air. The resulting cobalt species then binds water. This resulting cobalt aqua complex is then intrinsically acidic and reacts with additional water generating a cobalt hydride species and hydroxide ($2 \text{H}_2\text{O} + 2\text{e}^- \rightarrow \text{H}_2 + 2 \text{OH}^-$) of the labile triphenylphosphine or *bis*(phosphine) ligands, in (PPh₃)₂CoCl₂ (**3.3a**), (dtbpx)CoCl₂ (**3.6a**), or PNNP-Ph)CoCl₂ (**3.7a**), with hydration of resulting cobalt(II) chloride species results in the reduction of two CO₂ moieties to formate alongside the generation of HCl as a by-product.



Scheme 3.19 Proposed, simplified pathway for the formation of $[(COOH)_2Co(OH_2)_2]$ (**3.12**) from $(P^A P)CoX_2$.

While the formation of $[(COOH)_2Co(OH_2)_2]$ (**3.12**) was interesting, the transformation typically took 2-3 weeks under ambient conditions (by crystal growth rates). In addition, this transformation likely takes place at the expense of phosphine/diphosphine moieties, and therefore was not investigated any further.

3.4 Summary and Outlook

In this chapter, a small series of (α -diimine)CoBr₂ complexes (**3.2a-e**) have been synthesised with a variety of substituents on the N-aryl group and with variation to the α -diimine ligand scaffold backbone. These (α -diimine)CoBr₂ complexes (**3.2a-e**) were structurally characterised through X-ray diffraction, their steric constraints assessed using the %V_{bur} approach, and their electronic properties investigated through analysis of their electronic and vibrational spectra. It was found that introduction of an acenaphthyl-backbone [BIAN] to diimine ligand caused a twisting of the N-aryl groups present, which disrupted π -conjugation between the N-aryl group and the diimine motif hence any electronic effects through introduction of substituents at the N-aryl group will likely be inductive only. The complex {BIE-*p*-NMe₂}CoBr₂ (**3.2b**) contains an ethyl backbone (BIE) and the N-aryl groups are orientated such that they line in plane of the P-Co-P metallacycle. Structural analysis and analysis of the vibrational spectra ($\nu_{C=N}$) suggests that the -NMe₂ substituent is in conjugation with the extended π -system of the diimine ligand. As such, substitution of the *para*-position in BIE-based systems could be envisioned to allow electronic control over the reactivity of (α -diimine)CoBr₂ complexes within olefin oligomerisation reactions. Substitution in the *para*-position of the N-aryl group in BIAN and BIE based systems and the twisting of N-aryl groups in BIAN-based ligand systems, such that they approach orthogonal arrangement when compared to the plane of the metallacycle, does not have a great influence on the overall steric bulk of the systems, as determined by the values of %V_{bur} determined.

As the steric properties are predicted to have a great influence on the selectivity of any potential (α -diimine)CoBr₂-mediated olefin oligomerisation reactions, the introduction of bulky *ortho*-substituents on the N-aryl group would be of interest in the future. For gaining electronic control over reactivity of (N[^]N)CoBr₂ in olefin oligomerisation reactions in the future, the use of [BIE] backbones is desirable to allow conjugation of the π -system between substituents and the diimine motif. The obvious next step for these prepared and characterised (α -diimine)CoBr₂ complexes would be to investigate their reactivity towards ethylene. However, the time scale of this thesis did not allow for these investigations to be undertaken and is something that will be studied in the future.

Additionally, a library of diphosphine cobalt(II) halides complexes (**3.3-3.10**) were synthesised and described in this chapter. In order to probe the electronic impact of the variously-substituted diphosphines used, the corresponding diphosphine diselenides (**3.11a-3.11k**) were prepared. Analysis of the measured $|^1J_{SeP}|$ coupling constants revealed that the phosphine moieties investigated span a wide range of σ -donor capabilities ($|^1J_{SeP}| = 757-635$ Hz). Investigation of the solid-state structures of the (P[^]P)CoX₂ complexes revealed the expected impact that the phosphine-substituent has upon steric congestion around the cobalt centre, as indicated through the range of values of %V_{bur} obtained (50.1–

57.8%). In addition, the presence of sterically demanding phosphine-substituents result in a deviation from idealised tetrahedral geometry of the (P[^]P)CoX₂ systems as indicated through measurement of the dihedral angle, θ , measured between the planes P1-Co-P2 and P1-C...C-P2 of the backbone (6.7–40.5°, Section 3.3.2.1), X-Co-X bond angles (101.25(1)° in **3.6b** to 119.45(2)° in **3.4d**) and values of the four-coordinate geometry index (τ_4 , 0.874 in **3.4c** to 0.937 in **3.5a**, Section 3.3.2.1).

An investigation into the vibrational energies of the Co-X bonds within complexes **3.3-3.10** by Raman spectroscopic analysis showed that variation of the diphosphine ligand has little effect on the Co-X bond vibration, despite the significant difference in the donor capacities measured for the diphosphine ligands. The electronic spectra obtained of *pseudo*-tetrahedral complexes **3.3-3.10** all show a characteristic band in the visible region containing three maxima corresponding to the expected ${}^4T_1({}^4P) \leftarrow {}^4A_2({}^4F)$ transition. These three maxima are attributed to a lifting of degeneracy within the *d* orbitals of these distorted four-coordinate complexes. A loose trend was observed that indicated that as the donor character of the diphosphine ligand is decreased, the bandwidth of the ${}^4T_1({}^4P) \leftarrow {}^4A_2({}^4F)$ transition increases. However, this trend is also affected by the steric contributions imposed on the four-coordinate cobalt by the diphosphine and halide ligands. A NIR-UV-Vis spectroscopic study of a small number of (P[^]P)CoX₂ complexes was undertaken in order to determine nephelauxetic series for these diphosphine cobalt(II) complexes (**3.4d**, **3.5a**, **3.6b**, **3.6f**). However, when the structural (XRD, including τ_4) and spectroscopic (and resulting nephelauxetic series) data are considered together, it is clear that the bonding within the *pseudo*-tetrahedral (P[^]P)CoX₂ complexes cannot be described simply in terms of σ -donation. Consequently, a computational study of the structure and bonding of the various (P[^]P)CoX₂ complexes is underway (by Dr M. A. Fox, Durham University) in order to investigate the structure and bonding characteristics of these complexes, in particular the factors that dictate significant distortions from C_{2v} symmetry and the potential implications this has for the reactivity of these cobalt(II) systems. Unfortunately, the results and final analysis of these computational data were not available at the time of writing of this thesis.

This library of prepared and characterised (P[^]P)CoX₂ complexes (**3.3-3.10**) where the diphosphine ligands are systematically varied are expected to exhibit a range of reactivity. Chapter 4 discusses investigations into the reduction and reactivity chemistry of complexes **3.3-3.10**.

3.5 References

- 1 G. Wilkinson and F. A. Cotton, *Advanced Inorganic Chemistry*, Wiley-Interscience, New York, 5th edn., 1988, p45-48.
- 2 W. Beck and K. Sünkel, *Chem. Rev.*, 1988, **88**, 1405–1421.
- 3 W.-J. Van Zeist, R. Visser and F. M. Bickelhaupt, *Chem. - A Eur. J.*, 2009, **15**, 6112–6115.
- 4 T. Korenaga, K. Abe, A. Ko, R. Maenishi and T. Sakai, *Organometallics*, 2010, **29**, 4025–4035.
- 5 P. C. J. Kamer and P. W. N. M. van Leeuwen, *Phosphorous(III) Ligands in Homogeneous Catalysis*, John Wiley & Sons, Chichester, 2012, p20-25.
- 6 P. C. J. Kamer, P. W. N. M. Van Leeuwen and J. N. H. Reek, *Acc. Chem. Res.*, 2001, **34**, 895–904.
- 7 J. F. Hartwig, *Inorg. Chem.*, 2007, **46**, 1936–1947.
- 8 C. P. Casey, G. T. Whiteker, M. G. Melville, L. M. Petrovich, J. A. Gavney and D. R. Powell, *J. Am. Chem. Soc.*, 1992, **114**, 5535–5543.
- 9 B. Dudle, K. Rajesh, O. Blacque and H. Berke, *J. Am. Chem. Soc.*, 2011, **133**, 8168–8178.
- 10 B. L. Small, R. Rios, E. R. Fernandez, D. L. Gerlach, J. A. Halfen and M. J. Carney, *Organometallics*, 2010, **29**, 6723–6731.
- 11 L. Deng, T. K. Woo, L. Cavallo, P. M. Margl and T. Ziegler, *J. Am. Chem. Soc.*, 1997, **119**, 6177–6186.
- 12 H. Van Der Poel, G. Van Koten and K. Vrieze, *Inorg. Chem.*, 1980, **19**, 1145–1151.
- 13 C. M. Killian, D. J. Tempel, L. K. Johnson and M. Brookhart, *J. Am. Chem. Soc.*, 1996, **118**, 11664–11665.
- 14 S. D. Ittel, L. K. Johnson and M. Brookhart, *Chem. Rev.*, 2000, **100**, 1169–1203.
- 15 L. K. Johnson, C. M. Killian and M. Brookhart, *J. Am. Chem. Soc.*, 1995, **117**, 6414–6415.
- 16 S. A. Svejda and M. Brookhart, *Organometallics*, 1999, **18**, 65–74.
- 17 L. Deng, P. Margl and T. Ziegler, *J. Am. Chem. Soc.*, 1997, **119**, 1094–1100.
- 18 T. K. Woo, P. M. Margl, P. E. Blochl and T. Ziegler, *J. Phys. Chem. B*, 1997, **101**, 7877–7880.
- 19 A. Michalak and T. Ziegler, *Organometallics*, 1999, **18**, 3998–4004.
- 20 D. G. Musaev, R. D. J. Froese and K. Morokuma, *Organometallics*, 1998, **17**, 1850–1860.
- 21 V. Rosa, S. A. Carabineiro, T. Avilés, P. T. Gomes, R. Welter, J. M. Campos and M. R. Ribeiro, *J. Organomet. Chem.*, 2008, **693**, 769–775.
- 22 H. Zhong, M. R. Friedfeld and P. J. Chirik, *Angew. Chemie - Int. Ed.*, 2019, **58**, 9194–9198.
- 23 M. R. Friedfeld, H. Zhong, R. T. Ruck, M. Shevlin and P. J. Chirik, *Science*, 2018, **360**, 888–893.
- 24 L. D. Field and A. J. Ward, *J. Organomet. Chem.*, 2003, **681**, 91–97.
- 25 C. Wang, W. J. Teo and S. Ge, *ACS Catal.*, 2017, **7**, 855–863.
- 26 F. Yu, X. C. Zhang, F. F. Wu, J. N. Zhou, W. Fang, J. Wu and A. S. C. Chan, *Org. Biomol. Chem.*, 2011, **9**, 5652–5654.

Chapter 3

- 27 S. M. Jing, V. Balasanthiran, V. Pagar, J. C. Gallucci and T. V. RajanBabu, *J. Am. Chem. Soc.*, 2017, **139**, 18034–18043.
- 28 G. Ricci, A. Sommazzi, F. Masi, M. Ricci, A. Boglia and G. Leone, *Coord. Chem. Rev.*, 2010, **254**, 661–676.
- 29 H. Y. Rhyoo, B. Y. Lee, H. K. Bae Yu and Y. K. Chung, *J. Mol. Catal.*, 1994, **92**, 41–49.
- 30 M. A. Carins and J. F. Nixon, *J. Organomet. Chem.*, 1974, **64**, C19–C21.
- 31 H. Kanai and K. Ishii, *Bull. Chem. Soc. Jpn.*, 1981, **54**, 1015–1018.
- 32 H. Kanai and M. Okada, *Chem. Lett. Chem. Soc. Jpn.*, 1975, 167–168.
- 33 K. Kawakami, T. Mizoroki and A. Ozaki, *Bull. Chem. Soc. Jpn.*, 1978, **51**, 21–24.
- 34 K. Kawakami, T. Mizoroki and A. Ozaki, *Chem. Lett. Chem. Soc. Jpn.*, 1975, 903–904.
- 35 H. Kanai, Y. Watabe and T. Nakayama, *Bull. Chem. Soc. Jpn.*, 1986, **59**, 1277–1278.
- 36 I. Knopf, M. A. Courtemanche and C. C. Cummins, *Organometallics*, 2017, **36**, 4834–4843.
- 37 K. Kawakami, T. Mizoroki and A. Ozaki, *J. Mol. Catal.*, 1979, **5**, 175–187.
- 38 W. Keim and G. N. Schnauzer, *Transition Metals in Homogeneous Catalysis*, Marcel Dekker Inc., New York, 1971, p59.
- 39 I. Knopf, M. A. Courtemanche and C. C. Cummins, *Organometallics*, 2017, **36**, 4834–4843.
- 40 H. Zhong, M. R. Friedfeld, J. Camacho-Bunquin, H. Sohn, C. Yang, M. Delferro and P. J. Chirik, *Organometallics*, 2019, **38**, 149–156.
- 41 G. R. Morello, H. Zhong, P. J. Chirik and K. H. Hopmann, *Chem. Sci.*, 2018, **9**, 4977–4982.
- 42 J. V. Obligacion and P. J. Chirik, *Nat. Rev. Chem.*, 2018, **2**, 15–34.
- 43 J. M. Neely, M. J. Bezdek and P. J. Chirik, *ACS Cent. Sci.*, 2016, **2**, 935–942.
- 44 K. Duvvuri, K. R. Dewese, M. M. Parsutkar, S. M. Jing, M. M. Mehta, J. C. Gallucci and T. V. Rajanbabu, *J. Am. Chem. Soc.*, 2019, **141**, 7365–7375.
- 45 G. J. P. Britovsek and D. S. McGuinness, *Chem. - A Eur. J.*, 2016, **22**, 16891–16896.
- 46 J. D. Nobbs, A. K. Tomov, C. T. Young, A. J. P. White and G. J. P. Britovsek, *Catal. Sci. Technol.*, 2018, **8**, 1314–1321.
- 47 A. G. Orpen and N. G. Connelly, *J. Chem. Soc. Chem. Commun.*, 1985, 1310–1311.
- 48 N. Fey, A. C. Tsipis, S. E. Harris, J. N. Harvey, A. G. Orpen and R. A. Mansson, *Chem. - A Eur. J.*, 2005, **12**, 291–302.
- 49 T. Leyssens, D. Peeters, A. G. Orpen and J. N. Harvey, *New J. Chem.*, 2005, **29**, 1424–1430.
- 50 N. F. Curtis, *Coord. Chem. Rev.*, 1969, **3**, 3–47.
- 51 M. Tanabiki, Y. Sunada and H. Nagashima, *Organometallics*, 2007, **26**, 6055–6058.
- 52 M. N. Alnajrani, S. A. Alshimri and O. A. Alsager, *RSC Adv.*, 2016, **6**, 113803–113814.
- 53 E. K. Cope-Eatough, F. S. Mair, R. G. Pritchard, J. E. Warren and R. J. Woods, *Polyhedron*, 2003, **22**, 1447–1454.

- 54 L. Falivene, Z. Cao, A. Petta, L. Serra, A. Poater, R. Oliva, V. Scarano and L. Cavallo, *Nat. Chem.*, 2019, **11**, 872–879.
- 55 W. J. Evans, J. C. Brady and J. W. Ziller, *Inorg. Chem.*, 2002, **41**, 3340–3346.
- 56 C. A. Tolman, *Coord. Chem. Rev.*, 1977, **77**, 313–348.
- 57 K. Hasan and E. Zysman-Colman, *J. Phys. Org. Chem.*, 2013, **26**, 274–279.
- 58 E. P. Clark, *Ind. Eng. Chem. Anal. Ed.*, 1941, 820–820.
- 59 L. Yang, D. R. Powell and R. P. Houser, *J. Chem. Soc. Dalton Trans.*, 2007, 955–964.
- 60 Cambridge Structural Database, <http://webo.csd.ccdc.cam.ac.uk/index.php>, Nov 2019.
- 61 K. Hasan and E. Zysman-Colman, *Eur. J. Inorg. Chem.*, 2013, **6**, 4421–4429.
- 62 M. L. Laury, M. J. Carlson and A. K. Wilson, *J. Comput. Chem.*, 2012, **33**, 2380–2387.
- 63 C. Hansch, S. D. Rockwell, P. Y. C. Jow, A. Leo and E. E. Steller, *J. Med. Chem.*, 1977, **20**, 304–306.
- 64 C. J. Adams, N. Fey, Z. A. Harrison, I. V. Sazanovich, M. Towrie and J. A. Weinstein, *Inorg. Chem.*, 2008, **47**, 8242–8257.
- 65 V. Rosa, C. I. M. Santos, R. Welter, G. Aullón, C. Lodeiro and T. Avilés, *Inorg. Chem.*, 2010, **49**, 8699–8708.
- 66 A. Paulovicova, U. El-Ayaan, K. Shibayama, T. Morita and Y. Fukuda, *Eur. J. Inorg. Chem.*, 2001, 2641–2646.
- 67 V. Rosa, T. Avilés, G. Aullon, B. Covelo and C. Lodeiro, *Inorg. Chem.*, 2008, **47**, 7734–7744.
- 68 G. M. Clore and J. Iwahara, *Chem. Rev.*, 2009, **109**, 4108–4139.
- 69 K. Murugesan, Z. Wei, V. G. Chandrashekhar, H. Neumann, A. Spannenberg, H. Jiao, M. Beller and R. V. Jagadeesh, *Nat. Commun.*, 2019, **10**, 5443.
- 70 P. W. Dyer, J. Fawcett, M. J. Hanton, R. D. W. Kemmitt, R. Padda and N. Singh, *Dalton Trans.*, 2003, 104–113.
- 71 T. Fanjul, G. Eastham, N. Fey, A. Hamilton, A. G. Orpen, P. G. Pringle and M. Waugh, *Organometallics*, 2010, **29**, 2292–2305.
- 72 R. L. Carlin, R. D. Chirico, E. Sinn, G. Mennenga and L. J. de Jongh, *Inorg. Chem.*, 1982, **21**, 2218–2222.
- 73 A. K. Mondal, M. Sundararajan and S. Konar, *Dalton Trans.*, 2018, **47**, 3745–3754.
- 74 M. D. Brown, W. Levason, G. Reid and R. Watts, *Polyhedron*, 2005, **24**, 75–87.
- 75 M. M. P. Grutters, J. I. Van Der Vlugt, Y. Pei, A. M. Mills, M. Lutz, A. L. Spek, C. Müller, C. Moberg and D. Vogt, *Adv. Synth. Catal.*, 2009, **351**, 2199–2208.
- 76 K. Heinze, G. Huttner, L. Zsolnai and P. Schober, *Inorg. Chem.*, 1997, **36**, 5457–5469.
- 77 G. Pacchioni and P. S. Bagus, *Inorg. Chem.*, 1992, **31**, 4391–4398.
- 78 M. P. Mitoraj and A. Michalak, *Inorg. Chem.*, 2010, **49**, 578–582.
- 79 D. J. Eliot, D. G. Holah, A. N. Hughes, V. R. Magnuson, I. M. Moser and R. J. Puddephatt, *Bull. Chem. Soc. Fr.*, 1992, **129**, 676–679.

Chapter 3

- 80 G. Kiefer, H. Vrubel, R. Scopelliti and K. Severin, *Eur. J. Inorg. Chem.*, 2013, 4916–4921.
- 81 D. A. Thornton, *J. Coord. Chem.*, 1991, **24**, 261–289.
- 82 A. B. P. Lever, *Inorganic Electronic Spectroscopy*, Elsevier Publishing Company, Amsterdam, 1968, p322-333.
- 83 J. E. Huheey, *Inorganic Chemistry: Principles of Structure and Reactivity*, Harper and Row Publishers Inc., New York, 3rd edn., 1983, p23-33.
- 84 B. N. Figgis and M. A. Hitchman, *Ligand Field Theory and its Applications*, Wiley-VCH, New York, 2000, p32-45.
- 85 U. C. Davis, Accessed Oct 2019, *ChemistryLibreTexts*, https://chem.libretexts.org/Bookshelves/Physical_a.
- 86 A. B. P. Lever and S. M. Nelson, *J. Chem. Soc. A Inorganic, Phys. Theor.*, 1966, 859–863.
- 87 R. J. Lancashire, <http://wwwchem.uwimona.edu.jm/courses/Tanabe-Sugano/TShelp.html>, 2019, Tanabe-Sugano diagrams via JAVA Applets.
- 88 F. A. Cotton, D. M. L. Goodgame and M. Goodgame, *J. Am. Chem. Soc.*, 1961, **83**, 4690–4699.
- 89 F. A. Cotton and M. Goodgame, *J. Am. Chem. Soc.*, 1961, **83**, 1777–1780.
- 90 P. Atkins, T. Overton, J. Rourke, M. Weller and F. Armstrong, *Shriver and Atkins: Inorganic Chemistry*, Oxford University Press, Oxford, 5th edn., 2009, p138.
- 91 A. L. Tchougreeff and R. Dronskowski, *Int. J. Quantum Chem.*, 2009, **109**, 2606–2621.
- 92 D. A. Safin, P. Mlynarz, F. D. Sokolov, M. Kubiak, F. Ekkehardt Hahn, M. G. Babashkina, N. G. Zabiroy, J. Galezowska and H. Kozlowski, *J. Inorg. Gen. Chem.*, 2007, **633**, 2089–2096.
- 93 M. D. Spicer, *Univ. Southampton, StudyLib.*, <<http://studylib.net/doc/5874303/magnetism>>, Acces.
- 94 V. V. Grushin, *Chem. Rev.*, 2004, **104**, 1629–1662.
- 95 A. Kaufman, C. Afshar, M. Rossi, D. E. Zacharias and J. P. Glusker, *Struct. Chem.*, 1993, **4**, 191–198.

CHAPTER 4

– The Role of Zn in the Reduction
Chemistry of Diphosphine Cobalt(II)
Halide Complexes

“I have not failed. I have successfully discovered 10,000 things that will not work.”

– Thomas Edison

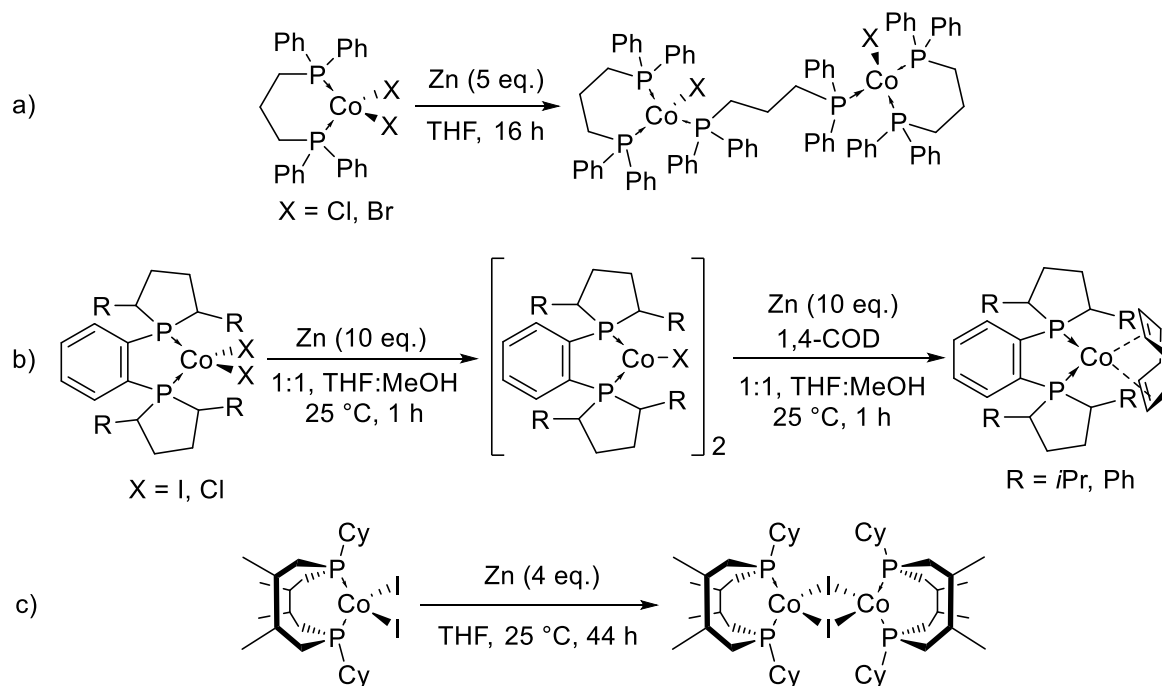
4.1 Introduction

Homogeneous cobalt-based catalysis is dominated by the successful formation of relatively stable cobalt(I) pre-catalysts.¹ As discussed in Chapter 3, there is precedent in the literature for the successful single-electron reduction of (P[^]P)CoX₂ systems through treatment with Zn metal to form new complexes with general, empirical formula “(P[^]P)CoX”. Several examples of the resulting “(P[^]P)CoX” systems that have been isolated, characterised and reported within literature were discussed in Chapter 3. However, it is much more common in the literature for the zinc reduction of (P[^]P)CoX₂ complexes to be performed *in situ* during catalysis. As a result, the identity/nature of the resulting cobalt-containing species is often unknown. Consequently, this chapter discusses the relationship between diphosphine ligand and effects upon the observed reactivity and reduction chemistry of corresponding (P[^]P)CoX₂ complexes (**3.3-3.10**) towards zinc metal. The findings of the investigations herein are then discussed in terms of the wider ramifications for generation of cobalt(I) species *in situ* for catalytic reactions based on reduced (P[^]P)CoX₂ precursors. In particular, the role of the inherently generated ZnX₂ species within (P[^]P)CoX₂ based systems are investigated. Selected reported examples of catalytic transformations whereby a Zn reduction of (P[^]P)CoX₂ *in situ* or *ex situ* are used to generate the catalytic pro-catalyst “(P[^]P)CoX” species are included in a brief literature overview.

4.1.1 Previously Reported Reduction of (P[^]P)CoX₂ Complexes with Zn where Resulting “(P[^]P)CoX” species have been Isolated

As discussed in Chapter 3, there are a few examples in the literature in which diphosphine cobalt(I) complexes have been prepared and isolated *ex situ* (**Scheme 4.1**). For example, in 2017, Rajanabu and co-workers reported the solid state structure of a diphosphine cobalt(I) complex that was used for the enantioselective hetero-dimerisation reaction of acrylates with 1,3-dienes (**Scheme 4.1a**).² In addition to this study by Rajanbabu, Chirik’s group have recently published their work on the synthesis of diphosphine cobalt(I) complexes.^{3-6*} In this work Chirik *et al.* reported the one-electron reduction of a number of different cobalt(II) precursors to produce complexes with empirical formula “(P[^]P)Co^IX” (**Scheme 4.1b**). Similarly, Cummins and co-workers have reported the single-electron reduction of a macrocyclic diphosphine-containing cobalt(II) complex through treatment with an excess of zinc metal (**Scheme 4.1c**).⁷

* Note, this work by Chirik was published while the studies described in this thesis were on-going.

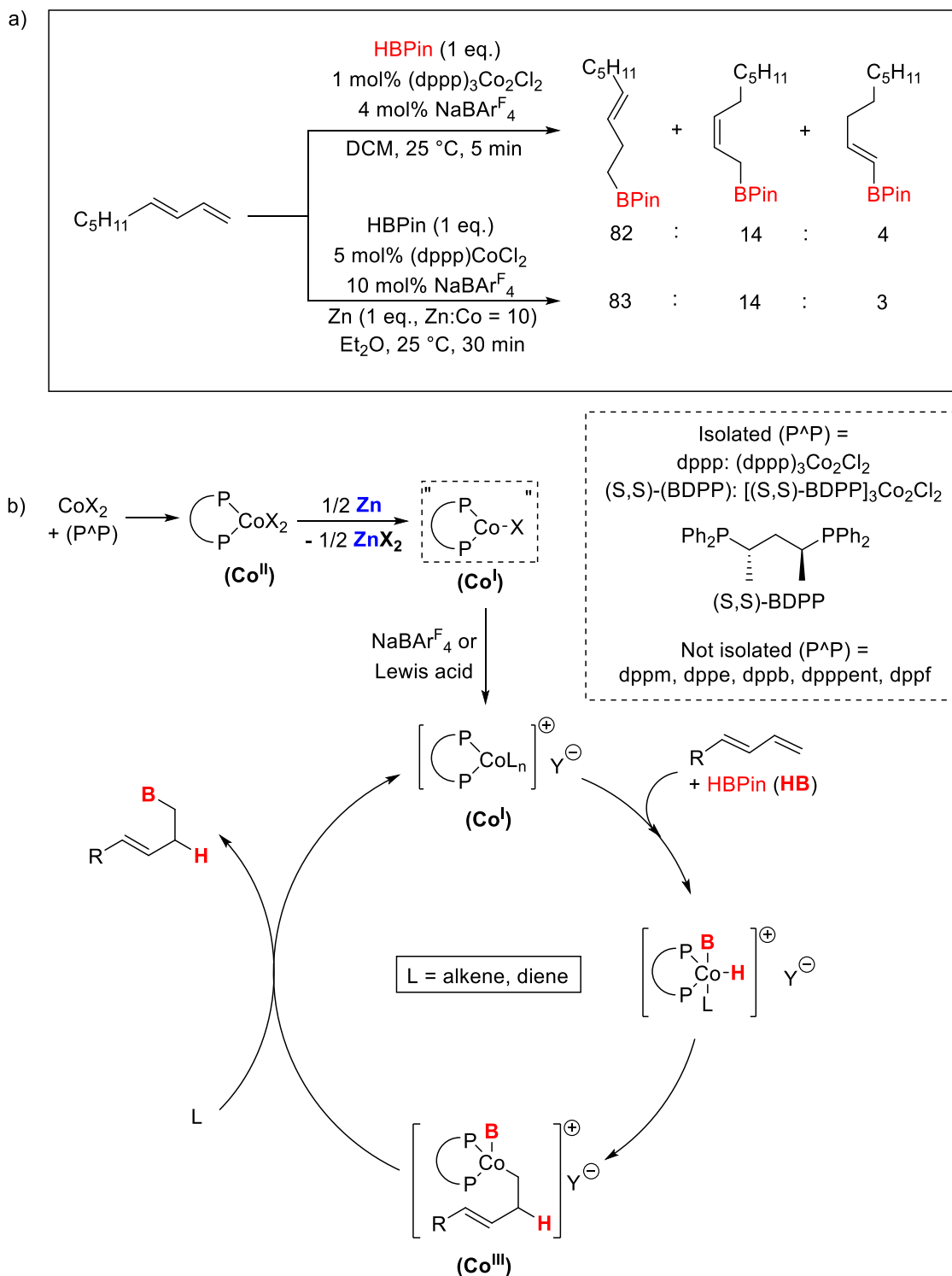


Scheme 4.1 Reported syntheses and structures of “(P^ΛP)Co^IX” complexes through treatment with Zn dust.^{2,3,7}

The above studies demonstrate the apparent relative ease with which diphosphine cobalt(II) complexes can undergo chemical reduction to “L_nCo^IX” through reaction with excess zinc metal.^{2,3,7,8} However, these studies (summarised in **Scheme 4.1**) are somewhat unusual since the cobalt(II) complexes have been both isolated and characterised. However, it is noteworthy that as discussed in Chapter 3, these “pre-reduced” systems have a tendency to demonstrate lower catalytic activity when compared to the same systems prepared by reduction and used *in situ* during catalysis. An exception to this comes from the work of Rajanbabu.⁹

Rajanbabu *et al.* recently published a report on cobalt(I)-catalysed regio- and stereo-selective hydroboration of 1,3-dienes. Notably, the isolated cobalt(I) species [(dppp)₃Co₂Cl₂] (structure shown in **Scheme 4.1a**) and *in situ* generation of a cobalt(I) pro-initiator for hydroboration of 1,3-diene with HBPIn in the presence of NaBAR^F₄ gave the same product mixture. However, Rajanbabu and co-workers noted that the cobalt(I) species that had been prepared and isolated gave much faster reaction times (complete conversion in 5 minutes) when compared to the cobalt(I) species prepared by reduction *in situ* (complete conversion in 30 minutes). However, the reaction conditions used are not identical (*c.f.* Co:NaBAR^F₄ ratio and solvents used in **Scheme 4.2a**). In particular, the use of an ethereal solvent for the *in situ* preparation of cobalt(I) may result in slower reaction times through coordination of the solvent to vacant sites on cobalt; inhibiting the reaction. Additionally, the solubility of the active cobalt(I) catalyst and NaBAR^F₄ activator will be affected by changing the solvent used.

Unfortunately, the authors did not perform experiments that would allow direct comparison of the isolated cobalt(I) species and cobalt(I) prepared *in situ* in the presence of an excess of Zn metal.⁹



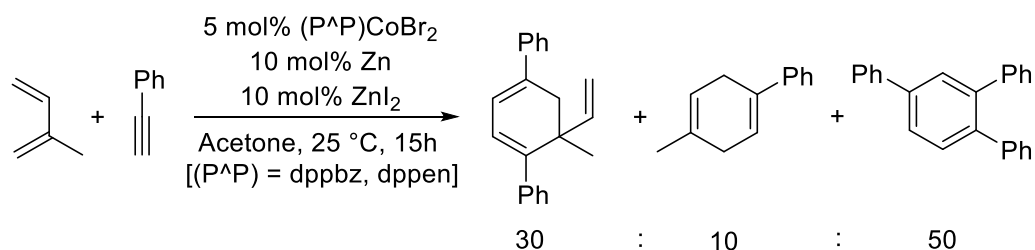
Scheme 4.2 a) Reported hydroboration of 1,3-dienes with HBPIn using *ex situ* reduced (P^AP)CoX₂ and “*in situ*” approach. b) Proposed reaction mechanism for cobalt(I) mediated hydroboration.⁹

Rajanbabu and co-workers proposed a straightforward mechanism for the hydroboration of 1,3-dienes, which is shown in **Scheme 4.2b**.⁹ Pre-reduction of (P[^]P)CoX₂ is proposed to generate a cobalt(I) complex, which can then undergo halide abstraction by NaBAR^F₄ to form a catalytically active, cationic cobalt(I) species. Complete conversion to the hydroborated product was observed after 30 minutes in the presence of both Zn and NaBAR^F₄ when using (dppp)CoCl₂ as pre-catalyst.⁹ Of note, the authors report that no conversion to the hydroborated products was observed in the absence of an activator (*e.g.* NaBAR^F₄). However, a slow reaction was observed in the absence of Zn (when *in situ* preparation of cobalt(I) was applied; 88% conversion after 30 minutes), suggesting that HBPin itself may be sufficient to perform the reduction forming the active cationic catalyst species.⁹

4.1.2 Reported Reduction of (P[^]P)CoX₂ Complexes with Zn *in situ*

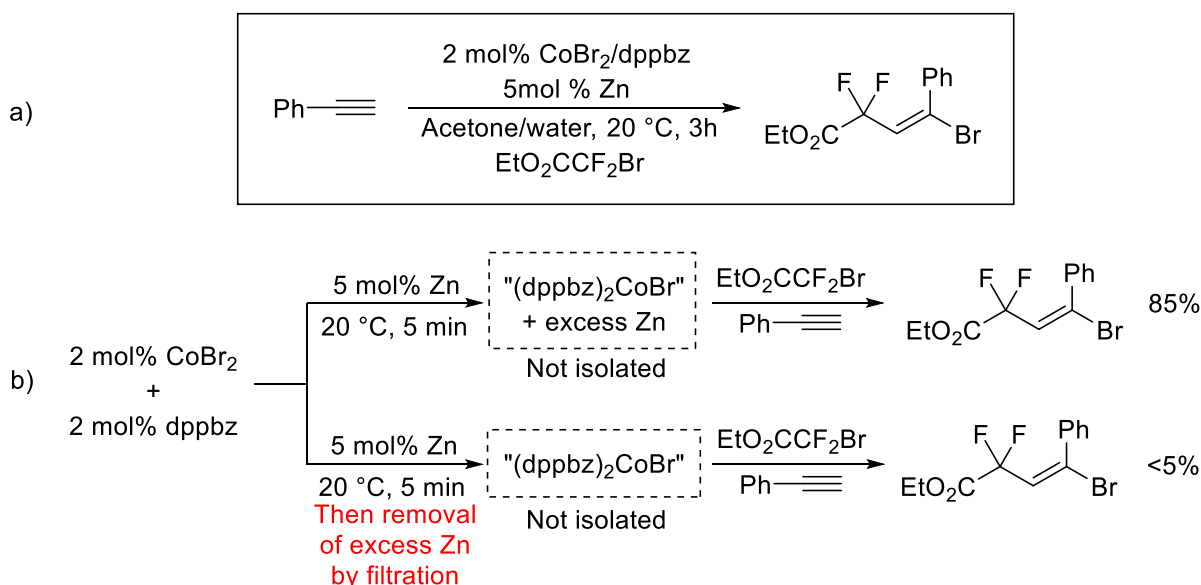
The vast majority of “(P[^]P)CoX”-mediated transformations that have been reported in the literature use Zn metal *in situ* to reduce (P[^]P)CoX₂ species to produce the necessary “(P[^]P)CoX” species. Several reports of the requirement for an excess of zinc (relative to cobalt) to achieve high conversions and activities within cobalt-based catalytic transformations have been published recently, although few reports have investigated the precise role of zinc in these reactions. The following brief literature review aims to highlight the extensive use of pre-catalyst (P[^]P)CoX₂ systems employed with *in situ* generation of cobalt(I) to mediate the catalytic transformations, despite limited knowledge in the literature on the role of zinc within these transformations.

In 2008, Harms and co-workers reported the use of (P[^]P)CoX₂ complexes in the presence of an excess of Zn and the Lewis acid ZnI₂ for use in [2+2+2] cycloadditions (**Scheme 4.3**).¹⁰ Harms *et al.* found that the solvent used for the reaction had a significant impact upon the selectivity of the transformation, with acetone giving rise to a system with the greatest selectivity (30%) to the target 1,3-cyclohexadiene derivative. Indeed, polar solvents were found to be favoured generally, something likely to result from increasing the solubility of the pre-catalyst (P[^]P)CoBr₂.¹⁰ Unfortunately, there were no mechanistic studies or attempts to isolate catalytic species performed by the authors here.



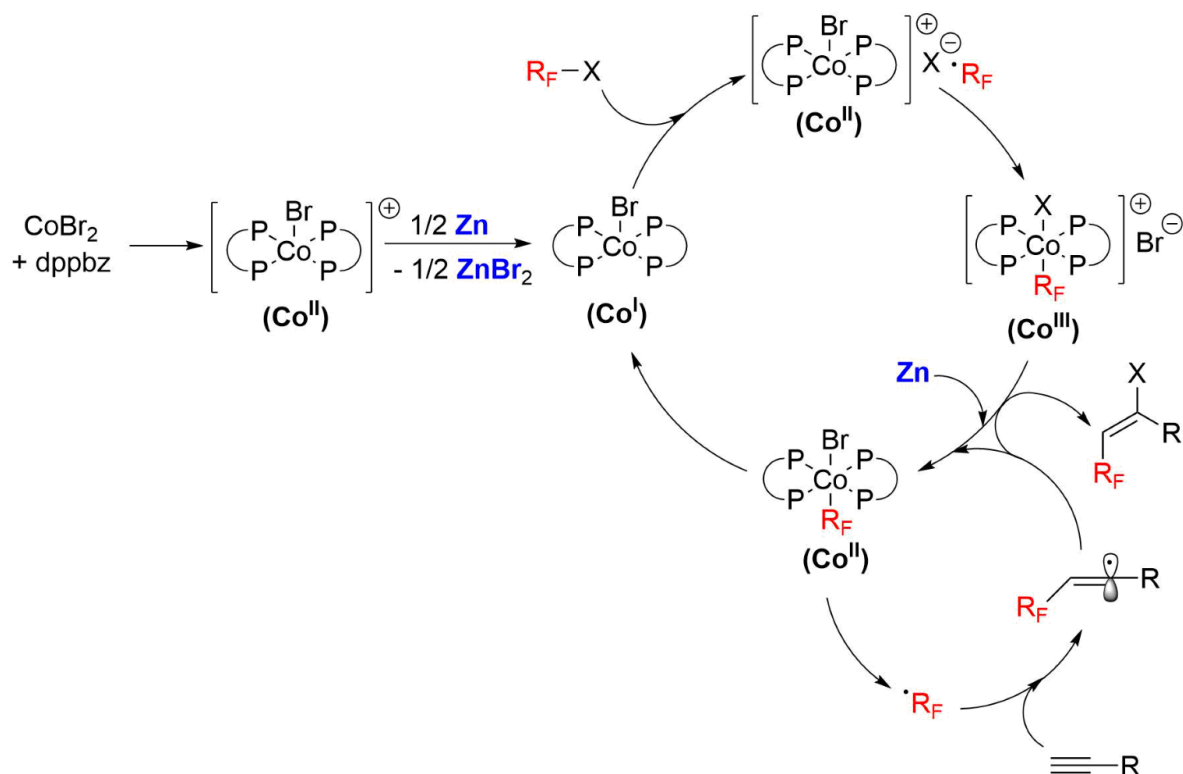
Scheme 4.3 Reported *in situ* generation of cobalt(I) for [2+2+2] cycloaddition catalysed by (P[^]P)CoBr₂/Zn/ZnI₂.¹⁰

In 2018, Wu and von Wangelin reported the selective hydrofluorination of alkynes mediated by *in situ*-generated cobalt(I) species *via* reduction of a cobalt(II) pre-catalyst with an excess of zinc metal (Zn:Co = 2.5: **Scheme 4.4a**).¹¹ Of note, the authors report that to obtain good conversion to the hydrofluorinated product, there must remain an excess of zinc metal within the reaction mixture, *i.e.* filtration to remove excess Zn before substrate addition dramatically reduced conversion (**Scheme 4.4b**).¹¹



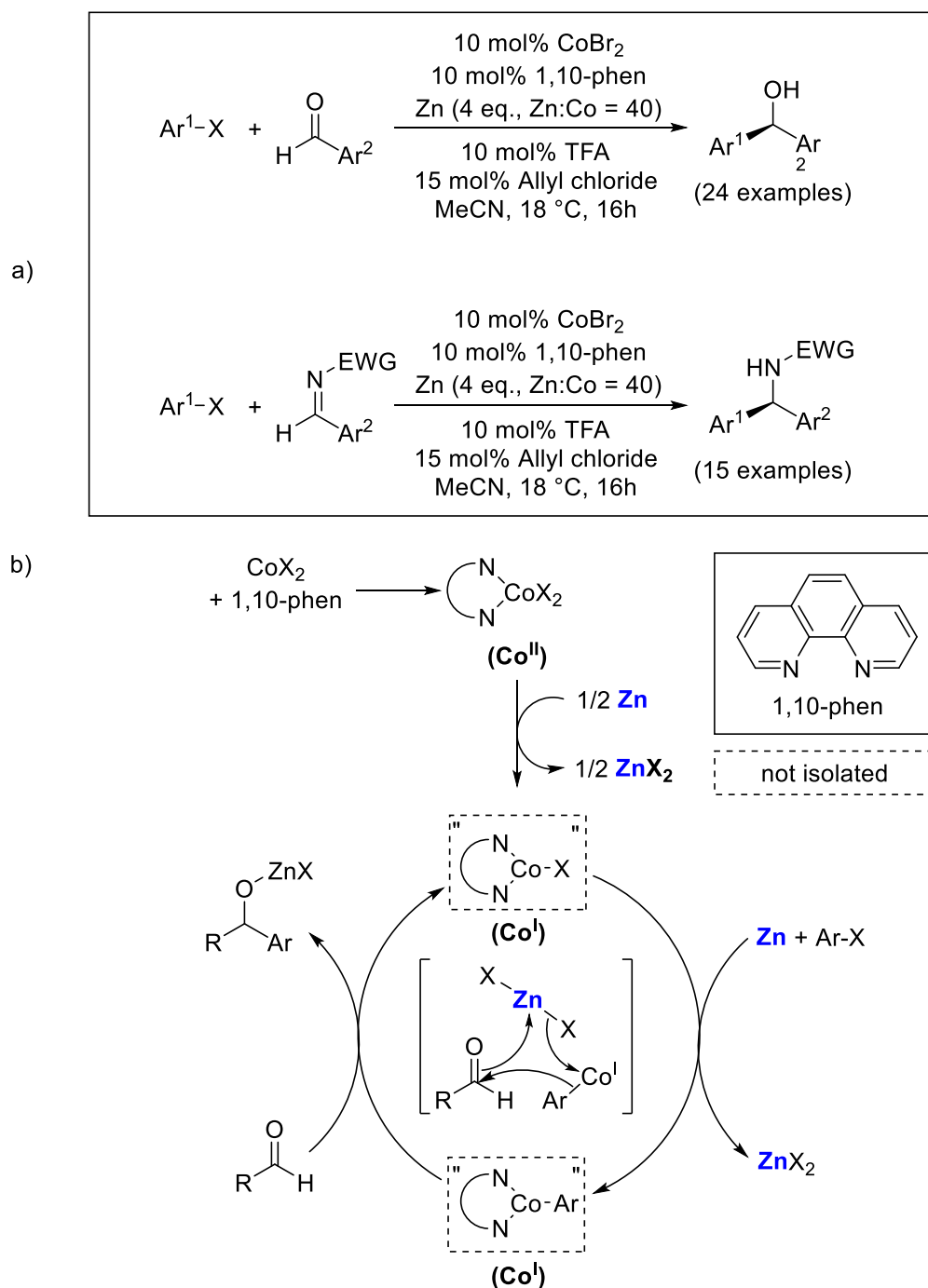
Scheme 4.4 a) Reported hydrofluorination of alkynes through application of a dppbz/CoBr₂/Zn system. b) Hydrofluorination conversions with and without the presence of excess Zn.¹¹

The authors attribute the necessity for the excess zinc within the reaction (**Scheme 4.4**) to allow for a second reduction of a proposed intermediate cobalt(III) species, which is generated upon addition to the Co^{II} species of an R_F radical species generated by reductive single electron activation of R_F-X (*e.g.* Et₂OCCF₂Br), as shown in **Scheme 4.5**.¹¹ This intermediate cobalt(III) species was proposed to take part in an atom transfer radical addition to produce the desired hydrofluorinated product. The mechanism proposed by the authors is complex, but does recognise the catalytic role of zinc within cobalt-based catalytic transformations. It should also be noted here that the reduction of (P[^]P)CoX₂ complexes with Zn metal will produce ZnBr₂ as a by-product, which will be present within the reaction mixture.¹¹



Scheme 4.5 Proposed reaction mechanism for the hydrofluorination of alkynes through application of a dppbz/ CoBr_2/Zn system.¹¹

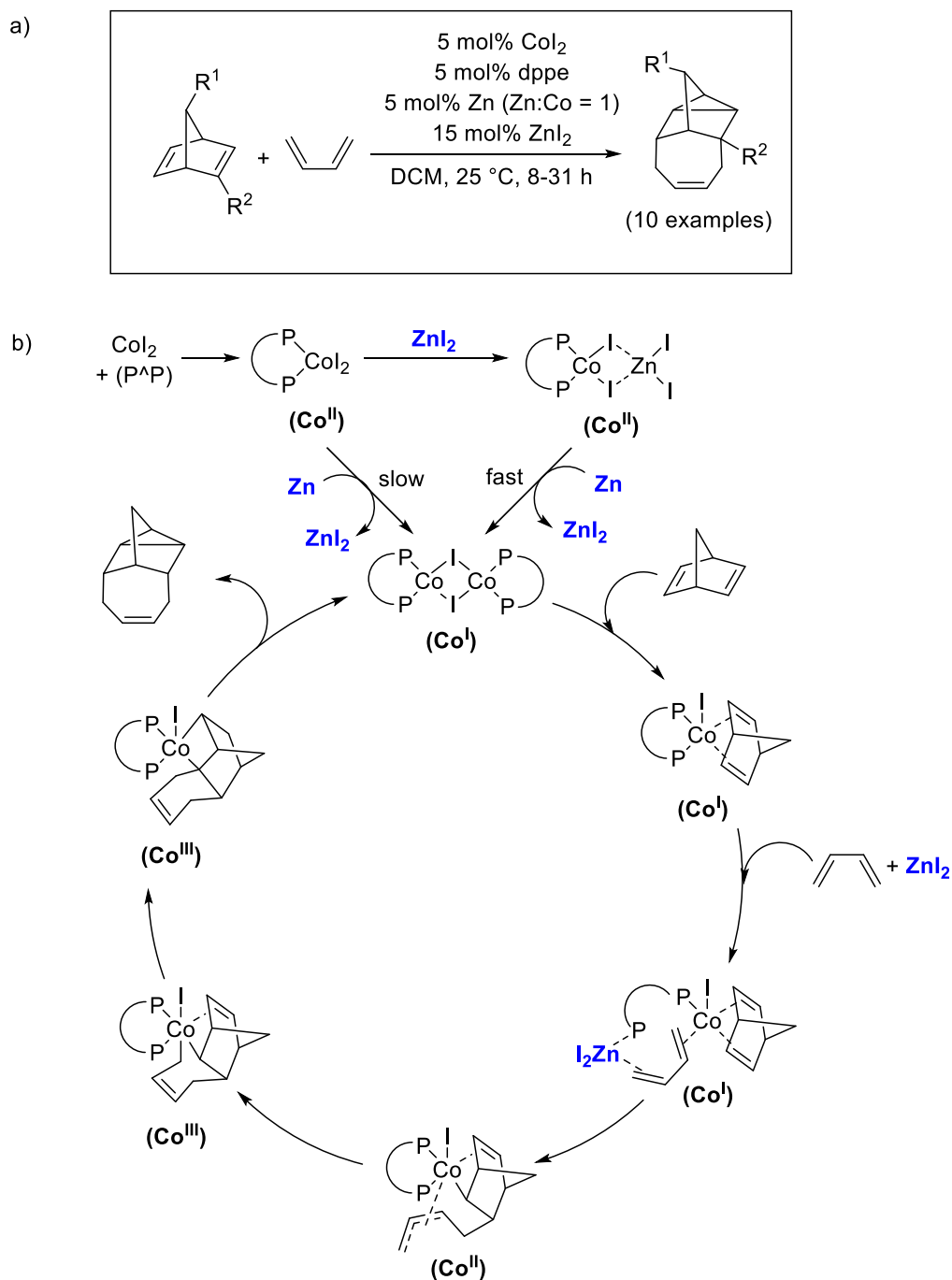
The production of ZnX_2 generated *in situ* as a by-product of the reduction of pre-catalyst species $(\text{P}^{\wedge}\text{P})\text{CoX}_2$ for cobalt(I)-mediated catalysis has been explored and utilised within Barbier reactions of aromatic halides and aromatic aldehydes and imines.¹² Le Gall and co-workers reported the catalytic formation of organo-zinc species mediated by a low valent cobalt(I) system (**Scheme 4.6a**).¹² Here, Le Gall *et al.* use a high Zn:Co ratio of 40:1. This large excess of zinc is proposed to be required in order to reduce the cobalt(II) pre-catalyst to the active cobalt(I) species envisaged to be “ $[(\text{N}^{\wedge}\text{N})\text{Co}^{\text{I}}\text{X}]$ ”, which can then undergo reaction with additional Zn and Ar-X to produce ZnX_2 and the metal aryl species “ $[(\text{N}^{\wedge}\text{N})\text{Co}^{\text{I}}\text{-Ar}]$ ”. This latter cobalt(I) species can then, in turn, react with aldehyde or imine substrate along with the generated ZnX_2 *via* a six-membered transition state to produce the desired organo-zinc product. While the presence of Zn within the report by Le Gall *et al.* is not catalytic, it does highlight the potential reactivity between low-valent cobalt species and ZnX_2 .¹²



Scheme 4.6 a) Reported Barbier reactions between aromatic halides and aromatic aldehydes and imines catalysed by $\text{CoBr}_2/1,10\text{-phen}/\text{Zn}$. b) Proposed reaction mechanism.¹²

Snyder and Ma also report the importance of ZnX_2 ($\text{X}=\text{I}$) in the [4+2+2] cycloaddition reaction of functionalised norbornenes with 1,4-butadiene (**Scheme 4.7a**).¹³ The authors found that this [4+2+2] cycloaddition could be catalysed by *in situ* generation of cobalt(I) through employing $\text{CoBr}_2/\text{dppe}/\text{Zn}/\text{ZnI}_2$ (1:1:1:3). Of note, the presence of a Lewis acid (ZnI_2) was found to be necessary for the success of the transformation, along with the presence of a reducing agent to produce the

presumed “(dppe)CoI” dimeric cobalt(I) catalyst.¹³ Snyder and Ma proposed that the addition of ZnI₂ to the reaction mixture allows for increasing the efficiency of reduction of cobalt(II) precursor through formation of a bimetallic Co/Zn species; weakening the Co-I bonds and making the pre-catalyst more susceptible to reduction. In addition, the presence of ZnI₂ was suggested to promote dissociation of a phosphine moiety to create a vacant site and allow 1,3-butadiene coordination to the cobalt centre. From this ZnI₂-stabilised cobalt(I) species, metallacyclisation can occur, followed by olefin insertion and reductive elimination to produce the [4+2+2] cycloadduct product (**Scheme 4.7b**).¹³

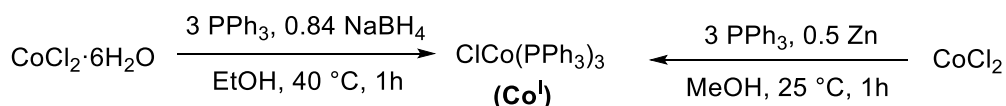


Scheme 4.7 a) Reported [4+2+2] cycloaddition of functionalised norbornenes and 1,4-butadiene. b) Proposed reaction mechanism for [4+2+2] cycloaddition of nobornadienes mediated by ZnI₂ and cobalt(I).¹³

4.1.3 Reported Reduction of (P[^]P)CoX₂ Complexes *in* or *ex situ*: Non-Zn reductants

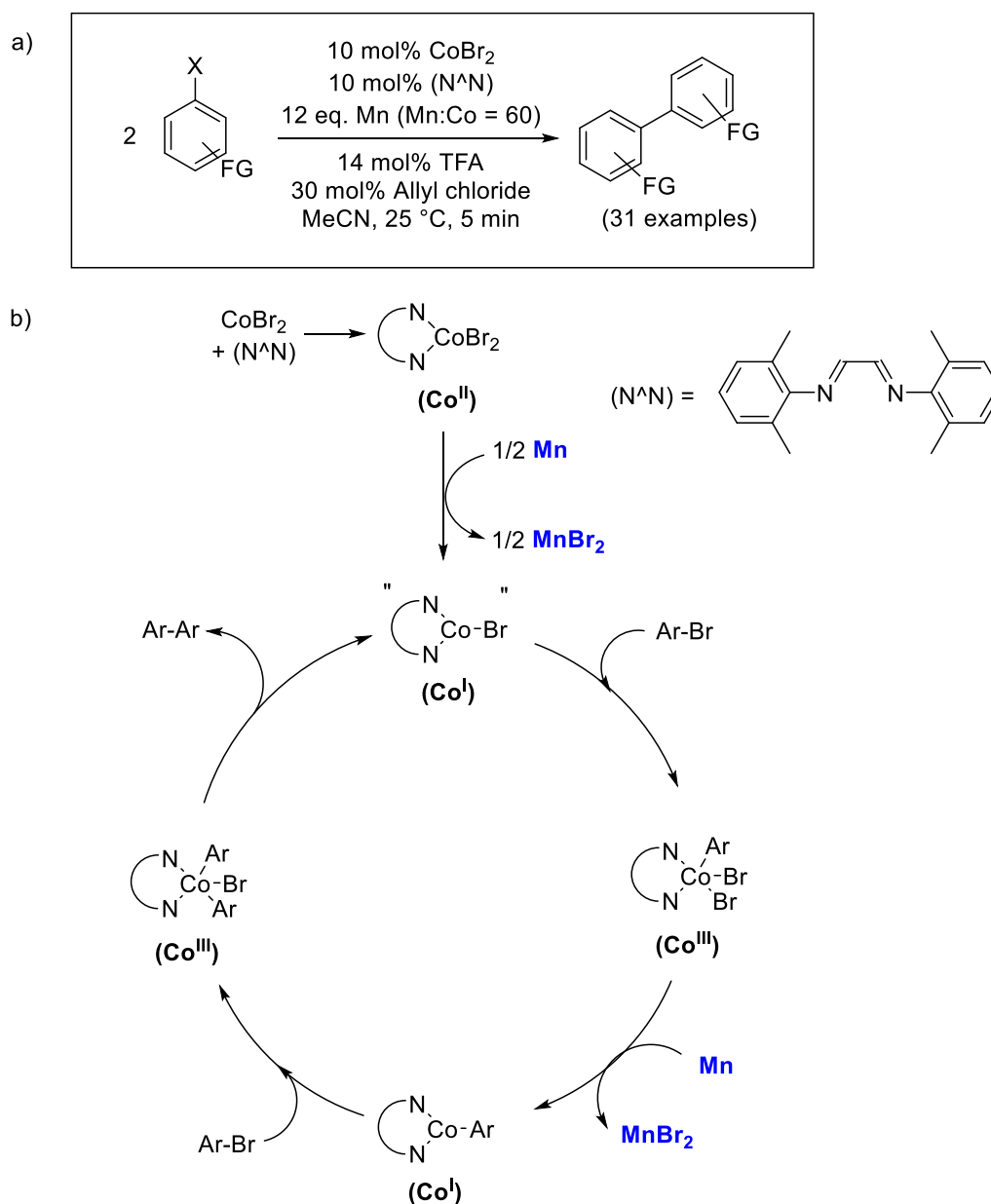
Of course, Zn is not the only reducing agent that can be used when it comes to preparation of cobalt(I) complexes *in* or *ex situ*. It would be remiss not to include some of the alternative reducing agents that have been employed for reduction of (P[^]P)CoX₂ complexes in the literature.

Perhaps one of the most widely used cobalt(I) catalysts, (PPh₃)₃CoCl is commercially available and readily prepared from reduction of CoCl₂·6H₂O with NaBH₄ (or through reduction with Zn; **Scheme 4.8**).^{14,15} Some examples of the catalytic activity of this complex were discussed in Chapter 3.



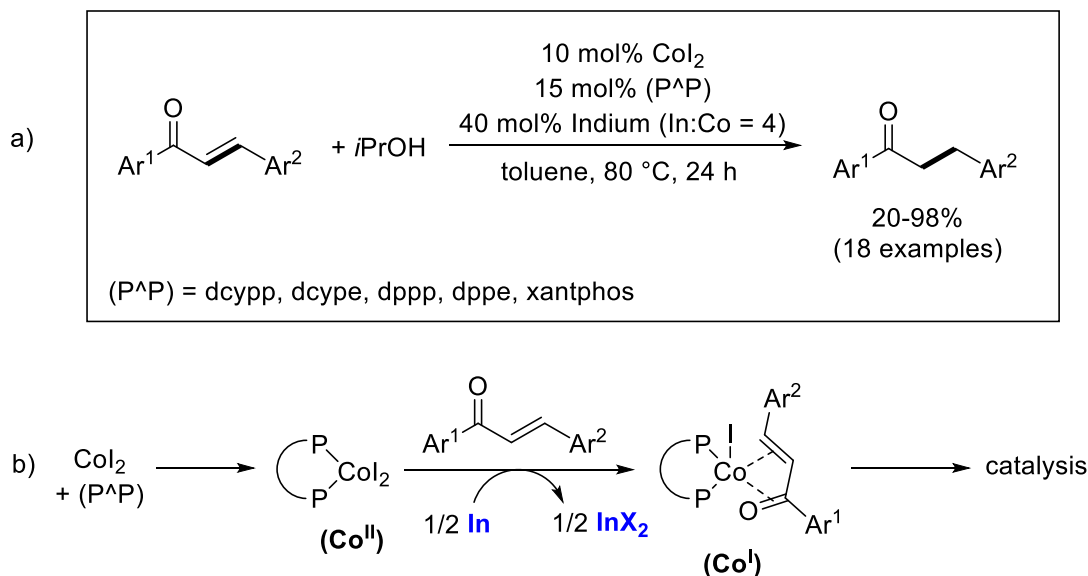
Scheme 4.8 Reported synthesis of ClCo(PPh₃)₃ *via* reduction of cobalt(II) with NaBH₄ or Zn.¹⁴

In 2009, Gosmini and co-workers reported the homo-coupling of aryl-bromides mediated by a cobalt(I)/cobalt(II) catalytic cycle (**Scheme 4.9a**).¹⁶ Here, the α -diimine cobalt(II) complex is reduced *in situ* to produce the presumed “(N[^]N)CoBr” cobalt(I) complex through addition of excess manganese. The authors also proposed a mechanism for the homo-coupling transformation based upon DFT calculations at the B3LYP and PBE0 levels, which were based on the assumption that the starting point for catalysis was “(N[^]N)CoBr” (**Scheme 4.9b**).¹⁶ Oxidative addition of aryl bromide to the *in situ*-generated cobalt(I) complex produced a cobalt(III) intermediate. This can then undergo two-electron reduction by reaction with further manganese dust to produce a cobalt(I) aryl species. Oxidative addition of a second equivalent of aryl-bromide then allowed formation of diaryl-cobalt(III), which is proposed to then undergo reductive elimination (driven by the exothermic formation of C-C bond) to regenerate the cobalt(I) catalyst and release the homo-coupled di-aryl product.¹⁶ This mechanism is comparable to those that have been reported previously for cobalt/zinc-mediated homo-coupling reactions.^{17–20}



Scheme 4.9 a) Reported cross-coupling of aryl-halides catalysed by $\text{CoBr}_2/(\text{N}^{\wedge}\text{N})/\text{Mn}$. b) Proposed reaction mechanism.¹⁶

Indium metal has also been reported for use as a one-electron reducing agent for $(\text{P}^{\wedge}\text{P})\text{CoX}_2$ species. Zhang *et al.* reported chemoselective transfer hydrogenation of C=C and C=O bonds in α,β -unsaturated ketones with alkanols (**Scheme 4.10a**).²¹ Using an excess of indium dust (In:Co = 4), diphosphine, and CoI_2 , *in situ* generation of cobalt(I) was applied for successful transfer hydrogenation in 20-98% yield with a wide substrate scope. Of interest, Zhang and co-workers take into account the presence of the substrate during the *in situ* reduction of the cobalt(II) pre-catalyst. The authors propose that the α,β -unsaturated ketone substrate could act to stabilise the cobalt(I) species, generated through single-electron reduction by indium; this would allow formation of the 18-electron cobalt(I) species shown in **Scheme 4.10b**.²¹

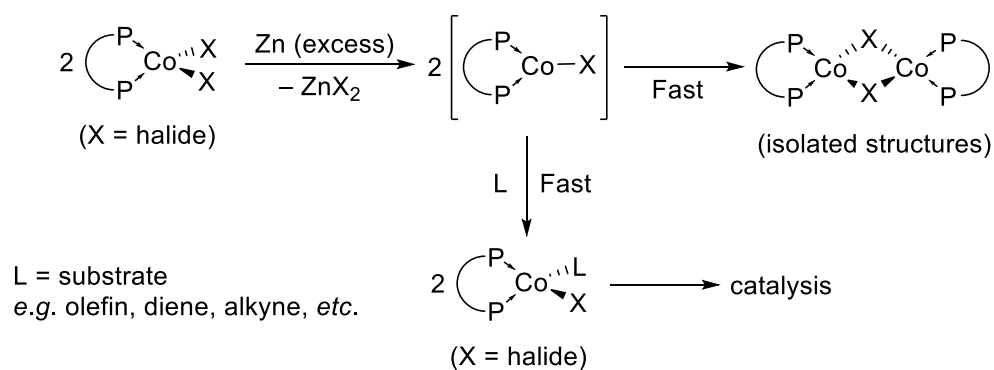


Scheme 4.10 a) Reported transfer hydrogenation of C=C and C=O bonds mediated by $\text{CoI}_2/(\text{P}^{\wedge}\text{P})/\text{Indium}$. b) Proposed formation of the catalytically active cobalt(I) species.²¹

4.1.4 Literature Review Summary

From the brief literature overview presented above, it is clear there is considerable interest in the use of complexes of cobalt bearing a diphosphine ligand with general formula $(\text{P}^{\wedge}\text{P})\text{CoX}_2$ in several different catalytic transformations with a variety of substrates (dienes, ketones, olefins, alkynes, *etc.*). It is evident that it is much more common to prepare the proposed catalytically-active cobalt(I) species *in situ* through treatment with a large excess of reducing agent (often Zn) during catalysis, rather than to attempt to isolate and characterise these extremely unstable and reactive cobalt(I) complexes.

From the few reports where cobalt(I) diphosphine complexes have been successfully isolated, it appears these complexes have a propensity to dimerise to form complexes with general formula $(\text{P}^{\wedge}\text{P})\text{Co}(\mu_2\text{-X})\text{Co}(\text{P}^{\wedge}\text{P})$. This dimerisation process is likely to be very fast and hence allows for the stabilisation of the low coordinate and low valent cobalt(I) species (**Scheme 4.11**). Alternatively, where *in situ* generation of cobalt(I) occurs during catalysis, the substrate of catalysis (*e.g.* L) is proposed to aid in stabilisation of the generated cobalt(I) complex (**Scheme 4.11**). As the mechanisms by which many of the reported catalytic transformations take place are not well understood, a good place to start would be the preparation and isolation of a series of cobalt(I) complexes bearing diphosphine ligands. Consequently, this thesis chapter describes studies around the reduction of $(\text{P}^{\wedge}\text{P})\text{CoX}_2$ complexes (**3.3-3.10**) with a focus on the observed reactivity of these complexes with Zn.



Scheme 4.11 General representation of the reported modes of stabilisation of generated cobalt(I) complexes prepared through reduction of $(\text{P}^{\wedge}\text{P})\text{CoX}_2$.

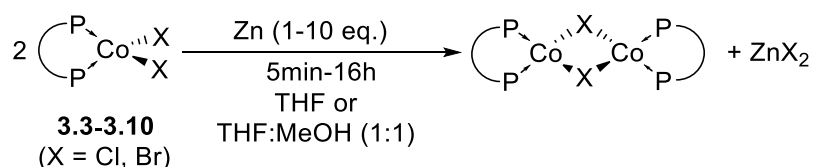
From the literature involving cobalt diphosphine complex-mediated catalytic transformations, it is evident that there is not a great understanding about the role that the presence of zinc metal in a large excess plays during catalysis. However, the requirement for a large excess of zinc to be present during catalysis has been noted in several reports. In addition, for cobalt(I) generated *in situ* during catalysis, there is little discussion over the possible role that generated ZnX_2 species might play within catalytic transformations mediated by diphosphine cobalt complexes. As such, an investigation into the reactivity of ZnX_2 species with diphosphine cobalt complexes has also been launched and the results reported herein.

4.2 Investigating the Reduction Chemistry of (P[^]P)CoX₂ Complexes

The single-electron reduction of (P[^]P)CoX₂ complexes (**3.3-3.10**) synthesised within this work was attempted through their treatment with an excess of Zn dust,[†] in accordance to literature precedent, in an attempt to produce cobalt(I) complexes with general formula “(P[^]P)CoX”. The following chapter sections are focused upon our studies of the reactivity and reduction chemistry of (P[^]P)CoX₂ complexes with Zn. For ease, the section has been split into two parts: successful single-electron reduction of (P[^]P)CoX₂ complexes with Zn and alternative reactivity of (P[^]P)CoX₂ complexes with Zn.

4.2.1 Successful Single-electron Reduction of (P[^]P)CoX₂ Complexes with Zn Dust

The single-electron reduction of (P[^]P)CoX₂ complexes (**3.3-3.10**) synthesised during this work was explored through treatment of **3.3-3.10** with activated Zn dust in THF or THF:MeOH. (1:1) in accordance to reported literature procedures for the reduction of (P[^]P)CoX₂ complexes (**Scheme 4.12**).^{2,3,9} It is proposed that the resulting cobalt(I) complexes are binuclear 16-electron cobalt species with bridging halide ligands. This hypothesis is based upon the work of Chirik and Cummins who have isolated dimeric cobalt-phosphine complexes in the solid state with the general structure shown in **Scheme 4.12**.



Scheme 4.12 General scheme for the single-electron reduction of (P[^]P)CoX₂ complexes and proposed structure of the cobalt(I) complexes formed.

As discussed in the introduction to this chapter, few examples of fully characterised diphosphine cobalt(I) complexes have been reported previously in the literature; the vast majority of diphosphine cobalt(I) complexes are produced *in situ* during catalysis. Of the examples where a diphosphine cobalt(I) complex has been isolated, single crystal X-ray diffraction appears to be the go-to method of characterisation. However, despite significant efforts, no single crystals of any cobalt(I) complexes reduced *ex situ* during the work presented in this thesis were obtained.

Synthesised cobalt(I) species containing diphosphine ligands are inherently difficult to characterise due to their paramagnetic nature (*pseudo*-tetrahedral, d⁸) and high reactivity towards moisture and

[†] Zn dust was activated through heating under vacuum before storage in a glovebox under inert atmosphere. The same batch of Zn dust was used throughout all the experiments presented herein.

oxygen. Excluding single crystal XRD, there is little data available on these complexes in the literature. Alongside a solid-state structure, Chirik reports solution state ^1H NMR (δ range -4 to $+75$ ppm) spectroscopic analysis of isolated $(\text{P}^{\wedge}\text{P})\text{Co}(\mu_2\text{-X})_2\text{Co}(\text{P}^{\wedge}\text{P})$ complexes.³ As a part of the work presented in this thesis, ^1H NMR spectroscopic data (d_8 -THF, 200 MHz) of the diphosphine cobalt(II) complexes (**3.3-3.10**) and subsequent reduction products were collected. However, the spectra obtained span a wide spectral window (δ -20 to $+120$ ppm) with very broad and difficult to interpret signals. For this reason, the ^1H NMR spectra obtained of these complexes will not be discussed further.

In the work of Rajanbabu and colleagues, the MALDI mass spectra of (some) “ $(\text{P}^{\wedge}\text{P})\text{CoX}$ ” complexes were reported. For the reported $(\text{dppp})_3\text{Co}_2\text{Br}_2$ system the only fragments reported to be observed by MALDI MS were $[(\text{dppp})_2\text{Co}]^+$ and $[(\text{dpppO}_2)\text{CoBr}]^+$. However, the work presented in this thesis shows that mass spectrometric analysis is ambiguous in determining whether a cobalt(I) complex has truly been produced. For instance, the fragment ions reported by Rajanbabu, $[(\text{dppp})_2\text{Co}]^+$ and $[(\text{dpppO}_2)\text{CoBr}]^+$, are also generated within the ionisation of $(\text{dppp})\text{CoBr}_2$ under standard ASAP⁺ MS and MALDI MS conditions, as a result of fragment recombination within the instrument. Despite this complication, mass spectra (*i*ASAP⁺) were collected of the reaction products of each of the reduction attempts performed as a part of this thesis and, as shall be discussed, can be used to provide valuable insight, especially in cases where single-electron reduction of $(\text{P}^{\wedge}\text{P})\text{CoX}_2$ complexes by Zn is *not* the only reaction pathway occurring. As solid state molecular structures could not be obtained of any of the cobalt(I) complexes prepared herein, and mass spectrometric analysis did not unambiguously prove single-electron reduction has taken place, additional methods of characterisation were sought.

In the absence of an effective crystallisation method for purification, the large excess of zinc used within the reduction attempts of $(\text{P}^{\wedge}\text{P})\text{CoX}_2$ complexes (**3.3-3.10**) and associated formation of ZnX_2 made elemental analysis unreliable for confirmation of reduction. The by-product, ZnX_2 , is particularly difficult to remove as it has sparing solubility in a range of organic solvents. Although non-polar solvents could be imagined to allow removal of ZnX_2 (as its solubility is greatly reduced), however, the cobalt(I) complexes prepared are also insoluble in, *e.g.* hexanes.

Due to these limitations, the work presented herein uses Raman and UV-Vis spectroscopic analyses to gain insight into the reduction of $(\text{P}^{\wedge}\text{P})\text{CoX}_2$ complexes (**3.3-3.10**) using Zn metal. As discussed in Chapter 3, Raman spectroscopy allows measurement of the vibrational energies of Co-Br bonds; which will differ significantly between $(\text{P}^{\wedge}\text{P})\text{CoX}_2$ and “ $(\text{P}^{\wedge}\text{P})\text{CoX}$ ” species. UV-Vis spectroscopy can be used to observe the formation of new cobalt(I) species through changes to the visible region of the spectrum (principally $d \leftarrow d$ transitions). A summary of the successful single-electron reductions, as determined by UV-Vis and Raman spectroscopic analysis of $(\text{P}^{\wedge}\text{P})\text{CoX}_2$ complexes performed with Zn metal are

shown in **Table 4.1**. Where not included within the text, spectroscopic data (UV-Vis, Raman) can be found in the Appendix with assignments being reported in the Experimental chapter.

Table 4.1 Single-electron reductions of (P[^]P)CoX₂ complexes with Zn metal in THF, which ultimately gives rise to the formation of (some) cobalt(I) species.

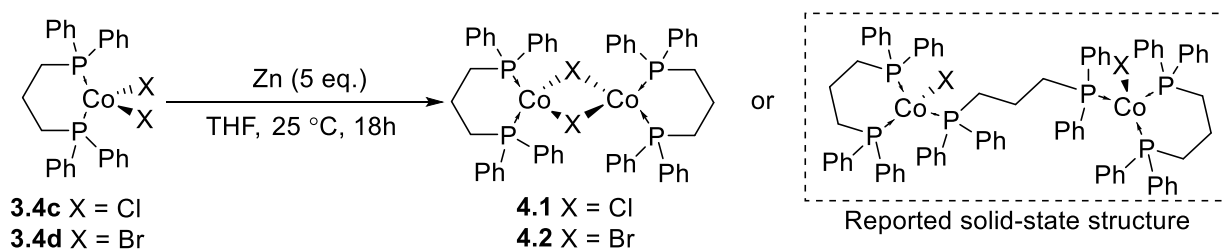
Entry	(P [^] P)CoX ₂ Complex	Eq. Zn	Time /h	Temp. /°C	Product(s)
1	3.4c (dppp)CoCl ₂	5	18	25	4.1
2	3.4d (dppp)CoBr ₂	5	18	25	4.2
3 ^a	3.4d (dppp)CoBr ₂	5	144	25	CoBr ₂ [*]
4 ^b	3.4d (dppp)CoBr ₂	10	1	25	4.2, 4.2·THF
5 ^c	3.4e (dppb)CoCl ₂	10	64	25	Co ⁰ _(s)
6	3.4e (dppb)CoCl ₂	5	48	40	4.3, Zn-5.1
7	3.4f (dppb)CoBr ₂	5	24	25	4.4
8	3.4a (dppm)CoBr ₂	5	4	25	4.5^d
9	3.6f (dppx)CoBr ₂	5	18	25	4.6, Zn-5.2
10	3.7b (PNNP-Ph)CoBr ₂	1	18	25	4.7
11	3.6b (dtbpx)CoBr ₂	5	18	25	Zn-5.3, 3.6b, Co⁰_(s)
12 ^a	3.6b (dtbpx)CoBr ₂	5	22	25	CoBr₂, Zn-5.3, 3.6b, Co⁰_(s)
13 ^b	3.6b (dtbpx)CoBr ₂	10	5 min	25	Zn-5.3, 3.6b, CoBr₂
14 ^b	3.6b (dtbpx)CoBr ₂	10	30 min	25	Zn-5.3, 3.6b, 4.8, Co⁰_(s)
15	3.6a (dtbpx)CoCl ₂	5	120	25	Zn-5.4, 3.6a, Co⁰_(s)

^aUV-Vis scale reaction, ^b1:1 MeOH:THF, ^cToluene added after 16 hours, ^dMixed valence dimer: BrCo(μ²-dppm)₂ (μ²-Br)CoBr,^{*} as determined by UV-Vis spectroscopic analysis through comparison to the spectrum obtained of an authentic sample.

The following sections discuss the reductions of (P[^]P)CoX₂ complexes, outlined in **Table 4.1**, with Zn metal. The reactions were investigated by UV-Vis (THF solutions) and Raman spectroscopic techniques (solid state) and subject to mass spectrometric analysis.

4.2.1.1 The Reduction of (dppp)CoX₂ (X = Cl **3.4c** and X = Br **3.4d**) with Zn Metal

Rajanbabu *et al.* have previously reported the reduction of (dppp)CoX₂ (X = Cl, Br) (**3.4c** and **3.4d**) with an excess of zinc metal, this synthesis was therefore repeated in order to confirm their findings.^{2,9} The general method used for the reduction of **3.4c** or **3.4d** using Zn is shown in **Scheme 4.13** alongside a representation of the previously reported solid-state structures of the cobalt(I) species **4.1** and **4.2**.



Scheme 4.13 One-electron reduction of (dppp)CoX₂ (**3.4c** and **3.4d**) with excess Zn metal to generate **4.1** and **4.2** and the previously reported structure for the cobalt(I) species generated.^{2,9}

The Raman spectra of (dppp)CoX₂ complexes (**3.4c** and **3.4d**) contain a band corresponding to Co-X_{symm}. Upon reduction to cobalt(I) species, **4.1** and **4.2**, this band will no longer be present. The Raman spectra of (dppp)CoCl₂ (**3.4c**) and “(dppp)CoCl” (**4.1**) are shown in **Figure 4.1**. It can be seen that the stretch corresponding to νCo-Cl_{symm} (320 cm⁻¹ in **3.4c**) is not in the spectrum of **4.1**, indicating successful single-electron reduction of **3.4c** has taken place. Additionally, new bands at 297 cm⁻¹ and 395 cm⁻¹ were observed, which have been attributed to the bridging halide stretch corresponding to that expected for **4.1** (c.f. νCo-Br-Co 365 cm⁻¹; νCo-Cl appear at higher wavenumber than νCo-Br, as discussed in Chapter 3). In the case of the bromide analogue, the Raman spectrum of complex **4.2** shows the presence of new shouldered bands at 298 cm⁻¹ and 366 cm⁻¹, which have been assigned as Co-(μ₂-Br) stretches in **4.1** (c.f. νCo-Br_{symm} 284 cm⁻¹ in **3.4d**) (**Figure 4.1**). Both the spectra for complexes **4.1** and **4.2** contain bands that could be attributed to bridging halide stretches when compared to those data obtained and calculated for Co-X-Co (Chapter 3, Section 3.3.4.1). It is therefore proposed that the reduced complexes **4.1** and **4.2** are dinuclear with bridging halide ligands in the solid-state as shown in **Scheme 4.13**.

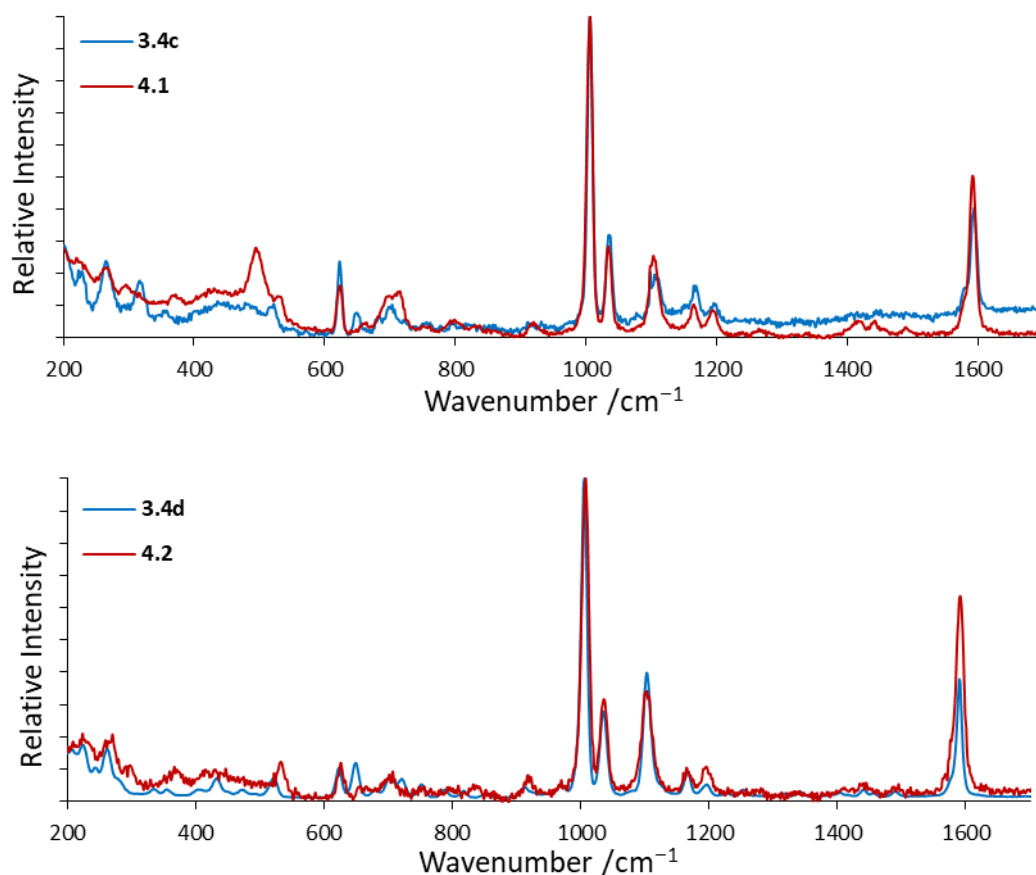


Figure 4.1 Comparison of the Raman spectra (LIR, 532 nm) obtained of Top: (dppp)CoCl₂ (**3.4c**) and (dppp)Co(μ-Cl)₂Co(dppp) (**4.1**); Bottom: (dppp)CoBr₂ (**3.4d**) and (dppp)Co(μ-Br)₂Co(dppp) (**4.2**). *note: broad band at ~500 cm⁻¹ in **4.1** results from contributions of the glass sample holder during measurement.

Comparison of the UV-Vis spectra obtained of (dppp)CoCl₂ (**3.4c**) and **4.1** (dppp)Co(μ₂-Cl)Co(dppp) (**4.1**) revealed that both contain peaks with ν_{\max} at 13569, 15723 and 17094 cm⁻¹, which correspond to transition bands ${}^4T_1({}^4F) \leftarrow {}^4A_2$ for (dppp)CoCl₂ (**Figure 4.2**: LHS),^{22,23} although, new bands corresponding to the cobalt(II) complex **4.1** are present at ν_{\max} 11261, 14599 and 15060 cm⁻¹. Observation of this ${}^4T_1({}^4F) \leftarrow {}^4A_2$ transition corresponding to **3.4c** in the UV-vis spectrum recorded for **4.1** suggests that there remains some unreacted (dppp)CoCl₂ (**3.4c**) within the mixture, which is contradictory to the data obtained within the Raman spectroscopic analysis.

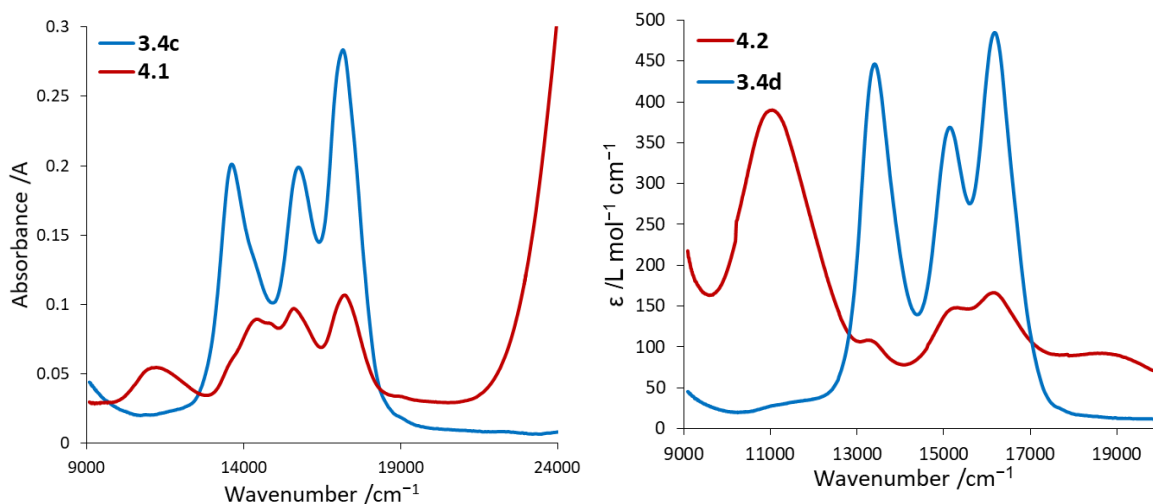
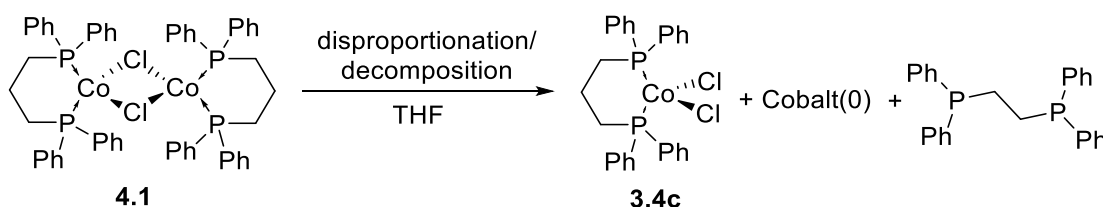


Figure 4.2 Comparison of the UV-Vis spectra collected for LHS: (dppp)CoCl₂ (**3.4c**) and (dppp)Co(μ₂-Cl)₂Co(dppp) (**4.1**); RHS: (dppp)CoBr₂ (**3.4d**) and (dppp)Co(μ₂-Br)₂Co(dppp) (**4.2**).

Some solids were observed to precipitate from solution during measurement of the UV-Vis spectrum of **4.1** as a solution in THF, as such, the comparison spectra are reported here in terms of absorbance only. It is possible that the generated cobalt(I) species **4.1** is unstable in solution, resulting in disproportionation to the cobalt(II) species and cobalt(0) (**Scheme 4.14**). This is consistent with the observation of trace blue precipitate after UV-Vis measurement; (dppp)CoCl₂ (**3.4c**) is blue. However, no black solid (corresponding to cobalt(0)) was observed, although it is likely that the small quantity that may have been produced was not observable on the scale of the UV-vis sample measured (~3 mg of **4.1** in 2 mL THF). The disproportionation of cobalt(I) complex (PPh₃)₃CoCl to produce (PPh₃)₂CoCl₂ and cobalt(0) has been reported in the literature and was discussed in Chapter 3, Section 3.2.2.1.²⁴ Even very slow rates of disproportionation of complex **4.1** in solution could have a dramatic effect on the UV-Vis spectrum obtained, as (dppp)CoCl₂ (**3.4c**) is only sparingly soluble in THF and subsequent precipitation could drive the disproportionation of **4.1** to produce **3.4c** and cobalt(0). This decomposition pathway could explain the disparity between the data as observed by Raman (showed **4.1**) and UV-Vis spectroscopic (showed **3.4c**) techniques.



Scheme 4.14 Proposed disproportionation of (dppp)Co(μ₂-Cl)₂Co(dppp) (**4.1**) into (dppp)CoCl₂ (**3.4c**), dppp and cobalt(0) in solution.

UV-Vis spectroscopic analysis of complex **4.2** (in THF) gave very similar data to those described above for complex **4.1** with the ${}^4T_1({}^4F) \leftarrow {}^4A_2$ transition band of $(\text{dppp})\text{CoBr}_2$ (**3.4d**) (ν_{max} 13423, 15175 and 16234 cm^{-1}) being present in the product mixture alongside additional tetrahedral cobalt(I)-related transitions with ν_{max} 11038 cm^{-1} and 18833 cm^{-1} (**Figure 4.2**: RHS). Based upon the calculated absorption coefficient of the transitions associated with complex **3.4d** (reported and discussed in Chapter 3), and the assumption that the rest of the cobalt species in solution is the dimeric cobalt(I) complex **4.2**, it can be determined from the UV-vis spectrum of "**4.2**" that this solution is an approximate 1:1 mixture of **3.4d**:**4.2**. As discussed for complex **4.1**, the presence of **3.4d** in solution could be the result of incomplete reduction or through disproportionation of the resulting cobalt(I) species, **4.2**, in solution.

The reduction of $(\text{dppp})\text{CoBr}_2$ (**3.4d**) with an excess of Zn metal (as per **Scheme 4.13**) was repeated in a more dilute solution to allow for reaction progress to be monitored by UV-Vis spectroscopy (**Table 4.1**: Entry 3). Analysis of the reaction progress by UV-Vis spectroscopy of **3.4d** with 5 equivalents of activated Zn metal is shown in **Figure 3**. After 1.5 hours, the peaks associated with **3.4d** begin to decrease in intensity. After 24 hours, a new band emerged with λ_{max} 685 nm, the intensity of which increased over the course of the reaction monitoring period (144 hours). This new peak has been assigned to cobalt(II) bromide (through comparison to spectra recorded within this work, Chapter 3, Section 3.3.4.3). Bands associated with $(\text{dppp})\text{Co}(\mu_2\text{-Br})_2\text{Co}(\text{dppp})$ (**4.2**) at ν 11038 cm^{-1} (λ_{max} 906 nm) were not observed at any point during monitoring of this reaction. It is proposed that the low concentration used within this reaction (0.16 mM **3.4d** in THF) promotes slow dissociation of the dppp ligand from **3.4d**. Possible side reactions that may play a significant role within this reaction are discussed in detail in Section 4.2.4. However, this reaction between **3.4d** and Zn does highlight the relative stability of **3.4d** in solution, as even after 144 hours at very low dilution there still remains some **3.4d** present.

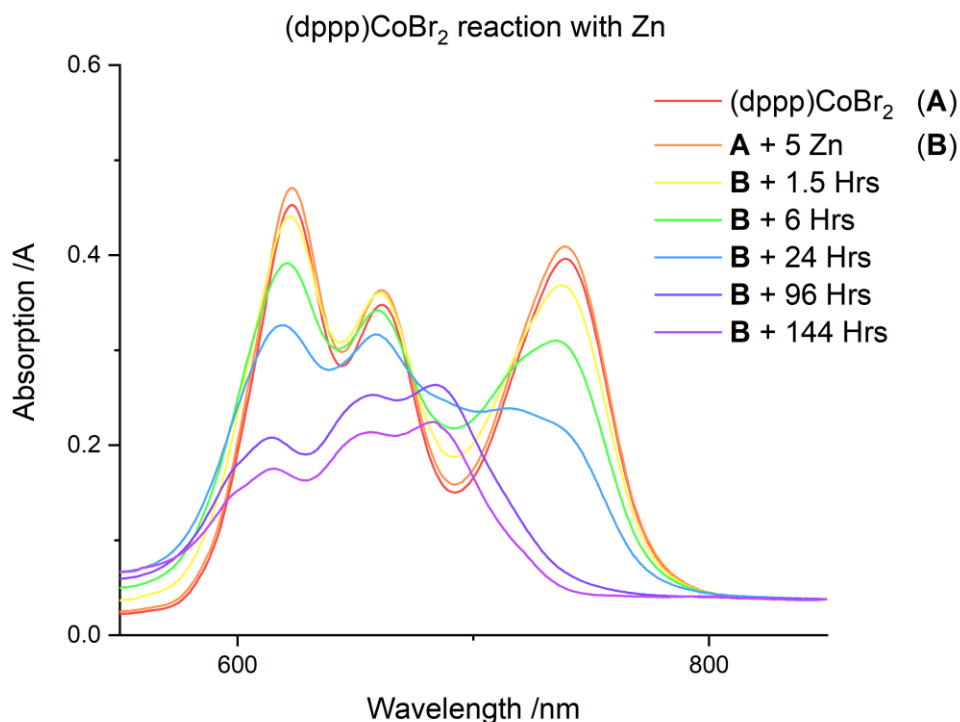
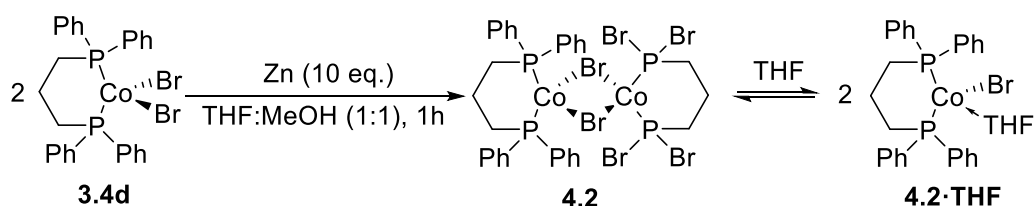


Figure 3 UV-Visible spectrum of reaction of (dppp)CoBr₂ (**3.4d**) with 5 eq. Zn over time.

The above reductions of **3.4b** with Zn metal were carried out in THF in accordance with the procedure outlined by Rajanbabu *et al.*² However, in contrast, the reduction method for (P[^]P)CoX₂ complexes reported by Chirik and co-workers uses different conditions. For instance, Chirik uses a 1:1 THF:MeOH solvent system (presumably to aid Zn solvation and modify the reduction potential in solution) along with a larger excess of Zn (Chirik uses 10 eq. Zn vs Rajanbabu's 5 eq. Zn).³ As the reduction of (P[^]P)CoX₂ complexes is likely to be very condition-dependant, the reduction of **3.4b** to produce **4.2** was repeated using the conditions outlined by Chirik (**Table 4.1**: Entry 4) (**Scheme 4.15**). The Raman spectrum obtained of the product, **4.2**, produced using the "Chirik method" was identical to that obtained previously when 5 eq. of Zn in THF was used, *i.e.* the lack of a $\nu_{\text{Co-Br}}_{\text{symm}}$ (284 cm⁻¹ in complex **3.4d**) and presence of two new bands assigned as Co-(μ_2 -Br)-Co at 295 cm⁻¹ and 365 cm⁻¹. UV-Vis spectroscopic analysis of the products of the reaction between **3.4d** and 10 equivalents of Zn in MeOH:THF (**Table 4.1** Entry 4) were very similar to that obtained previously for the reaction of **3.4b** with 5 equivalents of Zn in THF (**Table 4.1**: Entry 2) with bands associated with cobalt(I) species, **4.2**, observed at ν_{max} 11050 cm⁻¹ along with some contribution arising from **3.4d** (either residual or the disproportionation product).



Scheme 4.15 Reduction of **3.4d** with Zn metal in MeOH:THF to produce **4.2** in accordance to modifications to the “Chirik method”³ and proposed solution state equilibrium to form **4.2·THF**.

Mass spectrometric analysis of complex **4.1** (Table 4.1: Entry 4) gives rise to fragments that suggest complexation of THF to the cobalt centre. For instance, the fragment corresponding to $[(\text{dppp})\text{CoBrTHF}]^+$ is observed at m/z 622.019 Da (calc. m/z 622.060 Da with the correct isotope pattern). Comparison of the mass spectra obtained of complexes **3.4d** and **4.2** from Table 4.1: Entry 4 are shown in Figure 4.4. In addition, the ^1H NMR (200 MHz, CD_2Cl_2) spectrum obtained of complex **4.2** produced *via* the “Chirik method” shows two broadened singlet resonances at δ_{H} 3.79 ($\nu_{1/2}$ 18 Hz) and 1.86 ($\nu_{1/2}$ 17 Hz), which have been attributed to the presence of coordinated THF at the cobalt centre. Taking the MS and NMR analytical data together, it is proposed that the dimeric complex **4.2** can dissociate in THF, resulting in formation of $(\text{dppp})\text{CoBr}(\text{THF})$ (**4.2·THF**), the proposed structure of which is shown in Scheme 4.15.

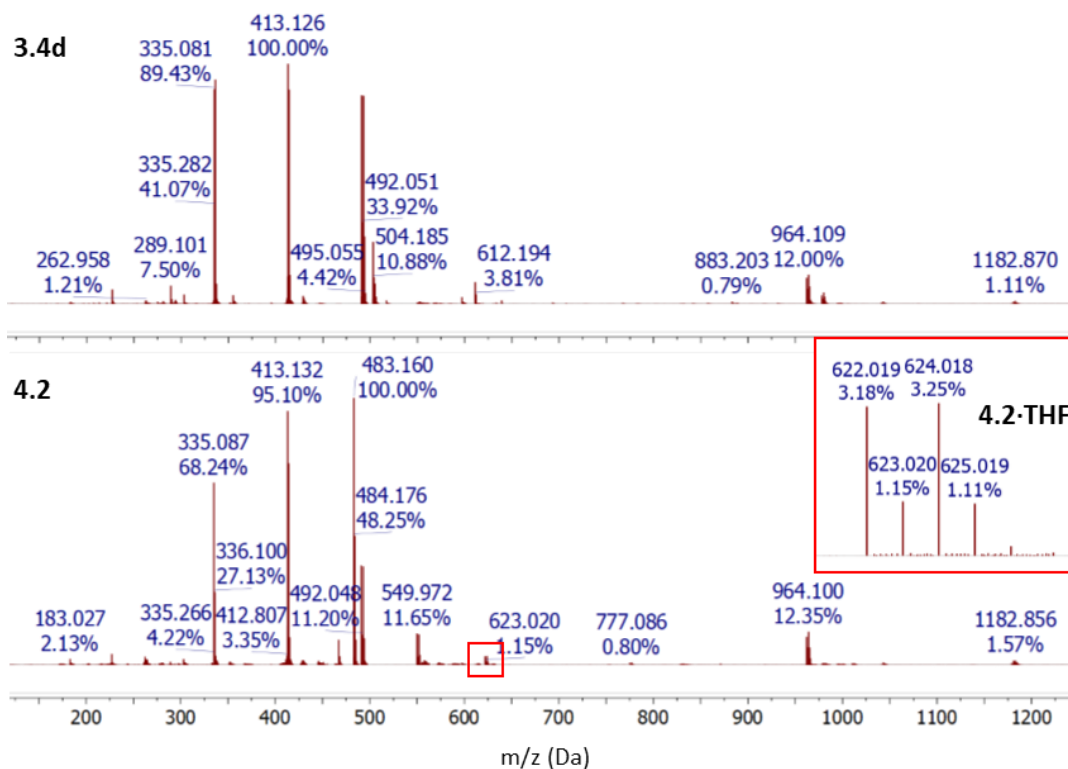
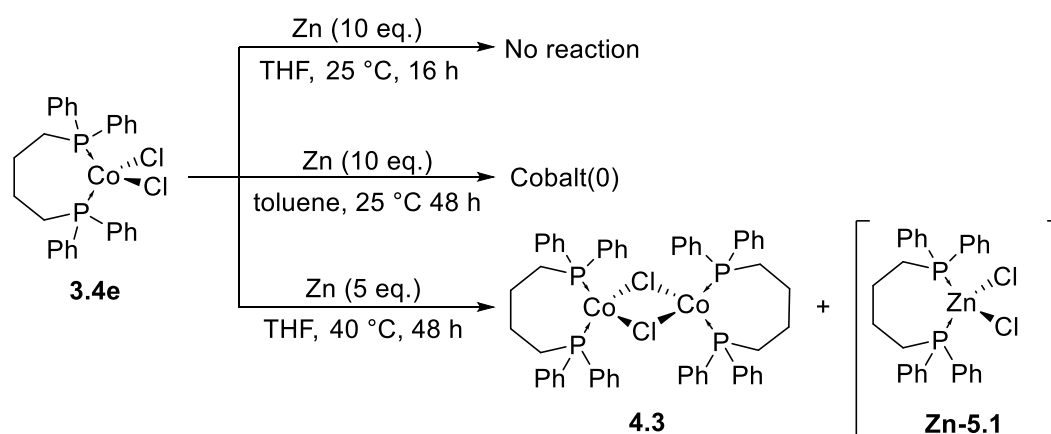


Figure 4.4 Comparison of MS (*iASAP*⁺) spectra of **3.4d** and **4.2** (as obtained from Table 4.1: Entry 4) where solid line insert shows the molecular ion of **4.2·THF**.

4.2.1.2 The Reduction of (dppb)CoX₂ (X = Cl **3.4e**, X = Br **3.4f**) with Zn Metal

The first attempt for single-electron reduction of (dppb)CoCl₂ (**3.4e**) was performed using 10 equivalents of Zn in THF (**Table 4.1**: Entry 5). However, after 16 hours no colour change was observed for the reaction. This observed lack of reactivity between **3.4e** and Zn in THF at 25 °C is proposed to be the result of poor solubility of **3.4e**. Toluene was then added to aid solvation of complex **3.4e**. After 48 hours from addition of toluene, a black, magnetic and insoluble material was observed, which has been attributed to the decomposition of **3.4e** to produce cobalt(0) under these reducing conditions (**Scheme 4.16**). The single-electron reduction of (dppb)CoCl₂ (**3.4e**) was therefore repeated in THF at 40 °C (to aid solvation of **3.4e**) and the successful reduction to (dppb)Co(μ₂-Cl)₂Co(dppb) (**4.3**) was confirmed through Raman and UV-Vis spectroscopic analyses (**Table 4.1**: Entry 6).



Scheme 4.16 Reaction conditions tested for the reduction of **3.4e** to form **4.3** and observed formation of (dppb)ZnCl₂ (**Zn-5.1**).

The Raman spectra obtained of complex **4.3** did not show a band for $\nu_{\text{Co-Cl}_{\text{symm}}}$ (310 cm⁻¹ in **3.4e**), as shown in **Figure 4.5**. However, no clear bands associated with a new Co-Cl stretching were observed (however, these can be very weak) and so the halide coordination configuration (terminal vs bridging) in **4.3** cannot be directly determined (**Figure 4.5**).

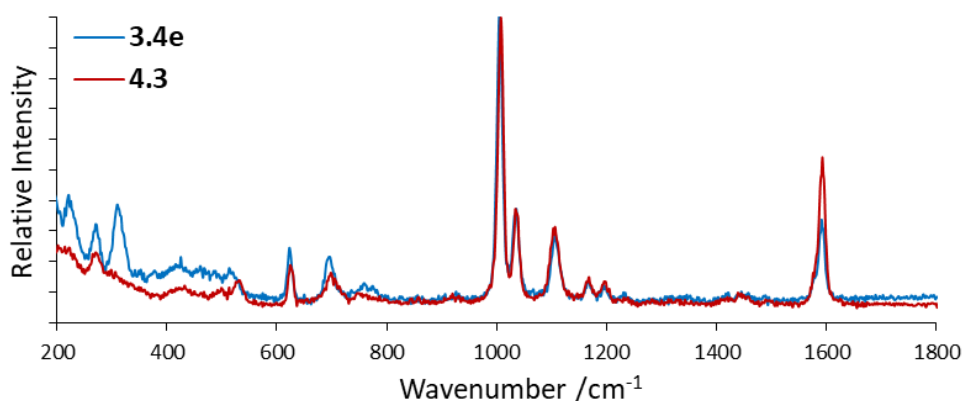


Figure 4.5 Comparison of the Raman spectra (LIR, 532 nm) obtained for $(\text{dppb})\text{CoCl}_2$ (**3.4e**) and $\text{dppbCo}(\mu_2\text{-Cl})_2\text{Co}(\text{dppb})$ (**4.3**) as defined in **Table 4.1**: Entry 6.

UV-Vis spectroscopic analysis of complex **4.3** showed a strong absorption at 10929 cm^{-1} , indicative of a cobalt(I) complex (shown in **Figure 4.6**). Mass spectrometric analysis of complex **4.3** shows fragments corresponding to, *e.g.* $[(\text{dppp})_2\text{CoCl}]^+$ at m/z 947.244 Da (calc. 947.243 Da, with the correct isotope pattern) and $[(\text{dppp})_2\text{Co-H}]^+$ at m/z 911.235 Da (calc. 911.267 Da, with the correct isotope pattern). Of note, the mass spectrometric analysis of the product obtained from the reaction of $(\text{dppb})\text{CoCl}_2$ (**3.4e**) with Zn also showed the presence of $(\text{dppb})\text{ZnCl}_2$ (**Zn-5.1**) with, *e.g.* m/z 559.048 Da $[(\text{M-H})^+]$ calc. 559.026 Da, with the correct isotope pattern) within the product mixture containing **4.3**. The formation of $(\text{P}^{\wedge}\text{P})\text{ZnX}_2$ complexes, such as **Zn-5.1**, within reduction reactions of $(\text{P}^{\wedge}\text{P})\text{CoX}_2$ complexes was observed in many cases in the work presented in this thesis. The formation of $(\text{P}^{\wedge}\text{P})\text{ZnX}_2$ in these reactions is discussed in detail in Section 4.2.4.

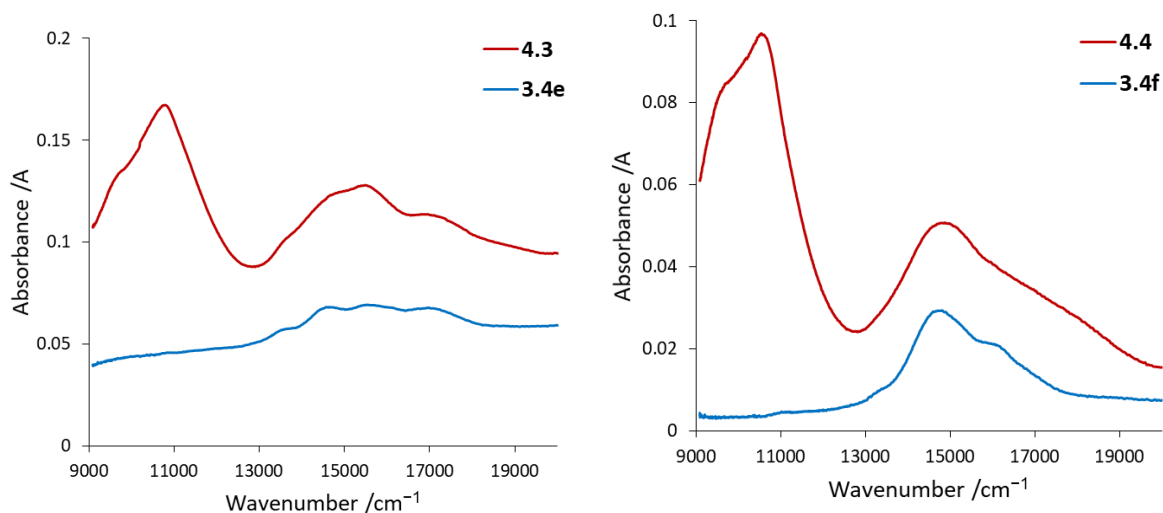
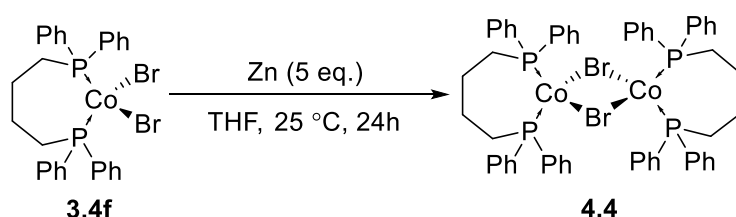


Figure 4.6 Comparison of UV-Vis spectra in THF for: LHS $(\text{dppb})\text{CoCl}_2$ (**3.4e**), $\text{dppbCo}(\mu_2\text{-Cl})_2\text{Co}(\text{dppb})$ (**4.3**); RHS $(\text{dppb})\text{CoBr}_2$ (**3.4f**) and $\text{dppbCo}(\mu_2\text{-Br})_2\text{Co}(\text{dppb})$ (**4.4**).

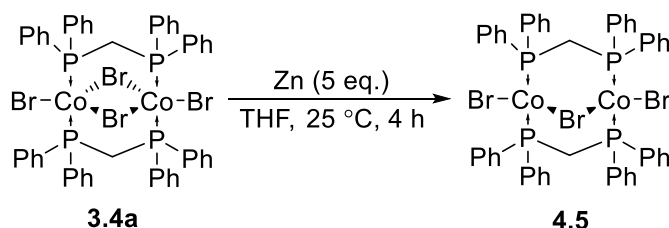
The reduction of $(\text{dppb})\text{CoBr}_2$ (**3.4f**) was carried out in THF using 5 eq. Zn in THF over a 24 hour period (**Scheme 4.17**); successful reduction to $(\text{dppb})\text{Co}(\mu_2\text{-Br})_2\text{Co}(\text{dppb})$ (**4.4**) was confirmed through Raman and UV-Vis spectroscopic analyses (**Table 4.1**: Entry 7). The Raman spectra obtained of the resulting complex $(\text{dppb})\text{Co}(\mu_2\text{-Br})_2\text{Co}(\text{dppb})$ (**4.4**) shows no band attributable to $\nu\text{Co-Br}_{\text{symm}}$ (286 cm^{-1} in **3.4f**), suggesting that the reduction to cobalt(I) has taken place. In addition, new bands were observed at 270 cm^{-1} and 356 cm^{-1} , which were assigned as the asymmetric and symmetric stretches of bridging bromide ligands; the band corresponding to $\nu\text{Co-P}$ did not move significantly (*c.f.* 775 cm^{-1} in **3.4f** and 761 cm^{-1} in **4.4**). The UV-Vis spectrum of complex **4.4** showed a strong absorbance at 10605 cm^{-1} , indicating the presence of cobalt(I) (**Figure 4.6**: RHS). Mass spectrometric analysis of complex **4.4** showed only the presence of the ligand, dppb, for instance, $[\text{dppb}+\text{H}]^+$ at m/z 497.212 Da.



Scheme 4.17 Reduction of $(\text{dppb})\text{CoBr}_2$ (**3.4f**) with Zn metal to produce $(\text{dppb})\text{Co}(\mu_2\text{-Br})_2\text{Co}(\text{dppb})$ (**4.4**).

4.2.1.3 The Reduction of $[\text{BrCo}(\mu_2\text{-dppm})_2(\mu_2\text{-Br})_2\text{CoBr}]$ (**3.4a**) with Zn Metal

The reduction of $[\text{BrCo}(\mu_2\text{-dppm})_2(\mu_2\text{-Br})_2\text{CoBr}]$ (**3.4a**) (**Table 4.1**: Entry 1) was attempted by treatment of **3.4a** with an excess of Zn metal in THF (**Table 4.1**: Entry 8). The solid obtained from this reaction was recrystallised from THF/hexanes to yield crystals suitable for single crystal X-ray diffraction and determined to be complex **4.5**. Subsequently, the product of this reaction was determined to be a mixed-valence ($\text{Co}^{\text{II}}/\text{Co}^{\text{I}}$) dimeric species 74%, $\text{BrCo}(\mu_2\text{-dppm})_2(\mu_2\text{-Br})\text{CoBr}$ (**4.5**), shown in **Scheme 4.18**. Discussion of the solid-state structure obtained for **4.5** can be found in Section 4.8.



Scheme 4.18 Formation of $[\text{BrCo}(\mu_2\text{-dppm})_2(\mu_2\text{-Br})\text{CoBr}]$ (**4.5**) from reduction of **3.4a** $[\text{BrCo}(\mu_2\text{-dppm})_2(\mu_2\text{-Br})_2\text{CoBr}]$.

The Raman spectrum obtained of complex **4.5** suffered from a degree of fluorescence, making assignments of weak Co-Br stretches difficult. However, UV-Vis spectroscopic analysis of complex **4.5** revealed a broad band with three maxima at 13513, 15220 and 16393 cm^{-1} . This UV-Vis spectrum of complex **4.5** is markedly different from that obtained for $\text{BrCo}(\mu_2\text{-dppm})_2(\mu_2\text{-Br})_2\text{CoBr}$ (**3.4a**), which was identical to that of solvated CoBr_2 (due to dppm ligand dissociation in THF) that has a broad band with ν_{max} 14771 cm^{-1} and shoulder at 16835 cm^{-1} (**Figure 4.7**). Notably, the UV-Vis spectrum of **4.5** did not have a strong absorbance around 11000 cm^{-1} , as was observed for the previously discussed cobalt(I) complexes **4.1-4.4**, and was more similar in features to those of the UV-Vis spectra obtained for *pseudo*-tetrahedral (P^\wedgeP) CoX_2 complexes **3.3-3.10**.

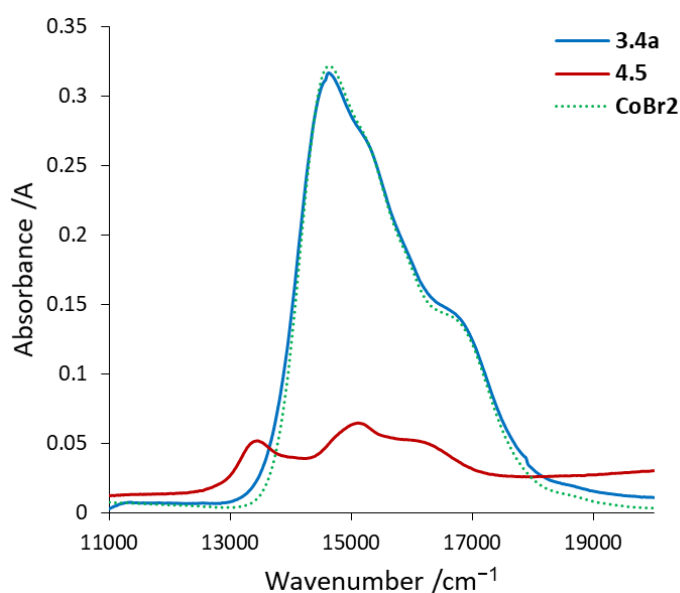
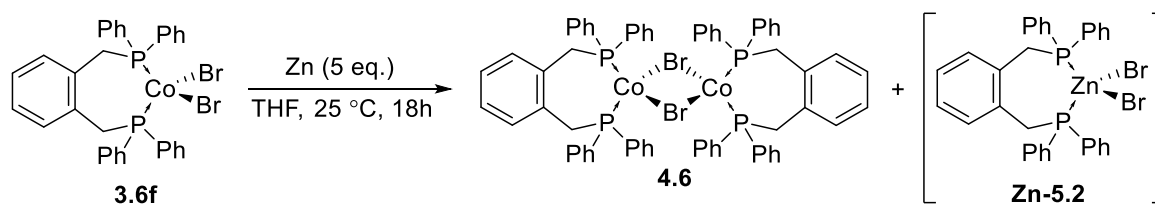


Figure 4.7 Comparison of UV-Vis spectra of $\text{BrCo}(\mu_2\text{-dppm})_2(\mu_2\text{-Br})_2\text{CoBr}$ (**3.4a**), $\text{BrCo}(\mu_2\text{-dppm})_2(\mu_2\text{-Br})\text{CoBr}$ (**4.5**) and CoBr_2 in THF.

4.2.1.4 The Reduction of $(\text{dppx})\text{CoBr}_2$ (**3.6f**) with Zn Metal

The reduction of $(\text{dppx})\text{CoBr}_2$ (**3.6f**) to produce $(\text{dppx})\text{Co}(\mu_2\text{-Br})_2\text{Co}(\text{dppx})$ (**4.6**) took place in 18 hours through treatment of **3.6f** with 5 eq. Zn in THF (**Table 4.1**: Entry 9) (**Scheme 4.19**). The UV-Vis spectrum of complex **4.6** showed a strong absorption at 10661 cm^{-1} , something which is indicative of the presence of a cobalt(I) complex, **4.6**. The UV-Vis spectrum obtained also contained bands associated with the cobalt(II) complex **3.6f** (*c.f.* 13405, 15060 and 16393 in **4.6** and 13175, 15060 and 16155 cm^{-1} in **3.6f**).



Scheme 4.19 Reduction of (dppx)CoBr₂ (**3.6f**) to produce (dppx)Co(μ₂-Br)₂Co(dppx) (**4.6**) and observed side product, (dppx)ZnBr₂ (**Zn-5.2**).

Raman spectroscopic analysis of the product, (dppx)Co(μ₂-Br)₂Co(dppx) (**4.6**), did not have a νCo-Br_{symm} band associated with the cobalt(II) starting material (283 cm⁻¹ in **3.6f**). A very weak band is observed within the Raman spectrum of **4.6** at ν = 336 cm⁻¹, which is within the expected range for a bridging bromide ligand (**Figure 4.8**). Mass spectrometric analysis (ASAP⁺) of the products of the reaction between (dppx)CoBr₂ (**3.6f**) and Zn show fragments that could correspond to either **3.6f** or **4.6** e.g. [(dppxO)₂CoBr]⁺ at *m/z* 1118.060 Da (calc. 1118.17 Da, with the correct isotope pattern) and [(dppxO)CoBr]⁺ at *m/z* 627.947 Da (calc. 628.013 Da, with the correct isotope pattern). The partial phosphine oxidation observed within the mass spectrum, *i.e.* the presence of dppxO, is likely the result of the sample briefly being exposed to air during MS measurement, as the sample of **4.6** was not run using the *inert*ASAP (*i*ASAP⁺ method). The MS spectrum also showed the presence of a zinc containing species, (dppx)ZnBr₂ (**Zn-5.2**) with [(dppxO)ZnBr]⁺ observed at *m/z* 632.944 Da (calc. 633.009 Da, with the correct isotope pattern), the structure of Zn-5.2 is shown in **Scheme 4.19**.

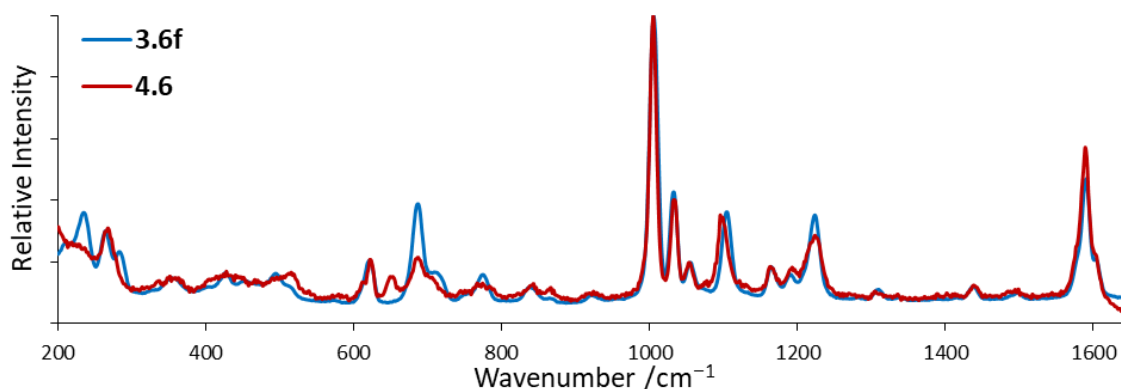
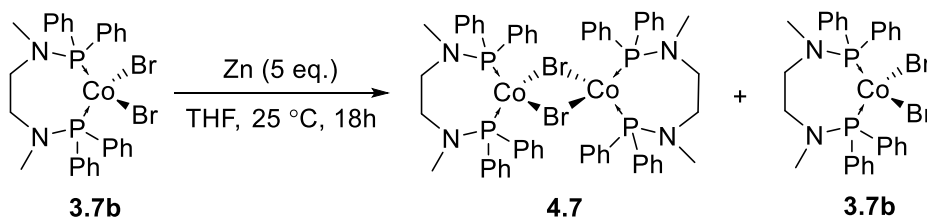


Figure 4.8 Comparison of the Raman spectra (LIR, 532 nm) obtained for (dppx)CoBr₂ **3.6f** and (dppx)Co(μ₂-Br)₂Co(dppx) **4.6**.

4.2.1.5 The Reduction of (PNNP-Ph)CoBr₂ (**3.7b**) with Zn Metal

The reduction of (PNNP-Ph)CoBr₂ (**3.7b**) with an excess of Zn metal was partially successful (**Table 4.1**: Entry 10). Both the Raman and UV-Spectroscopic analysis of the product mixture containing the

reduced species, (PNNP-Ph)Co(μ_2 -Br) $_2$ Co(PNNP-Ph) (**4.7**) showed the presence of residual **3.7b** (Scheme 4.20).



Scheme 4.20 Attempted reduction of (PNNP-Ph)CoBr $_2$ (**3.7b**) with Zn to produce (PNNP-Ph)Co(μ_2 -Br) $_2$ Co(PNNP-Ph) (**4.7**).

The UV-Spectrum obtained for the products of the reaction between **3.7b** and Zn in THF (Table 4.1: Entry 10) contains bands associated with cobalt(II) species **3.7b** along with a new band at 10764 cm $^{-1}$, which has been attributed to the presence of the complex (PNNP-Ph)Co(μ_2 -Br) $_2$ Co(PNNP-Ph) (**4.7**) (Figure 4.9). The Raman spectroscopic analysis of complex **4.7** also showed the presence of residual starting complex **3.7b** as a very weak shoulder is observed at ν 293 cm $^{-1}$ (c.f. ν Co-Br 296sh cm $^{-1}$ in **3.7b**).

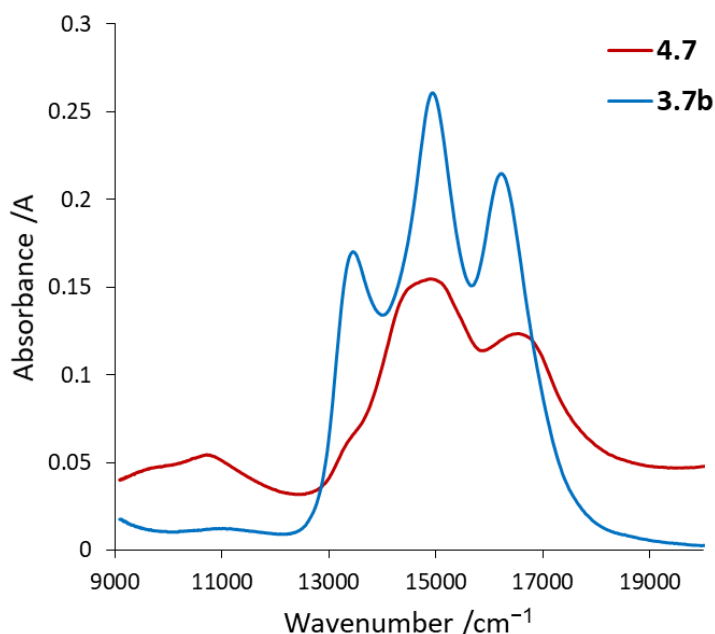
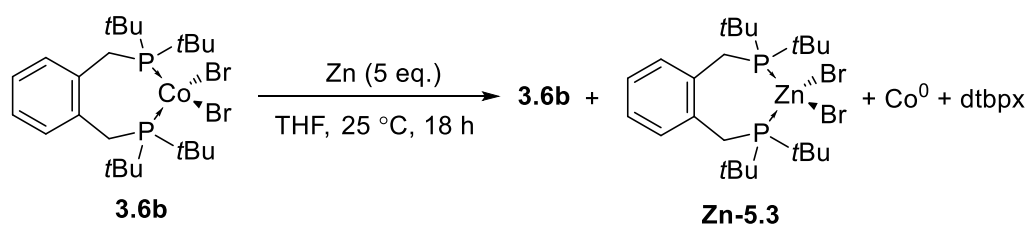


Figure 4.9: Comparison of the UV-Vis spectra (THF) of (PNNP-Ph)CoBr $_2$ (**3.7b**) and (PNNP-Ph)Co(μ_2 -Br) $_2$ Co(PNNP-Ph) (**4.7**).

4.2.1.6 The Reduction of (dtbpx)CoBr $_2$ (**3.6b**) with Zn Metal

The data in Entries 11-14 of Table 4.1 all correspond to attempts to reduce (dtbpx)CoBr $_2$ (**3.6b**) using an excess of Zn metal. When the reduction of complex **3.6b** with 5 eq. Zn was performed in THF (Table 4.1: Entry 11) over the course of 18 hours, no colour change occurred and a black, magnetic and

insoluble solid was observed to form, which was attributed to formation of cobalt(0) and some decomposition of **3.6b**. After removal of cobalt(0) *via* filtration, the remaining non-volatile components of the reaction mixture were collected. Raman spectroscopic analysis of these materials showed results very similar to those of **3.6b**, with $\nu_{\text{Co-Br}}^{\text{symm}}$ at 281 cm^{-1} (282 cm^{-1} in **3.6b**), indicating the presence of **3.6b**. The Raman spectra of the products of the reaction between (dtbpx)CoBr₂ and Zn metal over 18 hours had a sloping baseline, which was attributed to the presence of a fluorescent species. UV-Vis spectroscopic analysis of the material obtained from the reaction only indicated the presence of (dtbpx)CoBr₂ (**3.6b**). Mass spectrometric analysis of the products of this reaction shows the presence of both (dtbpx)CoBr₂ (**3.6b**) and (dtbpx)ZnBr₂ (**Zn-5.3**) with respective $[\text{M-Br}]^+$ at m/z 532.134 Da (calc. 532.143 Da, with correct isotope pattern) and 537.132 Da (calc. 537.139 Da, with correct isotope pattern). The structure of **Zn-5.3** is shown in **Scheme 4.21**.



Scheme 4.21 Observed formation of (dtbpx)ZnBr₂ (**Zn-5.3**) and cobalt(0) during reaction of (dtbpx)CoBr₂ (**3.6b**) with Zn.

³¹P NMR spectroscopic analysis of the reaction mixture obtained (**Scheme 4.21**) showed two singlet resonances at δ_{P} 24.2 and 18.4 ppm, which were attributed to free dtbpx and the diamagnetic complex (dtbpx)ZnBr₂ (**Zn-5.3**, *vide infra*), respectively. The formation of **Zn-5.3** as a major product within this reaction was confirmed through recrystallisation of the reaction mixture obtained (layering THF with hexanes), which yielded crystals suitable for X-ray diffraction. The solid-state structures of **3.6b** and **Zn-5.3** are isomorphous, as such, the resulting structure obtained from a mixture of **3.6b** and **Zn-5.3** has the general formula (dtbpx)MBr₂ where M = Zn/Co (**ZnCo-5.3**). The chemical occupancy of M in this mixed occupancy complex was found to be 3:1 Zn:Co (**Figure 4.10**). Discussion of the solid-state structures of **3.6b** and **Zn-5.3** are included in Section 4.3.2.

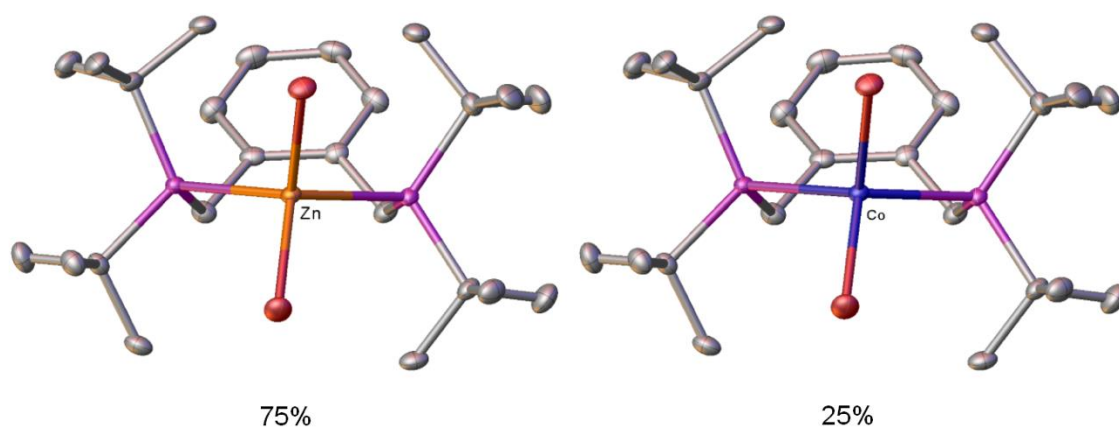
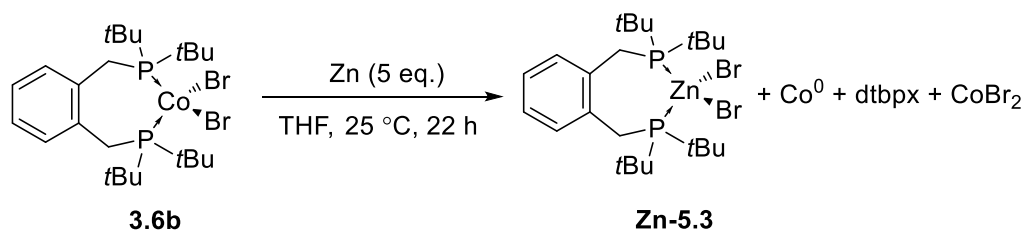


Figure 4.10 Molecular structure obtained of **ZnCo-5.3** [(dtbpx)MBr₂, M = 3:1 Zn:Co]. Zn and Co occupy the same crystallographic site: shown here side by side for clarity. ORTEPs set at 50% probability, hydrogen atoms and a second molecule present in the unit cell ($z = 2$) are omitted for clarity.

The formation of (dtbpx)ZnBr₂ (**Zn-5.3**) within this reaction between (dtbpx)CoBr₂ (**3.6b**) and Zn indicated that the diphosphine ligand, dtbpx, is being sequestered by ZnBr₂ (presumably formed *in situ*) which, in turn, suggests that the diphosphine ligand dtbpx is labile on cobalt. In order to understand the apparent ligand sequestering by zinc observed during reaction of **3.6b** with Zn, the reaction was repeated (**Table 4.1**: Entry 12) and the reaction progress monitored using UV-Vis spectroscopy by removal of aliquots of the reaction mixture at set time intervals (**Scheme 4.22**). This repeated reaction between (dtbpx)CoBr₂ (**3.6b**) and Zn, again, showed the formation of (dtbpx)ZnBr₂ (**Zn-5.3**), as determined by mass spectrometric analysis.



Scheme 4.22 Reaction of (dtbpx)CoBr₂ (**3.6b**) with Zn to produce (dtbpx)ZnBr₂ (**Zn-5.3**). The reaction progression was also followed by UV-Vis spectroscopy.

UV-Vis spectroscopy allowed monitoring of the presence of cobalt-containing species in the reaction shown in **Scheme 4.22**; zinc(II) is d^{10} and therefore no $d \leftarrow d$ transitions are expected to be observed. Immediately after addition of zinc metal to (dtbpx)CoBr₂ (**3.6b**) in THF solution, the characteristic three bands associated with Co^{II} tetrahedral ${}^4T_1({}^4F) \leftarrow {}^4A_2$ transitions disappeared and were replaced with shouldered bands at 690, 615 and 592 nm (**Figure 4.11**). After 22 hours there is no further change to

the spectrum obtained and the resulting signals were found to correspond to solvated CoBr_2 (shouldered bands at 596, 651 and 685 nm). The formation of CoBr_2 from this reaction suggests that the diphosphine, dtbpx, is labile in solution, which could contribute to the ease with which it was sequestered by zinc. The lability of dtbpx on cobalt is further suggested through observation of non-coordinated dtbpx within the ^{31}P NMR spectra obtained throughout this reaction (dtbpx, δ_{P} 24.1 ppm). In addition to the production of CoBr_2 , a black, magnetic and insoluble material was also observed to form within the reaction (**Table 4.1**: Entry 12) after 18 hours (cobalt(0)). Mass spectrometric and ^{31}P NMR spectroscopic analysis of the mixture obtained showed the presence of $(\text{dtbpx})\text{ZnBr}_2$ (**Zn-5.3**) (m/z 517.14 Da [M-Br], δ_{P} 18.4 ppm). The products of this reaction are shown in **Figure 4.11**.

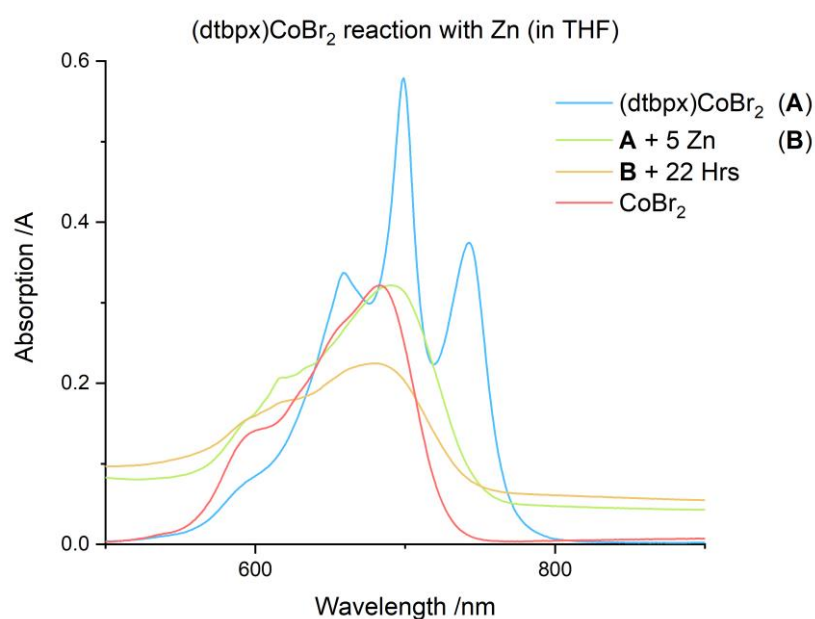
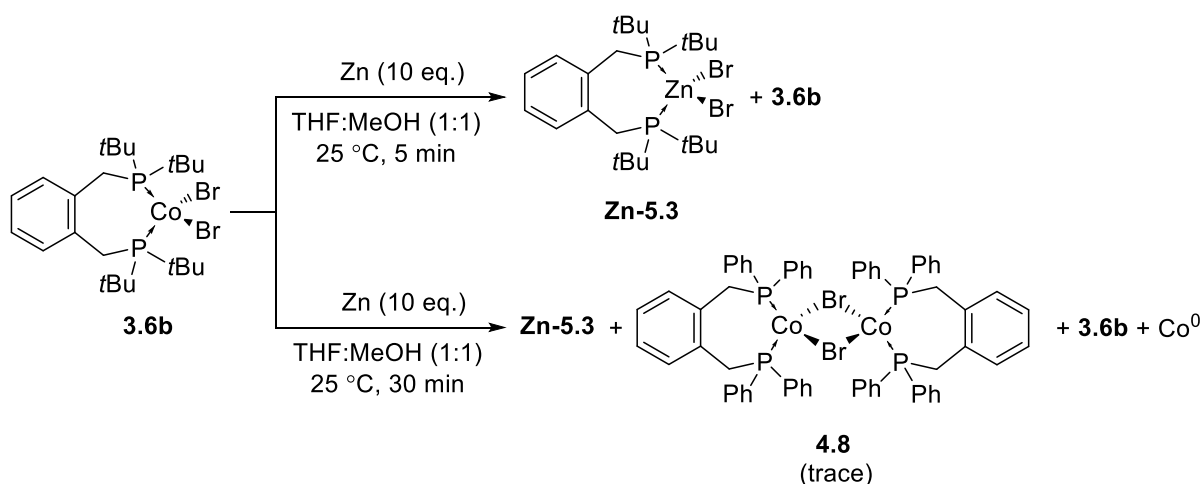


Figure 4.11 UV-Visible spectrum (THF) of reaction of $(\text{dtbpx})\text{CoBr}_2$ (**3.6b**) with 5 eq. Zn over time.

Further attempts to reduce complex $(\text{dtbpx})\text{CoBr}_2$ **3.6b** were carried out in a mixture of THF:MeOH with 10 eq. of Zn, in accordance with the conditions used by Chirik (**Table 4.1**: Entries 13 and 14). Immediately upon addition of MeOH to the reaction mixture, a colour change from blue to purple occurred, something attributed to MeOH coordination to cobalt. The reaction was then left for 5 minutes (**Table 4.1**: Entry 13) or 30 minutes (**Table 4.1**: Entry 14) before volatile components were removed, residual solids were redissolved in THF and filtered through a plug of Celite and subsequently concentrated to give a light blue/green solid. Analysis of the solids obtained from the reactions of **3.6b** with Zn in MeOH:THF by UV-Vis and Raman spectroscopies and mass spectrometry showed the presence of $(\text{dtbpx})\text{ZnBr}_2$ (**Zn-5.3**) (**Scheme 4.23**). When the reaction was left for 30 minutes (**Table 4.1**: Entry 14), trace amounts of $(\text{dtbpx})\text{Co}(\mu_2\text{-Br})_2\text{Co}(\text{dtbpx})$ (**4.8**) were observed to form.



Scheme 4.23 Reaction of (dtbpx)CoBr₂ (**3.6b**) with Zn in THF:MeOH in 5 minutes to produce (dtbpx)ZnBr₂ (**Zn-5.3**) or 30 minutes to produce **Zn-5.3** and trace amounts of (dtbpx)Co(μ₂-Br)₂Co(dtbpX) (**4.8**).

The Raman spectrum of the solid obtained from the reaction between (dtbpx)CoBr₂ (**3.6b**) and Zn in MeOH:THF for 5 minutes (**Scheme 4.23**: top) showed a weak band at 282 cm⁻¹ (νCo-Br_{symm}, **3.6b**). The mass spectrum of the products obtained which was a light blue/green solid showed [M-Br]⁺ ions for both **3.6b** and **Zn-5.3** at *m/z* 232.119 Da and 237.119 Da, respectively. UV-spectroscopic analysis of this solid shows an identical spectrum to that obtained for (dtbpx)CoBr₂ (**3.6b**); no bands corresponding to a cobalt(I) species were observed (**Figure 4.12**). While no cobalt(I) species were observed by UV-Vis spectroscopic analysis, the results were promising as the major Co species in the products was **3.6b** and not CoBr₂, which suggests that the diphosphine ligand, dtbpx, is less labile in MeOH:THF mixture when compared to THF.

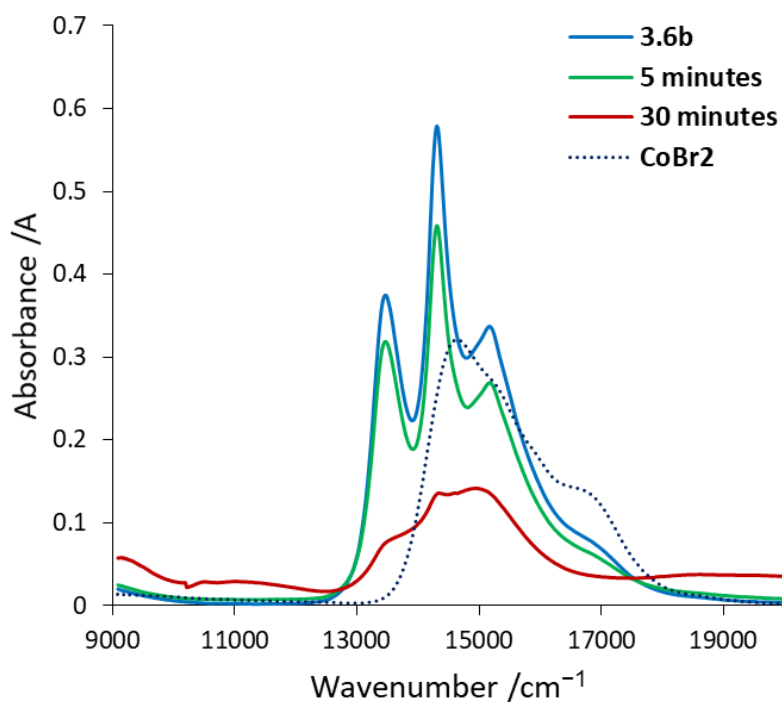


Figure 4.12 Comparison of the UV-Vis spectra (THF) after reaction of (dtbpx)CoBr₂ (**3.6b**) with Zn in MeOH:THF after 5 minutes (**Table 4.1**:Entry 13) and 30 minutes (**Table 4.1**:Entry 14).

The reaction of (dtbpx)CoBr₂ (**3.6b**) and Zn in THF:MeOH was repeated and left for 30 minutes (**Table 4.1**: Entry 14), after which time a black and magnetic solid was observed (cobalt(0), **Scheme 4.23**: bottom). Solids were removed by filtration and volatile components were removed *in vacuo* to yield a blue/green solid. Crystals suitable for X-ray diffraction were grown through layering a solution of the solid products in DCM with hexanes; the solid-state structure obtained was that of (dtbpx)CoBr₂ (**3.6b**). Raman spectroscopic analysis of the bulk material obtained from this reaction between **3.6b** and Zn showed a band at 279 cm⁻¹ which corresponds to $\nu_{\text{Co-Br}}^{\text{sym}}$ in **3.6b** (**Figure 4.13**). The Raman spectrum obtained of the products has a sloping baseline, which is attributed to the presence of a fluorescent species, in this case, (dtbpx)ZnBr₂ (**Zn-5.3**). The formation of complex **Zn-5.3** and the presence of unreacted **3.6b** from this reaction were confirmed by MS analysis with [M-Br]⁺ at m/z 537.125 Da (**Zn-5.3**) and 532.129 Da (**3.6b**). However, UV-Vis spectroscopic analysis of the products obtained from the reaction between **3.6b** and Zn in MeOH:THF for 30 minutes (**Figure 4.12**) showed a weak absorbance at 11161 cm⁻¹, with a band rising into the near-IR region, which could indicate the presence of a cobalt(I) species, (dtbpx)Co(μ_2 -Br)₂Co(dtbpx) (**4.8**) as previously observed cobalt(I) species (**4.1-4.7**) also contained bands in this region of the UV-Vis.

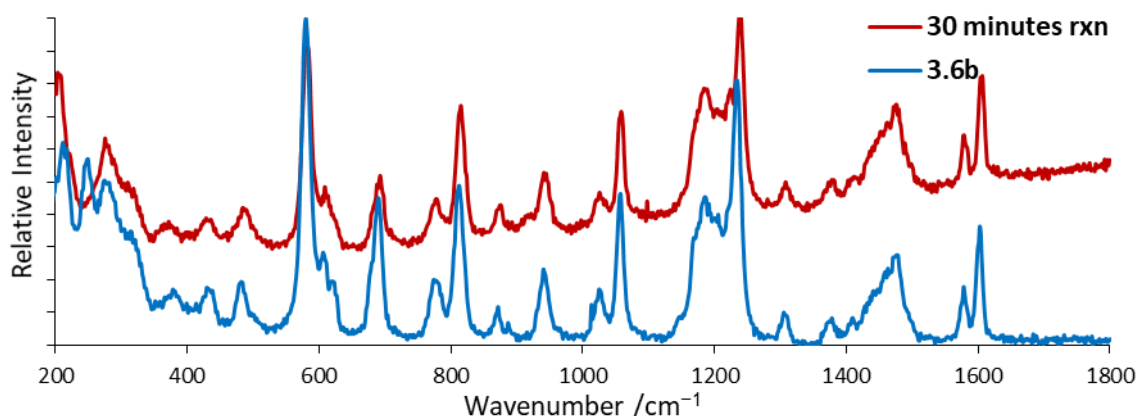
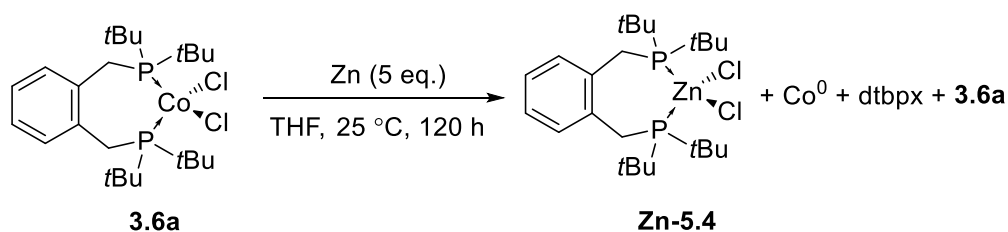


Figure 4.13: Comparison of the Raman spectra obtained for (dtbpx)CoBr₂ (**3.6b**) and reaction mixture obtained from the reaction between **3.6b** and Zn in MeOH:THF for 30 minutes (**Table 4.1:** Entry 14).

4.2.1.6 The Reaction of (dtbpx)CoCl₂ (**3.6a**) with Zn Metal

The reaction of (dtbpx)CoCl₂ (**3.6a**) with an excess of Zn in THF was performed (**Scheme 4.24**). No changes were observed for this reaction until a period of 120 hours had passed, after which time a black, magnetic and insoluble material formed, presumably cobalt(0). MS (ASAP⁺) analysis of the solids obtained from the reaction of **3.6a** with Zn showed unreacted starting material within the reaction mixture, *e.g.* [M-Cl]⁺ at *m/z* 488.184 Da (calc. 488.194 Da, with the correct isotope pattern). The presence of complex **3.6a** was corroborated by unit cell comparisons of single crystals obtained after a sample of the reaction mixture was recrystallised. A ³¹P{¹H} NMR spectrum of the reaction mixture had two peaks at δ_p 24.3 and 21.9 ppm, corresponding to dtbpx and (dtbpx)ZnCl₂ (**Zn-5.4**), respectively (*vide infra*).



Scheme 4.24 Reaction of (dtbpx)CoCl₂ (**3.6a**) with Zn in THF to produce (dtbpx)ZnCl₂ (**Zn-5.4**), dtbpx and cobalt(0).

In several of the reduction attempts of (P[^]P)CoX₂ complexes with Zn, there was some formation of by-products, cobalt(0) (**Table 4.1:** Entries 5, 11, 12, 14 and 15) or (P[^]P)ZnX₂ complexes (**Zn-5.1** – **Zn-5.4**, **Table 4.1:** Entries 6, 9, 11-15) observed. The following section describes additional attempted single-electron reductions of (P[^]P)CoX₂ complexes (**3.3-3.10**) with Zn where no cobalt(I) species were formed, and the reaction produced Co⁰_(s) or (P[^]P)ZnX₂ species as the major products of reaction.

4.2.2 Reaction of Zn with (P[^]P)CoX₂ Complexes Without Formation of Cobalt(I).

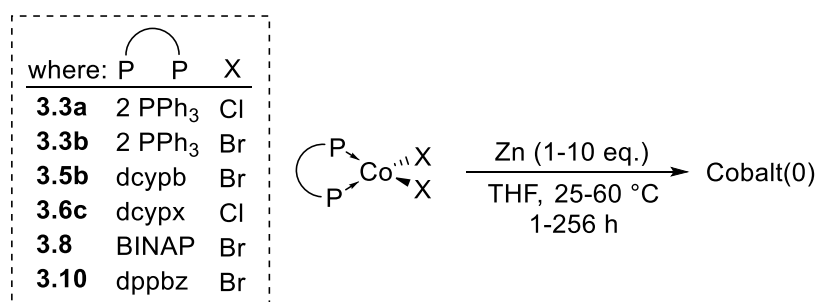
In many of the attempted reductions of (P[^]P)CoX₂ complexes (**3.3-3.10**), no cobalt(I) complex could be identified within the product mixture. These reactions were all carried out in THF with 1-10 eq. of Zn dust. A summary of each attempt is given in **Table 4.2**.

Table 4.2 Summary of attempted reductions of (P[^]P)CoX₂ complexes **3.3-3.10** by Zn in THF where a cobalt(I) complex was not the main reaction product.

Entry	(P [^] P)CoX ₂	Eq. Zn	Time /h	Temp. /°C	Outcome
1	3.3a (PPh ₃) ₂ CoCl ₂	5	256	25	Co ⁰ _(s)
2	3.3a (PPh ₃) ₂ CoCl ₂	1	48	60	Co ⁰ _(s)
3	3.3b (PPh ₃) ₂ CoBr ₂	10	16	25	Co ⁰ _(s)
4	3.3b (PPh ₃) ₂ CoBr ₂	5	1	25	Co ⁰ _(s)
5 ^a	3.4b “(dppe)CoBr ₂ ”	5	288	25	3.4b : no reaction
6 ^{a,b}	3.4b “(dppe)CoBr ₂ ”	5	1	25	3.4b : no reaction
7	3.5b (dcypb)CoBr ₂	5	144	40 ^c	Co ⁰ _(s)
8	3.6c (dcypx)CoCl ₂	10	120	25	Co ⁰ _(s)
9	3.6g (diprpx)CoBr ₂	5	18	25	3.6g, Zn-5.5
10	3.8 (BINAP)CoBr ₂	5	56	25	Co ⁰ _(s)
11	3.9 (Xantphos)CoBr ₂	5	57	25	3.9 : no reaction
12 ^d	3.10 “(dppbz)CoBr ₂ ”	5	18	25	Co ⁰ _(s)
13 ^d	3.10 “(dppbz)CoBr ₂ ”	1.2	16	25	(dppbz)ZnBr ₂ , 3.10

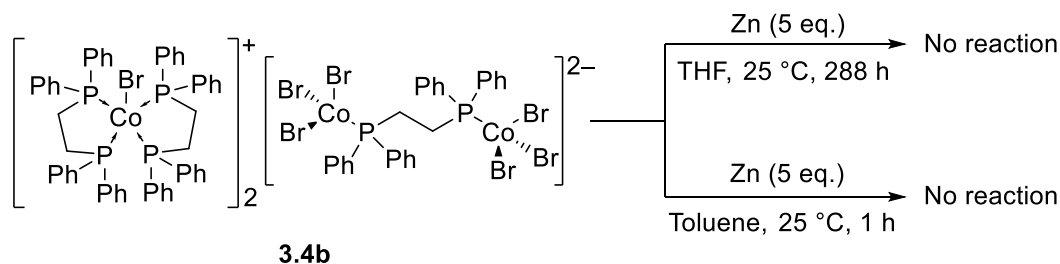
^a[(dppe)₂CoBr₂][Br₃Co(μ₂-dppe)CoBr₃], ^bReaction carried out in toluene, ^cReaction heated to aid solubility of **3.5b**, ^d[(dppbz)₂CoBr₂][Co₂Br₆].

In many of the reactions of (P[^]P)CoX₂ complexes with Zn outlined in **Table 4.2**, large quantities of magnetic, black and insoluble particulates of cobalt(0) were observed to form (**Table 4.2**: Entries 1-4, 7, 8, 10 and 12) as a result of over reduction of the cobalt(II) starting materials (**3.3a**, **3.3b**, **3.5b**, **3.6c**, **3.8** and **3.10**). As the quantity of pyrophoric cobalt(0) produced within these reactions was significant, suggesting the majority of the cobalt-containing species had undergone over-reduction, no spectroscopic characterisation was undertaken on the reaction mixtures obtained of these reactions (**Scheme 4.25**).



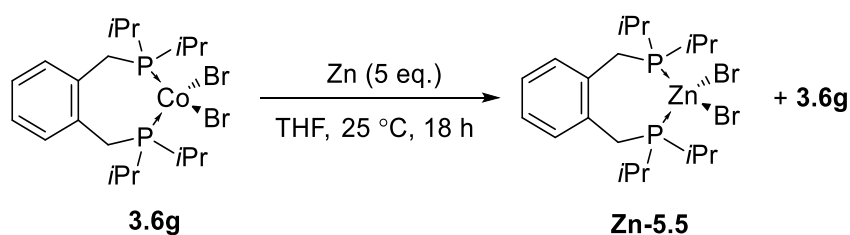
Scheme 4.25 Observed formation of cobalt(0) upon treatment of various (P[^]P)CoX₂ complexes (detailed in scheme) with Zn metal.

Entries 5 and 6 in **Table 4.2** correspond to reduction attempts of [(dppe)₂CoBr]₂[Br₃Co(μ₂-dppe)CoBr₃] (**3.4b**) with 5 equivalents of Zn (**Scheme 4.26**). When the reaction between **3.4b** and Zn was performed in THF (**Table 4.2**: Entry 5), no colour change was observed to occur over the course of 288 hours. After this time, residual Zn was removed from the reaction by filtration and volatile components were removed *in vacuo* to yield a blue solid. The Raman spectrum obtained of the reaction mixture had a fluorescent component, raising the baseline and resulting in weak signals being observed. However, a weak band at 345 cm⁻¹ was observed, which was attributed to the anion in **3.4b** (*c.f.* bands associated with νCo-Br in **3.4b**: 254 and 300 cm⁻¹). The fluorescence associated with the Raman spectrum of the products obtained from the reaction of **3.4b** and Zn is indicative of the presence of a (dppe)ZnBr₂ complex, however, MS analysis of the mixture only reveals the presence of the starting material, **3.4b**, *e.g.* [(dppe)₂CoBr]⁺ at *m/z* 934.077 Da (calc. 934.222 Da, with the correct isotope pattern). It was hypothesised that the poor solubility of **3.4b** in THF was the cause of the lack of reaction observed and so the reduction of **3.4b** with 5 eq. Zn metal was repeated in toluene (**Table 4.2**: Entry 6). This reaction of complex **3.4b** with Zn in toluene also gave a Raman spectrum that showed the presence of complex **3.4b** as evidenced by weak bands at ν253, 309 and 350 cm⁻¹. Mass spectrometric analysis (ASAP⁺) of the products of the attempted reduction of **3.4b** with Zn in Toluene (**Table 4.2**: Entry 6) only showed ions corresponding to oxidised dppe ligand, *e.g.* [dppeO₂-H]⁺ at *m/z* 429.006 Da (calc. 429.118 Da).



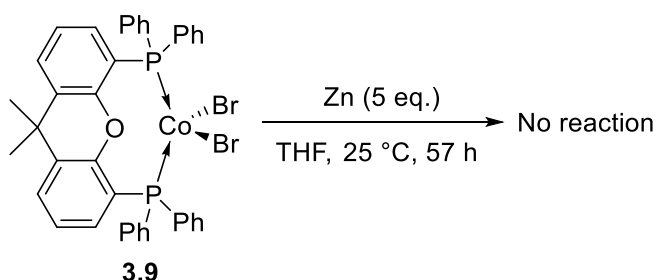
Scheme 4.26 Attempted reactions of [(dppe)₂CoBr]₂[Br₃Co(μ₂-dppe)CoBr₃] (**3.4b**) with Zn metal in THF or Toluene.

The reduction of (diprpx)CoBr₂ (**3.6g**) with an excess of Zn metal was carried out under the conditions outlined in **Table 4.2**: Entry 9. Raman spectroscopic analysis of the solid obtained showed a shouldered band at $\nu_{298} \text{ cm}^{-1}$ (*c.f.* **3.6g** $\nu_{\text{Co-Br}_{\text{symm}}} 296 \text{ cm}^{-1}$). UV-Vis spectroscopic analysis of the solids obtained showed the characteristic three peaks associated with a *pseudo*-tetrahedral cobalt(II) complex with energies matching those obtained for complex **3.6g**. Residual **3.6g** was also observed in the mass spectrum obtained (m/z 476.056 Da, $[\text{M-Br}]^+$, calc. 476.081 Da with the correct isotope pattern) along with a zinc species with m/z 481.053 Da ($[(\text{diprpx})\text{ZnBr}]^+$, calc. 481.077 Da with the correct isotope pattern) attributed to the formation of (diprpx)ZnBr₂ (**Zn-5.5**) (**Scheme 4.27**).



Scheme 4.27 Formation of (diprpx)ZnBr₂ (**Zn-5.5**) from treatment of (diprpx)CoBr₂ (**3.6g**) with Zn.

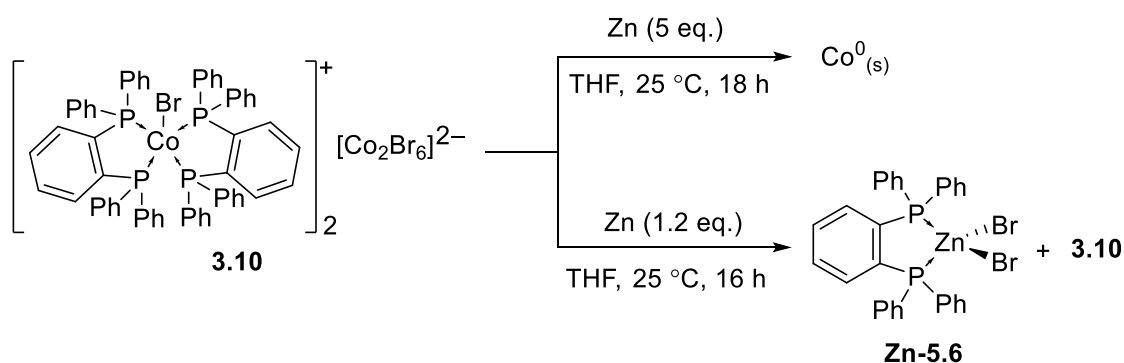
When (xantphos)CoBr₂ (**3.9**) was treated with 5 eq. of Zn metal (**Table 4.2**: Entry 11), no reaction was observed to occur even after 57 hours (**Scheme 4.28**). Raman spectroscopic analysis of the solids obtained after work up of the reaction showed the presence of complex **3.9** (*c.f.* observed: 273 cm^{-1} , **3.9** $\nu_{\text{Co-Br}_{\text{symm}}} 275 \text{ cm}^{-1}$). The starting complex **3.9** was also observed in the mass spectrum obtained of the solids obtained of the reaction with $[\text{M-Br}]^+$ at m/z 716.081 Da (calc. 716.044 Da, with the correct isotope pattern). No indication of any other xantphos-containing species was observed by MS.



Scheme 4.28 Attempted reduction of (xantphos)CoBr₂ (**3.9**) with Zn metal in THF.

The initial attempt to reduce $[(\text{dppbz})_2\text{CoBr}][\text{Co}_2\text{Br}_6]$ (**3.10**) with 5 eq. of Zn in THF resulted in decomposition into Co⁰(s) (**Table 4.2**: Entry 12). The reaction was therefore repeated with 1.2 eq. of Zn (**Table 4.2**: Entry 13). The Raman spectrum of the solids obtained from the reaction had a raised baseline due to the presence of a fluorescent species. However, weak bands were observed at 243,

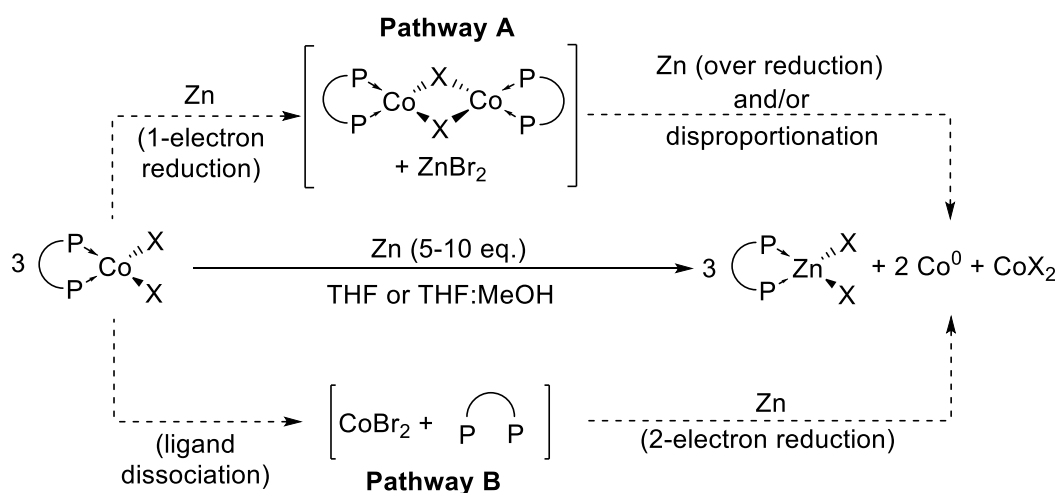
300 and 346 cm^{-1} , which were attributed to the starting complex **3.10** ($\nu_{\text{Co-Br}}$ 250, 298, 345 and 373 cm^{-1}). Mass spectrometric analysis of the solids obtained from reaction of **3.10** with 1.2 eq. of Zn revealed both **3.10** ($[\text{M}]^+$ m/z 1030.081 Da (calc. 1030.122 Da with the correct isotope pattern) and $(\text{dppbz})\text{ZnBr}_2$ (**Zn-5.6**) ($[\text{M-Br}]^+$ m/z 588.956 Da (calc. 588.983 Da with correct isotope pattern) (**Scheme 4.29**). No resonances were observed by ^{31}P NMR spectroscopy due to the presence of the paramagnetic complex, **3.10**.



Scheme 4.29 Reaction of **3.10** with Zn metal to produce $\text{Co}^0_{(s)}$ (**Table 4.2**: Entry 12) or $(\text{dppbz})\text{ZnBr}_2$ (**Zn-5.6**) (**Table 4.2**: Entry 13).

4.2.3 Summary of the Observed Reactions of Zn with $(\text{P}^{\wedge}\text{P})\text{CoX}_2$ Complexes

For many of the reduction attempts of a wide variety of $(\text{P}^{\wedge}\text{P})\text{CoX}_2$ complexes with Zn studied herein, insoluble, magnetic, black particulates (cobalt(0)) were observed to form, *i.e.* when $(\text{P}^{\wedge}\text{P}) = 2 \text{PPh}_3$, dppb, dcyph, dtbpx, BINAP and dppbz and when $\text{X} = \text{Cl}$ or Br (**Table 4.1**: Entries 5, 11, 12, 14 and 15 and **Table 4.2**: Entries 1-4, 7, 8, 10 and 12). The formation of cobalt(0) from over-reduction of these $(\text{P}^{\wedge}\text{P})\text{CoX}_2$ complexes along with the observation of the formation of $(\text{P}^{\wedge}\text{P})\text{ZnX}_2$ complexes (**Zn-5.1 - Zn-5.6**) suggested that zinc metal within the reaction mixture was acting to reduce the cobalt species present by two electrons, *i.e.* over reduction, rather than the desired single-electron reduction. It is possible that the desired one-electron reduction to produce cobalt(I) complexes with general formula $[(\text{P}^{\wedge}\text{P})\text{Co}(\mu_2\text{-Br})_2\text{Co}(\text{P}^{\wedge}\text{P})]$ did occur within these reactions, but then underwent further reduction by Zn to release free diphosphine ligand and metallic cobalt. Any cobalt(I) species produced *in situ* may also be unstable and undergo disproportionation to release metallic cobalt, $(\text{P}^{\wedge}\text{P})\text{CoX}_2$ complex and free ligand that can then be sequestered by ZnX_2 , which is formed during the reaction (**Scheme 4.30**: Pathway A). It is also possible that the lability of the diphosphine ligand on cobalt plays a large role in the formation of $(\text{P}^{\wedge}\text{P})\text{ZnX}_2$ species. Ligand dissociation from $(\text{P}^{\wedge}\text{P})\text{CoX}_2$ complexes would leave liberated CoBr_2 susceptible to over reduction by Zn to produce ZnX_2 (which can pick up free diphosphine) and metallic cobalt (**Scheme 4.30**: Pathway B).



Scheme 4.30 Proposed routes for the formation of $(P^P)ZnX_2$, Co^0 , CoX_2 and free diphosphine from the reaction of $(P^P)CoX_2$ excess Zn metal.

If Pathway A (**Scheme 4.30**) is the major pathway occurring to produce $(P^P)ZnX_2$ complexes and cobalt(0) from the starting material $(P^P)CoX_2$ complexes, then it could be imagined that performing the single-electron reduction of $(P^P)CoX_2$ complexes in the presence of a stabilising, neutral donor ligand could stabilise the generated cobalt(I) complex. Consequently, several attempts were made to form cobalt(I) complexes with general formula $(P^P)CoX(L)$, where $L = 1$ -hexene or PPh_3 .

4.2.4 Attempted $(P^P)CoX_2$ Single Electron-reductions in the Presence of a Stabilising Ligand

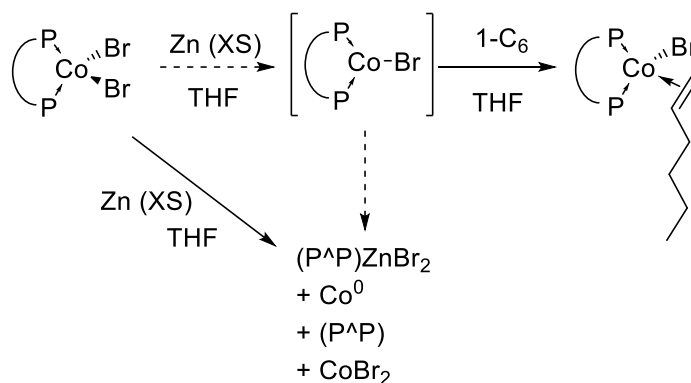
The over-reduction observed following the attempted reductions of $(P^P)CoX_2$ with an excess of Zn metal could be the result of inherent instability of the postulated cobalt(I) intermediate. As such, several attempts were made in an effort to stabilise this possible cobalt(I) intermediate (**Scheme 4.31**); the zinc reductions were carried out in the presence of a neutral donor ligand (PPh_3 or 1-hexene). A summary of the attempted reductions of $(diprpx)CoBr_2$ (**3.6b**), $(dtbpx)CoBr_2$ **3.6g** and $[(dppbz)_2CoBr]_2[Co_2Br_6]$ (**3.10**) in the presence of a neutral donor ligand is shown in **Table 4.3**

Table 4.3 Attempted Reductions of $(P^P)CoBr_2$ complexes (THF) in the presence of a neutral donor ligand, L ($L = PPh_3, C_2H_4$).

Entry	$(P^P)CoBr_2$	Eq. Zn	L (eq.)	Products
1	3.6g $(diprpx)CoBr_2$	5	1-hexene (1)	3.6g , $diprpx$
2	3.6b $(dtbpx)CoBr_2$	5	1-hexene (1)	3.6b , $dtbpx$, Zn-5.3
3 ^a	3.10 " $(dppbz)CoBr_2$ "	5	1-hexene (1)	3.10 , Zn-5.6
4	3.6b $(dtbpx)CoBr_2$	1.2	PPh_3 (1)	3.6b , $Co^0_{(s)}$
5	3.6b $(dtbpx)CoBr_2$	1.2	PPh_3 (2)	3.6b , Zn-5.3 , $Co^0_{(s)}$

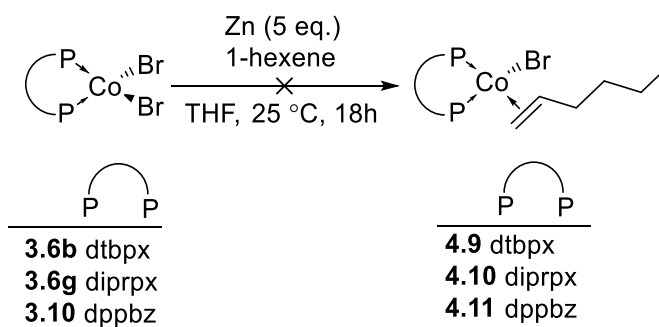
^a $[(dppbz)_2CoBr]_2[Co_2Br_6]$

Cobalt diphosphine complexes have been shown to be active towards olefins within the literature,^{7,9} therefore, 1-hexene was chosen as a possible stabilising ligand towards any cobalt(I) intermediates formed during the reaction of (P[∧]P)CoBr₂ with Zn. It was hypothesised that 1-hexene could coordinate and stabilise any low coordinate, unstable cobalt(I) intermediates produced during the reaction, as shown in **Scheme 4.31**.



Scheme 4.31 Proposed stabilisation of low coordinate cobalt(I) intermediate by 1-hexene coordination.

Attempted stabilisation of cobalt(I) complexes with 1-hexene was performed with a variety of (P[∧]P)CoBr₂ complexes (**3.6b**, **3.6g**, **3.10**), **Table 4.3**: Entries 1, 2, 3. However, in all cases, no 1-hexene-containing species were isolated (**Scheme 4.32**).

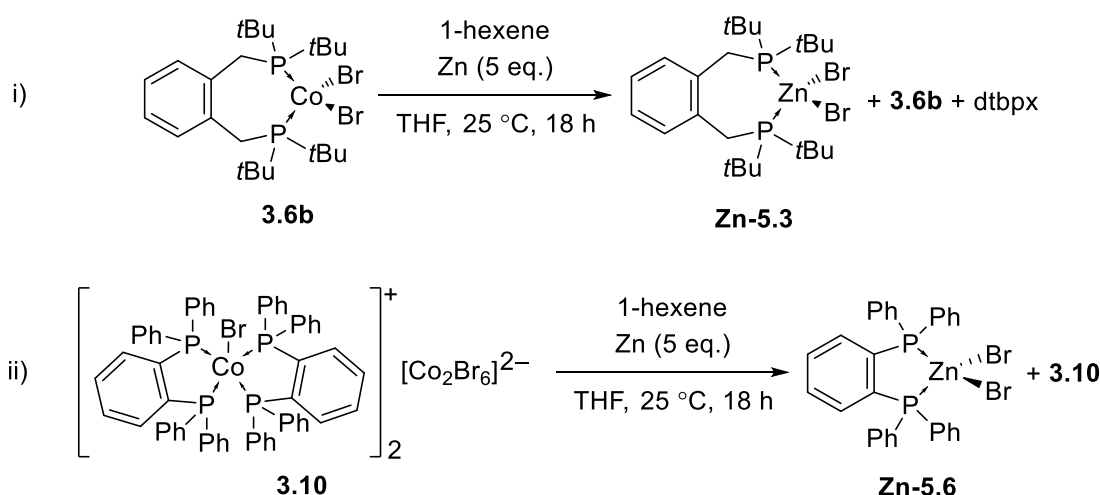


Scheme 4.32 Attempted synthesis of (P[∧]P)(1-C₆)CoBr complexes.

The attempted reduction of (diprpx)CoBr₂ (**3.6g**) in the presence of 1-hexene (**Table 4.3**: Entry 1) was unsuccessful. The mass spectrum (ASAP⁺) of the material gained post reaction showed only the presence of **3.6g** (m/z 555.970 Da [M]⁺). Additionally, no change to the Raman spectra of the reaction mixture, when compared to that of the starting material, **3.6g**, was observed. A ³¹P NMR spectrum obtained of the product mixture (following removal of volatile components under vacuum) showed a

resonance at $\delta_P -4.3$ ppm (*c.f.* free diprpx δ_P 5.2 ppm).²⁵ This resonance was attributed to the formation of (diprpx)ZnBr₂ (**Zn-5.5**).

Attempted zinc reduction of complexes (dtbpx)CoBr₂ (**3.6b**) and [(dppbz)₂CoBr]₂[Co₂Br₆] (**3.10**) in the presence of 1-hexene (**Table 4.3**: Entries 3 and 4, respectively) both resulted in the formation of (P[^]P)ZnBr₂ (**Zn-5.3** where (P[^]P) = dtbpx and **Zn-5.6** where (P[^]P) = dppbz) (**Scheme 4.33**). In the case of the attempted reduction of (dtbpx)CoBr₂ (**3.6b**) (**Table 4.3**: Entry 2), the mass spectrum (ASAP⁺) of the product mixture obtained contained fragments corresponding to both (dtbpx)CoBr₂ (**3.6b** m/z 532.117 Da [(dtbpx)CoBr]⁺) and (dtbpx)ZnBr₂ (**Zn-5.3** m/z 536.109 Da [(dtbpx)ZnBr-H]⁺), indicating the formation of **Zn-5.3** (**Scheme 4.33i**). Raman spectroscopic analysis of the product mixture indicated the presence of **3.6b** ($\nu_{\text{Co-Br}_{\text{symm}}}$ 284 cm⁻¹) and an additional fluorescent species. The complex **Zn-5.3** fluoresced under laser excitation and so the fluorescent species present in the product mixture has been attributed to the presence of **Zn-5.3**. Finally, complex **Zn-5.3** was also observed in the ³¹P NMR spectrum obtained of the products of the reaction between **3.6b** and Zn in the presence of 1-hexene (**Zn-5.3** δ_P 18.8 ppm) along with uncoordinated dtbpx (δ_P 24.5 ppm).

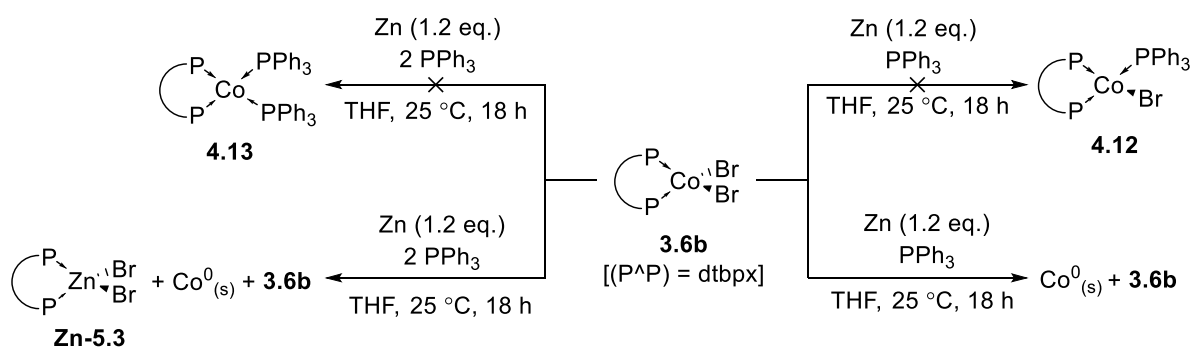


Scheme 4.33 Observed reaction between (P[^]P)CoX₂ complexes i) (dtbpx)CoBr₂ (**3.6b**) and ii) [(dppbz)₂CoBr]₂[Co₂Br₆] (**3.10**) with Zn in the presence of 1-hexene.

The mass spectrum of the solids obtained from reaction of [(dppbz)₂CoBr]₂[Co₂Br₆] (**3.10**) with Zn in the presence of 1-hexene (**Table 4.3**: Entry 3) presented ions corresponding the partial oxidation products of [(dppbz)₂CoBr]₂[Co₂Br₆] (**3.10**) and (dppbz)ZnBr₂ (**Zn-5.6**), for example, m/z 1062.059 Da [(dppbzO)₂CoBr]⁺ and m/z 604.948 Da [(dppbzO)ZnBr]⁺ (**Scheme 4.33ii**). The source of oxidation as inferred from the presence of the partially oxidised diphosphine ligand, dppbzO, within the ASAP MS spectrum is likely the result of the sample used for MS analysis being briefly exposed to air as this data was collected using standard ASAP techniques. No signals were observed in the ³¹P NMR spectrum

collected of this reaction and the Raman spectrum gathered included bands associated with Co-Br_{symm} stretch in [(dppbz)₂CoBr]₂[Co₂Br₆] (**3.10**) where $\nu_{\text{Co-Br}} = 250 \text{ cm}^{-1}$.

In addition to attempting to stabilise the postulated low-coordinate cobalt(I) intermediate with the presence of 1-hexene, attempts were also made to stabilise the proposed “(dtbpx)CoBr” species by performing the reduction of (dtbpx)CoBr₂ (**3.6b**) in the presence of 1 or 2 equivalents of triphenylphosphine (**Table 4.3**: Entries 4 and 5, 1 or 2 equivalents, respectively). In both cases, cobalt(0) was produced during the reaction, suggesting 2-electron reduction occurred under these reaction conditions (**Scheme 4.34**). Where 1 equivalent of triphenylphosphine was present during the reaction (**Table 4.3**: Entry 4), MS analysis and Raman and UV-Vis spectroscopic analysis of the product showed unreacted **3.6b** e.g. [M-Br]⁺ *m/z* 532.121 Da, $\nu_{\text{Co-Br}_{\text{symm}}} = 275 \text{ cm}^{-1}$ and $\lambda = 659, 694, 738 \text{ nm}$ (**3.6b**).



Scheme 4.34 Two-electron reduction of (dtbpx)CoBr₂ (**3.6b**) with Zn in the presence of triphenylphosphine (1 or 2 equivalents) to produce cobalt(0) and (dtbpx)ZnBr₂ (**Zn-5.3**).

Where two equivalents of triphenylphosphine were present during the reduction of (dtbpx)CoBr₂ (**3.6b**) (**Table 4.3**: Entry 5), unreacted **3.6b** remained (*m/z* 532.121 Da [(M-Br)⁺] and (dtbpx)ZnBr₂ (**Zn-5.3**) was again observed to form during the reaction (*m/z* 537.122 Da [M-Br]⁺). The mass spectrum obtained of the product from the reaction of **3.6b** with zinc in the presence of two equivalents of triphenylphosphine also contained a fragment with *m/z* 754.137 Da which has the correct isotope pattern to correspond to [(dtbpx)(PPh₃)CoBr-tBu+H+O]⁺ (calc. 754.167 Da) (**Figure 4.14**). However, as no evidence for a new cobalt-containing species was observed in the UV-Vis spectrum obtained of the reaction products ($\lambda_{\text{max}} = 660, 699, 744 \text{ nm}$; **3.6b**), this ion observed in the MS was likely the result of ionisation and recombination within the mass spectrometer.

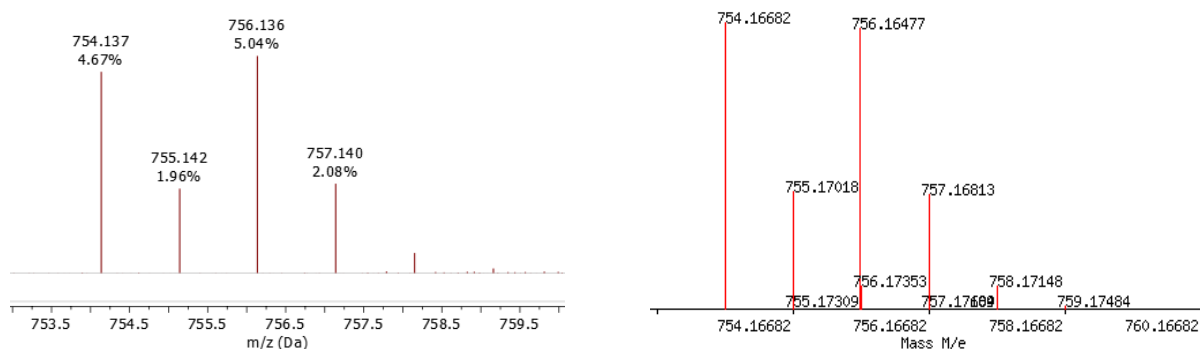
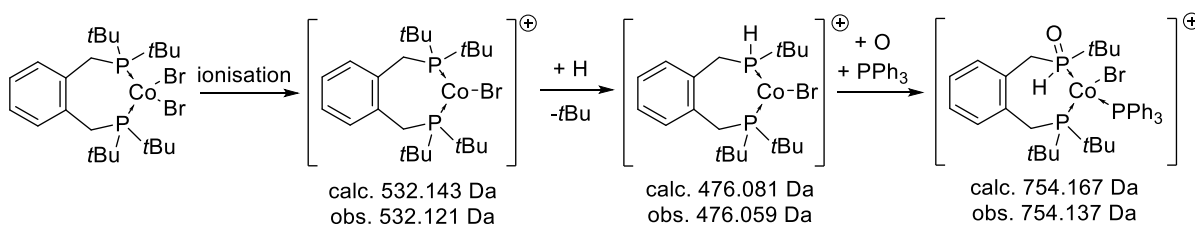


Figure 4.14 Observed (LHS) and calculated²⁶ (RHS) isotope patterns for $[\text{C}_{38}\text{H}_{51}\text{BrCoOP}_3]^+$

The fragment shown in **Figure 4.14** contains oxygen and is likely the result of introduction of a water impurity to the sample, either from the instrument (residual aqueous lock mass solution) or from brief exposure to the atmosphere during sample introduction. A mechanism of formation and proposed structure for the fragment with m/z 754.137 Da is shown in **Scheme 4.35** and is based upon additional observed ions within the mass spectrum obtained.



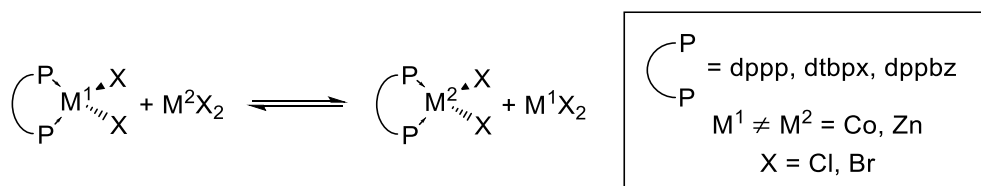
Scheme 4.35 Proposed structure and mechanism of formation of $[(\text{dtbpx})(\text{PPh}_3)\text{CoBr-tBu+H+O}]^+$ within the mass spectrometer.

Attempts, therefore, to stabilise the postulated $(\text{P}^{\wedge}\text{P})\text{Co}(\text{I})$ intermediate in pathway A (**Scheme 4.30**) in the presence of a neutral donor ligand were unsuccessful. With this in mind, it is of great interest to understand the lability of diphosphine ligands on cobalt, which appears to be a significant factor in determining the success of a reduction using Zn. The reaction of ZnX_2 species with diphosphines and with $(\text{P}^{\wedge}\text{P})\text{CoX}_2$ complexes was therefore explored. A small series of $(\text{P}^{\wedge}\text{P})\text{ZnX}_2$ complexes was synthesised and the apparent diphosphine ligand-exchange reaction between cobalt and zinc explored.

4.3 Synthesis of $(\text{P}^{\wedge}\text{P})\text{ZnX}_2$ Complexes

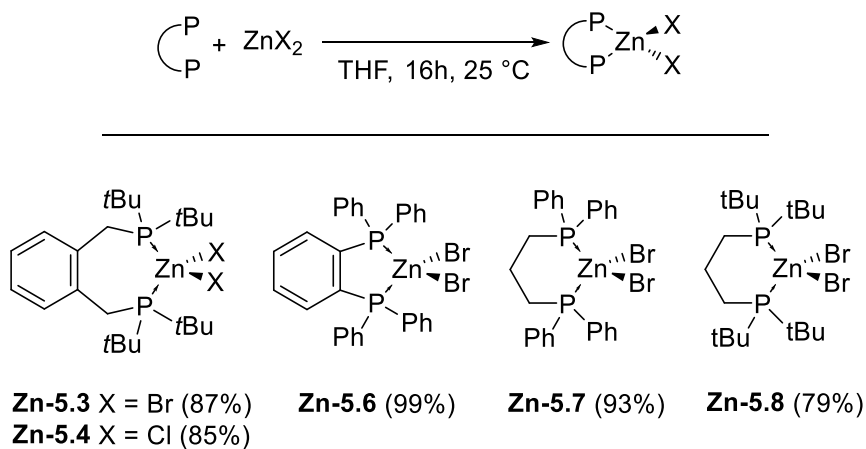
After the observed formation of $(\text{dtbpx})\text{ZnX}_2$ ($\text{X} = \text{Cl}, \text{Br}$) in the reactions described above (Section 4.2), it was of interest to investigate the ligand-exchange reactions between $(\text{P}^{\wedge}\text{P})\text{M}^1\text{X}_2$ ($\text{M}^1 = \text{Co}, \text{Zn}, \text{X} = \text{Br}$,

Cl, {P[^]P} = dtbpx, dppx, dppp, dtbpp, dppbz) and M²X₂ (M² = Co, Zn, X = Cl, Br). It is proposed that there exists an equilibrium of the diphosphine ligand-exchange between cobalt(II) and zinc(II) dihalide complexes.



Scheme 4.36 Ligand exchange reactions between equivalent Co and Zn complexes.

To investigate this potential dynamic exchange of diphosphine between MX₂ (M = Co, Zn) complexes, a series of (P[^]P)ZnX₂ complexes were therefore synthesised. This series of (P[^]P)ZnX₂ [(P[^]P) = dtbpx, dppp, dtbpp, dppbz and X = Cl, Br] complexes (**Zn-5.3**, **Zn-5.4**, **Zn-5.6-8**) were synthesised in accordance to the procedure shown in **Scheme 4.37**. These diphosphine zinc(II) halide complexes (**Zn-5.3**, **Zn-5.4**, **Zn-5.6-8**) were isolated in excellent yields (79-99%) and were characterised using ¹H, ¹³C{¹H} and ³¹P NMR and Raman spectroscopies and mass spectrometry (ASAP⁺).

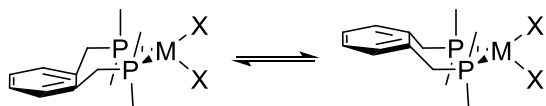


Scheme 4.37 Synthesis of (P[^]P)ZnX₂ complexes (**Zn-5.3**, **Zn-5.4**, **Zn-5.6-8**). Isolated yields in parenthesis.

4.3.1 Spectroscopic and Spectrometric Characterisation of (P[^]P)ZnX₂ Complexes

The ³¹P NMR spectra of (P[^]P)ZnX₂ complexes (**Zn-5.3 – Zn-5.8**) all show a singlet corresponding to the respective diphosphine ligand coordinated to zinc in a bidentate manner. For all the (P[^]P)ZnBr₂ complexes (**Zn-5.3**, **Zn-5.4**, **Zn-5.6-8**), the resonance observed by ³¹P NMR spectroscopy (δ_P **Zn-5.3** 19.4., **Zn-5.4** 22.4 **Zn-5.6** 21.9, **Zn-5.7** 9.36 and **Zn-5.8** 25.4 ppm) was shifted relative to that of the free diphosphine ligand (δ_P dtbpx 26.0, dppp 17.7, dtbpp 27.4 and dppbz –13.0 ppm, respectively), which was indicative of coordination to zinc (*i.e.* a coordination chemical shift).

The ^1H NMR spectra of complexes **Zn-5.3** and **Zn-5.4** (containing the dtbpx ligand) showed multiplets corresponding to methyl protons and methylene protons on the diphosphine ligand as a result of the presence of inequivalent environments. It has been reported previously in the literature that inequivalence of these protons within complexes containing dtbpx ligand is the result of dynamic “puckering” of the back-bone, the rate of which is slower than the NMR time scale (**Scheme 4.38**).²⁷



Scheme 4.38 Dynamic backbone “puckering” of dtbpx ligand in metal complexes.

The ASAP MS spectra of the (P[^]P)ZnX₂ complexes **Zn5.3**, **Zn-5.4**, **Zn5.6-5.8** were obtained under standard ASAP conditions. A summary of characteristic fragments observed is given in **Table 4.4**. Mass spectrometric analysis of complexes (dtbpx)ZnBr₂ (**Zn-5.3**), (dppbz)ZnBr₂ (**Zn-5.6**) and (dppp)ZnBr₂ (**Zn-5.7**) showed the presence of [M–X]⁺ fragment within the spectra obtained. All these (P[^]P)ZnX₂ show fragments corresponding to the diphosphine ligand, *i.e.* [M–ZnX₂]⁺.

Table 4.4 MS (ASAP+) fragmentation data from the analysis of (P[^]P)ZnX₂ complexes synthesised herein. Masses in Da, % intensities in parentheses.

Complex	[M–X] ⁺	[M–ZnX ₂] ⁺
Zn-5.3 (dtbpx)ZnBr ₂	537.110 (1.36%)	395.266 (91.10%) ^a
Zn-5.4 (dtbpx)ZnCl ₂		395.291 (51.9%)
Zn-5.6 (dppbz)ZnBr ₂	588.951 (3.37%)	446.110 (14.62%)
Zn-5.7 (dppp)ZnBr ₂	554.977 (9.83%)	412.125 (100%)
Zn-5.8 (dtbpp)ZnBr ₂		332.267 (43.25%)

^a[M–ZnX₂+H]⁺

The mass spectra obtained of complexes (dtbpx)ZnCl₂ (**Zn-5.4**) and (dtbpp)ZnBr₂ (**Zn-5.8**) did not show the presence of any “(P[^]P)Zn”-containing species. However, the NMR spectroscopic analysis of complexes **Zn-5.4** and **Zn-5.8** suggested complexation to zinc of the diphosphine ligand had occurred and so the lack of signal containing “(P[^]P)Zn” within the mass spectroscopic data is not indicative of non-coordination.

For all the (P[^]P)ZnX₂ complexes synthesised (**Zn5.3**, **Zn-5.4**, **Zn5.6-5.8**), attempts to obtain Raman spectroscopic data were made. However, in all cases, the collection of the Raman spectra were

hampered by significant fluorescence, resulting in vibrational resonances being obscured. The fluorescent nature of these complexes under laser irradiation was noted previously when $(P^{\wedge}P)ZnX_2$ complexes produced during reduction attempts of $(P^{\wedge}P)CoX_2$ complexes with Zn metal were analysed (*vide supra*).

4.3.2 Structural Characterisation of $(P^{\wedge}P)ZnX_2$ Complexes

Where possible, molecular structures of the diphosphine zinc(II) halide complexes were obtained by single crystal XRD studies. Investigation of the solid state structures allows insight into the steric effects of the ligand present to be probed. The solid-state molecular structures of tetrahedral $(P^{\wedge}P)ZnX_2$ complexes, which have not been previously reported, are shown in **Figure 4.15**.

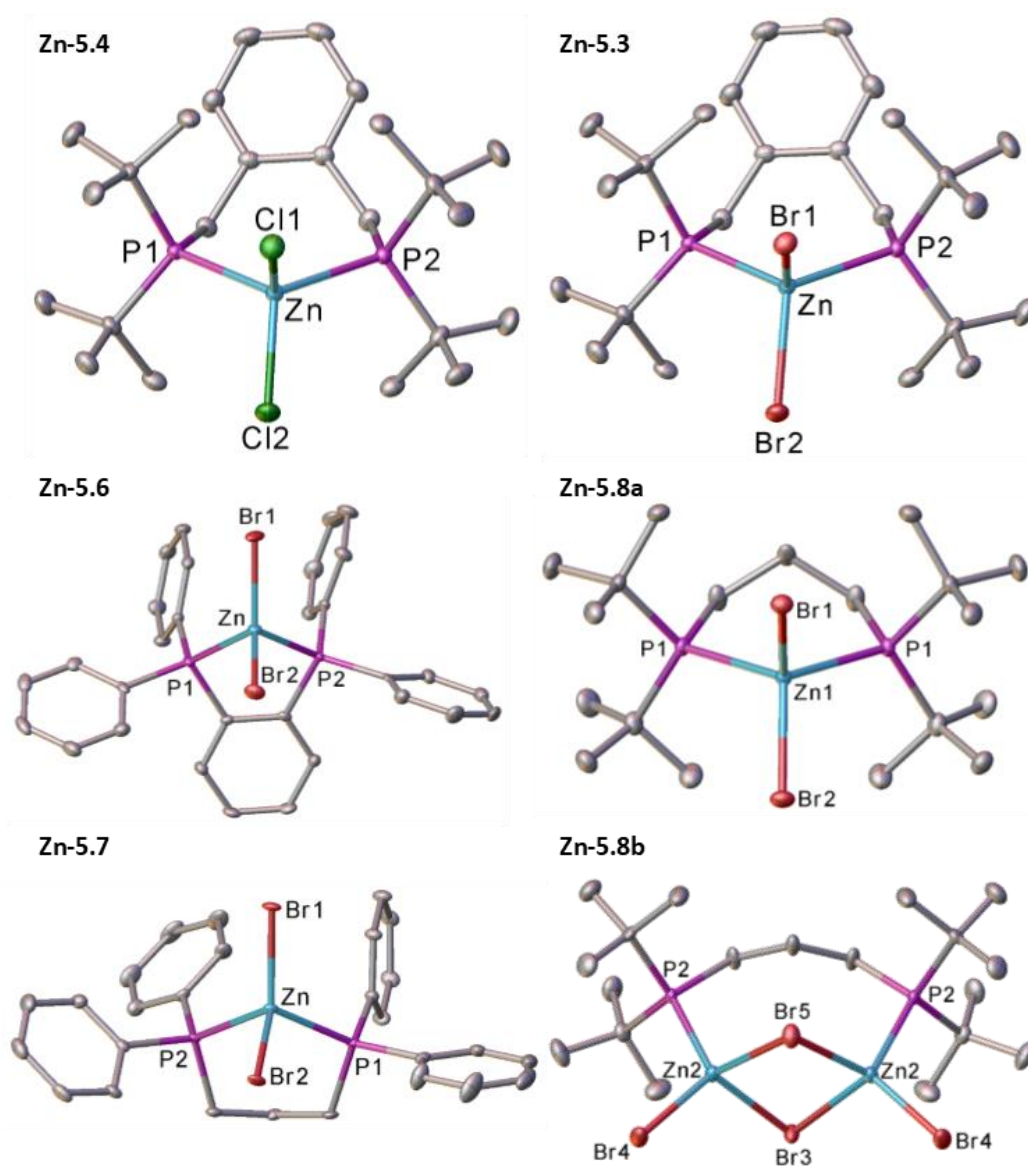


Figure 4.15 Molecular structures determined by XRD of various $(P^{\wedge}P)ZnX_2$ complexes ($(dtbpx)ZnCl_2$ ($Z=2$) (**Zn-5.4**), $(dtbpx)ZnBr_2$ ($Z=2$) (**Zn-5.3**), $(dppbz)ZnBr_2$ (**Zn-5.6**), $(dppp)ZnBr_2$ (**Zn-5.7**), $(dtbpp)ZnBr_2$ (**Zn-5.8a**), $BrZn(\mu^2-dtbpp)(\mu^2-Br)_2ZnBr$ (**Zn-5.8b**). ORTEPs are set at 50% probability and hydrogen atoms and a disordered DCM solvate in **Zn-5.6** are removed for clarity.

A summary of selected bond distances and bond angles measured in the solid-state structures of the various (P[^]P)ZnX₂ complexes can be found in **Table 4.5**. The molecular structure of **Zn-5.8** contains two chemically inequivalent complexes, (dtbpp)ZnBr₂ (**Zn-5.8a**) and [(μ₂-Br)₂(μ₂-dtbpp){ZnBr₂}₂] (**Zn-5.8b**). It is proposed that, due to the lability of the dtbpp ligand, the molecular structure obtained is not representative of the bulk of the sample.

Table 4.5 Selected bond distances and bond angles for (P[^]P)ZnX₂ complexes (**Zn-5.3**, **Zn-5.4**, **Zn-5.6**, **Zn-5.7**, **Zn-5.8**). Standard deviation in parenthesis. For comparison, values for corresponding (P[^]P)CoX₂ complexes have also been included.

(P [^] P)ZnX ₂ :	Zn-5.4 (dtbpx)ZnCl ₂	Zn-5.3 (dtbpx)ZnBr ₂	Zn-5.6 (dppbz)ZnBr ₂	Zn-5.8a (dtbpp)ZnBr ₂	Zn-5.7 (dppp)ZnBr ₂
<i>Selected bond distances / Å</i>					
P-Zn ^a	2.4596(10)	2.4666(12)	2.4279(9)	2.4691(8)	2.4027(7)
Zn-X ^a	2.2616(9)	2.4076(8)	2.3442(7)	2.4012(10)	2.3793(6)
<i>Selected bond angles / °</i>					
P1-Zn-P2	105.17(3)	106.15(3)	82.06(2)	102.68(1)	97.09(2)
X1-Zn-X2	103.35(3)	101.92(1)	117.33(2)	108.24(2)	119.34(2)
P-Zn-X ^a	112.14(6)	112.25(6)	113.05(4)	111.47(3)	109.25(4)
θ	6.74 ^a	8.89 ^a	41.96	10.36	40.49
τ ₄	0.943	0.934	0.883	0.954	0.881
(P [^] P)CoX ₂ :	3.6c (dtbpx)CoCl ₂	3.6b (dtbpx)CoBr ₂	^b	3.5a (dtbpp)CoBr ₂	3.4b* (dppp)CoBr ₂
<i>Selected bond distances / Å</i>					
P-Co ^a	2.4373(9)	2.452(2)	-	2.4334(9)	2.3458(8)
Co-X ^a	2.245(2)	2.396(2)	-	2.3874(6)	2.3594(6)
<i>Selected bond angles / °</i>					
P1-Co-P2	104.86(3)	105.97(3)	-	102.03(2)	98.07(2)
X1-Co-X2	102.67(3)	101.25(1)	-	104.05(2)	119.25(2)
θ	8.7	6.7	-	12.0	40.5
τ ₄	0.939	0.929	-	0.937	0.888

^aAverage value, ^b"(dppbz)CoBr₂" is not tetrahedral: [(dppbz)₂CoBr]₂[Co₂Br₆] *data obtained from WebCSD.

Upon variation of the halide ligand, there is no significant change to the Zn-P bond distance measured (c.f. 2.4596(10) Å in (dtbpx)ZnCl₂ (**Zn-5.4**) and 2.4666(12) Å in (dtbpx)ZnBr₂ (**Zn-5.3**)) (**Table 4.5**). Bond

lengths measured for Zn-X were longer when X = Br (2.4076(8) Å in **Zn-5.3**) than X = Cl (2.2616(9) Å in **Zn-5.4**) as expected.

In the absence of steric effects and any π -bonding contributions, the Zn-P bond distance measured in the solid-state structures of these (P[^]P)ZnX₂ complexes (**Zn-5.3**, **Zn5.6-8**) can be directly related to the σ -donor capacity of the diphosphine ligand (**Figure 4.16**). As the donor capacity of the diphosphine ligand is increased (decrease in $|^1J_{\text{SEP}}|$), the Zn-X bond distance increases. This trend is likely the result of electrostatic repulsion between the lone pair on the electron rich phosphine with the filled zinc *d* orbitals (Zinc(II), d¹⁰).

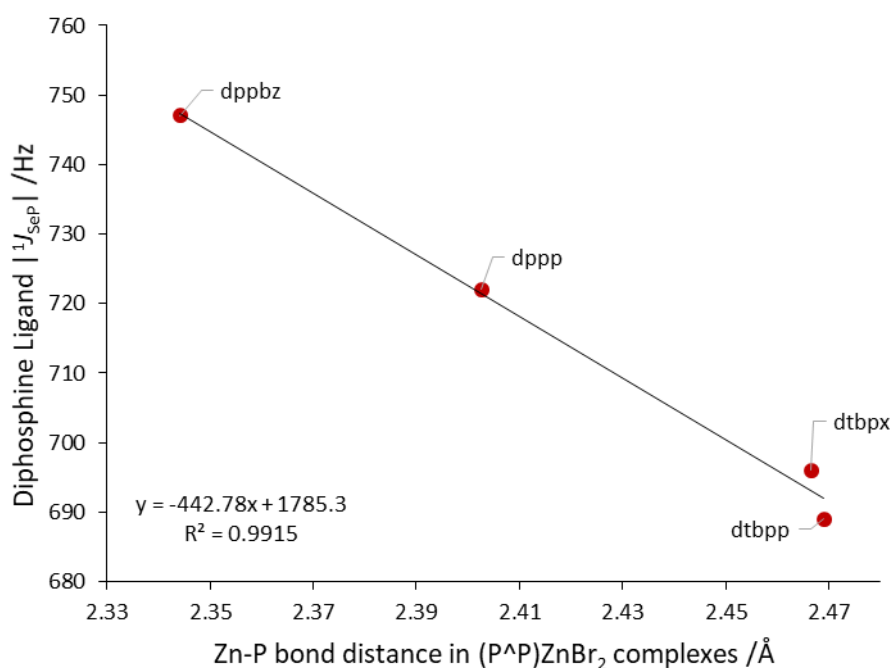


Figure 4.16 Relationship between Zn-P bond distance and donor capacity of the ligand, as measured by $|^1J_{\text{SEP}}|$.

Within the series of (P[^]P)ZnX₂ complexes, the P-Zn-P bond angle measured varies between 82.06(2)° in (dppbz)ZnBr₂ (**Zn-5.6**) and 106.05(3)° in (dtbpx)ZnBr₂ (**Zn-5.3**). This wide range of P-Zn-P bite angles is attributed to the relative flexibility of the diphosphine ligands investigated and as a result of the ring size of the subsequently formed metallacycle. For instance, dppbz that has a very rigid backbone and forms a 5-membered metallacycle with Zn means that the bite angle (\angle P-Zn-P) is essentially fixed by the ligand. In contrast, dtbpx has a much more flexible backbone and forms a 7-membered metallacycle with Zn and hence can give a large P-Zn-P.

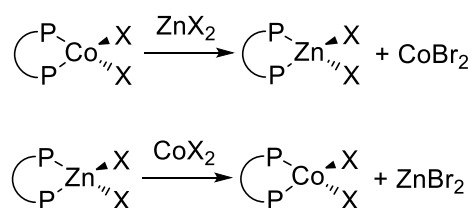
The X-Zn-X bond angles measured in the (P[^]P)ZnBr₂ complexes (**Table 4.5**) also varied significantly. Both (P[^]P)ZnBr₂ complexes with Ph-substituted phosphines (**Zn-5.7** and **Zn-5.6**) have wide Br-Zn-Br

angles (119.34(2)° and 117.33(2)°, respectively). These wide Br-Zn-Br angles are reflected in the values of τ_4 for complexes **Zn-5.7** and **Zn-5.6** (τ_4 0.881 and 0.883, respectively); indicating that complexes **Zn-5.7** and **Zn-5.6** exhibit trigonal pyramidal distortions of their *pseudo*-tetrahedral geometries. The X-Zn-X bond angles measured for (P[^]P)ZnBr₂ complexes with *t*Bu-substituted phosphines (**Zn-5.3** and **Zn-5.8a**) are smaller and are measured as 101.92(1)° in **Zn-5.4** and 108.24(2)° in **Zn-5.8a**, likely the result of bromide displacement due to steric repulsions between the bromide ligand and bulky *t*Bu-groups (θ is 8.89° in **Zn-5.3** and 10.86° in **Zn-5.8a**).

The structural data obtained for the (P[^]P)ZnX₂ complexes (**Zn5.3**, **Zn-5.4**, **Zn5.6-5.8a**) can be compared to those of the isomorphous (P[^]P)CoX₂ complexes (**3.6b**, **3.6c**, **3.5a** and **3.4b**). No significant changes to the X-M-X (X = Cl, Br, M = Co, Zn), P-M-P or dihedral angle (θ , as described in Chapter 3, Section 3.3.2) were observed. Additionally, only small variations in the value of τ_4 were observed between cobalt and zinc analogues of (P[^]P)MX₂ complexes.

4.4 Diphosphine Ligand Exchange Between CoX₂ and ZnX₂ Complexes

With (P[^]P)ZnX₂ complexes (**Zn5.3**, **Zn-5.4**, **Zn5.6-5.8**) and (P[^]P)CoX₂ complexes (**3.4d**, **3.5a**, **3.4b**, **3.4c**, **3.10**) in hand, an investigation into the diphosphine ligand-exchange reaction between cobalt and zinc complexes was undertaken. These reactions involved exchange between equivalent cobalt and zinc complexes (2+ oxidation state) (**Scheme 4.36**) and were followed by UV-Vis spectroscopy in order to probe ligand-metal coordination, and the resulting reaction mixtures analysed by MS (ASAP⁺) and ³¹P NMR spectroscopy.



Scheme 4.39 Top: 'Forward' ligand exchange reaction to produce (P[^]P)ZnBr₂ complexes. Bottom: 'reverse' ligand exchange reaction to produce (P[^]P)ZnBr₂ complexes.

The ligand exchange reactions were investigated in both '*forwards*' and '*reverse*' manners (**Scheme 4.39**). Various diphosphine and halide ligands were tested to determine the effects of differing electronic and steric effects upon the resulting ligand exchange reaction.

It was postulated that the use of a coordinating solvent may increase the lability of the diphosphine ligand through stabilisation of the resulting solvated MX₂ complexes. As such, the ligand exchange reactions were carried out in THF and DCM solution in order to determine whether the observed ligand

exchange occurs only in the presence of coordinating solvent (THF). The results of the investigations into these ligand exchange reaction have been summarised in **Table 4.6** for ease of reference. A typical procedure for the ligand exchange reactions carried out is as follows: a 25 mL volumetric solution of (P[^]P)M¹X₂ (M¹ = Zn, Co; P[^]P = dppp, dtbpx, dppbz; X = Cl, Br) (0.016 mmol) in THF or DCM was prepared in a nitrogen filled glovebox and an aliquot removed and measured by UV-Vis spectroscopy. The aliquot was then returned to the bulk solution in a Schlenk tube and the whole solution transferred by cannula into a Schlenk tube containing M²X₂ (M¹ = Co then M² = Zn; M¹ = Zn then M² = Co; X = Cl, Br) (0.016 mmol). Aliquots were removed periodically for UV-Vis analysis under anaerobic conditions.

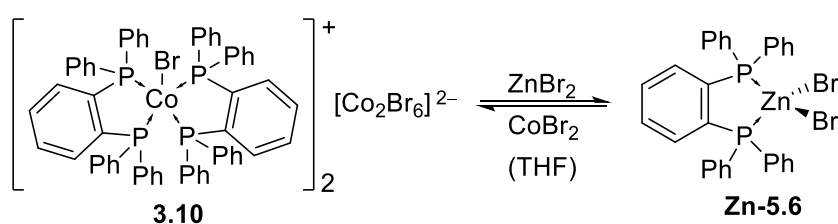
Table 4.6 Summary of forward and reverse ligand exchange reactions between (P[^]P)M¹X₂ and M²X₂ and conditions used (P[^]P = dppbz, dtbpx, dppp, X = Cl, Br, M = Zn, Co) and T = time.

Entry	(P [^] P)M ¹ X ₂	M ² X ₂	T / h	Solvent	Observed Products	
<i>“forward” reactions</i>						
1	3.10	(dppbz)CoBr ₂	ZnBr ₂	24	THF	(dppbz)ZnBr ₂ , “(dppbz)CoBr ₂ ”
2	3.6b	(dtbpx)CoBr ₂	ZnBr ₂	18	THF	(dtbpxO)ZnBr ₂ , CoBr ₂
3	3.6b	(dtbpx)CoCl ₂	ZnCl ₂	22	THF	(dtbpx)ZnCl ₂ , CoCl ₂
4	3.6b	(dtbpx)CoBr ₂	ZnBr ₂	18	THF	(dtbpxO)ZnBr ₂ , CoBr ₂
5	3.6b	(dtbpx)CoBr ₂	ZnBr ₂	1.5	DCM	(dtbpx)ZnBr ₂
6	3.4d	(dppp)CoBr ₂	ZnBr ₂	96	DCM	(dppp)ZnBr ₂
7	3.4d	(dppp)CoBr ₂	ZnBr ₂	144	THF	(dppp)ZnBr ₂ , (dppp)CoBr ₂
<i>“reverse” reactions</i>						
8	Zn-5.6	(dppbz)ZnBr ₂	CoBr ₂	24	THF	(dppbz)CoBr ₂ , (dppbz)ZnBr ₂
9	Zn-5.3	(dtbpx)ZnBr ₂	CoBr ₂	18	THF	(dtbpx)CoBr ₂ , (dtbpx)ZnBr ₂ , dtbpx,
10	Zn-5.3	(dtbpx)ZnBr ₂	CoBr ₂	20	THF	(dtbpx)CoBr ₂ , CoBr ₂
11	Zn-5.3	(dtbpx)ZnBr ₂	CoBr ₂	720	THF	(dtbpxO)ZnBr ₂ , (dtbpx)CoBr ₂ , CoBr ₂
12	Zn-5.4	(dtbpx)ZnCl ₂	CoCl ₂	18	THF	(dtbpx)CoCl ₂ , (dtbpx)ZnCl ₂
13	Zn-5.7	(dppp)ZnBr ₂	CoBr ₂	18	THF	(dppp)CoBr ₂

Using a combination of UV-Vis, Raman and NMR (³¹P) spectroscopies and mass spectrometry, the diphosphine ligand exchange reactions between cobalt(II) halide and zinc(II) halide can be investigated. The following sections discuss the outcomes of the ligand exchange reactions (**Table 4.6**) performed.

4.4.1 The Exchange of dppbz Between Zn^{II} and Co^{II} in THF

In both the reactions of (dppbz)MBr₂ complexes (M = Zn (**Zn-5.6**) and M = Co (**3.10**)) with MX₂, reversible ligand exchange between cobalt and zinc was observed (**Table 4.6**: Entries 1 and 8, respectively) as shown in **Scheme 4.40**. The ³¹P NMR spectra recorded of the reaction mixtures of both the “forward” reaction (Entry 1) and the “reverse” reaction (Entry 8) did not show any resonances, suggesting the presence of a paramagnetic species within both reactions (*i.e.* CoBr₂, or [(dppbz)₂CoBr][Co₂Br₆] (**3.10**)). The Raman spectrum obtained of the reaction mixture corresponding to Entry 1 had a significant fluorescent character, obscuring most vibrational bands, this suggests the presence of (dppbz)ZnBr₂ (**Zn-5.6**), which fluoresces during laser induced excitation. However, a weak band at 254 cm⁻¹ was observed, which corresponds to νCo-(μ-Br)_{symm} (arising from the dianion, [Co₂Br₆]²⁻) as discussed in Chapter 3, suggesting some starting material [(dppbz)₂CoBr][Co₂Br₆] (**3.10**) remained. The mass spectrum obtained of the reaction mixture from upon reaction of **3.10** with ZnBr₂ (Entry 1) showed the presence of both zinc and cobalt complexes containing dppbz *e.g.* *m/z* 662.896 Da (54.48% [(dppbz)CoBr₂]⁺ (**3.10**)) and *m/z* 588.977 Da (1.76% [(dppbz)ZnBr]⁺ (**Zn-5.6**)). The Raman spectrum obtained for the reaction mixture obtained upon reaction of **Zn-5.6** with CoBr₂ (Entry 8) matched that of **3.10** (νCo-Br 253 cm⁻¹ and 300 cm⁻¹) with no significant fluorescence observed, indicating ligand exchange from zinc to cobalt of the dppbz diphosphine ligand. The mass spectrum of the reverse reaction (Entry 8) shows the presence of both zinc and cobalt complexes of dppbz, *e.g.* *m/z* 1030.090 Da (4.75% [(dppbz)₂CoBr]⁺ (**3.10**)) and *m/z* 587.980 Da (0.54% [(dppbz)ZnBr]⁺ (**Zn-5.6**)). There is therefore reversible exchange of dppbz ligand between cobalt and zinc(II) bromides in THF solution (**Scheme 4.40**).



Scheme 4.40 Observed reversible exchange of dppbz between ZnBr₂ and CoBr₂ to produce [(dppbz)₂CoBr][Co₂Br₆] (**3.10**) or (dppbz)ZnBr₂ (**Zn-5.6**).

4.4.2 The Exchange of dtbpx Between Zn^{II} and Co^{II} in THF

The “forward” ligand-exchange reaction between (dtbpx)CoBr₂ (**3.6b**) and ZnBr₂ was investigated and followed by UV-Vis spectroscopy (**Table 4.6**: Entries 2 and 4). Over the course of 18 hours, UV-Vis spectroscopic analysis of these “forward” ligand exchange reactions showed the loss of bands

associated with complex **3.6b** and the appearance of bands associated with solvated CoBr_2 (λ_{max} 594, 655 and 684 nm) as the diphosphine ligand, dtbpx, is sequestered by zinc(II) bromide (**Figure 4.17**).

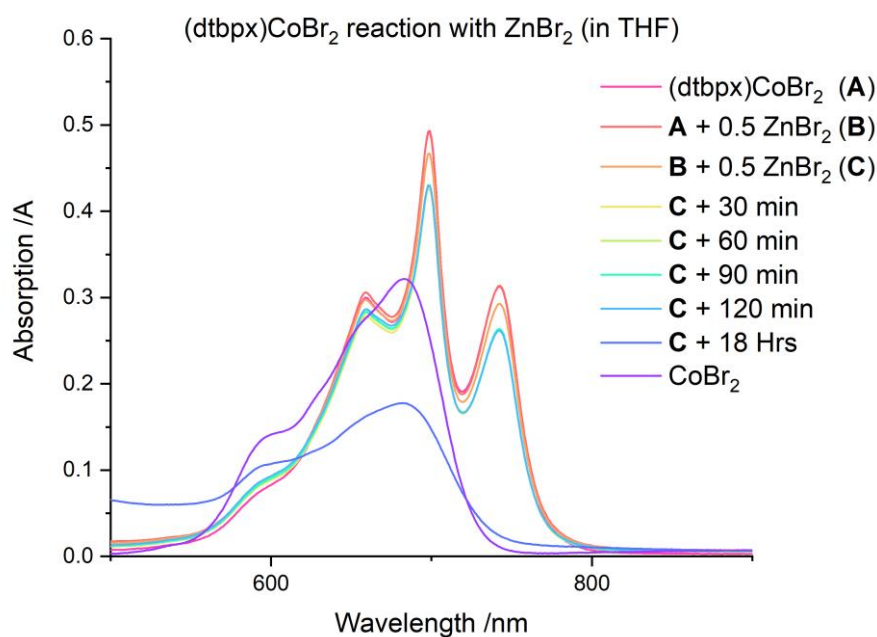
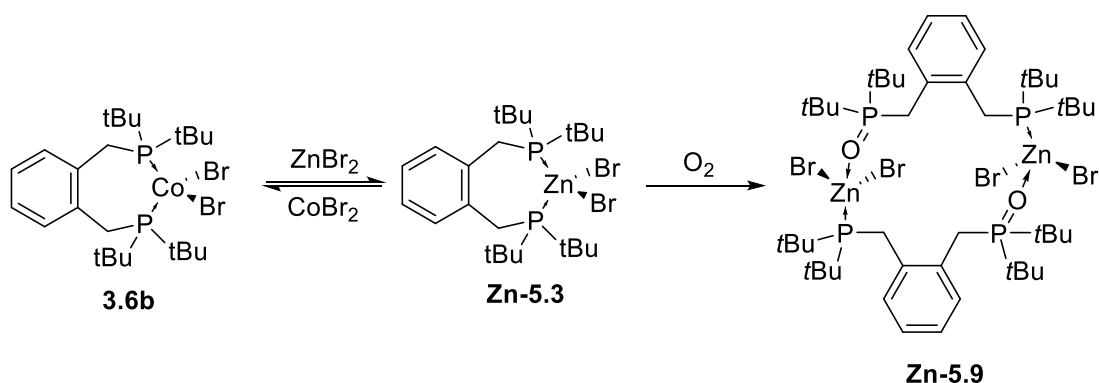


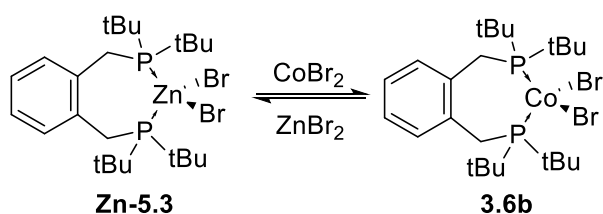
Figure 4.17 UV-Vis spectra of “forward” ligand-exchange reaction between $(\text{dtbpx})\text{CoBr}_2$ (**3.6b**) and ZnBr_2 showing loss of **3.6b** and formation of CoBr_2 over 18 hours.

The ^{31}P NMR spectrum obtained of the products obtained from reaction of $(\text{dtbpx})\text{CoBr}_2$ (**3.6b**) with ZnBr_2 (**Table 4.6**: Entry 2) showed two doublets, which were unchanged upon proton decoupling, *i.e.* $^{31}\text{P}\{^1\text{H}\}$ NMR δ_{P} 72.0 (d, $^3J_{\text{PP}}$ 69 Hz) and 37.8 (d, $^3J_{\text{PP}}$ 70 Hz) ppm. It is proposed that these signals in the ^{31}P NMR spectra corresponded to the partially oxidised diphosphine zinc species, $[(\mu_2\text{-dtbpxO})\text{ZnBr}_2]_2$ (**Zn-5.9**), and arise from $^3J_{\text{PP}}$ coupling through Zn ($^3J_{\text{PP}}$ coupling constants have been reported within the range 35-154 Hz).²⁸ Partially oxidised (P[^]PO) ligands have a preference for bridging two metal centres rather than forming an unstable 8-membered metallacycle, as has been seen for $[(\mu_2\text{-dppbO})\text{CoX}_2]_2$, the proposed structure for **Zn-5.9** is shown in **Scheme 4.41**. After observation of this partial oxidation product, **Zn-5.9**, within the products obtained from this reaction between **3.6b** and ZnBr_2 (**Table 4.6**: Entry 2), the reaction was repeated (**Table 4.6**: Entry 4). However, the UV-Vis and NMR spectra collected of the products of this repeated reaction were identical to those obtained previously.



Scheme 4.41 Reversible ligand exchange of dtbpx between cobalt(II) and zinc(II) and proposed structure of $[(\mu_2\text{-dtbpxO})\text{ZnBr}_2]_2$ (**Zn-5.9**) with bridging, partially oxidised, dtbpxO, ligands.

The “reverse” ligand exchange reaction between $(\text{dtbpx})\text{ZnBr}_2$ (**Zn-5.3**) and CoBr_2 (**Scheme 4.42**) was also explored (**Table 4.6**: Entries 9, 10 and 11). The products corresponding to Entry 9 were analysed through ^{31}P NMR and Raman spectroscopies and mass spectrometry. The mass spectrum obtained for the products of the “reverse” ligand-exchange reaction (**Table 4.6**: Entry 9) showed the presence of $(\text{dtbpx})\text{CoBr}_2$ (**3.6b**) (e.g. m/z 532.122 Da $[(\text{dtbpx})\text{CoBr}]^+$). The Raman spectrum obtained of the products of the reaction between **Zn-5.3** and CoBr_2 (Entry 9) also showed the presence of complex **3.6b** through appearance of a band at 278 cm^{-1} , which corresponds to $\nu_{\text{Co-Br}}^{\text{sym}}$. ^{31}P NMR spectroscopic analysis of the products obtained showed the presence of free dtbpx ligand (δ_{P} 24.0 ppm) along with $(\text{dtbpx})\text{ZnBr}_2$ (**Zn-5.3**) (δ_{P} 18.5 ppm).



Scheme 4.42 Reversible ligand exchange of dtbpx between zinc(II) bromide and cobalt(II) bromide.

This “reverse” reaction between complex **Zn-5.3** and CoBr_2 (**Table 4.6**: Entry 9) was repeated on a smaller scale under dilute conditions to allow the reaction to be followed by UV-Vis spectroscopy (**Table 4.6**: Entry 10). Almost immediately upon addition of CoBr_2 to the reaction, the UV-Vis spectrum of the reaction mixture showed the presence of $(\text{dtbpx})\text{CoBr}_2$ (**3.6b**) (λ_{max} 659, 699 and 744 nm). However, after 20 hours, the UV-Vis spectrum of the reaction mixture showed the presence of CoBr_2 , alongside **3.6b**; highlighting the lability of this ligand on cobalt (**Figure 4.18**).

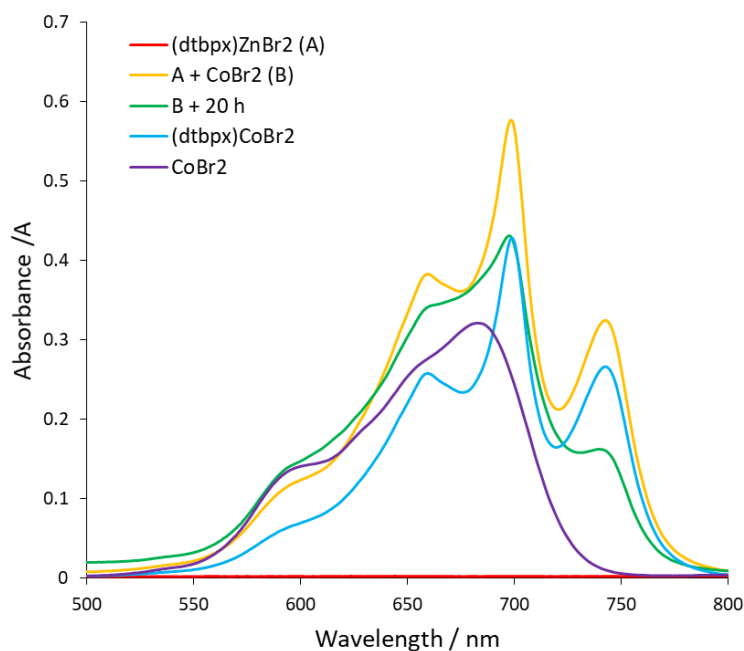
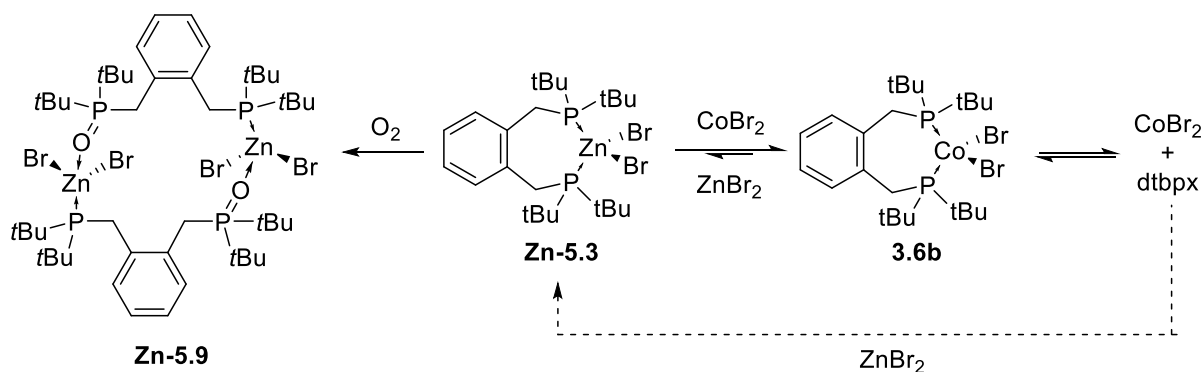


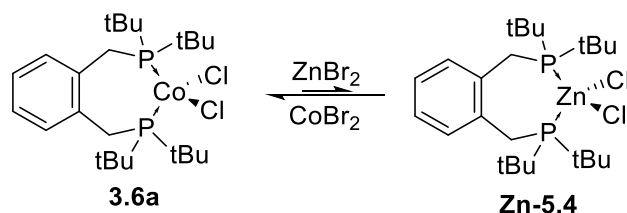
Figure 4.18 UV-Vis spectroscopic analysis of “reverse” reaction between (dtbpx)ZnBr₂ (**Zn-5.3**) and CoBr₂ to form (dtbpx)CoBr₂ (**3.6b**) in THF.

This “reverse” reaction (**Zn-5.3** and CoBr₂) was again repeated, but left for 720 hours (Entry 11) in an attempt to determine whether the reaction would eventually result in complete formation of (dtbpx)CoBr₂ (**3.6b**). This reaction was followed by UV-Vis spectroscopy, however, after 720 hours, the UV-Vis spectrum only shows the presence of CoBr₂: λ_{max} 596sh, 656sh and 679 nm. The mass spectrum of the products of the reaction between **Zn-5.3** and CoBr₂ (Table 4.6: Entry 11) showed the presence of a partially oxidised zinc species, presumed to be **Zn-5.9** e.g. m/z 873.184 Da [(dtbpxO)ZnBr]⁺, suggesting the reaction came into contact with oxygen, which resulted in the observed formation of CoBr₂ (Scheme 4.43). This oxidation is also indicated by ³¹P NMR spectroscopic analysis as peaks corresponding to **Zn-5.9** were observed (δ_{P} 71.5 (d, ³J_{PP} 69 Hz) and 38.8 (d, ³J_{PP} 68 Hz) ppm). It is possible that partial oxidation of the ligand prevented formation of a dtbpx cobalt complex.



Scheme 4.43 Reversible ligand exchange of dtbpx between CoBr₂ and ZnBr₂ and side reaction to form [(μ_2 -dyltbpox)ZnBr]₂ (**Zn-5.9**).

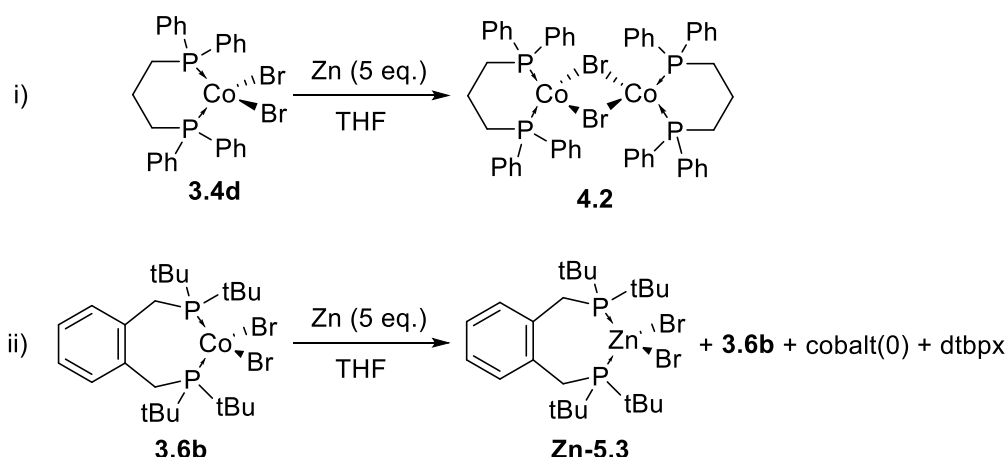
The effect of the halide ligands present on cobalt and zinc complexes upon the ligand exchange reaction was investigated. The data in **Table 4.6**: Entries 3 and 12 correspond to the “forward” and “reverse” dtbpx ligand-exchange reactions, respectively. In both the “forward” and “reverse” reactions, $^{31}\text{P}\{^1\text{H}\}$ NMR spectroscopic analysis indicated the presence of (dtbpx)ZnCl₂ (**Zn-5.4**) (δ_{P} 21.0 ppm). UV-Vis spectroscopic analysis of the products obtained from the “forward” reaction (Entry 3) shows (dtbpx)CoCl₂ (**3.6a**), with a slight hypsochromic shift as a result of the presence of CoCl₂. Raman spectroscopic analysis of the “forward” reaction product mixture displayed a weak band at 320 cm⁻¹, which corresponds to (dtbpx)CoCl₂ (**3.6a**). The mass spectrum obtained for the product of the reaction between **Zn-5.4** and CoBr₂ (**Table 4.6**: Entry 3) indicated the presence of (dtbpx)CoCl₂ (**3.6a**) (e.g. m/z 488.19 Da [(dtbpx)CoCl]⁺). No fragments corresponding to a zinc-containing species were seen in the mass spectrum for **Table 4.6**: Entry 3. The Raman spectrum of the products of the “reverse” reaction (**Table 4.6**: Entry 12) contained a species with some fluorescent character (attributed to (dtbpx)ZnCl₂ (**Zn-5.4**)), but also showed a shouldered band at ν 323 cm⁻¹ corresponding to $\nu_{\text{Co-Cl}_{\text{symm}}}$ in **3.6a**. The mass spectrum obtained of the products of **Table 4.6**: Entry 12 shows fragments associated only with the fragmentation of (dtbpx)CoCl₂ (**3.6a**), e.g. m/z 488.187 Da [(dtbpx)CoCl]⁺. When these data from the “forward” and “reverse” reactions containing dtbpx and metal(II) chloride species (**Table 4.6**: Entries 3 and 12) are considered together, there appears to be a preference for diphosphine (dtbpx) coordination to CoCl₂ to form (dtbpx)CoCl₂ (**3.6a**). However, there does still exist some ligand-exchange to form (dtbpx)ZnCl₂ (**Zn-5.4**), as shown by the $^{31}\text{P}\{^1\text{H}\}$ NMR spectra obtained (**Scheme 4.44**).



Scheme 4.44 Reversible exchange of dtbpx between cobalt(II) chloride and zinc(II) chloride where the equilibrium is proposed to lie towards the left hand side.

4.4.3 The Exchange of dppp Between Zn^{II} and Co^{II} in THF

An investigation into the ligand-exchange reaction of dppp ligand between zinc and cobalt(II) bromide complexes was also launched (**Table 4.6**: Entries 7 and 13, “forward” and “reverse” reactions, respectively). As (dppp)CoBr₂ (**3.4d**) undergoes successful single electron reduction using Zn metal as a reducing agent (**Scheme 4.45i**), it was expected that the extent of ligand exchange to produce (dppp)ZnBr₂ (**Zn-5.7**) would be less using dppp than with, for instance, dtbpx as (dtbpx)CoBr₂ (**3.6b**) does not undergo single electron reduction in the presence of Zn dust (**Scheme 4.45ii**).



Scheme 4.45 Observed difference in the observed reactivities of (dppp)CoBr₂ (**3.4d**) and (dtbpx)CoBr₂ (**3.6b**) towards Zn metal.

The “forward” ligand-exchange reaction between (dppp)CoBr₂ (**3.4d**) and ZnBr₂ (**Table 4.6**: Entry 7) was followed by UV-Vis spectroscopy. After 144 hours, UV-Vis spectroscopic analysis of the reaction corresponding to **Table 4.6**: Entry 7 displayed the presence of a mixture of **3.4d** and CoBr₂ (λ_{\max} 611, 659, 694 and 742 nm, shown in **Figure 4.19**) suggesting there is appreciable ligand-exchange between **3.4d** and CoBr₂ to produce (dppp)ZnBr₂ (**Zn-5.7**). ³¹P NMR spectroscopic analysis of the products of the reaction between (dppp)CoBr₂ (**3.4d**) and ZnBr₂ (**Table 4.6**: Entry 7) did not show any resonances, likely due to the presence of paramagnetic species (**3.4d** and CoBr₂) in solution.

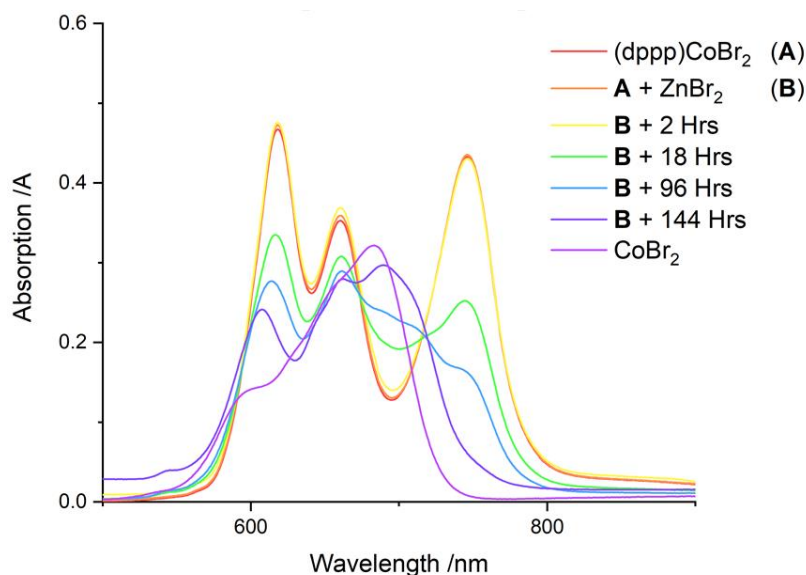


Figure 4.19 UV-Vis spectroscopic analysis of the “forward” ligand-exchange reaction between (dppp)CoBr₂ (**3.4d**) and ZnBr₂ in THF.

UV-Vis spectroscopic analysis of the “reverse” ligand exchange reaction between (dppp)ZnBr₂ (**Zn-5.7**) and CoBr₂ (**Table 4.6**: Entry 13) showed complete conversion to (dppp)CoBr₂ (**3.4d**) after 18 hours (λ_{\max} 620, 663 and 748 nm). No resonances were observed in the ³¹P NMR spectra obtained of the products from this reaction. The products of this “reverse” ligand-exchange were also analysed by Raman spectroscopy and mass spectrometry; both of which showed only the presence of **3.4d**. For instance, in the Raman spectrum, there is appearance of a shouldered band at 283 cm⁻¹ which corresponds to $\nu_{\text{Co-Br}}^{\text{sym}}$ of **3.4d** and the mass spectrum shows the molecular ion for **3.4d** in high intensity at m/z 628.897 Da (64.50% [(dppp)CoBr₂]⁺) (**Figure 4.20**).

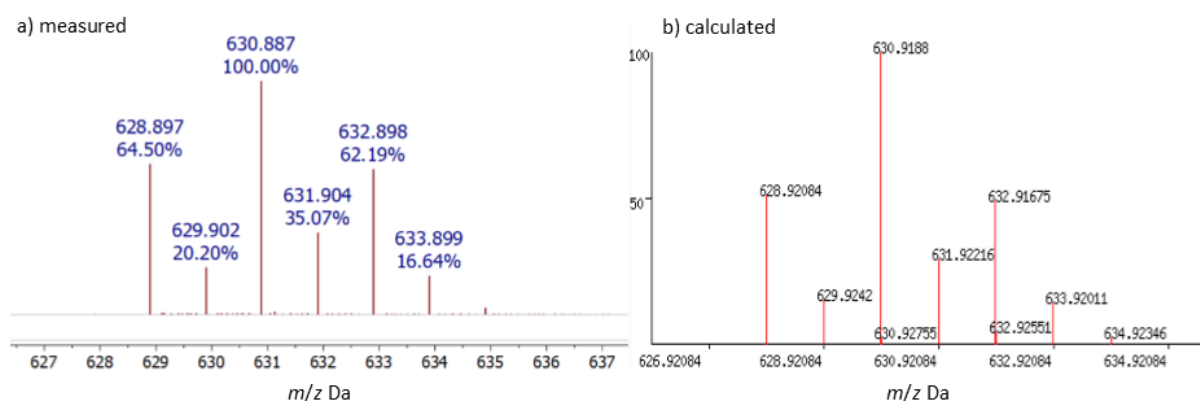
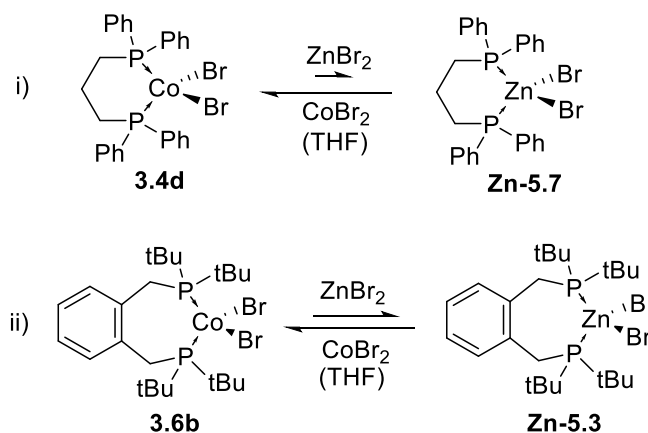


Figure 4.20 Comparison of a) measured and b) calculated isotope patterns for (dppp)CoBr₂ (**3.4d**).

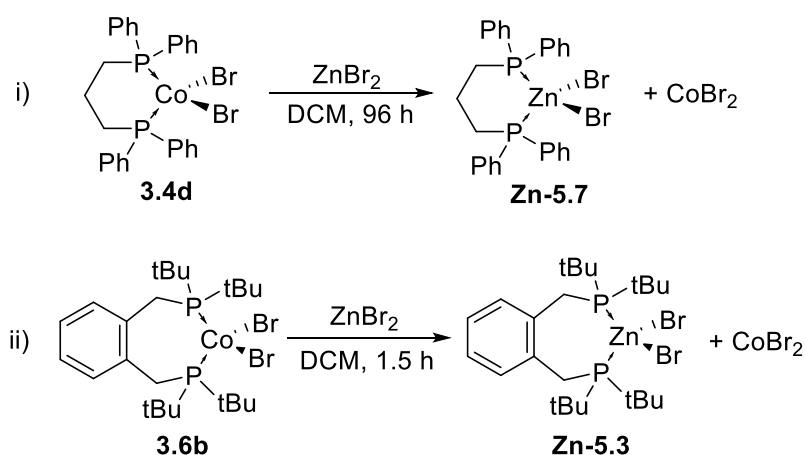
When these data from the “forward” and “reverse” dppp ligand exchange reactions between CoBr₂ and ZnBr₂ are considered together, it is apparent that dppp has a much greater propensity for coordination to cobalt over zinc (**Scheme 4.46i**). It is also suggested that dppp has a greater propensity for coordination to cobalt than that observed for dtbpx (**Scheme 4.46ii**).



Scheme 4.46 Proposed preference for dppp coordination to cobalt(II) bromide over zinc(II) bromide and comparison to that observed for dtbpx.

4.4.4 The Exchange of Diphosphine Ligands (dppp or dtbpx) Between Zn^{II} and Co^{II} in DCM

The “forward” ligand-exchange reaction of diphosphine ligand between (P[^]P)CoBr₂ (P[^]P = dtbpx (**3.6b**), Entry 5, or dppp (**3.4d**), **Table 4.6**: Entry 6) and ZnBr₂ in a non-coordinating solvent (DCM) were also investigated (**Scheme 4.47**). The ³¹P{¹H} NMR spectroscopic analysis of the reaction products obtained from these reactions showed no resonances. The Raman spectra obtained of the products of the reaction outlined between (dtbpx)CoBr₂ (**3.6b**) and ZnBr₂ in DCM (**Table 4.6**: Entry 5) did not display any discernible bands due to fluorescence of the sample, indicating the presence of (dtbpx)ZnBr₂ (**Zn-5.3**). Similarly, the Raman spectra of the products from the reaction between (dppp)CoBr₂ (**3.4d**) and ZnBr₂ in DCM (**Table 4.6**: Entry 6) also displayed a significant degree of fluorescence, indicating the presence of (dppp)ZnBr₂ (**Zn-5.7**).



Scheme 4.47 Observed complete conversion of (P[^]P)CoBr₂, i) (P[^]P) = dppp (**3.4d**), ii) (P[^]P) = dtbpx (**3.6b**), into corresponding (P[^]P)ZnBr₂ complexes in DCM.

Both these “forward” reactions (**Scheme 4.47**) were followed by UV-Vis spectroscopy. In the exchange-reaction of (dtbpx)CoBr₂ (**3.6b**) with ZnBr₂ (**Table 4.6**: Entry 5), after 1.5 hours, all bands corresponding to **3.6b** or CoBr₂ were no longer observed within the UV-Vis spectrum obtained (**Figure 4.21**: LHS). The UV-Vis spectra therefore suggested that complete transformation into (dtbpx)ZnBr₂ (**Zn-5.3**) had occurred after 1.5 hours. However, as no bands corresponding to CoBr₂ were observed, this complete exchange is likely driven by precipitation of CoBr₂ (insoluble in DCM) from the reaction mixture. The “forward” exchange reaction between (dppp)CoBr₂ (**3.4d**) and ZnBr₂ indicated a dependence on the solvent for complete exchange to form (dppp)ZnBr₂ (**Zn-5.7**). However, in the case of the reaction between (dppp)CoBr₂ (**3.4d**) and ZnBr₂, this was much slower than in the case of the reaction between (dtbpx)CoBr₂ with ZnBr₂, and nears completion after 96 hours (**Figure 4.21**: RHS).

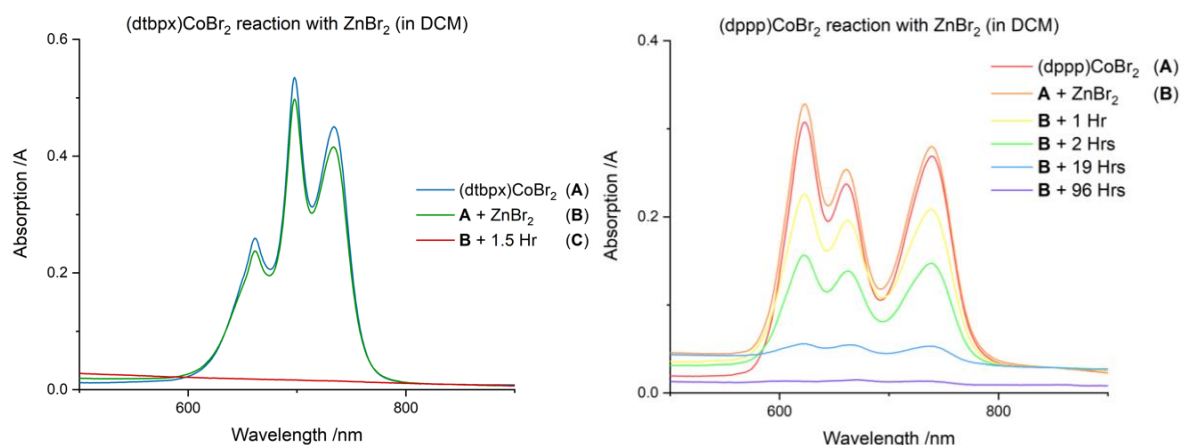


Figure 4.21 LHS: Ligand-exchange reaction between (dtbpx)CoBr₂ (**3.6b**) and ZnBr₂ in DCM. Complete consumption of **3.6b** after 1.5 hours. RHS: Ligand-exchange reaction between (dppp)CoBr₂ (**3.4d**) and ZnBr₂ in DCM, nearing completion after 96 hours.

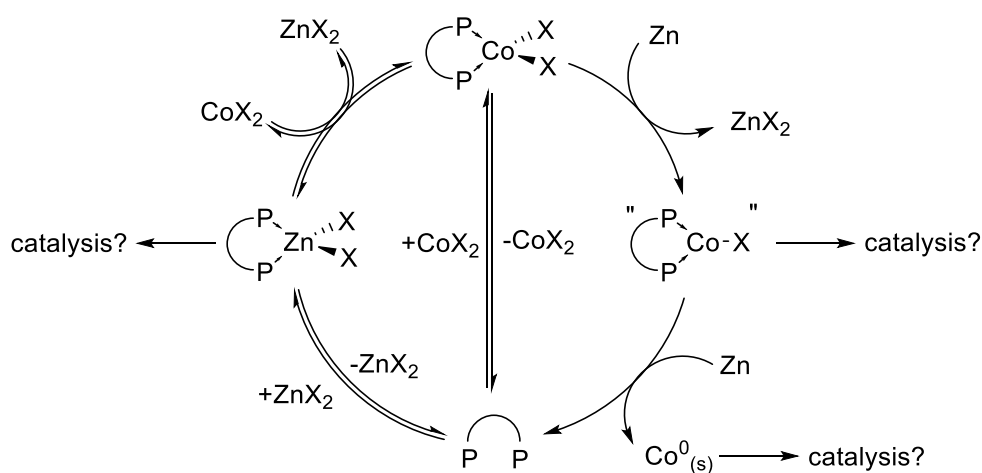
4.4.5 Summary of the Exchange of Diphosphine Ligands Between Zn^{II} and Co^{II}

The “forward” and “reverse” ligand-exchange reactions between zinc(II) dihalide and cobalt(II) dihalide (halide = Cl, Br) sources (**Table 4.6**) all demonstrated the ability of the diphosphine ligand (where (P[^]P) = dpbz, dtbpx, and dppp) to participate in ligand exchange. It is apparent that the rate of “forward” ligand exchange where (P[^]P) = dppp (**Table 4.6**: Entry 7 - incomplete exchange after 144 hours) is much less than that when (P[^]P) = dtbpx (**Table 4.6**: Entry 4 - complete exchange after 18 hours). The preference for dppp coordination to cobalt(II) over zinc(II) relative to dtbpx was also apparent within the “reverse” ligand exchange reactions (*c.f.* **Table 4.6**: Entry 13 (dppp) - complete exchange after 18 hours and Entry 10 (dtbpx) - incomplete exchange after 20 hours). The solvent in which the reaction is performed was also of significant importance, as the relative solubilities of products and reactants can act to drive the ligand-exchange to completion (*c.f.* **Table 4.6**: Entry 4 - complete exchange from (dtbpx)CoBr₂ (**3.6b**) to produce (dtbpx)ZnBr₂ (**Zn-5.3**) after 18 hours in THF, and Entry 5 - complete exchange after 1.5 hours in DCM).

As discussed in Sections 4.1.1-4.1.4 of this chapter, there are few examples of the use of “(P[^]P)Co^IX” where the cobalt(I) pre-catalyst has undergone pre-reduction, isolation and subsequent characterisation before cobalt(I) complex use, for instance, the recent work of Chirik, Cummins and Rajanbabu.^{2,3,7} The *in situ* reduction of cobalt systems with general formula (P[^]P)CoX₂ with Zn metal is much more widely applied for use in cobalt-mediated catalytic transformations. However, as standard, little or no characterisation is typically performed on the active pre-catalytic species generated *in situ*, which is merely assumed to be cobalt(I).

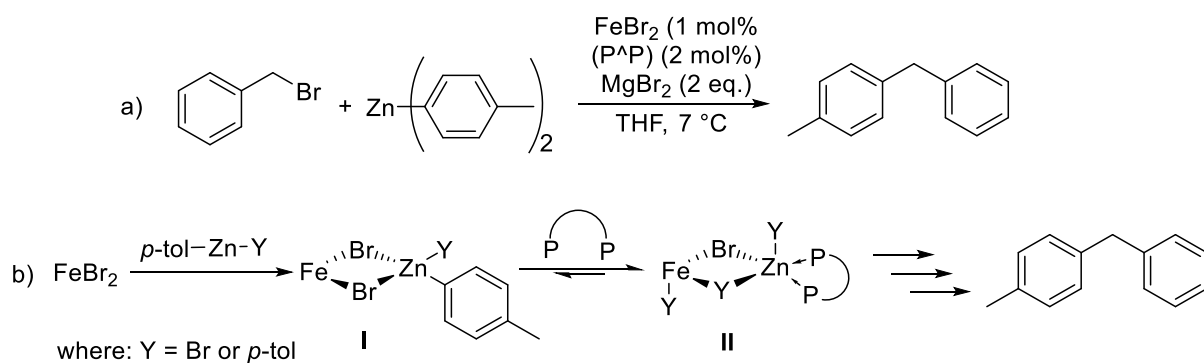
Consider the *in situ* reduction of $(P^{\wedge}P)CoX_2$ species. Upon reduction of $(P^{\wedge}P)CoX_2$ complexes by Zn, ZnX_2 species will be produced, which, as demonstrated within the ligand-exchange reactions performed herein, can then act to scavenge the diphosphine ligand from the cobalt species. It can therefore be imagined that for some catalytic transformations, which include formation of the pre-catalyst *in situ* through halide abstraction by Zn, there could be significant ligand-exchange occurring within the reaction mixture. This ligand-exchange could have several implications upon catalytic activity: 1) The catalytic activity could decrease as a result of removal of active pro-initiator species if this species is based upon “ $(P^{\wedge}P)CoX$ ” species. 2) The catalytic activity could increase if the transformation is catalysed by the $(P^{\wedge}P)ZnX_2$ species, which would be generated *in situ*. 3) The catalytic activity could increase if the catalytic species is heterogeneous cobalt, which would be formed as a result of ligand-exchange causing a decrease in stability towards reduction of resulting $CoBr_2$ species, allowing over-reduction to cobalt(0) to occur.

Together these observations suggest that it is possible that during catalytic transformations mediated by cobalt diphosphine species, where the reduction is performed *in situ*, that there are many competing reaction pathways. A representation of the pathways that could result in formation of various catalytically active species is shown in **Scheme 4.48**.



Scheme 4.48 Possible catalytically-active species and pathways for the formation from starting material $(P^{\wedge}P)CoX_2$.

The observations made within the work of this thesis are reminiscent of those very recently reported by the Bedford group.²⁹ The 2019 paper by Bedford and co-workers discusses diphosphine ligand exchange between iron(II) and zinc(II) during Negishi cross-coupling reactions (**Scheme 4.49**).



Scheme 4.49 a) Representative iron catalysed Negishi cross-coupling reaction. b) Observed formation of catalytically inactive species (I) and catalytically active species (II) where diphosphine ligand is coordinated to Zn.²⁹

Bedford and co-workers noted that, under the conditions used for catalysis where there is typically 80-100× more Zn than Fe, the diphosphine ligand (*e.g.* dppbz) will coordinate to zinc in preference to iron.²⁹ In addition, through application of time-resolved *operando* XAFS (X-ray fine structure) spectroscopy, Bedford *et al.* showed that, during catalysis, there was no observation of any (P[^]P)Fe species present. The authors propose the formation of a Zn-Fe bimetallic species (**Scheme 4.49: II**), which was shown to be formed before the rate-determining step of the reaction. The choice of diphosphine ligand is well established to significantly impact the activity observed of iron-catalysed Negishi cross-coupling reactions.³⁰⁻³⁴ However, until the recent report by Bedford and co-workers,²⁹ it was assumed that the diphosphine was coordinated to an iron-centre during turn-over. The activity observed within such iron/Zn mediated Negishi cross-coupling reactions may therefore also depend upon the ability of a given diphosphine to coordinate to Zn during catalysis.

4.5 Electrochemical Investigation into (P[^]P)CoBr₂ Complexes

As the diphosphine ligand present on cobalt(II) halide was observed to have a significant effect upon the ability of the given complex to under-go single electron reduction (Section A.B.C), it was of interest to look into the electrochemical behaviour of these complexes. As such, cyclic voltammetry (CV) was employed to probe the redox chemistry of the various (P[^]P)CoBr₂ complexes. A selection of (P[^]P)CoBr₂ complexes were selected, where (P[^]P) is dppp (**3.4d**), dtbpp (**3.5a**), dtbpx (**3.6b**) and dppx (**3.6f**), as these complexes exhibited different behaviour towards reaction with Zn metal, but had comparable structures: backbone and phosphine-substituent.

During testing of the selected diphosphine cobalt(II) complexes the scan rate was varied (**Figure 4.23**) to give insight into the mechanism of electrochemical reactions in play. In all cases, the peak-peak separation observed ($i_{p,a} - i_{p,c}$) increases as scan rate increases, suggesting, that under the conditions employed, the couple observed is electrochemically *quasi-reversible*.³⁵

The reversibility of an electrochemical process observed can be probed through use of the Randles-Sevcik equation (**Equation 1**).^{36,37} The Randles-Sevcik equation describes the relationship between the peak current measured, i_p , and the scan rate used, and can be used to determine electron-transfer reversibility along with the diffusion coefficient of the species under analysis.

$$i_p = 0.443 nFA C \left(\frac{nFvD}{RT} \right)^{1/2}$$

Equation 1: Randles-Sevcik equation where: i_p = peak current (A), n = no. electrons transferred in redox event, A = electrode area (cm^2), F is the Faraday Constant (C mol^{-1}), D = diffusion coefficient ($\text{cm}^2 \text{s}^{-1}$), C = concentration of the sample (mol cm^{-3}), v = scan rate (V s^{-1}), R = gas constant ($\text{J K}^{-1} \text{mol}^{-1}$) and T = temperature (K).

A simple plot of current vs \sqrt{v} (scan speed) will give an indication as to whether the electron transfer being probed is reversible. If a linear plot is obtained as scan speed is varied, then the transfer is reversible. A plot of $i_{p,c}$ and $i_{p,a}$ currents the *quasi*-reversible wave observed is shown in **Figure 4.22**.

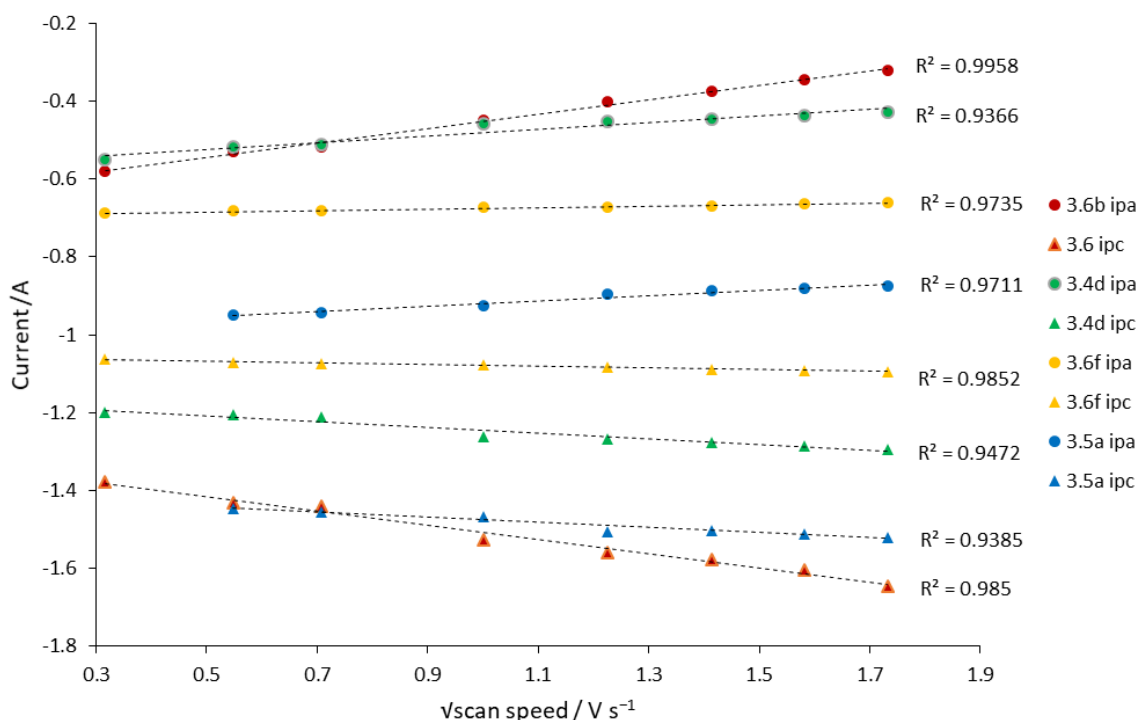


Figure 4.22 Peak current $i_{p,a}$ (circles) and $i_{p,c}$ (triangles) vs root scan speed for the complexes investigated. R^2 values shown correspond to linear goodness-of-fit of trendlines (dashed lines) shown. (dppp)CoBr₂ (**3.4d**), (dtbpb)CoBr₂ (**3.5a**), (dtbpx)CoBr₂ (**3.6b**) and (dppx)CoBr₂ (**3.6f**).

For all of the systems investigated here, all processes first appear to be reversible, *i.e.* linear plots of I vs \sqrt{v} (scan speed) are obtained for $i_{p,c}$ and $i_{p,a}$ processes, despite notable effects arising from suspected

competing irreversible chemical processes (discussed below). However, for the systems investigated here although i_p has been shown to have a linear relationship with ν (scan speed), Randles-Sevcik analysis is only valid when there is a truly reversible process, *i.e.* in addition, E_p values should remain constant with variation in scan speed. It can therefore be concluded that the electron transfer events under investigation here are *quasi*-reversible under the electrochemical conditions employed. The CVs of these complexes (**3.4d**, **3.5a**, **3.6b** and **3.6f**) are shown in **Figure 4.23**.

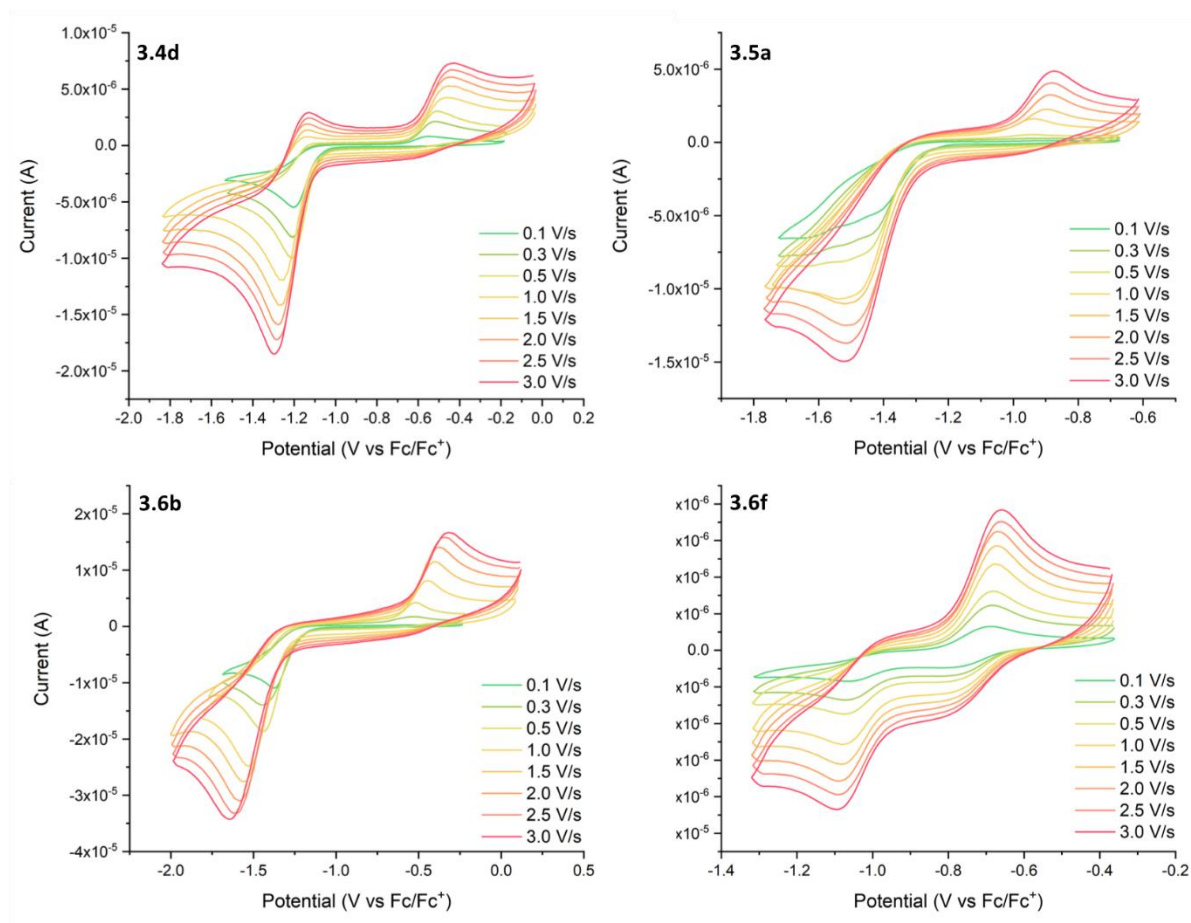


Figure 4.23 Cyclic Voltammograms (CVs) obtained of solutions of (P⁺P)CoBr₂ complexes in DCM with 0.1 M solution of TBAPF₆ electrolyte and platinum electrode with varying scan rate for (dppp)CoBr₂ (**3.4d**), (dtbpp)CoBr₂ (**3.5a**), (dtbpx)CoBr₂ (**3.6b**) and (dppx)CoBr₂ (**3.6f**).

The electrochemical data collected with varying scan rate (0.1 V s^{-1} to 3 V s^{-1}) for the cobalt(II) bromide complexes of dtbpx and dtbpp (**3.6b** and **3.5a**, respectively) appear similar in profile (**Figure 4.24**). These data show clear reduction events during the initial cathodic sweep at all scan rates tested. However, as scan rate was decreased, the corresponding oxidation peak within the anodic sweep was not observed below scan rates of 1.0 V s^{-1} and 0.5 V s^{-1} (for **3.5a** (dtbpp)CoBr₂ and **3.6b** (dtbpx)CoBr₂, respectively), suggesting competition with an irreversible chemical reaction. The cyclic voltammograms (CVs) of these complexes suggest an $E_{qr}C_i$ coupled mechanism, *i.e.* *quasi*-reversible

electron transfer in competition with an irreversible homogeneous chemical reaction. It is proposed that after initial single-electron reduction (**Equation 2**), the corresponding oxidation (**Equation 3**) of the redox process is in competition with a decomposition event, C_i , likely the release of the sterically hindered and electron-rich *tert*-butyl-substituted diphosphine ligand (**Equation 4**):



To understand the complex EC coupled process observed within the CV recorded for these complexes, consideration of both the steric and electronic influences of the diphosphine ligand on cobalt is required. The electronic contribution of the ligand *via* its donor capability is significant, as additional or reduced electron density on the cobalt centre will alter its electrochemical response. Additionally, the steric influence of the ligand is important, as it is likely that conformational changes to the geometry around the cobalt centre occur during electrochemical measurement, which vary the redox chemistry associated with cobalt. Something which has been reported previously for copper complexes when Rorabacher *et al.* investigated the Cu^{II}/Cu^{I} redox potential with a series of tripodal ligands.³⁸ The $E_{1/2}$ values for $(P^{\wedge}P)CoX_2$ complexes investigated are shown in **Scheme 4.7**, along with the donor characteristics of the diphosphine ligands ($|^1J_{SeP}|$) and information about the geometry of these complexes (τ_4).

Table 4.7 Selected bond angles measured from single crystal X-ray diffraction data (where numbers in parenthesis are standard deviation error) and Co^{II}/Co^{I} $E_{1/2}$ values for $(P^{\wedge}P)CoBr_2$ complexes. With phosphorus-selenium coupling constant measured for the selenated-ligand ($^{31}P\{^1H\}$ NMR, 121 MHz, $CDCl_3$). *vs Fc/Fc^{+} $E_{1/2} = 0$ V.

Ligand	$\angle P-Co-P^{\circ}$	$\angle Br-Co-Br^{\circ}$	τ_4	$^1J_{SeP}$ (Hz)	$E_{1/2}$ (V)*
dppp	98.07(2)	119.25(2)	0.888	722	-0.86
dtbpp	102.03(2)	104.05(2)	0.937	689	-1.20
dtbpx	106.02(4)	101.68(2)	0.929	696	-0.98
dppx	107.96(6)	119.06(6)	0.894	724 ^b	-0.88

^avalue obtained from literature.³⁹

The electron donating character of the ligands present in the cobalt(II)bromide complexes investigated was revealed through comparison of the $|^1J_{SeP}|$ phosphorus-selenium coupling constants measured for the ligand selenides, which has an inverse relationship with donor capability.⁴⁰ The donor capacity of these ligands can be ordered: dtbpp > dtbpx > dppp > dppx (**Table 4.7**: $|^1J_{SeP}|$ 689 < 696 < 722 < 724 Hz, respectively), the *t*Bu-groups present on dtbpp and dtbpx significantly increases the electron density present on cobalt, resulting in these electron-rich complexes becoming less susceptible to

reduction when compared to the corresponding complexes bearing dppp or dppx. This decreased ease of reduction as donor capacity is increased across the set is exemplified by the measured $E_{1/2}$ couple values (**Table 4.7**: $E_{1/2}$ dtbpp -1.20 V $<$ dtbpx -0.98 V $<$ dppx -0.88 V $<$ dppp -0.86 V) (**Figure 4.25**: LHS). The trend observed between donor capability of the ligand and the resulting $E_{1/2}$ value measured is not perfect ($R^2 = 0.799$), and so it is likely that additional factors are also correlating with the measured $E_{1/2}$ values. Additionally, increased electron density could also act to destabilise the Co^+ complex formed *in situ* during the cathodic sweep, increasing the likelihood of the proposed irreversible chemical reaction (decomposition), C_i (**Equation 4**).

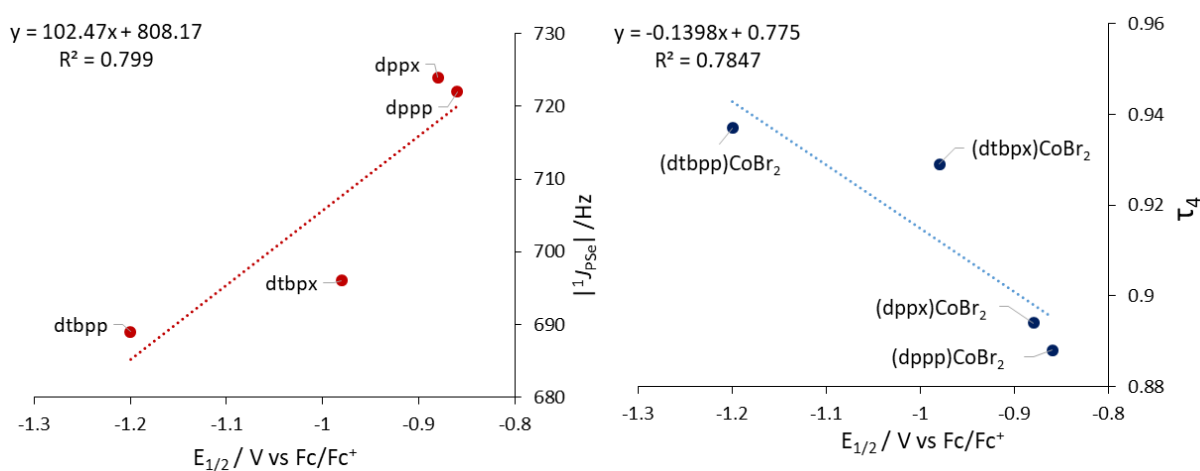


Figure 4.25 LHS: Relationship between the σ -donor ability of the diphosphine ligand and the value of $E_{1/2}$ measured for $(\text{P}^{\text{A}}\text{P})\text{CoBr}_2$ complexes. **RHS:** Relationship between the 4-coordinate geometry index (τ_4) and the measured $E_{1/2}$ values for $(\text{P}^{\text{A}}\text{P})\text{CoBr}_2$ complexes.

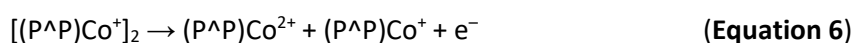
As was discussed in Chapter 3, there is a correlation between the donor capacity of the diphosphine ligand and the 4-coordinate geometry index (τ_4) of the resulting $(\text{P}^{\text{A}}\text{P})\text{CoBr}_2$ complex. There is therefore also a relationship between the τ_4 values of the $(\text{P}^{\text{A}}\text{P})\text{CoBr}_2$ complexes and the measured $E_{1/2}$ values (**Figure 4.25**). The dppx and dppp cobalt(II) bromide complexes, (**3.6f**) and (**3.4d**) respectively, (0.894 and 0.888, respectively) have greater distortion from tetrahedral geometry ($\tau_4 = 1.00$) towards trigonal pyramidal ($\tau_4 = 0.85$) than (dtbpp)CoBr₂ and (dtbpx)CoBr₂ (0.937 and 0.929, respectively). The magnitude of the differences in τ_4 for these complexes is small, and so the observed trend between $E_{1/2}$ and τ_4 may simply be an echo of that that was observed for the donor capacity of the ligand and $E_{1/2}$.

In contrast to the CVs obtained for (dtbpp)CoBr₂ (**3.5a**) and (dtbpx)CoBr₂ (**3.6b**), the cyclic voltammograms collected for (dppp)CoBr₂ (**3.4d**) and (dppx)CoBr₂ (**3.6f**) showed more structure at the scan rates tested. Both complexes **3.4d** and **3.6f** have similar $E_{1/2}$ values recorded for the *quasi*-reversible electron couple: -0.86 V and -0.88 V for (dppp)CoBr₂ (**3.4d**) and (dppx)CoBr₂ (**3.6f**),

respectively (**Table 4.7**). The phosphorus-selenium coupling constants for the diphosphines bound in these complexes reflect the similar reduction potentials measured for the corresponding (P[^]P)CoBr₂ complexes ($|^1J_{\text{SeP}}|$ 722 Hz and 724 Hz for dppp and dppx respectively), suggesting these complexes have similar electronic character (**Figure 4.25**).

In the case of (dppp)CoBr₂ (**3.4d**) as scan rate is decreased, the intensity of $i_{p,a}$ is observed to decrease to a greater extent than that of $i_{p,c}$, suggesting that an E_{qr}C_i mechanism is again at play. The cyclic voltammograms obtained of (dppx)CoBr₂ (**3.6f**) showed the least dramatic decrease in the intensity of $i_{p,a}$ vs $i_{p,c}$. As $i_{p,a}$ peaks are observed at all scan rates tested for **3.4d** and **3.6f** complex, the chemically irreversible reaction (**Equation 4**) present must occur at a greatly reduced rate than that for (dtbpp)CoBr₂ (**3.5a**) and (dtbpx)CoBr₂ (**3.6b**) such that: $k_{Ci}(\mathbf{3.6f}) < k_{Ci}(\mathbf{3.4d}) \ll k_{Ci}(\mathbf{3.6b}) < k_{Ci}(\mathbf{3.5a})$.

An additional feature is also observable within the anodic sweep of the CV obtained for (dppp)CoBr₂ (**3.4d**), with $i_{p,a} \approx -1.14$ V. It is likely that the reverse wave to this process is obscured by the initial single-electron reduction (**Equation 2**). It is proposed that this event with $i_{p,a} \approx -1.14$ V can be attributed to a geometry change within the generated Co^I species. Based upon the products of chemical reduction of complex **3.4d**, it is suggested that this geometry change corresponds to the formation of a dimeric cobalt(I) species with general formula (P[^]P)Co(μ₂-X)₂Co(P[^]P) (as has been observed during chemical reductions (Section 4.2.1)). It is further proposed that this generated dimeric species can then undergo its own redox process, meaning the wave observed in the cathodic sweep is likely coupled. Together, therefore, this suggests that the electrochemical mechanism proposed for (dppp)CoBr₂ (**3.4d**) is E_{qr}C_rE_{qr}C_i *i.e.* a *quasi*-reversible single-electron transfer (**Equations 2 and 3**) in competition with a *quasi*-reversible single-electron electron transfer in the postulated dimeric complex generated by chemical reaction (**Equations 5, 6 and 7**), both of which are in competition with a chemically irreversible reaction, likely decomposition (**Equation 4**).



The CV data obtained for (dppx)CoBr₂ (**3.6f**) is also complicated. Both cathodic and anodic sweeps likely have coupled waves due to chemical formation of the proposed dimeric cobalt(I) species during measurement. Electrochemical formation of this proposed dimeric Co^I species is observed within both anodic (**Equations 5, 6 and 7**) and cathodic sweeps. These observations suggested that the formation of a cobalt(I) complex from (dppx)CoBr₂ (**3.6f**) is much more favoured, *i.e.* (P[^]P)Co^I is more stable when

compared to any of the other complexes electrochemically investigated here. The electrochemical mechanism proposed for redox changes of $(\text{dppx})\text{CoBr}_2$ (**3.6f**) is therefore $E_{\text{qr},\text{C}_i}E_{\text{qr},\text{C}_i}$.

The UV-Vis spectra recorded for the chemically reduced species (Section 4.2.1) gave values of extinction coefficient $\epsilon > 100 \text{ L mol}^{-1} \text{ cm}^{-1}$, which is indicative of the geometry of any cobalt(I) species produced likely being tetrahedral in nature. Raman spectroscopic analysis of the chemically reduced species **4.1-4.8** indicate that these cobalt(I) complexes are dinuclear, *i.e.* contain bridging halides between two cobalt centres (See section 4.2.1).

The electrochemical data obtained for all of these $(\text{P}^{\wedge}\text{P})\text{CoBr}_2$ complexes were very complicated. It appeared as though *dppp* and *dppx* ligands were able to stabilise a cobalt(I) complex generated *in situ* through a geometry change to produce $[(\text{P}^{\wedge}\text{P})\text{Co}^{\text{I}}\text{Br}_2]^-$ or through generation of a new dimeric species, *i.e.* irreversible chemical reaction to generate $(\text{P}^{\wedge}\text{P})\text{Co}(\mu^2\text{-Br})_2\text{Co}(\text{P}^{\wedge}\text{P})$. However, at this time, which, if either, mechanism is in play cannot be definitely concluded.

A tentative explanation for the observed reactivity of these complexes towards Zn (Ph-substituted diphosphines are able to undergo successful single electron reduction to produce complexes with general formula $(\text{P}^{\wedge}\text{P})\text{Co}(\mu_2\text{-Br})_2\text{Co}(\text{P}^{\wedge}\text{P})$ (*e.g.* **4.1** and **4.6** where $(\text{P}^{\wedge}\text{P}) = \text{dppp}$ and *dppx*, respectively) can therefore be postulated. It is proposed that the distorted complexes, $(\text{dppx})\text{CoBr}_2$ (**3.6f**) and $(\text{dppp})\text{CoBr}_2$ (**3.4d**), are able to undergo a stabilising geometry change during reduction, which the sterically-locked geometries of $(\text{dtbpx})\text{CoBr}_2$ (**3.6b**) and $(\text{dtbpp})\text{CoBr}_2$ (**3.5a**) cannot. A spectroelectrochemical investigation is therefore of great interest as it would allow investigation into the postulated geometry change which may be taking place upon reduction. Work in this area is ongoing.

4.6 Attempted Reductions of $(\text{P}^{\wedge}\text{P})\text{CoX}_2$ Complexes Without Zn Metal

Much of the literature surrounding one-electron reduction of cobalt diphosphine complexes is focused upon the use of zinc as a reducing agent. However, work in this thesis has shown that for many of the $[(\text{P}^{\wedge}\text{P})\text{CoX}_2]$ complexes investigated herein, zinc is not a suitable choice and will inherently result in the formation of $(\text{P}^{\wedge}\text{P})\text{ZnX}_2$ complexes and/or over-reduction. It was therefore of significant interest to investigate alternative reducing agents (with a range of reduction potentials) to perform the desired one-electron reduction to produce cobalt(I) species. The reducing agents employed are summarised by reaction and corresponding reduction potential, E^0 , in **Table 4.8**.

Table 4.8 Reduction potentials of employed reducing agents and corresponding reaction.

Reaction	E^0 / V
$\text{Zn}^{2+} + 2 \text{e}^- \rightarrow \text{Zn}$	-0.7618^{41}
$\text{Mg}^{2+} + 2 \text{e}^- \rightarrow \text{Mg}$	-2.372^{41}
$\text{Sm}^{3+} + \text{e}^- \rightarrow \text{Sm}^{2+}$	-1.55^{41}
$\text{K}^+ + \text{e}^- \rightarrow \text{K}$	-2.931^{41*}
$\text{Zr}^{4+} + 4 \text{e}^- \rightarrow \text{Zr}$	-1.45^{41}
$\text{Cp}_2\text{Co}^{2+} + \text{e}^- \rightarrow \text{Cp}_2\text{Co}^+$	-0.90^{42}

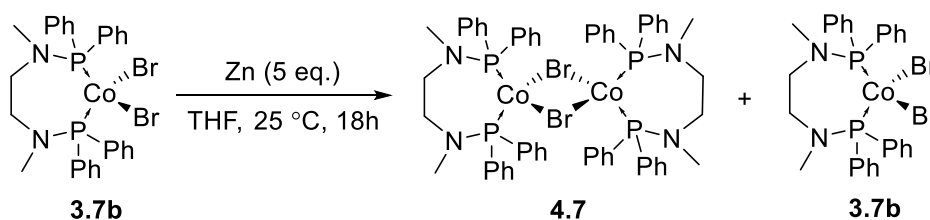
*Employed reagent is KC_8 , which has no recorded reduction potential due to insolubility.

4.6.1 Attempted Single-electron Reduction of $(\text{PPh}_3)_2\text{CoX}_2$ (**3.3a,b**) with Magnesium

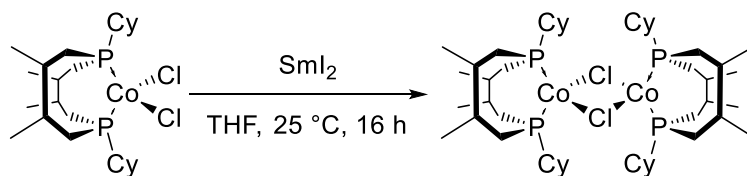
The reaction of $(\text{PPh}_3)_2\text{CoX}_2$ ($\text{X} = \text{Cl}$ (**3.3a**), Br (**3.3b**)) with Zn metal results in a two-electron reduction to form ZnBr_2 and essential decomposition of the starting material into cobalt(0) and triphenylphosphine (Section 4.2.2). As the attempted formation of a cobalt(I) species with Zn metal from **3.3a** or **3.3b** was not successful, the reduction of complexes **3.3a** and **3.3b** was also attempted using magnesium turnings. These complexes were chosen as the monophosphine substituents (rather than chelating diphosphines) might allow free geometry changes. However, treatment of complexes **3.3a** and **3.3b** with Mg quickly resulted in over-reduction to produce a black precipitate of cobalt(0). The reduction potential of magnesium has been measured to be -2.372 V ($\text{Mg}^{2+} + 2 \text{e}^- \rightarrow \text{Mg}$)⁴¹, and the monodentate triphenylphosphine ligands are very labile, as such, it is not surprising that over-reduction of cobalt(II) to cobalt(0) was observed within these reactions.

4.6.2 Attempted Single-electron Reduction of $(\text{PNNP-Ph})\text{CoBr}_2$ (**3.7b**) with SmI_2

The initial attempted reduction of $(\text{PNNP-Ph})\text{CoBr}_2$ (**3.7b**) with Zn metal showed a small portion of the reaction mixture to be the desired product $(\text{PNNP-Ph})\text{Co}(\mu_2\text{-Br})_2\text{Co}(\text{PNNP-Ph})$ (**4.7**), as discussed in Section 4.2.1.5 (**Scheme 4.50**). Importantly though, there was no evidence within this reaction for the formation of any Zn complexes.

**Scheme 4.50** Partially successful reduction of $(\text{PNNP-Ph})\text{CoBr}_2$ (**3.7b**) with Zn metal.

It was therefore postulated that this complex **3.7b** is able to undergo successful single-electron reduction but that the reaction with Zn is not efficient. Samarium iodide (SmI_2) is a well-known single electron reducing agent. Indeed, Cummins *et al.* have demonstrated the use of SmI_2 for the single-electron reduction of their macrocyclic diphosphine cobalt(II) complex (**Scheme 4.51**).⁷



Scheme 4.51 Reported reduction of $(\text{P}_2\text{-macrocyle})\text{CoCl}_2$ with SmI_2 .⁷

The reduction of $(\text{PNNP-Ph})\text{CoBr}_2$ (**3.7b**) was therefore carried out under the conditions reported by Cummins.⁷ Upon addition of a solution of SmI_2 to **3.7b** in THF, an immediate colour change from blue to green was observed. The reaction was left to stir at room temperature for 16 hours after which time a deep green precipitate was observed in a brown/green solution. The solids were collected and analysed by mass spectrometry and Raman spectroscopy. However, only the ligand ion $[(\text{PNNP-Ph})+\text{H}]^+$ (m/z 457.167 Da, calc. 457.196 Da) could be identified out of the very complicated mass spectrum that was obtained. Raman spectroscopic analysis of the product obtained from treatment of **3.7b** with SmI_2 showed a dramatic change had taken place, with several new bands appearing (when compared to **3.7b**). Additionally, the majority of bands associated with vibrations within the PNNP-Ph ligand were not observed in the Raman spectrum of the product. There was also a strong contribution from $\nu\text{Sm-I}$ (375 cm^{-1}) observed in the Raman spectrum, suggesting a significant samarium salt impurity present (**Figure 4.26**). No further attempts to use SmI_2 as a reducing agent were undertaken due to the difficulty in removing Sm(III) salts from the reaction mixture and the resulting difficult to interpret spectra of the product.

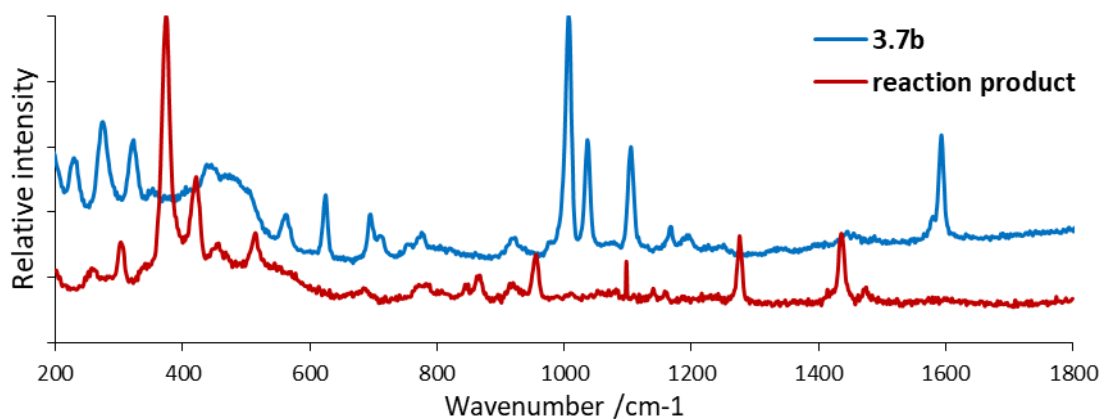
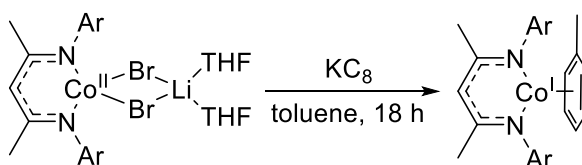


Figure 4.26 Comparison of the Raman spectra of $(\text{PNNP-Ph})\text{CoBr}_2$ (**3.7b**) and the product of the reaction between SmI_2 and **3.7b**.

4.6.3 Attempted Single-electron Reduction of (dtbpx)CoBr₂ (**3.6b**) with KC₈

Potassium graphite (KC₈) has been employed in the literature to perform single-electron reduction of [L₂CoX₂] complexes previously.⁴³ For example, Holland and co-workers have shown its use for the reduction of (NacNac)CoX₂ (X = Cl, Br) complexes in the presence of toluene to produce toluene-stabilised (N[^]N)Co^I(η⁶-tol) complexes (**Scheme 4.52**).⁴³

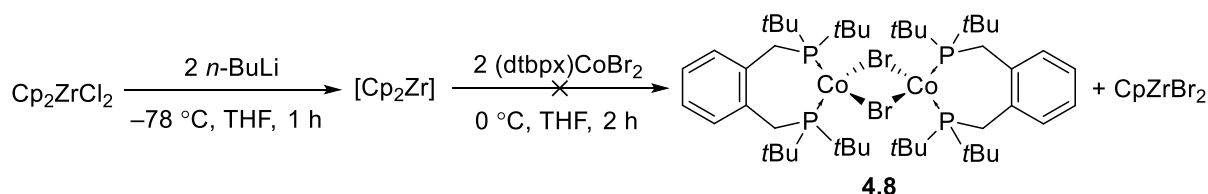


Scheme 4.52 Literature preparation of a (N[^]N)Co^I(η⁶-tol) complex *via* single electron reduction using KC₈.⁴³

Consequently, an attempt was made to reduce (dtbpx)CoBr₂ (**3.6b**) with KC₈ following the literature procedure employed for the aforementioned diimine complexes. Unfortunately, Raman and UV-Vis spectroscopic analysis of the product mixture revealed the predominant species present post-reaction to be **3.6b** (λ 644, 700 and 743 nm, ν_{Co-Br} 275 cm⁻¹). In addition, a black, magnetic solid (cobalt(0)) was also observed, suggesting that, where reduction had taken place, it was *via* a two-electron process.

4.6.4 Attempted Single-electron Reduction of (dtbpx)CoBr₂ (**3.6b**) with Zirconocene

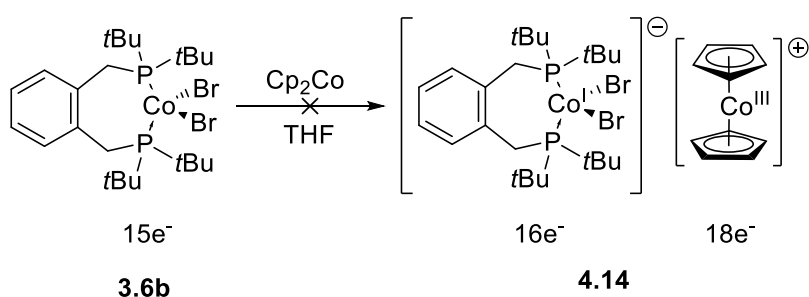
It was hypothesised that highly reactive zirconocene [Cp₂Zr] (generated *in situ* through treatment of Cp₂ZrCl₂ with two equivalents of *n*-butyllithium) could be used to abstract a halide from (dtbpx)CoBr₂ (**3.6b**) in an attempt to produce (dtbpx)Co(μ²-Br)₂Co(dtbpX) (**4.8**). However, Raman spectroscopic and mass spectrometric analysis of the solids obtained from the reaction showed the presence of **3.6b** only, *e.g.* [(dtbpxO₂)CoBr]⁺ at *m/z* 564.111 Da (calc. 564.133 Da, with the correct isotope pattern) and ν_{Co-Br_{symm}} 297 cm⁻¹ (*c.f.* 282 cm⁻¹ in **3.6b**), **Scheme 4.53**.



Scheme 4.53 Attempted halide abstraction from (dtbpx)CoBr₂ (**3.6b**) with [Cp₂Zr].

4.6.5 Attempted Single-electron Reduction of (dtbpx)CoBr₂ (**3.6b**) with Cobaltocene

Cobaltocene is a well-known and effective single electron reducing agent.⁴⁴ This sandwich complex has a formal electron count of 19 valence shell electrons, and as such it is liable to donate a single electron to achieve a greater stability as the 18-electron cobaltocenium cationic species. It was therefore postulated that treatment of (dtbpx)CoBr₂ (**3.6b**) with cobaltocene could result in single electron reduction of **3.6b** to produce the salt (**4.14**) shown in **Scheme 4.54**. The reaction was carried out through mixing cobaltocene with (dtbpx)CoBr₂ (**3.6b**) in THF for 18 hours at room temperature, the reaction was observed to change colour from initial blue to green. However, recrystallisation of the reaction products did not yield the expected product.



Scheme 4.54 Attempted reduction of (dtbpx)CoBr₂ (**3.6b**) with cobaltocene (Cp₂Co), where the reaction resulted in formation of [CoBr₄]²⁻ anion.

A sample of the product produced within this reaction was recrystallised and crystals suitable for single crystal X-ray diffraction were grown through slow layering of a solution in DCM with hexanes; the resulting structure was revealed to be [CoBr₄]²⁻[Cp₂Co]⁺₂ (**4.14**) (**Figure 4.27**). Spectroscopic (UV-Vis, Raman) and spectrometric analysis showed that the bulk of the material produced within this reaction was **4.14**. Interestingly, these crystals were unstable to flash cooling prior to diffraction measurement and so had to be slowly cooled over a period of 24 hours under a nitrogen stream prior to data collection.

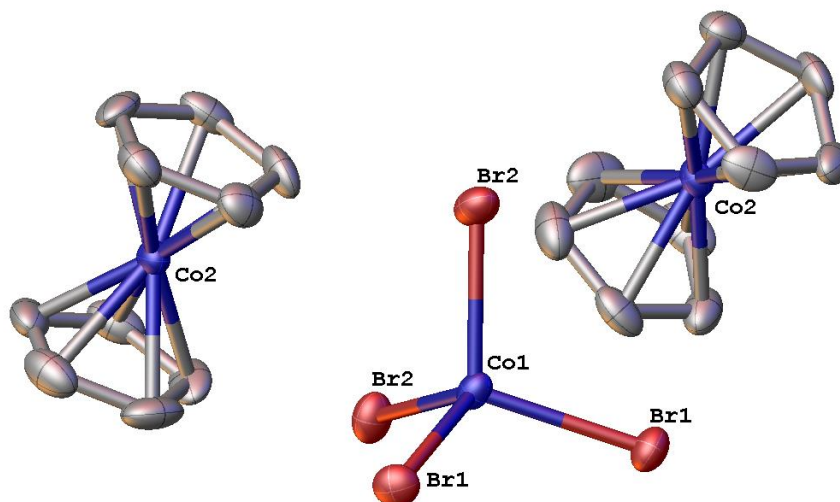
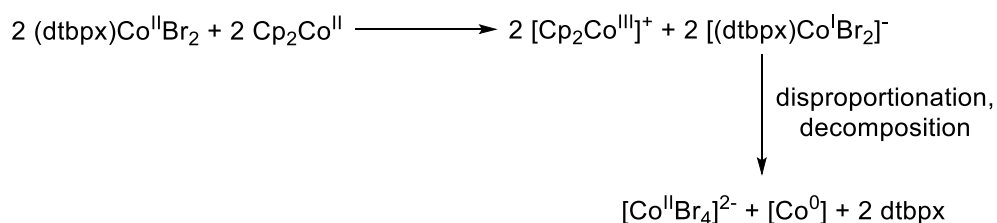


Figure 4.27 Molecular structure of $[\text{Cp}_2\text{Co}]_2^+[\text{CoBr}_4]^{2-}$ (**4.14**) where hydrogen atoms and a single DCM solvate molecule have been omitted for clarity (ORTEPs set at 50% probability).

The structural data of **4.14** further suggests the unlikelihood of forming a stable $(\text{dtbpx})\text{Co}^{\text{I}}$ complex *via* a single electron chemical reduction of $(\text{dtbpx})\text{CoBr}_2$ (**3.6b**) as to form $[\text{CoBr}_4]^{2-}$ by reaction of cobaltocene with $(\text{dtbpx})\text{CoBr}_2$ (**3.6b**) suggests not a two-electron reduction by two discrete cobaltocene complexes (each contributing a single electron) towards one $(\text{dtbpx})\text{CoBr}_2$ (**3.6b**) complex, rather, single electron reduction of two $(\text{dtbpx})\text{CoBr}_2$ complexes by two cobaltocene complexes followed by immediate disproportionation to produce the comparatively stable dianion $[\text{CoBr}_4]^{2-}$. The ^{31}P NMR spectrum obtained contains a single peak at δ_{P} 26.1 ppm, which corresponds to the free dtbpx ligand, indicating a decomposition event to produce metallic cobalt(0) with no ligand bound is likely to have occurred. From these observations, a proposed reaction pathway is shown in **Scheme 4.55**.



Scheme 4.55 Proposed reaction pathway for formation of cobalt bromide dianion from reaction of cobaltocene with $(\text{dtbpx})\text{CoBr}_2$ (**3.6b**).

Raman and UV-Vis spectroscopic analysis of the bulk product obtained of the reaction of $(\text{dtbpx})\text{CoBr}_2$ (**3.6b**) with cobaltocene (Cp_2Co) (**Scheme 4.54**) corroborate the solid state structure obtained (**Figure 4.28**). The UV-Vis spectrum of the product obtained showed a complex band in the visible region where

d←d transitions would be expected, with many overlapping transitions. The profile of this spectra matched that of a cobalt bromide dianion, $[\text{CoBr}_4]^{2-}$ when compared to literature values.⁴⁵ The extinction coefficient measured for these transitions was also consistent with the presence of a tetrahedral dianion ($>500 \text{ L mol}^{-1} \text{ cm}^{-1}$) in solution (**Figure 4.28**). It should be noted here that no bands corresponding to the starting material, $(\text{dtbpx})\text{CoBr}_2$ (**3.6b**), were observed in the UV-Vis spectrum. Complete consumption of **3.6b** during the reaction with cobaltocene was also evident as the Raman spectrum of the products (**4.14**) did not show any bands associated with the starting material (**3.6b**). The Raman spectrum of **4.14** showed a very strong, band at 317 cm^{-1} corresponding to Co-Br stretch $[\text{CoBr}_4]^{2-}$, alongside a broad band $\sim 1550 \text{ cm}^{-1}$, which can be attributed to C=C stretches from the Cp moiety within the cation(s).

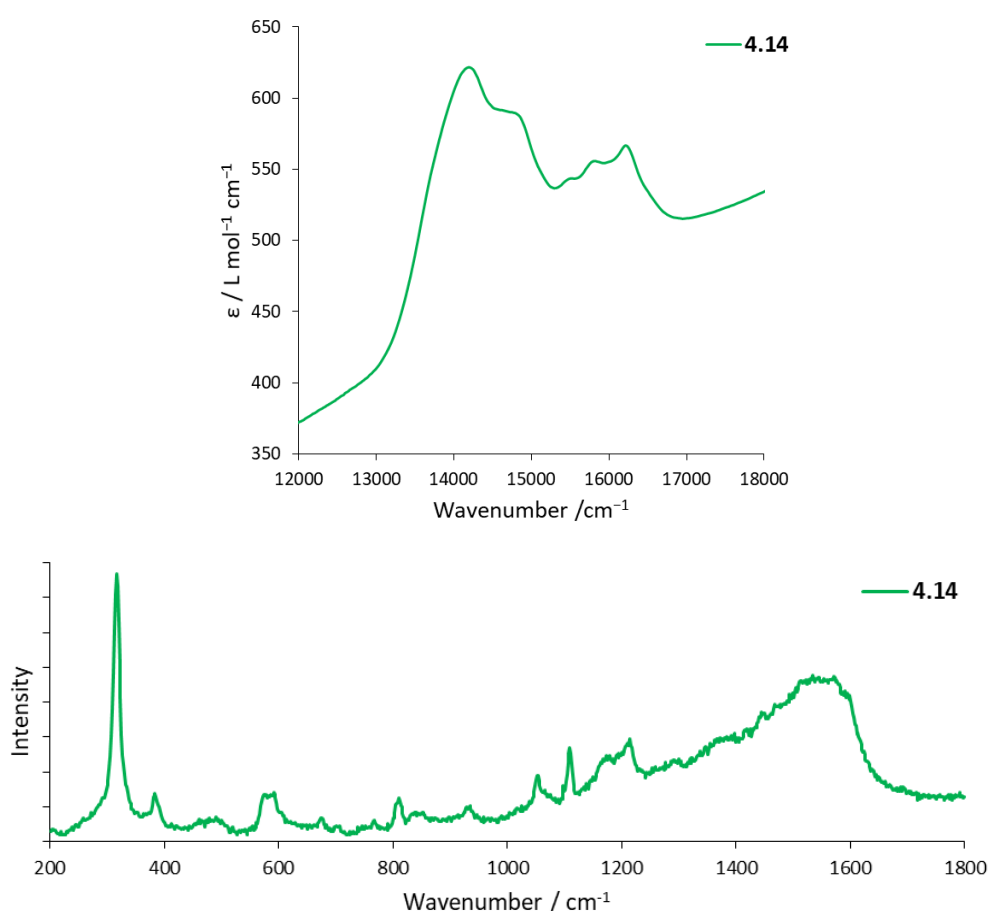


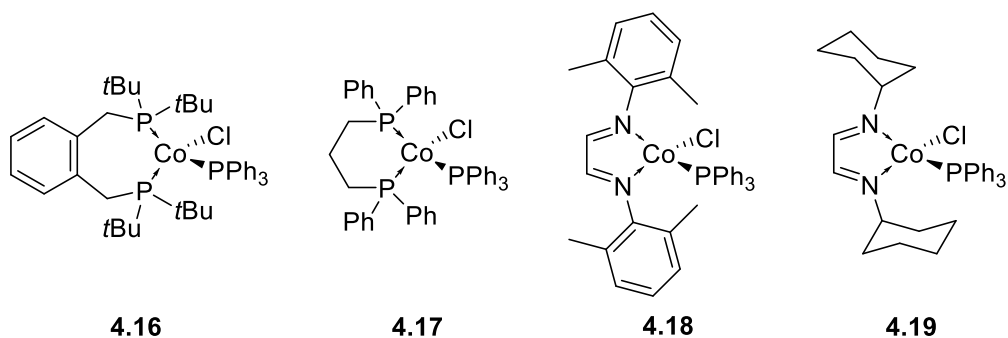
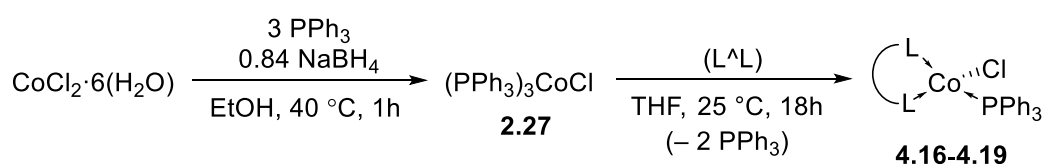
Figure 4.28 Top: UV-Vis spectrum (THF) obtained of $[\text{CoBr}_4][\text{Cp}_2\text{Co}]_2$. (**4.14**). Bottom: Raman (LIR, 532 nm) of **4.14**.

4.7 A Direct Approach to the Synthesis of $(\text{L}^{\wedge}\text{L})\text{cobalt(I)}$ Complexes

From the work presented in Sections 4.2-4.6, it is apparent that a single-electron reduction of $(\text{P}^{\wedge}\text{P})\text{CoX}_2$ -type complexes and subsequent formation of stable complexes with general formula $[(\text{P}^{\wedge}\text{P})\text{Co}(\mu_2\text{-X})_2]$ is not a universal method for preparing these cobalt(I) complexes. Most notably, the

diphosphine ligand present on cobalt and resulting steric and electronic effects on the cobalt(II) centre will determine whether successful single electron reduction can occur. Ultimately, it appears that the geometry of the parent cobalt(II) complex (as a result of the diphosphine ligand) is one of the most significant determining factors dictating the reactivity of $(P^{\wedge}P)CoX_2$ with reducing agents, such as Zn. It is very likely that the stability of the resulting cobalt(I) species, which is influenced significantly by the diphosphine, is key. Generally, it appears that diphosphine ligands with phenyl-substituents on the phosphine moieties are able to form stable cobalt(I) dinuclear species of the type $[(P^{\wedge}P)Co(\mu_2-Br)]_2$. Diphosphine ligands with bulky and/or very donating substituents on the phosphine moiety appear to be unsuitable for the formation of stable dinuclear cobalt(I) complexes and appear to be much more labile on cobalt when compared to their phenyl-substituted analogues. However, if cobalt(I) complexes are to be applied in catalytic applications, it is of importance to be able to access cobalt(I) systems with diphosphine ligands (and other $L^{\wedge}L$ ligands, such as diimines) that feature a range of different steric and electronic attributes. For instance, $L^{\wedge}L$ ligands with strong donor properties character (*e.g.* aliphatic-substituted L moieties where $L = P$ or N) and sterically demanding $L^{\wedge}L$ ligands. For this reason, a direct (*i.e.* no reduction step) synthetic route towards cobalt(I) complexes with chelating neutral donor ligand has been developed.

Throughout this work, the lability of phosphine ligands on cobalt(II) and (I) has become apparent. Thus, in order to access the desired $[(P^{\wedge}P)Co^I(\mu_2-X)]_2$ -type complexes it was envisaged that use of a well-defined cobalt(I) starting material with labile ligands, such as *tris*(triphenylphosphine)cobalt(I) chloride (**2.27**), could be used to produce the target $(L^{\wedge}L)(PPh_3)CoCl$ complexes. The lability of the triphenylphosphine ligands is advantageous in this instance, as they can undergo a ligand-exchange reaction with chelating bidentate neutral ligands (*e.g.* $(P^{\wedge}P)$ or $(N^{\wedge}N)$), as shown in **Scheme 4.56**.



Scheme 4.56 General scheme for the attempted synthesis of $(L^{\wedge}L)(PPh_3)CoCl$ complexes **4.16-4.19**.

Using the synthetic route outlined in **Scheme 4.56**, the synthesis of a small series of (L^Λ)(PPh₃)CoCl complexes (**Table 4.9**) was attempted, which included examples of diphosphine and diimine ligands. This ligand-exchange reaction, where successful, proceeded in excellent yield (81-96%). However, removal of liberated triphenylphosphine from the reaction mixture was difficult and required multiple (5+) extractions into hexanes at -78 °C.

Table 4.9 Summary of (L^Λ)(PPh₃)CoCl complexes synthesised and yield obtained.

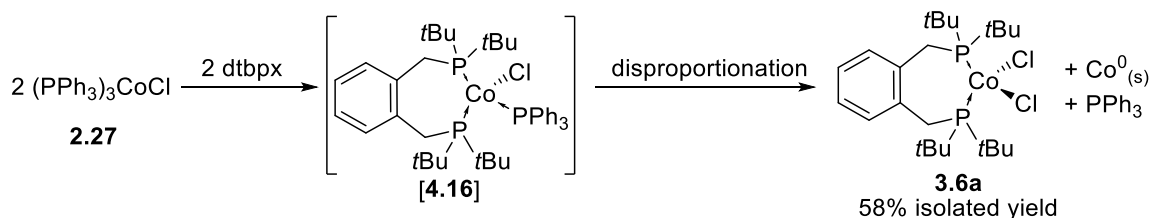
Entry	(L ^Λ)	Product	Yield (%)
1	dtbpx	3.6a ^a	58 ^a
2	dppp	4.17	89
3	<i>N,N'</i> -bis(2,5-dimethylphenyl)-1,2-diiminoethane	4.18 ^b	81 ^b
4	<i>N,N'</i> -bis(cyclohexyl)-1,2-diiminoethane	4.19	96

^aDisproportionation product, ^bsuggested product.

Using a combination of Raman, UV-Vis and NMR spectroscopic techniques and mass spectrometric analysis, the composition of the products from the reactions outlined in **Table 4.9** can be determined. The following sections discuss the observed outcomes of the reactions of L^ΛL ligands (diphosphines or diimines) with (PPh₃)₃CoCl.

4.7.1 The Attempted Synthesis of (P^ΛP)(PPh₃)CoCl Complexes

Using the ligand exchange reaction outlined in **Scheme 4.56**, an attempt was made to prepare the cobalt(I) complex (dtbpx)(PPh₃)CoCl (**4.16**). Following work-up, spectroscopic (Raman, UV-Vis, ³¹P NMR) and mass spectrometric analysis of the products obtained did not show any clear evidence of the presence of **4.16** and instead suggested the formation of (dtbpx)CoBr₂ (**3.6a**) (**Scheme 4.57**).



Scheme 4.57 Proposed disproportionation of unstable **4.16** to produce **3.6a**.

Triphenylphosphine ionises extremely well under ASAP conditions and, as such, often masks the signals from additional fragments. A ^{31}P NMR spectrum obtained of the solids obtained from the reaction between $(\text{PPh}_3)_3\text{CoCl}$ (**2.27**) and dtbpx (**Scheme 4.57**) did not show any resonances; this was attributed to the presence of a paramagnetic species in solution (^{31}P NMR spectroscopic analysis of **2.27** shows a broad resonance at $\delta_{\text{p}} -5.3$ ppm). Raman spectroscopic analysis of the products obtained from the reaction shown in **Scheme 4.57** provided evidence for the complexation of dtbpx to cobalt. The Raman spectrum of the solids obtained from this reaction is markedly different to that of the starting material, **2.27**, suggesting that all **2.27** has been consumed in the reaction. A band is observed in the Raman spectrum with $\nu = 323\text{ s cm}^{-1}$, which has been attributed to the presence of **3.6a** ($\nu_{\text{Co-Cl}}$ in **3.5a** is 318 cm^{-1}) (**Figure 4.29**).

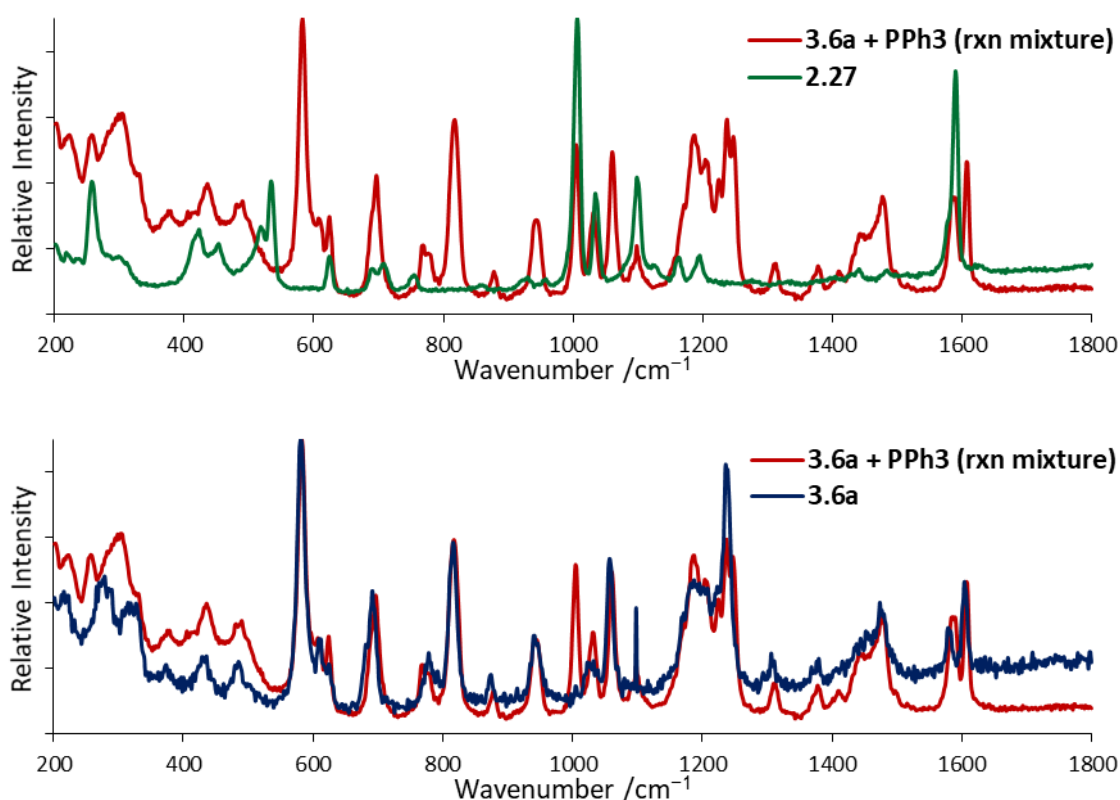


Figure 4.29 Comparison of Raman spectra (LIR, 532 nm) between the product of the reaction between $(\text{PPh}_3)_3\text{CoCl}$ (**2.27**) and dtbpx (**3.6a + PPh₃**) and Top: **2.27** and Bottom: $(\text{dtbpx})\text{CoCl}_2$ (**3.6a**).

The presence of **3.6a** is further evidenced in the UV-Vis spectrum obtained of the product mixture from the reaction shown in **Scheme 4.57**. UV-Vis spectroscopic analysis of the products of this reaction showed a broad band in the visible region with three peaks (ν 13699, 14870 and 15974 cm^{-1}), which is characteristic of cobalt(II) in a *pseudo*-tetrahedral geometry (**Figure 4.30**), and the spectrum obtained is clearly consistent with a disproportionation pathway having taken place to produce $(\text{dtbpx})\text{CoCl}_2$

(**3.6a**) (ν 13699, 14881, 15974 cm^{-1}). The formation of complex **3.6a** from **2.27** and dtbpx further demonstrates the inability of the dtbpx ligand to stabilise a cobalt(I) complex.

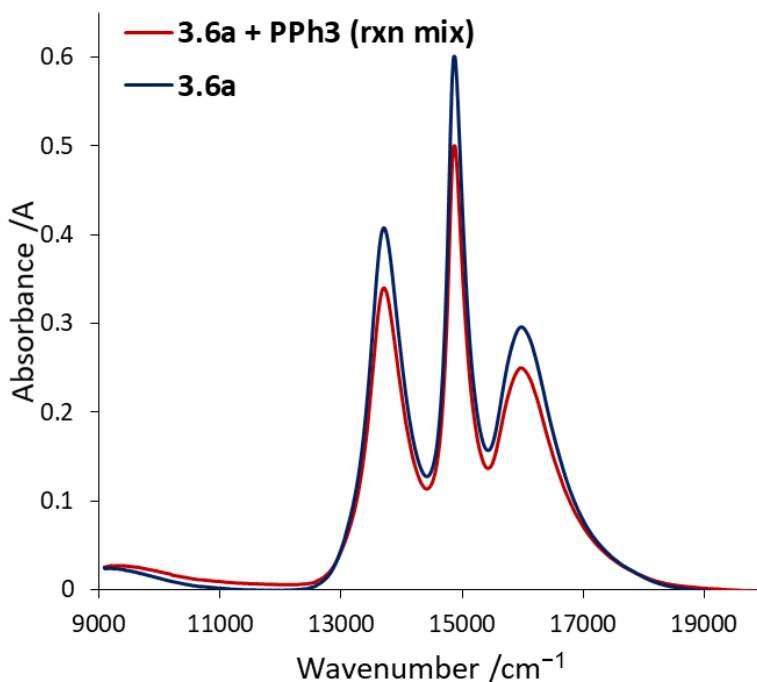
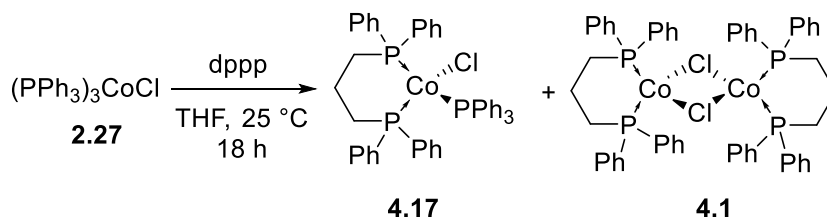


Figure 4.30 Comparison of the UV-Vis spectra (THF) of dtbpxCoCl₂ (**3.6a**) and product from reaction of (PPh₃)₃CoCl (**2.27**) with dtbpx that contained **3.6a** and PPh₃.

The ligand exchange reaction between dppp and triphenylphosphine to produce complex (dppp)(PPh₃)CoCl (**4.17**) was also attempted (**Table 4.9**: Entry 2). The cobalt(II) complexes (dppp)CoX₂ (X = Cl, **3.4c** or X = Br, **3.4d**) can successfully be reduced with Zn to produce complexes (dppp)Co(μ_2 -X)₂Co(dppp) (X = Cl, **4.1** or X = Br, **4.2**). Consequently, it was postulated that this dppp ligand may be able to stabilise the desired cobalt(I) product, **4.17**. UV-Vis and Raman spectroscopic analysis of the products obtained from the reaction of **2.27** with dppp suggested the formation of the desired product, **4.17**, and the presence of some (dppp)Co(μ_2 -Cl)₂Co(dppp) (**4.1**), as shown in **Scheme 4.58**.



Scheme 4.58 Reaction between (PPh₃)₃CoCl (**2.27**) and dppp to produce (dppp)(PPh₃)CoCl (**4.17**) and (dppp)Co(μ_2 -Cl)Co(dppp) (**4.1**).

Mass spectrometric analysis of the products obtained from the reaction shown in **Scheme 4.58** showed the molecular ion of **4.17** [(dppp)(PPh₃)CoCl]⁺, albeit with weak intensity (0.03%) at m/z 768.111 Da (calc. 768.144 Da, with correct isotope pattern). UV-Vis spectroscopic analysis of the product obtained shows a broad band at ν 11338 cm⁻¹, which is indicative of a cobalt(I) complex (c.f. (dppp)Co(μ_2 -Cl)Co(dppp) (**4.1**), ν 11261 cm⁻¹), **Figure 4.31**. Raman spectroscopic analysis of this proposed mixture containing **4.17** and **4.1** also showed the presence of **4.17** with a clear band at 297 cm⁻¹, which was assigned as ν Co-Cl in this *pseudo*-tetrahedral complex, **4.17**. A weak band at 395 cm⁻¹ was also visible in the Raman spectrum, suggesting some form of halide-bridged species (likely **4.1**) was also present.

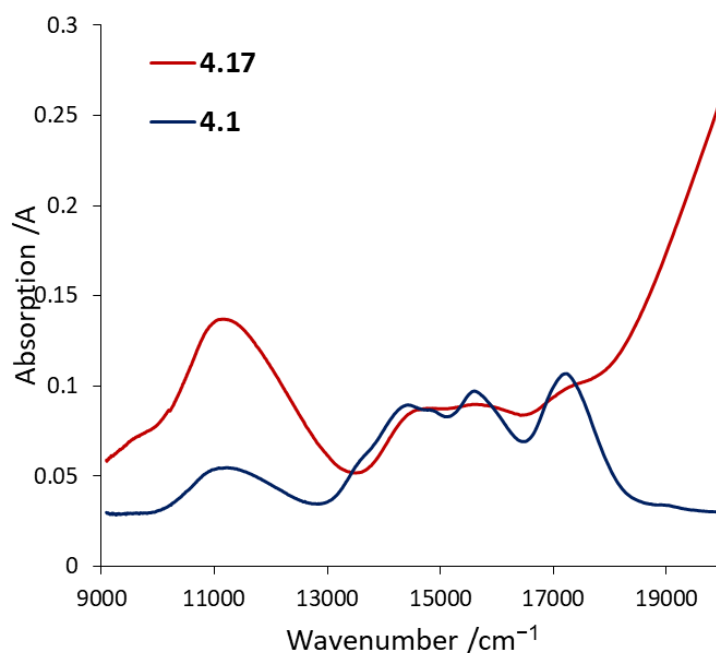
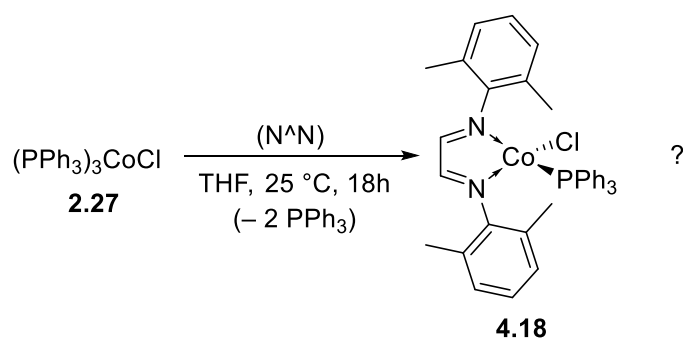


Figure 4.31 Comparison of the UV-Vis spectra (THF) of complexes (dtbpx)(PPh₃)CoCl (**4.17**) and (dppp)Co(μ_2 -Cl)₂Co(dppp) (**4.1**).

4.7.2 The Attempted Synthesis of (N[^]N)(PPh₃)CoCl Complexes

The ligand exchange reaction shown in **Scheme 4.56** was also attempted using diimine ligands. The reaction was performed using *N,N'*-bis(2,6-dimethylphenyl)-1,2-diiminoethane (**Table 4.9**: Entry 3). Analysis of the solids obtained from this reaction (shown in **Scheme 4.59**) was inconclusive and therefore the formation of complex **4.18** was not confirmed.



Scheme 4.59 The reaction between $(\text{PPh}_3)_3\text{CoCl}$ (**2.27**) and N,N' -bis(2,6-dimethylphenyl)-1,2-diiminoethane ($\text{N}^{\wedge}\text{N}$).

UV-Vis spectroscopic analysis of the resulting product from the reaction shown in **Scheme 4.59** showed no discernible bands in the visible region of the spectrum where $d \leftarrow d$ transitions would be expected. The UV-Vis spectrum was dominated by a charge transfer band at 28410 cm^{-1} [Note: no $d \leftarrow d$ are observed for $(\text{N}^{\wedge}\text{N})\text{CoX}_2$ complexes **3.2a-d** as discussed in Chapter 3: Section 3.2.2.4]. Comparison of the Raman spectrum of the solids obtained from this reaction with those of the starting material $(\text{PPh}_3)_3\text{CoCl}$ (**2.27**) showed the presence of a new strong vibration at 1633 cm^{-1} , which was assigned as $\nu\text{C=N}$ arising from the diimine ligand. In addition, the Raman spectrum of the product also showed a band at 345 cm^{-1} , which was tentatively assigned as $\nu\text{Co-Cl}$ in the *pseudo*-tetrahedral complex **4.18**. Although the molecular ion corresponding to **4.18** was not observed, mass spectrometric analysis (ASAP⁺) of **4.18** did contain ions that include the diimine ligand with cobalt, suggesting complexation had occurred, for instance, $[(\text{N}^{\wedge}\text{N})(\text{PPh}_3)\text{Co}+\text{H}]^+$ at m/z 586.238 Da (calc. 586.194 Da) and $[(\text{N}^{\wedge}\text{N})\text{CoCl-H}]^+$ at m/z 357.053 Da (calc. 357.057 Da, with correct isotope pattern) and $[(\text{N}^{\wedge}\text{N})(\text{Co})]^+$ at m/z 323.082 Da (calc. 323.096 Da, with correct isotope pattern). There is evidence for the formation of **4.18** from the ligand exchange reaction performed, however, together these data are currently inconclusive in the absence of future work.

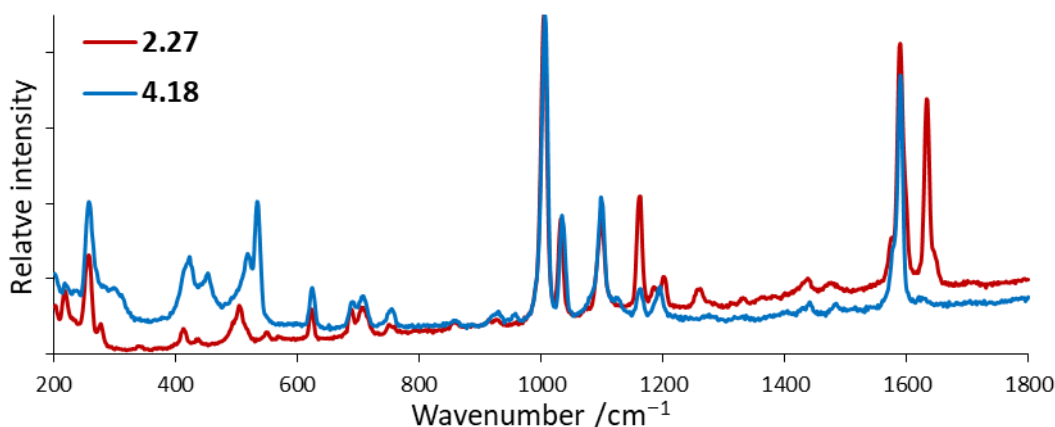
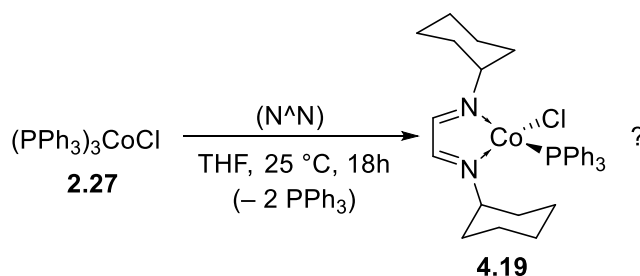


Figure 4.32 Comparison of the Raman spectra of $[(\text{PPh}_3)_3\text{CoCl}]$ (**2.27**) and possible $[(\text{N}^{\wedge}\text{N})(\text{PPh}_3)\text{CoCl}]$ (**4.18**) where $(\text{N}^{\wedge}\text{N}) = N,N'$ -bis(2,6-dimethylphenyl)-1,2-diiminoethane.

Finally, the ligand exchange reaction outlined in **Scheme 4.56** was carried out with an aliphatic diimine ligand, *N,N'*-bis(cyclohexyl)-diiminoethane (**Table 4.9**: Entry 4) to determine whether the exchange would be effected by imine-substituents, as has been observed for variously-substituted diphosphine ligands. Analysis of the products from this reaction (shown in **Scheme 4.60**) suggest the formation of the desired cobalt(I) diimine complex, **4.19**, however, as the data stands, this cannot be confirmed.



Scheme 4.60 The reaction between $(\text{PPh}_3)_3\text{CoCl}$ (**2.27**) and *N,N'*-bis(cyclohexyl)-diiminoethane ($\text{N}^{\wedge}\text{N}$).

UV-Vis spectroscopic analysis of the solids obtained from the reaction outlined in **Scheme 4.60** showed a series of charge transfer bands at λ_{max} 432, 478, 525, 567, 560s and 590s nm, which are likely a mixture of LC and LMCT (as discussed in Chapter 3: Section 3.2.2.4). Again, no clear bands were observed within the electronic absorbance spectrum of the products that might correspond to $d \leftarrow d$ transitions. The Raman spectrum obtained of the solids obtained from this reaction (**Scheme 4.60**) had a sloping baseline as a result of sample fluorescence. Any visible bands within the Raman spectrum obtained directly relate to triphenylphosphine, with the exception of a weak band observed at 1651 cm^{-1} , which was tentatively assigned as $\nu_{\text{C}=\text{N}}$ of the diimine ligand (**Figure 4.33**). Mass spectrometric analysis of the product of the reaction between **2.27** and *N,N'*-bis(cyclohexyl)-diiminoethane suggested successful formation of the desired product $(\text{N}^{\wedge}\text{N})(\text{PPh}_3)\text{CoCl}$ (**4.19**), for example, the protonated molecular ion is observed $[\text{M}+\text{H}]^+$ at m/z 557.105 Da (calc. 577.194 Da, with the correct isotope pattern), along with $[\text{M}-\text{PPh}_3]^+$ at m/z 314.084 Da (calc. 314.096 Da, with the correct isotope pattern) and $[\text{M}-\text{PPh}_3-\text{Cl}]^+$ at m/z 279.081 Da (calc. 279.127 Da, with the correct isotope pattern). As with complex **4.18**, there is evidence for the formation of **4.19**, however, as the data stands, the formation of **4.19** cannot be stated with certainty.

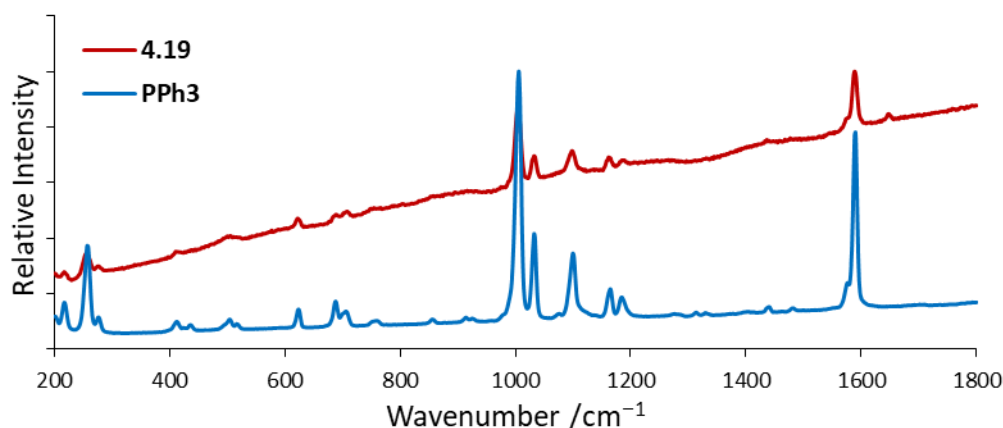


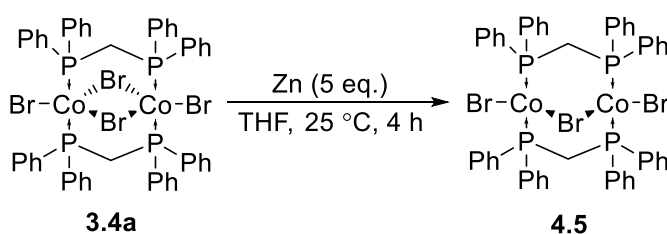
Figure 4.33 Comparison of the Raman spectrum obtained for triphenylphosphine and (N^N)(PPh₃)CoCl (**4.19**).

4.7.3 Summary of Direct Approach to the Synthesis of (L^L)Cobalt(I) Complexes

From the ligand exchange reactions outlined in **Scheme 4.56**, several conclusions can be drawn. Previously, disproportionation or decomposition products from reactions involving the dtbpx ligand have been seen in the presence of a Lewis acid or an excess of reductant (Sections 4.2-4.6). The formation of **3.5a** *via* a disproportionation pathway within the reaction of (PPh₃)₃CoCl (**2.27**) and dtbpx clearly shows the inability of this dtbpx ligand to stabilise a cobalt(I) species. The ligand exchange reaction between (PPh₃)₃CoCl (**2.27**) and dppp shows clear formation of a cobalt(I) complex (dppp)(PPh₃)CoCl (**4.17**) along with (dppp)Co(μ₂-Cl)Co(dppp) (**4.1**). The formation of complex **4.1** from the ligand exchange reaction between **2.27** and dtbpx is likely the result of the lability of PPh₃ ligands in solution. Loss of labile PPh₃ would result in a very unstable and coordinatively unsaturated 14e⁻ intermediate “(dppp)CoCl” which, with another cobalt(I) complex, will quickly dimerise to gain stability. This result is particularly interesting as an excess of PPh₃ was available within the reaction mixture (liberated from starting complex **2.27**), suggesting that these halide-bridged-dimeric complexes, once formed, are fairly robust to cleavage by a neutral donor ligand. In the literature it has been noted previously that when cobalt(I) complexes, which have been prepared *ex situ* to catalysis, are used within catalytic transformations, their activity is typically lower than analogous cobalt(I) species which are produced *in situ*. The formation of complex **4.1** from the reaction between **2.27** and dtbpx (**Table 4.9**: Entry 2) is clear evidence for the claims within the literature of the relative stability of dinuclear cobalt(I) complexes.^{7,8} The ligand exchange reactions involving diimine ligands appear to have produced diimine cobalt complexes – however, at this point it is difficult to say with any certainty the oxidation state or geometry of the cobalt species produced.

4.8 A Molecular “A-Frame”: The Solid-state structure of $[\{\text{BrCo}(\mu_2\text{-dppm})\}_2(\mu_2\text{-Br})]$ (**4.5**)

As described in Section 4.2.1.3, the attempted reduction of $[\{\text{BrCo}(\mu_2\text{-dppm})(\mu_2\text{-Br})\}_2]$ (**3.4a**) with Zn metal resulted in the formation of a mixed valence species, $[\text{BrCo}(\mu_2\text{-dppm})_2(\mu_2\text{-Br})\text{CoBr}]$ (**4.5**). The formation of **4.5** from **3.4a** is shown in **Scheme 4.61**.



Scheme 4.61 Formation of $[\text{BrCo}(\mu_2\text{-dppm})_2(\mu_2\text{-Br})\text{CoBr}]$ (**4.5**) from reduction of $[\text{BrCo}(\mu_2\text{-dppm})_2(\mu_2\text{-Br})_2\text{CoBr}]$ (**3.4a**).

The solid-state structure obtained for complex **4.5** is shown in **Figure 4.34**. Both cobalt centres are *pseudo*-tetrahedral in geometry and have a terminal bromide ligand. Bridging dppm ligands span the cobalt centres along with a single bridging bromide ligand, which results in an “A-frame”-type structure. As discussed in Chapter 3, Section 3.3.2.3, dppm ligands are much more likely to bridge two metal centres than coordinate in a bidentate manner due to repulsions between the lone pairs of each phosphine moiety. Selected bond distances and bond angles obtained from the solid-state structure of **4.5** are shown in **Table 4.10**.

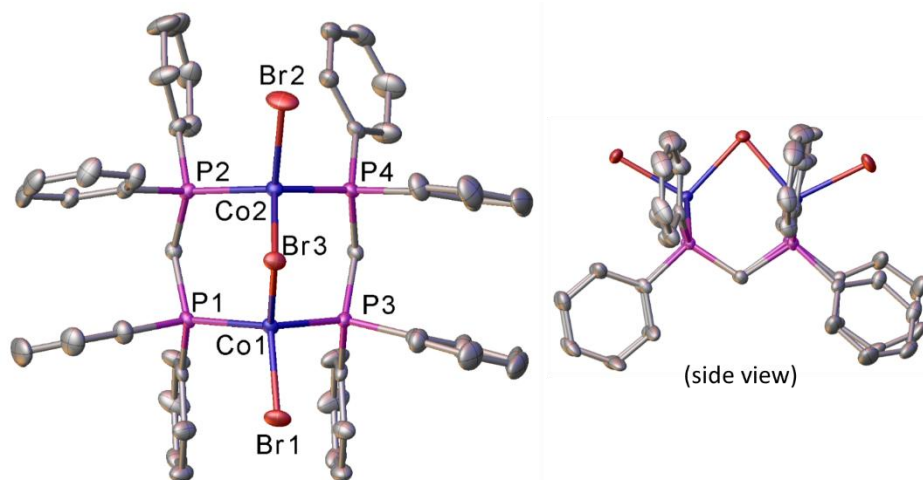


Figure 4.34 Solid state structure of $[\text{BrCo}(\mu_2\text{-dppm})_2(\mu_2\text{-Br})\text{CoBr}]$ (**4.5**). ORTEPs are set at 50% probability. Hydrogen atoms and a disordered THF solvate molecule have been omitted for clarity.

Table 4.10 Selected bond distances and bond angles of [BrCo(μ_2 -dppm) $_2$ (μ_2 -Br)CoBr] (**4.5**). Standard deviation in parenthesis.

Bond distance /Å		Co1 Bond Angles /°		Co2 Bond Angles /°	
Co1-Br1	2.3852(5)	Br1-Co1-Br3	103.15(2)	Br2-Co2-Br3	104.56(2)
Co2-Br2	2.3718(4)	P1-Co1-P3	106.37(2)	P2-Co2-P4	112.49(2)
Co1-Br3	2.4219(4)	P-Co1-Br1 ^a	108.61(3)	P-Co2-Br2 ^a	107.08(3)
Co2-Br3	2.3987(5)	P-Co1-Br3 ^a	114.93(3)	P-Co2-Br3 ^a	112.53(3)
Co-P ^a	2.2981(13)	τ_4^b	0.923	τ_4^b	0.928
Co1...Co2	3.2069(5)	Co1-Br3-Co2		83.40(2)	

^aAverage value, ^b4-coordinate geometry index.

The Co-Br bond distances measured in the solid-state structure of complex **4.5** range between 2.3718(4) Å (Co2-Br2) and 2.4219(4) Å (Co1-Br3) (**Table 4.10**). The Co-Br3 (bridging bromide) bond distance measured is shortest to Co2 (*c.f.* Co2-Br3 2.3718(4) and Co1-Br3 2.4219(4) Å), suggesting that Co2 has a greater degree of electron density than Co1 in this solid-state structure of the mixed valence (Co^{II}/Co^I, d^7/d^8 , $15e^-/16e^-$) dinuclear complex **4.5**. The Co-P bond distances do not vary greatly and range between 2.2902(7) Å and 2.3149(6) Å. There is no bond between the two cobalt centres as the Co...Co distance is found to be 3.2069(5) Å (Co-Co reported within the range 2.47-2.52 Å).⁴⁶

Both cobalt centres in the solid-state structure of **4.5** can be described as *pseudo*-tetrahedral and have very similar values of 4-coordinate geometry index, τ_4 , 0.923 and 0.928 for Co1 and Co2, respectively, with coordination angles ranging between 103.15(2)° and 114.93(3)° (**Table 4.10**). The Co1-Br3-Co2 bond angle is 83.40(2)°, which is smaller than that for the dihalide bridged dianion [Co₂Br₆]²⁻ present in **3.10**, which is 86.07(2)° (Chapter 3, Section 3.3.2.3). The small Co-Br-Co bond angle present in **4.5** is likely the result of steric repulsions between the phenyl groups present in dppm and the bridging halide, as shown in the side view of **4.5** in **Figure 4.34**.

Structures that can be described as molecular “A-Frames” have been investigated for cobalt in the past. However, previously-reported structures have included an additional neutral donor ligand to stabilise the structures: these are known as Type II complexes.⁴⁷ From a search of the Cambridge Structural Database,⁴⁸ complex **4.5** appears to be the first example of a Type I “A-Frame” complex of cobalt (**Figure 4.35**). Type I “A-frame” structures of rhodium and iridium (where a M-M bond is or is not present) have been of interest for catalysis historically due to their ability to reversibly coordinate a neutral donor ligand into the vacant bridging site.⁴⁹⁻⁵¹ However, from the solid-state structure of complex **4.5**, it is likely that the vacant bridging coordination site in complex **4.5** is likely to be blocked

by the bridging dppm ligands. Nevertheless, future studies on the reactivity of complex **4.5** with small molecules would be of interest.

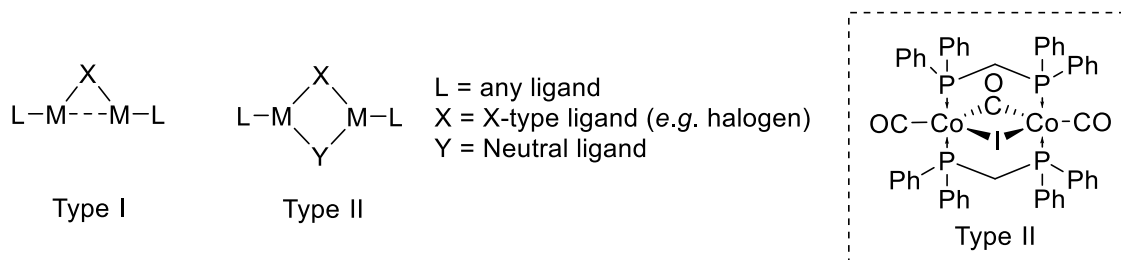
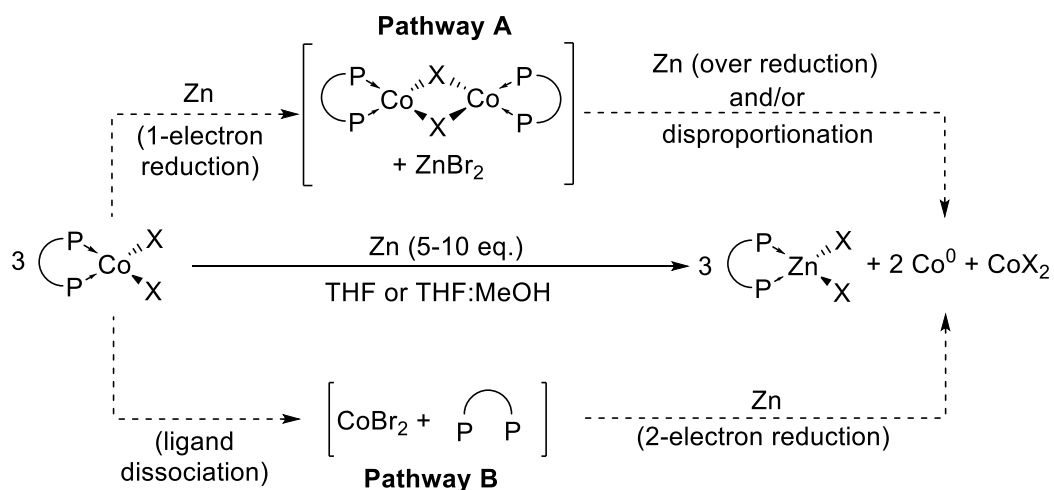


Figure 4.35 Representation of Type I and Type II "A-frame" structures, and an example of a previously reported cobalt Type II structure.⁴⁷

4.9 Summary and Conclusions

In this chapter, a series of cobalt(I) complexes (**4.1-4.8**) have been synthesised through treatment of the parent (P[^]P)CoX₂ complexes (X = Cl or Br) with an excess of zinc metal (1-10 equivalents) in THF or a THF:MeOH mixture. From spectroscopic analyses (Raman, UV-Vis) and literature support, the structures of these cobalt(I) complexes (**4.1-4.8**) are proposed to be dimeric in nature with bridging halide ligands between two *pseudo*-tetrahedral cobalt centres to stabilise these reactive complexes such that the general structure is (P[^]P)Co(μ₂-X)₂Co(P[^]P).

Throughout attempts to reduce (P[^]P)CoX₂ complexes (**3.3-3.10**) using an excess of Zn metal, the formation of (P[^]P)ZnX₂ complexes (**Zn-5.1-Zn-5.9**) and the generation of metallic cobalt(0) was observed. Two pathways for the formation of these (P[^]P)ZnX₂ complexes were proposed (**Scheme 4.62**). Based upon the experimental evidence within this chapter, it is likely that both reaction pathways to generate (P[^]P)ZnX₂ complexes from (P[^]P)CoX₂ complexes and Zn are occurring. For instance, Pathway A is observed through disproportionation of (PPh₃)₃CoCl (**2.27**) in the presence of dtbpx (and the absence of Zn) to generate the cobalt(II) species (dtbpx)CoCl₂ (**3.6a**), cobalt(0) and free triphenylphosphine or the decomposition of (dtbpx)CoBr₂ (**3.6b**) in the presence of cobaltocene to form [CpCo]₂[CoBr₄] (**4.15**). Pathway B was observed within UV-Vis spectroscopic measurements through dissociation of diphosphine ligands to generate CoBr₂ *in situ*. Attempts to stabilise any *in situ* generated cobalt(I) species to disproportionation through the addition of a neutral donor ligand (PPh₃ or 1-hexene) were unsuccessful.



Scheme 4.62 Proposed routes for the formation of (P[^]P)ZnX₂, Co⁰, CoX₂ and free diphosphine from the reaction of (P[^]P)CoX₂ excess Zn metal.

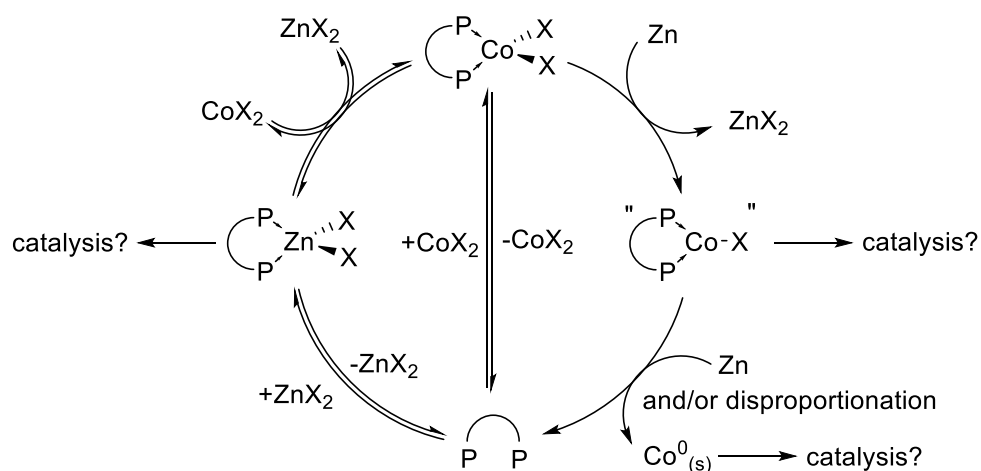
A small series of (P[^]P)ZnX₂ complexes (**Zn-5.3**, **Zn-5.4**, **Zn-5.6-Zn-5.8**) were synthesised through reaction of a 1:1 ratio of ZnX₂ (X = Cl or Br) and diphosphine ligand. These (P[^]P)ZnX₂ complexes were characterised by NMR spectroscopic and mass spectrometric techniques. A structural investigation (by single crystal X-ray diffraction) revealed these complexes to be isomorphs to their cobalt derivatives. Application of these (P[^]P)ZnX₂ complexes (**Zn-5.3**, **Zn-5.4**, **Zn-5.6-Zn-5.8**) and (P[^]P)CoX₂ complexes (**3.4-3.10**) in so-called ligand exchange reactions with either CoX₂ or ZnX₂ revealed a reversible equilibrium between diphosphine coordination to a zinc or a cobalt centre. For cases where a successful single-electron reduction of parent (P[^]P)CoX₂ complexes (**3.4a**, **3.4c-f**, **3.6f** and **3.7a**) to generate (P[^]P)Co(μ²-X)Co(P[^]P) complexes (**4.1-4.7**), the ligand exchange reactions observed (where possible and performed) were found to favour diphosphine coordination to cobalt over Zn. Where the treatment of parent (P[^]P)CoX₂ complexes with Zn resulted in formation of (P[^]P)ZnX₂ species and/or formation of metallic cobalt, the diphosphine ligands were found to be much more labile on cobalt or zinc.

Of note, the successfully prepared cobalt(I) complexes (**4.1-4.7**) all contained Ph-substituted diphosphine ligands. A preliminary electrochemical investigation was undertaken to try to determine any underlying bias for the successful single-electron reduction of (P[^]P)CoBr₂ complexes with Ph-substituted diphosphine ligands (**3.4d** and **3.6f**) over *t*Bu-substituted diphosphine ligands (**3.5a** and **3.6b**). The redox potentials measured for these (P[^]P)CoX₂ complexes appear to correlate to the σ-donor capability of the diphosphine ligand (as measured by |¹J_{SeP}|) such that as donor capacity is increased (lower magnitude of |¹J_{PSe}|) the E_{1/2} value is decreased, *i.e.* Ph-substituted complexes (**3.4d** and **3.6f**) are more susceptible to electrochemical reduction than the *t*Bu-substituted complexes (**3.5a** and **3.6b**). The cyclic voltammograms obtained were complex and may contain coupled waves making data interpretation difficult. However, what is clear is that the Ph-substituted diphosphine complexes (**3.4d** and **3.6f**) are more stable to electrochemical redox process than *t*Bu-substituted complexes (**3.5a** and **3.6b**) under the conditions applied through comparison of the “reversibility” of the redox event observed. Work in this field remains ongoing at the time of writing this thesis.

A direct approach to the synthesis of cobalt(I) complexes with general formula (L[^]L)(PPh₃)CoCl was trialled through application of a ligand exchange reaction between cobalt(I) species (PPh₃)₃CoCl (**2.27**) and a bidentate neutral donor ligand (where L[^]L = diphosphine or diimine). From the limited scope and data obtained, it appears as though the formation of stable complexes with general formula (L[^]L)(PPh₃)CoCl are privy to the same rules as observed for single-electron reduction of (P[^]P)CoX₂ complexes. Such that, Ph-substituted diphosphine, dppp, undergoes successful ligand exchange with (PPh₃)₃CoCl to form (dppp)(PPh₃)CoCl (**4.17**) (along with small amounts of (dppp)Co(μ₂-Cl)Co(dppp) (**4.1**)) and treatment of **2.27** with *t*Bu-substituted diphosphine, dtbpx, results in disproportionation of

the cobalt(I) complex. While not a ubiquitous method for the formation of cobalt(I) diphosphine complexes, this route could be employed for the synthesis of cobalt(I) complexes where the resulting product will be free from any impurities resulting from a reducing agent, *e.g.* ZnX_2 is produced during reductions of $(\text{P}^{\wedge}\text{P})\text{CoX}_2$ complexes with Zn. However, any small impurities of residual liberated triphenylphosphine from reaction of diphosphine with **2.27** could have the potential to inhibit any catalytic transformations these complexes might be employed in.

In the literature, it is common practice to employ a wide variety of diphosphine ligands in cobalt-mediated catalytic transformations using a so-called “all-in-one” approach, such that the reduction of pre-catalyst species $(\text{P}^{\wedge}\text{P})\text{CoX}_2$ is performed *in situ* through addition of, often, a large excess of Zn metal. As such, the ramifications of the observed range of reactivities that $(\text{P}^{\wedge}\text{P})\text{CoX}_2$ complexes have towards Zn and ZnX_2 species, as observed from the work presented in this chapter, upon possible catalytic transformations were considered. The nature of the diphosphine ligand (donor capacity) and steric constraints (phosphine-substituents) were found to influence the reactivity of $(\text{P}^{\wedge}\text{P})\text{CoX}_2$ complexes towards Zn metal, such that there are several pathways which should be considered whenever an *in situ* approach to generate a diphosphine cobalt(I) species is undertaken (**Scheme 4.63**).



Scheme 4.63 Possible catalytically active species and pathways for the formation of, from starting materials $(\text{P}^{\wedge}\text{P})\text{CoX}_2$ and Zn.

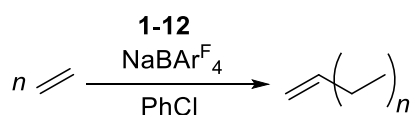
4.10 Future Work

It is apparent there remains work to be done to further investigate the observed reactivity of $(\text{P}^{\wedge}\text{P})\text{CoX}_2$ towards reduction. A spectro-electrochemical investigation (UV-Vis-Electrochemistry) would be beneficial to attempt to observed the proposed change in geometry of the $(\text{P}^{\wedge}\text{P})\text{CoX}_2$ complexes upon electrochemical reduction. Further electrochemical measurements at low temperature and/or faster scan speeds should allow observation of the processes present for all $(\text{P}^{\wedge}\text{P})\text{CoX}_2$ complexes. In addition,

it would also be beneficial to perform the electrochemical measurements in the presence of a halide through choice of the electrolyte employed as this may also help to stabilise any short lived species which form during electrochemical measurement.

Computational studies on the relative stabilities of dimeric vs monomeric cobalt(I) species would also be beneficial to help support the experimental evidence for the proposed formation of complexes with general formula $(P^{\wedge}P)Co(\mu^2-X)_2Co(P^{\wedge}P)$. As mentioned in Chapter 3, a computational investigation into the effects upon bonding within $(P^{\wedge}P)CoX_2$ complexes by distortions to the geometries of the complexes (τ_4 values) would be very interesting.

This work set out to attempt to understand the role that Zn (and Zn species such as ZnX_2) may play in catalytic transformations. It stands, therefore, that a lot of work remains to be done to determine the role such species may play in catalysis. For this reason, a catalytic investigation into the reactivity of a variety of species towards ethylene oligomerisation should be launched whereby possible catalytically active species could be investigated through the following possible control reactions:



1. $(P^{\wedge}P)CoX_2$
2. $CoX_2 + Zn$ (in excess or 1:1)
3. $(P^{\wedge}P)CoX_2 + Zn$ (in excess or 1:1)
4. $(P^{\wedge}P)CoX_2 + ZnX_2$ (in excess or 1:1)
5. $(P^{\wedge}P)ZnX_2$
6. $(P^{\wedge}P)ZnX_2 + Zn$ (in excess or 1:1)
7. $(P^{\wedge}P)ZnX_2 + ZnBr_2$ (in excess or 1:1)
8. $(P^{\wedge}P)Co(\mu^2-X)_2Co(P^{\wedge}P)$
9. $(P^{\wedge}P)Co(\mu^2-X)_2Co(P^{\wedge}P) + ZnX_2$ (in excess or 1:1)
10. $(P^{\wedge}P)Co(\mu^2-X)_2Co(P^{\wedge}P) + Zn$ (in excess or 1:1)
11. Metallic cobalt
12. Metallic zinc

4.11 References

- 1 G. Kiefer, H. Vrubel, R. Scopelliti and K. Severin, *Eur. J. Inorg. Chem.*, 2013, 4916–4921.
- 2 S. M. Jing, V. Balasanthiran, V. Pagar, J. C. Gallucci and T. V. RajanBabu, *J. Am. Chem. Soc.*, 2017, **139**, 18034–18043.
- 3 M. R. Friedfeld, H. Zhong, R. T. Ruck, M. Shevlin and P. J. Chirik, *Science*, 2018, **360**, 888–893.
- 4 H. Zhong, M. R. Friedfeld, J. Camacho-Bunquin, H. Sohn, C. Yang, M. Delferro and P. J. Chirik, *Organometallics*, 2019, **38**, 149–156.
- 5 R. Arevalo and P. J. Chirik, *J. Am. Chem. Soc.*, 2019, **141**, 9106–9123.
- 6 J. V. Obligacion and P. J. Chirik, *Nat. Rev. Chem.*, 2018, **2**, 15–34.
- 7 I. Knopf, M. A. Courtemanche and C. C. Cummins, *Organometallics*, 2017, **36**, 4834–4843.
- 8 H. Zhong, M. R. Friedfeld and P. J. Chirik, *Angew. Chemie - Int. Ed.*, 2019, **58**, 9194–9198.
- 9 K. Duvvuri, K. R. Dewese, M. M. Parsutkar, S. M. Jing, M. M. Mehta, J. C. Gallucci and T. V. Rajanbabu, *J. Am. Chem. Soc.*, 2019, **141**, 7365–7375.
- 10 G. Hilt, W. Hess and K. Harms, *Synthesis (Stuttg.)*, 2008, 75–78.
- 11 G. Wu and A. J. Von Wangelin, *Chem. Sci.*, 2018, **9**, 1795–1802.
- 12 M. Pisset, J. Paul, G. N. Cherif, N. Ratnam, N. Laloi, E. Léonel, C. Gosmini and E. Le Gall, *Chem. - A Eur. J.*, 2019, **25**, 4491–4495.
- 13 B. Ma and J. K. Snyder, *Organometallics*, 2002, **21**, 4688–4695.
- 14 M. Aresta, M. Rossi and A. Sacco, *Inorganica Chim. Acta*, 1969, **3**, 227–231.
- 15 H. Kanai and K. Ishii, *Bull. Chem. Soc. Jpn.*, 1981, 54, 1015–1018.
- 16 A. Moncomble, P. Le Floch and C. Gosmini, *Chem. - A Eur. J.*, 2009, **15**, 4770–4774.
- 17 I. Colon and D. R. Kelsey, *J. Org. Chem.*, 1986, **51**, 2627–2637.
- 18 J. H. Li, Y. X. Xie and D. L. Yin, *J. Org. Chem.*, 2003, **68**, 9867–9869.
- 19 K. Abiraj, G. R. Srinivasa and D. C. Gowda, *Synlett*, 2004, 877–879.
- 20 J. Hashim and C. O. Kappe, *Adv. Synth. Catal.*, 2007, **349**, 2353–2360.
- 21 B. L. Jiang, S. S. Ma, M. L. Wang, D. S. Liu, B. H. Xu and S. J. Zhang, *ChemCatChem*, 2019, **11**, 1701–1706.
- 22 A. B. P. Lever, *Inorganic Electronic Spectroscopy*, Elsevier Publishing Company, Amster, 1968, p322-333.
- 23 A. B. P. Lever and S. M. Nelson, *J. Chem. Soc. A Inorganic, Phys. Theor.*, 1966, 859–863.
- 24 K. Kawakami, T. Mizoroki and A. Ozaki, *Bull. Chem. Soc. Jpn.*, 1978, 51, 21–24.
- 25 A. J. Rucklidge, G. E. Morris, A. M. Z. Slawin and D. J. Cole-Hamilton, *Helv. Chim. Acta*, 2006, **89**, 1783–1800.
- 26 *Adapt. Solut.* <https://www.sisweb.com/mstools/isotope.htm>, Accessed 2019.
- 27 M. D. Brown, W. Levason, G. Reid and R. Watts, *Polyhedron*, 2005, **24**, 75–87.

- 28 G. A. Webb, *Nuclear Magnetic Resonance: Volume 20*, Royal Society of Chemistry, Cambridge, 1991, p161-162.
- 29 A. M. Messinis, S. L. J. Luckham, P. P. Wells, D. Gianolio, E. K. Gibson, H. M. O'Brien, H. A. Sparkes, S. A. Davis, J. Callison, D. Elorriaga, O. Hernandez-Fajardo and R. B. Bedford, *Nat. Catal.*, 2019, **2**, 123–133.
- 30 R. B. Bedford, M. Huwe and M. C. Wilkinson, *Chem. Commun.*, 2009, 600–602.
- 31 R. B. Bedford, M. A. Hall, G. R. Hodges, M. Huwe and M. C. Wilkinson, *Chem. Commun.*, 2009, 6430–6432.
- 32 K. G. Dongol, H. Koh, M. Sau and C. L. L. Chai, *Adv. Synth. Catal.*, 2007, **349**, 1015–1018.
- 33 T. Hatakeyama, Y. Kondo, Y. I. Fujiwara, H. Takaya, S. Ito, E. Nakamura and M. Nakamura, *Chem. Commun.*, 2009, 1216–1218.
- 34 S. Kawamura and M. Nakamura, *Chem. Lett.*, 2013, **42**, 183–185.
- 35 N. Elgrishi, K. J. Rountree, B. D. McCarthy, E. S. Rountree, T. T. Eisenhart and J. L. Dempsey, *J. Chem. Educ.*, 2018, **95**, 197–206.
- 36 S. R. Crouch and D. A. Skoog, *Principles of Instrumental Analysis*, Cengage Learning, Boston, 2006, p304-359.
- 37 P. Zanello, *Inorganic Electrochemistry: Theory, Practice and Application*, Royal Society of Chemistry, Cambridge, 2003, p12-38.
- 38 E. A. Ambundo, M.-V. Deydier, A. J. Grall, N. Aguera-Vega, L. T. Dressel, T. H. Cooper, M. J. Heeg, L. A. Ochrymowycz and D. B. Rorabacher, *Inorg. Chem.*, 1999, **38**, 4233–4242.
- 39 T. Fanjul, G. Eastham, N. Fey, A. Hamilton, A. G. Orpen, P. G. Pringle and M. Waugh, *Organometallics*, 2010, **29**, 2292–2305.
- 40 P. W. Dyer, J. Fawcett, M. J. Hanton, R. D. W. Kemmitt, R. Padda and N. Singh, *Dalton Trans.*, 2003, 104–113.
- 41 P. Vanysek, *Electrochemical Series in CRC Handbook of Chemistry and Physics*, CRC Press Taylor and Francis, 96th edn., 2016, p580-589.
- 42 A. J. Bard, E. Garcia, S. Kukharenko and V. V. Strelets, *Inorg. Chem.*, 1993, **32**, 3528–3531.
- 43 C. Chen, M. B. Hecht, A. Kavara, W. W. Brennessel, B. Q. Mercado, D. J. Weix and P. L. Holland, *J. Am. Chem. Soc.*, 2015, **137**, 13244–13247.
- 44 N. G. Connelly and W. E. Geiger, *Chem. Rev.*, 1996, **96**, 877–910.
- 45 W. R. Brode, *J. Am. Chem. Soc.*, 1931, **53**, 2457–2467.
- 46 L. Pauling, *Proc. Natl. Acad. Sci. U. S. A.*, 1976, **73**, 4290–4293.
- 47 E. C. Lisic and B. E. Hanson, *Organometallics*, 1987, **6**, 512–516.
- 48 Cambridge Structure Database, <http://webcds.ccdc.cam.ac.uk/index.php>, Nov 2019.
- 49 C. P. Kubiak, C. Woodcock and R. Eisenberg, *Inorg. Chem.*, 1980, **19**, 2733–2739.
- 50 C. P. Kubiak and R. Eisenberg, *J. Am. Chem. Soc.*, 1977, **99**, 6129–6131.
- 51 M. Cowie, J. T. Mague and A. R. Sanger, *J. Am. Chem. Soc.*, 1978, **100**, 3628–3629.

CHAPTER 5

– Development of an *Inert* Mass Spectrometric Analysis Technique

“Discard everything that does not spark joy.”

– Marie Kondo

5.1 Introduction

As discussed in previous chapters, the bulk of the work carried out within this project involved working with air- and moisture-sensitive samples. As such, it was of great interest to develop a mass spectrometric (MS) technique to allow analysis of these samples. However, gathering mass spectra of these complexes without oxidation occurring is a difficult task. This chapter is therefore a short discussion of the development of a new delivery method for use within vertically-loaded mass spectrometers to allow mass spectrometric analysis under inert conditions. This work was carried out in collaboration with the Durham Chemistry mass spectrometry department (Dr Jackie Mosely, Dr David Parker, and Mr Peter Stokes), Durham Chemistry glassblowing department (Mr Aaron Brown and Mr Malcolm Richardson) and Durham Chemistry Mechanical Workshop (Mr Neil Holmes and Mr Paul White).

5.1.1 Atmospheric Solids Analysis Probe (ASAP) Mass Spectrometry

While the internal conditions of a mass spectrometer are completely inert (usually under vacuum and fed with nitrogen gas supply), often, the method of delivery of a sample results in the sample briefly being exposed to air. For the analysis of air-/moisture sensitive samples, there are a few examples within the literature for MS analysis using e.g. LIFDI (Liquid Injection Field Desorption Ionisation) and ESI (Electrospray Ionisation) MS techniques.¹⁻³ However, these techniques all utilise coupling of a mass spectrometer to a glove box to provide an inert atmosphere, which incurs significant cost.

ASAP (Atmospheric Solids Analysis Probe) MS is a direct ionisation technique which removes the need for sample preparation through solvation.⁴ The ASAP MS technique can be applied to both solid and liquid samples.⁴ Compounds which have poor solubility (such as polymers) are increasingly analysed by ASAP MS in preference to other ionisation techniques, such as MALDI (Matrix-assisted Laser Desorption Ionisation).⁵ ASAP has been shown to be particularly useful in the analysis of samples which suffer from solvent suppression (dampening of the sample signal due to interactions with the solvent) in ESI (Electrospray Ionisation) or APCI (Atmospheric Pressure Chemical Ionisation).^{6,7} As the ASAP MS technique does not require sample preparation in a solvent, this technique is particularly attractive for the analysis of air-/moisture-sensitive samples as the need for rigorously dried and degassed solvents for use in MS is removed.

The use of ASAP MS for the analysis of air-/moisture-sensitive has been recognised previously by Messinis and Mosely.⁸ The authors report successful analysis of two highly air-sensitive samples through application of a novel delivery method of the sensitive sample to the mass spectrometer.⁸ Messinis and co-workers sealed solid-state air-/moisture-sensitive samples in a capillary in a nitrogen

filled glovebox. The sample was then transported (sealed under N₂) to the mass spectrometer which was fitted with ASAP and introduced to the ASAP chamber using a modified capillary holder such that the end of the sealed capillary was within the chamber. Within the internal ionisation chamber of the machine, the baffle (primary use allows or prevents lock-spray introduction to the sampling cone through systematic rotation) was then used to snap the capillary at a point of weakness (introduced deliberately during flame sealing of the capillary) during collection of the spectrum, thus freeing the sample from the capillary such that it could be vaporised and ionised for analysis by MS.⁸ While this approach worked well for the samples tested by Messinis *et al.*, the broken glass shards generated during sample analysis need to be removed after each sample measurement.⁸ Thus, the ionisation chamber is exposed to ambient conditions between sample measurements and generates an accrued time cost through cleaning and regeneration of the conditions required for MS analysis (*e.g.* reheating to correct temperatures and regaining gas pressure equilibrium within the ionisation chamber). This Chapter therefore describes an advancement to the previously reported system used by Messinis and co-workers to avoid the generation of broken glass within the MS ionisation chamber.

5.2 Development of *inert* ASAP MS

The delivery method designed herein for measurement of air-/moisture-sensitive samples by ASAP MS is based upon the 'traditional' delivery method used for a vertically loaded ASAP. To obtain a mass spectrum using ASAP MS for a standard (air stable) sample, a solid sample is loaded onto the end of a sealed capillary tube. This capillary is placed within a holder, which, in turn, is then placed within the mass spectrometer such that the loaded tip of the capillary is within the ASAP MS chamber. The chamber is kept at atmospheric pressure and has a nitrogen atmosphere. To ionise the sample, a corona discharge is used and the ionised sample can then enter the sample cone (which has an applied voltage gradient) before being taken by vacuum to the mass detector. A simplified schematic of the 'traditional' ASAP MS process is shown in **Figure 5.1**. This simple delivery method for ASAP MS does, briefly, result in the exposure of the sample for analysis to air. For the highly air-/moisture-sensitive complexes used throughout this thesis, this brief exposure to air was ample time to allow oxidation to occur (*e.g.* oxidation of diphosphine ligands in $(P^{\wedge}P)CoX_2$ complexes).

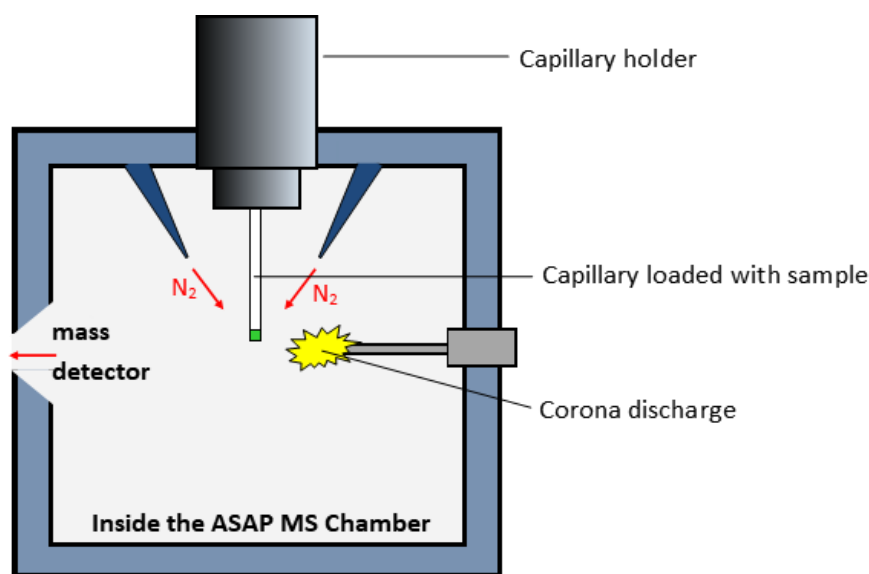


Figure 5.1 Simplified representation of a traditional ASAP MS chamber.

Building on the 'traditional' delivery method for ASAP MS analysis, a simple design was envisioned. A series of 'glass probes' were designed (manufactured in house) which allow transportation and delivery of a sample-dipped capillary into the ionisation chamber of an ASAP adapted mass spectrometer. The following sections describe the design and implementation of these glass probes along with optimisation of the conditions required for this inert ASAP (*i*ASAP) MS technique.

5.2.1 Glass Probe Design and Implementation

The glass probes were made by the Durham University Glassblowing Workshop to specifications to fit two mass spectrometers (*LCT Premiere XE QToF mass spectrometer* and *Water's Xevo QToF mass spectrometer*) capable of ASAP analysis. A probe holder to provide a seal between the external of the probe and the mass spectrometer was made by the Durham University Mechanical Workshop to specifications to fit both the probes and the mass spectrometers. The glass probes produced can be oven dried and taken into a glovebox to allow inert sample delivery as the sample can be loaded onto a capillary within the glovebox and then sealed between two PTFE taps under a glovebox atmosphere before transportation to the machine (**Figure 5.2**). This approach avoids the need to either house an MS instrument in a glovebox or to couple the sample injection system with a glovebox, both of which are non-trivial and costly to achieve.

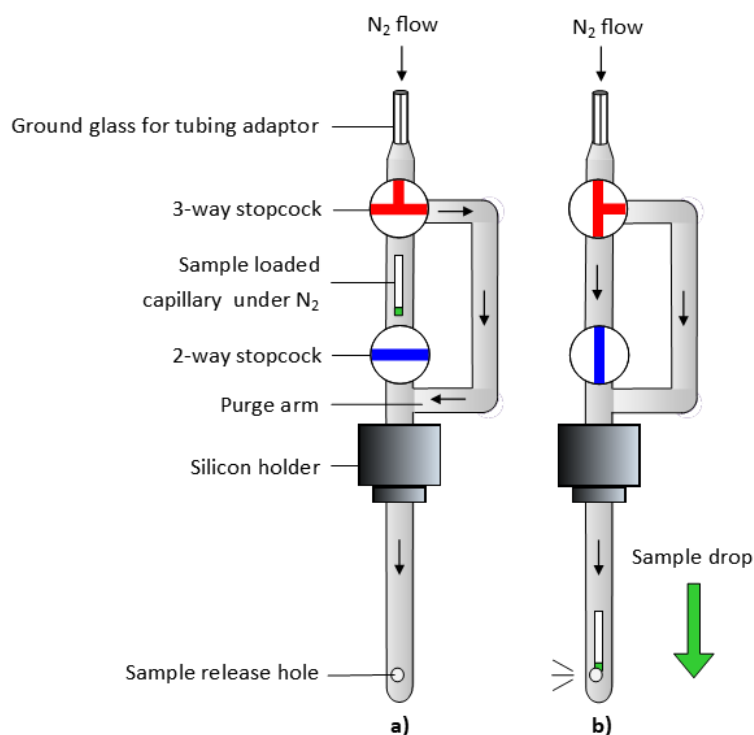


Figure 5.2 Representation of *iASAP* Probe design a) during purge of the probe, b) during analysis.

Once at the machine, the side-arm present and the three-way PTFE tap allows purging of the probe through connection to an inert gas source. The probe can then be inserted into the mass spectrometer such that the tip of the probe resides within the ASAP Chamber. Finally, to allow sample measurement, under a flow of inert gas from the top of the probe (vertical gas flow), both PTFE taps are opened and the sample-loaded capillary drops down to the base of the probe, where it can be ionised by corona

discharge and released from the probe *via* a sample release hole for analysis by the mass detector as normal (**Figure 5.3**).

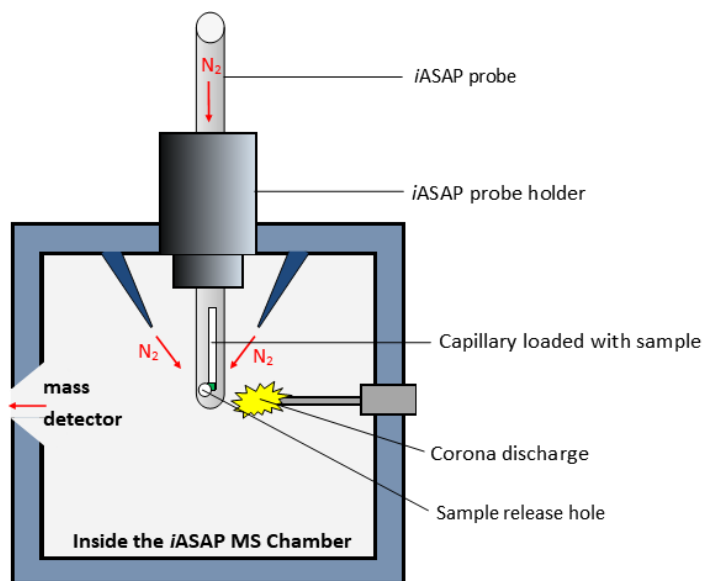


Figure 5.3 Simplified representation of the *iASAP* chamber.

5.2.2 Optimisation of the *iASAP*⁺ MS Process

Mass spectrometer conditions for *iASAP* analysis were optimised using a series of air-stable organometallic complexes [*(N,N'*-bis(2,6-dimethylphenyl)-1,2-diimino-1,2-dimethylethane)CoBr₂ (**MS-1**), (COD)Rh(dpm) (**MS-2**) and Pd(acac)₂ (**MS-3**)] in an attempt to produce spectra of matching quality and fragmentation to that of traditional ASAP MS (**Figure 5.4**). The variables considered were: machine used (LCT or Xevo), desolvation gas temperature (*i.e.* temperature of the nitrogen gas injected into the chamber: 300-600 °C), vertical flow rate (0-15 mL min⁻¹), cone voltage (15-60 V), source block temperature (temperature of the ionisation source: 120-150 °C) and probe design (1 or 2 sample release holes). Details of the experiments performed can be found in the appendix. It should be noted here that standard ASAP MS experiments are performed with introduction of a 'lock-mass' solution, which is used as an internal calibrant. Currently, the lock-mass employed is an aqueous-based mixture and therefore all *iASAP* MS experiments are run without the presence of this internal calibrant. Work is on-going to determine a suitable, inert/dry, alternative calibrant for use in *iASAP* MS.

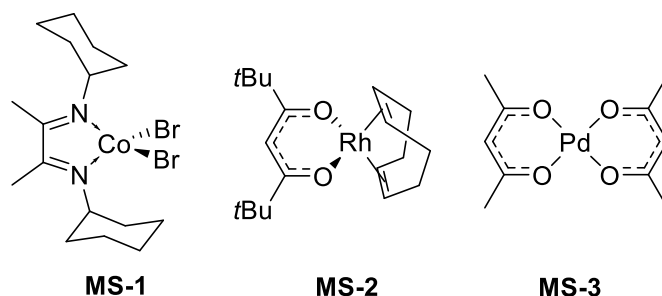


Figure 5.4 Organometallic complexes used within the *i*ASAP MS study, (N[^]N)CoBr₂ (**MS-1**), Rh(COD)(dpm) (**MS-2**) and Pd(acac)₂ (**MS-3**).

5.2.2.1 Maximising Signal Intensity in *i*ASAP MS

In all the *i*ASAP MS experiments undertaken, the intensity of the signal obtained was lower than that obtained with traditional ASAP MS. It is likely this is the result of a cooling effect caused by the addition of a vertical gas flow to the probe, which reduces the degree of volatilisation of the solid sample in the ASAP chamber. In particular it was found that low (5 mL min⁻¹) and high (≥15 mL min⁻¹) rates of the vertical gas flow cause reduced intensity in the signal measured. At low vertical flow rates, the signal intensity is reduced comparative to standard ASAP MS as a result of this cooling effect. However, increasing the vertical flow rate to 10 mL min⁻¹ results in higher signal intensity. It is thought that this is the result of sample being blown out of the glass probe into the ionisation chamber where it can then be vaporised and analysed (characterised by a sharp signal with high intensity immediately upon sample introduction (**Figure 5.5**)).

Despite this sample ejection phenomena, further increase to the vertical flow (≥15 mL min⁻¹) results in a reduction in the intensity of the spectra obtained as both the cooling effect and sample ejection are intensified (**Figure 5.5**). This more aggressive sample ejection from the probe/capillary (with ≥15 mL min⁻¹) was inferred from the observation of 'sprayed/deposited' sample upon the walls and door of the MS chamber post analysis, such that the sample is out with the main heated zone of the ionisation chamber and does not undergo vaporisation. As such, fast vertical gas flow rates are not recommended. However, the intensity of MS signal can be increased simply by increasing the temperature of the desolvation gas within the chamber to combat the cooling effects of the vertical flow and allowing the glass of the probe within the chamber time to warm up before data collection.

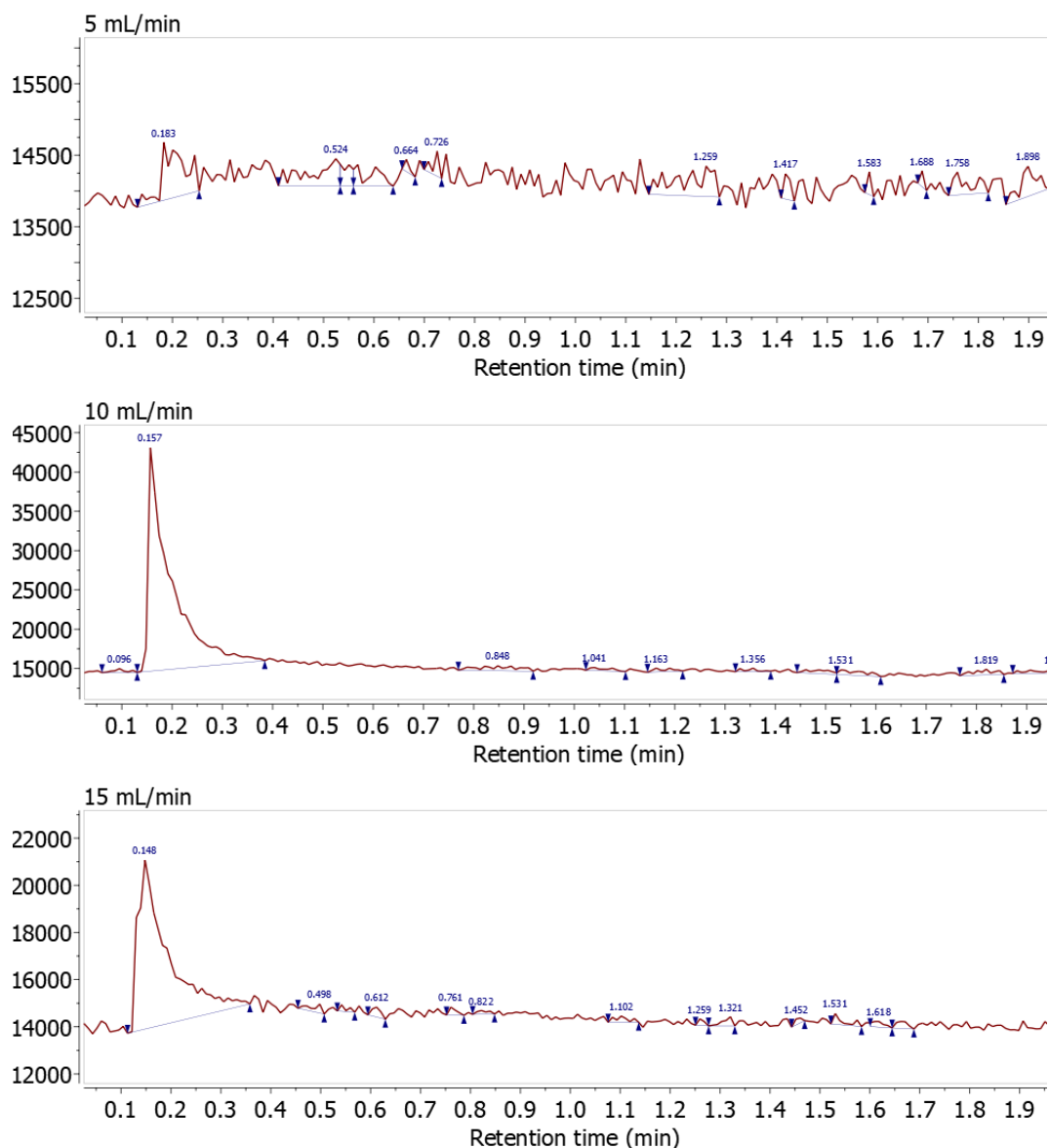


Figure 5.5 Comparison of signal intensities (MS trace) using the *i*ASAP MS technique with various vertical N_2 gas flow rates and all other conditions constant for a sample of $(N^N)CoBr_2$ (**MS-1**): Top: 5 mL/min; middle: 10 mL/min; bottom: 15 mL/min.

Varying the sample cone voltage used throughout *i*ASAP MS experiments was found to have a significant impact upon the fragmentation observed within the spectra obtained. This is also true of traditional ASAP MS, and the trend observed is the same: increasing sample cone voltage will result in an increase in fragmentation observed.⁹ The degree of fragmentation observed does not differ greatly between *i*ASAP MS spectra and ASAP MS spectra and so the sample cone voltage recommended for *i*ASAP MS analyses is that used for traditional ASAP MS. The temperature of the source block was not found to have any influence on the spectra obtained, and so it can be decreased from that which is used within traditional ASAP experiments simply to save energy.

The original design of the probe included a single sample release hole positioned so as to face the sample cone to maximise signal. However, this results in the corona pin facing glass (**Figure 5.6**), and as such, sample must presumably first exit the probe by vaporisation before sample ionisation can take place. Addition of a second sample release hole to the *i*ASAP probe opposite the first, therefore facing the corona pin, aided in increasing the intensity of signal by both providing a greater means of escape for the sample and by allowing the corona discharge to directly impinge upon the sample within the probe.

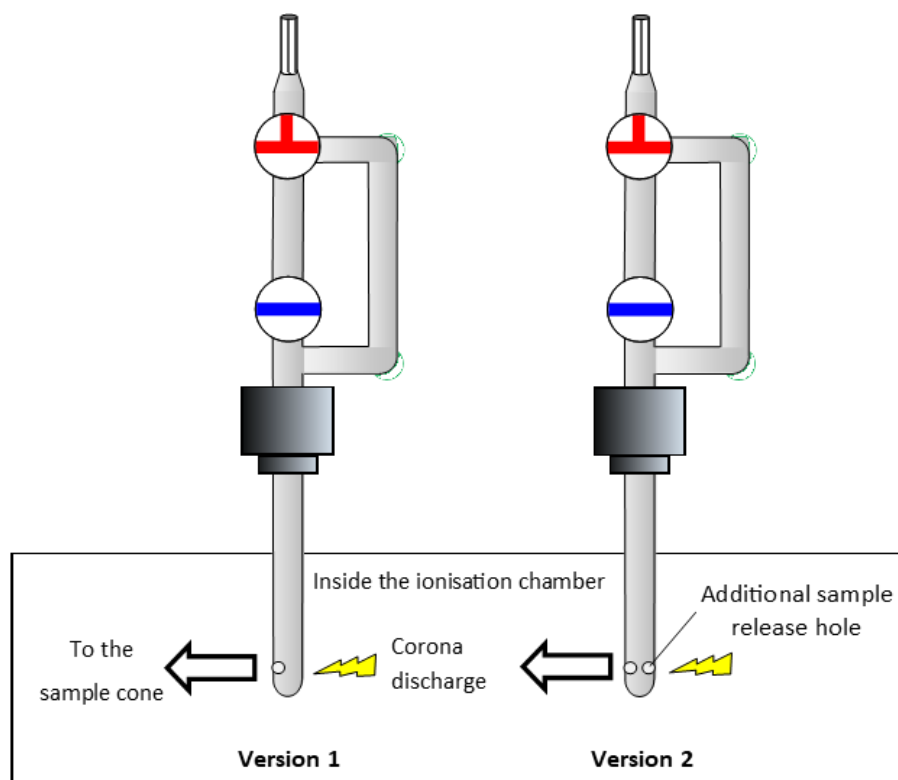


Figure 5.6 Versions 1 and 2 of the *i*ASAP glass delivery probe where addition of a second sample release hole in version 2 enables better ionisation of the sample.

5.3 Comparison of ASAP⁺ with *i*ASAP⁺

From the studies to attempt to maximise the signal intensity of the *i*ASAP MS method, a standard set of running conditions can be recommended. A summary of the conditions used to obtain spectra of similar quality within traditional ASAP MS and *i*ASAP MS is shown in **Table 5.1**.

Table 5.1 Conditions used within ASAP MS and *i*ASAP MS data collection.

Variable	ASAP MS	<i>i</i> ASAP MS
Vertical gas flow / mL min ⁻¹	-	10
Desolvation gas temperature / °C	350 ^a or 450 ^b	450 ^a or 550 ^b
Cone voltage / V	30	30
Source block temperature / °C	150	120
Probe design	-	2 holes
Lock mass solution	on	off

^aLCT Premiere XE QToF mass spectrometer, ^bWater's Xevo QToF mass spectrometer

Using the defined 'standard' conditions of *i*ASAP and ASAP MS techniques, comparative MS spectra can be obtained. In all cases using the *i*ASAP MS technique, the signal obtained within the MS trace is sharp and occurs immediately after 'sample drop' into the ionisation chamber (**Figure 5.7**). As mentioned, this is attributed to sample 'spraying' out of the sample release holes in the *i*ASAP probe.

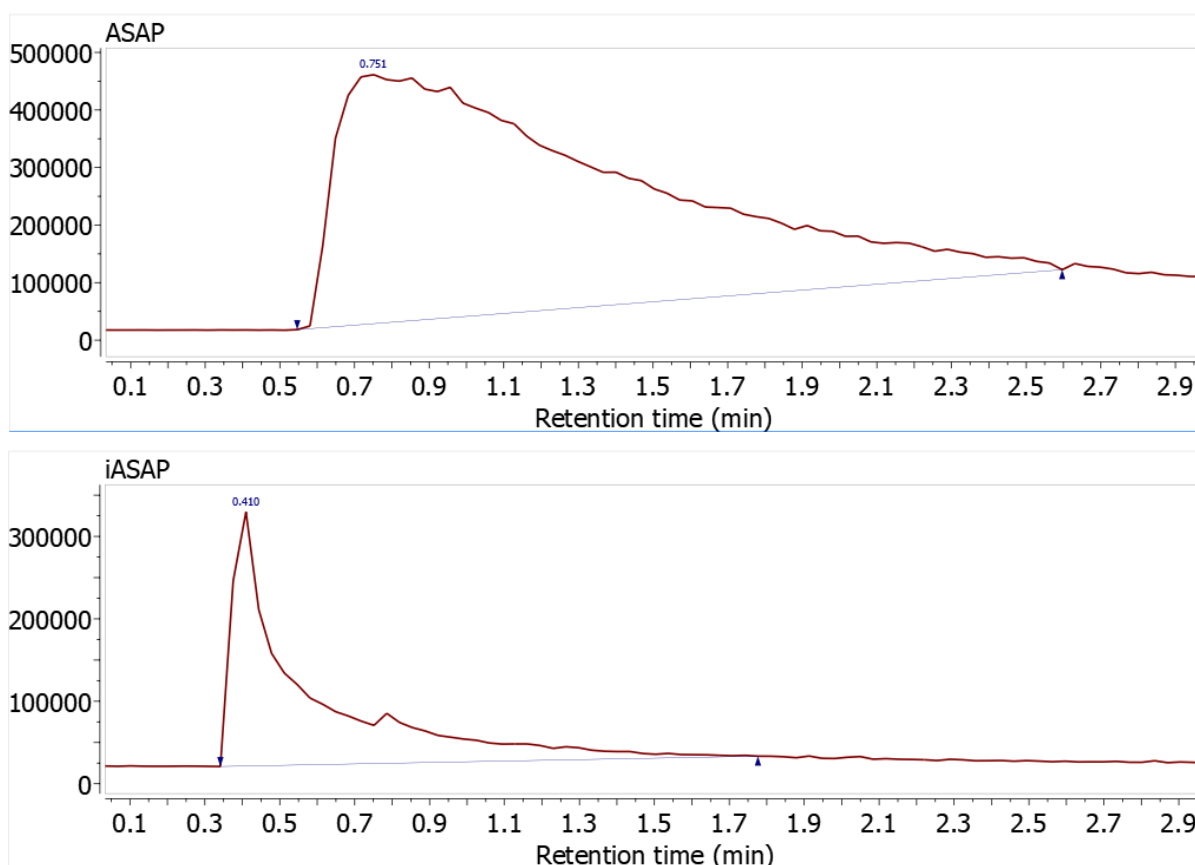


Figure 5.7 Comparison of the mass spectrum trace for the same sample (dtbpx)CoBr₂ (**3.6b**) run in ASAP⁺ conditions and *i*ASAP⁺ conditions on a Water's Xevo QToF mass spectrometer.

The mass spectra (taken as an average across all scans within the signal trace) obtained of an air stable sample (**MS-3**) shows that comparable spectra to those obtained with ASAP MS technique can be obtained with *i*ASAP MS technique. **Figure 5.8** shows a comparison of the mass spectra for a sample of (*N,N'*-bis(2,6-dimethylphenyl)-1,2-diimino-1,2-dimethylethane)CoBr₂ (**MS-3**) under ASAP and *i*ASAP conditions. Of note, both techniques show the [M-Br]⁺ ion as the highest intensity (100%) ion present. In addition, both ASAP and *i*ASAP techniques show some recombination of ions within the mass spectrometer to generate the ion corresponding to [2M-Br]⁺ at *m/z* 851.072 Da. Using the *i*ASAP technique, the relative intensity of this recombination product (compared to the [M-Br]⁺ ion) produced within the mass spectrometer is reduced comparative to when using ASAP MS technique. It is proposed that the cooling effect of the vertical N₂ flow rate through the *i*ASAP probe dampens the production of recombination products such as these.

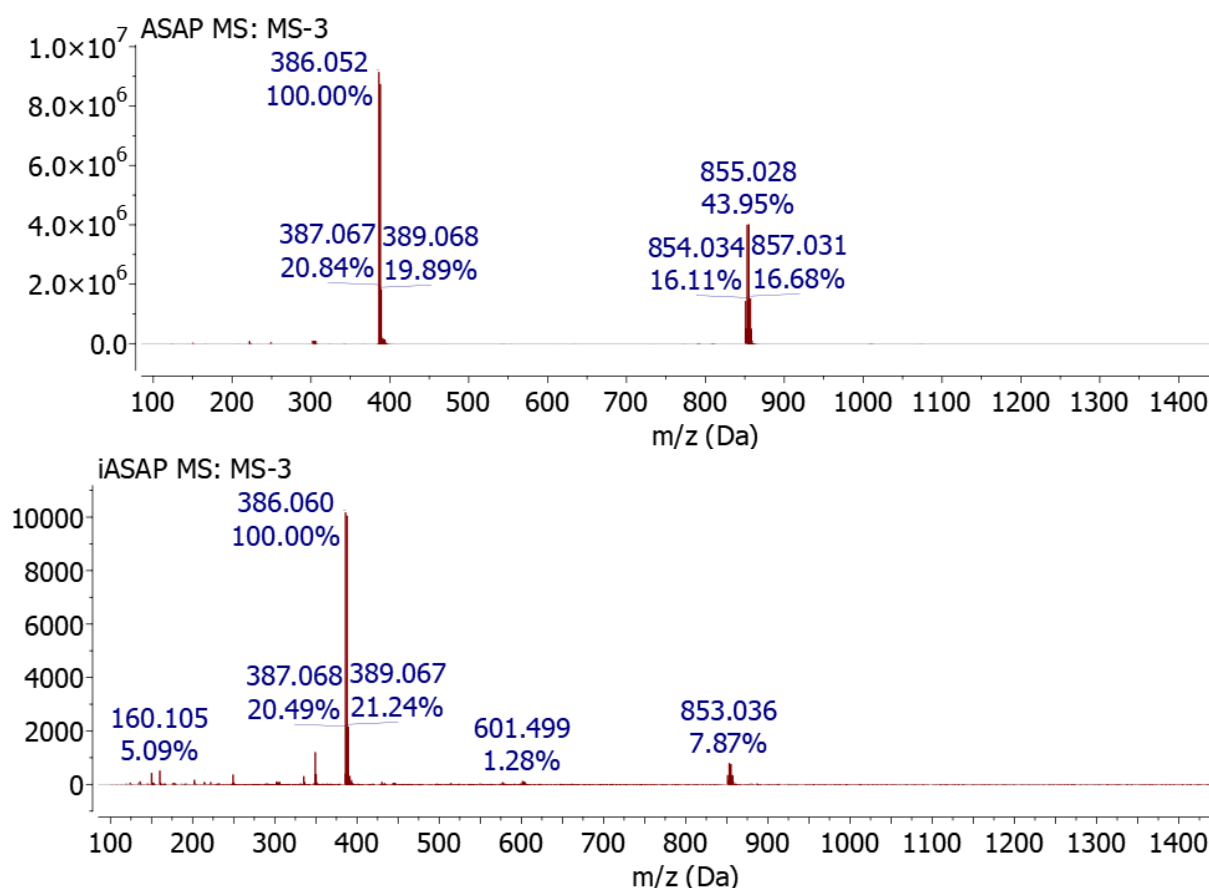


Figure 5.8 Comparison of the mass spectra obtained for a sample of (*N,N'*)CoBr₂ (**MS-3**) under ASAP (top) and *i*ASAP (bottom) conditions.

With spectra of similar quality to those obtained using ASAP MS able to be obtained using *i*ASAP MS technique, the *i*ASAP probes were tested on air sensitive samples. As an example of the benefits of the *i*ASAP methodology, the mass spectra obtained of an air-sensitive sample obtained from a crude reaction mixture predominantly containing (dtbpx)CoBr₂ (**3.6b**) using both traditional ASAP and *i*ASAP

MS methods is shown in **Figure 5.9**. Within the *i*ASAP MS spectrum, there is a significant decrease observed of the oxidation of the diphosphine (dtbpx) as shown by the highest intensity ion [M–CoBr₂+H]⁺ at *m/z* 395.283 Da whereas the ASAP MS technique shows the highest intensity ion as being the partial oxidation product [M–CoBr₂+OH]⁺ at *m/z* 411.278 Da. The *i*ASAP MS technique also allows observation of the [M–Br]⁺ molecular ion of (dtbpx)CoBr₂ at *m/z* 532.125 Da (calc. *m/z* 532.143 Da), whereas the ASAP technique shows a weaker signal corresponding to [M–Br+O]⁺ at *m/z* 548.120 Da (calc. *m/z* 548.138 Da). For the sample shown in **Figure 5.9**, neither the ASAP MS technique nor the *i*ASAP MS technique display the expected molecular ion with any significant intensity.

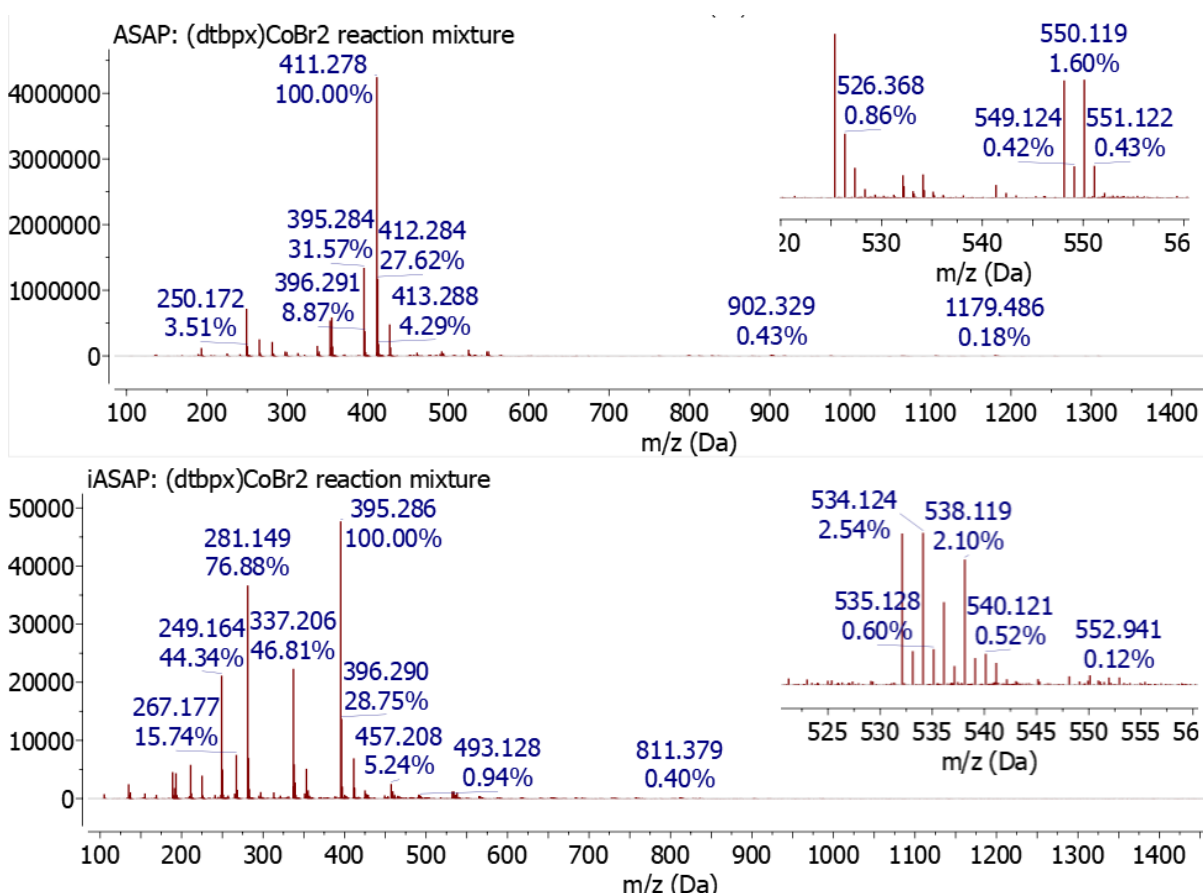


Figure 5.9 Comparison of the ASAP (top) and *i*ASAP (bottom) mass spectra obtained from a reaction mixture containing (dtbpx)CoBr₂ (**3.6b**).

5.4 Conclusions and Future Work

In this chapter, a straightforward delivery method for the analysis of air-/moisture-sensitive samples by *i*ASAP MS was presented. The use of a glass probe to transport and deliver samples to an ASAP fitted mass spectrometer is beneficial both in cost (*c.f.* glovebox-coupled MS^{2,3}) and through removal

of the issue of broken glass collecting in the mass spectrometer source (*c.f.* previous report on *i*ASAP MS⁸).

It was found that a higher temperature is required to achieve satisfactory vaporisation of the organometallic complexes tested for *i*ASAP MS analysis (450-550 °C) when compared to ASAP MS analysis (350-450 °C) to compensate for the cooling effect of the vertical flow of nitrogen through the glass probe into the ionisation chamber. The signal intensity of *i*ASAP MS measurement is lower than that obtained under standard ASAP conditions, however, the signal within *i*ASAP remains sufficient for confident assignments to be made. The mass spectra obtained using the *i*ASAP MS technique are comparable to those obtained using the ASAP MS technique.

In the future, it would be of interest to investigate pre-heating of the inert gas used within the vertical flow to reduce the observed cooling effect and subsequent decrease in signal intensity. In addition, the *i*ASAP MS technique does not currently offer the option of accurate mass determination, which is achieved in ASAP MS through introduction of an aqueous based 'lock-mass' solution. Work is currently underway within the Durham University Mass Spectrometry department to investigate suitable compounds for use in *i*ASAP MS to allow accurate mass determination of air-/ moisture-sensitive samples.

5.5 References

- 1 T. M. Böhme, C. Keim, K. Kreutzmann, M. Linder, T. Dingermann, G. Dannhardt, E. Mutschler and G. Lambrecht, *J. Med. Chem.*, 2003, **46**, 856–867.
- 2 J. H. Gross, N. Nieth, H. B. Linden, U. Blumbach, F. J. Richter, M. E. Tauchert, R. Tompers and P. Hofmann, *Anal. Bioanal. Chem.*, 2006, **386**, 52–58.
- 3 A. T. Lubben, J. S. McIndoe and A. S. Weller, *Organometallics*, 2008, **27**, 3303–3306.
- 4 C. N. McEwen, R. G. McKay and B. S. Larsen, *Anal. Chem.*, 2005, **77**, 7826–7831.
- 5 M. J. P. Smith, N. R. Cameron and J. A. Mosely, *Analyst*, 2012, **137**, 4524–4530.
- 6 C. Pettucci and J. Diffendal, *J. mass Spectrom.*, 2007, 1342–1347.
- 7 E. A. Bruns, V. Perraud, J. Greaves and B. J. Finlayson-Pitts, *Anal. Chem.*, 2010, **82**, 5922–5927.
- 8 J. A. Mosely, P. Stokes, D. Parker, P. W. Dyer and A. M. Messinis, *Eur. J. Mass Spectrom.*, 2018, **24**, 74–80.
- 9 A. B. Attygalle, H. Xia and J. Pavlov, *J. Am. Soc. Mass Spectrom.*, 2017, **28**, 1575–1586.

CHAPTER 6

– Experimental

“Everything is chemicals!”

– Tim Minchin

6.1 General Considerations

Air sensitive manipulations were carried out under an atmosphere of dry nitrogen or argon using standard Schlenk-line and glove box (*Saffron Scientific; Innovative Technologies*) techniques. All solvents, excluding petroleum ether (100 – 120 °C), xylenes, DMF, THF, DCM, MeCN and chlorobenzene were dried using *Innovative Technologies Solvent Purification System* facilities. Petroleum ether (100 – 120 °C), DMF, DCM and chlorobenzene were dried by distillation from calcium hydride. Xylenes and MeCN were dried by distillation from phosphorus pentoxide. MeCN used within UV-Vis spectroscopic studies was pre-dried over activated 4 Å molecular sieves, refluxed over CaH₂ and distilled. THF was dried by heating at reflux over sodium wire with benzophenone indicator, followed by distillation. d₈-THF, C₆D₆ and CD₂Cl₂ were dried over CaH₂ and vacuum transferred. All solvents were degassed prior to use using freeze-pump-thaw techniques, except deuterated solvents which were frozen solid and placed under vacuum for 30-60 minutes.

Chemicals used were purchased from *Sigma Aldrich, Alfa Aesar, Fisher Scientific* or *Apollo Scientific* and used without further purification with the following exceptions: 1,3-cyclohexadiene was filtered through activated alumina and degassed using freeze-pump-thaw techniques immediately before each use; 1,2,3,4,5-pentamethylcyclopentadiene, 2-bromo-2-butene, di-*tert*-butylphosphine, methyl-3-methoxypropionate and methyl-3-*N,N*-dimethylaminopropionate were degassed and stored under nitrogen before use; *n*-butyllithium in hexanes was degassed, stored under nitrogen and titrated against *N*-benzylbenzamide to determine accurate concentration; fluorene was purified by sublimation before use; *p*-TSA was recrystallised from ethanol and dried *via* vacuum desiccation over calcium chloride; 1,2-*bis*(*di**tert*butylphosphinomethyl)benzene was provided by Lucite International and recrystallised from methanol; 1,2-dibromoethane and 1,2-dichloroethane were vacuum-transferred, stored under nitrogen and degassed before use. Indene was dried by distillation from calcium hydride and degassed before use; cyclopentadiene was prepared immediately before each use *via* cracking, distillation and degassing of dicyclopentadiene; deuterated solvents (C₆D₆, CDCl₃, (CD₃)₂CO, CD₂Cl₂, d₈-THF) were dried by distillation over calcium hydride, degassed and stored under nitrogen.

6.1.1 NMR Spectroscopy

Solution-phase NMR spectra were collected on a Bruker Avance 400, a Varian Mercury-400, a Varian Mercury-200 or a Varian VNMRs-700 or 600 at ambient probe temperatures (290 K). Chemical shifts were referenced to residual *protio* impurities in the deuterated solvent (¹H), ¹³C shift of the solvent

($^{13}\text{C}\{^1\text{H}\}$) or to external 85% H_3PO_4 aqueous solution (^{31}P , $^{31}\text{P}\{^1\text{H}\}$). Chemical shifts are reported in ppm and coupling constants in Hz. Solvent residual proton shifts used are: CDCl_3 7.26 (s); C_6D_6 , 7.15 (s); $(\text{CD}_3)_2\text{CO}$, 2.05 (s) and CD_2Cl_2 , 5.35 (s).¹ Solvent residual carbon shifts employed: CDCl_3 , 77.0 (t); C_6D_6 , 128.0 (t); $(\text{CD}_3)_2\text{CO}$, 206.2 (s), 29.8 (spt) and CD_2Cl_2 , 53.0 (quin).¹

6.1.2 X-Ray Crystallography

The crystallographic data were obtained using an *R8V_Mo Diffractometer* with confocal optics Mo- $\text{K}\alpha$ (λ 0.71073 Å) at $-180(1)$ °C. All calculations were performed using the Olex2 software package except for refinement, which was performed using SHELXT.² Non-hydrogen atoms were refined anisotropically, hydrogen atoms were assigned riding isotropic displacement parameters and constrained to idealised geometries. Images were produced using OLEX-2 v1.2.8, with ORTEPS set at 50%.³ Searches of the Cambridge Structure Database were performed using WebCSD.⁴ All structures were collected and solved by Dr Andrei Batsanov or Dr Dimitry Yufit (Durham Chemistry Department). Steric maps were generated and $\%V_{\text{bur}}$ calculated using the web software *SambVca 2.1*.⁵

6.1.3 Effective Magnetic Moment

The effective magnetic moment (μ_{eff}) was determined in the solid state through use of a Johnson-Matthey-Evans (JME) magnetic susceptibility balance (*Johnson-Matthey*). The value of μ_{eff} for solutions of complexes were determined using the Evans method: a sample of the analyte was dissolved in CDCl_3 to a known concentration in an NMR tube fitted with a J Young's valve. Example calculations for the determination of the values of μ_{eff} obtained through use of a JME balance and the Evans method are presented in Section 6.5.

6.1.4 Raman, Infrared, UV/Vis and NIR-UV/Vis Spectroscopies

Infrared spectra were recorded in the solid-state using a *Perkin Elmer Frontier ATR-FT-IR* or as a Nujol mull suspension on KBr discs using a *Perkin Elmer Frontier FT-IR*, or through use of a *Perkin Elmer FT-IR Spectrum 2 Spectrometer* with UATR attachment. Laser Induced Raman spectra were recorded within the range $100 - 1800 \text{ cm}^{-1}$ using a *Horiba LabRAM HR* using either 532nm (green) or 663 nm (red) laser excitation source. Samples were measured in the solid-state in sealed glass J Young's NMR

tubes and the sample checked for degradation after each measurement through use of a video microscope.

UV-Vis spectroscopic analyses were carried out using a *Perkin Elmer Lambda 25 UV/Vis spectrometer* in dual beam mode with 10 mm path length quartz or glass cuvettes. Air-/moisture-sensitive samples were analysed using a purpose-made cuvette: quartz cuvette fitted with a 100 quartz-to-glass gradient joint and a J Young's tap glass cuvette fitted with a female B19 ground glass joint (sample measurement after preparation in a glovebox). Unless otherwise specified, all samples were recorded as solutions in THF.

Near-IR-UV-Vis spectroscopic analysis was carried out using a *CARY 5000 Series UV/Vis-NIR spectrometer* and samples were measured in made-for-purpose 10 mm path length quartz cuvette fitted with a J Young's tap. Single beam spectroscopic methods were employed when collecting NIR-UV/Vis spectra to minimise contributions which arise due to the non-parity of the cuvettes available, *i.e.* 1) 100% transmission taken with "blank" sample (cuvette + solvent), 2) machine zeroed to 100% transmission to create baseline, 3) sample transmission taken (same cuvette + same solvent + added stock solution of desired sample in same solvent). All samples were recorded as solutions in THF.

6.1.7 Computational Details

All computations were performed using Gauss View 6.0.16, WinSCP r2 and PuTTY softwares. Where possible, solid-state geometries were used as a starting point before geometry optimisation. IR and Raman spectra were calculated at the B3LYP/3-21G* level of density functional theory (DFT).

6.1.5 Mass spectrometry, Elemental Analysis and Gas Chromatography

ASAP (Atmospheric Solids Analysis Probe) mass spectra (ES) were acquired with an LCT *Premier XE mass spectrometer* or Waters *Xevo QToF Mass Spectrometer*. MALDI mass spectra were obtained using a Bruker Daltonik GmbH *Autoflex II ToF/ToF Mass Spectrometer*: samples were prepared as a solution in DCM in a nitrogen filled glovebox and incorporated into a *trans-2-[3-(4-tert-butylphenyl)-2-methyl-2-propenylidene]malononitrile* matrix immediately before running under an air atmosphere. GC-MS spectra were collected using a Shimadzu *QP201-Ultra Mass Spectrometer*. ESI mass spectra were obtained using a Waters *TQD Mass Spectrometer* and Waters *Acquity UPLC* (Ultra Performance Liquid Chromatography).

Elemental Analyses were performed by Stephen Boyer of the Service Technical Support Unit of London Metropolitan University or Emily Unsworth of Durham University (Exeter CE-440 Elemental Analyser).

Gas chromatographs were gathered using a *Perkin Elmer Clarus 400 Gas Chromatograph* fitted with a PONA column and operated as follows: manual injection ($1 \mu\text{L}$) at $40 \text{ }^\circ\text{C}$, hold for 10 minutes, ramp 1 at $20 \text{ }^\circ\text{C min}^{-1}$ to $170 \text{ }^\circ\text{C}$, hold for 12 minutes, ramp 2 at $20 \text{ }^\circ\text{C min}^{-1}$ to $300 \text{ }^\circ\text{C}$, hold for 5 minutes.

6.1.5.1 *i*ASAP

In conjunction with the Mass Spectrometry department in Durham University (Chemistry), an air-sensitive mass spectrometry technique was developed during the course of this project, for the purpose of obtaining additional analysis on air- and/or moisture-sensitive complexes synthesised within this project; the technique developed is termed '*i*ASAP,' *i.e.* inert Atmospheric Solids Analysis Probe. This new technique for Durham Chemistry Department allows the user to obtain an ASAP-MS spectrum upon a solid sample, while keeping the sample and experiment under inert conditions throughout. Samples were run at a temperature of $450 \text{ }^\circ\text{C}$, unless otherwise stated. The probe designed for and used within this project is detailed in **Figure 6.1** and described in detail in Chapter 5.

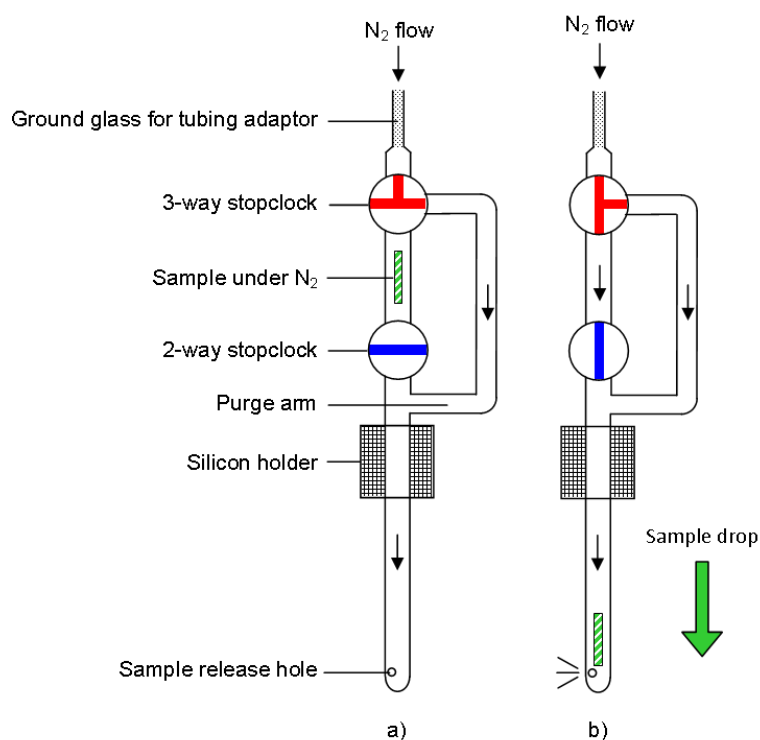


Figure 6.1 *i*ASAP probe diagram showing N_2 gas flow during a) probe purge and b) sample measurement

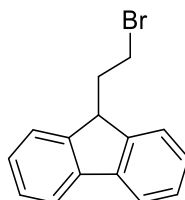
6.1.6 Electrochemical Measurements

Electrochemical measurement of cyclic voltammograms of analytically pure diphosphine cobalt(II) bromide complexes were collected using an *Autolab PGSTAT30 Potentiostat* with autolab software *GPES V4.9*. Tetrabutylammonium hexafluorophosphate was recrystallised from ethanol and dried before use. Solvents used were rigorously dried and degassed and all measurements performed in a nitrogen atmosphere glovebox. The desired complex was dissolved to a concentration of 0.72 mM in a pre-prepared DCM solution of 0.1 M $[\text{NBu}_4]^+[\text{PF}_6]^-$. Electrodes were cleaned and polished (alumina/water slurry) before use and between experiments; platinum wire encased in glass was used for both reference and counter electrodes with a 2.5 mm diameter platinum working electrode. Unless otherwise specified, data collected was subjected to smoothing using 10 point adjacent averaging.

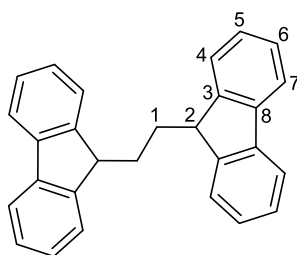
6.2 Chapter 2 Experimental Details

6.2.1 L₂X-CH₂CH₂-X type ligands

6.2.1.1 Attempted synthesis of 1-bromo-2-(9-fluorenyl)ethane



The attempted synthesis of 1-bromo-(9-fluorenyl)ethane was carried out in accordance with the literature procedure.⁶ Fluorene (5 g, 30 mmol) was dissolved in diethyl ether and cooled to $-78\text{ }^{\circ}\text{C}$ before dropwise addition of *n*BuLi (15.7 mL, 36 mmol, 2.3 M in hexanes) to form a bright yellow precipitate. The solution was allowed to warm to room temperature and stirred for an additional 3 hours. Subsequent cooling to $-78\text{ }^{\circ}\text{C}$ and dropwise addition to an excess of 1,2-dibromoethane (15.7 mL, 180 mmol) at $-40\text{ }^{\circ}\text{C}$ allowed formation of the substituted fluorenyl compound. The remaining mixture was allowed to warm to room temperature. Unfortunately, a hot plate error resulted in interruption to stirring overnight, resulting in loss of the desired “infinite dilution” conditions required to obtain mono-substitution of fluorene upon 1,2-dibromoethane. Concentration of the mother liquor resulted in precipitation of a cream solid which by ^1H and $^{31}\text{C}\{^1\text{H}\}$ NMR spectroscopy was confirmed to be 1-*bis*(di-9'-fluorenyl)ethane through comparison to literature values.⁷

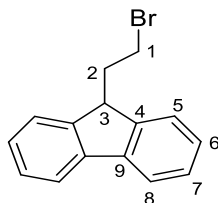


^1H NMR (400 MHz, CDCl_3): δ_{H} 7.77 (d, 2H, $^3J_{\text{HH}}$ 7.5 Hz, H-7), 7.38 (td, 2H, $^3J_{\text{HH}}$ 7.0 Hz, $^4J_{\text{HH}}$ 1.2 Hz, H-4), (m, 4H, H-5,6), 3.86 (s, H-2), 1.75 (m, 2H, H-1).

$^{13}\text{C}\{^1\text{H}\}$ NMR (176 MHz, CDCl_3): δ_{C} 146.9 (s, qC-3), 141.5 (s, qC-8), 127.1 (s, C-5), 127.0 (s, C-6), 124.3 (s, C-4), 119.9 (s, C-7), 47.2 (s, C-2), 26.8 (s, C-1).

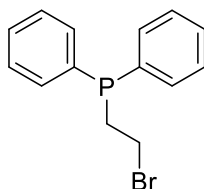
6.2.1.2 Synthesis of 1-bromo-2-(9-fluorenyl)ethane

The above procedure was repeated with no interruption to stirring and yielded the title compound as a beige solid (5.58g, 68%, 20.4 mmol), with ^1H and $^{13}\text{C}\{^1\text{H}\}$ NMR spectra in agreement with literature values.⁶



^1H NMR (600.1 MHz, CDCl_3): δ_{H} 7.77 (d, 2H, $^3J_{\text{HH}}$ 7.5 Hz, H-8), 7.54 (d, 2H, $^3J_{\text{HH}}$ 7.5 Hz, H-5), 7.40 (t, 2H, $^3J_{\text{HH}}$ 7.5 Hz, H-6) 7.34 (t, 2H, $^3J_{\text{HH}}$ 7.7 Hz, H-7), 4.18 (t, 1H, $^3J_{\text{HH}}$ 6.2 Hz, H-3), 3.31 (t, 2H, $^3J_{\text{HH}}$ 7.6 Hz, H-1), 2.52 (m, 2H, H-2).

$^{13}\text{C}\{^1\text{H}\}$ NMR (176 MHz, CDCl_3): δ_{C} 145.9 (s, qC-4), 141.2 (s, qC-9), 127.6 (s, C-6), 127.3 (s, C-7), 124.5 (s, C-5), 120.2 (s, C-8), 46.5 (s, C-3), 36.7 (s, C-2), 30.5 (s, C-1).

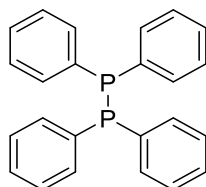
6.2.2 X- $\text{CH}_2\text{CH}_2\text{-ER}_n$ type ligands6.2.2.1 Attempted synthesis of 1-bromo-2-(diphenylphosphino)ethane using $\text{CsOH}\cdot\text{H}_2\text{O}$ 

A modification to the literature procedure was used in the attempted synthesis of 1-bromo-2-(diphenylphosphino)ethane.⁸ Caesium hydroxide monohydrate (1.0 g, 5.95 mmol) was added to activated 4 Å molecular sieves in DMF (30 mL). Upon addition of diphenylphosphine (1.04 mL, 5.95 mmol) the solution turned deep red in colour and the resulting solution allowed to stir for one hour. 1,2-Dibromoethane (3.09 mL, 35.7 mmol) was added in one portion, turning the mixture milky white, and the reaction then stirred for 24 hours. Basic water (aq. NaOH, pH ~9, 20 mL) was added, the organic layer separated and attempted extractions were carried out with DCM (3 × 30 mL), hexanes (2 × 50 mL), Et_2O (2 × 50 mL) and xylenes (2 × 50 mL). In each case, $^{31}\text{P}\{^1\text{H}\}$ NMR spectra obtained of the aqueous phase displayed a single resonance (δ_{P} 21.2 ppm), while no phosphorus-containing species present within the organic layers. An excess of sodium chloride was then added to the solution, before again attempting extraction with DCM (50 mL); however, once again the phosphorous species

remained within the aqueous layer. The pH of the solution was then brought to pH 7 using degassed aq. HCl; subsequent extraction with DCM (50 mL) was unsuccessful. This was then repeated at pH 4, but extraction into DCM was again unsuccessful. The pH of the bulk solution was then reduced to pH 1 through portion wise addition of degassed aq. HCl, at which point a white precipitate was observed, which was collected by filtration. The $^{31}\text{P}\{^1\text{H}\}$ NMR spectrum of this precipitate displayed a single resonance at δ_{P} 30.8 ppm.

6.2.2.2 Attempted synthesis of 1-bromo-2(diphenylphosphino)ethane using *n*-butyllithium

Diphenylphosphine (0.5 mL, 2.87 mmol) in diethyl ether (30 mL) was cooled to $-78\text{ }^{\circ}\text{C}$ before dropwise addition of *n*-butyllithium (1.80 mL, 1.9 M in hexanes, 3.45 mmol). The resulting solution was stirred and allowed to warm to room temperature over the course of three hours. After subsequent cooling to $-78\text{ }^{\circ}\text{C}$, 1,2-dibromoethane (1.50 mL, 17.22 mmol) was added in one portion and the solution allowed to warm to room temperature overnight. Subsequently, volatile components were removed *in vacuo* to yield a white solid which analysis by ^1H , $^{13}\text{C}\{^1\text{H}\}$, $^{31}\text{P}\{^1\text{H}\}$ and ^{31}P NMR spectroscopies showed to be tetraphenyldiphosphine (0.75 g, 70% if LiBr present in 1:1, $\text{P}_2\text{Ph}_4:\text{LiBr}$). The NMR spectroscopic data obtained are in agreement with the literature values for P_2Ph_4 .⁹



^1H NMR (700.0 MHz, C_6D_6): δ_{H} 7.55 (m, 2H, *o*-H), 6.96 (m, 3H, *m*-H and *p*-H).

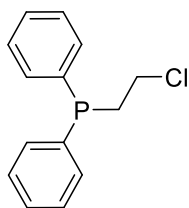
$^{13}\text{C}\{^1\text{H}\}$ NMR (176 MHz, C_6D_6): δ_{C} 136.6 (*i*-C), 134.8 (t, $^3J_{\text{CP}}$ 12.9 Hz, *o*-C), 128.9 (s, *p*-C), 128.6 (t, $^4J_{\text{CP}}$ 3.3 Hz, *m*-C).

$^{31}\text{P}\{^1\text{H}\}$ NMR (162 MHz, C_6D_6): δ_{P} -15.0 (s)

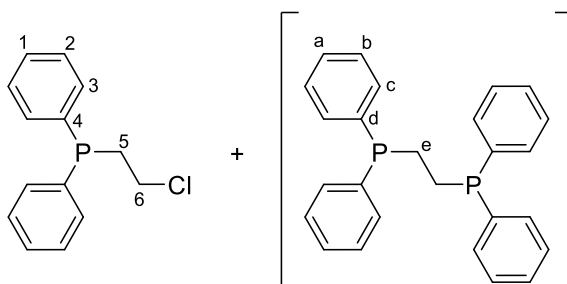
^{31}P NMR (162 MHz, C_6D_6): δ_{P} -15.0 (s)

MS (ASAP+): m/z 371.1 (100%, M+H).

6.2.2.3 Synthesis of 1-chloro-2-(diphenylphosphino)ethane



Attempt 1: *n*-Butyllithium (2.8 mL, 2.3 M in hexanes, 6.5 mmol) was added dropwise to a cooled (-78 °C) solution of diphenylphosphine (1 mL, 5.75 mmol) in ether (20 mL) and the reaction allowed to warm to room temperature overnight. Over the course of 2 hours, this lithiated species was added to a solution of 1,2-dichloroethane (0.43 mL, 5.5 mmol) in ether (10 mL) at -78 °C. The reaction was allowed to warm to room temperature overnight with stirring before quenching with degassed water (15 mL). The aqueous layer was separated and extracted with ether (3×10 mL) and organic fractions combined, dried over MgSO_4 , filtered and volatile components removed *in vacuo* to afford a white solid of a 1:1 mixture (by ^1H and ^{31}P NMR) of dppe (*bis*(1,2-diphenylphosphino)ethane) (0.67 g, 1.67 mmol) and 1-chloro-2-(diphenylphosphino)ethane (0.42 g, 1.67 mmol, 30%).



^1H NMR (C_6D_6 , 400 MHz): δ_{H} 7.34-7.30 (m, 2H, H-3), 7.26-7.23 (m, 3H, H-1,2), 3.34-3.29 (m, 1H, H-6), 2.32-2.28 (m, 1H, H-5).

$^{31}\text{P}\{^1\text{H}\}$ NMR (C_6D_6 , 162 MHz): δ_{P} -20.1 (s)

^{31}P NMR (C_6D_6 , 162 MHz): δ_{P} -20.1 (h, $^2J_{\text{PH}}$ 13.6, $^3J_{\text{PH}}$ 6.7 Hz)

^1H NMR (dppe, C_6D_6 , 400 MHz): δ_{H} 7.03-6.99 (m, 5H, H-a,b,c), 2.21 (t, $^2J_{\text{HP}}$ 4.2 Hz, 2H, H-e)

^{31}P NMR (dppe, C_6D_6 , 162 MHz): δ_{P} -12.9 (s)

$^{31}\text{P}\{^1\text{H}\}$ NMR (dppe, C_6D_6 , 162 MHz): δ_{P} -12.9 (s)

Due to the formation of dppe within the product mixture, the synthesis of 1-chloro-2-(diphenylphosphino)ethane was repeated with a large excess of 1,2-dichloroethane, as detailed below:

Attempt 2: *n*-Butyllithium (16.2 mL, 2.3 M in hexanes, 37.4 mmol) was added dropwise to a cooled (-78 °C) solution of diphenylphosphine (5 mL, 28.8 mmol) in ether (100 mL) and the reaction allowed to

warm to room temperature overnight. Over the course of 2 hours, this lithiated species was added to a solution of 1,2-dichloroethane (13.7 mL, 150.6 mmol) in ether (20 mL) at $-40\text{ }^{\circ}\text{C}$. The reaction was allowed to warm to ambient temperature and stirred for 2 hours before quenching with degassed water (40 mL). The aqueous layer was separated and extracted with ether ($3 \times 30\text{ mL}$) and the organic fractions combined, dried over MgSO_4 , isolated by filtration and volatile components removed *in vacuo* to afford 1-chloro-2-(diphenylphosphino)ethane (6.95 g, 28.0 mmol, 97%) as a white solid.

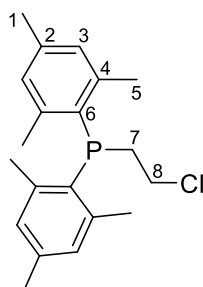
$^1\text{H NMR}$ (C_6D_6 , 400 MHz): δ_{H} 7.27-7.22 (m, 2H, H-3), 7.04-7.00 (m, 3H, H-1,2), 3.34-3.29 (m, 2H, H-6), 2.32-2.28 (m, 2H, H-5).

$^{13}\text{C}\{^1\text{H}\}$ NMR (C_6D_6 , 101 MHz): δ_{C} 138.0 (d, $^1J_{\text{CP}}$ 14.3 Hz, qC-4), 133.0 (d, $^2J_{\text{CP}}$ 19.3 Hz, C-3), 129.0 (d, $^3J_{\text{CP}}$ 9.8 Hz, C-2), 128.8 (s, C-1), 41.8 (d, $^2J_{\text{CP}}$ 29.0 Hz, C-6), 32.8 (d, $^1J_{\text{CP}}$ 16.7 Hz, C-5).

$^{31}\text{P}\{^1\text{H}\}$ NMR (C_6D_6 , 162 MHz): δ_{P} -20.1 (s)

^{31}P NMR (C_6D_6 , 162 MHz): δ_{P} -20.1 (h, $^2J_{\text{PH}}$ 13.6, $^3J_{\text{PH}}$ 6.7 Hz)

6.2.2.4 Synthesis of 1-chloro-2-(dimesitylphosphino)ethane



To a cooled ($-78\text{ }^{\circ}\text{C}$) solution of dimesitylphosphine (0.50 g, 1.85 mmol) in THF (20 mL), *n*-butyllithium (0.88 mL, 2.3 M in hexanes, 2.03 mmol) was added dropwise with stirring and the reaction allowed to warm to room temperature. The solution was cooled to $-35\text{ }^{\circ}\text{C}$ and added over the course of 1 hour to a cooled ($-35\text{ }^{\circ}\text{C}$) solution of 1,2-dichloroethane (1.0 mL, 12.6 mmol) and the reaction stirred for 2 hours, allowing the reaction to warm to room temperature. The resulting solution was quenched with water (20 mL) and extracted with diethylether ($4 \times 10\text{ mL}$). The organic layers were combined, dried over MgSO_4 and volatile components were removed *in vacuo* to yield 1-chloro-2-(dimesitylphosphino)ethane (0.475 g, 1.73 mmol, 77%) as a white solid.

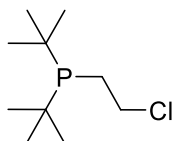
$^1\text{H NMR}$ (400.0 MHz, C_6D_6): δ_{H} 6.62 (d, $^4J_{\text{HP}}$ 2.3 Hz, 2H, H-3), 3.41-3.30 (m, 1H, H-8), 2.92-2.87 (m, 1H, H-7), 2.22 (s, 6H, H-5), 2.04 (s, 3H, H-1)

$^{13}\text{C}\{^1\text{H}\}$ NMR (176 MHz, C_6D_6): δ_{C} 142.1 (d, $^2J_{\text{CP}}$ 14.0 Hz, qC-4), 137.9 (s, qC-2), 132.5 (d, $^1J_{\text{CP}}$ 22.2 Hz, qC-6), 130.53 (s, C-3), 48.8 (d, $^1J_{\text{CP}}$ 38.9 Hz, C-7), 32.5 (d, $^2J_{\text{CP}}$ 19.0 Hz, C-8), 23.2 (d, $^3J_{\text{CP}}$ 13.9 Hz, C-5), 20.8 (s, C-1).

$^{31}\text{P}\{^1\text{H}\}$ NMR (162 MHz, C_6D_6): δ_{P} -28.3 (s)

^{31}P NMR (162 MHz, C_6D_6): δ_{P} -28.3 (s)

6.2.2.5 Synthesis of 1-chloro-2-(di-*tert*-butylphosphino)ethane



Attempt 1: *n*-Butyllithium (2.4 mL, 2.3 M in hexanes, 5.5 mmol) was added dropwise to a cooled (-78 °C) solution of di-*tert*-butylphosphine (10 mL, 0.5 M in hexanes, 5.0 mmol) in ether (35 mL) and the reaction allowed to warm to room temperature overnight. Over the course of 2 hours this lithiated species was added to a solution of 1,2-dichloroethane (2.9 mL, 30.0 mmol) in ether (10 mL) at -30 °C. The reaction was allowed to warm to ambient temperature with stirring, after which point an aliquot of the reaction mixture was removed and a ^{31}P NMR spectrum obtained with use of a C_6D_6 lock tube. The spectrum obtained displayed two major phosphorus-containing species: tetra(*tert*-butyl)diphosphane and di-*tert*-butylchlorophosphine, corresponding to 42% and 32% of the phosphorus-containing species present. Additionally, trace amounts of di-*tert*-butylphosphine oxide and additional unassigned impurities were observed.

$^{31}\text{P}\{^1\text{H}\}$ NMR (C_6D_6 , 162 MHz): 147.6 (s, $t\text{Bu}_2\text{PCl}$), 42.8 (s, $t\text{Bu}_4\text{P}_2$), 30.0 (s, unassigned P), 27.8 (s, unassigned P), 23.2 (s, $t\text{Bu}_2\text{PH}$).

^{31}P NMR (C_6D_6 , 162 MHz): 147.6 (m, $t\text{Bu}_2\text{PCl}$), 42.8 (m, $t\text{Bu}_4\text{P}_2$), 30.0 (m, unassigned P), 27.8 (s, unassigned P), 23.2 (d, $t\text{Bu}_2\text{PH}$).

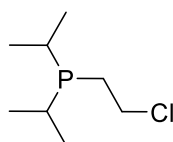
Due to the presence of multiple phosphorus-containing impurities, the above procedure was repeated using THF as a solvent in an attempt to prevent side-reactions.

Attempt 2: *n*-Butyllithium (2.4 mL, 2.3 M in hexanes, 5.4 mmol) was added dropwise to a stirred and cooled (-78 °C) solution of di-*tert*-butylphosphine (10 mL, 0.5 M in hexanes, 5.0 mmol) in THF (15 mL) over 20 minutes. The solution was then allowed to warm to room temperature overnight before being added dropwise to a solution of dichloroethane (2.38 mL, 30 mmol) in THF (10 mL) at -35 °C. The

mixture was warmed to room temperature and stirred for 48 hours before an aliquot of the reaction was analysed by ^{31}P NMR spectroscopy using a C_6D_6 lock tube. The ^{31}P NMR spectrum obtained displayed multiple peaks summarised in the table below:

	ClP^tBu_2	HP^tBu_2	$\text{HP(O)}^t\text{Bu}_2$	$^t\text{Bu}_2\text{P-P}^t\text{Bu}_2$	$\text{Cl-CH}_2\text{CH}_2\text{-P}^t\text{Bu}_2$	Unassigned
Proportion (%)	58	9	3	3	26	1
Shift (ppm)	146.6	20.2	65.5	40.1	25.3	64.7

6.2.2.6 Attempted synthesis of 1-chloro-2-(diisopropylphosphino)ethane



Attempt 1: *n*-Butyllithium (2.13 mL, 2.2 M in hexanes, 4.68 mmol) was added dropwise to a solution of di-*iso*-propylphosphine (5.0 mL, 10 wt.% in hexanes, 4.25 mmol) in ether (20 mL) at $-78\text{ }^\circ\text{C}$. The reaction was allowed to warm to room temperature over 2 hours before addition of 1,2-dichloroethane (4 mL, 26.0 mmol). The solution was then allowed to stir overnight, after which time a white precipitate was observed. A ^{31}P NMR spectrum obtained after 16 hours stirring at room temperature displayed 5 signals, with the major phosphorus-containing product being identified as tetra-*iso*-propyldiphosphine (62% of the phosphorus containing species by ^{31}P NMR) by comparison to literature values.¹⁰

^{31}P NMR (C_6D_6 , 162 MHz): δ_{P} 9.5 (m, unassigned), 3.0 (m, unassigned), 1.6 (m, unassigned), -12.3 ($^i\text{Pr}_2\text{P-P}^i\text{Pr}_2$), -15.7 (m, LiP^iPr_2).

Due to the mixture of products observed within the previous attempted synthesis of 1-chloro-2-(diisopropylphosphino)ethane, a second attempt at synthesis was undertaken; increasing the number of equivalents of 1,2-dichloroethane used.

Attempt 2: *n*-Butyllithium (2.13 mL, 2.2 M in hexanes, 4.68 mmol) was added dropwise to a solution of diisopropylphosphine (5.0 mL, 10 wt.% in hexanes, 4.25 mmol) in THF (20 mL) at $-78\text{ }^\circ\text{C}$ and the reaction allowed to warm to room temperature overnight before 1,2-dichloroethane (8 mL, 52 mmol) was added in one portion at $-35\text{ }^\circ\text{C}$. The reaction was monitored by ^{31}P NMR spectroscopy: after 2 hours, 73% of the phosphorus containing species present remained as diisopropylphosphinolium ($\delta_{\text{P}} -12.9$ ppm) while 27% was a new phosphorus-containing species at $\delta_{\text{P}} 1.1$ ppm. The reaction was

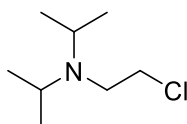
therefore left for an additional 72 hours in an attempt to reach completion, however, after these 72 hours, no change was observed by a ^{31}P NMR spectrum obtained. At this point, the reaction was quenched with degassed water (15 mL) and stirred for 30 minutes before and organics were extracted with ether (3×10 mL) and dried over MgSO_4 .

Unreacted di-*iso*-propylphosphinolium was therefore hydrolysed into a mixture of products, as indicated by ^{31}P NMR spectroscopic analysis. However, the resonance at δ_{P} 1.1 ppm remained present post quench. The valency of this species was then investigated through an NMR-scale experiment whereby elemental selenium was added to the NMR tube containing a sample of the reaction mixture and sonicated for 1 hour before an additional ^{31}P NMR spectrum was obtained with the view to exploring whether formation of the corresponding P^{V} selenide was possible.

The disappearance of the peak at δ_{P} 1.1 ppm, coupled with the appearance of a doublet of multiplets at δ_{P} 44.6 ppm within the ^{31}P NMR spectrum obtained post-Se addition shows that the species formed in 27% during the reaction was trivalent, and therefore could be the desired product. However, the small scale of this reaction along with the presence of multiple phosphorus-containing impurities (formed upon hydrolysis of LiP^iPr_2) meant that isolation of the species with shift δ_{P} 1.1 ppm was unachievable.

In an attempt to see whether the reaction could reach completion, an aliquot of the reaction mixture, taken pre-quench, was monitored by ^{31}P NMR spectroscopy. This sample was then heated in the NMR tube at 40°C for 34 days, however no further LiP^iPr_2 was consumed within this reaction as evidenced by integration against an internal standard. The only change observed within this time period was that a small proportion of the species present at δ_{P} 1.1 ppm was consumed, yielding a new species at δ_{P} 59.1 ppm, likely the oxidation product of the species at δ_{P} 1.1 ppm.

6.2.2.7 Attempted synthesis of 1-chloro-2-(di-*iso*-propylamino)ethane



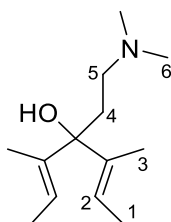
Attempt 1: To a cooled (-78°C) solution of di-*iso*-propylamine (5.0 mL, 35.4 mmol) in ether (20 mL), *n*-butyllithium (17.7 mL, 2.2 M in hexanes, 39.0 mmol) was added dropwise over 30 minutes. The solution was allowed to warm to room temperature overnight before further cooling to -78°C and adding dropwise to a solution of 1,2-dichloroethane (16.7 mL, 213.0 mmol) in ether (20 mL) at -78°C over the course of 1 hour. The reaction was allowed to warm to room temperature and stirred for 2 hours

Chapter 6

before quenching with degassed water (20 mL). The product was extracted with ether (3 × 5 mL), the organic fractions were combined and dried over MgSO₄. The reaction flask was placed under reduced pressure to remove diethyl ether and excess 1,2-dichloroethane, however the products of this reaction also proved to be volatile and as such were also removed.

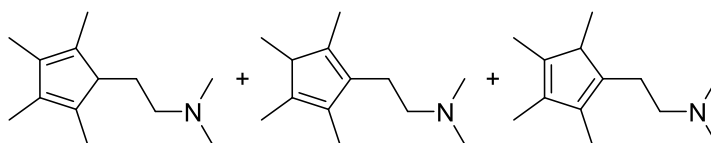
The synthesis of 1-chloro-2-(diisopropylamino)ethane was therefore repeated, using LDA as a substrate.

Attempt 2: LDA (0.5 g, 4.67 mmol) was dissolved in THF (20 mL), cooled to –35 °C and added dropwise to a cooled (–35 °C) of 1,2-dichloroethane (0.22 mL, 28.02 mmol) in THF (10 mL) and left to warm to room temperature with stirring over 16 hours. After this time, a GC-MS analysis of the reaction mixture was run following hydrolysis of an aliquot of the reaction mixture and it was observed that the reaction had produced >20 products visible within the GC trace obtained. At this point the reaction was abandoned.

6.2.3 L₂X-CH₂CH₂-ER_n type ligands6.2.3.1 Synthesis of 4-[2-(*N,N*-dimethylamino)ethyl]-3,5-dimethylhepta-2,5-diene-4-ol

The synthesis of 4-[2-(*N,N*-dimethylamino)ethyl]-3,5-dimethylhepta-2,5-diene-4-ol was carried out in accordance with the literature procedure.¹¹ 2-Bromo-2-butene (5 mL, 49.2 mmol) was added dropwise to a stirred suspension of lithium (0.68 g, 98.0 mmol) in ether (30 mL) and heated at reflux overnight. After cooling the reaction to 0 °C, methyl-3-*N,N*-dimethylaminopropionate (3.5 mL, 24.6 mmol) was added dropwise to the reaction mixture before heating at reflux overnight. Unreacted lithium was quenched *via* dropwise addition of propan-2-ol before a saturated solution of NH₄Cl (4 × 10 mL) was added and left for one hour before extracting with ether (3 × 20 mL). The combined extracts were dried (MgSO₄) and volatile components removed *in vacuo* to afford 4-[2-(*N,N*-dimethylamino)ethyl]-3,5-dimethylhepta-2,5-diene-4-ol as a viscous orange oil (2.91 g, 13.8 mmol, 56%). The ¹H NMR spectrum obtained is in agreement with the literature data.¹¹

¹H NMR (400 MHz, CDCl₃): 5.68 – 5.32 (m, 2H, H-1), 2.43 – 2.35 (m, 2H, H-5), 2.26, 2.23, 2.19 (3s, 6H, H-6), 1.92 – 1.87 (m, 2H, H-4), 1.75 – 1.58 (m, 12H, H-1/3)

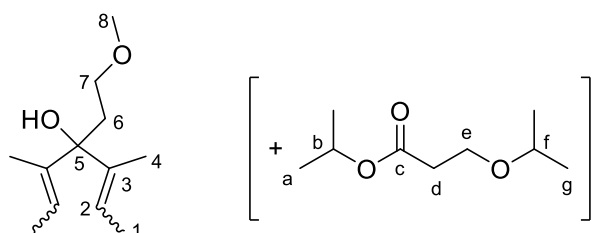
6.2.3.2 Synthesis of 1-[2-(*N,N*-dimethylamino)ethyl]-2,3,4,5-cyclopentadiene

The synthesis of 1-[2-(*N,N*-dimethylamino)ethyl]-2,3,4,5-cyclopentadiene was carried out in accordance with the literature procedure.¹¹ 4-[2-(*N,N*-Dimethylamino)ethyl]-3,5 dimethylhepta-2,5-diene-4-ol (2.48 g, 11.7 mmol) in ether (10 mL) was added slowly to *p*-TsOH·H₂O (2.78 g, 14.6 mmol) in ether (15 mL) and heated at reflux overnight. The resulting solution was neutralised with a saturated K₂CO₃ solution (~1 mL). Distilled water was added (20 mL) and the product extracted with ether (3 × 15 mL). The combined extracts were dried (MgSO₄) and removal of the solvent affords the crude product as a yellow oil. The ¹H NMR spectrum of the crude product was in agreement with that

reported in the literature, with additional impurities.¹¹ Unfortunately, purification by distillation under reduced pressure using a Kugelrohr caused decomposition of the product above 70 °C.

¹H NMR (crude): δ_{H} (400 MHz, CDCl₃) 2.65 – 2.53 (m, 3H, CH), 2.51 – 2.30 (m, 6H, CH₂N), 2.29, 2.26, 2.18 (3s, 18H, NCH₃), 1.83 – 1.76 (m, 18H, =CCH₃), 1.71 – 1.58 (m, 6H, CCH₂), 1.02 – 0.96 (m, 6H, C-CH₃).

6.2.3.3 Synthesis of 4-(2-methoxyethyl)-3,5-dimethylhepta-2,5-diene-4-ol



Attempt 1: A modification to the literature procedure was used for the synthesis of 4-(2-methoxyethyl)-3,5-dimethylhepta-2,5-diene-4-ol.¹¹ 2-Bromo-2-butene (5 mL, 49.2 mmol) was added dropwise to a stirred suspension of lithium (0.68 g, 98.0 mmol) in ether (30 mL) and heated at reflux overnight. Methyl-3-methoxypropionate (2.9 mL, 24.6 mmol) was added dropwise at 0 °C before heating at reflux overnight. Unreacted lithium was quenched *via* dropwise addition of propan-2-ol before a saturated solution of NH₄Cl (3 × 10 mL) was added which was then poured onto additional saturated NH₄Cl (20 mL) and left for one hour before extracting with ether (3 × 15 mL). The combined extracts were dried (MgSO₄) and volatile components removed *in vacuo* to afford a mixture of products, which were determined to be 4-(2-methoxyethyl)-3,5-dimethylhepta-2,5-diene-4-ol and isopropyl-(2-isopropoxy)ethanoate by ¹H and ¹³C{¹H} NMR spectra obtained and comparison to literature data.^{11,12}

¹H NMR (dienol: EE, ZZ and EZ isomers) (400 MHz, CDCl₃): δ_{H} 5.64-5.54 (m, 2H, H-2), 3.50 (t, 2H, ³J_{HH} 5.7 Hz, H-7), 3.38, 3.37, 3.35 (3s, H-8), 2.05 (t, 2H, ³J_{HH} 5.7 Hz, H-6), 1.66-1.62 (m, 12H, H-1/4)

¹³C{¹H} NMR (dienol: EE, ZZ, EZ isomers) (176 MHz, CDCl₃): δ_{C} 139.6, 139.1, 138.3 and 138.1 (4s, C-3) 122.7, 122.7, 119.1 and 118.1 (4s, C-2), 81.3, 81.1 and 80.0 (3s, C-5), 70.7, 70.6 and 70.6 (3s, C-7) 59.0, 58.9 and 58.9 (3s, C-8), 37.9, 34.5 and 29.8 (3s, C-6), 23.6, 22.9 and 22.2 (3s, C-4), 14.9, 14.6, 13.6, 13.3, 12.5 and 12.4 (6s, C-1).

¹H NMR (ester) (400 MHz, CDCl₃): δ_{H} 4.99 (h, 1H, ³J_{HH} 6.3 Hz, H-b), 3.64 (t, 2H, ³J_{HH} 6.5 Hz, H-e), 3.55 (h, 1H, ³J_{HH} 6.1 Hz, H-f), 3.31 (s, CH₃OH), 2.48 (t, 2H, ³J_{HH} 6.5 Hz, H-d), 1.20 (d, 6H, ³J_{HH} 6.3 Hz, H-a), 1.11 (d, 6H, ³J_{HH} 6.1 Hz, H-g).

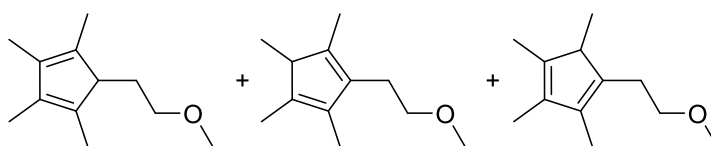
$^{13}\text{C}\{^1\text{H}\}$ NMR (ester) (176 MHz, CDCl_3): δ_{C} 171.4 (s, C-c) 71.8 (s, C-f), 67.8 (s, C-b), 63.7 (s, C-e), 36.0 (s, C-d), 22.1 (s, C-a), 21.9 (s, C-g).

Attempt 2: The above procedure was repeated as described with the following amendment: unreacted lithium was not quenched *in situ*, rather, the solution was filtered from the remaining lithium solids before pouring onto aq. NH_4Cl solution. This amended procedure resulted in the successful synthesis of 4-(2-methoxyethyl)-3,5-dimethylhepta-2,5-diene-4-ol (2.47 g, 12.5 mmol, 51 %), with spectroscopic data obtained in agreement with the literature values.¹¹

^1H NMR (400 MHz, CDCl_3): δ_{H} 5.66-5.54 (m, 2H, H-2), 3.50 (t, 2H, $^3J_{\text{HH}}$ 5.7 Hz, H-7), 3.38, 3.37, 3.35 (3s, H-8), 2.05 (t, 2H, $^3J_{\text{HH}}$ 5.7 Hz, H-6), 1.67-1.60 (m, 12H, H-1/4)

$^{13}\text{C}\{^1\text{H}\}$ NMR (176 MHz, CDCl_3): δ_{C} 139.6, 139.1, 138.3 and 138.1 (4s, C-3) 122.7, 122.7, 119.1 and 118.1 (4s, C-2), 81.3, 81.1 and 80.0 (3s, C-5), 70.7, 70.6 and 70.6 (3s, C-7) 59.0, 58.9 and 58.9 (3s, C-8), 37.9, 34.5 and 29.8 (3s, C-6), 23.6, 22.9 and 22.2 (3s, C-4), 14.9, 14.6, 13.6, 13.3, 12.5 and 12.4 (6s, C-1).

6.2.3.4 Attempted synthesis of $\text{Cp}^*\text{CH}_2\text{CH}_2\text{OMe}$



Attempt 1: The attempted synthesis of $\text{Cp}^*\text{CH}_2\text{CH}_2\text{OMe}$ was carried out in accordance to the literature procedure.¹¹ 4-[2-(Methoxy)ethyl]-3,5-dimethylhepta-2,5-diene-4-ol (3.00 g, 15.1 mmol) was added slowly to *p*- $\text{TsOH}\cdot\text{H}_2\text{O}$ (3.59 g, 18.9 mmol) in ether (40 mL) and heated at reflux overnight. The resulting deep red solution was neutralised with a saturated K_2CO_3 solution (~2 mL). Distilled water (30 mL) was added and the product extracted with ether (2 \times 20 mL). The combined extracts were dried (MgSO_4) and volatile components removed *in vacuo*. However, the ^1H NMR spectrum obtained could not be attributed. TLC analysis of the mixture (10:1, hexane:ethyl acetate) suggested the presence of at least three compounds in the product mix, however, when the same solvent system was applied to a larger scale separation on a silica column, clear separation was not obtained.

Attempt 2: The above procedure (without column) was repeated and resulted in the same unattributable ^1H NMR spectrum. The product(s) obtained from this were then dissolved in hexane (50 mL) before conc. sulfuric acid (25 mL) was added dropwise. Distilled water (60 mL) was added dropwise and a vigorous reflux established immediately. After stirring for 2 hours, the resulting mixture was poured onto a saturated aq. K_2CO_3 solution. The organic layer was separated, washed with one portion

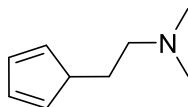
Chapter 6

each of aq. K_2CO_3 , aq. NH_4Cl and H_2O (30 mL) and dried ($MgSO_4$). Removal of the solvent under reduced pressure yielded a red oil, which was not attributable by 1H NMR spectroscopy.

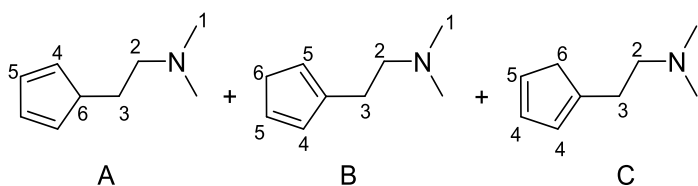
6.2.3.5 Attempted synthesis of $Cp^*-CH_2CH_2-OMe$ via $MsCl$

To a flask containing dienol (0.8 g, 4.03 mmol) in DCM (20 mL) at 0 °C, trimethylamine (0.57 mL, 4.10 mmol) was added and the solution stirred for one hour. $MsCl$ (0.47 mL, 6.05 mmol) was then added dropwise at 0 °C and the reaction allowed to warm to room temperature with stirring overnight, after which time the orange solution was observed to turn black with a visible precipitate. Degassed water (20 mL) was then added and the solution stirred for 30 minutes before the organic layer was separated and the aqueous layer extracted with DCM (3 × 20 mL). The organic layers were combined, dried over $MgSO_4$ and volatile components removed *in vacuo* to afford a sticky black solid. A GC-MS spectrum obtained in DCM of the black solid produced in this reaction displayed the presence of >15 species: no attempt was made to separate these.

6.2.3.6 Synthesis of 2-(cyclopentadienyl)-1-*N,N*-dimethylethylamine



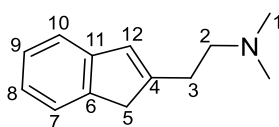
2-Chloro-1-*N,N*-dimethylethylamine hydrochloride (1.00 g, 6.94 mmol) was suspended in THF and cooled to -78 °C before *n*-butyllithium (3.17 mL, 2.3 M in hexanes, 7.63 mmol) was added dropwise over the course of 30 minutes. The solution was then allowed to warm to room temperature overnight. Cyclopentadienyl sodium was dissolved in THF (20 mL) and added to the 2-chloro-1-*N,N*-dimethylethylamine solution over the course of 2 hours to form a light pink solution. The reaction was then heated at reflux for 21 hours before quenching with degassed water (20 mL). The product was extracted in diethyl ether (3 × 15 mL), the organic fractions were combined and dried over $MgSO_4$ before being isolated by filtration and removal of volatile components under reduced pressure to yield 2-(cyclopentadienyl)-1-*N,N*-dimethylethylamine as an orange oil (0.31g, 2.25 mmol, 33%) consisting of geminal and facial isomers (shown below). Spectroscopic data are in good agreement when compared to literature values.¹³



$^1\text{H NMR}$ (700 MHz, CDCl_3): δ_{H} 6.43-6.41, 6.40-6.38, 6.23-6.22, 6.17-6.15 and 6.03-6.01 (m, ring CH=CH: H-4/5 of A, B and C), 2.92-2.87 (dm, ring CH_2 : H-6 of A, B and C), 2.57-2.55, 2.53-2.50 and 2.48-2.46 (m, Cp- $\text{CH}_2\text{CH}_2\text{-NMe}_2$: H-2 of A, B and C) 2.46-2.43 and 2.38-2.33(m, Cp- $\text{CH}_2\text{CH}_2\text{-NMe}_2$: H-3 of A, B and C) 2.26, 2.24 and 2.23 (s, CH_3 : H-1 of A, B and C).

MS (ESI): 137.15 (0.72%, $[\text{M}]^+$), 58.05 (100%, $[\text{M-CpCH}_2]^-$), 44.05 (1.54%, $[\text{M-CpCH}_2\text{CH}_2]^-$).

2.6.3.7 Synthesis of 2-(2-indenyl)-N,N-dimethylethylamine



A modification to the literature procedure was used.¹⁴ 2-Chloro-*N,N'*-dimethylethylamine hydrochloride (1.0 g, 6.94 mmol) was suspended in THF (30 mL) and cooled to $-78\text{ }^\circ\text{C}$, to which *n*-butyllithium (3.17 mL, 2.4 M in hexanes, 7.63 mmol) was added dropwise over 10 minutes and the solution allowed to warm to room temperature overnight with stirring. To a cooled ($-78\text{ }^\circ\text{C}$) solution of indene (0.81 mL, 6.94 mmol) in THF (20 mL), *n*-butyllithium (3.17 mL, 2.4 M in hexanes, 7.63 mmol) was added dropwise. The solution was allowed to warm to room temperature overnight with stirring.

The resulting indenyllithium solution was added dropwise to a solution of 2-chloro-*N,N'*-dimethylamine in THF over two hours before the reaction was heated at reflux for 16 hours in the dark. The reaction was then quenched *via* addition of water (20 mL), and the organic fraction extracted in ether ($3 \times 15\text{ mL}$) and dried over MgSO_4 before volatile components were removed *in vacuo* to yield the title compound as an orange oil (1.196 g, 6.90 mmol, 99%).

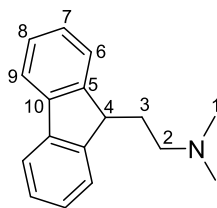
$^1\text{H NMR}$ (700 MHz, CDCl_3): δ_{H} 7.47 (d, 1H, $^3J_{\text{HH}}$ 7.4 Hz, H-10), 7.41 (d, 1H, $^3J_{\text{HH}}$ 7.6 Hz, H-7), 7.33 (t, 1H, $^3J_{\text{HH}}$ 7.5 Hz, H-9), 7.23 (t, 1H, $^3J_{\text{HH}}$ 7.4 Hz, H-8), 6.26 (s, 1H, H-12), 3.35 (s, 2H, H-5), 2.83-2.73 (m, 2H, H-3), 2.73-2.60 (m, 2H, H-2), 2.36 (s, 6H, H-1).

$^{13}\text{C}\{^1\text{H}\}$ NMR (176 MHz, CDCl_3): δ_{C} 145.3 (s, qC-11), 144.4 (s, qC-6), 142.4 (s, qC-4), 128.4 (s, C-12), 126.0 (s, C-9), 124.6 (s, C-8), 123.8 (s, C-10), 118.9 (s, C-7), 58.4 (s, C-2), 45.5 (s, C-1), 37.8 (s, C-5), 26.2 (s, C-3).

EI (GC-MS, Da): 187.10 (2.22%, $[\text{M}]^+$), 141.10 (2.25%, $[\text{M-NMe}_2]^+$), 115.40 (4.98%, $[\text{M-C}_2\text{H}_4\text{NMe}_2]^+$), 58.10 (100%, $[\text{CH}_2\text{NMe}_2]^+$).

Chapter 6

6.2.3.8 Synthesis of Flu-CH₂CH₂-NMe₂



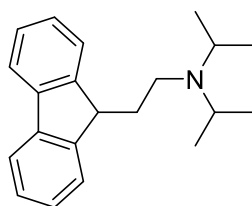
Prepared according to the literature procedure.¹⁴ *n*-Butyllithium (2.65 mL, 2.5 M in hexanes, 6.62 mmol) was added dropwise to a stirred solution of fluorene (1 g, 6.02 mmol) in THF (15 mL) at $-78\text{ }^{\circ}\text{C}$ before being allowed to warm to room temperature overnight. In tandem, *n*-Butyllithium (2.65 mL, 2.5 M in hexanes, 6.62 mmol) was added dropwise to a stirred solution of 2-chloro-*N,N*-dimethylethylamine hydrochloride (0.87 g, 6.02 mmol) in THF (15 mL) at $-78\text{ }^{\circ}\text{C}$ before being allowed to warm to room temperature overnight.

The solution of 2-chloro-*N,N*-dimethylethylamine was added dropwise to the that containing fluorenyl-lithium over the course of one hour before heating at reflux for 20 hours. The resulting red/brown solution was allowed to cool to room temperature before addition of degassed water (20 mL) and stirring for 2 hours. The aqueous layer was separated and extracted with ether ($3 \times 20\text{ mL}$), the organic fraction combined and dried over MgSO_4 before volatile components were removed *in vacuo*, leaving an orange oil. Impurities of fluorene were removed through recrystallization in diethyl ether at $-20\text{ }^{\circ}\text{C}$ to yield 1-(*N,N'*-dimethylamino)-2-(9'-fluorenyl)ethane as an orange oil (0.78 g, 3.29 mmol, 55%).

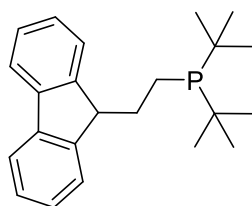
¹H NMR (700 MHz, CDCl_3): δ_{H} 7.77 (2H, d, $^3J_{\text{HH}}$ 7.5 Hz, H-9), 7.54 (2H, d, $^3J_{\text{HH}}$ 8.1 Hz, H-6), 7.38 (2H, t, $^3J_{\text{HH}}$ 7.6 Hz, H-8), 7.34-7.32 (2H, m, H-7), 4.08 (1H, t, $^3J_{\text{HH}}$ 5.8 Hz, H-4), 2.25-2.21 (2H, m, H-3), 2.21 (6H, s, CH_3), 2.20-2.15 (2H, m, H-2).

¹³C{¹H} NMR (176 MHz, CDCl_3): δ_{C} 147.1 (s, C-5), 141.1 (s, C-10), 127.1 (s, C-8), 127.0 (s, C-7), 124.4 (s, C-6), 119.9 (s, C-9), 56.0 (s, C-2), 45.7 (s, C-4), 45.5 (s, C-1), 31.1 (s, C-3).

EI (GC-MS, Da): m/z 237.192 (33.51% [M]⁺), 192.100 (9.16 [M-NMe₂-H]), 165.100 (9.47% [M-CH₂CH₂-NMe₂]), 58.100 (100% [M-Flu-CH₂]).

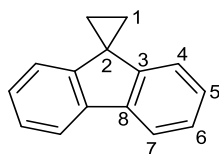
6.2.3.9 Attempted synthesis of Flu-CH₂CH₂-NⁱPr₂ via 2,6-lutidine and HNR₂

The reaction was monitored by GC-MS. 2,6-lutidine (0.23 mL, 2.0 mmol) and di-*iso*-propylamine (0.26 mL, 1.83 mmol) in THF (10 mL) were cooled to 0 °C and stirred for 3 hours. This solution was then added dropwise to 2-bromo-1-(9H'-fluorenyl)ethane (0.5 g, 1.83 mmol) in THF (20 mL) over the course of 20 minutes at 0 °C before the reaction was allowed to warm to room temperature overnight with stirring. A GC-MS spectrum of the reaction mixture was obtained, displaying the presence of starting materials only. Chlorobenzene (10 mL) was then added to the reaction mixture in attempt to aid the substitution reaction, and the mixture stirred for 5 days at room temperature, after which time no reaction was determined to have taken place by GC-MS. The reaction was then heated at reflux for 12 hours, with no change being achieved. After this point, caesium carbonate (0.60 g, 1.83 mmol) in acetonitrile (30 mL) was added to the solution and the reaction heated at reflux for 12 hours. A GC-MS spectrum of an aliquot of the reaction mixture obtained at this point showed the production of *spiro*[cyclopropane-1,9'-fluorene] at the expense of the starting material, so the reaction was therefore abandoned.

6.2.3.10 Attempted synthesis of 1-(di-*tert*-butylphosphino)-2-(9-fluorenyl)ethane

n-Butyllithium (2.3 mL, 1.9 M in hexanes, 4.39 mmol) was added dropwise to a cooled (-78 °C) and stirred solution of di-*tert*-butylphosphine (5.45 mL, 0.68 M in hexanes, 3.70 mmol) in ether (50 mL). The solution was left to stir for 3 hours before allowing the mixture to slowly warm to room temperature. A suspension of 1-bromo-2-(9-fluorenyl)ethane (1.01 g, 3.70 mmol) in ether (50 mL) was added dropwise to the reaction at room temperature, before heating to ~45 °C then heating at reflux for 2 hours. After cooling and stirring overnight, volatile components were removed *in vacuo* to yield an orange solid, which ¹H and ¹³C{¹H} NMR spectroscopy revealed to be *spiro*[cyclopropane-1,9'-

fluorene] (0.649 g, 3.32 mmol, 92%), shown below. The spectroscopic data obtained were in agreement with those reported in literature.¹⁵

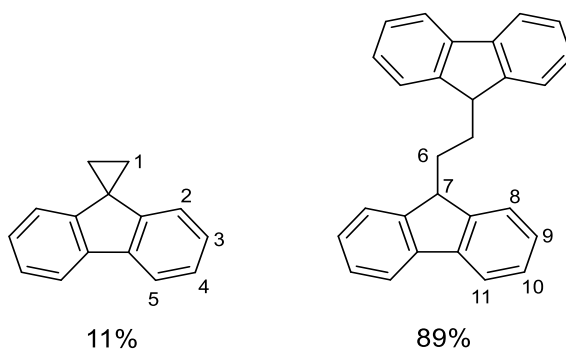


¹H NMR (400 MHz, CDCl₃): δ_H 7.69 (d, 1H, ³J_{HH} 7.5 Hz, H-7), 7.24 (td, 1H, ³J_{HH} 7.5 Hz, ⁴J_{HH} 1.1 Hz, H-6), 7.16 (td, 1H, ³J_{HH} 7.5 Hz, ⁴J_{HH} 1.1 Hz, H-5), 6.74 (d, 1H, ³J_{HH} 7.5 Hz, H-4), 1.37 (s, 2H, H-1).

¹³C{¹H} NMR (176 MHz, CDCl₃): δ_C 148.5 (s, qC-3), 140.5 (s, qC-8), 127.0 (s, C-6), 126.3 (s, C-5), 120.3 (s, C-7), 118.9 (s, C-4), 29.6 (s, qC-2), 18.2 (s, C-1).

6.2.3.11 Attempted synthesis of *spiro*[cyclopropane-1,9'-fluorene] *via n*-butyllithium

A solution of fluorene (1.74 g, 10.45 mmol) in Et₂O (20 mL) was treated with *n*-butyllithium (5 mL, 11.50 mmol, 2.3 M in hexanes), at -78 °C and left to warm to room temperature overnight with stirring. The resulting bright orange solution of fluorenyllithium was then added dropwise to a solution of 1,2-dibromoethane (1.91 mL, 10.45 mmol) in Et₂O (20 mL) over the course of two hours. The resulting mixture was left to stir at room temperature overnight after which time a white precipitate was observed. The reaction was quenched *via* addition of degassed water (30 mL) and organic components extracted into Et₂O (3 × 20 mL), and dried over MgSO₄. Volatile components were removed under reduced pressure to yield a white crystalline solid (0.152 g) which was determined to be predominantly 1,2-*bis*(9-*H'*-fluorenyl)ethane by ¹H NMR spectroscopy, with only 11% conversion to the title compound.

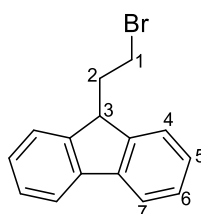


¹H NMR (CDCl₃, 400 MHz): δ_H 7.76 (dt, 2H, ³J_{HH} 7.6 Hz, ⁴J_{HH} 1.0 Hz, H-11), 7.41-7.36 (m, 2H, H-8), 7.35-7.28 (m, 4H, H-9/10), 3.85 (s, H-7), 1.78-1.72 (m, 2H, H-6), 1.54 (s, H-1).

In retrospect, it not surprising that slow addition of fluorenyllithium to 1,2-dibromoethane would yield 1,2-*bis*(9-*H'*-fluorenyl)ethane.

6.2.3.12 Attempted synthesis of *spiro*[cyclopropane-1,9'-fluorene] from 1-bromo-2-(9'-H-fluorenyl)ethane

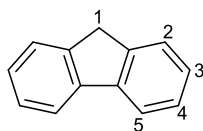
A modification to the literature procedure for the preparation of *spiro*[2.4]hepta-4,6-diene was used.¹⁶ To a round bottomed flask equipped with a condenser, 1-bromo-2-(9'-H-fluorenyl)-ethane (3.04 g, 11.1 mmol) and benzylammonium chloride (1.0 g, 6.91 mmol) suspended in Et₂O (150 mL) was charged, followed by a solution of NaOH (1 M, 100 mL). The reaction was immediately observed to change colour from yellow to deep orange and was left to stir at room temperature for 2 hours. The solution was cooled to room temperature and degassed water (50 mL) was added to the reaction. The organic layer was separated, washed with NaOH (1 M, 30 mL) and dried over MgSO₄. Volatile components were removed *in vacuo* to leave a white solid (0.982 g) which was determined by ¹H NMR spectroscopy to be unreacted 1-bromo-2-(9'-H-fluorenyl)ethane.



¹H NMR (CDCl₃, 400 MHz): δ_H 7.77 (dt, 2H, ³J_{HH} 7.6 Hz, ⁴J_{HH} 1.0 Hz, H-7), 7.54 (dq, 2H, ³J_{HH} 7.3 Hz, ⁴J_{HH} 1.0 Hz, H-4), 7.43-7.37 (m, 2H, H-5), 7.33 (td, ³J_{HH} 7.4 Hz, ⁴J_{HH} 1.3 Hz, H-6), 4.18 (t, 1H, ³J_{HH} 6.1 Hz, H-3), 3.31 (t, 2H, ³J_{HH} 7.6 Hz, H-1), 2.52 (td, 2H, ³J_{HH} 7.6 Hz, ³J_{HH} 6.1 Hz, H-2).

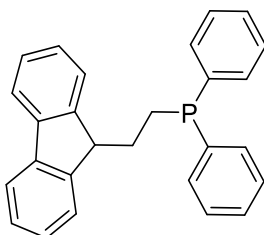
6.2.3.13 Attempted synthesis of *spiro*[cyclopropane-1,9'-fluorene] from fluorene *via* NaOH

A modification to the literature procedure for the preparation of *spiro*[2.4]hepta-4,6-diene was used.¹⁶ A 50% aqueous NaOH solution (100 mL) and benzylammonium chloride (0.34 g, 1.23 mmol) were heated to 55 °C in a round necked flask equipped with a condenser. To this reaction flask, a solution of fluorene (5.0 g, 30.08 mmol) and 1,2-dichloroethane (2.34 mL, 29.50 mmol) in Et₂O (30 mL) were added dropwise down the condenser. The reaction was heated at 55 °C for 4 hours before cooling to room temperature and left stirring for 3 days. With removal of stirring, the layers separated and the now yellow organic layer was collected, washed with NaOH (1M solution, 2 × 50 mL) and dried over MgSO₄. The filtrate was collected and volatile components were removed *in vacuo* to yield a bright yellow solid (4.668 g) which was shown by ¹H NMR spectroscopy to be unreacted fluorene.



$^1\text{H NMR}$ (CDCl_3 , 400 MHz): δ_{H} 7.82 (d, 1H, $^3J_{\text{HH}}$ 7.5 Hz, H-5), 7.57 (d, 1H, $^3J_{\text{HH}}$ 7.5 Hz, H-2), 7.41 (t, 1H, $^3J_{\text{HH}}$ 7.4 Hz, H-4), 7.35-7.29 (m, 1H, H-2), 3.92 (s, 1H, H-1).

6.2.3.13 Attempted synthesis of 1-(diphenylphosphino)-2-(9-fluorenyl)-ethane from Flu- $\text{CH}_2\text{CH}_2\text{-Br}$ using *n*-BuLi



n-BuLi (2.3 mL, 1.9 M in hexanes, 4.39 mmol) was added dropwise to a cooled ($-78\text{ }^\circ\text{C}$) and stirred solution of diphenylphosphine (0.65 mL, 3.70 mmol) in ether (50 mL). The solution was left to stir for 3 hours before allowing the mixture to slowly warm to room temperature. A suspension of 1-bromo-2-(9-fluorenyl)ethane (1.01 g, 3.70 mmol) in ether (50 mL) was added dropwise to the reaction mixture and left to stir overnight. After 24 hours, the reaction was heated to $\sim 45\text{ }^\circ\text{C}$ and heated at reflux for 2 hours. After cooling to room temperature, volatile components were removed *in vacuo* to yield an orange, oily product. The ^{31}P NMR spectrum obtained displays HPPH_2 as the major (64%) phosphorus-containing product.¹⁷ Additional phosphorus species present within the ^{31}P NMR spectrum were not attributable and further analysis could not be carried out due to the small quantity of sample produced.

$^{31}\text{P}\{^1\text{H}\}$ NMR (162 MHz, CDCl_3): δ_{P} -14.7 (s), -15.9 (s), -16.0 (s), -21.5 (s), -40.3 (s, HPPH_2).

^{31}P NMR (162 MHz, CDCl_3): δ_{P} -14.7 (s), -15.9 (s), -16.0 (s), -21.5 (s), -40.3 (dp, $^1J_{\text{PH}}$ 212 Hz, $^3J_{\text{PH}}$ 7.0 Hz, HPPH_2).

6.2.3.14 Attempted synthesis of 1-(diphenylphosphino)-2-(9-fluorenyl)-ethane from Flu- $\text{CH}_2\text{CH}_2\text{-Br}$ using DABCO

1-Bromo-2-(9-fluorenyl)ethane (1.0 g, 3.66 mmol) and diphenylphosphine (0.64 mL, 3.66 mmol) were dissolved in THF (30 mL) and cooled to $0\text{ }^\circ\text{C}$ before a THF solution (10 mL) of DABCO (0.41 g, 3.66 mmol) was added dropwise over the course of 1 hour. A precipitate was observed and the mixture was

allowed to warm to room temperature and stirred for an additional hour. The solution was filtered to remove the precipitate and volatile components were removed from the clear solution *in vacuo* to afford a yellow oily solid. A ^1H NMR spectrum of this solid was obtained in C_6D_6 and revealed the product to be a mixture of, 1-bromo-2-(9'-fluorenyl)ethane, *spiro*[cyclopropane-1,9'-fluorene], DABCO and diphenyl phosphine.

6.2.3.15 Attempted synthesis of 1-(diphenylphosphino)-2-(9-fluorenyl)-ethane from Flu- $\text{CH}_2\text{CH}_2\text{-Br}$ via a Grignard reagent

Attempt 1: Magnesium turnings (0.06 g, 2.38 mmol) were stirred under vacuum overnight before covering with THF (~5 mL) after which point an aliquot (~1 mL) of a solution of 1-bromo-2-(9'-fluorenyl)ethane (0.5 g, 1.83 mmol) in THF (~5 mL) was added and the reaction activated. Portionwise addition of the remaining 1-bromo-2-(9'-fluorenyl)ethane solution with additional THF (30 mL) was carried out over the course of one hour. The reaction was then heated at reflux for 12 hours. The solution was cooled to $-78\text{ }^\circ\text{C}$ and ClPPh_2 (0.32 mL, 1.80 mmol) was added dropwise, the solution was stirred for one hour before allowing to warm to room temperature overnight. The reaction was quenched with water (20 mL) before organic components were extracted in ether ($3 \times 15\text{ mL}$). The organic layers were combined, dried over MgSO_4 and volatile components were removed under reduced pressure. The ^1H NMR spectrum obtained of the waxy solid revealed the presence of starting material (1-bromo-2-(9'-fluorenyl)ethane), 1,2-*bis*(9'-fluorenyl)ethane and *spiro*[cyclopropane-1,9'-fluorene]. The ^{31}P NMR spectrum of the reaction mixture pre-quench displayed the presence of unreacted diphenylphosphine alongside additional hydrolysis and oxidation products of this.

^{31}P NMR (C_6D_6 , 162 MHz): δ_{P} 30.4 (s, $\text{Ph}_2\text{P(=O)-P(=O)Ph}_2$), 18.8 (d, $^1J_{\text{PH}}$ 482 Hz, HP(=O)Ph_2), -40.6 (m, LiPPh_2).

$^{31}\text{P}\{^1\text{H}\}$ NMR (C_6D_6 , 162 MHz): δ_{P} 30.4 (s, $\text{Ph}_2\text{P(=O)-P(=O)Ph}_2$), 18.8 (s, unassigned), -40.6 (s, LiPPh_2).

From the NMR data obtained, it is clear the Grignard reagent did not form in completeness and so the reaction was repeated as detailed below, using 1,4-dioxane as a solvent to aid formation of the Grignard reagent.

Attempt 2: 1-Bromo-2-(9H'-fluorenyl)ethane (0.5 g, 1.83 mmol) in THF (20 mL) and 1,4-dioxane (40 mL) was added dropwise to activated magnesium turnings (0.058 g, 2.38 mmol). The reaction was initiated through application of heat using a heat-gun and then the mixture heated at reflux for 12 hours, after which time an aliquot was extracted, hydrolysed and a GC-MS analysis made, which displayed only starting material. A flake of iodine was added to the reaction mixture and stirred for 4

hours in an attempt to activate the Grignard formation, however a GC-MS spectrum obtained displayed this not to be the case. A final attempt to activate the reaction was made through the addition of tetrachloromethane (0.2 mL). After 48 hours of stirring at room temperature, a GC-MS spectrum displayed the formation of *spiro*[cyclopropane-1,9'-fluorene] within the reaction mixture, and so the reaction was quenched and abandoned.

6.2.3.16 Attempted synthesis of 1-(diphenylphosphino)-2-(9-fluorenyl)-ethane from *spiro*[cyclopropane-1,9'-fluorene]

Attempt 1: A modification of the literature procedure was used in the attempted ring-opening of *spiro*[cyclopropane-1,9'-fluorene].¹⁸ *n*BuLi (1.17 mL, 1.9 M in hexanes, 2.22 mmol) was added dropwise to diphenylphosphine (0.32 mL, 1.85 mmol) in ether (50 mL) at -78 °C. The mixture was allowed to warm to room temperature overnight to yield a yellow solution. The mixture was cooled to -78 °C before addition of *spiro*[cyclopropane-1,9'-fluorene] (0.36 g, 1.85 mmol) in Et₂O (50 mL). The reaction was allowed to warm to room temperature and left to stir for 2 days, after which time the solution had turned orange. Volatile components were removed *in vacuo* leaving an orange residual solid. This residue was dissolved in THF (30 mL) to form a red solution, which was then washed with degassed water (15 mL), extracted with DCM (3 × 20 mL) and dried over MgSO₄. The resulting mixture was filtered and MgSO₄ washed with DCM (3 × 20 mL), after which point a ³¹P{¹H} NMR spectrum was obtained, displaying HPPH₂ as 84% of the phosphorus-containing species by integration.

³¹P{¹H} NMR (162 MHz, CDCl₃): δ_p 19.7 (s), -15.6 (s), -40.3 (s, HPPH₂).

Attempt 2: A modification of the literature procedure was used in the attempted ring-opening of *spiro*[cyclopropane-1,9'-fluorene].¹⁸ Diphenylphosphine (0.43 mL, 2.49 mmol) in ether (30 mL) was cooled to -78 °C before dropwise addition of *n*BuLi (1.44 mL, 1.9 M in hexanes, 2.74 mmol). The mixture was allowed to warm to room temperature overnight before re-cooling to -78 °C. TMEDA (0.82 mL, 5.48 mmol) was added to the mixture and allowed to stir for 1 hour before addition of *spiro*[cyclopropane-1,9'-fluorene] (0.48 g, 2.49 mmol) in ether (50 mL). The mixture was then allowed to warm to room temperature overnight, after which time HPPH₂ was observed by ³¹P{¹H} NMR spectroscopy. The solution was then heated at reflux at ~ 45 °C for 60 hours before cooling to room temperature and volatile components removed *in vacuo*. The residue was dissolved in THF (20 mL), washed with degassed water (15 mL), extracted with DCM (3 × 20 mL) and dried over MgSO₄. Volatile components were then removed under reduced pressure, before addition of petroleum ether (30 mL) and cooling to -78 °C, at which temperature a precipitate was formed. Attempts to isolate the solid

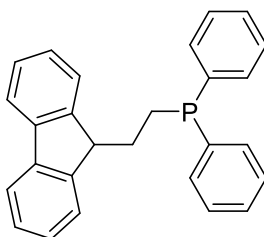
were unsuccessful due to the small quantity present, with the majority lost during the filtration process.

Attempt 3: A modification to the literature procedure was used.¹⁹ *n*-Butyllithium (0.77 mL, 2.2 M in hexanes, 1.71 mmol) was added dropwise to a solution of diphenylphosphine (0.27 mL, 1.56 mmol) in THF (20 mL) at $-78\text{ }^{\circ}\text{C}$, creating a bright orange suspension. The solution was allowed to warm to room temperature overnight before dropwise addition to a solution of *spiro*[cyclopropane-1,9'-fluorene] (0.30 g, 1.56 mmol) in THF (15 mL). The solution was heated at reflux for 4 days before cooling to room temperature. Volatiles were removed *in vacuo*, washed with water and the product extracted into toluene to yield a yellow sticky solid (0.521 g) which was determined to be unreacted starting materials by NMR spectroscopic analysis.

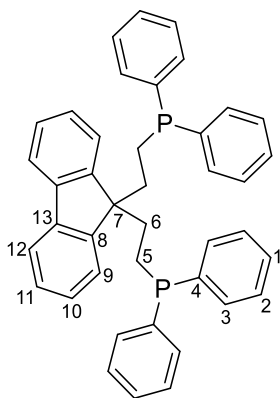
³¹P NMR (C₆D₆, 162 MHz): δ_{P} -40.7 (s, HPPH₂).

¹H NMR (C₆D₆, 400 MHz): δ_{H} 7.61-7.52 (m, 1H, Flu-H), 7.48-7.41 (m, 1H, Flu-H), 7.38-7.34 (m, 4H, *o*-H), 7.28-7.21 (m, 1H, Flu-H), 7.11-7.05 (m, 1H, Flu-H), 7.04-7.93 (m, 6H, *m*-H/*p*-H), 5.19 (d, ¹J_{PH} 2.16 Hz, P-H), 1.48 (br s, CH₂ (*spiro*-propyl ring)).

6.2.3.17 Attempted Synthesis of 2-(9H'-fluorenyl)-1-(diphenylphosphino)ethane



Fluorenyllithium was formed through dropwise addition of *n*-butyllithium (1.44 mL, 2.3 M in hexanes, 3.3 mmol) to a solution of fluorene (0.5 g, 3 mmol) in THF (20 mL) over 30 minutes at $-78\text{ }^{\circ}\text{C}$. The bright orange fluorenyllithium solution was allowed to warm to room temperature overnight before being added dropwise to a solution of 1-chloro-2-(diphenylphosphino)ethane (0.75 g, 3 mmol) in THF (20 mL) at $-35\text{ }^{\circ}\text{C}$. The reaction was then stirred at room temperature for 14 hours before quenching through the addition of 20 mL degassed water in one portion. The solution was extracted with ether (3 \times 20 mL), organic layers were combined and dried over MgSO₄ before volatile components were removed *in vacuo* to yield a yellow sticky solid. This solid was then washed with hexanes (4 \times 30 mL) at $-20\text{ }^{\circ}\text{C}$ to yield a white solid which dried under reduced pressure and determined by NMR spectroscopy to be 2-(9H'-fluorenyl)-1,1'-bis[(diphenylphosphino)ethane] (0.12 g, 0.20 mmol, 14%).

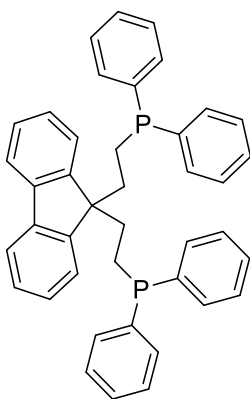


$^1\text{H NMR}$ (400 MHz, C_6D_6): δ_{H} 7.49 (dt, 1H, $^3J_{\text{HH}}$ 7.4 Hz, $^4J_{\text{HH}}$ 1.0 Hz, H-9), 7.19-7.17 (m, 4H, o-H), 7.16-7.14 (1H, m, H-10), 7.12 (td, 1H, $^3J_{\text{HH}}$ 7.4 Hz, $^4J_{\text{HH}}$ 1.2 Hz, H-12), 6.96-6.93 (m, 1H, H-11), 6.93-6.91 (m, 6H, m-H/*p*-H), 2.20-2.09 (2H, m, H-6), 1.50-1.43 (2H, m, H-5).

$^{31}\text{P}\{^1\text{H}\}$ NMR (162 MHz, C_6D_6): δ_{P} -15.3 (s)

$^{13}\text{C}\{^1\text{H}\}$ NMR (101 MHz, C_6D_6): δ_{C} 148.5 (s, qC-8), 141.6 (s, qC, C-13), 138.8 (d, $^1J_{\text{CP}}$ 14.4 Hz, qC-4), 132.6 (d, C-3), 128.2 (d, C-2), 128.1 (s, C-11), 127.9 (s, C-12), 127.3 (s, C-10), 122.8 (s, C-1), 120.0 (s, C-9), 56.4 (t, $^3J_{\text{CP}}$ 13.5 Hz, C-7), 36.1 (d, $^2J_{\text{CP}}$ 19.9 Hz, C-6), 21.9 (d, $^1J_{\text{CP}}$ 12.5 Hz, C-5).

6.2.3.18 Attempted synthesis of 2-(9H'-fluorenyl)-1,1'-bis[(diphenylphosphino)ethane]

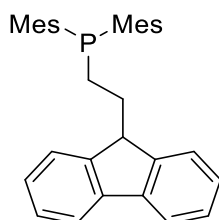


Fluorenyllithium was prepared in THF (30 mL) through dropwise addition of *n*-butyllithium (0.34 mL, 0.82 mmol, 2.4 M in hexanes) to fluorene (0.07 g, 0.40 mmol) at $-78\text{ }^\circ\text{C}$ and stirring at room temperature overnight. The fluorenyl lithium solution was then added dropwise to a solution of 1-chloro-2-(diphenylphosphino)ethane (0.20 g, 0.80 mmol) at $-35\text{ }^\circ\text{C}$. The reaction was allowed to warm to room temperature overnight with stirring, after which time it was quenched through addition on degassed water (30 mL). Organic components were extracted into Et_2O ($3 \times 20\text{ mL}$) and dried over MgSO_4 . Volatile components were removed *in vacuo* and the residue washed with hexanes ($3 \times 20\text{ mL}$)

at $-20\text{ }^{\circ}\text{C}$ to yield a white solid which was determined to be a mixture of products by ^{31}P NMR spectroscopy.

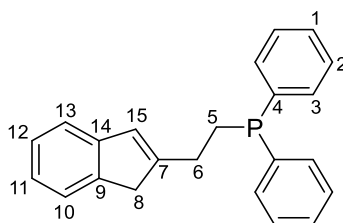
$^{31}\text{P}\{^1\text{H}\}$ NMR (C_6D_6 , 162 MHz): δ_{P} -7.5 (s), -10.9 (s), -12.9 (s, dppe), -15.1 (s, Ph_2PPh_2), -15.3 (s, $\text{Flu}\{\text{CH}_2\text{CH}_2\text{-PPh}_2\}_2$), -16.4 (s).

6.2.3.19 Attempted synthesis of 1-(dimesitylphosphino)-2-(9H'-fluorenyl)ethane



To a solution of fluorene (0.05 g, 0.30 mmol) in THF (10 mL), *n*-butyllithium (0.14 mL, 2.3 M in hexanes, 0.33 mmol) was added dropwise at $-78\text{ }^{\circ}\text{C}$ and the solution was left to warm to room temperature overnight. The fluorenyllithium was added dropwise over 30 minutes to a solution of 1-chloro-2-(dimesitylphosphino)ethane (0.10 g, 0.30 mmol) in THF (10 mL) which was cooled to $-35\text{ }^{\circ}\text{C}$. The reaction was monitored by ^{31}P NMR spectroscopy and, after no reaction was observed to take place after 26 hours at room temperature, the mixture was heated at reflux for 24 hours. A ^{31}P NMR spectrum obtained after this point displayed no reaction had occurred as only 1-chloro-2-(dimesitylphosphino)ethane was observed. THF was removed under reduced pressure and replaced with Et_2O (20 mL) and the mixture stirred for 48 hours at room temperature, however no reaction was observed and the attempted synthesis of 1-(dimesitylphosphino)-2-(9H'-fluorenyl)ethane abandoned.

6.2.3.20 Synthesis of 1-(diphenylphosphino)-2-(1'-indenyl)ethane



To a cooled ($-78\text{ }^{\circ}\text{C}$) solution of indene (0.35 mL, 3.02 mmol) in THF (20 mL), *n*-butyllithium (1.44 mL, 2.3 M in hexanes, 3.32 mmol) was added dropwise over the course of one hour. The orange indenyllithium solution was allowed to warm to room temperature overnight before 1-chloro-2-(diphenylphosphino)ethane (0.75 g, 3.02 mmol) in THF (20 mL) was added dropwise over 30 minutes before the reaction was heated at reflux for 19 hours. After cooling to room temperature, the reaction

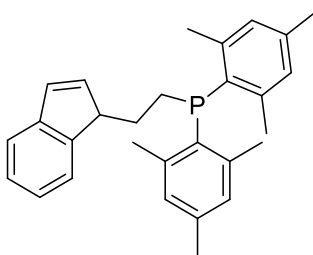
was quenched with water (20 mL), the product extracted in ether (3 × 20 mL) and organic layers combined and dried over MgSO₄. The solution was filtered and volatile components were removed *in vacuo* to yield viscous brown oil. This crude product was extracted into hexanes (40 mL) and hexanes removed under reduced pressure to yield a viscous yellow oil. This yellow oil was dissolved in the minimum volume of hexanes and cooled to −78 °C to yield a white precipitate which was collected by filtration, washed with cold (−78 °C) hexanes (3 × 20 mL) and dried under reduced pressure to afford the title compound as a white solid (0.33 g, 1.0 mmol, 33%).

¹H NMR (400 MHz, C₆D₆): δ_H 7.51-4.40 (m, 4H, H-3), 7.36-7.25 (m, 2H, H-10/13), 7.14-7.03 (m, 6H, H-1/2), 7.01-7.97 (m, 2H, H-11/12), 5.96 (s, 1H, H-15), 3.03-3.02 (m, 2H, H-8), 2.73-2.67 (m, 2H, H-6), 2.41-2.30 (m, 2H, H-5).

³¹P{¹H} NMR (162 MHz, C₆D₆): δ_P −15.7 (s).

³¹P NMR (162 MHz, C₆D₆): δ_P −15.7 (m).

6.2.3.21 Attempted synthesis of 1-(dimesitylphosphino)-2-(1H'-indenyl)ethane

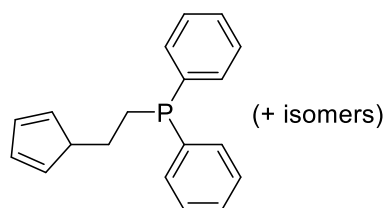


To a solution of indene (0.04 mL, 0.30 mmol) in THF (10 mL), *n*-butyllithium (0.14 mL, 2.3 M in hexanes, 0.33 mmol) was added dropwise at −78 °C and the solution was left to warm to room temperature overnight. The indenyllithium was added dropwise over 30 minutes to a solution of 1-chloro-2-(dimesitylphosphino)ethane (0.10 g, 0.30 mmol) in THF (10 mL) which was cooled to −35 °C. The reaction was monitored by ³¹P NMR spectroscopy and, after no reaction was observed to take place after 26 hours at room temperature, the mixture was heated at reflux for 48 hours. A ³¹P NMR spectrum obtained after this point displayed no reaction had occurred as only 1-chloro-2-(dimesitylphosphino)ethane was observed.

³¹P NMR (C₆D₆, 162 MHz): δ_P −28.0 (s, ClPMe₂).

³¹P{¹H} NMR (C₆D₆, 162 MHz): δ_P −28.0 (s, ClPMe₂).

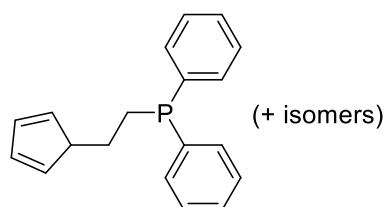
6.2.3.22 Attempted synthesis of 1-(diphenylphosphino)-2-(cyclopentadienyl)ethane with NaCp·THF



1-chloro-2-(diphenylphosphino)ethane (0.78 g, 3.12 mmol) was dissolved in THF (20 mL) and cooled to $-35\text{ }^{\circ}\text{C}$, to this, a cooled ($-35\text{ }^{\circ}\text{C}$) solution of NaCp·THF (0.50 g, 3.12 mmol) in THF (20 mL) was added dropwise over the course of 30 minutes. The reaction was allowed to warm to room temperature and stirred for 5 days, after which time a $^{31}\text{P}\{^1\text{H}\}$ NMR spectrum of the solution revealed the majority of the reaction mixture to be the starting phosphine. In an attempt to drive the reaction towards completion, the solution was heated at reflux overnight, but a ^{31}P NMR spectrum showed no change to the mixture. The reaction was sonicated for 4 hours before being stirred for an additional 10 days. No difference in the $^{31}\text{P}\{^1\text{H}\}$ NMR spectrum obtained was observed, therefore THF was removed *in vacuo* and replaced with ether (50 mL). The ethereal solution was stirred at room temperature for 6 days, however after this time, the $^{31}\text{P}\{^1\text{H}\}$ NMR spectrum obtained displayed a large proportion of starting material still present along with 6 additional phosphorus containing species.

$^{31}\text{P}\{^1\text{H}\}$ NMR (CDCl_3 , 162 Hz): δ_{P} 29.4 (s, $\text{Ph}_2\text{P}(\text{O})\text{CH}_2\text{CH}_2\text{P}(\text{O})\text{Ph}_2$), 21.9 (s, $\text{Ph}_2\text{P}(\text{O})\text{-P}(\text{O})\text{Ph}_2$), -10.1 (s, unassigned), -12.3 (s, dppe), -15.2 (s, P_2Ph_4), -15.5 (s, unassigned), -19.5 (s, $\text{ClCH}_2\text{CH}_2\text{PPh}_2$).

Due to the inherent side-reactions occurring within the reaction of cyclopentadienylsodium, an additional attempt to synthesise 1-(diphenylphosphino)-2-(cyclopentadienyl)ethane was made using cyclopentadienyllithium.

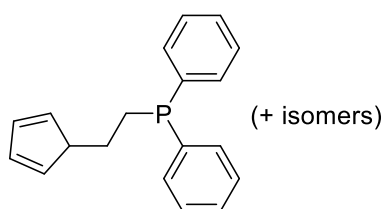
6.2.3.23 Attempted synthesis of 1-(diphenylphosphino)-2-(cyclopentadienyl)ethane with *n*-BuLi

Freshly distilled cyclopentadiene (0.34 mL, 4.02 mmol) was dissolved in THF (20 mL) and cooled to $-78\text{ }^{\circ}\text{C}$ before *n*-butyllithium (1.92 mL, 2.3 M in hexanes, 4.42 mmol) was added dropwise over 1 hour. The solution was left to warm to room temperature overnight, after which time it was observed to be bright violet in colour. The fresh cyclopentadienyllithium was added dropwise over 1 hour to a solution

of 1-chloro-2-(diphenylphosphino)ethane (1.0 g, 4.02 mmol) in THF (20 mL). The reaction was left stirring at room temperature and monitored by ^{31}P NMR, however, after 8 days no reaction was observed and so THF was removed *in vacuo*. Ether (30 mL) was added and the reaction was heated at reflux for 94 hours. A ^{31}P NMR spectrum of the mixture obtained at this point revealed no reaction had taken place.

As no reaction was observed when attempting to synthesis 1-(diphenylphosphino)-2-(cyclopentadienyl)ethane from cyclopentadienyllithium, the synthesis was reattempted with the use of cyclopentadienylthallium.

6.2.3.24 Attempted synthesis of 1-(diphenylphosphino)-2-(cyclopentadienyl)ethane with TICp

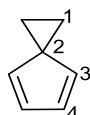


Cyclopentadienylthallium (1.08 g, 4.02 mmol) and 1-chloro-2-(diphenylphosphino)ethane (1.00 g, 4.02 mmol) were suspended in THF (30 mL) and left to stir at room temperature for 10 days. No reaction was observed by ^{31}P NMR at this point, therefore the mixture was heated at reflux for 8 days. However, a ^{31}P NMR spectrum after this time also revealed no reaction to have taken place. Volatile components were then removed under reduced pressure, replaced with chlorobenzene (25 mL) and heated at reflux for 12 days. After this period, a ^{31}P NMR spectrum obtained displayed 70% of the reaction mixture was unreacted starting material.

$^{31}\text{P}\{^1\text{H}\}$ NMR (C_6D_6 , 160.2 MHz): δ_{P} 29.0 (s, $\text{Ph}_2\text{P}(\text{O})\text{CH}_2\text{CH}_2\text{P}(\text{O})\text{Ph}_2$), 19.5 (s, unassigned,), -11.1 (s, unassigned), -13.2 (s, $\text{Ph}_2\text{P}-\text{PPh}_2$), -19.5 (s, $\text{ClCH}_2\text{CH}_2\text{PPh}_2$).

^{31}P NMR (C_6D_6 , 160.2 MHz): δ_{P} 29.0 (s, $\text{Ph}_2\text{P}(\text{O})\text{CH}_2\text{CH}_2\text{P}(\text{O})\text{Ph}_2$), 19.5 (s, $\text{Ph}_2\text{P}(\text{O})-\text{P}(\text{O})\text{Ph}_2$), -11.1 (s unassigned), -13.2 (s, $\text{Ph}_2\text{P}-\text{PPh}_2$), -19.5 (h, $^2J_{\text{PH}}$ 6.9 Hz, $\text{ClCH}_2\text{CH}_2\text{PPh}_2$).

6.2.3.25 Synthesis of *spiro*[2.4]hepta-4,6-diene



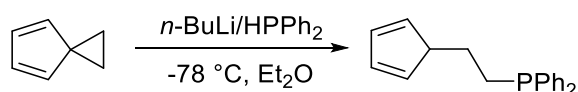
A modification to the literature procedure was used.¹⁶ Benzyltriethylammonium chloride (2.54 g, 11.1 mmol) was suspended in a 50% aqueous NaOH solution (200 mL) and heated to 45 °C. To this, a cooled (-10 °C) solution of freshly distilled cyclopentadiene (20 mL, 0.24 mol) and 1,2-dichloroethane (17.5

mL, 0.22 mol) was added portion wise over a period of 1.5 hours to avoid reflux. The solution was stirred at 55 °C for 2 hours, during which time a white precipitate was formed. The solution was cooled to room temperature and degassed water (60 mL) and pentane (40 mL) were added to aid separation of the layers. The organic layer was collected and washed with aq. 1 M NaOH (20 mL), dried over MgSO₄ and filtered. The filtrate was collected and pentane was fractionally distilled away from the product, leaving a yellow oil of *spiro*[2.4]hepta-4,6-diene (3.75 g, 40.67 mmol, 18%). Data obtained are in good agreement with reported values.¹⁶

¹H NMR (CDCl₃, 400 MHz): δ_H 6.63-6.47 (m, 1H, H-4), 6.23-6.11 (m, 1H, H-3), 1.68 (s, 2H, H-1).

¹³C{¹H} NMR (CDCl₃, 101 MHz): δ_C 139.5 (s, CCH₃), 129.3 (s, CCH₃), 38.0 (s, qC-2), 12.8 (s, C-1).

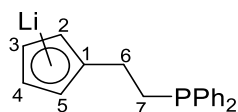
6.2.3.26 Attempted synthesis of 1-(diphenylphosphino)-2-cyclopentadienylethane



n-Butyllithium (5.75 mL, 2.2 M in hexanes, 12.7 mmol) was added dropwise to a solution of diphenylphosphine (2 mL, 11.5 mmol) in ether (20 mL) at –78 °C, creating a bright yellow suspension. The solution was allowed to warm to room temperature overnight before further cooling at –78 °C and dropwise addition to a solution of *spiro*[2.4]hepta-4,6-diene (1.06 g, 11.5 mmol) in ether (5 mL) at –78 °C. The solution was allowed to warm to room temperature and the reaction monitored by ³¹P NMR spectroscopy. The mixture was stirred in the dark for 1 week, after which time 70% of the phosphorus containing species remained as LiPPh₂, the reaction was therefore heated at reflux until no signal attributed to LiPPh₂ could be observed within the ³¹P NMR spectrum obtained: 4 days. The solution was quenched with degassed water (20 mL) and stirred for 1 hour before the organic layer was extracted with ether (3 × 20 mL), dried (MgSO₄) and concentrated under vacuum to yield a pale yellow oil. This yellow oil was determined to be a mixture of products by NMR spectroscopic analyses.

³¹P{¹H} NMR (162 Hz, C₆D₆): δ_P 18.2 (s, 4%), –12.9 (s, dppe, 6%), –14.9 (s, P₂Ph₄, 6%), –15.9 (s, 33%), –16.1 (s, 44%), –40.7 (s, HPPPh₂, 5%).

6.2.3.27 Synthesis of LiCp-CH₂CH₂-PPh₂



A modification to the literature procedure was used.¹⁹ *n*-Butyllithium (5.75 mL, 2.2 M in hexanes, 12.7 mmol) was added dropwise to a solution of diphenylphosphine (2 mL, 11.5 mmol) in ether (20 mL) at

−78 °C, creating a bright yellow suspension. The solution was allowed to warm to room temperature overnight before further cooling at −78 °C and dropwise addition to a solution of *spiro*[2.4]hepta-4,6-diene (1.06 g, 11.5 mmol) in ether (5 mL) at −78 °C. The solution was allowed to warm to room temperature and the reaction monitored by ³¹P NMR spectroscopy. After 18 hours at room temperature, 95% of the phosphorous containing species present within the reaction corresponded to LiPPh₂. The mixture was heated at reflux for 3 days. The reaction was cooled to room temperature and volatiles removed in vacuo to yield a crude yellow sticky solid which was washed with petroleum ether (60:40, 3 × 20 mL, 1 × 40 mL) to yield a light yellow powder of the title compound (2.60 g, 9.15 mmol, 80%).

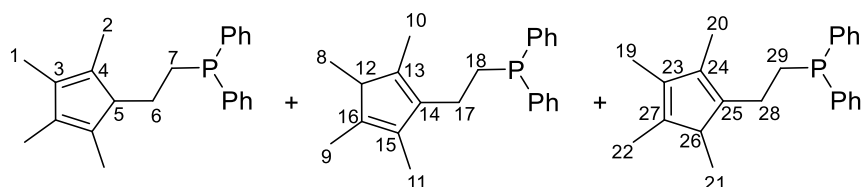
¹H NMR (d₈-THF, 700 MHz): δ_H 7.43-7.40 (m, 4H, *o*-H), 7.31-7.23 (m, 6H, *m*-H/*p*-H), 5.56 (dt, 4H, ³J_{HH} 18.2 Hz, ⁴J_{HH} 2.6 Hz, C₅H₄), 2.63-2.58 (m, 2H, H-7), 2.35-2.31 (m, 2H, H-6).

¹³C{¹H} NMR (d₈-THF, 176 MHz): δ_c 141.1 (d, ¹J_{CP} 13.1 Hz, *i*-qC), 133.8 (d, ²J_{CP} 18.1 Hz, *m*-C) 129.1 (d, ³J_{CP} 6.4 Hz, *m*-C), 129.0 (s, *p*-C), 102.8 (d, C₅H₄), 32.9 (d, ²J_{CP} 9.2 Hz, C-6), 27.5 (d, ¹J_{CP} 16.9 Hz, C-7).

³¹P NMR (d₈-THF, 283 MHz): δ_p −15.7 (s).

MS (*i*ASAP⁺): m/z 279.103 (100% [M-Li+H]⁺).

6.2.3.28 Synthesis of (Cp*)-CH₂CH₂-PPh₂



A modification to the literature procedure was used.¹⁹ *n*-Butyllithium (5.75 mL, 12.7 mmol, 2.3 M in hexanes) was added dropwise to a solution of HPPH₂ (2.0 mL, 11.5 mmol) in THF at −78 °C. The reaction was left to warm to room temperature with stirring overnight. The solution of LiPPh₂ was added dropwise to a solution containing 1,2,3,4,-tetramethylbicyclo[2,4]hepta-1,3-diene (1.70 g, 11.5 mmol) in THF (20 mL) and the resulting mixture left to stir at room temperature for three days. Volatile components were removed in vacuo to leave an off-white solid which was washed with petroleum ether (60:40, 3 × 50 mL). At this point a ³¹P NMR spectrum was obtained of the crude product which showed a small LiPPh₂ impurity. For this reason, the solid was then suspended in toluene and washed with dilute HCl (1 M, 30 mL) and water (30 mL). The product was extracted into toluene and dried over MgSO₄ before volatile components were removed in vacuo to yield a yellow pyrphoric oil of the title compound (1.79 g, 5.36 mmol, 47% (62% conversion by ³¹P NMR)). An impurity of HPPH₂ remains within the solution (accounted for within the yield quoted), observable within the NMR spectra obtained.

^1H NMR (C_6D_6 , 400 MHz): δ_{p} 7.53-7.40 (m, 4H, *o*-H), 7.40-7.33 (m, *o*-H: HPPH₂), 7.15-7.04 (m, 6H, *m*-H/*p*-H), 5.20 (d, $^1J_{\text{HP}}$ 2.16 Hz, HPPH₂), 2.65-2.50 (m, 1H, H-6/17/28), 2.48-2.30 (m, 1H, H-6/17/28), 2.22-2.05 (m, 1H, H-7/18/29), 1.95-1.82 (m, 1H, H-7/18/29), 1.81-1.58 (m, 11H, =CCH₃ (H-1/2/9/10/11/19/20/22)), 0.96 (d, 0.5H, $^3J_{\text{HH}}$ 7.6 Hz, H-8/21), 0.91 (d, 0.5H, $^3J_{\text{HH}}$ 7.6 Hz, H-8/21).

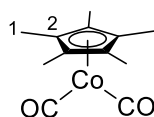
$^{31}\text{P}\{^1\text{H}\}$ NMR (C_6D_6 , 162 MHz): δ_{p} -14.3 (s), -15.6 (s), -16.1 (s), -40.7 (s, HPPH₂).

^{31}P NMR (C_6D_6 , 162 MHz): δ_{p} -14.3 (m), -15.6 (m), -16.1 (m), -40.7 (dp, $^1J_{\text{PH}}$ 215 Hz, $^3J_{\text{PH}}$ 7.6 Hz, HPPH₂)

MS (*i*ASAP+): *m/z* 334.165 (76.11% [M]⁺), 335.172 (100% [M+H]⁺).

6.2.4 (L_2X)Co(L)_n Complexes

6.2.4.1 Synthesis of Cp*Co(CO)₂



The synthesis of Cp*Co(CO)₂ was carried out using a modification of the literature procedure.²⁰ Co₂(CO)₈ (4 g, 11.7 mmol) was dissolved in DCM (35 mL) and the flask charged with 1,2,3,4,5-pentamethylcyclopentadiene (2.5 mL, 16.0 mmol) and 1,3-cyclohexadiene (1.6 mL, 16.8 mmol, filtered through activated alumina prior to use) and the mixture heated at reflux for 1 hour. The reaction was allowed to cool to room temperature before addition of a subsequent portion of 1,2,3,4,5-pentamethylcyclopentadiene (2.5 mL, 16.8 mmol) and heated at reflux for a further 2 hours, after which volatile components were removed *in vacuo* to yield Cp*Co(CO)₂ as red brown crystals suitable for X-ray diffraction (5.58 g, 22.3 mmol, 95 %). Successful synthesis of the title compound was confirmed through ^1H and $^{13}\text{C}\{^1\text{H}\}$ NMR and IR spectroscopic analyses; the ^1H NMR spectrum obtained in agreement with that quoted in the literature synthesis, however the $^{13}\text{C}\{^1\text{H}\}$ NMR and IR spectra had not previously been reported.²⁰

^1H NMR (400 MHz, C_6D_6): δ_{H} 1.62 (s, 15H, CH₃).

$^{13}\text{C}\{^1\text{H}\}$ NMR (176 MHz, C_6D_6): δ_{C} 208.7 (br s, CO), 96.3 (s, C-2), 10.4 (s, C-1).

IR (Nujol mull on KBr): ν cm⁻¹ 2006s (ν_{CO} asymmetric stretch), 1946 (ν_{CO} symmetric stretch).

Chapter 6

6.2.4.2 Repeat of Synthesis of Cp*Co(CO)₂

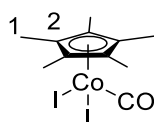
The above synthesis was repeated to yield Cp*Co(CO)₂ as red crystals (0.692 g, 2.94 mmol, 84 %). Samples of the collected volatile fractions were used for GC-analysis on a PONA column in an attempt to gain information on the mechanism of formation of Cp*Co(CO)₂ using the above method.

¹H NMR (400 MHz, C₆D₆): δ_H 1.62 (s, 15H, CH₃).

¹³C{¹H} NMR (176 MHz, C₆D₆): δ_C 208.7 (br s, CO), 96.3 (s, C-2), 10.4 (s, C-1).

GC Reaction mixture, min: 1.97 (98.92%, DCM), 3.42 (0.40%, 1,3-cyclohexadiene), 3.68 (0.28%, cyclohexene), 6.11 (0.34%, toluene).

6.2.4.3 Synthesis of Cp*Co(I)₂(CO)

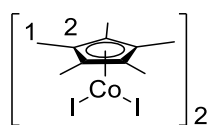


A modification to the literature procedure was employed during the synthesis of Cp*Co(I)₂(CO).²¹ To a stirred ethereal suspension (50 mL) of Cp*Co(CO)₂ (5.0 g, 20.0 mmol) an ethereal solution (100 mL) of iodine (10.15 g, 40.0 mmol) was added dropwise over the course of an hour. The mixture was left to stir for 20 hours before volatile components (including excess iodine) were removed *in vacuo* over 48 hours, to yield a black solid from which crystals suitable for X-ray diffraction were grown *via* slow evaporation of DCM. The X-ray structure obtained revealed co-crystallisation of the target complex with a molecule of I₂, and so the crude black solid contained excess iodine still. Consequently, the crude product was placed under dynamic vacuum for an additional 48 hours, before being twice recrystallised from DCM at -20 °C to yield Cp*Co(I)₂(CO) (9.49 g, 19.9 mmol, 99%). NMR spectroscopic data are not reported within the literature synthesis, however, the IR spectrum obtained is in agreement with the literature.²¹

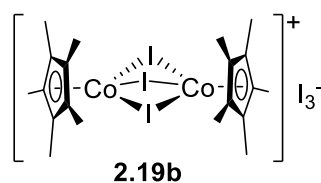
¹H NMR (400 MHz, C₆D₆): δ_H 1.58 (15H, s, CH₃).

¹³C{¹H} NMR (176 MHz, C₆D₆): δ_C 100.5 (s, C-2), 11.0 (s, C-1).

IR (Nujol mull on KBr): ν cm⁻¹ 2055 (ν_{CO} stretch).

6.2.4.4 Attempted synthesis of $[\text{Cp}^*\text{Co}(\text{I})_2]_2$ (**2.19a**)

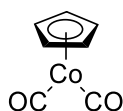
The synthesis of **3** was carried out with modifications to the literature procedure.²¹ $\text{Cp}^*\text{Co}(\text{I})_2(\text{CO})$ (7.491 g, 15.7 mmol) was dissolved in the minimum volume of octane (~240 mL) and heated at reflux under a flow of nitrogen for 56 hours to promote CO loss. Volatile components were removed *in vacuo* to produce a dark green solid, which was extracted in DCM (350 mL) *via* Soxhlet over 96 hours. DCM was then removed under reduced pressure to produce a black solid which was determined by single crystal X-ray diffraction to be $[\text{Cp}^*\text{Co}(\mu^2\text{-I})_3\text{CoCp}^*]^+[\text{I}_3]^-$, **2.19b** (6.48 g, 6.29 mmol, 81%).



$^1\text{H NMR}$ (400 MHz, C_6D_6): δ_{H} 1.60 (s, 15H, $\underline{\text{C}}\text{H}_3$).

$^{13}\text{C}\{^1\text{H}\}$ NMR (176 MHz, C_6D_6): δ_{C} 100.4 (s, $\underline{\text{C}}\text{H}_3$), 10.9 (s, Cp ring).

IR (Nujol mull on KBr): ν cm^{-1} no CO bands observed.

6.2.4.5 Synthesis of $\text{CpCo}(\text{CO})_2$ 

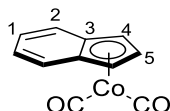
Cyclopentadienylcobalt dicarbonyl was prepared in accordance with the literature procedure.²² Freshly distilled cyclopentadiene (3.7 mL, 43.9 mmol) was added to dicobalt octacarbonyl (3 g, 8.8 mmol) in DCM (30 mL) and heated at reflux in the dark for 56 hours. The reaction was then allowed to cool to room temperature before DCM was removed by distillation (1 atm, 43 °C). A dark red liquid was then collected *via* vacuum transfer to yield $\text{CpCo}(\text{CO})_2$ (3.12 g, 13.0 mmol, 74%) which was stored under nitrogen in the dark at -20 °C. The successful synthesis of the title compound was confirmed through ^1H , $^{13}\text{C}\{^1\text{H}\}$ NMR and IR spectroscopic techniques, with the IR spectrum obtained in agreement with literature values, however the NMR spectrum of $\text{CpCo}(\text{CO})_2$ was not reported.^{22,23}

$^1\text{H NMR}$ (400 MHz, C_6D_6): δ_{H} 4.42 (s, 5H, H-1)

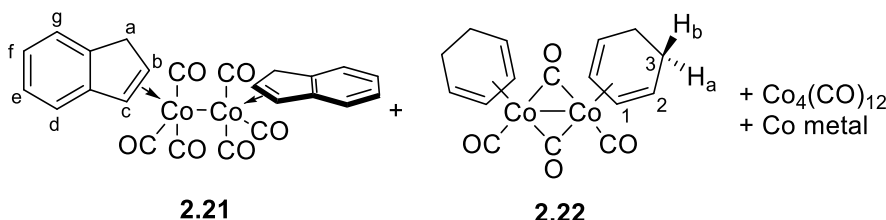
$^{13}\text{C}\{^1\text{H}\}$ NMR (176 MHz, C_6D_6): δ_{C} 205.5 (br s, $\underline{\text{CO}}$), 84.6 (s, Cp ring)

IR: (Nujol mull on KBr): ν cm^{-1} 2029 (ν_{CO} asymmetric stretch), 1968 (ν_{CO} symmetric stretch).

6.2.4.6 Attempted Synthesis of $(\eta^5\text{-Ind})\text{Co}(\text{CO})_2$



A modification of the literature procedure for the attempted synthesis of $(\text{Ind})\text{Co}(\text{CO})_2$.²⁰ $\text{Co}_2(\text{CO})_8$ (4 g, 11.7 mmol) was dissolved in DCM (35 mL) and the flask charged with indene (1.5 mL, 12.9 mmol) and 1,3-cyclohexadiene (1.5 mL, 15.2 mmol) and the mixture heated at reflux for 2 days. The reaction was allowed to cool to room temperature before addition of a subsequent portion of indene (1.5 mL, 12.9 mmol) and then heated at reflux for a further for 2 days. An orange precipitate of $[\text{Co}(\text{C}_6\text{H}_8)(\text{CO})(\mu\text{-CO})_2]$ (0.774 g, 1.98 mmol, 17%) was observed (as determined by ^1H NMR spectroscopy), isolated *via* cannula filtration and washed with cold DCM (2×10 mL). Volatile components were removed from the filtrate to yield a black powder of cobalt metal (2.592 g). From these volatile fractions a yellow liquid was obtained. ^1H NMR and IR spectroscopic methods suggest this liquid to be $[(\eta^2\text{-Indene})\text{Co}(\text{CO})_3]_2$ (1.098 g, 2.11 mmol, 18%).



^1H NMR (**2.21**, 400 MHz, CD_2Cl_2): δ_{H} 7.49 (br d, 2H, $\nu_{1/2}$ 74 Hz, $^3J_{\text{HH}}$ 45 Hz, $\underline{\text{H-e/f}}$), 7.27 (br d, 2H, $\nu_{1/2}$ 76 Hz $^3J_{\text{HH}}$ 44 Hz, $\underline{\text{H-d/g}}$), 6.94 (br s, 1H, $\nu_{1/2}$ 25 Hz, $\underline{\text{H-b}}$), 6.61 (br s, 1H, $\nu_{1/2}$ 25 Hz, $\underline{\text{H-c}}$) and 3.45 (br s, 2H, $\nu_{1/2}$ 26 Hz, $\underline{\text{H-a}}$).

IR (**2.21**, ATR-FTIR): ν cm^{-1} 3066w and 3042w (ν_{CH} CH_2 stretch), 2052m (ν_{CO} stretch), 1980s (ν_{CO} stretch), 1940w cm^{-1} (ν_{CO} stretch), 2894w and 2052w (ν_{CH} stretch), 1613 ($\nu_{\text{C=C}}$ stretch), 1457m (ν_{CH} CH_2 bend).

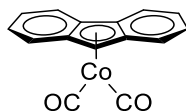
MS (**2.21**, ASAP+): m/z 519.15 Da (0.90% $[\text{M}]^+$), 291.059 (47.47% $[\text{M}-6(\text{CO})-\text{H}]^+$), 231.12 Da (100% $[(\text{M}-\text{CO})/2]+\text{H}]^+$).

^1H NMR (**2.22**, 400 MHz, $(\text{CD}_3)_2\text{CO}$): δ_{H} 4.90 (br s, 1H, $\nu_{1/2}$ 34 Hz, $\underline{\text{H-1}}$), 3.84 (br s, 1H, $\nu_{1/2}$ 34 Hz, $\underline{\text{H-2}}$), 1.93 (br s, 1H, $\nu_{1/2}$ 48 Hz, $\underline{\text{H-a}}$), 1.59 (br s, 1H, $\nu_{1/2}$ 51 Hz $\underline{\text{H-b}}$).

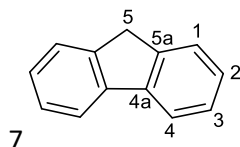
IR (2.22, ATR-FTIR): ν cm^{-1} 3064w and 3065w (ν_{CH} CH_2 stretch), 2937-2844m (ν_{CH} CH bend), 2000s and 1984vs (ν_{CO} terminal CO), 1764vs (ν_{CO} bridging CO).

IR ($\text{Co}_4(\text{CO})_{12}$, ATR-FTIR): ν cm^{-1} 2062, 2053 and 1865 cm^{-1} (ν_{CO}).

6.2.4.7 Attempted Synthesis of (η^5 -Flu)Co(CO)₂

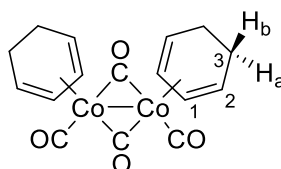


A modification to the literature procedure for the synthesis of $\text{Cp}^*\text{Co}(\text{CO})_2$ was used for the attempted synthesis of $(\text{Flu})\text{Co}(\text{CO})_2$.²⁰ $\text{Co}_2(\text{CO})_8$ (2 g, 5.85 mmol) was dissolved in DCM (30 mL) and the flask charged with an ethereal solution (10 mL) of fluorene (1.33 g, 8.0 mmol) and 1,3-cyclohexadiene (0.8 mL, 8.4 mmol, filtered through activated alumina) and the mixture heated at reflux for 2 hours. The reaction was allowed to cool to room temperature before addition of a subsequent ethereal solution (10 mL) of fluorene (1.33 g, 8.0 mmol) and further heating at reflux for 2 hours, after which time volatile components were removed *in vacuo* to yield a light brown powder. ^1H and $^{13}\text{C}\{^1\text{H}\}$ NMR and IR spectroscopic data revealed that this collected powder was a mixture of unreacted starting materials: fluorene and $\text{Co}_2(\text{CO})_8$, *cis*- and *trans*-isomers of $[(\text{C}_6\text{H}_8)(\text{CO})\text{Co}(\mu_2\text{-CO})]_2$ (4:3 mixture *cis:trans*).^{24,25}



^1H NMR Fluorene (400 MHz, C_6D_6): δ_{H} 7.81 (d, 1H, $^3J_{\text{HH}}$ 6.4 Hz, H-1), 7.57 (d, 1H, $^3J_{\text{HH}}$ 6.0 Hz, H-4), 7.38 (s, 1H, H-3), 7.31 (s, 1H, H-2), 3.92 (s, 1H, CH_2)

$^{13}\text{C}\{^1\text{H}\}$ NMR Fluorene (176 MHz, C_6D_6): δ_{C} 211.5 (br s $\underline{\text{CO}}$ ($\text{Co}_2(\text{CO})_8$), 143.9 (s, qC-4a), 142.2 (s, qC-5a) 127.3 (s, C-2), 127.2 (s, C-3), 125.6 (s, C-4), 120.3 (s, C-1), 37.5 (s, C-5)



^1H NMR *cis*- $[\text{Co}(\text{C}_6\text{H}_8)(\text{CO})(\mu_2\text{-CO})]_2$ (400 MHz, C_6D_6): δ_{H} 5.54 (br s, 1H, H-1), 4.17 (br s, 1H, H-2), 2.00 (br m, 1H, H-a), 1.52 (br m, 1H, H-b).

^1H NMR *trans*- $[\text{Co}(\text{C}_6\text{H}_8)(\text{CO})(\mu_2\text{-CO})]_2$ (400 MHz, C_6D_6): δ_{H} 4.90 (br s, 1H, H-1), 3.80 (br s, 1H, H-2), 1.93 (br m, 1H, H-a), 1.54 (br m, 1H, H-b).

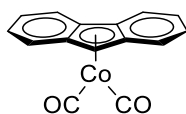
$^{13}\text{C}\{^1\text{H}\}$ NMR *cis*- $[\text{Co}(\text{C}_6\text{H}_8)(\text{CO})(\mu_2\text{-CO})_2]$ (176 MHz, C_6D_6): δ_{C} 96.0 (s, C-1), 79.8 (s, C-2), 23.7 (s, C-3)

$^{13}\text{C}\{^1\text{H}\}$ NMR *trans*- $[\text{Co}(\text{C}_6\text{H}_8)(\text{CO})(\mu_2\text{-CO})_2]$ (176 MHz, C_6D_6): δ_{C} 92.7 (s, C-1), 80.0 (s, C-2), 24.3 (s, C-3)

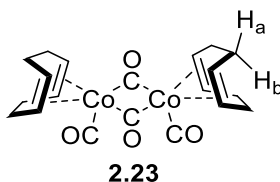
IR $[\text{Co}(\text{C}_6\text{H}_8)(\text{CO})(\mu_2\text{-CO})_2]$ (Nujol mull on KBr): ν cm^{-1} 2028s and 2008s (ν_{CO} terminal CO), 1841m (ν_{CO} bridging CO).

IR $\text{Co}_2(\text{CO})_8$ (Nujol mull on KBr): ν cm^{-1} 2072 and 2054s (ν_{CO} terminal CO), 1865m (ν_{CO} bridging CO).

6.2.4.8 Attempted synthesis of $(\eta^5\text{-Flu})\text{Co}(\text{CO})_2$ using COD



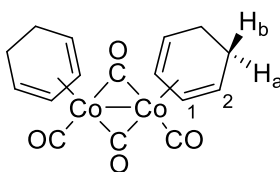
A modification to the literature procedure for the synthesis of **2.17a** was used for the attempted synthesis of **2.17d**.²⁰ $\text{Co}_2(\text{CO})_8$ (0.5 g, 1.46 mmol) was dissolved in DCM (30 mL) and the flask charged with an ethereal solution (10 mL) of fluorene (0.32 g, 1.9 mmol) and 1,4-cyclooctadiene (0.25 mL, 2.0 mmol) and the mixture heated at reflux for 2 hours. The reaction was allowed to cool to room temperature before addition of a subsequent ethereal solution (10 mL) of fluorene (0.32 g, 1.9 mmol) and further heating at reflux for 2 hours, after which time volatile components were removed *in vacuo* to yield a brown solid (1.05 g). ^1H and $^{13}\text{C}\{^1\text{H}\}$ NMR and IR spectroscopic data revealed that this collected powder was a mixture of unreacted starting materials: fluorene and $\text{Co}_2(\text{CO})_8$, and **2.23**.



^1H NMR (C_6D_6 , 400 MHz): δ_{H} 6.82 (br s, 1H, $\nu_{1/2}$ 176 Hz, =CH), 3.11 (br s, 1H, $\nu_{1/2}$ 178 Hz, $\underline{\text{H}}_a/\underline{\text{H}}_b$), -0.09 (br s, 1H, $\nu_{1/2}$ 174 Hz, $\underline{\text{H}}_a/\underline{\text{H}}_b$).

IR (Nujol Mull on KBr): ν cm^{-1} 2062s and 2054s (ν_{CO} terminal CO) and 1865m (ν_{CO} bridging CO).

6.2.4.9 Mechanistic Study *via* synthesis of $[\text{Co}(\eta_4\text{-C}_6\text{H}_8)(\text{CO})(\mu\text{-CO})_2]$



Following observation by ^1H NMR spectroscopy and single-crystal X-ray diffraction of the formation of $[\text{Co}(\eta^4\text{-C}_6\text{H}_8)(\text{CO})(\mu\text{-CO})]_2$ (**2.22**) within the attempted synthesis of $\text{IndCo}(\text{CO})_2$, the following experiments were conducted in an attempt to understand the mechanism by which either **2.22** or $\text{L}_2\text{XCo}(\text{CO})_2$ will form more favourably. A representative procedure of the experiments is detailed below:

Dicobaltoctacarbonyl (0.5 g, 1.46 mmol) was dissolved in chlorobenzene (20 mL) to form a deep red solution. 1,3-Cyclohexadiene (0.20 mL, 2.96 mmol) (filtered through activated alumina and degassed immediately before use) was added and the mixture heated to 60 °C for 48 hours. The solution was allowed to cool to room temperature and volatile components removed *in vacuo* to yield a mixture of $\text{Co}_2(\text{CO})_8$, C_6H_8 and $[\text{Co}(\eta^4\text{-C}_6\text{H}_8)(\text{CO})(\mu\text{-CO})]_2$.

The experiments carried out, along with isolated products, are summarised in Table 7.1. Spectroscopic data of those isolated products can be found below **Table 7.1**.

Table 7.1 Conditions and products isolated during attempted synthesis of $[\text{Co}(\text{C}_6\text{H}_8)(\text{CO})(\mu_2\text{-CO})]_2$.

Entry	Solvent	Temperature / °C	Time/ h	Isolated Products ^a
1	DCM	25	48	No observed reaction
2	DCM	40	48	Co black, $[\text{Co}(\text{C}_6\text{H}_8)(\text{CO})(\mu\text{-CO})]_2$
3	DCM	40	96	Co black, $[\text{Co}(\text{C}_6\text{H}_8)(\text{CO})(\mu\text{-CO})]_2$, $\text{Co}_2(\text{CO})_8$, C_6H_8 ^b
4 ^c	DCM	25	48	$[\text{Co}(\text{C}_6\text{H}_8)(\text{CO})(\mu\text{-CO})]_2$, $\text{Co}_2(\text{CO})_8$, C_6H_8 ^b
5	PhCl	60	48	$[\text{Co}(\text{C}_6\text{H}_8)(\text{CO})(\mu\text{-CO})]_2$, $\text{Co}_2(\text{CO})_8$, C_6H_8 ^b
6	Pet-ether	90	4	Metallic Co mirror
7	Xylenes	130	48	Metallic Co mirror

^a Due to the volatility of 1,3-cyclohexadiene, attempts were not made to specifically isolate this residual starting material. ^b Observed within ^1H NMR spectrum. ^c Sample placed in an ultrasound bath.

Entry 2:

IR $[\text{Co}(\text{C}_6\text{H}_8)(\text{CO})(\mu_2\text{-CO})]_2$ (ATR-FTIR): ν cm^{-1} 3066w and 3025w (ν_{CH} CH_2 stretch), 2937m and 2845m (ν_{CH} CH stretch), 1982s (ν_{CO} terminal CO), 1768s (ν_{CO} bridging CO), 1408m (ν_{CH} bend)

Chapter 6

^1H [$\text{Co}(\text{C}_6\text{H}_8)(\text{CO})(\mu_2\text{-CO})_2$] NMR (400 MHz, C_6D_6): δ_{H} 4.41 (br s, 1H, $\nu_{1/2}$ 17 Hz, H-1), 3.66 (br s, 1H, $\nu_{1/2}$ 18 Hz, H-2), 1.63 (br s, 1H, $\nu_{1/2}$ 51 Hz, H-a), 1.12 (br s, 1H, $\nu_{1/2}$ 37 Hz, H-b).

Entry 3:

^1H NMR [$\text{Co}(\text{C}_6\text{H}_8)(\text{CO})(\mu_2\text{-CO})_2$] (400 MHz, C_6D_6): δ_{H} 4.34 (br s, 1H, $\nu_{1/2}$ 254 Hz, H-1), 3.64 (br s, 1H, $\nu_{1/2}$ 266 Hz, H-2), 1.64-1.12 (br m, 2H, $\nu_{1/2}$ 466 Hz, H-a/b).

^1H NMR C_6H_8 (400 MHz, C_6D_6): δ_{H} 5.86-5.59 (br m, 2H, H-1/2), 2.25-1.94 (br m, 2H, H-a/b).

IR [$\text{Co}(\text{C}_6\text{H}_8)(\text{CO})(\mu_2\text{-CO})_2$] (Nujol mull on KBr): ν cm^{-1} 2012m and 1982, (ν_{CO} terminal CO), 1779 (ν_{CO} bridging CO).

IR $\text{Co}_2(\text{CO})_8$ (Nujol on KBr): ν cm^{-1} 2062m and 2053m (ν_{CO} terminal CO), 1865w (ν_{CO} bridging CO).

Entry 4:

^1H NMR spectrum displays suspected *cis*- and *trans*-isomers of [$\text{Co}(\text{C}_6\text{H}_8)(\text{CO})(\mu\text{-CO})_2$] in a ratio of 3:1, *cis:trans* respectively.

^1H NMR *cis*-[$\text{Co}(\text{C}_6\text{H}_8)(\text{CO})(\mu_2\text{-CO})_2$] (400 MHz, C_6D_6): δ_{H} 4.40 (brs, $\nu_{1/2}$ 24 Hz, 1H, H-1), 3.66 (br s, 1H, $\nu_{1/2}$ 27 Hz, H-2), 1.64 (br s, 1H, $\nu_{1/2}$ 36 Hz, H-a) 1.16 (br s, 1H, $\nu_{1/2}$ 36 Hz, H-b).

^1H NMR *trans*-[$\text{Co}(\text{C}_6\text{H}_8)(\text{CO})(\mu_2\text{-CO})_2$] (400 MHz, C_6D_6): δ_{H} 4.82 (br s, $\nu_{1/2}$ 19 Hz, 1H, H-1), 3.51 (br s, $\nu_{1/2}$ 25 Hz, 1H, H-2), 1.33 (br s, 1H, $\nu_{1/2}$ 45 Hz H-a), 0.68 (br s, 1H, $\nu_{1/2}$ 43 Hz H-b).

^1H NMR C_6H_8 (400 MHz, C_6D_6): δ_{H} 4.62 (br m, 2H, $\nu_{1/2}$ 59 Hz, H-1/2), 1.96 (br m, 2H, $\nu_{1/2}$ 72 Hz, H-a/b).

$^{13}\text{C}\{^1\text{H}\}$ *cis*-[$\text{Co}(\text{C}_6\text{H}_8)(\text{CO})(\mu_2\text{-CO})_2$] NMR (176 MHz, C_6D_6): δ_{C} 91.6 (s, C-1), 79.0 (s, C-2), 23.6 (s, C-3).

$^{13}\text{C}\{^1\text{H}\}$ *trans*-[$\text{Co}(\text{C}_6\text{H}_8)(\text{CO})(\mu_2\text{-CO})_2$] NMR (176 MHz, C_6D_6): δ_{C} 94.6 (s, C-1), 78.3 (s, C-2), 22.6 (s, C-3).

IR [$\text{Co}(\text{C}_6\text{H}_8)(\text{CO})(\mu_2\text{-CO})_2$] (Nujol mull on KBr): ν cm^{-1} 2009m and 1984m (ν_{CO} terminal CO), 1781 (ν_{CO} bridging CO).

IR $\text{Co}_2(\text{CO})_8$ (Nujol on KBr): ν cm^{-1} 2062s, 2054s and 2028m (ν_{CO} terminal CO), 1865 and 1843 (ν_{CO} bridging CO).

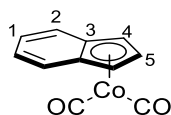
Entry 5:

$^1\text{H NMR C}_6\text{H}_8$ (400 MHz, C_6D_6): δ_{H} 5.81-5.69 (br m, $\nu_{1/2}$ 60 Hz, 1H, H-1), 5.66-5.56 (br m, 1H, $\nu_{1/2}$ 36 Hz, H-2), 1.40 (s, 2H, H-a/b).

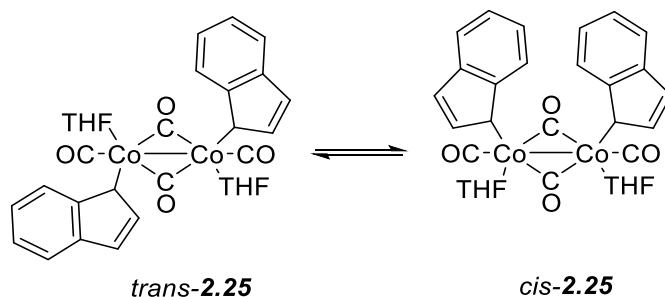
$^1\text{H NMR [Co(C}_6\text{H}_8\text{)(CO)(}\mu_2\text{-CO)]}_2$ (400 MHz, C_6D_6): δ_{H} 4.59 (br s, 1H, $\nu_{1/2}$ 18 Hz, H-1), 4.01 (br s, 1H, $\nu_{1/2}$ 16 Hz, H-2), 1.89-1.56 (br m, 1H, H-a/b), 1.19-0.92 (br m, 1H, H-a/b).

IR [Co(C₆H₈)(CO)(μ_2 -CO)]₂ (Nujol mull on KBr): ν cm^{-1} 2063s and 2054s (ν_{CO} terminal CO), 1991m (ν_{CO} bridging CO).

IR Co₂(CO)₈ (Nujol on KBr): ν cm^{-1} 2025 (ν_{CO} terminal CO), 1896w (ν_{CO} bridging CO), 1866m (ν_{CO} bridging CO).

6.2.4.10 Attempted synthesis of $(\eta^5\text{-Ind})\text{Co}(\text{CO})_2$ 

This reaction was carried out in the dark. Indenyllithium was prepared through slow addition of *n*-butyllithium (12.32 mL, 2.3 M in hexanes, 28.33 mmol) to a cooled ($-78\text{ }^\circ\text{C}$) solution of indene (3 mL, 25.75 mmol) in THF (60 mL). Iodocobalttetracarbonyl [$\text{ICo}(\text{CO})_4$] was freshly prepared *in situ* through dropwise addition of a solution of iodine (3.27 g, 12.87 mmol) in THF (25 mL) to a solution of cooled ($-78\text{ }^\circ\text{C}$) dicobaltoctacarbonyl (4.40 g, 12.87 mmol) in THF (50 mL) and the reaction allowed to proceed for 30 minutes. **Note: [$\text{ICo}(\text{CO})_4$] is only stable at $-78\text{ }^\circ\text{C}$ in the dark for approx. 1 hour.** To the solution of [$\text{ICo}(\text{CO})_4$] at $-78\text{ }^\circ\text{C}$, the solution of indenyllithium was added dropwise. The reaction was allowed to warm to room temperature overnight before volatiles were removed *in vacuo* to yield a crude oil, predominantly THF. Excess THF was removed under reduced pressure over 14 days to yield a very viscous deep red/brown oil which contains THF. No yield data has been collected due to the viscosity of this sample and associated difficulties in handling (e.g. gravimetric removal from reaction Schleck flask took several weeks). Crystals suitable for neutron diffraction grew over the course of six months, however, these decomposed during measurement. The $^1\text{H NMR}$ displays the presence of coordinated THF along with indene environments consistent with a η^1 -binding mode. IR spectroscopic analysis suggests a dimeric structure with terminal and bridging carbonyl groups.

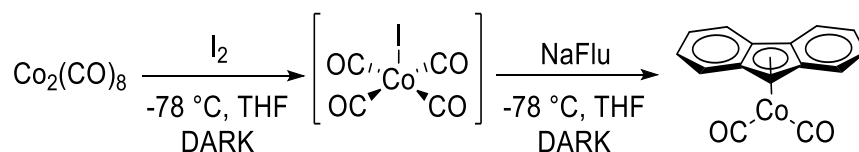


$^1\text{H NMR}$ (C_6D_6 , 400 MHz): δ_{H} 6.96-6.83 (m, 1H), 6.09 (br d, $\nu_{1/2}$ 51 Hz, 1H), 5.77 (br d, $\nu_{1/2}$ 51 Hz, 1H), 5.01-4.99 (m, 1H), 4.77 (d, 1H), 4.23 (br s, $\nu_{1/2}$ 4. Hz, Co-THF), 3.95 (s, 1H), 3.85 (s, 1H), 1.56 (br s, $\nu_{1/2}$ 20 Hz, Co-THF).

MS (ASAP⁺, Da): 130.084 (79.74% [(Ind)Co(CO)₂]⁺), 289.011 (100% [(Ind)₂Co]⁺).

IR (ATR-FTIR, ν cm^{-1}): 2980w (C-H aromatic), 2883w (C-H alkyl), 2013s and 1909s (terminal CO stretch), 1887s and 1837s (bridging CO stretch), 1460w (C=C), 1041s (C-C aromatic).

6.2.4.11 Attempted Synthesis of FluCo(CO)₂



The reaction was performed in the dark. Dicobaltoctacarbonyl (0.038 g, 0.11 mmol) was dissolved in THF (15 mL) and cooled to $-78\text{ }^{\circ}\text{C}$ before a solution of iodine (0.028 g, 0.11 mmol) in THF (5 mL) was added dropwise over 10 minutes. The solution was then left to stir at $-78\text{ }^{\circ}\text{C}$ for 30 minutes to allow formation of ICo(CO)_4 *in situ*.

To this cooled solution of ICo(CO)_4 , a solution of fluorenyl sodium (0.042 g, 0.22 mol) in THF (15 mL) was added dropwise over 20 minutes. Over the course of a few hours, the reaction mixture was observed to change colour from brown to green, after which time the reaction was allowed to warm to room temperature to result in a bright green clear solution. Volatile components were removed *in vacuo*, replaced with diethyl ether (30 mL) and the resulting cloudy mixture filtered to re-obtain a clear green solution. Volatile components were removed *in vacuo* to yield a waxy green solid which was then recrystallised from dissolution in THF and layering with hexane to obtain dark crystals which were too small for single crystal X-ray diffraction and decomposed upon exposure to neutron diffraction. The mass spectrum does show some small signals corresponding to the desired product or some

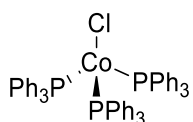
derivative of, but is dominated by a repeating pattern due to the presence of polymeric ring-opened, THF.

$^1\text{H NMR}$ (400 MHz, C_6D_6): δ_{H} 7.64 (br s, 1H, $\nu_{1/2}$ 30 Hz), 7.26 (br s, 1H, $\nu_{1/2}$ 39 Hz), 6.96 (br s, 1H, $\nu_{1/2}$ 32 Hz), 6.83 (br s, 1H, $\nu_{1/2}$ 37 Hz), 6.67 (br s, 1H, $\nu_{1/2}$ 33 Hz).

IR (Nujol Mull on KBr): ν cm^{-1} 2063vw, 2054vw, 2037vw, 2029vw and 2020vw (CO_{asymm} stretch), 1959vw and 1950vw (CO_{symm}), 1609s (multiple bands, C=C stretch), 1090s (C-C stretch), 1020s (C=C stretch).

MS (iASAP⁺, Da): 281.026 (9.52%, $[\text{M}+\text{H}]^+$), 223.047 (1.68 % $[\text{M}-2\text{CO}-\text{H}]^+$), 165.055 (26.48% $[\text{Flu}-\text{H}]^+$), 166.062 (100% $[\text{Fluorene}]^+$). Repeating units separated by 72 Da and 16 Da: polymeric ring-opened THF.

6.2.4.12 Synthesis of $\text{ClCo}(\text{PPh}_3)_3$



This complex was prepared in accordance to the literature procedure.²⁶ A solution of $\text{CoCl}_2 \cdot 6\text{H}_2\text{O}$ (3.00 g, 12.61 mmol) and triphenylphosphine (10.49 g, 40.0 mmol) in degassed ethanol (200 mL) was heated to 40 °C. A slurry of sodium borohydride (0.40 g, 10.59 mmol) in degassed ethanol (50 mL) was added to the reaction mixture portion-wise over the course of 1 hour, with immediate precipitation of a brown solid observed. The reaction was left to stir at 40 °C for an additional 2 hours before cooling to room temperature and the precipitate collected *via* filtration. The crude solid was washed with degassed water (2 × 25 mL) and degassed ethanol (2 × 25 mL) and dried under vacuum to yield a greenish-brown solid (8.60 g, 9.76 mmol, 92%). The mass spectrum was inconclusive due to the presence of triphenylphosphine.

$^{31}\text{P NMR}$ (CD_2Cl_2 , 162 MHz): δ_{P} -5.3 (br s, $\nu_{1/2}$ 60 Hz).

$^1\text{H NMR}$ (C_6D_6 , 400 MHz): δ_{H} 9.85 (br s, 2H, $\nu_{1/2}$ 35 Hz, *m*-H), 3.33 (br s, 2H, $\nu_{1/2}$ 407 Hz, *o*-H), 1.65 (s, 1H, $\nu_{1/2}$ 22 Hz, *p*-H).

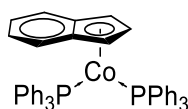
MS (ASAP⁺, Da): 263.091 (65.87 % $[\text{PPh}_3+\text{H}]^+$), 294.069 (100% $[\text{PPh}_3+2\text{O}]^+$), 556.161 (59.84% $[2(\text{PPh}_3+2\text{O})]^+$), 650.061 (1.32% $[\text{M}-\text{PPh}_3-\text{H}+2\text{O}]^+$).

Raman (532 nm): ν cm^{-1} 309m (Co-Cl), 624m (C-C), 707w, (C-P) 1006vs (C=C), 1036m (C-C), 1098m (C=C), 1590vs (C=C).

UV-Vis: λ_{max} 296 ($\pi^* \leftarrow \pi$), 375 (shoulder) nm.

Chapter 6

6.2.4.13 Attempted Synthesis of $(\eta^5\text{-Ind})\text{Co}(\text{PPh}_3)_2$



Indenyllithium was prepared over two hours at $-78\text{ }^\circ\text{C}$ by slow addition of *n*-butyllithium (0.10 mL, 2.4 M in hexanes, 0.24 mmol) to a stirred solution of indene (0.025 mL, 0.23 mmol) in THF (15 mL). The yellow solution of indenyllithium was allowed to warm to room temperature and added dropwise to a stirred green solution of $(\text{PPh}_3)_3\text{CoCl}$ (0.20 g, 0.23 mmol) in THF (30 mL) at $-78\text{ }^\circ\text{C}$. The reaction was observed to turn deep red after two hours and was left to warm to room temperature overnight. Volatile components were removed *in vacuo* and the residual solid extracted into toluene. Toluene was removed under reduced pressure and the resulting oily solid dried overnight under vacuum to yield a red solid. The mass spectrum of the solid obtained is inconclusive as it displays only peaks associated with triphenylphosphine. The NMR spectra obtained show the presence of $[(\text{PPh}_3)_3\text{CoCl}]$ and the IR spectra obtained is inconclusive as it could correspond to the desired product or to a mixture of starting materials. The Raman spectra collected contains bands associated with Co-Cl, therefore it can be concluded that the reaction did not proceed in totality.

MS (ASAP⁺, Da): 263.075 (89.56% $[\text{PPh}_3+\text{H}]^+$), 294.055 (94.05% $[\text{PPh}_3+2\text{O}]^+$), 556.125 (100% $[2(\text{PPh}_3+2\text{O})]^+$).

³¹P NMR (162 MHz, CD_2Cl_2): $\delta_{\text{P}} -5.7$ (br s, $\nu_{1/2}$ 1452 Hz) ppm.

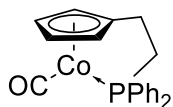
³¹P NMR (162 MHz, C_6D_6): $\delta_{\text{P}} -5.39$ (s, PPh_3) ppm.

¹H NMR ($[(\text{PPh}_3)_3\text{CoCl}]$, 400 MHz, C_6D_6): $\delta_{\text{H}} 9.85$ (br s, $\nu_{1/2}$ 42 Hz, *m*-H), 3.42 (br s, $\nu_{1/2}$ 405 Hz, *o*-H), 1.65 (br s, $\nu_{1/2}$ 34 Hz, *p*-H) ppm.

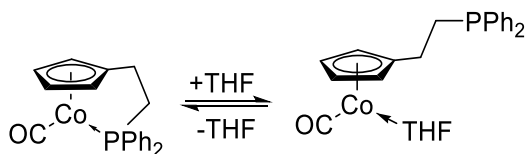
IR (ATR-FTIR, cm^{-1}): $\nu \text{ cm}^{-1}$ 3066w (C-H stretch, phenyl), 2964w (C-H stretch, indenyl), 1583w, 1475s, 1435s (C=C stretch, phenyl), 1260m (C=C stretch, indenyl), 1088-1024s multiple bands, C=C stretch, phenyl and indenyl), 798s (C=C stretch, indenyl), 741m (C-P, phenyl).

Raman (532 nm): $\nu \text{ cm}^{-1}$ 305m (Co-Cl), 438m (indenyl), 620m (C-C), 702w (C-P), 1000vs (C=C), 1030m (C=C, PPh_3), 1098m (C-C, PPh_3), 1342m (C-C, indenyl), 1536m (C=C, indenyl), 1589s (C=C, PPh_3).

UV-Vis: λ_{max} 289 ($\pi^* \leftarrow \pi$), 532 (shoulder, $d \leftarrow d$) nm.

6.2.4.14 $[(\kappa^2, \eta^6\text{-}(\text{L}_2\text{X})\text{-CH}_2\text{CH}_2\text{-ER}_n)\text{CoL}_n]$ Complex Synthesis6.2.4.14.1 Synthesis of $(\text{Cp-CH}_2\text{CH}_2\text{-PPh}_2)\text{Co}(\text{CO})$ 

Iodine flake (0.27 g, 1.06 mmol) in THF (20 mL) was added to a cooled ($-78\text{ }^\circ\text{C}$) solution of $\text{Co}_2(\text{CO})_8$ (0.36 g, 1.06 mmol) and left to stir for 30 minutes in the dark to form $2[\text{ICo}(\text{CO})_4]$ *in situ*. A solution of $(\text{CpLi})\text{-CH}_2\text{CH}_2\text{-PPh}_2$ (0.60 g, 2.11 mmol) in THF (20 mL) was added to the flask containing $[\text{ICo}(\text{CO})_4]$ at $-78\text{ }^\circ\text{C}$ and the reaction left to warm to room temperature overnight in the dark. Volatile components were removed *in vacuo* to reveal a red/brown oil which was extracted into toluene. Toluene was removed under reduced pressure and the flask left under dynamic vacuum for 24 hours to remove any residual iodine to yield a dark red/brown solid (1.09 g). NMR spectroscopic analysis showed broadened signals corresponding to THF, suggesting coordination of THF to cobalt. The ^1H NMR spectrum also displays a toluene impurity and so accurate yield cannot be determined. Multiple resonances were observed within the ^{31}P NMR spectrum, most broadened and one fairly sharp; suggesting hemi-labile behaviour of the phosphine-moiety, *e.g.*



^{31}P NMR (CD_2Cl_2 , 283 MHz): δ_{P} 85.4 (br s, $\nu_{1/2}$ 149 Hz), 84.4 (br s, $\nu_{1/2}$ 84 Hz), 83.7 (br s, $\nu_{1/2}$ 84 Hz), 49.2 (br s, $\nu_{1/2}$ 354 Hz), 48.7 (s).

^{31}P NMR (CD_2Cl_2 , 162 Hz): δ_{P} 85.4 (br s, $\nu_{1/2}$ 258 Hz), 60.1 (br s, $\nu_{1/2}$ 210 Hz), 55.3 (br s, 75 Hz), 49.3 (br s, $\nu_{1/2}$ 335 Hz).

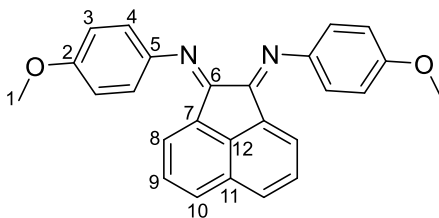
^1H NMR (CD_2Cl_2 , 400 MHz): δ_{H} 7.77-7.66 (m, *o*-H), 7.43-7.34 (m, *m*-H/*p*-H), 5.10-5.09 (m, 2H, C_5H_4), 5.06-5.00 (m, 2H, C_5H_4), 3.93-3.90 (m, Co-THF), 3.18-3.12 (overlapping multiplets, 2H, Cp-CH₂-CH₂), 2.13 (t, 1H, $^3J_{\text{HH}}$ 7.1 Hz, Cp-CH₂-CH₂), 2.06 (t, 1H, $^3J_{\text{HH}}$ 7.1 Hz, Cp-CH₂-CH₂), 1.97-1.82 (m, THF).

^1H NMR (CD_2Cl_2 , 700 MHz): δ_{H} 7.79-7.69 (m, *o*-H), 7.54-7.35 (m, *m*-H/*p*-H), 5.16-5.05 (m, 2H, C_5H_4), 5.00-4.90 (m, 2H, C_5H_4), 3.99 (br s, $\nu_{1/2}$ 30 Hz, Co-THF), 3.25 (br s, 2H, $\nu_{1/2}$ 30 Hz, Cp-CH₂CH₂), 3.15 (br s, 2H, $\nu_{1/2}$ 26 Hz), and 1.95 (br s, $\nu_{1/2}$ 15 Hz, Co-THF).

MS (*i*ASAP⁺): m/z 364.008 (100%, $[\text{M}]^+$), 435.061 (0.76% $[\text{M}+\text{THF}-\text{H}]^+$), 700.032 (7.91% $[\text{2M}-\text{CO}]^+$), and 798.941 (28.67% $[\text{2M}+\text{THF}]^+$).

6.3 Chapter 3 Experimental

6.3.1 Synthesis of Diimine Ligands

6.3.1.1 Synthesis of *bis*(4-methoxyphenyl)-acenaphthylquininediimine {(*p*-OMe)-BIAN}

To a round-bottomed flask charged with MgSO_4 and acenaphthylquinone (1.0 g, 5.49 mmol) in MeCN (150 mL) and equipped with a condenser and dropping funnel, 3 drops of formic acid are added down the condenser and the stirring reaction is heated to 65 °C. A solution of *p*-anisidine (1.48 g, 12.0 mmol) in MeCN (8 mL) was added dropwise to the reaction flask over the course of 20 minutes before the reaction was heated to reflux for 48 hours. The mixture was filtered under gravity and subsequently the volatile components removed from the resulting deep red solution *in vacuo* to leave a crude orange solid. Recrystallisation from ethanol yielded the title compound as crystalline orange needles (1.20g, 3.06 mmol, 57%).

$^1\text{H NMR}$ (600 MHz, C_6D_6): δ_{H} 7.32 (d, 1H, $^3J_{\text{HH}}$ 8.1 Hz, H-8), 7.19 (d, 1H, $^3J_{\text{HH}}$ 7.2 Hz, H-10), 7.07 (d, 2H, $^3J_{\text{HH}}$ 8.7 Hz, H-4), 6.91-9.87 (m, 1H, H-9), 6.85 (d, 2H, $^3J_{\text{HH}}$ 8.7 Hz, H-3), 3.37 (s, 3H, H-1).

$^{13}\text{C}\{^1\text{H}\}$ NMR (151Hz, C_6D_6): δ_{C} 160.5 (s, C-11), 156.9 (s, C-2), 145.8 (s, C-5), 141.5 (s, C-12), 131.3 (s, C-6), 129.3 (s, C-7), 128.1 (s, C-8), 127.2 (s, C-9), 123.2 (s, C-10), 119.3 (s, C-3), 114.8 (s, C-4), 54.6 (s, C-1).

IR (ATR-FTIR): ν cm^{-1} 3042w (C-H stretch aromatic), 2971-2842w (C-H stretch alkyl), 1642s (C=C stretch), 1584m (C=N asymm stretch), 1549s (C=C stretch), 1500vs (C=C stretch), 1485m (C=N symm stretch), 1232vs (C-O stretch).

Raman (532 nm): ν cm^{-1} 1122m (C-C stretch), 1173m (C-C stretch), 1480w (C=N_{symm} stretch), 1562vs (C=C stretch), 1588s (C=C stretch).

UV-Vis (DCM): λ_{max} 225, 232 and 441 nm.

6.3.2 Synthesis of (N^N)CoBr₂ Complexes

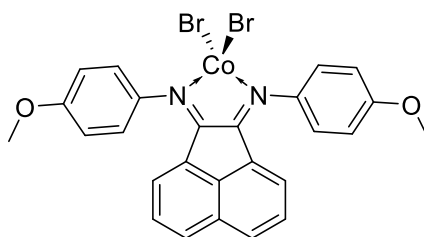
General Procedure: To a solution of diimine ligand (1 eq.) in THF, a solution of CoBr₂ (1 eq.) was added dropwise at room temperature. The reaction was stirred for 18 hours before volatile components were removed *in vacuo*. The resulting solid was washed with hexanes and dried to yield complexes with the general formula (N^N)CoBr₂, which were then stored in an N₂-filled glovebox. A summary of the (N^N)CoBr₂ complexes synthesised is given in **Table 6.2**.

Table 6.2 Summary of (N^N)CoBr₂ synthesis.

Entry	Ligand	(N^N) / g (mmol)	CoBr ₂ / g (mmol)	Yield / %
1	(p-OMe)-BIAN	0.50 (1.27)	0.28 (1.27)	76
2	(p-Me)BIAN	1.30 (3.61)	0.77 (3.53)	85
3	(p-NMe ₂)Et	0.45 (1.53)	0.33 (1.50)	92
4	(p-OMe)Et	0.50 (1.87)	0.40 (1.83)	85

Entry 1:

{(p-OMe)-BIAN}CoBr₂: 0.59g (0.97 mmol, 76%).



Crystals of the title complex suitable for single crystal X-ray diffraction were grown from layering a solution of [(p-OMe)-BIAN]CoBr₂ in DCM with hexanes at room temperature and confirmed the structure of this complex.

MS (ASAP⁺, Da): 608.892 (25.25% [M]⁺), 529.977 (34.80% [M-Br]⁺), 392.132 (100% [M-CoBr₂]⁺), 1138.872 (13.55% [2M-Br]⁺), 922.111 (23.58% [(p-OMe)-BIAN]₂CoBr⁺).

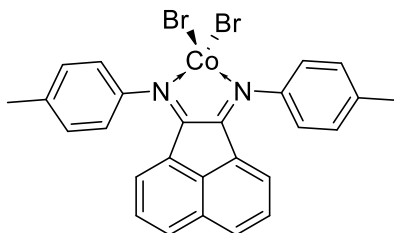
IR (ATR-FTIR): ν cm⁻¹ 2953w (C-H stretch, aromatic), 2953-2833w (C-H stretch, alkyl), 1623s (C=C stretch), 1589m (C=N_{symm} stretch), 1503vs (C=C stretch), 1480w (C=N_{symm} stretch) 1242vs (C-O stretch).

Raman (532 nm): ν cm⁻¹ 259w (Co-Br), 1122m (C=C), 1171m (C-C), 1480w (C=N_{symm} stretch), 1562vs (C=C stretch), 1625s (C=C stretch).

UV-Vis (DCM): λ_{\max} 465 and 673 nm.

Entry 2:

{{(p-Me)-BIAN}CoBr₂}: 1.74 g (3.00 mmol, 85%)



Crystals of the title complex suitable for single crystal X-ray diffraction were grown from layering a solution of [(p-Me)-BIAN]CoBr₂ in DCM with hexanes at room temperature.

MS (ASAP⁺, Da): 576.896 (59.70% [M]⁺), 497.981 (50.68% [M-Br]⁺), 360.139 (16.09% [M-CoBr₂]⁺), 1074.874 (12.98% [2M-Br]⁺), 858.121 (1.30% [(p-Me)-BIAN]₂CoBr⁺).

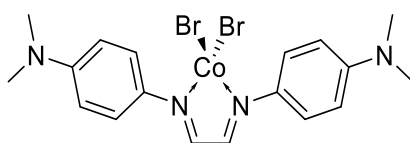
IR (ATR-FTIR): $\nu_{\text{cm}^{-1}}$ 3049w (C-H stretch, aromatic), 2973-2896w (C-H stretch, alkyl), 1659m (C=C stretch), 1626s (C=C stretch), 1588m (C=N_{asymm} stretch), 1488m (C=N_{symm} stretch), 1251s (C-N stretch).

Raman (633 nm): $\nu_{\text{cm}^{-1}}$ 250w and 340w (Co-Br), 613m (C-C), 1047m (C-C), 1123m (C=C), 1217m (C=C), 1502w (C=N_{symm} stretch), 1586vs (C=C stretch), 1626vs (C=C stretch).

UV-Vis (DCM): λ_{max} 266, 333, 469 nm.

Entry 3:

{{(p-NMe₂)-BIE}CoBr₂}: 0.71 g (1.38 mmol, 92%).



Crystals of the title complex suitable for single crystal X-ray diffraction were grown through slow evaporation of a concentrated DCM solution of [(p-NMe₂)-Et]CoBr₂ at room temperature and confirmed the structure of the complex.

MS (ASAP⁺, Da): 510.922 (5.51% [M]⁺), 432.010 (2.63% [M-Br]⁺), 294.161 (100% [M-CoBr₂]⁺),

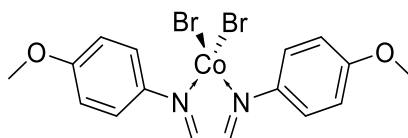
IR (ATR-FTIR): $\nu \text{ cm}^{-1}$ 3040w (C-H stretch, aromatic), 2907-2807w (C-H stretch, alkyl), 1600s (C=C stretch), 1588m (C=C stretch), 1536s (C=C stretch), 1482m (C=N_{asymm} stretch), 1299m (C=N_{symm} stretch), 1172s (C=C stretch).

Raman (663 nm): ν cm^{-1} 861w (C-C stretch), 1039m (C=C stretch), 1187m (C-N stretch), 1308w (C=N_{symm} stretch), 1363 (C-H stretch), 1459vs (C=C), 1514s (C=C stretch), 1611s (C=C stretch).

UV-Vis (DCM): λ_{max} 259, 308 and 450 and 660 nm.

Entry 4:

{{(p-OMe)-BIE}CoBr₂: 0.80 g (1.62 mmol, 85%)



MS (ASAP⁺, Da): 484.863 (7.12% [M]⁺), 405.949 (12.84% [M-Br]⁺), 268.096 (100% [M-CoBr₂]⁺), 890.812 (2.95% [2M-Br]⁺), 674.054 (32.39% [{(p-OMe)-Et}₂CoBr]⁺).

IR (ATR-FTIR): ν cm^{-1} 3036vw (C-H stretch, aromatic), 2973-2841w (C-H stretch, alkyl), 1614m (C=C stretch) 1579s (C=C stretch), 1463s (C=N_{asymm} stretch), 1257vs (C-O stretch), 1372m (C=N_{symm} stretch)

Raman (663 nm): ν cm^{-1} 873w (C-C stretch), 1037w (C=C stretch), 1165s (C-N stretch), 1371m (C=N_{symm} stretch), 1488vs (C=C stretch), 1568s (C=C stretch).

UV-Vis (DCM): λ_{max} 268, 326, 475, 500 and 678 nm.

Crystals suitable for single crystal X-ray diffraction were grown through slow evaporation of a solution of the title complex in aerated acetonitrile. Use of non-anhydrous, coordinating solvent for the recrystallisation resulting in formation of the octahedral complex: [{(p-OMe)-BIE}Co(OH₂)(NCMe)Br₂].

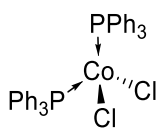
6.3.3 Synthesis of (P[^]P)CoCl₂ Complexes:

General procedure: To a solution of cobalt(II) chloride (0.95 eq.) in THF, diphosphine (1 eq.) in THF was added dropwise. The reaction was stirred at room temperature for 16 hours after which time precipitation was mediated through addition of hexane. The solids were collected *via* filtration and washed with three times with hexane before drying to yield a powder with general formula (P[^]P)CoCl₂. A summary of the reactions performed is provided in **Table 6.3**.

Table 6.3 Summary of (P[^]P)CoCl₂ syntheses.

Entry	Ligand	(P [^] P) /g (mmol)	CoCl ₂ /g (mmol)	Yield / %
1	2 PPh ₃	1.00 (7.70)	4.33 (16.50)	68
2	dppp	0.035 (0.31)	0.125 (0.29)	69
3	dppb	0.050 (0.40)	0.170 (0.38)	99
4	diprpb	0.100 (0.86)	0.250 (0.82)	100
5	dtbpx	0.150 (1.19)	0.470 (1.13)	39
6	dcypx	0.048 (0.40)	0.200 (0.38)	90
7	dadpx	0.017 (0.085)	0.100 (0.083)	29
8	PNNP-Ph	0.080 (0.66)	0.300 (0.62)	88
9	PNNP- <i>t</i> Bu	0.100 (0.81)	0.310 (0.77)	N/A*
10	PNNP- <i>t</i> Bu/Py	0.250 (0.20)	0.085 (0.19)	31

*hydrolysis product obtained.

Entry 1: (PPh₃)₂CoCl₂

Crystals suitable for X-ray diffraction were grown from layering DCM/hexane and comparison of the data with those reported previously in the literature showed the structure to be that of the title complex.²⁷ Mass spectrometric analysis gave inconclusive results due to the presence of triphenylphosphine ligands, which masked the sample spectrum, giving a spectrum identical to that of only triphenylphosphine. When (PPh₃)₂CoCl₂ is left in air as a solution in THF, over time (~6 weeks) small red crystals appear. These have been confirmed by single crystal X-ray diffraction to be cobalt formate dihydrate ((COOH)₂Co(H₂O)₂), which resulted from CO₂ activation by Co^{II} losing the phosphine in the process.

Yield: 3.412 g (5.21 mmol, 68%).

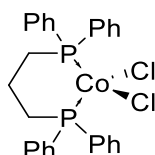
MS (*i*ASAP+, Da): 263.08 (100%, [PPh₃+H]), 279.07 (31.59%, [PPh₃O]).

IR (Nujol on KBr): ν cm⁻¹ 3022m (C-H stretch, aromatic), 1620w and 1336w (C-C, aromatic), 660 (C-H, aromatic).

Raman (532 nm): 318m (Co-Br), 1003vs (C-C stretch), 1029m (C-C), 1098s (C-C), 1587s (C=C).

UV-Vis (THF): λ_{max} 580, 634 and 693 nm.

Entry 2: (dppp)CoCl₂



A modification of the above general procedure was employed. To a solution of cobalt(II) chloride (0.95 eq.) in THF, diphosphine (1 eq.) in THF was added dropwise. The reaction was stirred at room temperature for 16 hours after which time hexane was layered over the reaction and the solution was left to stand for 48 hours before affording dark blue crystals. These crystals were suitable for single crystal X-ray diffraction, and unit cell check against the literature structure determined the obtained data to be consistent with those reported for (dppp)CoCl₂.²⁸

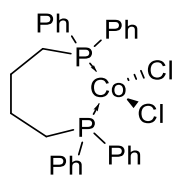
Yield: 0.111 g (0.20 mmol, 71%).

MS (*i*ASAP+, Da): 541.01 (9.02 %, [M]), 413.14 (31.22%, [M-CoCl₂]).

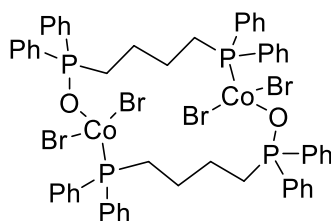
IR (Nujol on KBr): $\nu_{\text{cm}^{-1}}$ 2668m (C-H bend, alkane), 1587 (C-C, aromatic), 1151m and 1104s (C=C aromatic), 805m and 704s (C-H rock, alkane).

Raman (532 nm): ν cm⁻¹ 318w (Co-Cl), 622m (C-C), 717w (C-P), 1006s (C=C), 1034m (C-C), 1197m (CH₂), 1594s (C=C).

UV-Vis (THF): λ_{max} 583, 635 and 734 nm.

Entry 3: (dppb)CoCl₂

Attempt 1: Initial synthesis of the title compound yielded the partial oxidation product shown below. Crystals suitable for single crystal X-ray diffraction were grown from layering a solution in acetonitrile over mixed xylenes. It is speculated this is the result of an oxygen-/moisture-contaminated solvent. The crystal structure obtained reinforced the *i*ASAP MS result obtained which suggested the presence of oxidised *bis*phosphine ligand.



MS (*i*ASAP+): 349.11 (100%, [Ph₂P-C₄H₈-PPh₂]), 427.15 (28.7%, [M-CoCl₂]), 459.14 (14%, [Ph₂P(=O)-C₄H₈-P(=O)Ph₂]).

IR (Nujol on KBr): ν cm⁻¹ 3053w (C-H bend, aromatic), 2933w (C-H bend, alkane), 1602w, 1539w and 1485m (C-C in ring stretch, aromatic), 1435s (C-H bend, alkane), 1101s and 1028m (C-H stretch, aromatic), 692s (C-H rock, alkane).

Attempt 2: The reaction was repeated with freshly dried and distilled THF and yielded the title compound. UV-Vis spectroscopic analysis suggests some dissociation of the ligand within solution to produce CoCl₂ (λ_{max} 580, 634 and 693 nm).

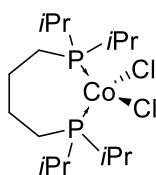
Yield: 1.30 g (2.43 mmol, 98%).

MS (*i*ASAP+, Da): 214.083 (26.40%, [C₁₄H₁₄P]), 427.152 (100%, [M+H-CoCl₂]), 443.155 (5.19 %, [MC₆H₅Cl]), 519.124 (1.03 %, M-HCl).

IR (Nujol on KBr): $\nu_{\text{cm}^{-1}}$ 2726m and 2669w (C-H stretch, alkane), 1305m (C-H rock, alkane), 1159m and 1100m (C-H stretch, aromatic), 723s (C-H rock, alkane)

Raman (532 nm): ν cm⁻¹ 309w (Co-Cl), 624w (C-C), 695w (C-P), 1004s (C=C), 1304m (C-C), 1593m (C=C), 2902 (C-H, alkyl), 3060m (C-H, aromatic).

UV-Vis (THF): λ_{max} 592, 641, 690, 741 nm.

Entry 4: (diprpb)CoBr₂

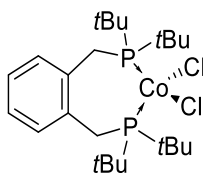
Yield: 0.332 g (0.79 mmol, 96%).

MS (*i*ASAP+, Da): 291.28 (33.54%, [M-CoCl₂+H]⁺), 384.19 (100%, [M-Cl]⁺), 419.20 (10.6%, [M]⁺).

IR (Nujol on KBr): ν cm⁻¹ 2723w (C-H stretch), 1302m (C-H alkane), 1262m (C=C aromatic), 1092-1026m (C-H aromatic), 798m (C-H rock).

Raman (532 nm): ν cm⁻¹ 309m (Co-Cl), 603s (C-C), 671w (C-P), 771m (C-C), 890s (C-C), 1019m (C-C), 1276w (CH₂), 1462m (CH₃).

UV-Vis (THF): λ_{max} 618, 653 (shoulder) and 734 nm.

Entry 5: (dtbpx)CoCl₂

Crystals suitable for single crystal X-ray diffraction were grown *via* layering hexane over an MeCN/THF (1:1) solution of the title complex.

Yield: 0.222 g (0.44 mmol, 39%).

MS (ASAP+, Da): 555.148 (0.91% [M+2O]), 488.187 (2.67% [M-Cl]), 395.36 (100%, [M-CoCl₂]).

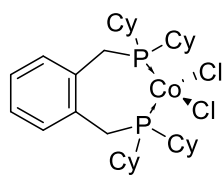
IR (Nujol on KBr): ν cm⁻¹ 2724m and 2670m (C-H bend, alkane), 1605w, (C-C stretch, aromatic), 1307w, (C-H, alkane) 1261m (C-C aromatic), 1150m (C-H aromatic) and 1064s (C-H rock, alkane).

Raman (532 nm): ν cm⁻¹ 318w (Co-Cl), 581s (C-C), 691w (C-P), 817m (C-C), 1057s (C=C), 1187m (C-C), 1236s (CH₂), 1474m (CH₂), 1604m (C=C).

UV-Vis (THF): λ_{max} 625, 668, and 721 nm.

Chapter 6

Entry 6: (dcypx)CoCl₂



Crystals suitable for single crystal X-ray diffraction were grown through slow diffusion of a THF/hexanes mixture and the structure was determined to be that of the title compound, existing in two distinct crystallographic environments.

Yield: 0.223 g (0.35 mmol, 93%).

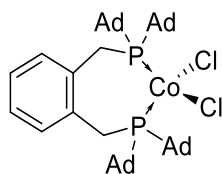
MS (*i*ASAP+, Da): 627.19 (43.40%, [M]), 592.23 (100%, [M-Cl]), 499.34 (87.74%, [M-CoCl₂]).

IR (Nujol on KBr): ν cm⁻¹ 1279m (C-H bend, alkane), 1621w and 1265w (C-C, aromatic), 1262m (C-H, aromatic), 1098s (C-H rock, alkane)

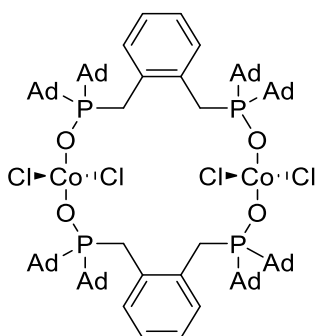
Raman (532nm): 312w (Co-Cl), 687m (C-P), 825s (C-C), 1013w (C=C), 1033s (C-C) 1054s (C=C), 1233s (C-C), 1449s (CH₂), 1610w (C=C).

UV-Vis (THF): λ_{max} 599, 637 and 733 nm.

Entry 7: (dadpx)CoCl₂



Attempt 1: Initial synthesis of the title complex yielded the oxidation product shown below. Crystals suitable for single crystal X-ray diffraction were grown through layering hexane over a solution of the solids obtained in DCM and were determined the oxidised structure shown below. The formation of this dimeric oxidised complex is the result of oxygen/moisture contamination of the solvents used.



52 MS (*i*ASAP+, Da): 707.47 (100%, [M-CoCl₂+H]), 800.36 (2.25%, [M-Cl]).

52ox MS (*i*ASAP, 350 °C, Da): 739.44 (100%, [Ad₂P(=O)-CH₂-C₆H₄-CH₂-P(=O)Ad₂])

Attempt 2: The reaction was repeated with freshly dried and distilled THF and yielded the title compound.

Crystals suitable for single crystal X-ray diffraction were grown through layering a solution in THF with hexanes at room temperature.

Yield: 0.056 g (0.060 mmol, 73%).

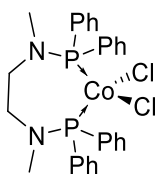
MS (*i*ASAP+, Da): 407.253 (100%, [M-CoBr₂C₂₀H₃₀P]), 571.318 (26.83%, [M-CoBr₂C₁₀H₁₅]), 746.431 (67.68%, [M-CoBr₂]), 844.27 (5.69 %, [M-Br]).

IR (Nujol on KBr): ν cm⁻¹ 2727m and 2625m (C-H bend, alkane), 1642w (C-C, aromatic), 1300m (C-H alkane), 1262w (C-C aromatic), 1088w (C-H aromatic), 723s (C-H rock, alkane).

Raman (532 nm): ν cm⁻¹ 315sh (Co-Cl), 672m (C-P), 777s (C-C), 978s (C-C), 1058m (C=C), 1111m (C=C), 1266s (CH₂), 1444m (C-C), 1607m (C=C).

UV-Vis (THF): λ_{max} 580, 677, and 726 nm.

Entry 8: (PNNP-Ph)CoCl₂



Yield: 0.32 g (0.55 mmol, 88%)

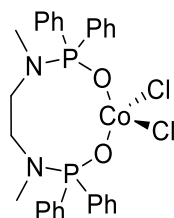
MS (*i*ASAP+, Da): 457.18 (59.19%, [M-CoCl₂+H]), 371.10 (100%, [Ph₂P-PPh₂]), 791.056 (0.88% [(PPh₂)₄CoCl+2O+2H]).

IR (Nujol on KBr): ν cm⁻¹ 2671m and 2614m (C-H bend, alkane), 1306w (C-H, alkane), 1156w (C-C aromatic), 1098 (C-H aromatic), 1067 (C-N stretch).

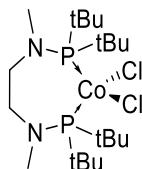
Raman (532 nm): ν cm⁻¹ 321m (Co-Cl), 625m (C-P), 1007s (C=C), 1036m (C-C), 1105m (C=C), 1445w (CH₂), 1595m (C=C).

UV-Vis (THF): λ_{max} 580, 641 and 681 nm.

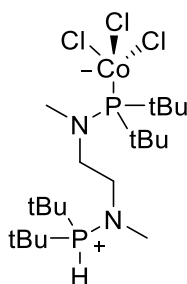
When a sample of the title complex as a solution in THF is exposed to air, over several weeks small red crystals were observed to form, which were determined to be $(\text{COOH})_2\text{Co}(\text{H}_2\text{O})_2$ by single crystal X-ray diffraction. An attempt was made to repeat this transformation through growth of crystals suitable for single crystal X-ray diffraction *via* slow evaporation of THF exposed to air, however, the resulting structure is that containing the oxidised phosphine, as shown below:



Entry 9: (PNNP-*t*Bu)CoCl₂



Crystals of the title complex suitable for single crystal X-ray diffraction were grown *via* layering a solution of this blue solid in DCM with hexane (0.191 g). The structure obtained was determined to be the trichloride species, shown below. It is thought this oxidation product is the result of water contaminated solvents used within the synthesis, as the *i*ASAP MS spectrum obtained of the blue solid prior to recrystallisation displays fragmentation associated with the structure of the hydrolysis product shown below. The Raman spectrum obtained displayed significant fluorescence, which obscured all bands.



μ_{eff} (JME balance): 9.41 μ_{B} at 19 °C

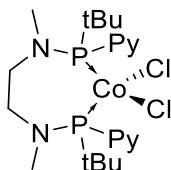
MS (*i*ASAP, 350 °C, Da): 447.429 (46.24%, [M-C₄H₁₁Cl]), 377.381 (100%, [M-CoCl₃H]), 319.300 (6.65% [M-CoCl₃C₄H₁₁])

IR (Nujol on KBr): ν cm^{-1} 2722m and 2672m (C-H bend, alkane), 1261m (C-C, aromatic), 1105s (C-N stretch).

Raman (532 nm): ν cm^{-1} no discernible bands.

UV-Vis (THF): λ_{max} 590, 644 and 697 nm.

Entry 10: (PNNP-*t*Bu/Py)CoCl₂



Yield: 0.034 g (0.06 mmol, 33%).

MS (*i*ASAP+, Da): 512.2 (100%, [M-Cl]), 252.3 (65%, [M-CoCl₂-P-*t*Bu-Py]).

IR (Nujol on KBr): ν cm^{-1} 2727m (C-H bend, alkane), 1589m (C-C, aromatic), 1261w (C-N, aromatic), 1165w (C-C, aromatic), 1096s (C-N stretch).

Raman (532 nm): ν cm^{-1} 334w (Co-Cl), 647w (C-P), 805w (C-C), 1019 (C=C), 1470m (CH₂), 1571m (CH₃), 1594m (C=C).

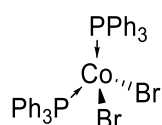
UV-Vis (THF): λ_{max} 582, 646 (shoulder) and 687 nm.

6.3.4 Synthesis of (P^ΛP)CoBr₂ complexes:

General procedure: To a solution of cobalt(II) bromide (0.95 eq.) in THF, diphosphine (1 eq.) in THF was added dropwise. The reaction was stirred at room temperature for 16 hours after which time precipitation was mediated through addition of hexane. The solids were collected *via* filtration and washed with three times with hexane before drying to yield a powder with general formula (P^ΛP)CoX₂. A summary of the reactions performed is provided in **Table 6.4**.

Table 6.4 Summary of (P^ΛP)CoBr₂ synthesis.

Entry	Ligand	(P ^Λ P) /g (mmol)	CoBr ₂ /g (mmol)	Yield / %
1	2 PPh ₃	4.50 (17.16)	1.58 (8.58)	98
2	dppm	0.97 (2.52)	0.50 (2.29)	98
3	dppe	1.79 (4.48)	1.00 (4.57)	98
4	dppp	3.00 (7.27)	1.49 (6.81)	96
5	dtbpp	1.00 (3.00)	0.62 (2.86)	92
6	dppb	0.50 (1.17)	0.25 (1.15)	87
7	dcypb	0.25 (0.56)	0.12 (0.55)	88
8	dppbz	1.00 (2.24)	0.48 (2.19)	99
9	dppx	0.50 (1.05)	0.23 (1.03)	78
10	dtbpx	0.50 (1.28)	0.27 (1.24)	90
11	diprpx	0.12 (0.35)	0.08 (0.34)	93
12	dadpx	0.06 (0.85)	0.018 (0.83)	73
13	PNNP-Ph	0.40 (0.88)	0.19 (0.86)	88
14	BINAP	0.20 (0.32)	0.07 (0.31)	81
15	Xantphos	0.50 (0.86)	0.18 (0.82)	90

Entry 1: (PPh₃)₂CoBr₂

Crystals of the title complex suitable for single crystal X-ray diffraction were grown from slow evaporation of DCM, and subsequent analysis by IR, Raman and UV-vis spectroscopies and mass spectrometry confirmed the identity of the crystals as being (PPh₃)₂CoBr₂.²⁷ Mass spectrometry gave

inconclusive results due to the presence of triphenylphosphine ligands which masked the sample spectrum, giving a spectrum identical to that of only triphenylphosphine.

Yield: 6.236 g (8.38 mmol, 98%)

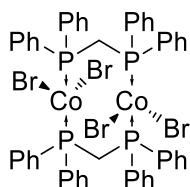
MS (*i*ASAP+, Da) : 263.07 (100%, [PPh₃+H]), 447.12 (46.92 %, [P₂C₃₀H₂₅]), 556.1 (16.91 %, [P₂O₂C₃₆H₃₀])

IR (Nujol on KBr): ν cm⁻¹ 3050m (C-H stretch, aromatic), 1585w (C-C aromatic), 1480s and 1432s (C-C, aromatic), 690s and 741s (C-H, aromatic).

Raman (532 nm): ν cm⁻¹ 273m (Co-Br), 526m (C-P), 625m (C-C), 697m (C-C), 1006s (C=C), 1035 (C-C), 1590s (C=C).

UV-Vis (THF): λ_{max} 596 (shoulder), 653 (shoulder) and 687 nm.

Entry 2: [(dppm)₂Co₂Br₄]



The Raman spectrum of the title complex contained significant contributions from the glass of the J Young's tube used for holding the sample during analysis between 300-600 cm⁻¹. The mass spectrum obtained only contained a peak corresponding to the ligand.

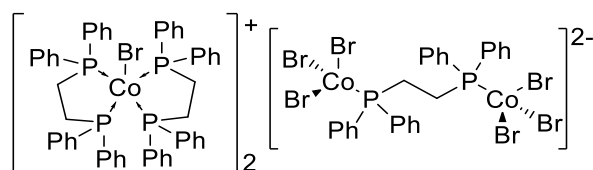
Yield: 1.48 g (1.23 mmol, 98%)

MS (ASAP+, Da): 723.141 (0.94% [(dppmO)₂Co+H₂O]), 385.100 (100% [dppm+H]⁺),

IR (ATR-FTIR): ν cm⁻¹ 3050w (C-H stretch, aromatic), 2967-2878w (C-H stretch, alkyl), 1572w and 1482m (C=C stretch, aromatic), 1434s (C-H bend, alkyl).

Raman (532 nm): ν cm⁻¹ 254-278m (Co-Br), 707w (C-P), 1007s (C=C), 1035m (C-C), 1104m (C-C), 1590 (C=C).

UV-Vis (THF): λ_{max} 595, 651 and 686 nm.

Entry 3: $[(dppe)_2CoBr]^+ [Br_3Co(\mu^2-dppe)CoBr_3]^{2-}$ 

Crystals of the title complex suitable for single crystal X-ray diffraction were grown through layering a solution in DCM with hexanes at room temperature under a N_2 atmosphere.

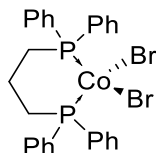
Yield: 2.58 g (0.89 mmol, 99%)

MS (*i*ASAP+, Da): 535.99 (3.98%, [M-Br]), 399.15 (100%, [M-CoBr₂]),

IR (ATR-FTIR): ν cm⁻¹ 3055m (C-H stretch, aromatic), 2934-2856m (C-H stretch, alkyl), 1574m and 1484m (C=C stretch, aromatic), 1434s (C-H bend, alkyl).

Raman (532 nm): ν cm⁻¹ 254s and 300w (Co-Br), 625w (C-C), 1007s (C=C), 1036m (C-C), 1440w (CH₂), 1592s (C=C).

UV-Vis (THF): λ_{max} 617 (shoulder) 652 (shoulder) and 693 nm.

Entry 4: (dppp)CoBr₂

Crystals of the title complex suitable for single crystal X-ray diffraction were grown from layering a solution in THF with hexane at room temperature, and comparison to literature cell structure confirmed the identity to be that of (dppp)CoBr₂.²⁸ The MALDI MS spectrum obtained contained significant oxidation products.

Yield: 4.117 g (6.52 mmol, 96%)

MS (*i*ASAP+, Da): 628.93 (1.12%, [M]), 550.01 (12.91%, [M-Br]), 413.16 (100%, [M-CoBr₂+H]).

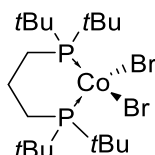
MS (MALDI⁺, DTCB matrix, Da): 931.064 (89.19% [2M-3HBr+3O]⁺), 661.214 (4.78%, [M+2O]⁺), 549.982 (2.95% [M-Br]⁺), 519.049 (91.26% [M-2Br+3O]⁺).

IR (ATR-FTIR): ν cm⁻¹ 3052m (C-H stretch, aromatic), 2930w-2865w (C-H stretch, alkyl), 1586m, 1572m and 1483s (C=C stretch, aromatic), 1433s (C-H bend, alkyl).

Raman (532 nm): ν cm^{-1} 284sh (Co-Br), 650w (C-C), 752w (C-P), 1008s (C=C), 1037m (C-C), 1104m (C-C), 1591s (C=C).

UV-Vis (THF): λ_{max} 620, 663 and 748 nm.

Entry 5: (dtbpp)CoBr₂



Crystals of the title complex suitable for single crystal X-ray diffraction were grown through layering a solution in DCM with hexanes and cooling to -20 °C.

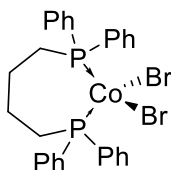
Yield: 1.45 g (2.63 mmol, 92%)

MS (ASAP⁺, Da): 549.022 (1.68% [M]⁺), 470.105 (20.59% [M-Br]⁺), 333.266 (74.24% [dtbpp+H]⁺, 275.185 (100% [dtbpp-tBu]⁺).

Raman (532 nm): ν cm^{-1} 279sh (Co-Br), 583s (C-C), 818m (C-C), 1031w (C-C), 1188m (CH₂), 1477s (CH₃).

UV-Vis (THF): λ_{max} 662, 699 and 744 nm.

Entry 6: (dppb)CoBr₂



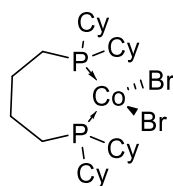
Yield: 0.642 g (1.00 mmol, 87 %)

MS (*i*ASAP⁺, Da): 602.9 (3.07 %, [M]), 564.0 (1.84 %, [M-Br]), 426.1 (100 %, [M-CoBr₂]).

IR (Nujol on KBr): ν cm^{-1} 2724w and 2716w (C-H stretch, alkyl), 1629w (C=C stretch, aromatic), 1268w (C=C stretch, aromatic).

Raman (532 nm): ν cm^{-1} 286m (Co-Br), 622w (C-C), 695w (C-P), 1006s (C=C), 1034m (C-C), 1593m (C=C), 2904w (C-H, alkyl), 3060m (C-H, aromatic).

UV-Vis (THF): λ_{max} 622 and 678 nm.

Entry 7: (dcypb)CoBr₂

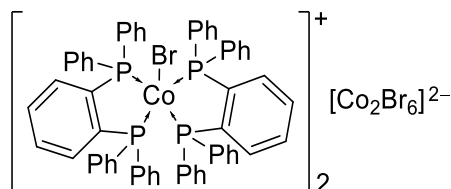
Yield: 0.322 g (0.48 mmol, 88%)

MS (*i*ASAP+, Da): 367.233 (100%, [M-CoBr₂C₆H₁₁]), 451.318 (66.42%, [M-CoBr₂], 588.160 (11.73 %, [M-Br]), 667.074 (7.94 %, [M])

IR (Nujol on KBr): ν cm⁻¹ 1301m (C-H alkane), 1260w (C=C), 1091-1023m (C-H aromatic), 799m (C-H rock)

Raman (532 nm): ν cm⁻¹ 270w (Co-Br), 825m and 858w (C-C), 1006m (C=C), 1034s (C-C), 1279m (C-C), 1303s (CH₂), 1447s (CH₂).

UV-Vis (THF): λ_{max} 642 (shoulder), 680 and 745 nm.

Entry 8: [(dppbz)₂CoBr]⁻[Co₂Br₆]⁺

Crystals of the title complex suitable for single crystal X-ray diffraction were grown through layering a solution in DCM with hexanes at room temperature.

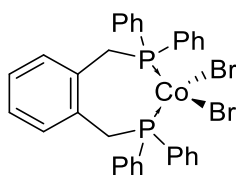
Yield: 1.45 g (0.54 mmol, 99%)

MS (ASAP⁺, Da): 1030.55 (2.21% [(dppbz)₂CoBr]⁺), 662.859 (44.03% [(dppbz)CoBr₂]⁺), 583.949 (39.69% [(dppbz)CoBr]⁺), 447.114 (78.83% [dppbz+H]⁺).

IR (ATR-FTIR): ν cm⁻¹ 3051w (C-H stretch, aromatic), 1481m (C=C, aromatic), 1435m (C-H bend), 1092s (C=C).

Raman (532 nm): ν cm⁻¹ 250m (Co-Br_{symm} anion), 298w (Co-Br cation), 345m (Co-Br_{asymm} anion), 373m (Co-Br_{asymm} anion), 700w (C-P), 1004s (C=C), 1034m (C-C), 1098m (C=C), 1588s (C=C).

UV-Vis (THF): λ_{max} 614 (shoulder), 639 (shoulder) and 709 nm.

Entry 9: (dppx)CoBr₂

Crystals of the title complex suitable for single crystal X-ray diffraction were grown through layering a solution in THF with hexanes at room temperature.

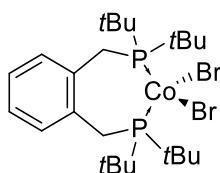
Yield: 0.56 g (0.81 mmol, 77%)

MS (ASAP⁺, Da): 690.948 (6.39% [M]⁺), 612.029 (10.73% [M-Br]⁺), 474.175 (4.50% [dppx]⁺), 397.133 (100% [dppx-Ph]⁺).

IR (ATR-FTIR): ν cm⁻¹ 3053w (C-H stretch, aromatic), 1483m (C=C stretch, aromatic), 1434s (C-H bend), 1100m (C=C).

Raman (532 nm): ν cm⁻¹ 283m (Co-Br), 622w (C-C), 687m (C-P), 775w (Co-P), 1006s (C=C), 1033w (C-C), 1224m (CH₂), 1590s (C=C).

UV-Vis (THF): λ_{max} 619, 664 and 759 nm.

Entry 10: (dtbpx)CoBr₂

Crystals of the title complex suitable for single crystal X-ray diffraction were grown through concentration of a sample in THF.

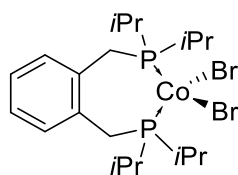
Yield: 0.688 g (1.12 mmol, 90%)

MS (ASAP⁺, 500 °C, Da): 532.15 (2.61%, [M-Br]), 395.31 (100%, [M-CoBr₂+H]).

IR (ATR-FTIR): ν cm⁻¹ 3064w (C-H stretch, aromatic), 2972-2868s (C-H stretch, alkyl), 1601w (C=C stretch, aromatic), 1472-1370s (C-H bend, alkyl).

Raman (532 nm): ν cm⁻¹ 282m (Co-Br), 580s (C-C), 690m (C-P), 812m (C-C), 942m (C=C), 1027w (C-C), 1057m (C=C), 1235s (CH₂), 1476m (CH₃), 1603m (C=C).

UV-Vis (THF): λ_{max} 658, 699 and 744 nm.

Entry 11: (diprpx)CoBr₂

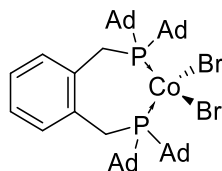
Yield: 0.22 g (0.32 mmol, 93%)

MS (ASAP⁺, Da): 555.012 (42.82% [M]⁺), 476.091 (42.80% [M-Br]⁺), 339.242 (66.72% [(diprpx+H)⁺], 295.175 (100% [diprpx-*i*Pr]⁺), 1031.100 (4.07% [2M-Br]⁺), 1110.039 (0.26% [2M]⁺).

IR (ATR-FTIR): ν cm⁻¹ 2958-2872m (C-H stretch, alkyl), 1460s-1391m (C-H bend, alkyl), 1046m (C=C), 1044m (C-C).

Raman (532 nm): ν cm⁻¹ 296sh (Co-Br), 613m (C-C), 721w (C-P), 890w (C-C), 1052s (C-C), 1230s (CH₂), 1471m (CH₃), 1603m (C=C).

UV-Vis (THF): λ_{max} 631 (shoulder), 664 and 746 nm.

Entry 12: (dadpx)CoBr₂

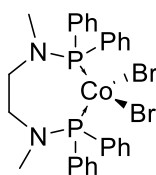
Yield: 0.056 g (0.06 mmol, 73%).

MS (*i*ASAP⁺, Da): 407.253 (100%, [M-CoBr₂C₂₀H₃₀P]), 571.318 (26.83%, [M-CoBr₂C₁₀H₁₅], 746.431 (67.68%, [M-CoBr₂]), 844.27 (5.69 %, [M-Br]).

IR (Nujol on KBr): ν cm⁻¹ 2727m and 2625m (C-H bend, alkane), 1642w (C-C, aromatic), 1300m (C-H alkane), 1262w (C-C aromatic), 1088w (C-H aromatic), 723s (C-H rock, alkane).

Raman (532 nm): ν cm⁻¹ 297w (Co-Br), 674m (C-C), 777s (C-C), 980s (C=C), 1060m (C-C), 1187s (CH₂), 1242m (CH₂), 1439m (CH₃), 1605w (C=C).

UV-Vis (THF): λ_{max} 661, 704 and 743 nm.

Entry 13: (PNNP-Ph)CoBr₂

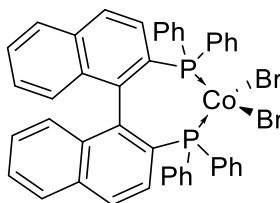
Yield: 0.51 g (0.76 mmol, 88%)

MS (ASAP⁺): 672.920 (1.00% [M]⁺), 594.006 (0.84% [M-Br]⁺), 457.165 (100% [(PNNP-Ph)+H]⁺), 1266.922 (0.16% [2M-Br]⁺), 1050.163 (3.56% [(PNNP-Ph)₂CoBr]⁺).

IR (ATR-FTIR): ν cm⁻¹ 3056w (C-H stretch, aromatic), 2960-2860w (C-H stretch, alkyl), 1440m (C-H bend, alkyl), 1432m (C=C stretch, aromatic), 1207w (C-C stretch, aromatic), 1095s (C-H bend, aromatic).

Raman (532 nm): ν cm⁻¹ 293sh (Co-Br), 623w (C-C), 713w (C-P), 778m (Co-P), 1006s (C=C), 1034m (C-C), 1102m (C=C), 1248w (CH₂), 1444w (CH₃), 1592s (C=C).

UV-Vis (THF): λ_{max} 616, 673 and 745 nm.

Entry 14: (BINAP)CoBr₂

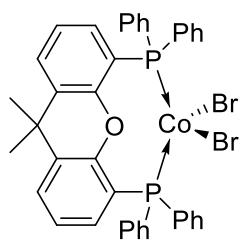
Yield: 0.212g (0.25 mmol, 81%)

MS (*i*ASAP⁺, Da): 759.96 (0.51%, [M-Br]), 623.21 (20.58%, [M-CoBr₂+H]), 437.15 (100%, [M-CoBr₂PPh₂])

IR (ATR-FTIR): ν cm⁻¹ 3058w (C-H stretch, aromatic), 1573m, 1482s and 1376s (C=C stretch, aromatic).

Raman (532 nm): ν cm⁻¹ 293sh (Co-Br), 703w (C-P), 868m (C-C), 1006s (C=C), 1036m (C-C), 1375s (C=C), 1588m and 1619m (C=C).

UV-Vis (THF): λ_{max} 597 (shoulder), 651 (shoulder), and 684 nm.

Entry 15: (Xantphos)CoBr₂

Crystals of the title complex suitable for single crystal X-ray diffraction were grown through layering a solution in THF with hexanes at room temperature. Unit cell comparison to the literature values confirmed the structure of (xantphos)CoBr₂.²⁹

Yield: 0.59 g (0.74 mmol, 90%)

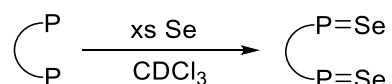
MS (ASAP⁺, Da): 716.030 (2.02% [M-Br]⁺), 579.189 (100% [M-CoBr₂+H]⁺), 1510.967 (0.10% [2M-Br]⁺), 1294.212 (0.78% [(Xantphos)₂CoBr]⁺).

IR (ATR-FTIR): ν cm⁻¹ 3058w (C-H stretch, aromatic), 2971w (C-H stretch, alkyl), 1612w (C=C stretch), 1436m-1408s (CH-bend, alkyl), 1242s (C=C stretch, aromatic).

Raman (532 nm): ν cm⁻¹ 275m (Co-Br), 623w (C-C), 702w (C-P), 1005s (C=C), 1035m (C-C), 1105m (C=C), 1443w (CH₃), 1592s (C=C).

UV-Vis (THF): λ_{max} 627 (shoulder), 658 and 756 nm.

6.3.5 Synthesis of diphosphinediselenides



General Procedure: A J Young's NMR tube was charged with diphosphine and excess selenium before addition of CDCl₃ (0.7 mL). The mixture was sonicated for 30-240 minutes and the resulting compound analysed by NMR spectroscopy. These compounds were not isolated as only the $|^{31}\text{P}-^{77}\text{Se}|$ coupling constant is of interest. The diphosphine ligands investigated and corresponding $|^{31}\text{P}-^{77}\text{Se}|$ coupling constants are summarised in **Table 6.5**.

Table 6.5 ^{31}P NMR shifts and $^{31}\text{P}-^{77}\text{Se}$ coupling constants of synthesised diphosphinediselenide compounds measured in CDCl₃ at 162 MHz.

Compound	δ_{P} /ppm	$^1J_{\text{PSe}}$ /Hz
dppmSe ₂	25.1	744
dppeSe ₂	36.0	735
dpppSe ₂	33.0	722
dppbSe ₂	33.7	720
dppbzSe ₂	38.3	747
dcypeSe ₂	57.6	697
dcypbSe ₂	53.3	680
dtbppSe ₂	76.8	689
dtbpxSe ₂	76.7	696
dadpxSe ₂	69.7	635
dppxSe ₂ ³⁰	32.9	724
BINAPSe ₂	33.6	738
XantphosSe ₂	31.5	757

6.4.4 Chapter 4 Experimental

6.4.1 Attempted Reductions of (P[^]P)CoX₂ with Zn metal:

General Procedure: A solution of (P[^]P)CoX₂ (1 eq.) and activated zinc powder (1, 5 or 10 eq.) was stirred in THF at room temperature. THF was removed *in vacuo* and the residue extracted into toluene. Volatile components were removed and the resulting solid dried before storage in an N₂-filled glovebox. A summary of the reactions performed is provided in **Table 6.6**.

Table 6.6 Summary of (P[^]P)CoX₂ reductions attempted with Zn metal.

Entry	(P [^] P)CoX ₂ /g	Zn / g (mmol)	Time /h	Temp. /°C	
1	(PPh ₃) ₂ CoCl ₂	0.50 (0.76)	0.25 (3.82)	256	25
2	(PPh ₃) ₂ CoCl ₂	0.09 (1.35)	0.09 (1.35)	48	60
3	(dppp)CoCl ₂	0.05 (0.09)	0.03 (0.50)	18	25
4 ^a	(dppb)CoCl ₂	0.25 (0.45)	0.29 (4.50)	64	25
5	(dppb)CoCl ₂	0.25 (0.45)	0.15 (2.25)	48	40
6	(dcypx)CoCl ₂	0.10 (0.16)	0.10 (1.60)	120	25
7	(dtbpx)CoCl ₂	0.10 (0.19)	0.06 (0.95)	97	25
8	(PPh ₃) ₂ CoBr ₂	0.20 (0.27)	0.18 (2.70)	16	25
9	(PPh ₃) ₂ CoBr ₂	0.20 (0.27)	0.09 (1.35)	1	25
10	(dppm)CoBr ₂	0.10 (0.18)	0.06 (0.90)	4	25
11	(dppe)CoBr ₂	0.20 (0.32)	0.11 (1.62)	288	25
12 ^b	(dppe)CoBr ₂	0.50 (0.81)	0.26 (4.05)	1	25
13	(dppp)CoBr ₂	0.60 (0.95)	0.31 (4.75)	18	25
14 ^c	(dppp)CoBr ₂	1.00 (1.58)	1.03 (15.8)	1	25
15	(dppb)CoBr ₂	0.25 (0.39)	0.13 (1.94)	24	25
16	(dcypb)CoBr ₂	0.10 (0.15)	0.05 (0.75)	144	40
17	(dppbz)CoBr ₂	0.75 (1.13)	0.37 (5.64)	18	25
18	(dppbz)CoBr ₂	0.33 (0.75)	0.06 (0.98)	16	25
19	(dtbpx)CoBr ₂	0.25 (0.41)	0.13 (2.04)	18	25
20 ^c	(dtbpx)CoBr ₂	0.50 (0.82)	0.53 (8.15)	5 min	25
21 ^c	(dtbpx)CoBr ₂	0.50 (0.82)	0.53 (8.15)	30 min	25
22	(dppx)CoBr ₂	0.25 (0.36)	0.12 (1.80)	18	25
23	(diprpx)CoBr ₂	0.75 (1.24)	0.41 (6.22)	18	25
24	(PNNP-Ph)CoBr ₂	0.20 (0.37)	0.03 (0.37)	18	25
25	(BINAP)CoBr ₂	0.10 (0.12)	0.04 (0.59)	56	25
26	(Xantphos)CoBr ₂	0.25 (0.31)	0.10 (1.55)	57	25

^a Toluene added after 16 hours, ^b Toluene, ^c 1:1 MeOH:THF, ^d final hour at 40 °C.

Entry 1:

Black insoluble, magnetic precipitate observed. Assumed to be cobalt(0) formed as a result of decomposition and so the reaction was abandoned.

Entry 2:

Black insoluble, magnetic precipitate observed. Assumed to be cobalt(0) formed as a result of decomposition and so the reaction was abandoned.

Entry 3:

0.209 g: mix of **4.1** and **3.4c**.

The mass spectrum obtained shows ring-opened THF. Attempts to remove this resulted in loss of the product and so no further analysis could be completed.

UV-Vis: λ_{\max} 583, 645, 672s, 694, 895 nm.

Raman (532 nm, cm^{-1}): ν 270w (Co-Cl), 495m (C-C), 624m (C-C), 717w (C-P), 1006s (C=C), 1036m (C-C), 1103w (CH_2), 1591s (C=C).

MS (ASAP⁺, Da): Repeating units separated by $\Delta m/z = 72$.

Entry 4:

Black insoluble, magnetic precipitate observed. Assumed to be cobalt(0) formed as a result of decomposition and so the reaction was abandoned.

Entry 5:

0.142 g – mixture of “dppbCoCl” and (dppb)ZnCl₂.

UV-Vis (THF): λ_{\max} 588, 649s, 739s, 930 nm.

Raman (532 nm, cm^{-1}): ν 642m (C-C), 696w (C-P), 1007s (C=C), 1034m (C-C), 1106m (CH_2), 1593s (C=C).

MS (ASAP⁺, Da): *m/z* 1073.175 (1.90% [(dppb)₃Zn₃Cl₃]), 1049.124 (3.76% [(dppb)₂Zn₂Cl₂], 1149.071 (12.7% [(dppb)₂Zn₃Cl₃]), 947.244 (5.08% [(dppb)₂CoCl]), 911.235 (0.17% [(dppb)₂Co]), 559.048 (14.07% [(dppbO)ZnCl₂-H]), 505.087 (13.32% [(dppbO)Zn]), 497.231 (100% [dppb-THF]).

¹H NMR (200 MHz, CD₂Cl₂): δ_H 16.64 (br s, 8H, *o*-H, *v*_{1/2} 73 Hz), 7.86-7.32 (br m, 12H, *m*-H/*p*-H, *v*_{1/2} 80 Hz), 3.77 (br s, THF O-CH₂, *v*_{1/2} 20 Hz), 2.62 (br s, 4H, CH₂CH₂, *v*_{1/2} 63 Hz), 1.85 (br s, THF CH₂CH₂, *v*_{1/2} 16 Hz), -4.22 (br s, 4H, P-CH₂, *v*_{1/2} 131 Hz).

Entry 6:

No reaction observed: solution remained blue at all times.

[NB: reaction was run prior to the knowledge that (P[^]P)ZnX₂ complexes can inherently result, so it is possible that (dcypx)ZnCl₂ could have been formed. Unfortunately, the reaction products were not retained and so analysis could not be performed.]

Entry 7:

Black, insoluble, magnetic precipitate observed. Assumed to be cobalt(0) formed as a result of decomposition. Crystals suitable for X-ray diffraction were grown through layering a solution in DCM with hexanes and found to be (dtbpx)CoCl₂.

MS (*i*ASAP⁺, Da): 488.184 (0.57% [M-Cl]⁺), 395.286 (19.78% [dtbpx]⁺), 337.200 (100% [dtbpx-tBu]⁺).

Raman (532 nm): *v* cm⁻¹ 321sh (Co-Cl), 582s (C-C), 698m (C-P), 814m (C-C), 1060s (C=C), 1186m (C-C), 1234s (CH₂), 1475m (CH₂), 1607s (C=C).

³¹P NMR (THF, unlocked, 162 MHz): δ_P 24.5-23.8 (m, dtbpx), 23.1-22.5 (m, (dtbpx)ZnCl₂).

³¹P{¹H} NMR (THF, unlocked, 162 MHz): δ_P 24.3 (s, dtbpx), 21.9 (s, (dtbpx)ZnCl₂).

Entry 8:

Black insoluble, magnetic precipitate observed. Assumed to be cobalt(0) formed as a result of decomposition and so the reaction was abandoned.

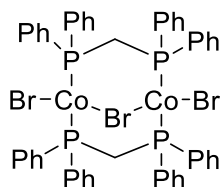
Entry 9:

Black insoluble, magnetic precipitate observed. Assumed to be cobalt(0) formed as a result of decomposition and so the reaction was abandoned.

Entry 10:

0.52 g (0.46 mmol, 74%).

Upon treatment with activated zinc powder, $[\text{Co}(\text{dppm})\text{Br}_2]_2$ was reduced to the mixed valence dinuclear species shown below, with one bridging bromide between cobalt centres as determined by single crystal X-ray diffraction. ^1H NMR analysis suggested the phenyl environments on phosphorus are inequivalent.



UV-Vis (THF): λ_{max} 622sh, 644 and 745 nm.

^{31}P NMR (162 MHz, C_6D_6): δ_{P} no signals observed.

^1H NMR (400 MHz, C_6D_6): δ_{H} 7.39-6.21 (overlapping multiplets, 10H), 2.10 (s, 1H, CH_2).

Raman (532 nm, cm^{-1}): ν 283w (Co-Br), 311vw (brCo-Br), 707w (C-P), 1006s (C=C), 1035m (C-C), 1098s (CH_2), 1591m (C=C).

MS (ASAP⁺, Da): m/z 938.308 (62.56% [$(\text{dppmO})_2\text{CoBr}$]), 954.229 (10.12% [$(\text{dppmO})(\text{dppmO}_2)\text{CoBr}$]), 38.220 (58.24% [dppm]), 401.129 (40.82% [dppmO]), 275.163 (100% [$(\text{dppm}-\text{PPh}_2+\text{H})\text{Co}$]).

Entry 11:

The Raman spectra obtained had a fluorescent component, raising the baseline by several hundred counts. The mass spectrum obtained shows the starting material.

Raman (532 nm, cm^{-1}): ν 345vw (Co-Br), 530w (C-C), 701w (P-C), 1007s (C=C), 1034m (C-C), 1059m (C=C).

MS (ASAP⁺, Da): *m/z* 934.077 (3.27% [(dppe)₂CoBr]), 950.062 (8.62% [(dppeO)(dppe)CoBr]), 966.055 (24.40% [(dppeO)₂CoBr]), 982.046 (13.33% [(dppeO₂)(dppeO)CoBr₂]), 998.036 (0.12% [(dppeO₂)₂CoBr]), 583.152 (19.38% [(dppe)Co(PPh₂)·H₂O]), 399.117 (100% [dppe]).

Entry 12:

The mass spectrum was inconclusive due to excessive fragmentation of the ligand. The UV-Vis was inconclusive due to poor solubility in THF (NB: [(dppe)₂CoBr]⁺ [Co₂Br₆(dppe)]²⁻ is soluble in THF). The Raman spectra obtained suggests [(dppe)₂CoBr]⁺ [Co₂Br₆(dppe)]²⁻.

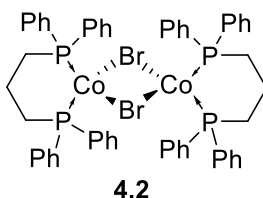
UV-Vis: λ_{max} Poor solubility in THF resulted in poor quality spectra.

Raman (532 nm, cm⁻¹): ν 253w, 309w and 350vw (Co-Br), 622w (C-C), 698w (C-P), 1004s (C=C), 1035m (C-C), 1102m (CH₂), 1590s (C=C).

MS (ASAP⁺, Da): *m/z* 429.006 (7.25% [dppeO₂-H]), 369.006 [15.48% [(PPh₂)₂], 217.05 (100% [Ph₂PO₂]).

Entry 13:

(dppp)CoBr(μ₂-Br)Co(dppp): 0.209 g (0.13 mmol, 22%)



UV-Vis (THF): λ_{max} 535, 619, 664s, 753 and 912 nm.

Raman (532 nm, cm⁻¹): ν 270w (Co-Br), 626w (C-C), 707w (C-P), 1008s (C=C), 1036m (C-C), 1103m (CH₂), 1591s (C=C).

MS (ASAP⁺, Da): *m/z* 1178.88 (0.31% [(dppp)₂Co₂Br₃]), 962.110 (3.97% [(dppp)₂CoBr]), 978.104 (7.35% [(dpppO)(dppp)CoBr]), 994.098 (4.80% [(dpppO)CoBr]), 1010.101 (0.62% [(dpppO₂)(dpppO)CoBr]), 549.979 (21.04% [dpppCoBr]), 491.031 (69.69% [dppp+Br]), 412.128 (61.85% [dppp]).

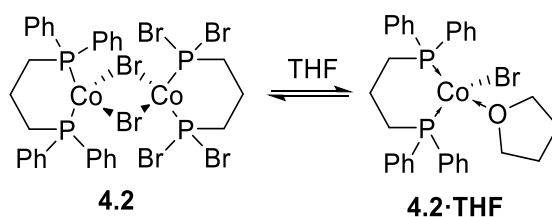
MS (MALDI⁺, DTCB matrix, Da): 931.077 (15.85% [2M-3HBr+3O]⁺), 883.101 (95.16% [M-CoBr]⁺), 628.25 (0.97% [M-(dppp)CoBr]⁺), 550.002 (15.36% [M/2]⁺), 471.117 (100% [M-(dppp)₂CoBr₂]⁺),

³¹P NMR (162 MHz, CD₂Cl₂): δ_P -21.4 (br s, ν_{1/2} 80 Hz).

$^1\text{H NMR}$ (200 MHz, CD_2Cl_2): δ_{H} 17.84 (br s, 8H, κ_2 -Ph-*o*-H, $\nu_{1/2}$ 167 Hz), 14.81 (br s, 4H, μ_2 -Ph-*o*-H, $\nu_{1/2}$ 128 Hz), 10.08 (br s, 2H, κ_2 -CH $_2$, $\nu_{1/2}$ 98 Hz), 7.30-7.12 (br m, 18H, all *m*-H/*p*-H, $\nu_{1/2}$ 112 Hz), 2.35 (br s, 2H, κ_2 -CH $_2$ -CH $_2$, $\nu_{1/2}$ 140 Hz), -3.94 (br s, 4H, κ_2 -P-CH $_2$, $\nu_{1/2}$ 194 Hz), -5.08 (br s, 2H, μ_2 -P-CH $_2$, $\nu_{1/2}$ 150 Hz).

Entry 14:

(dppp)CoBr·THF: 0.59 g (0.95 mmol, 60%).

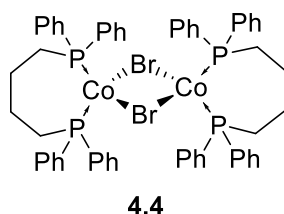


UV-Vis (THF): λ_{max} 533, 622, 661, 752 and 915 nm.

Raman (532 nm, cm^{-1}): ν 262w and 295w (Co-Br-Co), 366w (Co-Br-Co), 624w (C-C), 704w (C-P), 1006s (C=C), 1034m (C-C), 1103m (CH $_2$), 1591s (C=C).

MS (ASAP $^+$, Da): m/z 1178.86 (0.61% [(dppp) $_2$ Co $_2$ Br $_3$]), 962.095 (13.94% [(dppp) $_2$ CoBr]), 978.080 (2.65% [(dpppO)(dppp)CoBr]), 622.019 (3.18% [(dppp)CoBrTHF] $^+$), 549.968 (18.37% [dpppCoBr]), 491.037 (43.09% [dppp+Br]), 484.160 (100%, [dppp+THF-H] $^+$), 412.121 (51.61% [dppp]).

$^1\text{H NMR}$ (200 MHz, CD_2Cl_2): δ_{H} 18.14 (br s, 8H, *o*-H, $\nu_{1/2}$ 75 Hz), 7.66-7.41 (br m, 12H, *m*-H/*p*-H, $\nu_{1/2}$ 80 Hz), 3.79 (br s, 4H, THF CH $_2$ -CH $_2$, $\nu_{1/2}$ 18 Hz), 2.72 (br s, 2H, CH $_2$ -CH $_2$, $\nu_{1/2}$ 35 Hz), 1.86 (br s, THF O-CH $_2$, $\nu_{1/2}$ 17 Hz), -4.20 (br s, 4H, P-CH $_2$, $\nu_{1/2}$ 97 Hz).

Entry 15:

The mass spectrum showed only peaks corresponding to the ligand. The Raman and UV-Vis spectra show signals corresponding to **4.4**.

UV-Vis (THF): λ_{max} 585s, 673, 956 and 1050s nm.

Raman (532 nm, cm^{-1}): ν 270m (Co-Br), 356w (Co-Br), 637m (C-C), 698w (C=P), 761w (Co-P), 1006s (C=C), 1034m (C-C), 1106m (CH_2), 1591s (C=C).

MS (ASAP⁺, Da): m/z 497.212 (64.65% [dppb-H+THF]), 427.171 (100% [dppb+H]).

¹H NMR (200 MHz, CD_2Cl_2): 16.85 (br s, 8H, o-H, $\nu_{1/2}$ 30 Hz), 8.06-7.33 (br m, 12H, *m*-H/*p*-H/free dppb, $\nu_{1/2}$ 99 Hz), 3.69 (br s, THF $\text{CH}_2\text{-CH}_2$, $\nu_{1/2}$ 15 Hz), 2.77-2.36 (br m, 4H, $\text{CH}_2\text{-CH}_2$ /free dppb, $\nu_{1/2}$ 50 Hz), 1.82 (br s, THF O- CH_2 , $\nu_{1/2}$ 17.25 Hz), -3.90 (br s, 4H, P- CH_2 , $\nu_{1/2}$ 40 Hz).

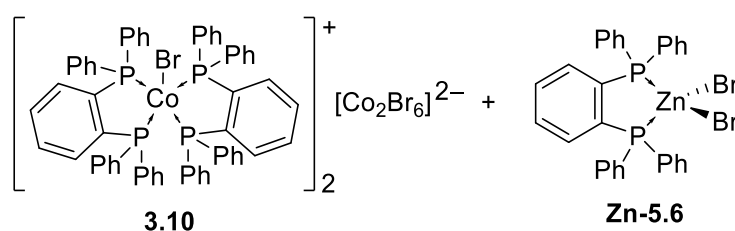
Entry 16:

Black insoluble, magnetic precipitate observed. Assumed to be cobalt(0) formed as a result of decomposition and so the reaction was abandoned.

Entry 17:

A black, insoluble and magnetic precipitate was observed to form, however, the reaction solution did change colour from blue to forest green. Volatiles were removed *in vacuo*, but attempts to extract the product of the reaction into toluene were unsuccessful.

Entry 18:



Found to be mixture of $(\text{dppbz})\text{ZnBr}_2$ and $[(\text{dppbz})_2\text{CoBr}]_2^+ [\text{Co}_2\text{Br}_6]^{2-}$:

Raman (532 nm, cm^{-1}): ν 243w and 275w (Co-Br), 705w (C-P), 1006s (C=C), 1098s (C=C), 1588m (C=C).

MS (ASAP⁺, Da): m/z 1030.081 (0.59% $[(\text{dppbz})_2\text{CoBr}]$), 1046.066 (3.29% $[(\text{dppbz})(\text{dppbzO})\text{CoBr}]$), 1060.060 (3.88% $[(\text{dppbzO})_2\text{CoBr}]$), 588.956 (2.87% $[(\text{dppbz})\text{ZnBr}]$), 447.121 (46.78% [dppbz]).

³¹P NMR (162 MHz, C_6D_6): δ_{P} no peaks observed.

¹H NMR (400 MHz, C₆D₆): δ_H 7.67 (m), 7.41 (m), 7.35 (m), 6.95 (m), 6.75 (m) [all correspond to free dppbz in solution; additional peaks obscured by C₆D₆].

Entry 19:

Crystals suitable for X-ray diffraction were grown through layering THF with hexanes at room temperature to show complex (dtbpx)MBr₂ where M = 3:1 Zn:Co. The Raman spectrum obtained has a sloping baseline as wavenumber increases; fluorescent character as a result of the presence of (dtbpx)ZnBr₂.

UV-Vis (THF): λ_{max} 660, 699, 744 nm [(dtbpx)CoBr₂]

Raman (532 nm, cm⁻¹): ν 286w (Co-Br), 580m (C-C), 696w (P-C), 1009m (C=C), 1028m (C-C), 1059m (C-C), 1184s (CH₂), 1241s (CH₃), 1478s (C-C), 1645s (C=C).

MS (ASAP⁺, Da): *m/z* 532.134 (0.36% [(dtbpx)CoBr]), 537.132 (0.23% [(dtbpx)ZnBr]), 315.396 (100% [dtbpx+H]).

³¹P NMR (162 MHz, unlocked THF): δ_P 24.2 (s, dtbpx) and 18.4 (s, (dtbpx)ZnBr₂).

Entry 20:

Found to contain (dtbpx)CoBr₂ from spectroscopic and spectrometric analysis. The Raman spectrum obtained has a sloping baseline as wavenumber increases; fluorescent character as a result of the presence of (dtbpx)ZnBr₂, which was also observed within the mass spectrum acquired.

UV-Vis (THF): λ_{max} 660, 799, 744 nm [(dtbpx)CoBr₂].

Raman (532 nm, cm⁻¹): ν 282w (Co-Br), 695w (C-P), 1059m (C-C), 1189-1237s (CH₂, CH₃), 1475m (C-C), 1643m (C=C).

MS (ASAP⁺, Da): *m/z* 232.119 (3.31% [dtbpxCoBr]), 237.119 (0.46% [dtbpxZnBr]), 395.280 (100% [dtbpx+H]).

Entry 21:

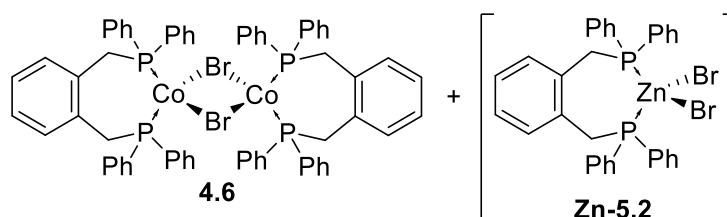
Crystals suitable for X-ray diffraction were grown through layering a solution in DCM with hexanes at room temperature and the structure determined to be (dtbpx)CoBr₂. Spectroscopic and spectrometric analysis suggested the bulk product is a mixture of: (dtbpx)CoBr₂, (dtbpx)ZnBr₂ and “dtbpxCoBr”:

UV-Vis (THF): λ_{\max} 538, 672, 741, 917 and 1095 nm. [(dtbpxCoBr₂ and “dtbpxCoBr”)].

Raman (532 nm, cm⁻¹): ν 281s (Co-Br *symm*), 218vw (Co-Br in Co^I), 583s (C-C), 696w (C-P), 817s (C-C), 1034w (C-C), 1058s (C-C), 1187-1141s (CH₂ and CH₃), 1477s (C-C), and 1606s (C=C).

MS (ASAP⁺, Da): m/z 537.125 (30.43% [dtbpxZnBr]), 532.129 (2.22% [(dtbpxCoBr)], 395.277 (100% [dtbpx]).

¹H NMR (200 MHz, CD₂Cl₂): δ_{H} 7.39 (br s, 1H, Ar-H, $\nu_{1/2}$ 30 Hz), 7.23 (br s, 1H, Ar-H, $\nu_{1/2}$ 36 Hz), 3.40 (br s, 2H, CH₂, $\nu_{1/2}$ 30 Hz), 1.50 (br s, 18H, CH₃, $\nu_{1/2}$ 27 Hz).

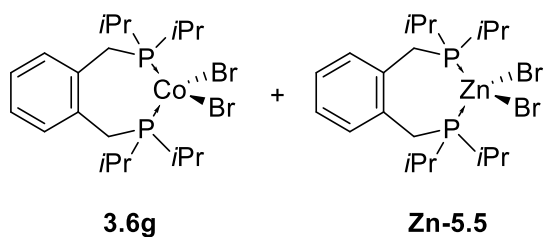
Entry 22:

The UV-Vis spectrum shows bands corresponding to “dppxCoBr.” The Raman shows loss of a band corresponding to Co-Br symmetric stretch of (dppx)CoBr₂. The Mass spectrum shows some formation of (dppx)ZnBr₂ and shows the presence of (dppx)Co species.

UV-Vis (THF): λ_{\max} 613, 665, 720, 762 and 945 nm.

Raman (532 nm, cm⁻¹): ν 386m (Co-Br), 623w (C-C), 689w (C-P), 773w (Co-P), 1005s (C=C), 1033m (C-C), 1099s (C=C), 1228s (CH₂), 1589s (C=C).

MS (ASAP⁺, Da): m/z 1118.060 (6.13% [(dppxO)₂CoBr]), 627.947 (7.01% [dppxCoBr]), 632.944 (3.68% [dppxZnBr]), 491.114 (100% [dppx+H+O]), 475.128 (48.55% [dppx+H]).

Entry 23:

The UV-Vis shows $[(\text{diprpx})\text{CoBr}_2]$, as do the mass and Raman spectra. The mass spectrum obtained also shows the presence of $[(\text{diprpx})\text{ZnBr}_2]$.

UV-Vis (THF): λ_{max} 480, 620, 662 and 748 nm.

Raman (532 nm, cm^{-1}): ν 296sh (Co-Br), 606m (C-C), 711m (C-P), 1050m (C-C), 1256-1299s (CH_2 , CH_3), 1465m (C-C), 1608m (C=C).

MS (ASAP⁺, Da): m/z 476.056 (13.51% $[(\text{diprpx})\text{CoBr}]$), 481.053 (5.47% $[(\text{diprpx})\text{ZnBr}]$), 492.051 (32.39% $[(\text{diprpxO})\text{CoBr}]$), 497.050 (8.45% $[(\text{diprpxO})\text{ZnBr}]$), 830.266 (2.20% $[(\text{diprpx})_2\text{CoBr}]$), 846.258 (11.84% $[(\text{diprpx})(\text{diprpxO})\text{CoBr}]$), 339.220 (43.75% $[(\text{diprpx})]$).

Entry 24:

The Mass spectrum is inconclusive and fragments could not be assigned. The UV-Vis shows some cobalt(I) species is present, however the mass spectrum contains residual cobalt(II).

UV-Vis (THF): λ_{max} 610, 680, 754 and 943 nm.

Raman (532 nm, cm^{-1}): ν 232sh (Co-Br), 624m (C-C), 697w (C-P), 1006s (C=C), 1033m (C-C), 1098m (C=C), 1591s (C=C).

MS (ASAP⁺, Da): m/z 185.0081 (70.19% $[\text{PPh}_2]$), 216.785 (20%), 293.783 (5.65%), 302.641 (43.10%), 406.722 (3.91%), 417.709%, 636.334 (1.12%), 641.334 (0.67%).

Entry 25:

Black insoluble, magnetic precipitate observed. Assumed to be cobalt(0) formed as a result of decomposition and so the reaction was abandoned.

Entry 26:

Crystals suitable for X-ray diffraction were grown through layering a solution in DCM with hexanes at room temperature and the structure was determined to be (xantphos)CoBr₂. The spectroscopic and spectrometric data obtained also suggest (xantphos)CoBr₂ as the main species present.

Raman (532 nm, cm⁻¹): ν 275w (Co-Br), 622m (C-C), 715w (C-P), 1005vs (C=C), 1035m (C-C), 1107m (C-C), 1170-1229m (CH₃), 1443m (C-C), 1592s (C=C)

MS (ASAP⁺, Da): m/z 716.081 (1.45% [(xantphos)CoBr]), 1310.199 (0.08% [(xantphos)₂Co]), 579.175 (100% [xantphos+H]).

6.4.2 Attempted Reductions of (P[^]P)CoX₂ Complexes with Zn in the presence of L6.4.2.1 Attempted synthesis of (P[^]P)(1-C₆)CoBr:

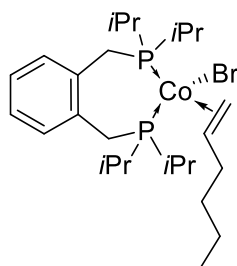
General Procedure: (P[^]P)CoBr₂ ((P[^]P) = diprpx, dppbz or dtbpx) (1 eq.), and activated Zn powder (5 eq.) were placed in a Schlenk and THF added to dissolve (P[^]P)CoBr₂ complex. 1-Hexene (1 eq.) was added immediately and the reaction allowed to stir at room temperature for 18 hours. Volatiles were removed *in vacuo* and the crude reaction mixture dried before storage in an N₂-filled glovebox. A summary of the reactions performed can be found in **Table 6.7**.

Table 6.7 Summary of attempted synthesis of complexes with general formula (P[^]P)(1-C₆)CoBr.

Entry	(P [^] P)CoBr ₂ /g (mmol)	Zn /g (mmol)	1-hexene /mL (mmol)
1	(diprpx)CoBr ₂	0.10 (0.18)	0.02 (0.18)
2	[(dppbz) ₂ CoBr] ₂ ⁺ [Co ₂ Br ₆] ²⁻	0.25 (0.41)	0.05 (0.41)
3	(dtbpx)CoBr ₂	0.75 (1.13)	0.14 (1.13)

*0.2 M solution in DCM

Entry 1: Attempted synthesis of (diprpx)(1-C₆)CoBr:

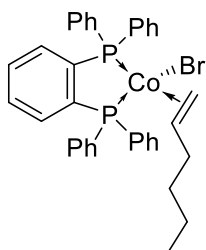


Found to be: (diprpx)CoBr₂

³¹P NMR (162 MHz, THF, unlocked): -4.3 (s) (free ligand shifted to low frequency due to paramagnetic species present in solution).

MS (ASAP⁺): *m/z* 555.970 (49.37% [M]⁺), 511.025 (7.75% [M+H-*i*Pr]⁺), 476.055 (27.25% [M-Br]⁺), 295.153 (100% [M-CoBr₂-*i*Pr]⁺)

Raman (532nm): ν cm⁻¹ 272w (Co-Br), 601m (C-P), 889s (C-C), 1051s (C=C), 1469 (CH₂), 1604 (C=C).

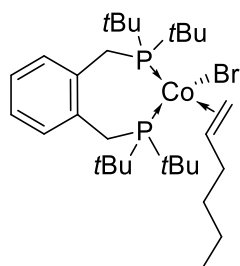
Entry 2: Attempted synthesis of (dbbpz)(1-C₆)CoBr:

Found to be mixture of $[(\text{dppbz})_2\text{CoBr}]_2^+ [\text{Co}_2\text{Br}_6]^-$ and $(\text{dppbz})\text{ZnBr}_2$

^{31}P NMR (162 MHz, THF, unlocked): no signals observed.

MS (ASAP⁺): m/z 1067.055 (4.01% $[(\text{dppbz})_2\text{ZnBr}+2\text{O}]^+$), 1062.059 (2.76% $[(\text{dppbz})_2\text{CoBr}+2\text{O}]^+$), 604.948 (11.09% $[\text{dppbz})\text{ZnBr}+\text{O}]^+$), 620.940 (14.12% $[(\text{dppbz})\text{ZnBr}+2\text{O}]^+$), 385.058 (100% $[\text{dppbz-Ph}+\text{O}]^+$).

Raman (532nm): ν cm^{-1} 250w (Co-Br), 435s (Si-O-Si), 555s (C-C), 705w (C-P), 1098s (C=C), 1598s (C=C).

Entry 3: Attempted synthesis of (dtbpx)(1-C₆)CoBr

Found to be mixture of: $(\text{dtbpx})\text{CoBr}_2$ and $(\text{dtbpx})\text{ZnBr}_2$

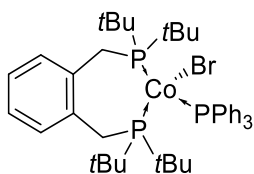
^{31}P NMR (162 MHz, THF, unlocked): δ_{P} 24.5 (s, free dtbpx), 18.8 (s, $(\text{dtbpx})\text{ZnBr}_2$)

MS (ASAP⁺): m/z 532.117 (0.54% $[(\text{dtbpx})\text{CoBr}]^+$), 536.109 (3.39% $[(\text{dtbpx})\text{ZnBr-H}]^+$), 395.277 (35.19% $[\text{dtbpx}+\text{H}]^+$), 337.191 (100% $[\text{dtbpx-tBu}]^+$).

Raman (532nm): ν cm^{-1} 249w and 282w (Co-Br), 580s (C-C), 817s (C-C), 1009m and 1060m (C=C), 1237s (CH_3), 1479m (CH_2), 1606s (C=C).

Chapter 6

6.4.2.2 Attempted synthesis of [(dtbpx)(PPh₃)CoBr]:



THF (25 mL) was added to a Schlenk containing (dtbpx)CoBr₂ (0.10g, 0.16 mmol), activated Zn powder (0.53 g, 0.81 mmol), and triphenylphosphine (0.042g, 0.16 mmol) and the mixture stirred at room temperature for 18 hours, after which time a black, magnetic and insoluble material (cobalt(0)) was visible. The reaction was filtered, filtrate collected and volatiles removed *in vacuo* to produce a blue/green powder, which was confirmed to be unreacted (dtbpx)CoBr₂ by MS (ASAP) spectrometric and Raman and UV-Vis spectroscopic analysis.

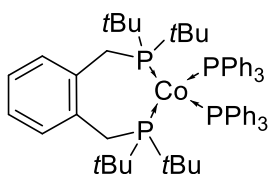
Found to be starting materials: (dtbpx)CoBr₂ and Zn.

MS (ASAP⁺): *m/z* 532.121 (6.37% [M-Br]⁺), 395.282 (100% [M-CoBr₂+H]⁺), 263.087 (74.17% [PPh₃+H]⁺).

Raman (532nm): ν cm⁻¹ 275w (Co-Br), 580s (C-C), 811s (C-C), 1004s and 103m (C=C), 1234s (CH₃), 1480 (CH₂), 1590s (C=C).

UV-Vis: λ_{\max} 659, 694, 738 nm [(dtbpx)CoBr₂].

6.4.2.3 Attempted synthesis of [(dtbpx)(PPh₃)₂Co]:



THF (25 mL) was added to a Schlenk containing (dtbpx)CoBr₂ (0.10g, 0.16 mmol), activated Zn powder (0.53 g, 0.81 mmol), and triphenylphosphine (0.084g, 0.32 mmol) and the mixture stirred at room temperature for 18 hours, after which time a black, magnetic and insoluble material (cobalt(0)) was visible. The reaction was filtered, filtrate collected and volatiles removed *in vacuo* to produce a blue/green powder which was confirmed to be a mixture of (dtbpx)ZnBr₂ and unreacted (dtbpx)CoBr₂ by MS (ASAP) spectrometric and Raman and UV-Visible spectroscopic analysis.

Found to be mixture of (dtbpx)CoBr₂ and (dtbpx)ZnBr₂

MS (ASAP⁺): *m/z* 532.121 (8.02% [(dtbpx)CoBr]⁺), 537.122 (0.79% [(dtbpx)ZnBr]⁺), 395.282 (100% [dtbpx]⁺), 263.086 (87.52% [PPh₃+H]⁺).

Raman (532nm): ν cm^{-1} 275w (Co-Br), 561m (C-C), 828w (C-C), 1004s (C=C), 1430w (CH_2), 1588s (C=C).

UV-Vis: λ_{max} 660, 699, 744 nm ((dtbpx)CoBr₂).

6.4.3 Synthesis of Diphosphine Zinc(II) Halides

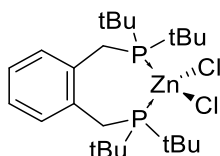
General Procedure: The diphosphine ligand (1.05 eq.) was dissolved in THF and added dropwise to a solution of zinc(II)halide (1 eq.) in THF. The reaction was left to stir at room temperature for 14 hours, after which THF was removed *in vacuo* and excess diphosphine was removed *via* washing with hexanes. Solvent residue was then removed *in vacuo* and the resulting complex stored in an N₂ atmosphere glovebox. A summary of the reactions performed can be found in **Table 6.8**.

Table 6.8 Summary of synthesis of (P[^]P)ZnX₂ complexes.

Entry	Ligand (g, mmol)	ZnX ₂ (g, mmol)	Yield / %
1	dtbpx 0.50 (1.27)	ZnCl ₂ 0.17 (1.27)	85
2	dtbpx 1.05 (2.66)	ZnBr ₂ 0.50 (2.22)	87
3	dppp 0.75 (1.82)	ZnBr ₂ 0.40 (1.78)	93
4	dtbpp 0.75 (2.26)	ZnBr ₂ 0.48 (2.14)	79
5	dppbz 0.99 (2.22)	ZnBr ₂ 0.50 (2.22)	99

Entry 1: (dtbpx)ZnCl₂

(1,2-bis(di-*tert*-butylphosphinomethyl)benzene)zinc(II) chloride: **0.57 g** (1.07 mmol, 85%).



Crystals of the title complex suitable for single crystal XRD were grown through layering a solution in THF with hexanes at room temperature.

¹H NMR (CD₂Cl₂, 600 MHz): δ_{H} 7.41-7.38 (m, 2H, *o*-H), 7.23-7.20 (m, 2H, *m*-H), 3.38-3.37 (m, 4H, CH_2), 1.47 (m, 36H, CH_3) ppm.

^{13}C NMR (CD_2Cl_2 , 151 MHz): δ_{C} 135.5 (s, q $\underline{\text{C}}$ -CH $_2$), 134.6 (s, o- $\underline{\text{C}}$), 127.9 (s, m- $\underline{\text{C}}$), 36.2 (s, - $\underline{\text{C}}\text{H}_3$), 26.7 (s, q $\underline{\text{C}}$ -CH $_3$), 26.1 (s, - $\underline{\text{C}}\text{H}_2$) ppm.

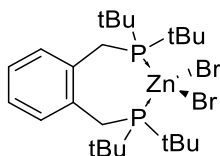
$^{31}\text{P}\{^1\text{H}\}$ NMR (243 MHz, CD_2Cl_2): δ_{P} 22.4 (s) ppm.

MS (ASAP $^+$): m/z 395.291 (51.9%, [M-ZnBr $_2$] $^+$), 337.247 (100%, [M-ZnBr $_2$ -tBu] $^+$).

Raman (cm^{-1} , 532 nm): The Raman spectrum collected for this complex had a significant fluorescent contribution, resulting in poor peak resolution.

Entry 2: (dtbpx)ZnBr $_2$

(1,2-bis(ditertbutylphosphinomethyl)benzene)zinc(II) bromide: **1.20 g** (1.94 mmol, 87%).



Crystals of the title complex suitable for single crystal XRD were grown through layering a solution in DCM with hexanes at room temperature.

^1H NMR (CD_2Cl_2 , 700 MHz): δ_{H} 7.41-7.39 (m, 2H, AA'BB', o- $\underline{\text{H}}$), 7.24-7.22 (m, 2H, AA'BB', m- $\underline{\text{H}}$), 3.41-3.40 (m, 4H, $\underline{\text{C}}\text{H}_2$), 1.51 (m, 36H, $\underline{\text{C}}\text{H}_3$) ppm.

$^{31}\text{P}\{^1\text{H}\}$ NMR (CD_2Cl_2 , 283 MHz): δ_{P} 19.0 (s) ppm.

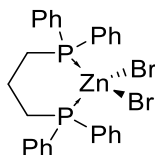
MS (ASAP $^+$): m/z 537.110 (1.36%, [M-Br]), 395.266 (91.10%, [M-CoBr $_2$ +H]), 337.188 (100%, [M-CoBr $_2$ tBu]).

IR (ATR-FTIR): ν cm^{-1} 3000-2820m (C-H stretch), 1474s and 1469s (C-H bend), 935m (C=C stretch).

Raman (532 nm): ν cm^{-1} The Raman spectrum collected for this complex has a significant fluorescent contribution, resulting in poor peak resolution.

Entry 3: (dppp)ZnBr₂

(1,3-bis(diphenylphosphino)propane)zinc(II) bromide: 1.04 g (1.65 mmol, 93%).



Crystals of the title complex suitable for single crystal XRD were grown through slow cooling of a saturated solution in MeCN to room temperature.

¹H NMR (CD₂Cl₂, 400 MHz): δ_H 7.68-7.63 (8H, m, *o*-H), 7.45-7.41 (4H, m, *p*-H), 7.37-7.32 (8H, m, *m*-H), 2.69 br s (4H, *v*_{1/2} 19 Hz, P-CH₂), 2.02-1.89 (2H, m, P-CH₂-CH₂).

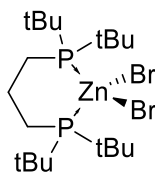
³¹P{¹H} NMR (CD₂Cl₂, 162 MHz): δ_P -21.9 (s) ppm.

MS (ASAP⁺): *m/z* 554.977 (9.83%, [M-Br]), 412.125 (100%, [M-ZnBr₂]).

Raman (cm⁻¹, 532 nm): ν 234 (ZnBr₂ symm), 275w, 624w, 698w, 1006s (C=C).

Entry 4: (dtbpp)ZnBr₂

(1,3-bis(ditertbutylphosphino)propane)zinc(II) bromide: 0.94 g (1.69 mmol, 79%).



Crystals of the title complex suitable for single crystal XRD were grown through layering a solution in DCM with hexane at room temperature.

¹H NMR (C₆D₆, 400 MHz): δ_H 1.29-1.20 (36 H, m, CH₃), 0.99-0.90 (6H, m, CH₂) ppm.

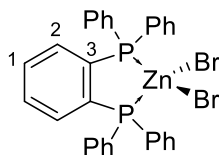
³¹P{¹H} NMR (C₆D₆, 162 MHz): δ_P 9.36 (s) ppm.

MS (ASAP⁺): *m/z* 332.267 (43.25%, [M-CoBr₂]), 275.187 (100%, [M-CoBr₂tBu]).

Raman (cm⁻¹, 532 nm): The Raman spectrum collected for this complex has a significant fluorescent contribution, resulting in poor peak resolution.

Entry 5: (dppbz)ZnBr₂

(1,2-bis(diphenylphosphino)benzene)zinc(II)bromide: 1.48 g (2.20 mmol, 99%).



Crystals of the title complex suitable for single crystal XRD were grown through layering a solution in DCM with hexanes at room temperature.

¹H NMR (CD₂Cl₂, 600 MHz): δ_H 7.62-7.59 (m, 1H, H-2), 7.46-7.43 (m, 4H, *m*-H), 7.40-7.38 (m, 2H, *p*-H), 7.38-7.36 (m, 1H, H-1), 7.30-2.28 (m, 4H, *o*-H) ppm.

¹³C{¹H} NMR (CD₂Cl₂, 151 MHz): δ_C 137.5 (t, ¹J_{PC} 27.3 Hz, C-3) 135.7 (t, ³J_{PC} 4.1 Hz, C-1), 134.8 (t, ³J_{PC} 7.0 Hz, *m*-C), 132.3 (s, C-2), 131.8 (s, *p*-C), 129.5 (t, ²J_{PC} 5.3 Hz, *o*-C), 127.0 (t, ¹J_{PC} 20.2 Hz, *i*-C) ppm.

³¹P{¹H} NMR (CD₂Cl₂, 243 MHz): δ_P 25.4 (s) ppm.

MS (ASAP⁺): *m/z* 588.951 (3.37% [M-Br]⁺), 510.087 (4.05% [M-2Br]⁺), 446.110 (14.62% [M-ZnBr₂]⁺), 385.062 (100% [M-ZnBr₂-Ph+O]⁺).

IR (ATR-FTIR): ν cm⁻¹ 3055-2850w (C-H stretch), 1482 and 1436 (C-H bend), 1099-906 (C=C bend).

Raman (532 nm): ν cm⁻¹ The Raman spectrum collected for this complex has a significant fluorescent contribution, resulting in poor peak resolution. However, the following peaks could be assigned: 266w (Zn-Br_{symm}), 1006s (C=C stretch), 1591s (C=C stretch).

6.4.4 Ligand Exchange Reactions

General procedure: (P[^]P)M¹X₂ (M¹ = Co, Zn, (P[^]P) = dppbz, dtbpx, dppp, X = Cl, Br) and M²X₂ (M² = Co, Zn, X = Cl, Br) were dissolved in THF or DCM and the resulting reaction followed by UV-Vis spectroscopy. Uptake of a ligand by a cobalt species was seen through emergence of bands within the visible region. Loss of a ligand by a cobalt species was seen through reduction in absorbance of bands present within the visible region as the concentration of this species decreases. A summary of the reactions performed is presented in **Table 6.9**.

Table 6.9 Summary of ligand exchange reactions and conditions used.

Entry	(P [^] P)M ¹ X ₂ (g, mmol)	M ² X ₂ (g, mmol)	Time / h	Solvent
1	(dppbz)CoBr ₂ 0.25 (0.19)	ZnBr ₂ 0.085 (0.38)	24	THF
2	(dtbpx)CoBr ₂ 0.01 (0.016)	ZnBr ₂ 0.004 (0.018)	18	THF
3	(dtbpx)CoCl ₂ 0.20 (0.38)	ZnCl ₂ 0.052 (0.38)	22	THF
4	(dtbpx)CoBr ₂ 0.01 (0.016)	ZnBr ₂ 0.003 (0.014)	18	THF
5	(dtbpx)CoBr ₂ 0.01 (0.016)	ZnBr ₂ 0.004 (0.018)	1.5	DCM
6	(dppp)CoBr ₂ 0.01 (0.016)	ZnBr ₂ 0.003 (0.014)	96	DCM
7	(dppp)CoBr ₂ 0.01 (0.016)	ZnBr ₂ 0.003 (0.014)	144	THF
8	(dppbz)ZnBr ₂ 0.25 (0.37)	CoBr ₂ 0.080 (0.37)	24	THF
9	(dtbpx)ZnBr ₂ 0.25 (0.40)	CoBr ₂ 0.088 (0.40)	18	THF
10	(dtbpx)ZnBr ₂ 0.01 (0.016)	CoBr ₂ 0.004 (0.018)	20	THF
11	(dtbpx)ZnBr ₂ 0.01 (0.016)	CoBr ₂ 0.004 (0.018)	720	THF
12	(dtbpx)ZnCl ₂ 0.20 (0.38)	CoCl ₂ 0.049 (0.38)	18	THF
13	(dppp)ZnBr ₂ 0.01 (0.016)	CoBr ₂ 0.003 (0.014)	18	THF

Entry 1:

The Raman spectrum obtained had significant fluorescent character as a result of the presence of (dppbz)ZnBr₂, obscuring most peaks.

³¹P NMR (162 MHz, unlocked, THF): δ_P no signals observed.

³¹P{¹H} NMR (162 MHz, unlocked, THF): δ_P no signals observed.

Raman (532 nm, cm⁻¹): ν 254w (Co-Br), 1006w (C=C), 1036w (C-C), 1098w (C-C) and 1590m (C=C).

MS (ASAP⁺, Da): m/z 446.127 (90.64% [dppbz]), 662.896 (54.48% [(dppbz)CoBr₂]), 583.987 (23.85% [(dppbz)CoBr]), 588.977 (1.76% [(dppbz)ZnBr]), 1030.116 (0.71% [(dppbz)CoBr]), 1109.033 (0.62% [(dppbz)₂CoBr₂]), 1246.873 (6.21% [(dppbz)₂Co₂Br₂]), 1325.792 (4.42% [(dppbz)₂Co₂Br₃]).

Entry 2:

The exchange reaction was followed by UV-Vis Spectroscopy: loss of bands corresponding to [(dtbpx)CoBr₂] and formation of bands corresponding to [CoBr₂] was observed. The ³¹P NMR spectrum obtained suggests some oxidation of the phosphine has occurred during the reaction *i.e.* observed species is [(dtbpxO)ZnBr₂].

UV-Vis: λ_{\max} 594, 655 and 684 nm [CoBr₂].

³¹P{¹H} NMR (162 MHz, unlocked, THF): δ_P 72.0 (d, ³J_{PP} 69 Hz, P=O-Zn), 37.8 (d, ³J_{PP} 70 Hz, P-Zn) ppm.

³¹P NMR (162 MHz, unlocked, THF): δ_P 72.0 (d, ³J_{PP} 69 Hz, P=O-Zn), 37.8 (d, ³J_{PP} 67 Hz, P-Zn) ppm.

Entry 3:

The ³¹P NMR spectrum obtained shows [(dtbpx)ZnCl₂], and the Raman and mass spectra show [(dtbpx)CoCl₂]. The UV-Vis shows [(dtbpx)CoCl₂], with a slight hypsochromic shift as a result of the presence of CoCl₂.

UV-Vis: λ_{\max} 626, 673 and 732 nm.

³¹P{¹H} NMR (162 MHz, C₆D₆): δ_P 21.0 (s, [(dtbpx)ZnCl₂]) ppm.

¹H NMR (400 MHz, C₆D₆): δ_H 8.31 (br s, 1H, $v_{1/2}$ 22 Hz, *o*-H), 8.14 (br s, 1H, $v_{1/2}$ 13 Hz, *m*-H), 3.61 (br s, $v_{1/2}$ 22 Hz, THF), 2.76 (br s, 2H, $v_{1/2}$ 12 Hz, CH₂), 1.42 (br s, $v_{1/2}$ 17 Hz, THF), 1.33-1.31 (br m, 18 H, $v_{1/2}$ 17 Hz, CH₃) ppm.

Raman (532 nm, cm⁻¹): ν 287m (Co-Cl), 320w (Co-Cl), 581s (C-C), 691m (C-C), 776w (C-P), 1032w (C-C), 1055s (C-C), 1184-1236s (CH₂ and CH₃), 1473m (C-C), 1604m (C=C).

MS (ASAP⁺, Da): m/z 488.19 (8.07% [(dtbpx)CoCl]), 395.290 (100% [dtbpx+H]).

Entry 4:

The exchange reaction was followed by UV-Vis Spectroscopy: loss of bands corresponding to [(dtbpx)CoBr₂] and formation of bands corresponding to [CoBr₂] was observed. The ³¹P NMR spectrum obtained suggests some oxidation of the phosphine has occurred during the reaction *i.e.* observed species is [(dtbpxO)ZnBr₂].

UV-Vis: λ_{max} 597s, 647s 694 nm [CoBr₂].

³¹P NMR (162 MHz, unlocked, THF): δ_P 73.4 (d, ²J_{PP} 67 Hz, P=O-Zn), 38.9 (d, ²J_{PP} 68 Hz, P-Zn).

³¹P{¹H} NMR (lb = 5 Hz, 162 MHz, unlocked, THF): δ_P 73.4 (d, ²J_{PP} 60 Hz, P=O-Zn), 38.7 (d, ²J_{PP} 60 Hz, P-Zn) ppm.

Entry 5:

The exchange reaction was followed by UV-Vis Spectroscopy: complete loss of bands corresponding to [(dtbpx)CoBr₂] was seen after 1.5 hours. The ³¹P NMR spectrum shows no signals. The Raman spectrum collected has a significant fluorescent character as a result of [(dtbpx)ZnBr₂].

³¹P NMR (162 MHz, unlocked, DCM): δ_P no signals observed.

³¹P{¹H} NMR (162 MHz, unlocked, DCM): δ_P no signals observed.

UV-Vis: λ_{max} no bands observed in the visible region.

Raman (532 nm, cm⁻¹): ν no discernible bands.

Entry 6:

The exchange reaction was followed by UV-Vis Spectroscopy: complete loss of bands corresponding to [(dppp)CoBr₂] was seen after 96 hours. The ³¹P NMR spectrum shows no signals.

³¹P NMR (162 MHz, unlocked, DCM): δ_P no signals observed.

UV-Vis: λ_{max} no bands observed in the visible region.

Entry 7:

The exchange was followed by UV-Vis Spectroscopy: after 144 hours, some [(dppp)CoBr₂] remained along with new bands corresponding to [CoBr₂] formation. The ³¹P NMR spectrum shows no signals.

³¹P NMR (162 MHz, unlocked, THF): δ_P no signals observed.

³¹P{¹H} NMR (162 MHz, unlocked, THF): δ_P no signals observed.

UV-Vis: λ_{max} 611, 659 and 694 nm [(dppp)CoBr₂] and [CoBr₂] mixture.

Entry 8:

The Raman spectrum obtained corresponds to [(dppbz)CoBr₂]. No signals were observed within the ³¹P NMR spectrum gathered. The mass spectrum obtained largely consists of [(dppbz)₂CoBr]⁺₂[Co₂Br₆]²⁻ with a small amount of [(dppbz)ZnBr₂].

³¹P NMR (162 MHz, unlocked, THF): δ_P no signals observed.

Raman (532 nm, cm⁻¹): ν 253m (Co-Br), 300w (Co-Br), 622w (C-C), 703w (C-P), 1006s (C=C), 1034m (C-C), 1098m (C-C), 1590s (C=C).

MS (ASAP⁺, Da): *m/z* 583.966 (19.28% [(dppbz)CoBr]), 587.980 (0.54% [(dbbpz)ZnBr]), 662.881 (26.00% [(dppbz)CoBr₂]), 1030.090 (4.75% [(dppbz)₂CoBr]), 1246.846 (4.21% [(dppbz)₂Co₂Br₃]), 446.118 (17.12% [dppbz]).

Entries 9, 10 and 11:

Entry 9: The ³¹P NMR spectra obtained shows the presence of (dtbpx)ZnBr₂. The Raman and mass spectrum obtained show the presence of (dtbpx)CoBr₂.

³¹P{¹H} NMR (162 MHz, unlocked, THF): δ_P 24.0 (s, [dtbpx]), 18.5 (s, [(dtbpx)ZnBr₂] ppm.

³¹P NMR (Ib = 5 Hz, 162 MHz, unlocked, THF): δ_P 25.1-23.6 (m [dtbpx]), 18.8-18.2 (m, (dtbpx)ZnBr₂) ppm.

Raman (532 nm, cm⁻¹): ν 278m (Co-Br), 580s (C-C), 779m (C-P), 1025w (C=C), 1058m (C-C), 1096-1235s (CH₂ and CH₃), 1474m (C-C), 1603m (C=C).

MS (ASAP⁺, Da): *m/z* 532.122 (2.08% [(dtbpx)CoBr]), 395.280 (29.28% [dtbpx+H]).

Entry 10: The reaction was repeated on a smaller scale and the progress followed by UV-Vis spectroscopy. No signals were observed within the ^{31}P NMR spectrum, however this is likely the result of the dilute concentration used in order to obtain clear UV-Vis spectra. After 20 hours all clear bands corresponding to CoBr_2 in the UV-Vis spectrum has disappeared and were replaced with bands corresponding to $[(\text{dtbpx})\text{CoBr}_2]$. However, the spectral shape within the UV-Vis suggests some small impurity of CoBr_2 remained.

^{31}P NMR (162 MHz, unlocked, THF): δ_{P} no signals observed.

$^{31}\text{P}\{^1\text{H}\}$ NMR (162 MHz, unlocked, THF): δ_{P} no signals observed.

UV-Vis: λ_{max} 659, 699 and 744 nm $[(\text{dtbpx})\text{CoBr}_2]$.

Entry 11: The reaction was repeated and left for 720 hours and the progress followed by UV-Vis spectroscopy. The UV-Vis spectrum show CoBr_2 . The mass spectrum shows the presence of $(\text{dtbpxO})_2\text{Zn}_2\text{Br}$: suggesting the reaction came into contact with oxygen. This oxidation is also displayed within the ^{31}P NMR as peaks corresponding to $(\text{dtbpxO})_2\text{ZnBr}$ were observed. It is likely that partial oxidation of the ligand has prevented formation of a dtbpx cobalt complex.

$^{31}\text{P}\{^1\text{H}\}$ NMR (162 MHz, THF, unlocked): δ_{P} 71.5 (d, $^3J_{\text{PP}}$ 69 Hz, P=O-Zn), 38.8 (d, $^3J_{\text{PP}}$ 68 Hz, P-Zn) ppm.

^{31}P NMR ($\text{lb} = 5$ Hz, 162 MHz, THF, unlocked): δ_{P} 72.1-70.0 (m, P=O-Zn), 39.1-38.3 (m, P-Zn) ppm.

UV-Vis: λ_{max} 596sh, 656sh, 697 nm $[\text{CoBr}_2]$.

MS (ASAP⁺, Da): m/z 873.184 (0.86% $[(\text{dtbpxO})_2\text{ZnBr}]$), 532.125 (2.24% $[(\text{dtbpx})\text{CoBr}]$), 552.968 (0.50% $[(\text{dtbpxO})\text{ZnBr}]$), 395.229 (100% $[\text{dtbpx}+\text{H}]$).

Entry 12:

The ^{31}P NMR spectrum shows $(\text{dtbpx})\text{ZnCl}_2$. The Raman spectrum and mass spectrum show the predominant presence of $(\text{dtbpx})\text{CoCl}_2$. The Raman spectrum contains a species with significant fluorescent character.

^{31}P NMR (162 MHz, C_6D_6): δ_{P} 21.0 (s, $[(\text{dtbpx})\text{ZnCl}_2]$).

^1H NMR (400 MHz, C_6D_6): δ_{H} 8.30 (br s, 1H, $\nu_{1/2}$ 24 Hz, *o*-H), 8.14 (br s, 1H, $\nu_{1/2}$ 14 Hz, *m*-H), 3.63 (br s, $\nu_{1/2}$ 33 Hz, THF), 2.77 (br s, 2H, $\nu_{1/2}$ 12 Hz, CH_2), 1.43 (br s, $\nu_{1/2}$ 21 Hz, THF), 1.34-1.31 (br m, $\nu_{1/2}$ 20 Hz, CH_3).

Raman (532 nm, cm^{-1}): ν 323sh (Co-Cl), 584s (C-C), 785w (C-P), 1041m (C-C), 1060s (C-C), 1187-1239s (CH_2 and CH_3), 1480m (C-C), 1067m (C=C).

MS (ASAP⁺, Da): m/z 555.128 (1.15% [(dtbpxO₂)CoCl₂]), 488.187 (3.89% [(dtbpx)CoCl]), 395.292 (46.00 [dtbpx+H]).

Entry 13:

The reaction was followed by UV-Vis spectroscopy: after 18 hours, only bands associated with (dppp)CoBr₂ were observed. No signals were seen by ³¹P NMR. The Raman and mass spectra obtained suggest only the presence of (dppp)CoBr₂.

³¹P NMR (162 MHz, unlocked, THF): δ_{P} no signals observed.

³¹P{¹H} NMR (162 MHz, unlocked, THF): δ_{P} no signals observed.

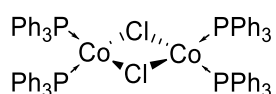
UV-Vis: λ_{max} 620, 663 and 748 nm [(dppp)CoBr₂].

Raman (532 nm, cm^{-1}): ν 283sh (Co-Br), 624m (C-C), 708w (C-P), 1006s (C=C), 1037m (C-C), 1103m (C-C), 1200w (CH_2), 1591m (C=C).

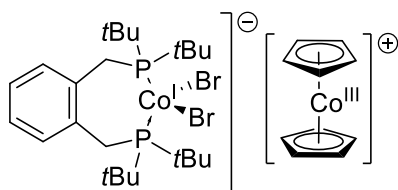
MS (ASAP⁺, Da): m/z 628.897 (64.50% [(dppp)CoBr₂]), 549.982 (49.59% [(dppp)CoBr]), 412.131 (100% [dppp]), 1178.879 (14.52% [(dppp)₂Co₂Br₃]).

6.4.5 Attempted Reductions of (P[^]P)CoX₂ Without Zn

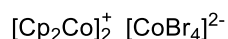
6.4.5.1 Attempted synthesis of [(PPh₃)₂Co(μ -Cl)]₂



THF (30 mL) was added to a Schlenk containing magnesium turnings (0.15 g, 6.17 mmol) and (PPh₃)₂CoCl₂ (0.40 g, 0.62 mmol) and the resulting deep blue mixture stirred at room temperature for 20 hours, after which time the solution colour had deepened and the presence of a black precipitate was noted. Volatile components were removed *in vacuo* to reveal the presence of cobalt(0).

6.4.5.2 Attempted synthesis of $[(dtbpx)CoBr_2]^- [Cp_2Co]^+$:

THF (20mL) was added to a Schlenk containing cobaltocene (0.031 g, 0.163 mmol) and $(dtbpx)CoBr_2$ (0.10 g, 0.163 mmol) and the solution allowed to stir at room temperature for 15 hours. An aliquot (3 mL) was removed for UV-Vis spectroscopic analysis, which revealed a new species present within solution. This aliquot was returned to the bulk solution and all volatile components removed *in vacuo* to yield a dark green solid (0.06 g). Crystals suitable for single crystal X-ray diffraction were grown though layering a solution in DCM with hexanes, and the product found to be:



The Raman spectrum shows one broad peak for Co-Br stretch, shifted to higher wavenumber when compared to $(dtbpx)CoBr_2$. The ^{31}P NMR shows only the presence of free dtbpx ligand. The 1H NMR shows both Cp and dtbpx moieties.

1H NMR (400 MHz, CD_2Cl_2): δ_H 7.53 (br s, 1H, $v_{1/2}$ 14 Hz, *o*-H), 7.04 (br s, 1H, $v_{1/2}$ 13 Hz, *m*-H), 4.43 (br s, $v_{1/2}$ 31 Hz, Cp), 3.04 (s, 2H, CH_2), 1.13 (s, 18 H, CH_3).

^{31}P NMR (162 MHz, CD_2Cl_2): δ_P 26.1 (s, free ligand)

UV-Vis (THF): λ_{max} 618, 635, 648, 677s, 708 nm $[CoBr_4]^{2-}$

Raman (532nm, cm^{-1}): ν 296s (Co-Br), 573s (C-C), 811s (C-C), 945m (C=C), 1045m (C-C), 1178-1212s (C-C), 1508m (C=C).

6.4.5.3 Attempted reduction of $(PNNP-Ph)CoBr_2$ with Sml_2

$(PNNP-Ph)CoBr_2$ (0.10 g, 0.17 mmol) was dissolved in THF and a solution of Sml_2 (1.70 mL, 0.1 M in THF, 0.17 mmol) added dropwise over 5 minutes. An immediate colour change was observed from blue to green and a green precipitate was observed. The reaction was left to stir at room temperature for 16 hours. The resulting deep green precipitate was collected *via* filtration, washed with hexanes and dried *in vacuo*. The resulting deep green solid was analysed by Raman spectroscopy and mass spectrometry, which gave unattributable results.

Raman (532 nm): ν cm^{-1} 306m, 374vs (Sm-I), 422m, 958m, 1276s and 1438m.

MS (ASAP⁺, Da): m/z 457.167 (29.09% [(PNNP-Ph)+H]⁺), 185.041 (40.49%), 217.029 (32.77%), 251.997 (76.75%), 382.985 (83.17%), 437.035 (45.97%), 496.979 (100%).

6.4.5.4 Attempted Reduction of (dtbpx)CoBr₂ with [ZrCp₂]

To a solution of ZrCp₂Cl₂ [0.036 g, 0.12 mmol] in THF (30 mL) at -78 °C, n-butyllithium (0.10 mL, 2.3 M in hexanes, 0.24 mmol) was added dropwise and the solution allowed to warm to 0 °C. Once at 0 °C, the solution containing [ZrCp₂] was added dropwise to a cooled (0 °C) solution of (dtbpx)CoBr₂ (0.15 g, 0.24 mmol) in THF (20 mL). The brown/green reaction mixture was left to stir at 0 °C for 2 hours before warming to room temperature. Volatile components were removed in vacuo to leave a brown residue which was extracted into toluene (60 mL) to yield a green filtrate. Toluene was removed under reduced pressure to leave a brown/yellow sticky solid which was then redissolved in THF to azeotrope the residual toluene. Final drying under reduced pressure yielded a yellow/brown solid 0.08g. Raman and mass spectrometric analysis show little to no reaction has taken place.

Raman (532 nm): ν cm⁻¹ 286m (Co-Br), 580s (C-C), 690m (C-P), 817m (C-C), 945m (C=C), 1059m (C=C), 1234s (CH₂), 1477m (CH₃), 1605m (C=C).

MS (ASAP⁺, Da): m/z 564.111 (5.16% [(dtbpxO₂)CoBr]⁺), 427.264 (100% [dtbpxO₂+H]⁺), 411.273 (20.65% [dtbpxO+H]⁺), 395.273 (40.04% [dtbpx+H]⁺).

6.4.5.5 Attempted synthesis of [(dtbpx)CoBr]₂ via reduction with KC₈

(dtbpx)CoBr₂ (0.10 g, 0.163 mmol) and KC₈ (0.022 g, 0.163 mmol) were suspended in THF (20 mL) and the reaction stirred for 4 hours, after which time black precipitates were observed. Volatile components were removed *in vacuo* and the resulting solids extracted into toluene (40 mL). Toluene was removed under reduced pressure and the resulting solid dried under vacuum. The isolated solid was found to be (dtbpx)CoBr₂ and the black precipitates are presumed to be cobalt(0) and graphite.

The Raman and UV-Vis spectra obtained both show (dtbpx)CoBr₂.

UV-Vis (THF): λ_{\max} 644, 700 and 743 nm [(dtbpx)CoBr₂].

Raman (532 nm): ν cm⁻¹ 275m (Co-Br), 575s (C-C), 688m (C-C), 773w (C-P), 1023w (C=C), 1053s (C-C), 1178-1232s (CH₂ and CH₃), 1469m (C-C), 1600m (C=C).

Chapter 6

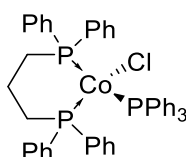
Raman (532 nm): ν cm^{-1} 304m (Co-Cl), 583m (C-C), 696m (C-P), 817s (C-C), 1004s (C=C), 1034m (C-C), 1060 (C-C), 1187-1247s (CH_2 , CH_3), 1477m (C-C), 1590s (C=C), 1608m (C=C).

MS (ASAP⁺, Da): m/z 263.093 (42.91% [PPh_3+H]), 294.071 (100% [PPh_3+2O]), 556.157 (30.01% [$2(\text{PPh}_3+2\text{O})$]), 395.289 (51.30% [$\text{dtbpx}+\text{H}$]).

³¹P NMR (162 MHz, THF, unlocked): δ_{P} no signals observed.

Entry 2:

(dppp)(PPh_3)CoCl: 0.19 g (0.25 mmol, 89%).



UV-Vis (THF): λ_{max} 581s, 640, 693s and 896 nm.

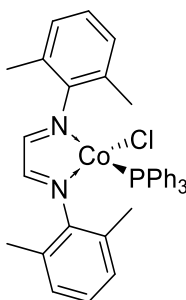
Raman (532 nm): ν cm^{-1} 297m (Co-Cl), 534s (C-C), 624m (C-C), 707w (C-P), 1007s (C=C), 1034m (C-C), 1100s (C-C), 1165-1196w (CH_2), 1590s (C=C).

MS (ASAP⁺, Da): m/z 768.111 (0.03% [M]), 506.035 (1.69% [M- PPh_3+H]), 413.141 (100% [dppp+H]), 263.087 (43.26% [PPh_3+H]).

Entry 3:

(*N,N'*-bis(2,6-dimethylphenyl)-1,2-diiminoethane)(PPh_3)CoCl: 0.14 g (0.23 mmol, 81%)

The UV-Vis spectrum did not show any peaks within the region expected for $d \leftarrow d$ transitions.



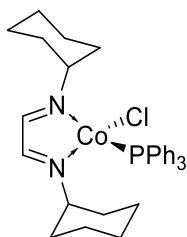
UV-Vis (THF): λ_{\max} 366 nm.

Raman (532 nm): ν cm^{-1} 617w (C-C), 705w (C-P), 1006s (C=C), 1034m (C-C), 1100m (C=C), 1063m (C-C), 1590m (C=C), 1633s (C=N).

MS (ASAP⁺, Da): m/z 586.238 (1.15% [M-Cl+H]), 357.053 (0.11% [M-PPh₃-H]), 323.082 (6.42% [M-Cl-PPh₃]), 263.087 (100% [PPh₃+H]), 264.262 (0.38% [M-PPh₃-Co-Cl+H]).

Entry 4:

(*N,N'*-bis(cyclohexyl)-1,2-diminoethane)(PPh₃)CoCl: 0.16 g (0.27 mmol, 96%).



The Raman spectrum obtained shows a significant fluorescent character which has obscured some peaks, likely the result of the large aliphatic character of the α -diimine in use.

UV-Vis (THF): λ_{\max} 432, 478, 525, 567, 560s and 590s nm.

Raman (532 nm): ν cm^{-1} 268w (PPh₃) 1006s (C=C), 1043m (C-C), 1098m (C-C), 1590s (C=C), 1651w (C=N).

MS (ASAP⁺, Da): m/z 577.105 (0.64% [M+H]), 314.084 (7.78% [M-PPh₃]), 279.081 (88.65% [M-Cl-PPh₃]), 263.086 (100% [PPh₃+H])

6.5 Example μ_{eff} calculations

6.5.1 JME Determination of Effective Magnetic Moment

The effective magnetic moments of selected complexes were determined using Equation 1-Equation 4. The mass magnetic susceptibilities, χ_g , were obtained using a Johnston Matthey Evans' (JME) balance. A sample of the paramagnetic species was packed uniformly into a Gouy tube and the sample weight and height accurately measured. The JME balance was zeroed before each use and a sample of $(\text{NH}_4)_2\text{Fe}(\text{SO}_4)_2 \cdot 6\text{H}_2\text{O}$ used to calibrate the machine at the measured temperature (K).

$$\chi_g = \frac{C l (R - R_0)}{10^7 \cdot m}$$

Equation 1 Equation for determining the mass magnetic susceptibility (χ_g) where C = calibration constant determined using $(\text{NH}_4)_2\text{Fe}(\text{SO}_4)_2 \cdot 6\text{H}_2\text{O}$, l = sample length, R = JME reading for the paramagnetic species, R_0 = JME reading for empty Gouy tube, and m = mass of paramagnetic sample present in the Gouy tube.³¹

$$\chi'_M = \chi_g \times RMM$$

Equation 2 Equation for determining the uncorrected molar magnetic susceptibility (χ_M) where χ_g = mass magnetic susceptibility and RMM = relative molecular mass of paramagnetic species.³¹

$$\chi_M = \chi'_M + \chi_D$$

Equation 3 Equation for determining the corrected molar magnetic susceptibility (χ_M) where χ'_M = uncorrected molar magnetic susceptibility, and χ_D = diamagnetic contribution.³¹

$$\mu_{\text{eff}} = 797.5(\chi_M T)^{1/2}$$

Equation 4 Equation for determining the effective magnetic moment (μ_{eff}) where χ_M = corrected molar magnetic susceptibility, and T = temperature (K).³¹

An example calculation for the effective magnetic moment (μ_{eff}) of $(\text{dppb})\text{CoCl}_2$. Details used within the calculation can be found in **Table 6.11** below.

Table 6.11 JME readings and sample details used within the example μ_{eff} calculation

	$(\text{NH}_4)_2\text{Fe}(\text{SO}_4)_2 \cdot 6\text{H}_2\text{O}$	$(\text{dppb})\text{CoCl}_2$
Path length (mm)	36	34
Temperature ($^{\circ}\text{C}$)	16	16
Sample Weight (mg)	-	46
Molecular mass (g mol^{-1})	392.14	556.31
JME measurement	1155	176

a) Calibration constant, C , using standard $(\text{NH}_4)_2\text{Fe}(\text{SO}_4)_2 \cdot 6\text{H}_2\text{O}$:

$$\chi_g \text{ at } 20^{\circ}\text{C} = 4.059 \times 10^{-7} \text{ m}^3 \text{ kg}^{-1}$$

$$\chi_g \text{ at } 16^{\circ}\text{C} = \frac{1.194}{274 + 16} \times 10^{-4} \text{ m}^3 \text{ kg}^{-1}$$

$$\chi_g \text{ at } 16^{\circ}\text{C} = 4.117 \times 10^{-7} \text{ m}^3 \text{ kg}^{-1}$$

$$4.117 \times 10^{-7} \text{ m}^3 \text{ kg}^{-1} = \frac{C \times 3.6 \times 10^{-2} \text{ m} (1155 - (-34))}{10^7 \times 1.566 \times 10^{-4} \text{ kg}}$$

$$C = 1.508 \times 10^{-5} \text{ m}^2$$

b) Mass susceptibility, χ_g , for sample $(\text{dppb})\text{CoCl}_2$:

$$\chi_g = \frac{C l (R - R_0)}{10^7 \cdot m}$$

$$\chi_g = \frac{1.508 \times 10^{-5} \text{ m}^2 \times 3.4 \times 10^{-2} \text{ m} (176 - (-34))}{10^7 \times 4.62 \times 10^{-5} \text{ kg}}$$

$$\chi_g = 2.33 \times 10^{-7} \text{ m}^3 \text{ kg}^{-1}$$

c) Molar susceptibility, χ_M :

$$\chi'_M = \chi_g \times RMM$$

$$\chi'_M = 2.33 \times 10^{-7} \text{ m}^3 \text{ kg}^{-1} \times 0.556 \text{ kg mol}^{-1}$$

$$\chi'_M = 1.296 \times 10^{-7} \text{ m}^3 \text{ mol}^{-1}$$

d) Diamagnetic Correction, χ_D :

$$\chi_D[(\text{dppb})\text{CoCl}_2] = \sum n(\chi_D[\text{Co}^{2+}, \text{PPh}_3, \text{Cl}^-])$$

$$\chi_D[(\text{dppb})\text{CoCl}_2] = 4.977 \times 10^{-9} \text{ m}^3 \text{ mol}^{-1}$$

e) Corrected molar susceptibility, χ_M' :

$$\chi_M = \chi_M' + \chi_D[(dppb)CoCl_2]$$

$$\chi_M = 1.296 \times 10^{-7} \text{ m}^3 \text{ mol}^{-1} + 4.977 \times 10^{-9} \text{ m}^3 \text{ mol}^{-1}$$

$$\chi_M = 1.346 \times 10^{-7} \text{ m}^3 \text{ mol}^{-1}$$

f) Effective magnetic moment, μ_{eff} :

$$\mu_{\text{eff}} = 797.5(\chi_M T)^{1/2}$$

$$\mu_{\text{eff}} = 797.5 (1.346 \times 10^{-7} \text{ m}^3 \text{ mol}^{-1} \times 290 \text{ K})^{1/2}$$

$$\mu_{\text{eff}} = 4.98 \mu_B \text{ at } 16^\circ \text{C}$$

6.5.2 Evans' Spectroscopic NMR Method for Determination of Effective Magnetic Moment

The effective magnetic moment of selected (P[^]P)CoX₂ were determined using the equations below. The mass magnetic susceptibilities, χ_a , were obtained *via* the Evans NMR method.³² 1 mL of a solution of known concentration of the sample in CDCl₃ was transferred to a Young's tap NMR tube which contained a sealed capillary filled with CDCl₃. A ¹H NMR spectrum (400 MHz) was recorded of the sample and $\Delta\nu$ (Equation 5) obtained.

$$\mu_{\text{eff}} = \sqrt{\frac{3k\chi_m T}{N_A}} = 2.828\sqrt{\chi_m T}$$

Equation 5 Equation for determining the effective magnetic moment (μ_{eff}) where k = Boltzmann constant, χ_m = molar magnetic susceptibility, T = temperature (K), and N_A = Avogadro constant.³²

$$\chi_m = \chi_m' - \chi_D$$

Equation 6 Equation for determining molar magnetic susceptibility (χ_m) where χ_m' = uncorrected molar magnetic susceptibility and χ_D = diamagnetic contribution.^{32,33}

$$\chi_m' = \chi_g \times RMM$$

Equation 7 Equation for determining the uncorrected molar magnetic susceptibility (χ_m') where χ_g = mass magnetic susceptibility and RMM = relative molecular mass of paramagnetic species.^{32,33}

$$\chi_g = \frac{\Delta\nu}{sF\nu c} + \chi_o$$

Equation 8 Equation for determining the mass magnetic susceptibility (χ_g) where $\Delta\nu$ = frequency difference (Hz) in ^1H NMR spectrum of paramagnetic species between residual solvent resonance for the bulk solvent and the standard present within the seal capillary, sF = shape factor (equal to $4\pi/3$ for a cylindrical sample in a superconducting NMR spectrometer), ν = spectrometer frequency (Hz), c = concentration of sample in NMR tube, and χ_o = mass susceptibility of solvent.

6.6 References

- 1 G. R. Fulmer, A. J. M. Miller, N. H. Sherden, H. E. Gottlieb, A. Nudelman, B. M. Stoltz, J. E. Bercaw and K. I. Goldberg, *Organometallics*, 2010, **29**, 2176–2179.
- 2 G. M. Sheldrick, *Acta Crystallogr. Sect. A Found. Crystallogr.*, 2007, **64**, 112–122.
- 3 O. V. Dolomanov, L. J. Bourhis, R. L. Gildea and H. Howard, J. A. K. Puschmann, *J. Appl. Crystallogr.*, 2009, **42**, 339–341.
- 4 Cambridge Structure. Database, <http://webcsd.ccdc.cam.ac.uk/index.php>, Nov 2019.
- 5 L. Falivene, Z. Cao, A. Petta, L. Serra, A. Poater, R. Oliva, V. Scarano and L. Cavallo, *Nat. Chem.*, 2019, **11**, 872–879.
- 6 J. Kukral, P. Lehmus, M. Klinga, M. Leskelä and B. Rieger, *Eur. J. Inorg. Chem.*, 2002, 1349–1356.
- 7 H. G. Alt, *J. Organomet. Chem.*, 1994, **472**, 113–118.
- 8 M. T. Honaker, B. J. Sandefur, J. L. Hargett, A. L. McDaniel and R. N. Salvatore, *Tetrahedron Lett.*, 2003, **44**, 8373–7377.
- 9 D. Crich, Ed., *Handbook of Reagents for Organic Synthesis, Reagents for Radical and Radical Ion Chemistry*, John Wiley and Sons, Online Edi., 2013, p580-598.
- 10 A. A. M. Ali, B. D. El-issa and N. I. Swiedan, *Phosphorus, Sulfur Relat. Elem.*, 1985, **24**, 311–319.
- 11 P. Jutzi and J. Dahlhaus, *Synthesis (Stuttg.)*, 1993, 684–686.
- 12 M. Helms and H. Fullbier, *J. Pract. Chem.*, 1986, **328**, 643–647.
- 13 A. Antiñolo, R. Fernández-Galán, A. Otero, S. Prashar, I. Rivilla, A. M. Rodríguez and M. A. Maestro, *Organometallics*, 2004, **23**, 5108–5111.
- 14 F. Taullaj, D. Armstrong, A. J. Lough and U. Fekl, *Polyhedron*, 2016, **108**, 30–35.
- 15 P. M. Nedorezorva, E. N. Veksler, E. S. Novikova, V. A. Optov, A. O. Baranov, A. M. Aladyshev, V. I. Tsvetkova, B. F. Shklyaruk, A. V. Churakov, L. G. Kuz'mina and J. A. K. Howard, *Russ. Chem. Bull. Int. Ed.*, 2005, **54**, 400–413.
- 16 E. V. Shulishov, O. A. Pantyukh, L. G. Menchikov and Y. V. Tomilov, *Tetrahedron Lett.*, 2019, **60**, 2043–2045.
- 17 Z. Rohlík, P. Holzhauser, J. Kotek, J. Rudovský, I. Němec, P. Hermann and I. Lukeš, *J. Organomet. Chem.*, 2006, **691**, 2409–2423.

Chapter 6

- 18 A. Doppiu, U. Englert and A. Salzer, *Chem. Commun.*, 2004, 2166–2167.
- 19 A. C. McConnell, P. J. Pogorzelec, A. M. Z. Slawin, G. L. Williams, P. I. P. Elliott, A. Haynes, A. C. Marr and D. J. Cole-Hamilton, *Dalton Trans.*, 2006, 91–107.
- 20 S. A. Frith and J. L. Spencer, *Inorganic Synthesis*, Wiley-Interscience, Vol. 23., 1985, p272.
- 21 D. M. Roe and P. M. Maitlis, *J. Chem. Soc. A*, 1971, 3173–3175.
- 22 R. A. Genetti and M. D. Rausch, *J. Org. Chem.*, 1970, **35**, 3888–3897.
- 23 O. Crichton, D. J. Taylor and J. Rest, Antony, *J. Chem. Soc. Dalton Trans.*, 1980, 167–173.
- 24 C. Kaya, D. Karaka and E. Üstün, *Indian J. Chem.*, 2007, **46A**, 1388–1392.
- 25 A. A. Fomichov, N. S. Prostakov and S. O. Lawani-Edogiawerie, *Org. Magn. Reson.*, 1983, **21**, 310–314.
- 26 M. Aresta, M. Rossi and A. Sacco, *Inorganica Chim. Acta*, 1969, **3**, 227–231.
- 27 R. L. Carlin, R. D. Chirico, E. Sinn, G. Mennenga and L. J. de Jongh, *Inorg. Chem.*, 1982, **21**, 2218–2222.
- 28 S. M. Jing, V. Balasanthiran, V. Pagar, J. C. Gallucci and T. V. RajanBabu, *J. Am. Chem. Soc.*, 2017, **139**, 18034–18043.
- 29 A. K. Mondal, M. Sundararajan and S. Konar, *Dalton Trans.*, 2018, **47**, 3745–3754.
- 30 T. Fanjul, G. Eastham, N. Fey, A. Hamilton, A. G. Orpen, P. G. Pringle and M. Waugh, *Organometallics*, 2010, **29**, 2292–2305.
- 31 D. F. Evans, *J. Phys. E.*, 1974, **7**, 247–249.
- 32 D. F. Evans, *J. Chem. Soc.*, 1959, **0**, 2003–2005.
- 33 D. F. Evans, G. V. Fazakerley and R. F. Phillips, *J. Chem. Soc. A Inorganic, Phys. Theor.*, 1971, **0**, 1931–1934.

CHAPTER 7

Appendices and
Supplementary Information

7.1 Appendices

7.1.1 Conferences: Contributions and Prizes

Chemistry PG Gala: Annual Postgraduate Symposium
15th June 2017, University of Durham, UK

Catalysis Fundamentals and Practice Summer School - Applied Catalysis Group RSC
17th-21st July 2017, University of Liverpool, UK

USIC-2017: The 51st Universities of Scotland Inorganic Chemistry Conference
29th-30th August 2017, University of St Andrews, Scotland

EWPC-15: The 15th European Workshop in Phosphorus Chemistry
14th-16th March 2018, Uppsala, Sweden

Poster Presentation: *“Homogeneous Systems for Selective Olefin Oligomerisation – Synthetic Routes towards Bidentate, Mixed-functional (L₂X^ΛL) Ligands”*

Chemistry PG Gala: Annual Postgraduate Symposium
21st June 2018, University of Durham, UK

Poster Presentation: *Homogeneous Systems for Selective Olefin Oligomerisation – Structural and spectroscopic investigations into (P^ΛP)CoX₂ precatalysts”*

Prize: Best L3 Inorganic Demonstrator (£100)

Scottish Regional Dalton Meeting - RSC
2nd July 2018, University of Durham, UK

USIC-2018: The 52nd Universities of Scotland Inorganic Chemistry Conference
3rd-4th September 2018, University of Edinburgh, Scotland

Oral Presentation: *“Synthetic Routes to Cobalt Half-Sandwich Complexes for Olefin Oligomerisation Catalysis”*

EWPC-16: The 16th European Workshop in Phosphorus Chemistry
24th-26th April 2019, University of Bristol, UK

Oral Presentation: *“Investigating the Reactivity and Reduction Chemistry of Cobalt Diphosphine Complexes”*

Sir Geoffrey Wilkinson Poster Symposium 2019 - RSC Dalton Division
30th April 2019, RSC, Burlington House, London, UK

Poster and Flash Presentations: *“Synthetic Routes To Cobalt Half-sandwich Complexes for Olefin Oligomerisation”*

Prize: Best Poster Presentation (£800 conference travel budget)

North East Regional Dalton Meeting – RSC
13th June 2019, University of York, UK

Oral Presentation: *“Investigating the Reduction and Reactivity of Cobalt Diphosphine Complexes”*

Prize: Best Oral Presentation

Chemistry PG Gala: Annual Postgraduate Symposium
21st June 2019, University of Durham, UK

Oral Presentation: *“Zinc: NOT always what you think!”*

UK-Spain Organometallic Chemistry Symposium

17th-19th September 2019, Alcalá de Henares, Spain

Oral Presentation: “Investigating the Reduction and Reactivity of Cobalt Diphosphine Complexes”

PBSi-2019: International Conference on Phosphorus, Boron and Silicon

2nd-4th December 2019, **Rome, Italy**

Oral Presentation: “Cobalt Diphosphine Complexes: Reduction and Reactivity”

7.1.2 Seminars attended

Synthesis of conjugated polymers for organic electronics: Making use of the triplet excited state

Dr Hugo Bronstein, University of Cambridge, UK, 19th October 2016

Substituent effects on TADF molecules for OLED applications

Dr Jonathon Ward, University of Durham, UK, 21st October 2016

Sodiumphosphaethynolate Na(OCP) as a building block

Dr Dominikus Heift, University of Durham, UK, 21st October 2016

Watching reactions take place at the atomic scale (and learning from them)

Dr Neema Sharma, University of New South Wales, Australia, 26th October 2016

New luminescent platinum and palladium complexes of 1,2,4-triazole and tetrazole ligands

Melissa Walden, University of Durham, UK, 18th November 2016

The Synthesis and Analysis of Potential Histone Deacetylase Inhibitors from Piano-Stool Complexes

Jasmine Cross, University of Durham, UK, 18th November 2016

Heterogeneous Ethylene trimerisation Catalysis: Probing Catalytic Behaviour and Reaction

Mechanism

Michael Lamb, University of Durham, UK, 18th November 2016

Diarylhydrazide-bridged cyclometalated diiridium phosphors and their matrix-dependent emission properties

Daniel Congrave, University of Durham, UK, 18th November 2016

Molecular porous materials – Heterogeneous gas storage, separation and catalysis

Dr Shan Jiang, University of Durham, UK, 25th November 2016

HD or not HD? That is the question

Dr Alan Kenwright, University of Durham, UK, 25th November 2016

When is a silk not a silk? How rheology has opened a can of worms for silk/melt processing

Dr Chris Holland, University of Sheffield, UK, 7th December 2016

Highly substituted pyrrolidines: From anti-cancer ETP-Alkaloid analogues to new diastereoselective trifluoro-acetylation reactions

Dr Marcus Baumann, University of Durham, UK, 9th December 2016

Proton coupled mixed valency and arene exchange catalysis

Dr Luke Wilkinson, University of Durham, UK, 9th December 2016

Nanoscale structures from supramolecular assembly of molecular magnets

Prof. Richard Winpenny, University of Manchester, UK, 25th January 2017

Ionic liquids – Solvents for sustainable chemistry

Prof. Tom Welton, Imperial College London, UK, 6th February 2017

Imposter Syndrome: Floating to Professor on a Magic Carpet of Success

Prof. Tom Welton, Imperial College London, UK, 6th February 2017

Developing heterobimetallic hydrides for catalysis

Dr Mark Crimmin, Imperial College London, UK, 8th February 2017

Using narrow carbon nanoreactors to explore chemistry at the molecular/atomic level

Dr Thomas Chamberlin, University of Leeds, UK, 10th February 2017

Catalytic biomass conservation in lignocellulosic bio-refineries

Prof. Bert Sels, Katholieke Universiteit te Leuven, Belgium, 15th March 2017

Exploiting the 'chemical memory' of materials to create new processes

Prof. Ian Metcalfe, University of Newcastle, 10th May 2017

Regioselective Functionalization of Aromatic and Heteroaromatic Compounds using Organometallic Reagents

Prof. Giuliano Clososki, Universidade de São Paulo, Brazil, 29th September 2017

Investigations of halide perovskites for optoelectronic applications: Tuning Properties and Searching for Environmentally Benign Alternatives

Prof. Patrick Woodward, Ohio State University, USA, 11th October 2017

Appendices and Supplementary Information

Casting Iron in softer catalytic roles

Prof. Robin Bedford, University of Bristol, UK, 25th October 2017

Structure-activity relationship in heterogeneous catalysis

Dr Justine Harmel, Utrecht University, Netherlands, 30th October 2017

Disorder in inorganic solids – exploiting multinuclear NMR spectroscopy and DTF calculations

Prof. Sharon Ashbrooke, University of St Andrews, UK, 1st November 2017

Harnessing non-covalent interactions for control of regioselectivity and site selectivity in catalysis

Dr Robert Phipps, University of Cambridge, UK, 14th February 2018

Asking questions in copper catalysis

Dr Allan Watson, University of St Andrews, UK, 28th February 2018

Bristol ChemLabS Outreach programme

Dr Tim Harrison, University of Bristol, UK, 5th April 2018

Regioselective borylation of heterocycles

Jay Wright, University of Durham, UK, 4th May 2018

New materials for a new age

Prof. Nicola Spaldin, ETH Zürich, Switzerland, 4th June 2018

From materials to cosmology – studying the early universe under the microscope

Prof. Nicola Spaldin, ETH Zürich, Switzerland, 5th June 2018

Hidden magnetoelectric multipoles in multiferronics and superconductors

Prof. Nicola Spaldin, ETH Zürich, Switzerland, 7th June 2018

Computational discovery of new materials

Dr Kim Jelfs, Imperial College London, UK, 16th January 2019

Designing new metal complexes and hybrid nanomaterials for multimodal imaging techniques

Prof. Sofia Pascu, University of Bath, UK, 30th January 2019

Theory meets experiments: The chemistry of P-containing anions

Dr Zoltán Benkő, Budapest University of Technology and Economics, Hungary, 31st January 2019

Cooperative catalysis – from frustrated Lewis pairs to advanced biofuels

Prof. Duncan Wass, University of Cardiff, UK, 20th February 2019

Changing the landscape: prospects for NMR and MRI through SABRE

Prof. Simon Duckett, University of York, UK, 27th February 2019

Teflon-coated molecules: electronic structure and reactivity

Prof. Linda Doerrer, Boston University, UK, 20th March 2019

Exploring computation with chemical reactions

Prof. Lee Cronin, University of Glasgow, UK, 1st May 2019

Synthesis and applications of Diamond

Prof. Mike Ashfold, University of Bristol, UK, 11th June 2019

The versatility of and joy in using ion-mobility mass spectrometry to measure protein structures and to diagnose Parkinson's disease

Prof. Perdita Barron, University of Manchester, UK, 12th June 2019

Probing the chemical physics of diamond chemical vapour deposition

Prof. Mike Ashfold, University of Bristol, UK, 12th June 2019

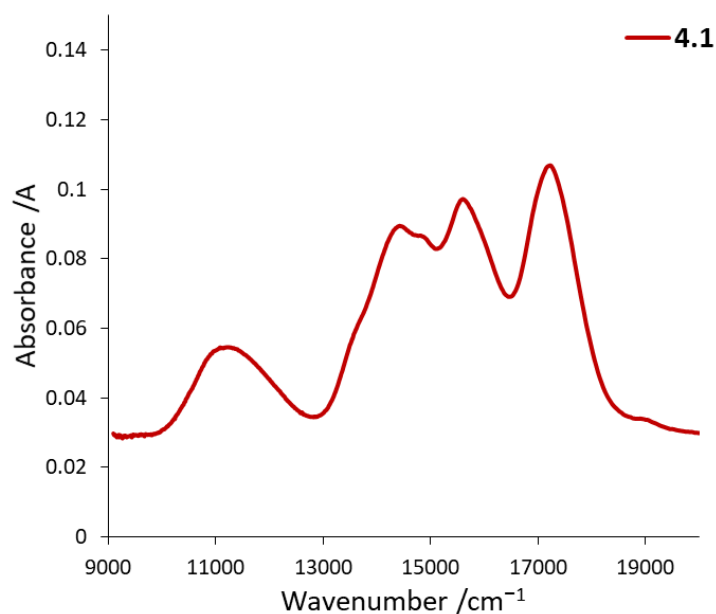
7.2 Supplementary Information:

7.2.1 UV-Vis and Raman Spectroscopic data for diphosphine Cobalt(I) Complexes

Table S1 Successful single-electron reductions of (P[^]P)CoX₂ complexes with Zn metal in THF.

Entry	(P [^] P)CoX ₂ Complex	Eq. Zn	Time /h	Temp. /°C	Product
1	3.4c (dppp)CoCl ₂	5	18	25	4.1 + 3.4c
2	3.4d (dppp)CoBr ₂	5	18	25	4.2 + 3.4d
3 ^a	3.4d (dppp)CoBr ₂	5	144	25	CoBr ₂ [*]
4 ^b	3.4d (dppp)CoBr ₂	10	1	25	4.2
5 ^c	3.4c (dppb)CoCl ₂	10	64	25	Co ⁰ _(s)
6	3.4e (dppb)CoCl ₂	5	48	40	4.3
7	3.4f (dppb)CoBr ₂	5	24	25	4.4
8 ^d	3.4a (dppm)CoBr ₂	5	4	25	4.5b
9	3.6f (dppx)CoBr ₂	5	18	25	4.6
10	3.7b (PNNP-Ph)CoBr ₂	1	18	25	4.7
13 ^{b,f}	3.6b (dtbpx)CoBr ₂	10	30 min	25	4.8

^aUV-Vis scale reaction, ^b1:1 MeOH:THF, ^cToluene added after 16 hours, ^dMixed valence dimer produced due partial reduction: BrCo(μ₂-dppm)₂(μ₂-Br)CoBr, ^etoluene, ^fPartial reduction only: discussed in text. *as determined by UV-Vis spectroscopic analysis.

**Figure S1** UV-Vis (THF) spectrum of [(dppp)CoCl]₂ (**4.1**).

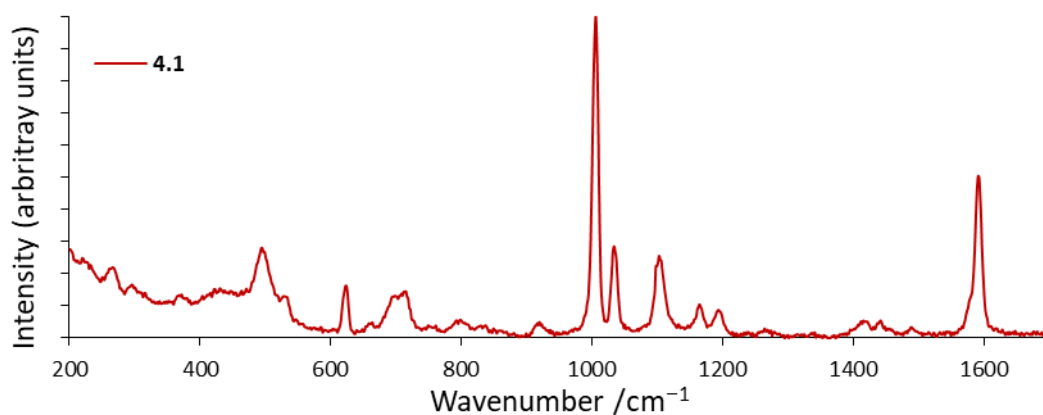


Figure S2 Raman (LIR, 532 nm) spectra of $[(\text{dppp})\text{CoCl}]_2$ (**4.1**).

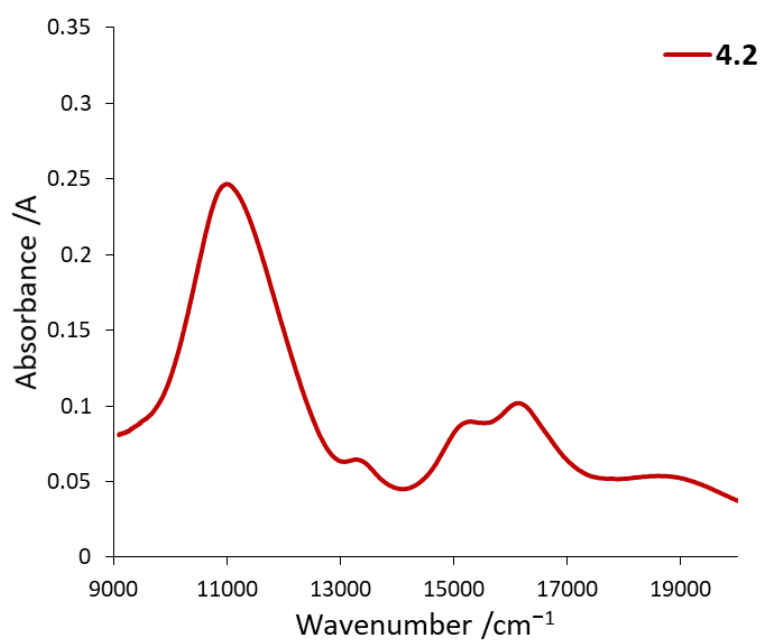


Figure S3 UV-Vis (THF) spectrum of $[(\text{dppp})\text{CoBr}]_2$ (**4.2**) prepared from $(\text{dppp})\text{CoBr}_2$ (**3.4d**) with 10 eq. Zn in THF.

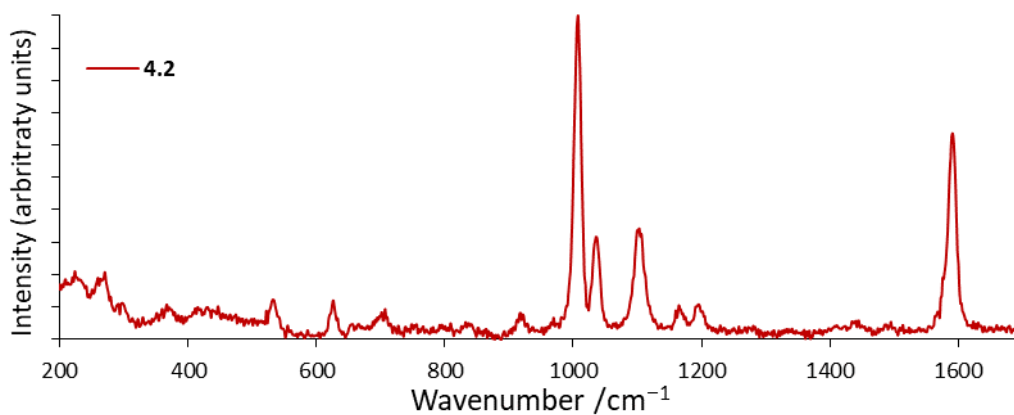


Figure S4 Raman (LIR, 532 nm) spectrum of $[(\text{dppp})\text{CoBr}]_2$ (**4.2**) prepared from $(\text{dppp})\text{CoBr}_2$ (**3.4d**) with 10 eq. Zn in THF.

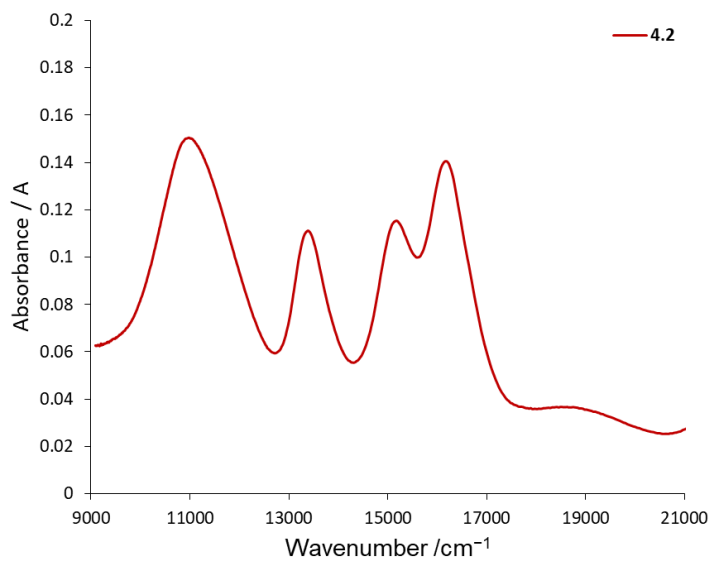


Figure S5 UV-Vis (THF) spectrum of [(dppp)CoBr₂] (**4.2**) prepared from (dppp)CoBr₂ (**3.4d**) with 5 eq. Zn in THF:MeOH.

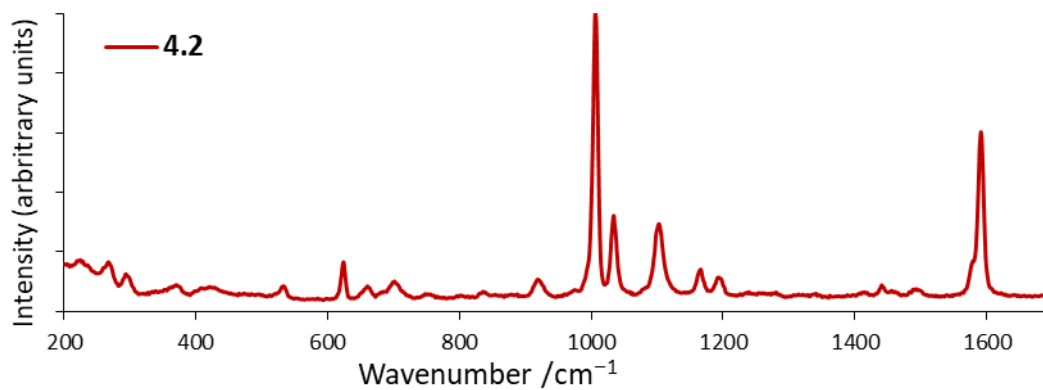


Figure S6 Raman (LIR, 532 nm) spectrum of [(dppp)CoBr₂] (**4.2**) prepared from (dppp)CoBr₂ (**3.4d**) with 5 eq. Zn in THF:MeOH.

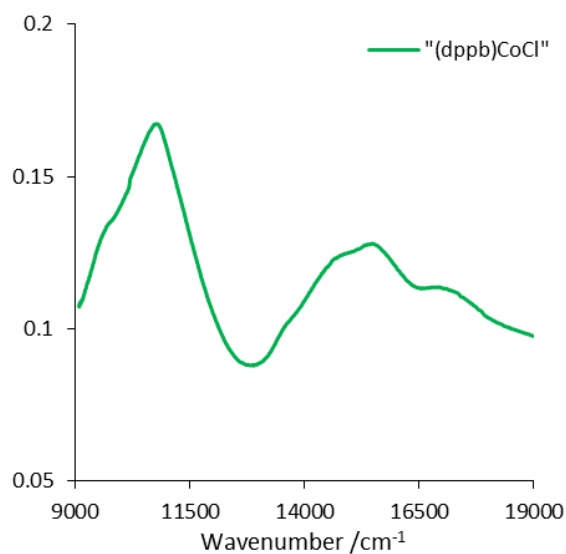


Figure S7 UV-Vis (THF) spectrum of [(dppb)CoCl]₂ (**4.3**).

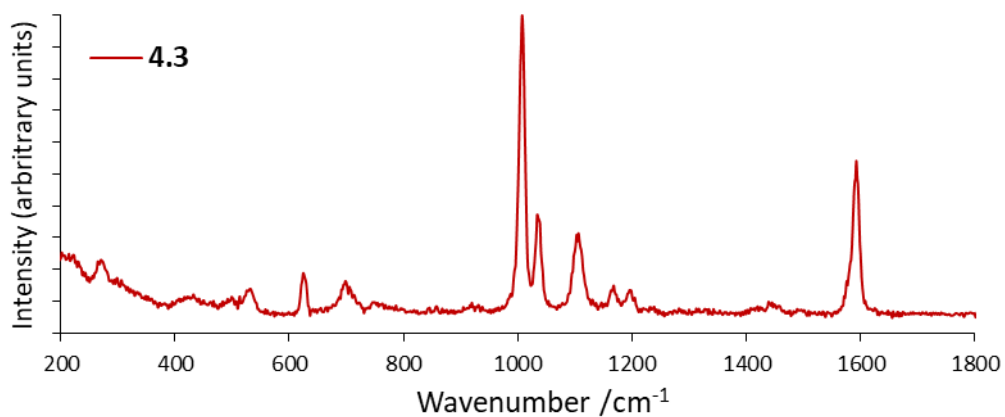


Figure S8 Raman (LIR, 532 nm) spectrum of $[(dppb)CoCl]_2$ (4.3).

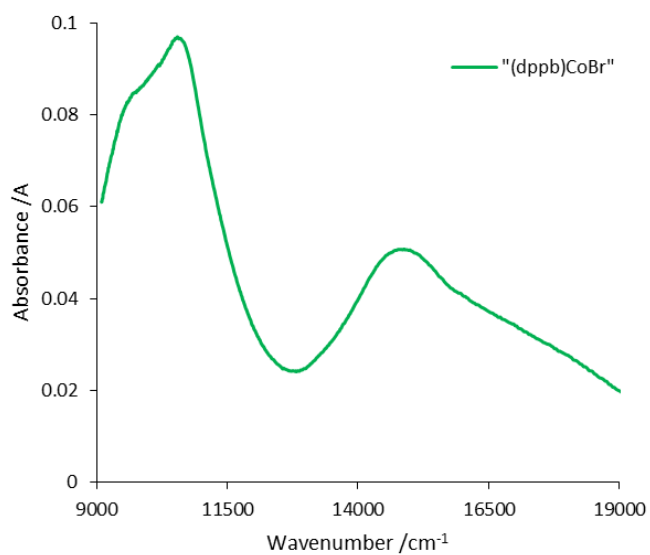


Figure S9 UV-Vis (THF) spectrum of $[(dppb)CoBr]_2$ (4.4).

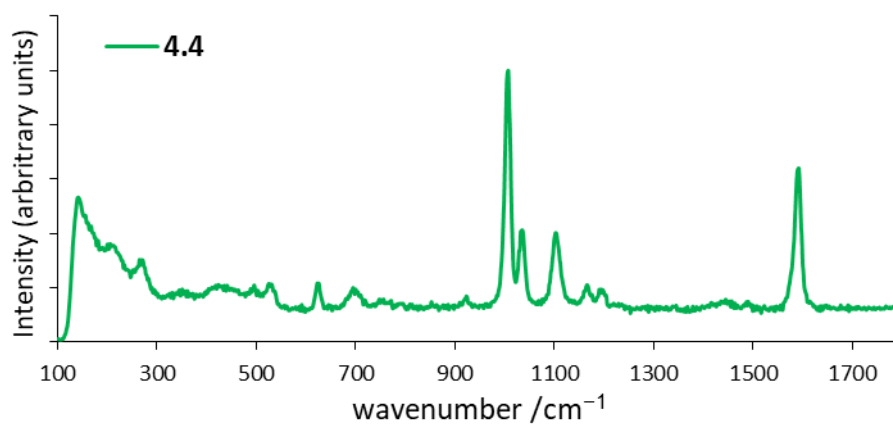


Figure S10 Raman (LIR, 532 nm) spectrum of $[(dppb)CoBr]_2$ (4.4).

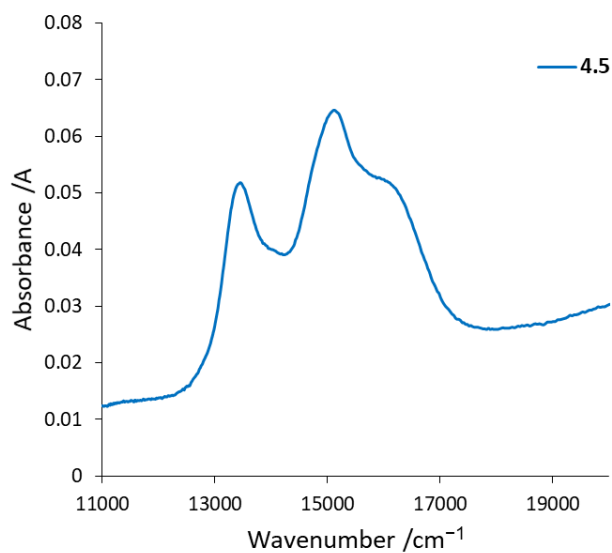


Figure S11 UV-Vis (THF) spectrum of [BrCo(μ₂-dppm)₂(μ₂-Br)CoBr] (4.5).

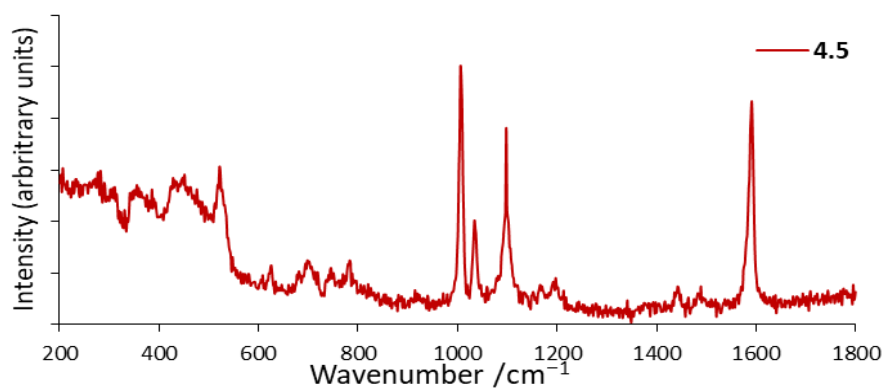


Figure S12 Raman (LIR, 532 nm) spectrum of [BrCo(μ₂-dppm)₂(μ₂-Br)CoBr] (4.5).

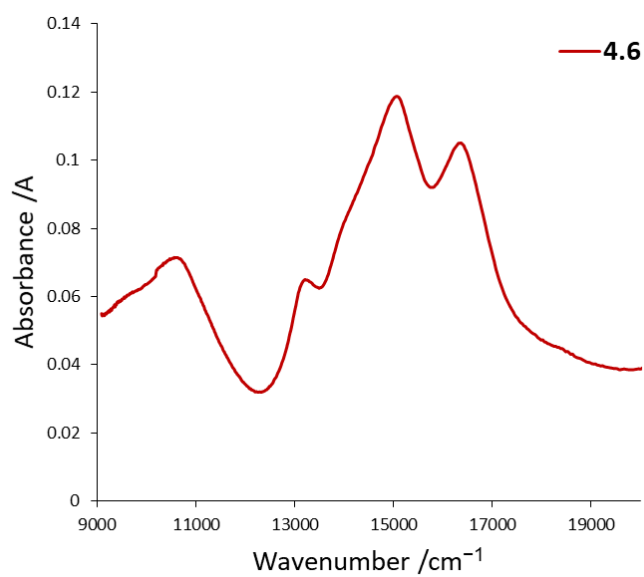


Figure S13 UV-Vis (THF) spectrum of [(dppx)CoBr]₂ (4.6).

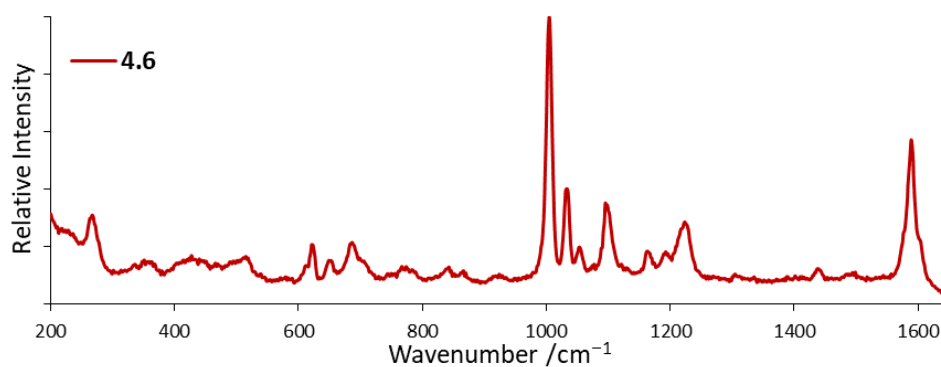


Figure S14 Raman (LIR, 532 nm) spectrum of [(dppx)CoBr]₂ (**4.6**).

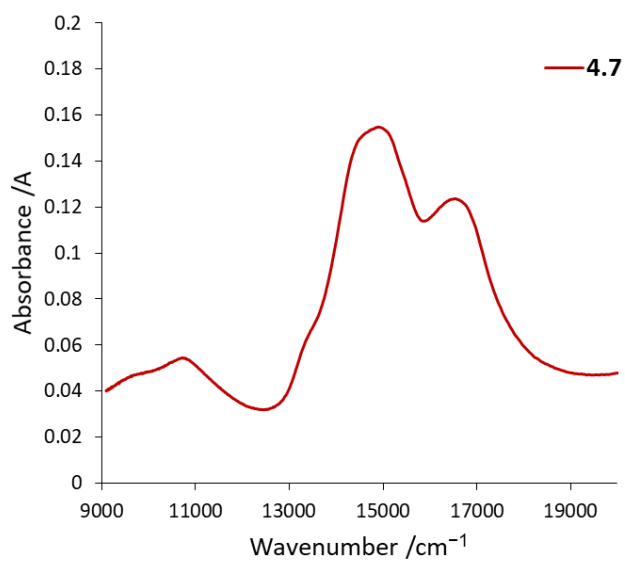


Figure S15 UV-Vis (THF) spectrum of [(PNNP-Ph)CoBr]₂ (**4.7**).

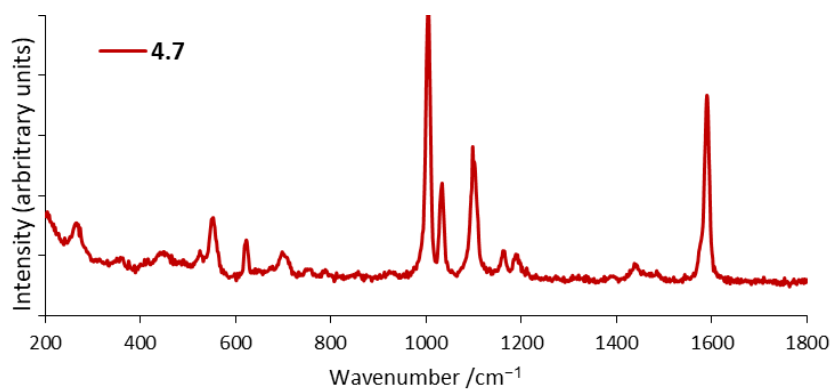


Figure S16 Raman (LIR, 532 nm) spectrum of [(PNNP-Ph)CoBr]₂ (**4.7**).

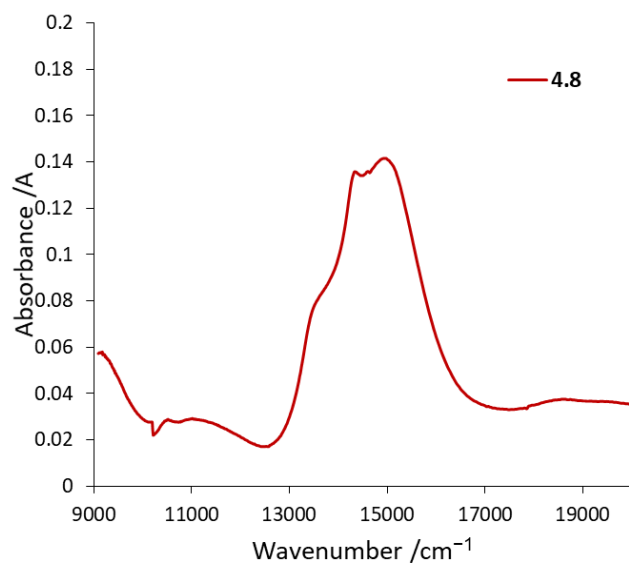


Figure S17 UV-Vis (THF) spectrum of [(dtbpx)CoBr₂]₂ (**4.8**).

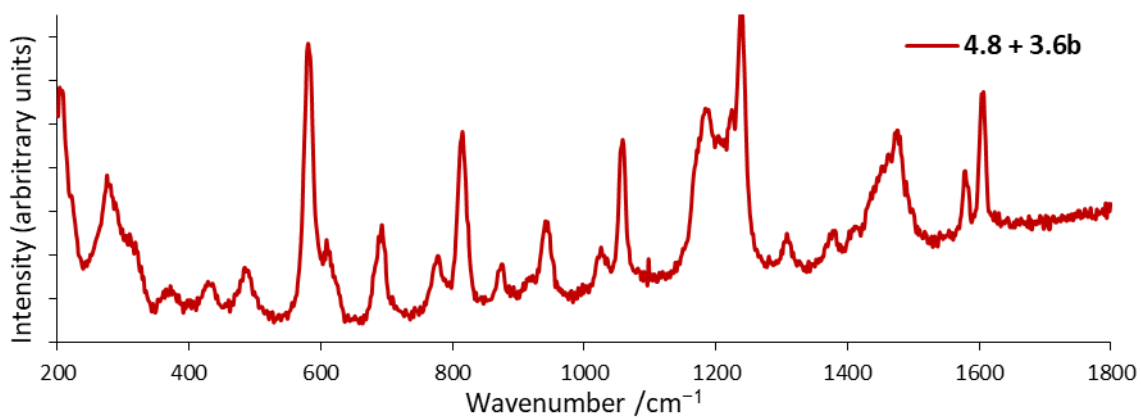


Figure S18 Raman (LIR, 532 nm) spectrum of the mixture of [(dtbpx)CoBr₂]₂ (**4.8**) and (dtbpx)CoBr₂ (**3.6b**).

7.2.2 Crystallographic Data

Complex	2.17a Cp*Co(CO) ₂	2.18 Cp*Co(I) ₂ (CO)·I ₂	2.19b Cp*Co(μ ₂ -I)CoCp*	2.22 [(CHD)(CO)Co(μ ₂ -CO)] ₂
<i>Identifier code</i>	17srv125	17srv139	17srv170	17srv109
<i>Empirical formula</i>	C ₁₂ H ₁₅ CoO ₂	C ₁₁ H ₁₅ CoI ₃ O	C ₂₀ H ₃₀ Co ₂ I ₆	C ₁₆ H ₁₆ Co ₂ O ₄
<i>Formula weight</i>	250.17	602.86	1149.70	390.15
<i>Temperature/K</i>	120	120	200	120.0
<i>Crystal system</i>	monoclinic	triclinic	monoclinic	orthorhombic
<i>Space group</i>	P2 ₁ /n	P-1	P2 ₁ /c	Cmcm
<i>a/Å</i>	7.3504(4)	7.5902(12)	12.6838(6)	9.8643(7)
<i>b/Å</i>	10.5413(5)	8.1706(13)	13.9516(6)	7.7748(5)
<i>c/Å</i>	15.1601(7)	13.949(2)	17.1423(8)	18.7627(13)
<i>α/°</i>	90	79.579(7)	90	90
<i>β/°</i>	98.054(2)	85.468(7)	100.1652(17)	90
<i>γ/°</i>	90	66.473(6)	90	90
<i>Volume/Å³</i>	1163.06(10)	780.0(2)	2985.9(2)	1438.97(17)
<i>Z</i>	4	2	4	4
<i>ρ_{calc}/cm³</i>	1.429	2.567	2.558	1.801
<i>μ/mm⁻¹</i>	1.452	7.017	7.321	2.319
<i>F(000)</i>	520.0	550.0	2088.0	792.0
<i>Crystal size/mm³</i>	0.345 × 0.225 × 0.128	0.348 × 0.324 × 0.046	0.323 × 0.178 × 0.092	0.3 × 0.22 × 0.18
<i>Radiation</i>	MoKα (λ = 0.71073)	MoKα (λ = 0.71073)	MoKα (λ = 0.71073)	MoKα (λ = 0.71073)
<i>2θ range for data collection/°</i>	4.722 to 67.43	5.512 to 60.292	4.378 to 56.564	6.672 to 59.998
<i>Index ranges</i>	-11 ≤ h ≤ 11, -16 ≤ k ≤ 10, -23 ≤ l ≤ 21	-10 ≤ h ≤ 10, -11 ≤ k ≤ 11, -19 ≤ l ≤ 19	-16 ≤ h ≤ 16, -18 ≤ k ≤ 18, -22 ≤ l ≤ 22	-13 ≤ h ≤ 13, -10 ≤ k ≤ 10, -26 ≤ l ≤ 26
<i>Reflections collected</i>	18088	9426	58547	13157
<i>Independent reflections</i>	4581 [R _{int} = 0.0354, R _{sigma} = 0.0407]	4476 [R _{int} = 0.0457, R _{sigma} = 0.0662]	7397 [R _{int} = 0.0349, R _{sigma} = 0.0207]	1127 [R _{int} = 0.0389, R _{sigma} = 0.0187]
<i>Data/restraints/parameters</i>	4581/0/146	4476/180/155	7397/469/294	1127/0/58
<i>Goodness-of-fit on F²</i>	1.028	1.005	1.035	1.096
<i>Final R indexes [I ≥ 2σ(I)]</i>	R ₁ = 0.0321, wR ₂ = 0.0660	R ₁ = 0.0448, wR ₂ = 0.1090	R ₁ = 0.0326, wR ₂ = 0.0632	R ₁ = 0.0226, wR ₂ = 0.0473
<i>Final R indexes [all data]</i>	R ₁ = 0.0520, wR ₂ = 0.0717	R ₁ = 0.0669, wR ₂ = 0.1212	R ₁ = 0.0462, wR ₂ = 0.0683	R ₁ = 0.0315, wR ₂ = 0.0507
<i>Largest diff. peak/hole /e Å⁻³</i>	0.52/-0.39	2.70/-2.01	1.86/-1.35	0.64/-0.24

Complex	3.2a { <i>p</i> -Me-BIAN}- CoBr ₂ ·DCM	3.2b { <i>p</i> -NMe ₂ -BIE}- CoBr ₂	3.2c { <i>p</i> -OMe-BIAN}- CoBr ₂ ·DCM	3.2e [{ <i>p</i> -OMe-BIE}- Co(NCMe)(OH ₂) ₂]
<i>Identifier code</i>	18srv488	18srv504	19srv105	19srv318
<i>Empirical formula</i>	C ₂₇ H ₂₂ Br ₂ Cl ₂ CoN ₂	C ₁₉ H ₂₄ Br ₂ Cl ₂ CoN ₄	C ₂₇ H ₂₂ Br ₂ Cl ₂ CoN ₂ O ₂	C ₁₈ H ₂₁ Br ₂ CoN ₃ O ₃
<i>Formula weight</i>	664.11	598.07	696.11	546.13
<i>Temperature /K</i>	120	120	120	120
<i>Crystal system</i>	monoclinic	monoclinic	monoclinic	monoclinic
<i>Space group</i>	P2 ₁ /c	P2 ₁ /c	P2 ₁ /c	P2 ₁ /n
<i>a/Å</i>	11.7222(6)	10.4397(7)	13.671(4)	12.0228(4)
<i>b/Å</i>	12.0482(6)	22.9213(16)	11.741(3)	8.9568(3)
<i>c/Å</i>	18.4994(10)	9.6849(8)	18.227(5)	19.2577(6)
<i>α/°</i>	90	90	90	90
<i>β/°</i>	98.362(2)	98.945(3)	108.994(7)	104.8410(10)
<i>γ/°</i>	90	90	90	90
<i>Volume /Å³</i>	2584.9(2)	2289.3(3)	2766.5(13)	2004.60(11)
<i>Z</i>	4	4	4	4
<i>ρ_{calc}/cm³</i>	1.706	1.735	1.671	1.810
<i>μ/mm⁻¹</i>	3.981	4.487	3.730	4.866
<i>F(000)</i>	1316.0	1188.0	1380.0	1084.0
<i>Crystal size/mm³</i>	0.259 × 0.2 × 0.088	0.822 × 0.118 × 0.022	0.163 × 0.111 × 0.035	0.304 × 0.223 × 0.136
<i>Radiation</i>	MoKα (λ = 0.71073)	MoKα (λ = 0.71073)	MoKα (λ = 0.71073)	MoKα (λ = 0.71073)
<i>2θ range for data collection/°</i>	4.45 to 63	3.95 to 54.996	4.686 to 50.33	4.376 to 68.676
<i>Index ranges</i>	-17 ≤ h ≤ 17, -17 ≤ k ≤ 17, -27 ≤ l ≤ 27	-13 ≤ h ≤ 13, -29 ≤ k ≤ 29, -12 ≤ l ≤ 12	-16 ≤ h ≤ 16, -14 ≤ k ≤ 14, -21 ≤ l ≤ 21	-18 ≤ h ≤ 19, -14 ≤ k ≤ 14, -30 ≤ l ≤ 30
<i>Reflections collected</i>	61204	33695	29512	53216
<i>Independent reflections</i>	8608 [R _{int} = 0.0406, R _{sigma} = 0.0276]	5265 [R _{int} = 0.0626, R _{sigma} = 0.0524]	4947 [R _{int} = 0.1394, R _{sigma} = 0.1145]	8289 [R _{int} = 0.0341, R _{sigma} = 0.0257]
<i>Data/restraints parameters</i>	8608/0/315	5265/0/262	4947/0/329	8289/0/259
<i>Goodness-of-fit on F²</i>	1.026	1.017	1.027	1.029
<i>Final R indexes [I >= 2σ(I)]</i>	R ₁ = 0.0249, wR ₂ = 0.0552	R ₁ = 0.0319, wR ₂ = 0.0621	R ₁ = 0.0657, wR ₂ = 0.1442	R ₁ = 0.0221, wR ₂ = 0.0468
<i>Final R indexes [all data]</i>	R ₁ = 0.0392, wR ₂ = 0.0592	R ₁ = 0.0528, wR ₂ = 0.0682	R ₁ = 0.1235, wR ₂ = 0.1677	R ₁ = 0.0331, wR ₂ = 0.0490
<i>Largest diff. peak/hole /e Å⁻³</i>	0.51/-0.35	0.84/-0.65	1.76/-0.69	0.50/-0.36

Complex	3.4c (dppp)CoCl ₂	3.5a (dtbpb)CoBr ₂ ·DCM	3.6a (dtbpx)CoCl ₂
<i>Identifier code</i>	17srv377	19srv242	19srv054
<i>Empirical formula</i>	C ₂₇ H ₂₆ Cl ₂ CoP ₂	C ₂₀ H ₄₄ Br ₂ Cl ₂ CoP ₂	C ₂₄ H ₄₄ Cl ₂ CoP ₂
<i>Formula weight</i>	542.25	636.14	524.36
<i>Temperature /K</i>	120	120	120
<i>Crystal system</i>	monoclinic	monoclinic	triclinic
<i>Space group</i>	P2 ₁ /c	P2 ₁ /c	P-1
<i>a/Å</i>	15.0170(7)	9.7237(4)	11.5209(2)
<i>b/Å</i>	11.1068(6)	12.4889(4)	15.7210(4)
<i>c/Å</i>	15.2302(7)	23.4156(9)	17.0080(5)
<i>α/°</i>	90	90	62.785(3)
<i>β/°</i>	90.7438(19)	101.5589(15)	87.060(2)
<i>γ/°</i>	90	90	79.731(2)
<i>Volume /Å³</i>	2540.0(2)	2785.88(18)	2693.98(13)
<i>Z</i>	4	4	4
<i>ρ_{calc}/cm³</i>	1.418	1.517	1.293
<i>μ/mm⁻¹</i>	1.026	3.797	0.964
<i>F(000)</i>	1116.0	1300.0	1116.0
<i>Crystal size/mm³</i>	0.63 × 0.331 × 0.213	0.247 × 0.227 × 0.224	0.481 × 0.3315 × 0.1428
<i>Radiation</i>	MoKα (λ = 0.71073)	MoKα (λ = 0.71073)	MoKα (λ = 0.71073)
<i>2θ range for data collection/°</i>	4.54 to 65.154	4.276 to 66.452	4.24 to 60.69
<i>Index ranges</i>	-22 ≤ h ≤ 22, -16 ≤ k ≤ 16, -23 ≤ l ≤ 23	-14 ≤ h ≤ 14, -15 ≤ k ≤ 19, -32 ≤ l ≤ 36	-14 ≤ h ≤ 16, -21 ≤ k ≤ 21, -23 ≤ l ≤ 23
<i>Reflections collected</i>	63389	54315	53159
<i>Independent reflections</i>	9258 [R _{int} = 0.0642, R _{sigma} = 0.0454]	10641 [R _{int} = 0.0344, R _{sigma} = 0.0300]	14316 [R _{int} = 0.0437, R _{sigma} = 0.0435]
<i>Data/restraints parameters</i>	9258/0/290	10641/0/269	14316/0/571
<i>Goodness-of-fit on F²</i>	1.028	1.065	1.026
<i>Final R indexes [I ≥ 2σ (I)]</i>	R ₁ = 0.0336, wR ₂ = 0.0761	R ₁ = 0.0348, wR ₂ = 0.0746	R ₁ = 0.0351, wR ₂ = 0.0758
<i>Final R indexes [all data]</i>	R ₁ = 0.0527, wR ₂ = 0.0831	R ₁ = 0.0475, wR ₂ = 0.0778	R ₁ = 0.0476, wR ₂ = 0.0822
<i>Largest diff. peak/hole /e Å⁻³</i>	0.71/-0.69	1.40/-0.89	0.40/-0.31

Complex	3.6b (dtbpx)CoBr ₂	3.6c (dcypx)CoCl ₂	3.6f (dppx)CoBr ₂
<i>Identifier code</i>	19srv020	18srv033	18srv418
<i>Empirical formula</i>	C ₂₄ H ₄₄ Br ₂ CoP ₂	C ₃₂ H ₅₂ Cl ₂ CoP ₂	C ₃₂ H ₂₈ Br ₂ CoP ₂
<i>Formula weight</i>	613.28	628.50	693.23
<i>Temperature /K</i>	120	120	120
<i>Crystal system</i>	triclinic	monoclinic	triclinic
<i>Space group</i>	P-1	P2 ₁ /c	P-1
<i>a/Å</i>	11.515(3)	7.1855(4)	8.9962(3)
<i>b/Å</i>	15.922(3)	38.874(3)	11.2365(4)
<i>c/Å</i>	17.312(4)	23.5682(15)	30.0477(11)
<i>α/°</i>	62.930(8)	90	99.9278(14)
<i>β/°</i>	86.480(8)	96.731(3)	97.8924(14)
<i>γ/°</i>	79.166(7)	90	90.0375(15)
<i>Volume /Å³</i>	2774.8(10)	6537.9(7)	2962.65(18)
<i>Z</i>	4	8	4
<i>ρ_{calc}/cm³</i>	1.468	1.277	1.554
<i>μ/mm⁻¹</i>	3.623	6.675	3.404
<i>F(000)</i>	1260.0	2680.0	1388.0
<i>Crystal size/mm³</i>	0.375 × 0.333 × 0.142	0.106 × 0.047 × 0.046	0.318 × 0.126 × 0.064
<i>Radiation</i>	MoKα (λ = 0.71073)	CuKα (λ = 1.54184)	MoKα (λ = 0.71073)
<i>2θ range for data collection/°</i>	4.21 to 63.012	4.406 to 117.34	4.17 to 51.998
<i>Index ranges</i>	-16 ≤ h ≤ 16, -23 ≤ k ≤ 23, -25 ≤ l ≤ 25	-7 ≤ h ≤ 7, -42 ≤ k ≤ 40, -26 ≤ l ≤ 23	-11 ≤ h ≤ 11, -13 ≤ k ≤ 13, -37 ≤ l ≤ 37
<i>Reflections collected</i>	67489	40120	47352
<i>Independent reflections</i>	18468 [R _{int} = 0.0355, R _{sigma} = 0.0413]	8737 [R _{int} = 0.1004, R _{sigma} = 0.1133]	11612 [R _{int} = 0.0358, R _{sigma} = 0.0379]
<i>Data/restraints parameters</i>	18468/0/572	8737/688/680	11612/8/670
<i>Goodness-of-fit on F²</i>	1.071	1.019	1.019
<i>Final R indexes [I >= 2σ(I)]</i>	R ₁ = 0.0279, wR ₂ = 0.0585	R ₁ = 0.0608, wR ₂ = 0.0988	R ₁ = 0.0379, wR ₂ = 0.0858
<i>Final R indexes [all data]</i>	R ₁ = 0.0471, wR ₂ = 0.0618	R ₁ = 0.1200, wR ₂ = 0.1152	R ₁ = 0.0572, wR ₂ = 0.0919
<i>Largest diff. peak/hole /e Å⁻³</i>	0.69/-0.74	0.62/-0.47	1.46/-0.66

Complex	3.4b (dppe) ₅ Co ₃ Br ₈ ·2DCM	3.10 (dppbz) ₄ Co ₄ Br ₈	3.7·HCl (PNNP-tBuH)CoCl ₃ ·2DCM
<i>Identifier code</i>	18srv490	18srv473	18srv105
<i>Empirical formula</i>	C ₁₃₄ H ₁₂₈ Br ₈ Cl ₈ Co ₄ P ₁₀	C ₁₂₉ H ₁₁₄ Br ₈ Cl ₁₈ Co ₄ P ₈	C ₂₂ H ₅₁ Cl ₇ CoN ₂ P ₂
<i>Formula weight</i>	3206.66	3425.06	712.66
<i>Temperature /K</i>	120	120	120
<i>Crystal system</i>	triclinic	monoclinic	orthorhombic
<i>Space group</i>	P-1	P2 ₁ /c	Pna2 ₁
<i>a/Å</i>	10.8916(8)	17.393(3)	10.8211(6)
<i>b/Å</i>	17.3954(13)	18.881(4)	20.2786(12)
<i>c/Å</i>	18.3130(13)	22.230(4)	15.8378(10)
<i>α/°</i>	95.727(2)	90	90
<i>β/°</i>	97.887(2)	112.193(7)	90
<i>γ/°</i>	107.910(2)	90	90
<i>Volume /Å³</i>	3233.0(4)	6759(2)	3475.4(4)
<i>Z</i>	1	2	4
<i>ρ_{calc}/cm³</i>	1.647	1.683	1.362
<i>μ/mm⁻¹</i>	3.315	3.346	1.139
<i>F(000)</i>	1606.0	3404.0	1492.0
<i>Crystal size/mm³</i>	0.227 × 0.079 × 0.024	0.451 × 0.342 × 0.116	0.328 × 0.083 × 0.033
<i>Radiation</i>	MoKα (λ = 0.71073)	MoKα (λ = 0.71073)	MoKα (λ = 0.71073)
<i>2θ range for data collection/°</i>	4.23 to 49.998	4.314 to 55	4.266 to 50
<i>Index ranges</i>	-12 ≤ h ≤ 12, -20 ≤ k ≤ 20, -21 ≤ l ≤ 21	-22 ≤ h ≤ 22, -24 ≤ k ≤ 24, -28 ≤ l ≤ 28	-12 ≤ h ≤ 12, -24 ≤ k ≤ 24, -18 ≤ l ≤ 18
<i>Reflections collected</i>	46757	127810	48003
<i>Independent reflections</i>	11371 [R _{int} = 0.0501, R _{sigma} = 0.0527]	15517 [R _{int} = 0.0522, R _{sigma} = 0.0322]	6120 [R _{int} = 0.0530, R _{sigma} = 0.0411]
<i>Data/restraints parameters</i>	11371/0/740	15517/0/770	6120/291/372
<i>Goodness-of-fit on F²</i>	1.026	1.014	1.037
<i>Final R indexes [I >= 2σ (I)]</i>	R ₁ = 0.0478, wR ₂ = 0.1109	R ₁ = 0.0380, wR ₂ = 0.0839	R ₁ = 0.0398, wR ₂ = 0.0860
<i>Final R indexes [all data]</i>	R ₁ = 0.0699, wR ₂ = 0.1190	R ₁ = 0.0566, wR ₂ = 0.0931	R ₁ = 0.0492, wR ₂ = 0.0903
<i>Largest diff. peak/hole /e Å⁻³</i>	2.62/-0.49	1.17/-1.74	0.64/-0.53

Complex	3.5c-ox [(dcybpO)CoCl ₂] ₂	3.4a-ox (dppmO ₂) ₃ Co ₂ Br ₄	3.6aO-HCl (dtbpxOH)CoCl ₃
<i>Identifier code</i>	18srv225	18srv484	18srv043
<i>Empirical formula</i>	C ₅₆ H ₁₀₄ Br ₄ Co ₂ O ₂ P ₄ × 2 C ₄ H ₈ O	C ₈₄ H ₈₄ Br ₄ Cl ₁₈ Co ₂ O ₆ P ₆	C ₂₄ H ₄₅ Cl ₃ CoOP ₂
<i>Formula weight</i>	1514.97	2450.93	576.82
<i>Temperature /K</i>	120.0	120	120
<i>Crystal system</i>	monoclinic	cubic	orthorhombic
<i>Space group</i>	P2 ₁ /c	P2 ₁ 3	Pca2 ₁
<i>a/Å</i>	14.2821(14)	21.672(2)	17.2540(9)
<i>b/Å</i>	14.8728(14)	21.672(2)	10.7488(6)
<i>c/Å</i>	18.1496(18)	21.672(2)	15.8208(8)
<i>α/°</i>	90	90	90
<i>β/°</i>	113.096(2)	90	90
<i>γ/°</i>	90	90	90
<i>Volume /Å³</i>	3546.2(6)	10178(3)	2934.1(3)
<i>Z</i>	2	4	4
<i>ρ_{calc}/g/cm³</i>	1.419	1.599	1.306
<i>μ/mm⁻¹</i>	2.854	2.511	8.230
<i>F(000)</i>	1580.0	4904.0	1220.0
<i>Crystal size/mm³</i>	0.1 × 0.06 × 0.02	0.21 × 0.176 × 0.132	0.15 × 0.034 × 0.033
<i>Radiation</i>	MoKα (λ = 0.71073)	MoKα (λ = 0.71073)	CuKα (λ = 1.54184)
<i>2θ range for data collection/°</i>	4.636 to 49.996	4.202 to 50.11	8.226 to 116.97
<i>Index ranges</i>	-16 ≤ h ≤ 16, -17 ≤ k ≤ 17, -21 ≤ l ≤ 21	-25 ≤ h ≤ 25, -25 ≤ k ≤ 25, -25 ≤ l ≤ 25	-18 ≤ h ≤ 18, -11 ≤ k ≤ 11, -16 ≤ l ≤ 17
<i>Reflections collected</i>	47253	138350	18273
<i>Independent reflections</i>	6360 [R _{int} = 0.1137, R _{sigma} = 0.0931]	6051 [R _{int} = 0.1499, R _{sigma} = 0.0611]	4001 [R _{int} = 0.1213, R _{sigma} = 0.1462]
<i>Data/restraints parameters</i>	6360/36/353	6051/244/319	4001/250/306
<i>Goodness-of-fit on F²</i>	1.044	1.042	0.954
<i>Final R indexes [I >= 2σ (I)]</i>	R ₁ = 0.0760, wR ₂ = 0.1711	R ₁ = 0.0577, wR ₂ = 0.1297	R ₁ = 0.0675, wR ₂ = 0.1437
<i>Final R indexes [all data]</i>	R ₁ = 0.1477, wR ₂ = 0.2022	R ₁ = 0.1058, wR ₂ = 0.1562	R ₁ = 0.1324, wR ₂ = 0.1767
<i>Largest diff. peak/hole /e Å⁻³</i>	1.64/-1.92	0.55/-0.43	0.72/-0.38

Complex	3.12 (H ₂ O) ₂ Co(O ₂ CH) ₂	3.7a-ox (PNNP-PhO ₂ CoCl ₂)
<i>Identifier code</i>	18srv017	18srv056
<i>Empirical formula</i>	C ₂ H ₆ CoO ₆	C ₂₈ H ₃₀ CoP ₂ O ₂ N ₂ Cl ₂
<i>Formula weight</i>	185.00	618.34
<i>Temperature /K</i>	120	120
<i>Crystal system</i>	monoclinic	triclinic
<i>Space group</i>	P2 ₁ /c	-P 1
<i>a/Å</i>	8.6552(11)	9.6729(5)
<i>b/Å</i>	7.1234(10)	11.7751(7)
<i>c/Å</i>	9.2579(11)	25.3222(14)
<i>α/°</i>	90	91.590(2)
<i>β/°</i>	97.514(4)	94.601(2)
<i>γ/°</i>	90	98.016(2)
<i>Volume /Å³</i>	565.89(13)	2844.6(3)
<i>Z</i>	4	2
<i>ρ_{calc}/cm³</i>	2.171	1.444
<i>μ/mm⁻¹</i>	2.991	
<i>F(000)</i>	372.0	1276
<i>Crystal size/mm³</i>	? × ? × ?	0.039x0.096x0.103
<i>Radiation</i>	MoKα (λ = 0.71073)	MoKα (λ = 0.71073)
<i>2θ range for data collection/°</i>	4.748 to 71.61	4.83 to 71.61
<i>Index ranges</i>	-14 ≤ h ≤ 13, -7 ≤ k ≤ 11, -14 ≤ l ≤ 10	-8 ≤ h ≤ 7, -6 ≤ k ≤ 5, -14 ≤ l ≤ 23
<i>Reflections collected</i>	6667	40543
<i>Independent reflections</i>	2346 [R _{int} = 0.0278, R _{sigma} = 0.0363]	11672 [R _{int} = 0.0483, R _{sigma} = 0.0961]
<i>Data/restraints parameters</i>	2346/0/110	11672/0/110
<i>Goodness-of-fit on F²</i>	1.043	4.83
<i>Final R indexes [I >= 2σ (I)]</i>	R ₁ = 0.0249, wR ₂ = 0.0588	R ₁ = 0.0961, wR ₂ = 0.0811
<i>Final R indexes [all data]</i>	R ₁ = 0.0469, wR ₂ = 0.0646	R ₁ = 0.0827, wR ₂ = 0.0606
<i>Largest diff. peak/hole /e Å⁻³</i>	0.74/-0.39	0.53/-0.45

Complex	ZnCo-5.3 (dtbpx)Co/ZnBr ₂	Zn-5.3 (dtbpx)ZnCl ₂	Zn-5.4 (dtbpx)ZnBr ₂
<i>Identifier code</i>	18srv238	19srv065	19srv205
<i>Empirical formula</i>	C ₂₄ H ₄₄ Br ₂ Co _{0.25} P ₂ Zn _{0.75}	C ₂₄ H ₄₄ Cl ₂ P ₂ Zn	C ₂₄ H ₄₄ Br ₂ P ₂ Zn
<i>Formula weight</i>	618.11	530.80	619.72
<i>Temperature /K</i>	120	120	120
<i>Crystal system</i>	triclinic	triclinic	triclinic
<i>Space group</i>	P-1	P-1	P-1
<i>a/Å</i>	11.4861(4)	11.5007(4)	11.4892(8)
<i>b/Å</i>	15.9246(6)	15.7062(6)	15.9287(11)
<i>c/Å</i>	17.2579(6)	17.0236(7)	17.2754(12)
<i>α/°</i>	62.6708(14)	62.7487(13)	62.663(3)
<i>β/°</i>	86.5109(15)	86.9340(15)	86.455(3)
<i>γ/°</i>	79.3381(15)	79.7367(15)	79.348(3)
<i>Volume /Å³</i>	2754.87(17)	2688.58(18)	2759.1(3)
<i>Z</i>	4	4	4
<i>ρ_{calc}/cm³</i>	1.490	1.311	1.492
<i>μ/mm⁻¹</i>	3.851	1.241	3.912
<i>F(000)</i>	1269.0	1128.0	1272.0
<i>Crystal size/mm³</i>	0.425 × 0.266 × 0.17	0.421 × 0.31 × 0.166	0.516 × 0.239 × 0.239
<i>Radiation</i>	MoKα (λ = 0.71073)	MoKα (λ = 0.71073)	MoKα (λ = 0.71073)
<i>2θ range for data collection/°</i>	4.224 to 63.01	4.248 to 61.996	4.224 to 60
<i>Index ranges</i>	-16 ≤ h ≤ 16, -23 ≤ k ≤ 23, -25 ≤ l ≤ 25	-16 ≤ h ≤ 16, -22 ≤ k ≤ 22, -24 ≤ l ≤ 24	-16 ≤ h ≤ 16, -22 ≤ k ≤ 22, -24 ≤ l ≤ 24
<i>Reflections collected</i>	61068	63221	61270
<i>Independent reflections</i>	18329 [R _{int} = 0.0442, R _{sigma} = 0.0488]	17145 [R _{int} = 0.0373, R _{sigma} = 0.0430]	16079 [R _{int} = 0.0565, R _{sigma} = 0.0564]
<i>Data/restraints parameters</i>	18329/0/571	17145/0/571	16079/0/572
<i>Goodness-of-fit on F²</i>	1.013	1.067	1.025
<i>Final R indexes [I >= 2σ(I)]</i>	R ₁ = 0.0320, wR ₂ = 0.0743	R ₁ = 0.0294, wR ₂ = 0.0680	R ₁ = 0.0300, wR ₂ = 0.0601
<i>Final R indexes [all data]</i>	R ₁ = 0.0530, wR ₂ = 0.0800	R ₁ = 0.0487, wR ₂ = 0.0721	R ₁ = 0.0526, wR ₂ = 0.0659
<i>Largest diff. peak/hole /e Å⁻³</i>	1.01/-0.92	0.44/-0.41	0.68/-0.60

Complex	Zn-5.6 (dppbz)ZnBr ₂	Zn-5.7 (dppp)ZnBr ₂	Zn-5.8 (dtbpp)ZnBr ₂
<i>Identifier code</i>	19srv035	19srv325	19srv169
<i>Empirical formula</i>	C ₃₁ H ₂₆ Br ₂ Cl ₂ P ₂ Zn	C ₂₇ H ₂₆ Br ₂ P ₂ Zn	C ₃₈ H ₈₄ Br ₆ P ₄ Zn ₃
<i>Formula weight</i>	756.55	637.61	1340.50
<i>Temperature /K</i>	120	100	120
<i>Crystal system</i>	monoclinic	monoclinic	monoclinic
<i>Space group</i>	P2 ₁ /c	P2 ₁ /n	P2 ₁ /m
<i>a/Å</i>	9.8018(6)	9.5788(6)	8.1552(9)
<i>b/Å</i>	16.8862(9)	15.7196(10)	22.980(2)
<i>c/Å</i>	18.1875(10)	17.1167(11)	14.0450(15)
<i>α/°</i>	90	90	90
<i>β/°</i>	92.739(2)	93.9830(15)	92.905(4)
<i>γ/°</i>	90	90	90
<i>Volume /Å³</i>	3006.9(3)	2571.1(3)	2628.7(5)
<i>Z</i>	4	4	2
<i>ρ_{calc}/cm³</i>	1.671	1.647	1.694
<i>μ/mm⁻¹</i>	3.779	3.859	6.065
<i>F(000)</i>	1504.0	1272.0	1344.0
<i>Crystal size/mm³</i>	0.73 × 0.405 × 0.379	0.1 × 0.058 × 0.014	0.168 × 0.16 × 0.083
<i>Radiation</i>	MoKα (λ = 0.71073)	synchrotron (λ = 0.6889)	MoKα (λ = 0.71073)
<i>2θ range for data collection/°</i>	4.16 to 54.998	3.414 to 59.996	4.582 to 64.064
<i>Index ranges</i>	-12 ≤ h ≤ 12, -21 ≤ k ≤ 21, -23 ≤ l ≤ 23	-13 ≤ h ≤ 13, -22 ≤ k ≤ 22, -24 ≤ l ≤ 24	-12 ≤ h ≤ 12, -34 ≤ k ≤ 32, -20 ≤ l ≤ 20
<i>Reflections collected</i>	56202	44696	63562
<i>Independent reflections</i>	6906 [R _{int} = 0.0564, R _{sigma} = 0.0346]	8195 [R _{int} = 0.0569, R _{sigma} = 0.0403]	9324 [R _{int} = 0.0478, R _{sigma} = 0.0374]
<i>Data/restraints parameters</i>	6906/0/348	8195/0/289	9324/0/271
<i>Goodness-of-fit on F²</i>	1.030	1.050	1.056
<i>Final R indexes [I ≥ 2σ(I)]</i>	R ₁ = 0.0285, wR ₂ = 0.0541	R ₁ = 0.0352, wR ₂ = 0.0964	R ₁ = 0.0395, wR ₂ = 0.0910
<i>Final R indexes [all data]</i>	R ₁ = 0.0439, wR ₂ = 0.0583	R ₁ = 0.0378, wR ₂ = 0.0975	R ₁ = 0.0554, wR ₂ = 0.0956
<i>Largest diff. peak/hole /e Å⁻³</i>	0.53/-0.46	2.10/-0.88	1.96/-1.54

Complex	4.14 Cp ₄ Co ₃ Br ₄	4.5 (dppm) ₂ Co ₂ Br ₃	Zn-5.9 (dtbpxO ₂)ZnBr ₂
<i>Identifier code</i>	19srv302	18srv474	19srv326
<i>Empirical formula</i>	C ₂₁ H ₂₂ Br ₄ Cl ₂ Co ₃	C ₅₂ H ₄₈ Br ₃ Co ₂ O _{0.5} P ₄	C ₂₄ H ₄₄ Br ₂ O ₂ P ₂ Zn
<i>Formula weight</i>	841.71	1162.37	651.72
<i>Temperature /K</i>	120.0	120	100
<i>Crystal system</i>	orthorhombic	monoclinic	monoclinic
<i>Space group</i>	Pbcn	P2 ₁ /c	P2 ₁ /n
<i>a/Å</i>	12.3828(11)	22.617(2)	13.111(5)
<i>b/Å</i>	16.4701(14)	13.5120(12)	15.903(6)
<i>c/Å</i>	12.9868(11)	16.1306(15)	13.793(5)
<i>α/°</i>	90	90	90
<i>β/°</i>	90	92.511(4)	90.596(7)
<i>γ/°</i>	90	90	90
<i>Volume /Å³</i>	2648.6(4)	4924.7(8)	2875.7(18)
<i>Z</i>	4	4	4
<i>ρ_{calc}/cm³</i>	2.111	1.568	1.505
<i>μ/mm⁻¹</i>	8.101	3.274	3.456
<i>F(000)</i>	1612.0	2332.0	1336.0
<i>Crystal size/mm³</i>	0.12 × 0.09 × 0.08	0.341 × 0.269 × 0.251	0.017 × 0.005 × 0.003
<i>Radiation</i>	MoKα (λ = 0.71073)	MoKα (λ = 0.71073)	synchrotron (λ = 0.6889)
<i>2θ range for data collection/°</i>	4.116 to 54.994	4.374 to 56.998	3.788 to 48.422
<i>Index ranges</i>	-16 ≤ h ≤ 16, -21 ≤ k ≤ 21, -16 ≤ l ≤ 16	-30 ≤ h ≤ 30, -18 ≤ k ≤ 18, -21 ≤ l ≤ 21	-12 ≤ h ≤ 13, -18 ≤ k ≤ 15, -10 ≤ l ≤ 16
<i>Reflections collected</i>	33247	98048	7640
<i>Independent reflections</i>	3049 [R _{int} = 0.1101, R _{sigma} = 0.0631]	12462 [R _{int} = 0.0520, R _{sigma} = 0.0350]	3536 [R _{int} = 0.0761, R _{sigma} = 0.1811]
<i>Data/restraints parameters</i>	3049/0/137	12462/30/577	3536/225/280
<i>Goodness-of-fit on F²</i>	1.134	1.024	1.031
<i>Final R indexes [I > 2σ(I)]</i>	R ₁ = 0.0615, wR ₂ = 0.1057	R ₁ = 0.0311, wR ₂ = 0.0666	R ₁ = 0.1071, wR ₂ = 0.2919
<i>Final R indexes [all data]</i>	R ₁ = 0.1035, wR ₂ = 0.1156	R ₁ = 0.0476, wR ₂ = 0.0710	R ₁ = 0.1887, wR ₂ = 0.3472
<i>Largest diff. peak/hole /e Å⁻³</i>	1.77/-0.88	1.67/-0.64	0.72/-0.49

7.3.3 *i*ASAP MS Variable Optimisation Experiments

Table S2 Summary of the ASAP and *i*ASAP MS optimisation experiment with observed fragments and intensities shown. Where DS = desolvation gas temperature, cV = cone voltage, VF = vertical flow rate, SB = Source block temperature, PD = probe design (1 or 2 denotes number of sample holes and cc and oc refer to the use of an 'open-ended' (oc) or 'closed' (cc) capillary).

CODE	Sample*	Machine	DS /°C	cV /V	VF /mL min-1	SB /°C	PD	Fragments observed: %observed (mass /Da)						
								M/M+H	Pd2L3	Pd2L4	Pd2L6			
T1	MS-3	LCT	300	30	N/a	120	N/a	100 (304.726)	90.61 (510.484)	11.51 (609.444)	12.35 (814.201)			
T2			100 (303.983)					14.25 (510.922)	1.14 (609.972)					
T3			100 (304.989)					4.29 (510.926)	0.23 (609.979)					
								M+H	M+Rh+COD	dpm+2H	M-Rh+2H			
T4	MS-2	LCT	300	30	n/a	120	1 - cc	100 (395.122)	49.85 (605.123)	7.37 (293.048)				
T5			75.05 (395.129)					2.56 (605.099)	7.16 (185.148)	100 (293.043)				
T6			67.84 (395.114)					100 (605.109)						
								M/ M+H	M+Rh+COD	M-dpm				
T7	MS-2	Xevo	350	15	N/a	120	N/a	84.2 (394.114)	100 (605.102)					
T8				20				88.38 (394.114)	100 (605.101)					
T9				30				55.92 (349.095) /76.48 (395.097)		100 (605.060)	28.83 (210.983)			
T10				450				20	96.28 (394.112)	100 (605.099)	1.59 (210.986)			
								M	Pd2L3	PdL	PdL+O	Pd2L2-H	Pd2L2+O	
T11	MS-1	Xevo	350	15	N/a	120	N/a	96.5 (303.976)	100 (510.911)	28.47 (204.940)	4.28 (220.965)	4.29 (408.869)	6.45 (424.895)	
T12				20				59.4 (303.976)	100 (510.909)	39.79 (204.938)	10.12 (220.964)	7.61 (408.868)	14.69 (424.895)	
T13				20				67.27 (303.976)	100 (510.910)	40.31 (204.939)	7.78 (220.963)	8.86 (408.868)	15.69 (424.896)	
T14			450	20		16.12 (303.979)		100 (510.908)	8.16 (204.941)	2.02 (220.968)	10.79 (408.868)	17.63 (424.897)		
T15				30		33.5 (303.976)		100 (510.892)	67.7 (204.933)	19 (220.966)	47.14 (408.864)	60.06 (424.890)		
T16				40		toast! Almost every O/C fragment possible								
								M-Br (386.0768)	Co2L2Br3 (851.0719)					
T17	MS-3	Xevo	450	5	30	120	1 - oc	96.59 (386.039)	4.56 (850.994)					
T18				10				100 (386.031)	21.38 (850.998)					
T19				350				5						
T20								100 (386.043)						
T21			400	10		100 (386.038)		7.83 (850.998)						
T22				15		95.51 (386.041)		3.25 (851.003)						
T23				450		10		1 - cc						

*Samples used: *N,N'*-bis(2,6-dimethylphenyl)-1,2-diimino-1,2-dimethylethane)CoBr₂ (MS-1), (COD)Rh(dpm) (MS-2), Pd(acac)₂ (MS-3), Pd₂(dba)₃·CH₃Cl (MS-4).

Table S2: continued.

CODE	Sample*	Machine	DS /°C	cV /V	VF /mL min-1	SB /°C	PD	Fragments observed: %observed (mass /Da)						
								dba+H						
T24	MS-4^a	LCT	400	30	N/a	120	N/a	100 (235.101)						
T25			450	30				100 (235.101)						
T26			450	40				100 (235.102)						
T27			450	50				100 (234.907)						
T28			450	60				100 (235.102)						
								M-Br (386.0768)	Co2L2Br3 (851.0719)	M (464.9951)	M-H (463.9873)	M+H (466.002)		
T29	MS-1	Xevo	450	30	N/A	140	N/A	100 (386.053)	15.70 (851.031)	0.01 (464.992)				
T30							10	100 (386.055)	0.09 (851.030)					
T31							15	100 (386.056)						
T32							15	100 (386.056)						
T33							500	2 - oc	100 (386.054)	3.01 (851.028)	0.10 (464.974)	0.23 (463.976)		
T34							550	10	100 (386.055)	3.00 (851.033)	0.43 (463.970)			
T35							600	100 (386.054)	21.86 (851.030)	461.9875				
T36							450	5	100 (386.057)	0.79 (851.046)				
T37							0	100 (386.058)	2.62 (851.035)	0.01 (464.976)	0.03 (463.969)			
T38							550	10	100 (386.058)	0.26 (851.037)				
T39							0	100 (386.060)	3.28 (851.041)					
T40							450	2 - oc	100 (386.065)					
T41							500	5	100 (386.050)	3.45 (851.043)				
T42							550	100 (386.058)	0.71 (851.045)	0.71 (461.986)				
T43							600	100 (386.060)	0.30 (851.049)					
T44							450	100 (386.060)	0.72 (851.045)					
T45							500	2 - oc	100 (386.063)	3.04 (851.045)	0.04 (463.976)			
T46							600	10	100 (386.061)	3.88 (851.045)	0.61 (461.989)	1.20 (463.986)	(overlapping)	
T46-LM									10	N/A	100 (386.050)	25.83 (851.044)	0.01 (466.146)	

*Samples used: *N,N'*-bis(2,6-dimethylphenyl)-1,2-diimino-1,2-dimethylethane)CoBr₂ (**MS-1**), (COD)Rh(dpm) (**MS-2**), Pd(acac)₂ (**MS-3**), Pd₂(dba)₃·CH₃Cl (**MS-4**). ^anot included in main discussion due to poor volatility for ionisation.